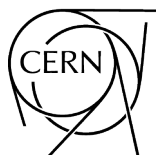


# **Conceptual design of an experiment at the FCC-hh, a future 100 TeV hadron collider**


Editors: M. Mangano and W. Riegler



CERN Yellow Reports: Monographs  
Published by CERN, CH-1211 Geneva 23, Switzerland

ISBN 978-92-9083-629-2 (Paperback)  
ISBN 978-92-9083-630-8 (PDF)  
ISSN 2519-8068 (Print)  
ISSN 2519-8076 (Online)  
DOI <https://doi.org/10.23731/CYRM-2022-002>

Copyright © CERN, 2022

 Creative Commons Attribution 4.0

This volume should be cited as:

Conceptual design of an experiment at the FCC-hh, a future 100 TeV hadron collider,  
M. Mangano and W. Riegler (eds.)  
CERN Yellow Reports: Monographs, CERN-2022-002 (CERN, Geneva, 2022)  
<https://doi.org/10.23731/CYRM-2022-002>.

Corresponding editor: [Werner.Riegler@cern.ch](mailto:Werner.Riegler@cern.ch).

Accepted in November 2022, by the [CERN Reports Editorial Board](#) (contact [Carlos.Lourenco@cern.ch](mailto:Carlos.Lourenco@cern.ch)).

Published by the CERN Scientific Information Service (contact [Jens.Vigen@cern.ch](mailto:Jens.Vigen@cern.ch)).

Indexed in the [CERN Document Server](#) and in [INSPIRE](#).

Published Open Access to permit its wide dissemination, as knowledge transfer is an integral part of the mission of CERN.

# Conceptual design of an experiment at the FCC-hh, a future 100 TeV hadron collider

M. Aleksa<sup>1</sup>, P. P. Allport<sup>2</sup>, S. Asai<sup>1</sup>, A. Ball<sup>1</sup>, M. I. Besana<sup>1,3</sup>, E. R. Bielert<sup>1</sup>, S. Bologna<sup>1,4</sup>, E. Boos<sup>5</sup>, L. Borghoni<sup>6</sup>, R. Bosley<sup>2</sup>, S. Braibant-Giacomelli<sup>6</sup>, J. Brooke<sup>4</sup>, F. Cerutti<sup>1</sup>, S. Chekanov<sup>7</sup>, B. Cui<sup>1</sup>, H. F. Da Silva<sup>1</sup>, D. Dannheim<sup>1</sup>, D. S. Denisov<sup>8,9</sup>, B. Di Micco<sup>10</sup>, Z. Drasal<sup>1</sup>, L. Dudko<sup>5</sup>, M. Elsing<sup>1</sup>, J. Faltova<sup>1,11</sup>, W. J. Fawcett<sup>12,13</sup>, E. Fontanesi<sup>6</sup>, D. Fournier<sup>14</sup>, A. Gaddi<sup>1</sup>, J. Gentil<sup>15</sup>, J. Gerwig<sup>1</sup>, F. Gianotti<sup>1</sup>, R. Gonçalo<sup>15,16</sup>, L. Gouskos<sup>1</sup>, H. Gray<sup>1,17</sup>, P. C. Harris<sup>18</sup>, B. Hegner<sup>1</sup>, C. Helsens<sup>1</sup>, A. M. Henriques Correia<sup>1</sup>, J. Hrdinka<sup>1</sup>, D. Jamin<sup>1</sup>, V. Klyukhin<sup>5</sup>, A. Karyukhin<sup>19</sup>, J. Kieseler<sup>1</sup>, O. Kortner<sup>20</sup>, A. Kotwal<sup>21,9</sup>, H. Kroha<sup>20</sup>, J. Lingemann<sup>1</sup>, P. Mandrik<sup>22</sup>, M. Mangano<sup>1</sup>, P. Mannelli<sup>1</sup>, M. Mentink<sup>1</sup>, F. Moortgat<sup>1</sup>, C. Neubuser<sup>1,23</sup>, G. Ortona<sup>24</sup>, E. Perez Codina<sup>25</sup>, L. Pontecorvo<sup>1</sup>, A. Price<sup>2</sup>, W. Riegler<sup>1</sup>, P. G. Roloff<sup>1</sup>, M. Saito<sup>26</sup>, A. Salzburger<sup>1</sup>, R. Sawada<sup>26</sup>, J. S. Schliwinski<sup>27</sup>, M. Selvaggi<sup>1</sup>, O. Solovyanov<sup>1,22</sup>, R. Stein<sup>28</sup>, A. Sznajder<sup>29</sup>, H. Ten Kate<sup>1</sup>, K. Terashi<sup>26</sup>, M. Testa<sup>24</sup>, N. Topiline<sup>19</sup>, V. Völkl<sup>1</sup>, M. Verducci<sup>24</sup>, N. Watson<sup>2</sup>, M. Widorski<sup>1</sup>, A. Winter<sup>2</sup>, C. Young<sup>30</sup>, and A. Zaborowska<sup>1</sup>

<sup>1</sup>European Organization for Nuclear Research (CERN), Switzerland

<sup>2</sup>University of Birmingham, United Kingdom

<sup>3</sup>Paul Scherrer Institut, Switzerland

<sup>4</sup>University of Bristol, United Kingdom

<sup>5</sup>Lomonosov Moscow State University, Russia

<sup>6</sup>University of Bologna, Italy

<sup>7</sup>Argonne National Laboratory, USA

<sup>8</sup>Brookhaven National Laboratory, USA

<sup>9</sup>Fermilab, USA

<sup>10</sup>Roma Tre University, Italy

<sup>11</sup>Charles University, Prague, Czech Republic

<sup>12</sup>University of Geneva, Switzerland

<sup>13</sup>University of Cambridge, England

<sup>14</sup>French National Institute of Nuclear and Particle Physics (CNRS-IN2P3), France

<sup>15</sup>Laboratory of Instrumentation and Experimental Particle Physics (LIP), Portugal

<sup>16</sup>University of Coimbra, Portugal

<sup>17</sup>UC Berkeley, USA

<sup>18</sup>Massachusetts Institute of Technology (MIT), USA

<sup>19</sup>Joint Institute for Nuclear Research (JINR), Russia

<sup>20</sup>Max Planck Institute for Physics, Germany

<sup>21</sup>Duke University, USA

<sup>22</sup>Kurchatov Institute, Russia

<sup>23</sup>Trento Institute for Fundamental Physics and Applications (TIFPA-INFN), Italy

<sup>24</sup>Ecole Polytechnique (LLR), France

<sup>25</sup>TRIUMF, Canada

<sup>26</sup>University of Tokyo, Japan

<sup>27</sup>Humboldt University of Berlin, Germany

<sup>28</sup>University of York, United Kingdom

<sup>29</sup>Rio de Janeiro State University, Brazil

<sup>30</sup>SLAC National Accelerator Laboratory, USA

***Volume editors:***

M. Mangano, W. Riegler

**Benchmark processes, detector requirements from physics**

*Editors:* H. Gray, C. Helsen, F. Moortgat, M. Selvaggi

**Experiment, detector requirements from environment**

*Editors:* I. Besana, W. Riegler

**Software**

*Editors:* C. Helsen, M. Selvaggi

**Magnet systems**

*Editors:* H. Ten Kate, M. Mentink

**Tracker**

*Editors:* Z. Drasal, E. Codina

**Calorimetry**

*Editors:* M. Aleksa, A. Henriques, C. Neubuser, A. Zaborowska

**Muons**

*Editors:* W. Riegler, K. Terashi

**Physics performance for benchmark channels**

*Editors:* M. Mangano, C. Helsen, M. Selvaggi



**Abstract**

This report summarises the study of a general purpose detector for the FCC-hh, a 100 TeV hadron collider with peak luminosity of  $3 \cdot 10^{35} \text{ cm}^{-2} \text{ s}^{-1}$ . A pileup of 1000 pp collisions per bunch-crossing, highly boosted objects as well as radiation levels up to  $10^{18}$  hadrons/cm<sup>2</sup> are just three of the challenges that such a collider poses. The general specifications for such a detector in terms of resolution, granularity, acceptance and radiation tolerance are discussed. A specific detector layout is proposed and its performance is simulated, discussed and parameterized. This parameterization is then used to evaluate the performance for key benchmark physics topics, such as the precision measurement of the Higgs boson couplings and the discovery reach for several frameworks beyond the Standard Model.



# Contents

<b>1</b>	<b>Introduction</b>	<b>1</b>
1.1	The FCC-hh accelerator context . . . . .	2
1.2	The overall features of an FCC-hh detector . . . . .	3
<b>2</b>	<b>Benchmark processes and detector requirements from physics</b>	<b>7</b>
2.1	General considerations on the acceptance . . . . .	8
2.1.1	Rapidity coverage . . . . .	8
2.1.2	Minimum momentum requirements . . . . .	9
2.2	Energy-momentum resolution . . . . .	11
2.2.1	The low energy limit . . . . .	11
2.2.2	The high energy limit . . . . .	13
2.3	Object reconstruction and identification performance . . . . .	14
2.3.1	Electrons . . . . .	14
2.3.2	Photons . . . . .	15
2.3.3	Muons . . . . .	15
2.3.4	Boosted topologies . . . . .	15
2.3.5	Heavy flavour . . . . .	16
<b>3</b>	<b>Detector requirements from environment</b>	<b>17</b>
3.1	Rates, collision parameters, cavern size . . . . .	17
3.2	Radiation . . . . .	18
3.2.1	Detector geometry and shielding conceptual design . . . . .	19
3.2.2	Source term characterisation . . . . .	22
3.2.3	Radiation calculations . . . . .	23
3.2.4	Forward dipole option . . . . .	28
3.2.5	Detector material activation . . . . .	28
<b>4</b>	<b>Software</b>	<b>31</b>
4.1	Introduction . . . . .	31
4.2	Event data model . . . . .	31
4.3	Full and fast simulation . . . . .	31
4.3.1	Full simulation . . . . .	32
4.3.2	Fast simulation . . . . .	32
4.4	Reconstruction software . . . . .	33
4.5	Analysis framework . . . . .	34
4.6	The FCC-hh detector parameterisation in DELPHES . . . . .	35
4.6.1	Introduction . . . . .	35
4.6.2	Tracking . . . . .	35
4.6.3	Calorimetry . . . . .	36
4.6.4	Particle-flow . . . . .	37

4.6.5	Object identification . . . . .	38
4.6.6	Leptons and photons . . . . .	38
4.6.7	Jets and missing energy . . . . .	39
4.6.8	Conclusion and discussion . . . . .	41
<b>5</b>	<b>Magnet systems</b>	<b>43</b>
5.1	Introduction . . . . .	43
5.1.1	Outline . . . . .	43
5.1.2	Requirements . . . . .	43
5.1.3	Evolution of the design . . . . .	45
5.2	Main solenoid with forward solenoids (Configuration used for the reference detector) . . .	46
5.2.1	Magnetic field configuration in detector and magnetic stray field in service cavern . . . .	47
5.2.2	Main solenoid . . . . .	48
5.2.3	Forward solenoids . . . . .	52
5.3	Electrical circuit, quench protection and controls . . . . .	55
5.4	Main solenoid with forward dipole magnets (Alternative layout) . . . . .	57
5.4.1	Magnetic field in the main solenoid—forward dipoles case . . . . .	58
5.4.2	Forward dipole magnets . . . . .	59
5.4.3	Cold mass . . . . .	60
5.4.4	Superconductor . . . . .	61
5.4.5	Cryostat . . . . .	62
5.5	Cryogenics . . . . .	63
5.6	Magnet system installation, shielding and infrastructure . . . . .	66
5.6.1	Main and side cavern . . . . .	66
5.6.2	Assembly and installation . . . . .	67
5.7	Alternative designs for the magnet system . . . . .	71
5.7.1	Actively shielded twin solenoid and forward dipoles . . . . .	71
5.7.2	Iron yoke solenoid with forward dipole/toroid . . . . .	71
5.7.3	Ultra-thin solenoid positioned inside the calorimeter . . . . .	72
5.8	Magnet R&D programme to complete the technical design report . . . . .	75
5.9	Conclusion and outlook . . . . .	75
<b>6</b>	<b>Tracker and vertex detector</b>	<b>77</b>
6.1	Overview and general challenges . . . . .	77
6.2	Mathematical approaches and software tools . . . . .	79
6.2.1	Analytical, approximative and numerical approaches . . . . .	79
6.2.2	CLIC software framework . . . . .	80
6.2.3	FCC software framework . . . . .	80
6.3	Reference layout and track parameter resolution . . . . .	81
6.3.1	Hermeticity and number of measurement layers/discs . . . . .	82
6.3.2	Granularity . . . . .	83
6.3.3	Material budget . . . . .	86

6.3.4	Track parameter resolution . . . . .	86
6.3.5	Effects of non-uniform magnetic field, dipole alternative . . . . .	89
6.4	Expected performance: vertexing, tracking and flavour tagging . . . . .	91
6.4.1	Progressive track filtering in pile-up and tilted layout . . . . .	93
6.4.2	Tracking efficiency in boosted objects . . . . .	96
6.4.3	Vertexing and pile-up mitigation by extra timing information . . . . .	102
6.4.4	Flavour tagging performance . . . . .	105
6.5	Triggering, occupancy and data rates . . . . .	109
6.5.1	Track trigger . . . . .	109
6.5.2	Expected occupancy and data rates . . . . .	112
6.A	Technical specification of tracker layout . . . . .	117
<b>7</b>	<b>Calorimetry</b>	<b>125</b>
7.1	Introduction . . . . .	125
7.1.1	Calorimetry at the FCC-hh . . . . .	125
7.1.2	Calorimeter requirements . . . . .	125
7.2	Layout of the calorimeter system . . . . .	131
7.2.1	Overview and reminder of FCC-hh detector environment . . . . .	131
7.2.2	Liquid argon calorimeters . . . . .	134
7.2.3	Scintillator tile calorimeters . . . . .	144
7.3	Software implementation . . . . .	155
7.3.1	Digitisation and reconstruction . . . . .	155
7.3.2	Noise . . . . .	162
7.3.3	Reconstruction and identification using deep neural networks . . . . .	167
7.4	Performance . . . . .	170
7.4.1	Electrons and photons . . . . .	170
7.4.2	Hadronic showers . . . . .	178
7.4.3	Pion and photon identification using multivariate analysis (MVA) techniques . . . . .	190
7.4.4	DNN based particle identification at $\langle\mu\rangle = 1000$ . . . . .	197
7.4.5	Jets . . . . .	197
7.5	Alternative technology for the EM barrel calorimeter . . . . .	202
7.5.1	Silicon tungsten calorimeter . . . . .	202
7.5.2	Software implementation . . . . .	204
7.5.3	Performance . . . . .	207
7.5.4	Discussion . . . . .	209
7.6	Summary and outlook . . . . .	210
<b>8</b>	<b>Muon system</b>	<b>213</b>
8.1	Introduction . . . . .	213
8.2	Momentum measurement . . . . .	213
8.3	Muon rates . . . . .	214
8.4	Simulation of the standalone performance . . . . .	215

8.4.1	Momentum reconstruction . . . . .	216
8.4.2	Momentum calibration . . . . .	218
8.4.3	Triggering . . . . .	218
8.4.4	Contribution from hadronic interaction background . . . . .	219
<b>9</b>	<b>Trigger/DAQ</b>	<b>225</b>
9.1	The FCC-hh trigger challenge . . . . .	225
9.2	State of the art . . . . .	225
9.3	Extrapolating CMS trigger rates to 100 TeV . . . . .	227
9.4	Track trigger studies . . . . .	228
<b>10</b>	<b>FCC-hh physics benchmark studies</b>	<b>229</b>
10.1	Introduction . . . . .	229
10.2	Higgs and electroweak symmetry breaking . . . . .	230
10.2.1	Higgs properties . . . . .	230
10.2.2	ttH production . . . . .	235
10.2.3	Measurement of di-Higgs production . . . . .	238
10.2.4	Measurement of vector boson scattering . . . . .	248
10.3	Searches for new physics . . . . .	250
10.3.1	Resonances: ee, $\mu\mu$ , $\tau\tau$ . . . . .	250
10.3.2	Resonances: WW, $t\bar{t}$ , jj . . . . .	253
10.3.3	Supersymmetry: top squarks . . . . .	255
10.3.4	Dark matter: monojet + DM, $t\bar{t}$ + DM, VBF + DM . . . . .	260
10.3.5	Dark matter: disappearing tracks . . . . .	264
10.3.6	Top quark FCNC couplings . . . . .	269
<b>11</b>	<b>Cost goals, strategic R&amp;D</b>	<b>277</b>
11.1	Cost goals . . . . .	277
11.2	Detector research and development . . . . .	277
	<b>Bibliography</b>	<b>278</b>

## Introduction

---

Particle physics has arrived at an important moment in its history. The discovery of the Higgs boson, with a mass of 125 GeV, completes the matrix of particles and interactions that has constituted the Standard Model (SM) for several decades. This model is a consistent and predictive theory, which has so far proven successful at describing all phenomena accessible to collider experiments. However, several experimental facts require the extension of the SM and explanations are needed for observations such as the abundance of matter over antimatter, the striking evidence for dark matter and the non-zero neutrino masses. Theoretical issues such as the hierarchy problem and, more generally, the dynamic origin of the Higgs mechanism, likewise point to the existence of physics beyond the SM.

The Future Circular Collider (FCC) facility is designed to be the most powerful post-LHC experimental infrastructure to address the key open questions of particle physics. The conceptual design report (CDR), describing the physics opportunities and the possible technical implementations, was published in three volumes during 2019 [1–3]. The  $e^+e^-$  collider phase, FCC-ee [2], will increase the size of the LEP and LEP2 data samples by several orders of magnitude, improving the precision with which electroweak (EW) parameters are known by one to two orders of magnitude. Operations at  $\sqrt{s} = 240$  GeV will produce in excess of one million Higgs bosons, providing an absolute and model-independent determination of the total Higgs width and reducing the uncertainty on its couplings to EW gauge bosons to the few per mille level, and below the percent level for its couplings to bottom and charm quarks, to tau leptons and to gluons. Operations above the  $t\bar{t}$  threshold will allow a precise measurement of the top quark mass and of its EW couplings. Sensitivity to the electron coupling to the Higgs boson could be achieved with dedicated running with  $\sqrt{s}$  at the Higgs mass,  $m_H$ . The large event samples, and the sensitivity of the detectors operating in the clean  $e^+e^-$  environment, could enable the direct discovery of new low-mass phenomena, elusive at the LHC. The second phase of the FCC integrated programme builds on a high-energy hadron collider, FCC-hh [3], with a centre-of-mass collision energy of 100 TeV and an integrated luminosity a factor of 5–10 larger than the HL-LHC. The FCC-hh will extend the current pp collisions center-of-mass energy by almost an order of magnitude. The mass reach for direct discovery will reach several tens of TeV and allow, for example, to produce new particles whose existence could be indirectly exposed by FCC-ee precision measurements.

The overall FCC physics potential is discussed in greater detail in Ref. [1]. This report reviews the current status of the baseline design for a general purpose detector for high-luminosity experiments at the FCC-hh. This introduction outlines the overall context set by the FCC-hh machine design and the general principles guiding the detector concept.

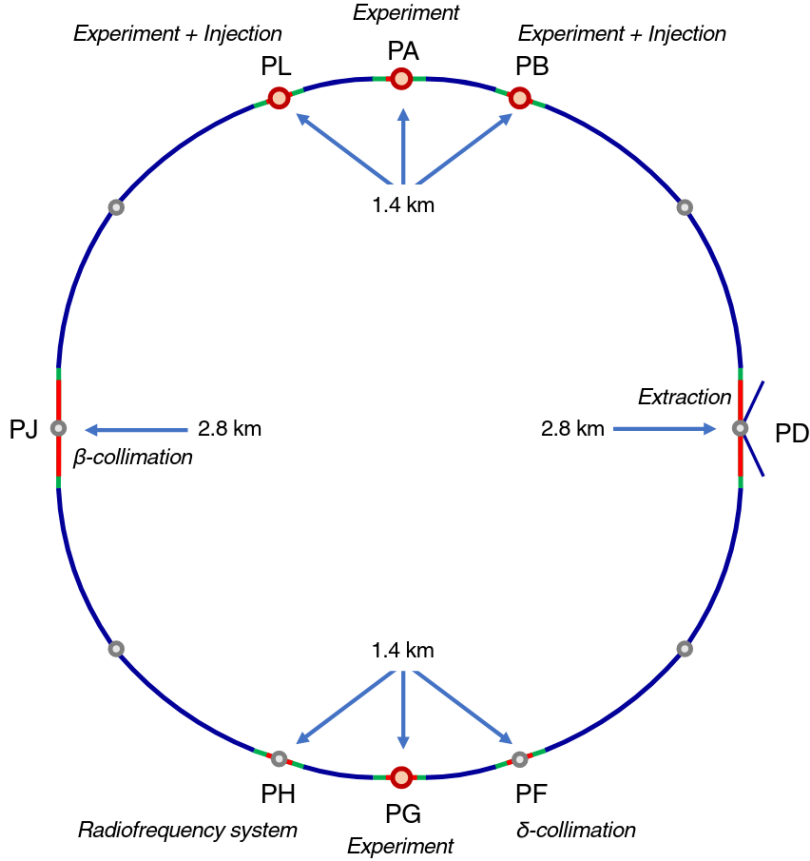


Fig. 1.1: Conceptual layout of the collider ring [3]. The experiment interaction points are at PA, PB, PG and PL. Injection takes place at PL and PB. PD hosts the beam extraction. Collimation takes place at PF and PJ. The radiofrequency systems are installed at PH.

## 1.1 The FCC-hh accelerator context

Here we introduce the overall environment in which the experiments will operate (for more details, see Ref. [3]). The FCC-hh is designed to collide protons at a centre-of-mass energy of 100 TeV, delivering a peak instantaneous luminosity of  $\mathcal{L} = 3 \cdot 10^{35} \text{ cm}^{-2} \text{ s}^{-1}$  in its ultimate phase. This will result in  $\mathcal{O}(20) \text{ ab}^{-1}$  of integrated luminosity, over 25 years of operation, for each of the two planned large general-purpose experiments. The combined data sets will thus significantly exceed the total of  $30 \text{ ab}^{-1}$  that will optimise the physics potential. Such high luminosity places stringent requirements on the radiation hardness of the detector, in particular in the forward region at small angular distances from the beampipe. While the FCC-hh is also planned to accelerate and collide ions, and to allow for electron-proton and electron-ion collisions, this document focuses on the description of the baseline design for a large pp general-purpose detector.

The layout of the collider is shown in Fig. 1.1 and key parameters are given in Table 1.1. The two high-luminosity experiments are located in opposite insertions (PA and PG). This ensures the highest luminosity, reduces unwanted beam-beam effects and is independent of the beam-filling pattern. The main experiments are located in 66 m long halls, sufficient for the detector to be described here, and ensuring that the final focus system can be integrated in the available length in the insertion. Two additional, lower luminosity experiments are located together with the injection systems in insertions PB and PL.

The proposed accelerator layout increases the collider robustness because the high radiation experiment and collimation sections are separated from the radiation sensitive equipment, i.e. the RF instrumentation and the extraction kickers. Also the short arcs between the main experiment in PA and the



additional experiments in PB and PL are long enough to avoid background from the collision debris in the main experiment, which would perturb the other experiments. Similarly, the RF insertion is protected from the main experiment in PG.

Table 1.1: Key FCC-hh baseline parameters compared to LHC and HL-LHC parameters.

	LHC	HL-LHC	FCC-hh	
			Initial	Nominal
<b>Physics performance and beam parameters</b>				
Peak luminosity <sup>1</sup> [ $10^{34} \text{ cm}^{-2} \text{ s}^{-1}$ ]	1.0	5.0	5.0	< 30.0
Optimum average integrated luminosity / day [ $\text{fb}^{-1}$ ]	0.47	2.8	2.2	8
Target turnaround time [h]			2	2
Assumed turnaround time <sup>2</sup> [h]			5	4
Peak number of inelastic events / crossing	27	135 levelled	171	1026
Total / inelastic cross section $\sigma$ proton [mbarn]		111 / 85		153 / 108
Luminous region RMS length [cm]			5.7	5.7
Distance IP to first quadrupole, $L^*$ [m]		23	40	40
<b>Beam parameters</b>				
Number of bunches n		2808		10400
Bunch spacing [ns]	25	25		25
Bunch population $N$ [ $10^{11}$ ]	1.15	2.2		1.0
Nominal transverse normalised emittance [ $\mu\text{m}$ ]	3.75	2.5	2.2	2.2
Number of IPs contributing to $\Delta Q$	3	2	2+2	2
IP beta function [m]	0.55	0.15 (min)	1.1	0.3
RMS IP spot size [ $\mu\text{m}$ ]	16.7	7.1 (min)	6.8	3.5
Full crossing angle [ $\mu\text{rad}$ ]	285	590	104	200 <sup>3</sup>

<sup>1</sup> For the nominal parameters, the peak luminosity is reached during the run.

<sup>2</sup> Turnaround time assumed for calculations of integrated luminosity, including typical recovery time for issues.

<sup>3</sup> The crossing angle will be compensated using the crab crossing scheme.

## 1.2 The overall features of an FCC-hh detector

The FCC-hh accelerator parameters allow the direct exploration of massive particles up to 40–50 TeV [4], approximately one order of magnitude improvement over the LHC sensitivity for discovering heavy resonant states. In addition, during its lifetime the FCC-hh is expected to produce trillions of top quarks and tens of billions of Higgs bosons, allowing for a rich SM precision programme [1, 5]. Most importantly, FCC-hh is the only machine under study today that will provide a few-percent-level measurement of the Higgs self-coupling [5, 6].

An experimental apparatus that operates within the FCC-hh must therefore operate optimally on two main fronts. Physics at the EW scale, in particular the Higgs, will produce objects in the detector with momenta in the  $p_T$  range 20–100 GeV. The LHC detectors were built to produce an optimal response in such an energy range. In addition, a new regime, at the energy frontier, will be characterised by the energy scale of decay products originating from high mass resonances (potentially as high as  $m_X = 50 \text{ TeV}$ ). An FCC-hh detector must therefore be capable of reconstructing leptons, jets, top quarks and H, W/Z bosons with momenta as large as  $p_T = 20 \text{ TeV}$ . Thus the detector must provide accurate measurements in the full energy range between tens of GeV and tens of TeV.

Figure 1.2 shows the layout of the FCC-hh reference detector. This detector concept does not represent the final design, but rather a concrete example that suits the performance and physics requirements and allows the identification of areas where dedicated further R&D efforts are needed. The detector has

a diameter of 20 m and a length of 50 m, comparable to the dimensions of the ATLAS detector but much heavier. The central detector, with a pseudo-rapidity coverage of  $|\eta| < 2.5$ , houses the tracking, electromagnetic calorimetry and hadron calorimetry inside a 4 T solenoid with a free bore diameter of 10 m. In order to reach the required performance for  $2.5 < |\eta| < 6$ , the forward parts of the detector are displaced along the beam axis by 10 m from the interaction point. Two forward magnet coils with an inner bore of 5 m provide the required bending power. These forward magnets are also solenoids with a 4 T field, providing a total solenoid volume of 32 m length for high precision momentum spectroscopy up to  $|\eta| \approx 4$  and tracking up to  $|\eta| \approx 6$ . As an option, replacing the forward solenoids with two forward dipoles is also being considered. The tracker cavity has a radius of 1.7 m with the outermost layer at around 1.6 m from the beam in the central and forward regions, providing the full spectrometer arm up to  $|\eta| = 3$ . The electromagnetic calorimeter (ECAL) has a thickness of around 30 radiation lengths ( $X_0$ ). The overall calorimeter thickness, including the hadron calorimeter (HCAL), exceeds 10.5 nuclear interaction lengths ( $\lambda$ ), ensuring 98 % containment of high energy hadron showers and limiting punch-through to the muon system. The ECAL is based on liquid argon (LAr) given its intrinsic radiation hardness. The barrel HCAL is a scintillating tile calorimeter with steel and Pb absorbers that uses wavelength shifting (WLS) fibres and silicon photomultipliers (SiPMs) for the readout. It is divided into a central barrel and two extended barrels. The HCALs for the endcap and forward regions are also based on LAr. The requirement of calorimetry acceptance up to  $|\eta| \approx 6$  translates into an inner active radius of only 8 cm at a  $z$ -distance of 16.6 m from the IP. The transverse and longitudinal segmentation of both the electromagnetic and hadronic calorimeters is  $\sim 4$  times finer than the present ATLAS calorimeters.

The muon system is placed outside the magnet coils. The barrel muon system provides muon identification, standalone muon spectroscopy by measurement of the angle of the muon track as well as precision muon spectroscopy by combining the tracker measurement with the measured space points in the muon chambers. The forward muon system can only provide spectroscopy if forward dipoles are used.

The reference detector does not assume any shielding of the magnetic field.

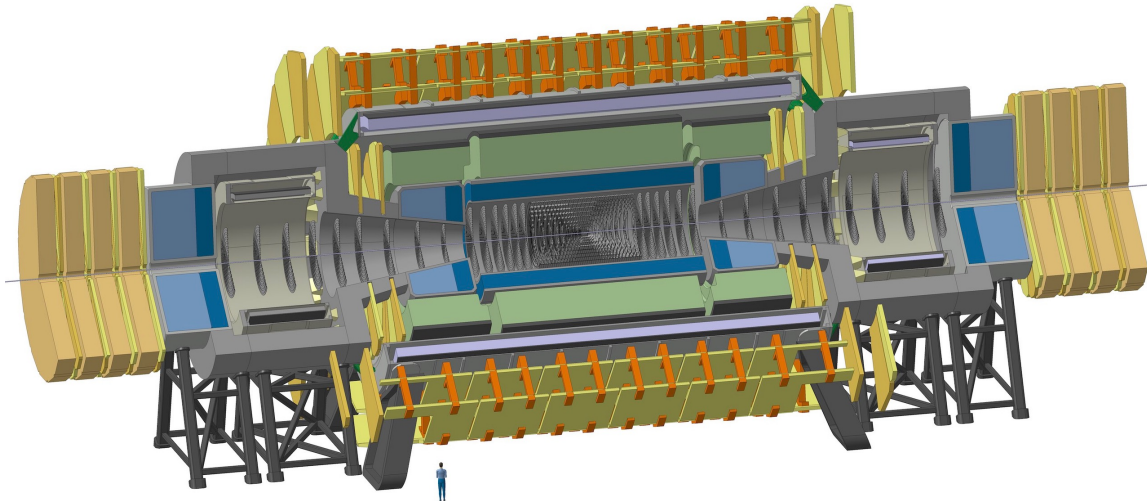


Fig. 1.2: The layout of the FCC-hh reference detector [3].

This document will review the individual detector components and their expected performance in more detail, assessed through a combination of fast and full detector simulations. Chapter 2 will outline the overall detector performance requirements, based on a set of benchmark processes that fully characterise the FCC-hh physics programme. Chapter 3 will define the requirements arising from the radiation environment. Chapter 4 introduces the software framework used for all studies. Chapter 5 discusses

the detector magnet systems. Chapters 6, 7 and 8 present the tracker, calorimeter and muon detectors, respectively. Chapter 9 discusses the trigger system, and Chapter 10 presents some concrete examples of detector performance and measurement potential for the chosen benchmark processes. Chapter 11 gives a first indication of the overall detector cost.



# Benchmark processes and detector requirements from physics

---

The physics programme of FCC-hh is extremely diverse, both in its reach and in the demands it sets on the detectors. As the Tevatron and the LHC have shown, hadron colliders can deliver high-precision measurements. In the context of the Higgs boson, in particular, current studies [1, 5] have shown the potential to complement the precision achievable by FCC-ee for the measurement of rare Higgs boson decays, such as  $H \rightarrow \gamma\gamma$ ,  $H \rightarrow \mu^+\mu^-$  and  $H \rightarrow Z\gamma$ , and in particular of the Higgs self-coupling. These precision measurements, in addition to those of the top quark, form the core of the ‘guaranteed deliverable’ part of the FCC-hh physics programme. The opportunity to further extend the FCC-ee reach in the detailed understanding of the Higgs and EW symmetry breaking sectors of the SM, including a possible understanding of the nature of the cosmological EW phase transition, must be matched by the appropriate detector performance.

The FCC-hh search programme extends from the exploration of the highest accessible energies, in the multi-TeV region, down to the search for subtle and potentially elusive rare signatures at lower energy. Among the key goals here is the search for dark matter candidates, particularly in the sector of weakly interacting massive particles, where the FCC-hh has the potential of either proving or conclusively ruling out their existence. A further goal is to push the search to higher masses for signatures of long-standing candidates for new physics scenarios, such as supersymmetry or new gauge interactions. Depending on the strength of the relevant couplings, the mass window spans between  $\mathcal{O}(100)$  GeV and several tens of TeV, with final states that can include combinations of all SM fermions and gauge bosons.

The benchmark processes selected in this report to test the performance of the baseline FCC-hh detector cover all the previous cases, and examples of the measurement potential will be given in Chapter 10. Further measurements and scientific opportunities arise at FCC-hh thanks to the heavy ion collision programme and to the ep and eA collisions option (FCC-eh). They are discussed in Ref. [1] and will not enter in this report. A programme of flavour physics, along the lines of the LHCb experiment at the LHC, of forward physics measurements (like TOTEM, ALFA, LHCf, PPS), and of searches for exotic signatures beyond the SM (like MoEDAL, FASER, SND etc), are also expected to emerge from future studies, but the respective dedicated detectors will not be considered here.

As just discussed, a multipurpose detector that collects data within the FCC-hh must operate optimally on three main fronts. Physics at the EW scale, in particular the Higgs, will produce objects in the detector with momenta in the range  $p_T = 20\text{--}100$  GeV. The LHC detectors were built to produce an optimal response in such an energy range. A new regime, at the energy frontier, will be characterised by the energy scale of decay products originating from high mass resonances (potentially as high as  $m_X = 50$  TeV). An FCC-hh detector must therefore be capable of reconstructing and identifying lep-

tons, jets, and potentially top, H and W/Z bosons with momenta as large as  $p_T = 20$  TeV to provide accurate measurements in a wide energy spectrum. Such a detector must also be able to identify elusive signatures, that might originate from compressed spectra of theories beyond the SM (BSM) [7–9]. Such signatures include soft leptons (with momenta as low as  $p_T = 5$  GeV), and more exotic final states originating from the production of long-lived particles (neutral or charged), such as disappearing tracks [10, 11] or displaced leptons or jets [12–14]. Since evidence for such signals would unambiguously indicate the presence of new physics, the FCC-hh experimental apparatus must also be designed and optimised to maximise its sensitivity to these elusive signatures.

This chapter introduces the general specifications that a detector operating in the FCC-hh environment should satisfy, in order to maximise the physics potential.

## 2.1 General considerations on the acceptance

Proton collisions at  $\sqrt{s} = 100$  TeV give access to a wide range of possible kinematics. The comparison of the kinematic coverage in the  $(x, M_X)$  plane between  $\sqrt{s} = 14$  TeV and  $\sqrt{s} = 100$  TeV is shown in Fig. 2.1, where  $x$  is the fraction of the proton longitudinal momentum and  $M_X$  is the characteristic mass-energy scale of the process under consideration. The large centre-of-mass energy allows for the production of resonances with masses up to  $M_X = 100$  TeV. Due to the rapid fall-off of the parton distribution functions (PDFs) in the high  $x$  region, however, the cross-section for producing heavy particles with masses  $M_X > 50$  TeV is negligible, even in the case of strongly coupled resonances. Energy-momentum conservation requires large  $M_X$  resonances to be produced in a relatively balanced collision, i.e. mostly at rest. A two body decay for a particle produced at rest results in a 95% probability that both decay products lie in  $|\eta| < 2.5$ . As a bare minimum, in order to allow for an exploration of the high energy frontier, a detector operating at  $\sqrt{s} = 100$  TeV must therefore be able to detect and measure decay products with high precision in such a geometrical acceptance.

### 2.1.1 Rapidity coverage

Processes occurring at a given characteristic energy scale  $Q^2 = M_X^2$  will be produced on average from collisions that are more asymmetric at  $\sqrt{s} = 100$  TeV compared to  $\sqrt{s} = 14$  TeV. This effect, clearly visible in Fig. 2.1, is due to the fact that, for a maximally imbalanced collision, the minimum available longitudinal momentum fraction is given by  $x_{\min} = \frac{M_X^2}{s}$ . A maximally imbalanced collision corresponds to one of the partons entering the collision carrying a momentum fraction  $x_{\max} \sim 1$  of the proton momentum. In practice, due to the rapidly falling PDFs at high  $x$ , one can assume  $x_{\max} \approx 0.5$ , which gives  $x_{\min} \approx \frac{2M_X^2}{s}$  corresponding to a maximal rapidity  $y_{\max} = -\ln(\frac{2M_X}{\sqrt{s}})$ . As a result, at the FCC-hh the decay products of the particles of interest will be, on average, produced more forward than at the LHC. For example, at  $\sqrt{s} = 14$  TeV, a Higgs boson originating from gluon fusion can be produced up to  $y_{\max} \approx 4$ , whereas at  $\sqrt{s} = 100$  TeV it can be produced up to  $y_{\max} \approx 6$ . This effect is illustrated in Fig. 2.2 where the pseudo-rapidity distribution of the most forward lepton in a  $H \rightarrow ZZ^* \rightarrow 4\ell$  decay (left) and the most forward jet in vector boson fusion Higgs (right) are shown for two different collision energies.

This aspect of  $\sqrt{s} = 100$  TeV collisions sets stringent requirements on the detector acceptance. In particular, in order to maintain high efficiency for reconstructing top, Higgs, W and Z particles, which will constitute a substantial part of the FCC-hh physics programme, the FCC-hh detector must be able to reconstruct decay products up to very large rapidity,  $\eta \approx 6$ . Since the forward region of the detector suffers from the largest levels of radiation and the worst achievable intrinsic detector performance (due to multiple scattering and a higher relative impact of pile-up), such a requirement on the design comes with significant challenges.

Provided that forward detectors can be operated in the extreme environment of the FCC-hh, the missing transverse energy  $E_T^{\text{miss}}$  performance can benefit from having a larger geometric acceptance.

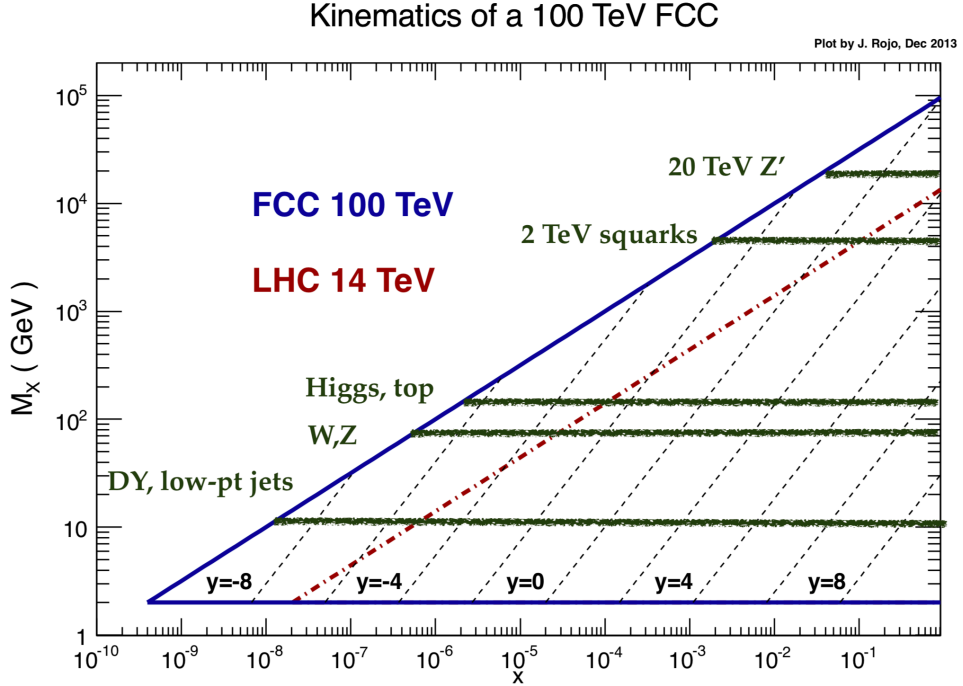


Fig. 2.1: Kinematic coverage in the  $(x, M_X)$  plane of a  $\sqrt{s} = 100$  TeV hadron collider (solid blue line), compared with the corresponding coverage of the LHC at  $\sqrt{s} = 14$  TeV (dot-dashed red line). The dotted lines indicate regions of constant rapidity  $y$  at the FCC. We also indicate the relevant  $M_X$  regions for phenomenologically important processes, from low masses (Drell–Yan, low  $p_T$  jets), electroweak scale processes (Higgs, W, Z, top), and possible new high-mass particles (squarks,  $Z'$ ). This figure is taken from Ref. [15].

The probability of reconstructing  $E_T^{\text{miss}}$  above some threshold in QCD events (that contain little to no generated invisible energy) is shown in Fig. 2.3 (left) for various assumptions on the detector  $\eta$  coverage. The tails in the  $E_T^{\text{miss}}$  distribution result from both the intrinsic resolution of the detector active element as well as the lack of hermeticity of the detector. A large acceptance definitely benefits the  $E_T^{\text{miss}}$  resolution. A reduction of the  $E_T^{\text{miss}}$  tails in QCD or Drell–Yan backgrounds can be highly beneficial to searches requiring large  $E_T^{\text{miss}}$  in the final states. This is the case for virtually all supersymmetric (SUSY) final states in R-parity conserving scenarios, where the  $E_T^{\text{miss}}$  is produced by the lightest super-symmetric particle (LSP).

Based on the above considerations, we require a pseudo-rapidity coverage up to  $|\eta| = 6$  for the FCC-hh detector. More specifically, we require tracking and precise calorimetry up to  $|\eta| = 6$ . Given the intrinsic limitations due to the multiple scattering in the forward region, the track momentum measurement (spectrometry) will only be required up to  $|\eta| = 4$ .

### 2.1.2 Minimum momentum requirements

Higgs and SM related processes are useful benchmarks in order to define minimal detector requirements for reconstructing and identifying low momentum objects. In particular, one of the golden Higgs decay modes is the  $H \rightarrow ZZ^* \rightarrow 4\ell$  channel. This decay channel features the presence of a very soft lepton ( $p_T \approx 5$  GeV) originating from the off-shell Z. Another important physics case for efficiently reconstructing low momentum leptons is electro-weakly produced SUSY. Electroweakinos in SUSY provide compelling weakly interacting dark matter candidates (WIMPs), the LSP. In the SUSY parameter space LSPs might lie in so-called *compressed* regions, where the mass difference between the next-to-LSP (NLSP) and the LSP is very small. This class of decay chains typically produce very soft leptons since it



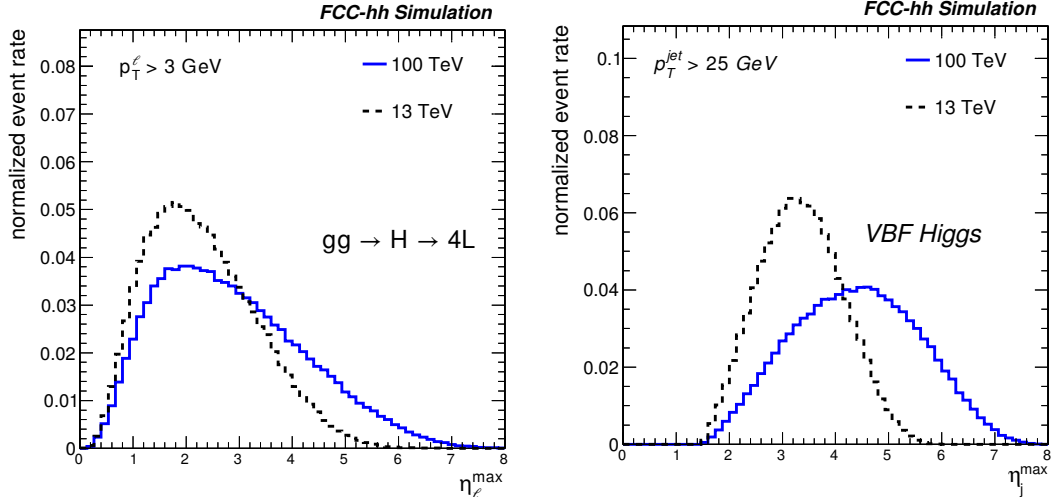


Fig. 2.2: Highest lepton pseudo-rapidity for gluon-gluon fusion Higgs decaying to 4 leptons (left) and maximum jet pseudo-rapidity for vector-boson fusion Higgs (right).

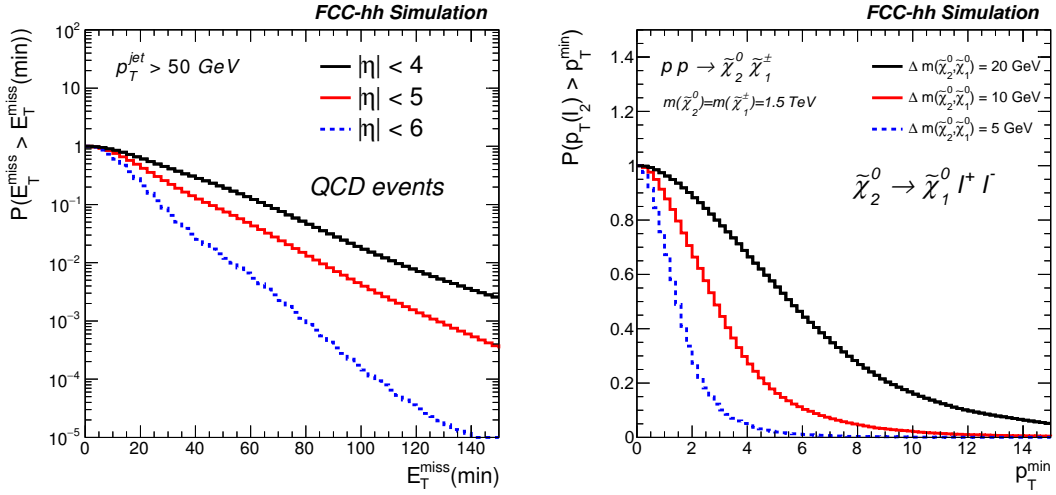


Fig. 2.3: Left: Probability of reconstructing  $E_T^{\text{miss}}$  greater than  $E_T^{\text{miss}}(\text{min})$  in di-jet QCD events for various assumptions on the detector acceptance. Right: Probability of reconstructing the softest lepton in electroweakino production for different scenarios of compressed super-symmetric spectra.

involves the production of highly off-shell W or Z bosons. The probability of reconstructing the softest leptons in  $p p \rightarrow \tilde{\chi}_1^\pm \tilde{\chi}_2^0 \rightarrow \tilde{\chi}_1^0 \nu \tilde{\chi}_1^0 \ell \ell$  events as a function of the threshold on the  $p_T$  of the lepton is given in Fig. 2.3 (right) for three hypothetical compressed SUSY scenarios. It clearly appears that, in order to maintain the largest possible sensitivity to such signatures, the FCC-hh detector will need to be able to reconstruct and unambiguously identify leptons down to momenta of a few GeV.

Electrons and muons are reconstructed as charged particle trajectories in the tracking volume. The identification of the electrons is performed via a combination of tracking and ECAL based observables. Due to the presence of a large magnetic field, electrons can be identified if their momenta are above some threshold  $p_T^{\text{min}}$ , defined as the momentum required to reach the ECAL. Likewise, muons can only be identified if they are able to reach the muon spectrometers. To be more concrete, we assume a multi-purpose detector setup with a tracking volume and a calorimeter embedded inside a solenoidal magnetic field. Muon chambers are placed outside of the solenoid, therefore the minimal momentum



for reconstructing and identifying muons  $p_T^{\min}$  is typically larger than for electrons. As discussed in the next section, a large magnetic field and a large detector volume are desirable in order to obtain a good tracking momentum resolution, which is in competition with the requirement of being able to identify low momentum leptons. Defining the maximum radial distance  $R_{\max}$  for the identification detector (ECAL for electrons and first muon station for muons), and using  $p_T = 0.3B\rho$ , where  $B$  is the solenoidal magnetic field strength in Tesla,  $\rho$  is the track curvature in m, and  $R_{\max} = 2\rho$ , we can derive  $R_{\max}$ . We find that, in order to reconstruct muons with  $p_T^{\min} = 4$  GeV, the first muon station needs to be placed at  $R_{\max} = 6.5$  m with a detector operating in a field  $B = 4$  T. If we consider the energy loss of muons in the calorimeter absorbers, the threshold increases by a few GeV to  $p_T^{\min} = 6-7$  GeV. With a tracking volume defined as a cylinder with  $R = 1.5$  m (corresponding approximately to the start of the ECAL), this corresponds to an electron identification threshold of  $p_T^{\min} = 1$  GeV. It should be noted, however, that in practice this should be considered as an idealised limit. In the current LHC multi-purpose experiments ATLAS and CMS, electrons with  $p_T < 3$  GeV are difficult to identify unambiguously due to energy loss, even with a lower lever-arm. We therefore set  $p_T^{\min} = 4$  GeV for electrons as a target.

## 2.2 Energy-momentum resolution

The scope of the FCC-hh is to carry out an extensive programme of SM and Higgs measurements and to explore the energy frontier by directly probing the production of multi-TeV resonances. Therefore the decay products of the particles of interest have to be detected and measured as precisely as possible in a wide range of energies.

The energy resolution in calorimeters, as a function of the incoming particle energy  $E$ , is given by

$$\frac{\sigma_E}{E} = \frac{a}{\sqrt{E}} \oplus \frac{b}{E} \oplus c \quad , \quad (2.1)$$

where  $a$  is the stochastic term,  $b$  is the noise term and  $c$  is the constant term. The relative resolution is a decreasing function of the energy. At high energy, the resolution asymptotically tends to  $c$ , which is ultimately determined by inhomogeneities in the detector and possible energy leakages due to partial shower containment.

The tracking gives access to the momentum of charged particles by measuring the curvature  $\rho$  (or the ‘sagitta’,  $s$ ) of the trajectory. The relative uncertainty on the momentum resolution is given by

$$\frac{\sigma_p}{p} = a \oplus b p \quad , \quad (2.2)$$

where  $a$  is the constant term determined by the amount of material responsible for multiple scattering in the tracking volume. In contrast to the energy measurement in calorimeters, the momentum resolution increases linearly with the incoming particle momentum, in the high energy limit. The constant  $b$  is proportional to  $\sigma_x/BL^2$ , where  $\sigma_x$  is the single point resolution of the tracking elements,  $B$  is the field strength and  $L$  is the tracker radius. The measurements provided by the tracking system and the calorimeters are therefore complementary, for particles like charged hadrons or electrons that deposit energy in both sub-detectors.

### 2.2.1 The low energy limit

#### 2.2.1.1 Tracking

It is crucial to design a detector that maximises the precision achievable in measurements of rare Higgs decay modes such as  $H \rightarrow Z\gamma$  or  $H \rightarrow \mu^+\mu^-$  since such measurements will still be statistically dominated at the end of HL-LHC. The precision expected in these modes relies on the reconstruction of a narrow mass peak over a large background continuum. Excellent electron and muon momentum resolution is needed in order to achieve the best possible precision. For charged particles in the low momentum regime

( $p_T < 100$  GeV) maximising the performance requires minimising the impact of multiple-scattering. This can be achieved both by minimising the total material budget in the tracker and the beam-pipe as, well by adopting a so-called *tilted module* geometry. For the FCC-hh detector we require a track momentum resolution  $\sigma_p/p \approx 0.5\%$  in the multiple scattering limit at  $\eta \approx 0$ , which corresponds roughly to  $0.2X_0$  radiation length of material for the entire tracking volume. In Fig. 2.4 (left) we show the impact of the muon momentum resolution on the  $H \rightarrow \mu^+\mu^-$  invariant mass peak obtained with the CMS-Phase II tracker [16] and the FCC-hh tracker prototype. The tracking requirements are summarised in Table 2.1. We note that the muon spectrometers have a negligible impact on the muon momentum resolution in the low momentum regime, and the resolution is driven almost entirely by the tracking system.

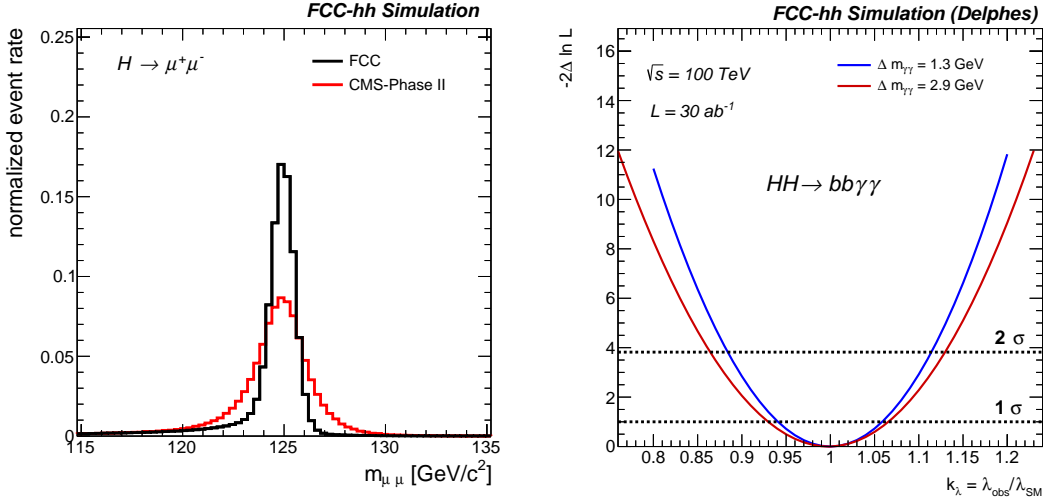


Fig. 2.4: Left: Reconstructed di-muon invariant mass spectrum of  $H \rightarrow \mu^+\mu^-$  decays obtained with the CMS-Phase II and the FCC-hh tracker designs. Right: Expected precision of the Higgs self-coupling modifier  $\kappa_\lambda$  obtained by varying the photon reconstruction performance in two scenarios with nominal ( $\Delta m_{\gamma\gamma} = 1.3$  GeV) and degraded ( $\Delta m_{\gamma\gamma} = 2.9$  GeV) energy resolution.

### 2.2.1.2 Calorimetry

The precise measurement of the Higgs self-coupling in the  $HH \rightarrow bb\gamma\gamma$  decay mode relies on excellent energy photon resolution in the  $E = 50\text{--}100$  GeV energy range. A di-photon invariant mass resolution  $\Delta m_{\gamma\gamma} \approx 1\%$  for photons from  $H \rightarrow \gamma\gamma$  decays can only be achieved if the stochastic term  $b$  defined in Eq. (2.1) is at the level of  $\sigma_E/E \sim 10\%/\sqrt{E}$  and the noise term is kept under control. Pile-up will lead to additional noise in the calorimeter. The effect of the noise term of pile-up on the photon energy resolution has been studied extensively in full simulation and is discussed in Chapter 7. The expected pile-up of  $\langle \mu \rangle = 200$  and  $\langle \mu \rangle = 1000$  for the FCC-hh baseline and ultimate scenarios, respectively, will lead to energy deposits from pile-up collisions on top of the hard scatter of interest. The degradation induced has been parameterised directly on the di-photon invariant mass and its impact on the expected precision of the Higgs self-coupling has been studied and summarised in Ref. [17]. The result of this study, shown in Fig. 2.4 (right), shows that the presence of  $\langle \mu \rangle = 200$  pile-up interactions can lead to an absolute degradation of  $\approx 1\%$  (or 20% relative) of the self-coupling precision. It should be noted that this study does not include the effect of pile-up on the photon isolation assumes a standalone calorimeter reconstruction. A combined reconstruction using tracking, calorimetry and timing information will be needed to reduce the impact of pile-up and achieve the target photon energy resolution.

Table 2.1: Requirements for tracking and calorimetry for the FCC-hh detector at  $|\eta| \approx 0$ .

	Transverse granularity, $\eta \times \phi$ (rad.)	# Layers	Resolution
Tracker	$0.001 \times 0.001$	12	$0.5\% \oplus (\frac{p_T}{[\text{TeV}]}) * 1\%$
ECAL	$0.01 \times 0.01$	8	$\frac{10\%}{\sqrt{E}} \oplus 0.3\%$
HCAL	$0.025 \times 0.025$	10	$\frac{50\%}{\sqrt{E}} \oplus 3\%$

## 2.2.2 The high energy limit

With the exception of muons and neutrinos, all particles originating from the collision end their journey in the calorimeters. Therefore, the energy resolution of electrons, photons and jets at high energy will be determined entirely by the calorimeter performance. In contrast, high energy muons traverse calorimeters and their momentum is determined through a combination of tracking, calorimeter and muon chambers measurements. Multi-TeV resonances constitute useful processes for determining detector performance goals in the high energy regime. A summary of the physics reach of the FCC-hh for heavy resonance searches can be found in Refs. [18, 19], and will be reviewed in Chapter 10.

### 2.2.2.1 Electrons, photons and hadrons

As discussed previously, the energy resolution at high energy is determined by the constant term defined in Eq. (2.1). The value of the constant term is different for electromagnetic (ECAL) and hadronic (HCAL) calorimeters. It is ultimately determined by the choice of the calorimeter technology and the design. Large constant terms typically originate from inhomogeneities among different detector elements and energy leakages due to sub-optimal shower containment. The calorimeters of the FCC-hh detector must therefore be capable of containing EM and hadronic showers in the multi-TeV regime in order to achieve small constant terms. For compatibility, with the LHC experiments, we require a performance of  $\sigma_E/E \approx 0.3\%$  and  $\sigma_E/E \approx 3\%$  for the ECAL and HCAL, respectively. As shown in Fig. 2.5 (left), the effect induced by the magnitude of the hadronic calorimeter constant term on the expected discovery reach for heavy  $Z'$  resonances decaying hadronically is sizeable. We note that, despite the fraction of electromagnetic energy from  $\pi^0$ s is large in jets, the sensitivity is entirely driven by the hadronic calorimeter resolution, given its worse intrinsic resolution. The shower maximum in the longitudinal direction grows logarithmically with the energy. Naïve scaling therefore leads to an increase, respectively, of  $1 X_0$  and  $1 \lambda_I$  compared to the calorimeters of the LHC experiments. More detailed studies, summarised in Chapter 7 and Ref. [20], show that an average 95% containment of  $E = 20$  TeV particle showers can be achieved with  $\approx 30 X_0$  radiation lengths for EM particles and a total thickness of  $\approx 11 \lambda_I$  for hadrons, allowing the required criteria for the electromagnetic and hadronic calorimeters constant terms to be matched.

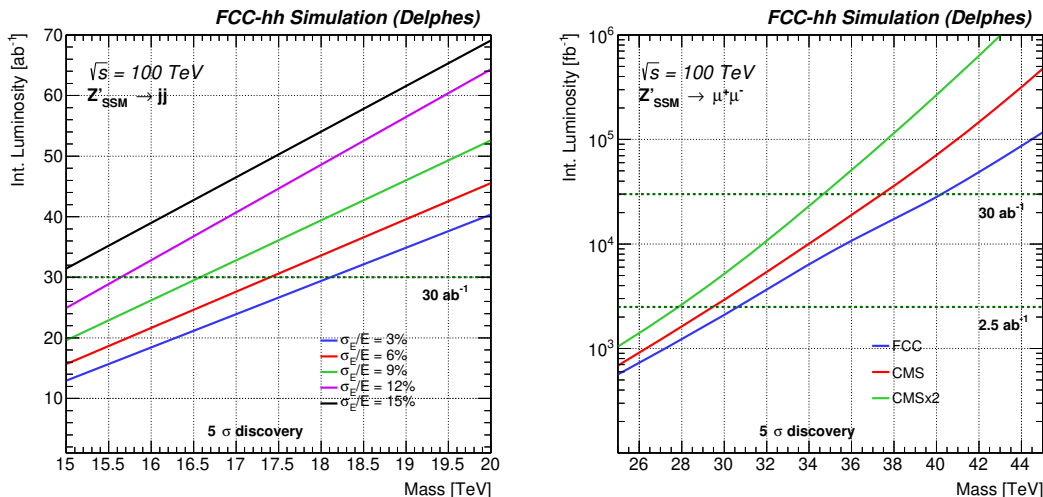


Fig. 2.5: Left: Expected discovery reach for heavy  $Z'$  resonances decaying to di-jet (left) and di-muon (right) for various assumptions on the hadronic calorimeter constant term (left) and muon momentum resolution (right). For the di-muon resonance we compare the nominal FCC resolution to the CMS resolution, and the CMS resolution degraded by a factor of two.

### 2.2.2.2 Muons

Since the muon momentum is obtained through a fit of the trajectory that uses a combination of tracker and muon spectrometer hits as input, the muon momentum resolution degrades with increasing momentum, as already shown in Eq. (2.2). As with jets, electrons and photons, a good muon momentum resolution at multi-TeV energy is crucial for maintaining a high sensitivity in searches for heavy new states that might decay to muons. The reach for a  $Z' \rightarrow \mu\mu$  resonance obtained with various assumptions on the muon resolution is illustrated in Fig. 2.5. The best sensitivity is achieved with an assumed  $\sigma_p/p \approx 5\%$  at  $p_T = 20$  TeV corresponding to our target for the FCC-hh detector, as opposed to the projected CMS resolution of  $\sigma_p/p \approx 40\%$ . In order to reconstruct and accurately measure the momentum of  $p_T = 20$  TeV, a large lever arm, an excellent spatial resolution, and precise alignment of the tracking plus muon systems, are needed. It should be noted that calorimetric information can help muon identification, especially at high energies. For example, a 20 TeV muon deposits, through radiative energy loss, on average  $\Delta E = 200$  GeV in 3 meters of iron, corresponding to 1% of the initial muon energy. The specifics of a design that allows such performance to be achieved is discussed in Chapter 8.

## 2.3 Object reconstruction and identification performance

As a general rule, object identification requires the use of the combined information of several sub-detector systems and relies on complex algorithms that need a detailed knowledge of the detector and a mature simulation framework, none of which is available at this stage. However, simple heuristics from first principles can help in defining the criteria for optimal performance object reconstruction and identification. High performance in object identification is equivalent to high identification efficiency for a low false-positive rate (or fake-rate).

### 2.3.1 Electrons

Electron identification requires the use of the tracker, ECAL and HCAL information. More specifically, an electron object is a track that matches an ECAL deposit, with the requirement of a small HCAL energy deposit. To ensure a small HCAL deposit for electrons in a wide range of energies, one must design an ECAL with a large enough number of  $X_0$ , which is already ensured by the requirement of a small

constant term in the energy resolution. The 3D shape of the EM shower in the calorimeter is distorted by the presence of bremsstrahlung photons in the  $\phi$  direction, which can help in discriminating against photons that accidentally match the extrapolation of a charged hadron trajectory (in jets for instance), or directly against charged hadrons that happen to have small HCAL deposits. A precise reconstruction of the full shower shape is therefore of vital importance in order to achieve a low electron fake-rate from charged hadrons, and can be achieved with a high granularity calorimeter that gives access to an ‘image’ of the shower.

### 2.3.2 Photons

Photon identification requires the presence of an ECAL deposit, the absence of a track with compatible momentum pointing to it, and a negligible HCAL deposit. The probability of reconstructing ‘fake’ photons from mis-reconstructed neutral hadrons can be kept small with a thick ECAL detector. However, the largest contribution of fake photons typically originates from  $\pi^0 \rightarrow \gamma\gamma$  decays, which are produced copiously at hadron colliders. To be more specific, a  $\pi^0$  with  $p_T = 20$  GeV will decay into two photons separated by an average angular distance  $\Delta R = \sqrt{\Delta\eta^2 + \Delta\phi^2} = 10$  mrad. A large prompt photon identification efficiency and low mis-identification probability can be obtained with a highly segmented calorimeter, both in the transverse and the longitudinal directions. An ECAL with transverse granularity of  $1 \text{ cm}^2$  (placed at  $> 1$  m from the IP) can achieve the required separation capability. In addition, the probability to resolve two photons from a  $\pi^0$  decay can be increased by exploiting the full 3D shower information, thus improving the  $\pi^0$  background rejection efficiency. The transverse and longitudinal calorimeter requirements are summarised in Table 2.1.

Due to the absence of a pointing track that can be associated with the hard interaction vertex, background photons from  $\pi^0$  decays become more severe in the presence of pile-up. The reduction of such background will therefore require high resolution timing detectors that allow linking of neutral energy deposits to given interaction vertices by triangulation. A large photon fake-rate can have a negative impact on flagship measurements at the FCC-hh, as shown in the case of the Higgs self-coupling in the  $HH \rightarrow b\bar{b}\gamma\gamma$  channel, see Fig. 2.6 (left).

### 2.3.3 Muons

The mis-identification of muons results from in-flight charged pion decays or punch-throughs, i.e. hadron showers that are not fully contained in the HCAL and leak into the muon system. Again, such phenomena can be contained by requiring a deep HCAL sub-detector, which is automatically ensured by requiring high energy resolution for hadrons in the multi-TeV regime.

### 2.3.4 Boosted topologies

In addition to the more standard leptons, photons, jets and missing energy final states, new physics will be searched for in final states that include the presence of boosted object topologies, i.e. boosted particles decaying hadronically and forming collimated jets. Such hadronic jets, as opposed to simple QCD jets, display an internal *sub-structure*, featuring 2 or more prongs. Moreover, the invariant mass of the jet,  $m_J \approx m_B$ , is of the order of the mass of the parent particle  $B$ , where  $B = \tau, W, Z, H, t$ <sup>1</sup>. The reconstruction of boosted topologies is highly complex and will necessarily rely on the combined measurement of several subdetectors. To be able to resolve the jet sub-structure, in addition to good energy resolution, an excellent angular resolution is necessary. For instance, in a W-jet with  $p_T = 10$  TeV, the two hard prongs will be separated on average by the angular distance  $\Delta R = 0.02$ , which is the typical transverse size of an ECAL crystal in the CMS detector. Reference [22] investigated the impact of different calorimeter granularities on the identification capability of highly boosted  $Z'$  decaying to top

<sup>1</sup>To further complicate things,  $\tau$  leptons are also long-lived, as discussed in Section 2.3.5. As a result, a significant fraction of multi-TeV  $\tau$  will produce highly displaced ( $\gamma c \tau > 5$  cm) vertices.

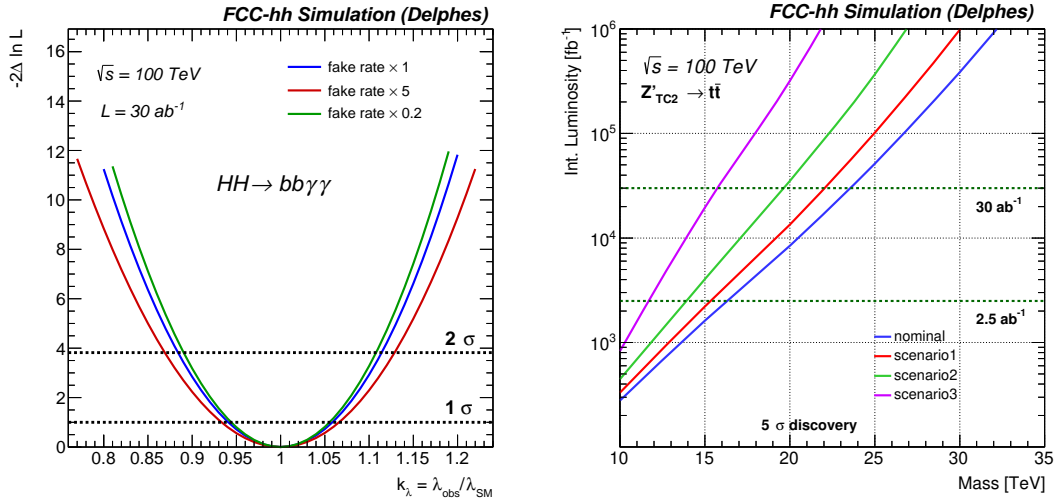


Fig. 2.6: Left: Expected precision on the Higgs self-coupling modifier  $\kappa_\lambda$  obtained for three scenarios of nominal-degraded ( $\times 5$ ) and improved ( $\times 0.2$ ) photon mistag rate. Right: Discovery potential for a  $Z'$  decaying to a  $t\bar{t}$  pair for various scenarios of b-tagging efficiencies at very large  $p_T$ . The nominal efficiency is given in Ref. [21], and scenarios 1, 2, and 3 correspond to the reduction of the slope in Table 7 by 25, 33 and 50%, respectively.

and W bosons. Whilst at moderate boost ( $p_T < 10$  TeV) a better granularity improves the identification efficiency, at large momenta ( $p_T > 10$  TeV) the efficiency saturates. Indeed extreme granularity at the calorimeter level will anyway be limited by the transverse size of the showers in the absorber, and only an optimised particle-flow approach that fully exploits tracking and calorimeter information can extract the maximum information from highly boosted topologies. From these preliminary studies it is clear that high transverse (and possibly longitudinal) granularity required for optimal boosted topologies identification performance, both in the tracking and the calorimeter systems. While further studies in full-simulation are needed to address this point, we set targets for the lateral and longitudinal segmentation of the FCC-hh calorimeters to fulfill the parameters given in Table 2.1.

### 2.3.5 Heavy flavour

New heavy states could decay to multi-TeV c and b quarks. FCC-hh detectors must therefore be capable of efficiently identifying multi-TeV long-lived hadrons. A  $p_T = 5$  TeV b-hadron is qualitatively very different from a  $p_T = 100$  GeV b-hadron. The latter decays, on average, within the vertex detector acceptance and can be identified by means of displaced vertex reconstruction. Conversely, the former, on average, decays at a distance  $\gamma c\tau = 50$  cm, well outside the pixel detector volume. Reconstructing such highly displaced b-jets will require a paradigm shift in heavy flavour reconstruction. Algorithms exploring large hit multiplicity discontinuities among subsequent tracking layers, see Ref. [23], are required. The success of such algorithms relies heavily on the excellent granularity of the tracking system, in both the longitudinal and transverse directions. High efficiencies ( $\epsilon_b > 60\%$ ) for corresponding low mis-identification probabilities ( $\epsilon_{u,d,s} < 1\%$ ) from light quark jets have to be achieved up to  $p_T = 5$  TeV. For example, searches for heavy resonances decaying to hadronic  $t\bar{t}$  pairs rely heavily on efficient b-tagging performance at such energies. The discovery reach for a specific  $Z'$  model, assuming several scenarios for b-jet identification at high energies, is shown in Fig. 2.6.

# Detector requirements from environment

## 3.1 Rates, collision parameters, cavern size

Particle physics detectors have shown significant performance improvements over recent decades. The development of large scale detector structures and access to a highly developed silicon industry with exponential performance growth have paved the way to ever more sophisticated detectors. The most recent incarnation of such detectors are e.g. the LHC detectors ALICE, ATLAS, CMS and LHCb. The original configuration of these detectors, their Phase-I upgrades, as well as their Phase-II upgrades in the middle of the decade, provide a good insight into the technology trends allowing for an initial projection of performance improvements and R&D challenges for the design of experiments at a future hadron collider.

Table 3.1 compares the detector challenges at the FCC-hh to those of LHC, HL-LHC and HE-LHC. The expected peak luminosity is around six times larger than at the HL-LHC while the bunch spacing is the same, 25 ns. Together with the moderate increase in total cross-section, this results in an average number of 950 pile-up events per bunch crossing, a 7.3 fold increase. Since the r.m.s.-bunch length has a value similar to the HL-LHC, the number of pileup events/mm (pile-up density) increases by the same factor, the average distance and time between these pile-up events are therefore only 125  $\mu\text{m}$  and 0.4 ps. This poses one of the main challenges to a detector at the FCC-hh collider: ultra low material budget of the first tracker layers ( $0.3 X_0/\text{layer}$ ), a position resolution of 5  $\mu\text{m}$  in the vertex tracker, and a timing capability of the order of 5 ps are required.

The number of charged particles per pp collision increases by 1.75 when going from 14 to 100 TeV, so the increase in hit rate and data rate when going from HL-LHC to FCC-hh is mainly due to the increase in luminosity. The track hit rate of 10 GHz/cm<sup>2</sup> in the first tracking layer is therefore about 15 times larger than at the HL-LHC. The total track rate of around 4000 GHz gives a glimpse at the significant data volume the tracker is producing. The 10 times larger integrated luminosity goal of the FCC-hh therefore leads to a formidable radiation number of almost  $10^{18}$  1 MeV neutron equivalent (1 MeV-neq) fluence hadrons/cm<sup>2</sup> and a total ionising dose of 300 MGy in the most exposed silicon layers, where the 1 MeV-neq is a key quantity to assess long-term damage for silicon sensors and electronics in general.

It is also noteworthy that the energy deposit per unit of rapidity at  $|\eta = 5|$  is around 4 kW, which poses an interesting challenge to the cryogenic system of the liquid argon calorimeter.

The  $b\bar{b}$  rate of 750 MHz, the high  $p_T$  jet rate of 90 MHz, the W rate of 390 kHz, and the Z rate of 120 kHz are all quite sizeable compared to the bunch-crossing rate of 30 MHz, so in addition to the trigger challenge there is also a serious challenge from the rate of physics data.



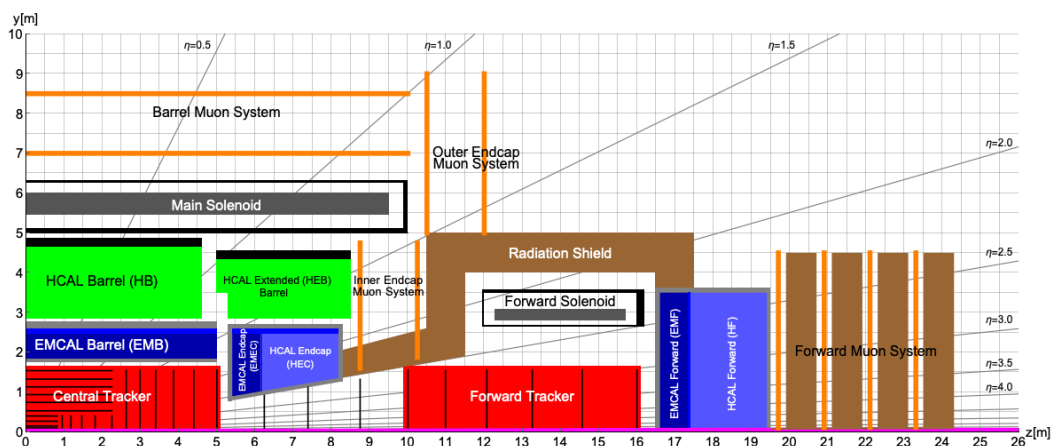


Fig. 3.1: Longitudinal cross-section of the FCC-hh reference detector. The installation and opening scenario for the detector requires a cavern length of 66 m, which is compatible with the baseline assumption of  $L^* = 40$  m for the FCC-hh accelerator.

A cross-section of the FCC-hh reference detector is shown in Fig. 3.1. The barrel and end-cap systems covering a rapidity range of  $|\eta| < 2.5$  are housed inside a 4T solenoid with an inner bore diameter of 10 m and length of 20 m. A forward system with a separate magnet coil of 5 m inner bore diameter covers the rapidity range of  $2.5 < |\eta| < 5-6$ . This brings the total length of the detector to around 50 m.

A muon system outside the magnet coil brings the enveloping diameter of the central system to 18 m, similar to the diameter of the ATLAS detector. It has to be noted that this reference detector is based on an un-shielded solenoid coil. Adding a flux return yoke would lead to a significant increase in the detector diameter and a significant increase in the cost of the magnet system. An active shielding coil around the muon system will slightly increase the detector radius but it also comes with a significant cost. The other problem of this solution is the need of a much larger shaft diameter for transport of the large shielding coil to the cavern. The un-shielded coil requires a shaft diameter of around 15 m, also similar to that of the ATLAS and CMS experiments.

A cross-section of the experiment cavern is shown in Fig. 3.2. A width of 35 m is sufficient to accommodate the FCC-hh reference detector as well as an FCC-ee detector with an IP that is radially displaced by 10.6 m. The diameter of the access shaft is 15 m. The service cavern that houses the detector services, like the cryogenic system, the gas systems, the cooling systems, the off detector electronics, etc., is 50 m from the main cavern. This distance allows the main and service caverns to be treated as independent constructions without the need for complex reinforcements between them. It also provides sufficient radiation shielding and it ensures that the magnetic stray field from the experiment magnet falls to below 5 mT. The additional latency of  $0.5 \mu\text{s}$  for control signals due to the round-trip distance of 100 m is small compared to typical trigger latencies of  $10 \mu\text{s}$ , as used for the trigger systems of the ATLAS and CMS experiments.

### 3.2 Radiation

The significant radiation levels expected at the FCC-hh create strong constraints on the choice of technologies for the various subsystems. While the average number of particles per collision is expected to increase by only a factor 1.6 due to the increase of centre-of-mass energy from 14 to 100 TeV from HL-LHC to FCC-hh, the increased collision rates, increased integrated luminosity goals, silicon layers very close to the beampipe, as well as increased forward acceptance, add one to two orders of magnitude of radiation load compared to the HL-LHC detectors.



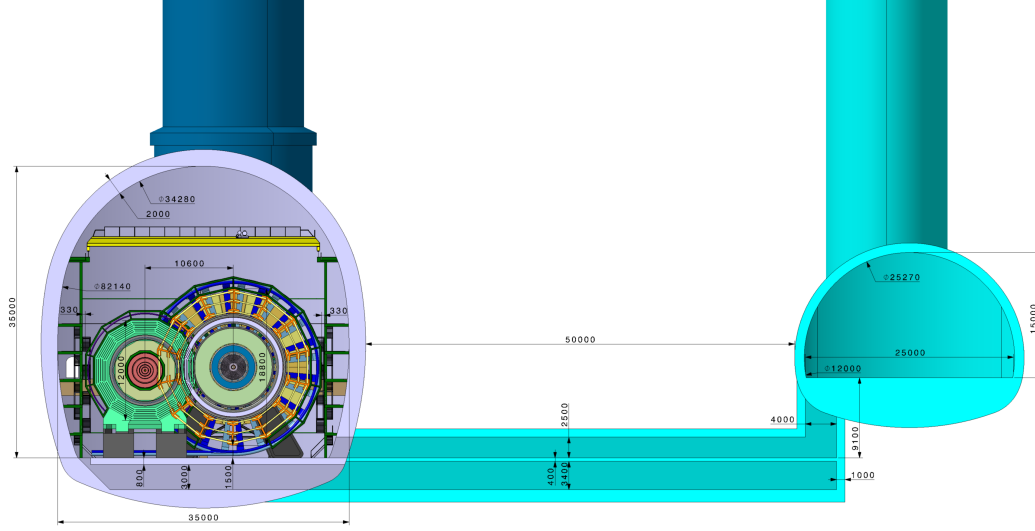


Fig. 3.2: Cross-section of the experiment cavern. A detector for the FCC-ee with a radial IP displacement of 10.6 m is shown as well. The total length of the cavern is 66 m.

For example, the charged particle flux on the first silicon sensor is expected to increase by one order of magnitude with respect to HL-LHC. Assuming that only primary hadrons pass through the first pixel layer and neglecting the bending in the magnetic field, the charged particle flux at a given radius  $r$  is  $L \times \sigma_{\text{inel}} \times \frac{dN}{d\eta} \times \frac{1}{2r^2\pi}$ . This number is indicated in Table 3.1 and does not depend on  $\eta$ , since  $\frac{dN}{d\eta}$  is constant. At  $r = 2.5$  cm this evaluates to around  $0.8 \text{ cm}^{-2}\text{s}^{-1}$  for HL-LHC and  $8 \text{ cm}^{-2}\text{s}^{-1}$  for FCC-hh. The 1 MeV-neq fluence can be calculated in a similar way. Assuming that only the primary hadrons impact the first tracker layer, the 1 MeV-neq fluence at a given radius is  $N_0 \times \frac{dN}{d\eta} \times \frac{1}{2r^2\pi}$ , where  $r = 2.5$  cm and  $N_0$  is the total number of collisions, amounting to  $3.2 \times 10^{18}$  for  $30 \text{ ab}^{-1}$  of pp collisions. For a silicon detector at a radial distance of 2.5 cm from the beamline, this evaluates to a fluence of  $8 \times 10^{17} \text{ cm}^{-2}$ , more than 20 times higher compared to the HL-LHC.

In order to obtain a reliable estimate of the radiation impact on each part of the detector, detailed Monte Carlo simulations are needed. They have been performed using FLUKA [26, 27], which is a Monte Carlo code benchmarked up to the TeV energy region and regularly used for beam-machine interaction studies [28], in particular, concerning the LHC and its upgrade.

### 3.2.1 Detector geometry and shielding conceptual design

The detector geometry has been modelled in FLUKA as shown in Figs. 3.3 and 3.4. All the different subdetectors, described in Section 1.2, have been included, as well as the magnetic field map. To optimise the computational time, only half of the detector has been implemented in FLUKA, but the contribution coming from the other half is accounted for by reflecting particles back at the  $z = 0$  plane. Particles produced in the  $z < 0$  half detector can indeed contribute to the load on the  $z > 0$  half of the detector and their contribution is equivalent to the one from particles produced in the  $z > 0$  half detector into the negative one.

A cylindrical cavern with a radius of 15 m, extending up to  $z = 33$  m, has been considered at this stage. The target absorber secondaries (TAS), the protection element in front of the final focus triplet, is located between 35.5 m and 38.5 m, according to the current design of the interaction region, which has a value of  $L^*$  of 40 m.

Table 3.1: Key numbers related to the detector challenges at different accelerators.

Parameter	unit	LHC	HL-LHC	HE-LHC	FCC-hh
$E_{\text{cm}}$	TeV	14	14	27	100
Circumference	km	26.7	26.7	26.7	97.8
Peak $\mathcal{L}$ , nominal (ultimate)	$10^{34} \text{ cm}^{-2} \text{ s}^{-1}$	1 (2)	5 (7.5)	16	30
Bunch spacing	ns	25	25	25	25
Number of bunches		2808	2760	2808	10600
Goal $\int \mathcal{L}$	$\text{ab}^{-1}$	0.3	3	10	30
$\sigma_{\text{inel}}$ [24]	mb	80	80	86	103
$\sigma_{\text{tot}}$ [24]	mb	108	108	120	150
BC rate	MHz	31.6	31.0	31.6	32.5
Peak pp collision rate	GHz	0.8	4	14	31
Peak av. PU events/BC, nominal (ultimate)		25 (50)	130 (200)	435	950
R.m.s luminous region $\sigma_z$	mm	45	57	57	49
Line PU density	$\text{mm}^{-1}$	0.2	1.0	3.2	8.1
Time PU density	$\text{ps}^{-1}$	0.1	0.29	0.97	2.43
$dN_{\text{ch}}/d\eta _{\eta=0}$ [24]		6.0	6.0	7.2	10.2
Charged tracks per collision $N_{\text{ch}}$ [24]		70	70	85	122
Rate of charged tracks	GHz	59	297	1234	3942
$\langle p_{\text{T}} \rangle$ [24]	GeV/c	0.56	0.56	0.6	0.7
Bending radius for $\langle p_{\text{T}} \rangle$ at $B = 4 \text{ T}$	cm	47	47	49	59
Total number of pp collisions	$10^{16}$	2.6	26	91	324
Charged part. flux at 2.5 cm, est.(FLUKA)	$\text{GHz cm}^{-2}$	0.1	0.7	2.7	8.4 (10)
1 MeV-neq fluence at 2.5 cm, est.(FLUKA)	$10^{16} \text{ cm}^{-2}$	0.4	3.9	16.8	84.3 (60)
Total ionising dose at 2.5 cm, est.(FLUKA)	MGy	1.3	13	54	270 (300)
$dE/d\eta _{\eta=5}$ [24]	GeV	316	316	427	765
$dP/d\eta _{\eta=5}$	kW	0.04	0.2	1.0	4.0
90% $b\bar{b} p_{\text{T}}^{\text{b}} > 30 \text{ GeV/c}$ [25]	$ \eta  <$	3	3	3.3	4.5
VBF jet peak [25]	$ \eta  <$	3.4	3.4	3.7	4.4
90% VBF jets [25]	$ \eta  <$	4.5	4.5	5.0	6.0
90% $H \rightarrow 4l$ [25]	$ \eta  <$	3.8	3.8	4.1	4.8
$b\bar{b}$ cross-section	mb	0.5	0.5	1	2.5
$b\bar{b}$ rate	MHz	5	25	250	750
$b\bar{b} p_{\text{T}}^{\text{b}} > 30 \text{ GeV/c}$ cross-section	$\mu\text{b}$	1.6	1.6	4.3	28
$b\bar{b} p_{\text{T}}^{\text{b}} > 30 \text{ GeV/c}$ rate	MHz	0.02	0.08	1	8
Jets $p_{\text{T}}^{\text{jet}} > 50 \text{ GeV/c}$ cross-section [24]	$\mu\text{b}$	21	21	56	300
Jets $p_{\text{T}}^{\text{jet}} > 50 \text{ GeV/c}$ rate	MHz	0.2	1.1	14	90
$W^+ + W^-$ cross-section [15]	$\mu\text{b}$	0.2	0.2	0.4	1.3
$W^+ + W^-$ rate	kHz	2	10	100	390
$W^+ \rightarrow l + \nu$ cross-section [15]	nb	12	12	23	77
$W^+ \rightarrow l + \nu$ rate	kHz	0.12	0.6	5.8	23
$W^- \rightarrow l + \nu$ cross-section [15]	nb	9	9	18	63
$W^- \rightarrow l + \nu$ rate	kHz	0.1	0.5	4.5	19

Table 3.2: Further key numbers related to the detector challenges at different accelerators.

Parameter	unit	LHC	HL-LHC	HE-LHC	FCC-hh
Z cross-section [15]	nb	60	60	100	400
Z rate	kHz	0.6	3	25	120
Z $\rightarrow ll$ cross-section [15]	nb	2	2	4	14
Z $\rightarrow ll$ rate	kHz	0.02	0.1	1	4.2
$t\bar{t}$ cross-section [15]	nb	1	1	4	35
$t\bar{t}$ rate	kHz	0.01	0.05	1	11

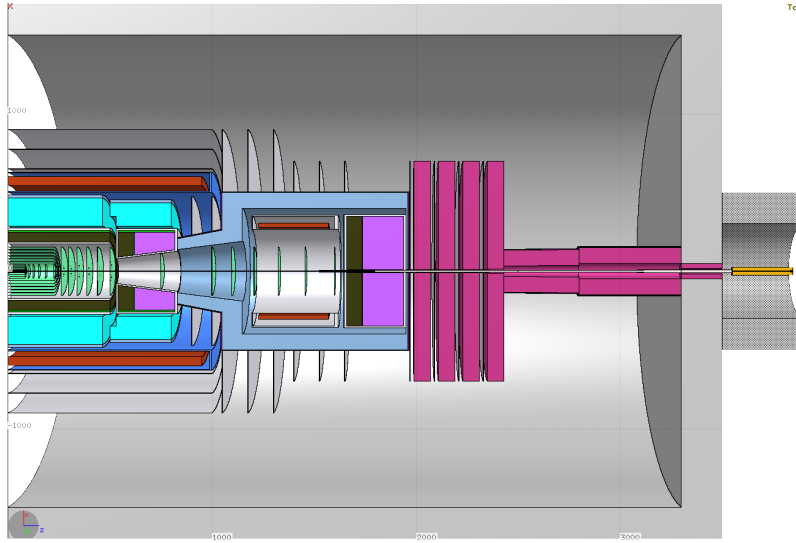


Fig. 3.3: Detector layout: top view at beam height. The  $x$  axis is in the horizontal plane, pointing outside the ring; the  $y$  axis is up (opposite to gravity), and the  $z$  axis is along the beam. The origin of the right-handed coordinate system corresponds to the nominal collision point.

Even though the TAS is located in the tunnel behind a 2 m thick concrete wall, it still represents a source of back-scattering into the detector. To prevent particles produced at the TAS from striking the detector components, a shielding concept has been proposed. The cavern entrance is filled with a conical shielding of cast iron down to  $|\eta| = 6$ . In addition to this, the cavern hosts forward shielding, which is composed of three different layers: a 1 m thick iron wall to remove high energy particles; a 5 cm thick layer of lithiated polyethylene placed externally to further slow down and capture neutrons; finally, a 1 cm thick layer of lead is added as outer boundary, in order to absorb the photons, already made rare due to the presence of lithium in the polyethylene that provides neutron capture without gamma emission. The shielding is conical up to  $|z| = 28$  m, and for larger values of  $z$  it is cylindrical.

Radiation values in the forward calorimeters are extremely high and previous studies [29] showed that particles created there populate the forward tracking stations, the external part of the HCAL barrel and the muon spectrometer in the barrel and in the endcap. In particular, the fluxes in the muon chambers have to be limited by adequate shielding. A massive shielding around the forward calorimeter which extends from the end of the endcap hadronic calorimeter to the end of the forward calorimeters has therefore been proposed. Like the forward shielding, it is composed of three layers, a 1 m thick layer of steel, a 5 cm thick layer of lithiated polyethylene, and finally a 1 cm thick layer of lead. Steel has been used instead of iron, due to the presence of a high magnetic field in this part of the detector. The shielding is effective and previous studies show that the neutron flux is reduced by 3–4 orders of

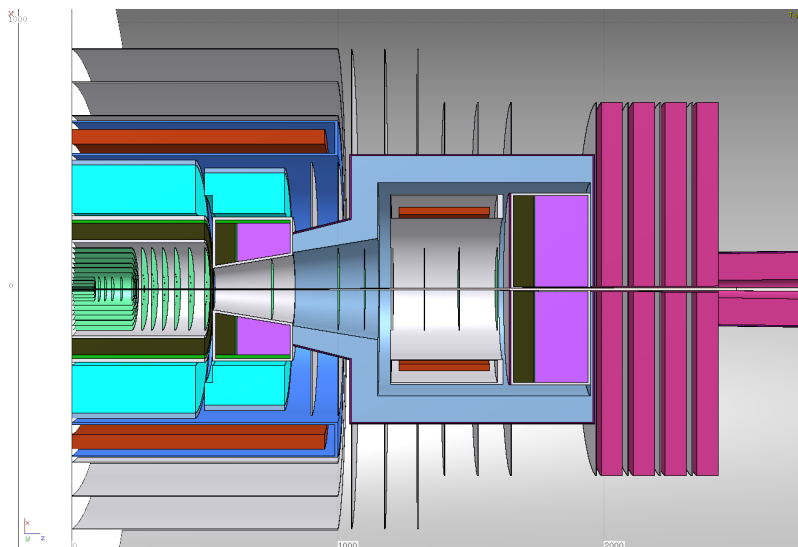


Fig. 3.4: Detector layout: zoom.

magnitude, depending on the location [29].

In order to reduce the rate on the forward tracking stations, shielding is also placed in front of the forward calorimeter. It is made of 5 cm of lithiated polyethylene, with a 2 mm thick aluminium cover on both sides. Despite its limited thickness, the shielding reduces the 1 MeV-neq fluence in the nearby tracking stations by up to a factor of three.

Finally, conical shielding made of iron is located between the beampipe and the forward muon chambers, extending from  $|\eta| = 6$  to 6.5. As will be discussed later, this shielding is very effective, even if the radiation levels on the forward muon spectrometer remain challenging.

### 3.2.2 Source term characterisation

Proton-proton collisions have been simulated using the DPMJET generator [30, 31], directly called from inside FLUKA. The proton-proton non-elastic cross section assumed, including inelastic scattering and single diffractive events, is 108 mbarn. The average number of particles generated in one collision is about 200. Moving away from the interaction point (IP), this multimodal population evolves, even before touching the surrounding material, because of the decay of unstable particles (in particular neutral pions decaying into photon pairs). At 5 mm from the IP the average number of particles (neglecting neutrinos) is around 250 and the main components are photons (almost 50%) and charged pions (40%). Neutral and charged kaons represent about 7.5% of the total, while protons and neutrons are 1.6% and 1.4% respectively. Antiprotons and antineutrons (1% each), and hyperons, contribute to the remaining fraction.

Figure 3.5a shows particle multiplicity, as a function of pseudorapidity for 100 TeV pp collisions, compared to 14 TeV pp collisions. Due to the larger centre-of-mass energy, the average number of particles is expected to increase by a factor 1.6. The distribution is characterised by two symmetric peaks around  $|\eta| = 1.5$ . About 80% of the particles are within the pseudorapidity coverage of the FCC detector,  $-6 < \eta < 6$ . Despite this large coverage, the majority of energy escapes from the detector. As can be seen from Fig. 3.5b, the energy distribution for pp collisions at 100 TeV peaks at  $|\eta|$  larger than 10 and the fraction of energy inside the detector acceptance is less than 5%. The total energy increase in the detector with respect to 14 TeV collisions is about a factor 5, assuming the pseudorapidity coverage of the present ATLAS and CMS detectors at 14 TeV ( $|\eta| < 5$ ).

Finally, the transverse momentum distribution of charged particles produced in 100 TeV collisions is shown in Fig. 3.6. The peak is at about 200 MeV and the average value is slightly above 600 MeV.

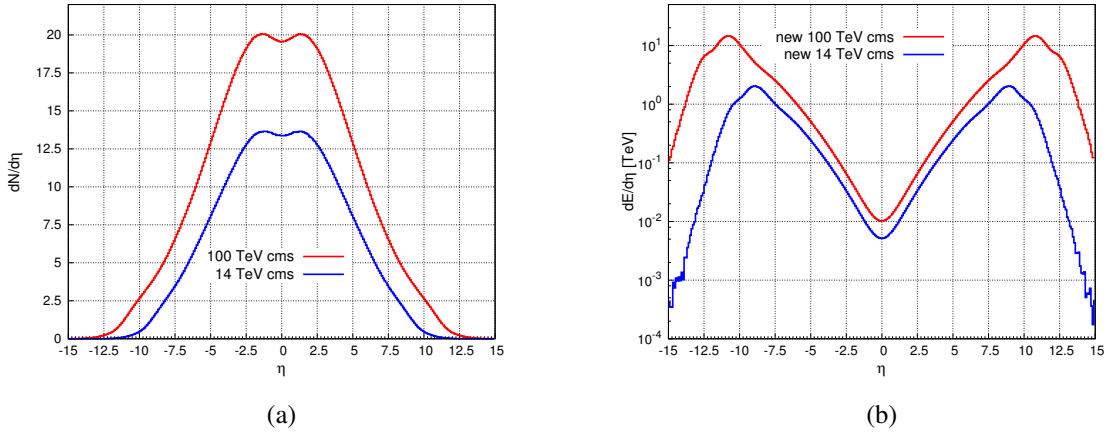


Fig. 3.5: Particle multiplicity distribution (a) and collision debris energy distribution (b) as a function of pseudorapidity, for 100 TeV pp collisions in red and 14 TeV pp collisions in blue, at 5 mm from the nominal interaction point, as calculated with DPMjet.

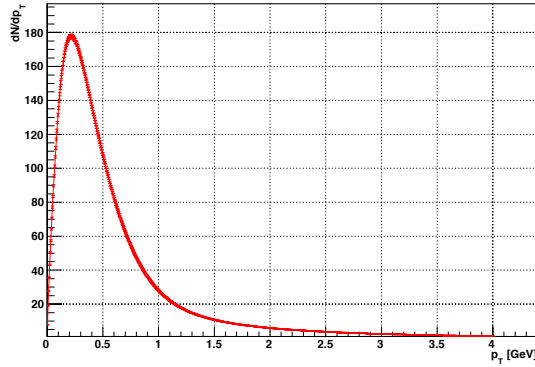


Fig. 3.6: Charged particle transverse momentum, for 100 TeV pp collisions, as calculated with DPMjet.

### 3.2.3 Radiation calculations

In order to assess the detector occupancy, fluxes have been evaluated for the ultimate target instantaneous luminosity of  $30 \cdot 10^{34} \text{ cm}^{-2} \text{ s}^{-1}$ . Only the charged particle flux is discussed in the following, but numbers for neutrals can be found in Ref. [29]. The long-term damage has been estimated in terms of dose and 1 MeV neutron equivalent fluence, taking the ultimate integrated luminosity of  $30 \text{ ab}^{-1}$  as reference.

An energy cutoff of 100 keV has been applied to all the particles, apart from electrons and positrons, for which a cutoff of 1 MeV is used, and for neutrons, which are considered down to thermal energies.

Since the detector is characterised by rotational symmetry, a cylindrical scoring has been considered and all the values are averaged over the azimuthal angle  $\phi$ . The resolution along the  $z$ -axis is 5 cm, while the radial resolution is 5 mm in the central region up to  $R = 175 \text{ cm}$  and 10 cm elsewhere.

#### 3.2.3.1 Charged particle fluxes

The charged particle flux in the  $R$ - $z$  plane is shown in Fig. 3.7. The rates have a significant radial dependence, but a weak dependence on  $z$ , as expected since  $\frac{dN}{d\eta}$  has only a weak dependence on  $\eta$ . Equi-fluence lines are essentially parallel to the  $z$  axis.

Figure 3.8 shows the charged particle fluxes in the tracker at five different longitudinal positions,

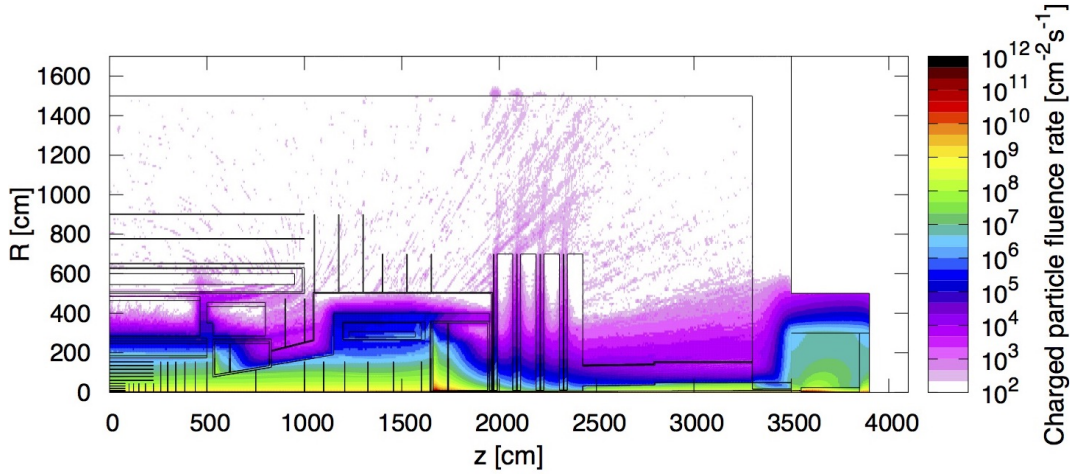


Fig. 3.7: Charged particle flux for an instantaneous luminosity of  $30 \cdot 10^{34} \text{ cm}^{-2} \text{ s}^{-1}$ . Values are averaged over the azimuthal angle  $\phi$ . The origin of the coordinate system corresponds to the nominal collision point.

two in the barrel tracker at 2.5 and 4.8 m and three in the forward tracker at 7.5, 12, and 16 m. Figure 3.8, in the right plot, also shows the flux distribution in the second forward muon chamber at  $z = 21$  m.

The values in the barrel tracker range from  $2 \cdot 10^{10} \text{ cm}^{-2} \text{ s}^{-1}$  in the first pixel layer at  $r = 2.5$  cm to  $10^6 \text{ cm}^{-2} \text{ s}^{-1}$  at larger radii. The peak structure, visible in the distributions at  $z = 2.5$  and 4.8 m, reflects the position of the cylindrical tracking stations. The flux rises above  $7 \cdot 10^6 \text{ cm}^{-2} \text{ s}^{-1}$  at the entrance of the ECAL, while it is reduced to  $1.5 \cdot 10^5 \text{ cm}^{-2} \text{ s}^{-1}$  at the entrance of the barrel HCAL.

Values are significantly higher in the endcap calorimeters, up to  $10^8 \text{ cm}^{-2} \text{ s}^{-1}$  in the ECAL and up to  $10^7 \text{ cm}^{-2} \text{ s}^{-1}$  in the HCAL. Particles produced in these subdetectors impact on the nearby tracking stations, as can be seen in Fig. 3.8. The fluence distribution in the forward tracking station at  $z = 7.5$  m shows a bump at a radial distance of about 90 cm, due to particles coming from the hot spot in the endcap ECAL. The second bump, followed by a rapid flux decrease, is due to the entrance into the endcap HCAL.

In the forward calorimeters the flux rises to  $10^{11} \text{ cm}^{-2} \text{ s}^{-1}$  in the ECAL and  $4 \cdot 10^{10} \text{ cm}^{-2} \text{ s}^{-1}$  in the HCAL. From there, particles populate the nearby tracking stations. Beyond a radius of 40 m, the flux values at  $z = 12$  and 16 m, presented in the right plot of Fig. 3.8, are a factor of two to three higher than those in the tracker barrel, shown on the left plot.

Thanks to the presence of the shielding around the forward calorimeter, the charged particle rate in the barrel and in the outer endcap muon chambers does not exceed  $500 \text{ cm}^{-2} \text{ s}^{-1}$ . The charged particle rate is dominated by electrons, created from high energy photons in the MeV range. These photons are created by processes related to thermalisation and capture of neutrons that are produced in hadron showers, mainly in the forward region. These processes immerse the muon system and the cavern in a ‘gas’ of high energy photons that convert to electrons in the muon chamber material. Because of their relatively low energy, these electrons curl around the magnetic field lines and reveal the B-field, as seen in Fig. 3.7. The rate in the inner endcap muon system goes up to  $10^4 \text{ cm}^{-2} \text{ s}^{-1}$  due to the leakage coming from the gap between barrel and endcap calorimeters. These rates are comparable to those in the ATLAS, CMS and LHCb muon systems and the gaseous detectors employed in these experiments can therefore be adopted in these regions. The values in the forward muon system are, instead, significantly higher, as shown by the orange curve in plot (b) of Fig. 3.8. The rate decreases by two orders of magnitude between 5 and 10 cm, thanks to the presence of the shielding between the beampipe and the muon chambers, but is still of the order of  $10^8 \text{ cm}^{-2} \text{ s}^{-1}$  for  $z > 20$  m, almost  $8 \cdot 10^8 \text{ cm}^{-2} \text{ s}^{-1}$  in the first muon chamber downstream the forward calorimeter. It is only at a radial distance of 1 m from the beampipe that the rate decreases to  $500 \cdot 10^3 \text{ cm}^{-2} \text{ s}^{-1}$ , comparable to the rates in the LHCb muon system.



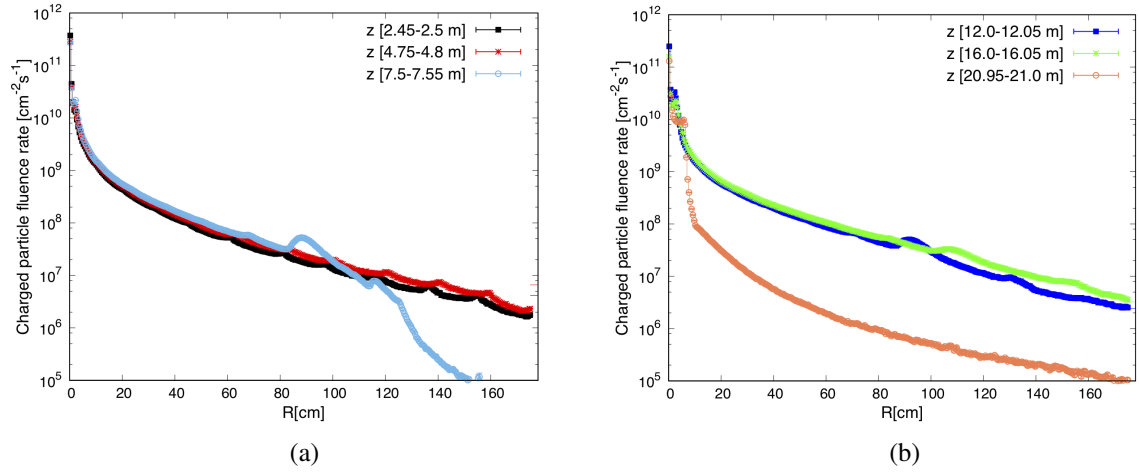


Fig. 3.8: Charged particle flux for an instantaneous luminosity of  $30 \cdot 10^{34} \text{ cm}^{-2} \text{ s}^{-1}$  as a function of distance from the beamline, at different  $z$  positions in the detector. The values are averaged by the azimuthal angle  $\phi$ .

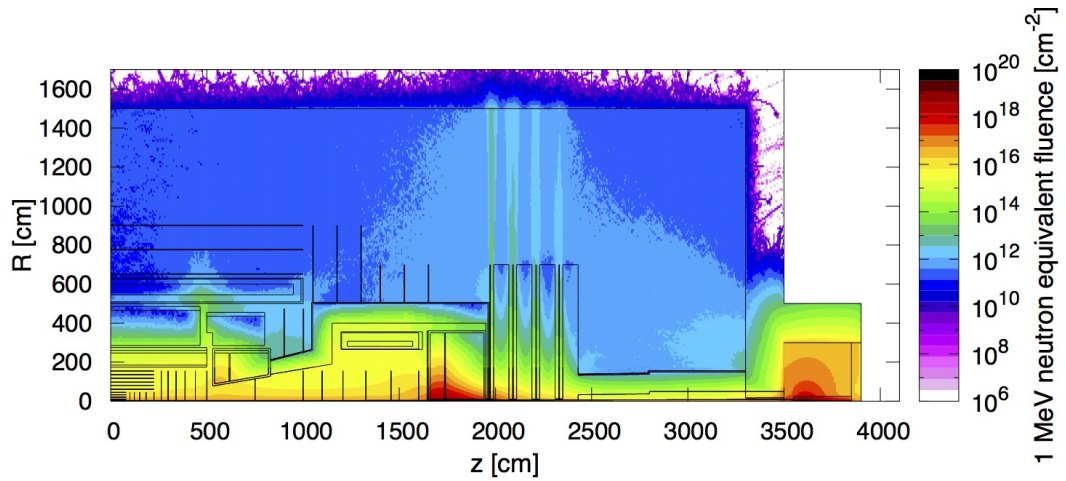


Fig. 3.9: 1 MeV neutron equivalent fluence for an integrated luminosity of  $30 \text{ ab}^{-1}$ . Values are averaged over the azimuthal angle  $\phi$ . The origin of the coordinate system corresponds to the nominal collision point.

### 3.2.3.2 1 MeV neutron equivalent fluence

Figure 3.9 shows the 1 MeV neutron equivalent fluence in the  $R$ - $z$  plane, while Fig. 3.10 shows 1 MeV-neq as a function of distance from the beam axis, at the longitudinal positions already considered in Fig. 3.8.

The 1 MeV-neq fluence in the first tracker layer is  $5.5 \cdot 10^{17} \text{ cm}^{-2}$ . Beyond a radius of 40 cm the value drops below  $10^{16} \text{ cm}^{-2}$  and in the outer parts it is around  $5 \cdot 10^{15} \text{ cm}^{-2}$ . Technologies used for the HL-LHC detectors are therefore applicable at radii larger than 40 cm. Novel sensors and readout electronics have to be developed for the innermost parts of the tracker.

The fluence in the centre of the detector at the entrance of the barrel ECAL is almost above  $4 \cdot 10^{15} \text{ cm}^{-2}$  and is then reduced by the calorimeters by several orders of magnitude, to below  $10^{12} \text{ cm}^{-2}$  on the external side of the HCAL. At  $z > 4 \text{ m}$ , the values in the outer part of the barrel HCAL stay above  $10^{14} \text{ cm}^{-2}$ , due to the particles coming from the gap between the barrel and the endcap calorimeters. In the gap itself, where the readout cables of the tracker will be routed, the 1 MeV-neq fluence is between

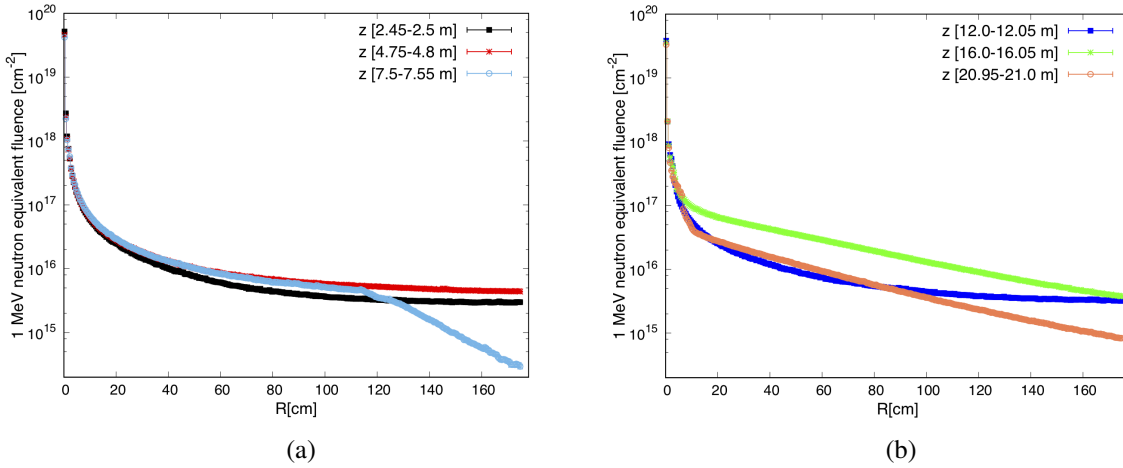


Fig. 3.10: 1 MeV neutron equivalent fluence after an integrated luminosity of  $30 \text{ ab}^{-1}$  as a function of distance from the beamline, at different  $z$  positions in the detector, as in Fig. 3.8. The values are averaged over the azimuthal angle  $\phi$ .

$10^{16}$  and  $10^{14} \text{ cm}^{-2}$ .

The values on the inner side of the endcap calorimeters are higher than in the barrel and are above  $10^{16} \text{ cm}^{-2}$  in both the ECAL and in the HCAL calorimeters. The effect of the backscattering from the endcap calorimeter is visible comparing the black and red curves in plot (a) of Fig. 3.10. For radial values above 50 cm, the fluence at  $z = 4.8 \text{ cm}$  is 20% higher with respect to  $z = 2.5 \text{ cm}$ . The fluence in the first forward tracking station is very similar to the fluence at  $z = 4.8 \text{ cm}$  up to a radial distance of 1.2 m, where it drops due to the entrance into the hadronic calorimeter.

In the inner part of the forward calorimeters, the radiation levels rise to extreme values of  $5 \cdot 10^{18} \text{ cm}^{-2}$  and decrease to below  $10^{16} \text{ cm}^{-2}$ , for radial distances larger than 2 m. Despite the presence of shielding in front of the forward calorimeter, particles produced there impact the forward tracker and the fluence in the tracking station at  $z = 16 \text{ m}$  is up to 4 times higher than the fluence at  $z = 12 \text{ m}$ .

The shielding around the forward calorimeter reduces the fluence by several orders of magnitude and the values in the barrel and the outer endcap muon chambers are of the order of  $10^{12} \text{ cm}^{-2}$ . The fluence in the inner endcap chambers is an order of magnitude higher. The fluence in the forward muon spectrometer is represented by the orange curve in Fig. 3.10. The values decrease by a factor of five between 5 and 10 cm, thanks to the presence of the conical shielding, but they remain above  $10^{16} \text{ cm}^{-2}$ ; almost  $2 \cdot 10^{17}$  in the first muon tracking station downstream of the forward calorimeter and about  $5 \cdot 10^{16} \text{ cm}^{-2}$  for  $z > 20 \text{ m}$ . The 1 MeV-neq fluence only decreases below  $10^{15} \text{ cm}^{-2}$  beyond 2 m from the beamline.

### 3.2.3.3 Total ionising dose

Another key number for long-term damage of electronics and detector elements is the total ionising dose, which is shown in Fig. 3.11. Figure 3.12 shows the integrated dose as a function of distance from the beam axis, at the longitudinal positions already considered in Fig. 3.8.

The expected dose in the first silicon layer is 300 MGy in the centre of the detector and almost 400 MGy at  $|z| = 70 \text{ cm}$ , about 30 times higher than what is expected at the HL-LHC. Present technologies cannot sustain these values and novel detectors need to be developed for the innermost part of the tracker, up to a radius of 40 cm. Beyond this value the dose is below 10 MGy, as can be seen in Fig. 3.12, and is reduced to 0.1 MGy in the external part of the tracker barrel.



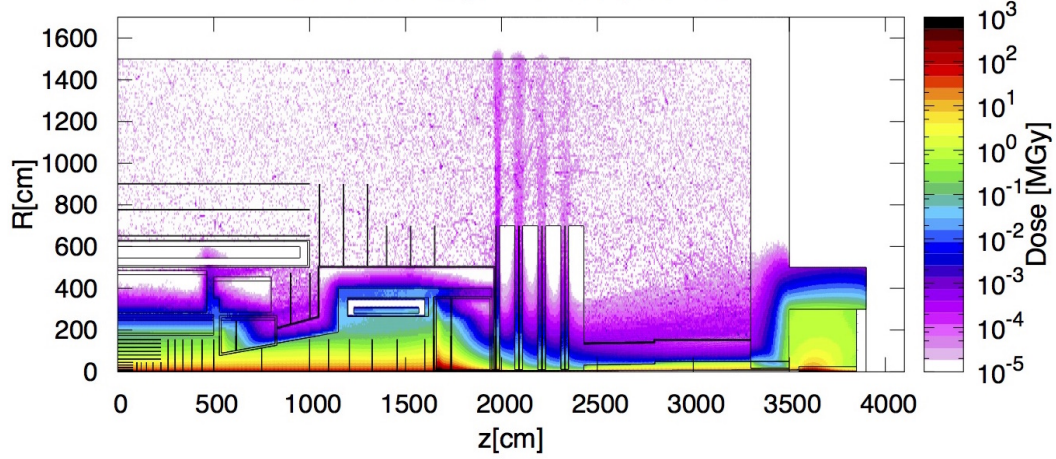


Fig. 3.11: Total ionising dose at  $30 \text{ ab}^{-1}$ . Values are averaged over the azimuthal angle  $\phi$ . The origin of the coordinate system corresponds to the nominal collision point.

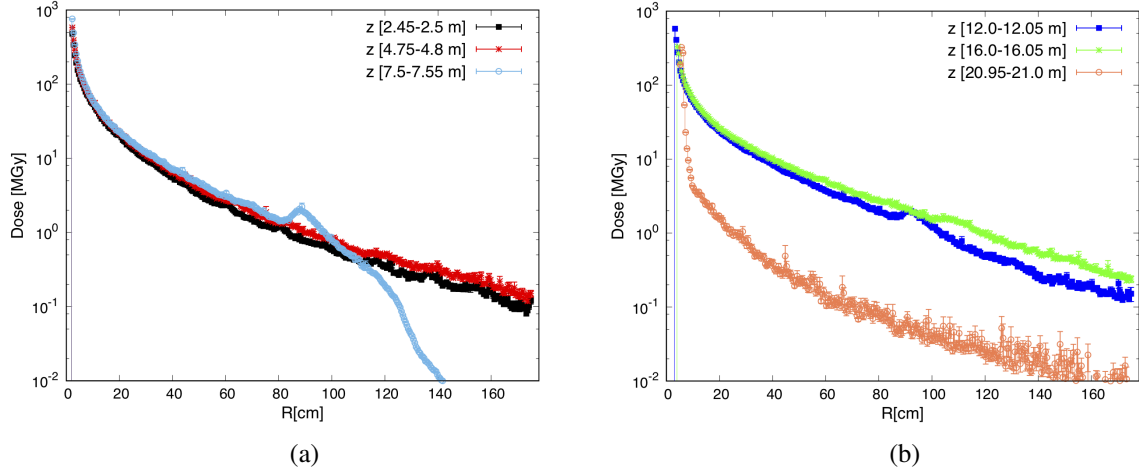


Fig. 3.12: Dose, after an integrated luminosity of  $30 \text{ ab}^{-1}$  as a function of distance from the beamline, at different  $z$  positions in the detector, as in Fig. 3.8. The values are averaged over the azimuthal angle  $\phi$ .

The maximum dose in the central region of the ECAL is 0.2 MGy, while the values are around 6 kGy in the HCAL barrel and 8 kGy in the HCAL extended barrel. Conventional organic scintillators can be considered for the hadronic calorimeter in the barrel region, since the dose is below 10 kGy, which is the limiting number for the use of this technology. On the other hand, the dose in the endcap is significantly higher and reaches almost 4 MGy in the ECAL and 0.7 MGy in the HCAL. A calorimeter based on liquid argon technology is therefore considered for this subdetector. Particles produced in endcap calorimeters strike the nearby tracking stations, as can be seen in plot (a) of Fig. 3.12. The fluence distribution in the forward tracking station at  $z = 7.5$  m shows a bump at a radial distance of about 90 cm, due to particles coming from the hot spot in the endcap ECAL. The curve drops at about 1.2 m due to the entrance into the endcap HCAL.

In the forward calorimeters the dose reaches extreme values of 5 GGy in the ECAL and 1 GGy in the HCAL. At a radial distance of 1.5 m the dose is below 10 MGy and present technologies can be used. The impact of particles coming from the forward calorimeters to the nearby tracking stations can be seen comparing the green and blue curves in plot (b) of Fig 3.12. Beyond 1 m from the beampipe, the values at  $z = 16$  m are about a factor of two higher than those at  $z = 12$  m.

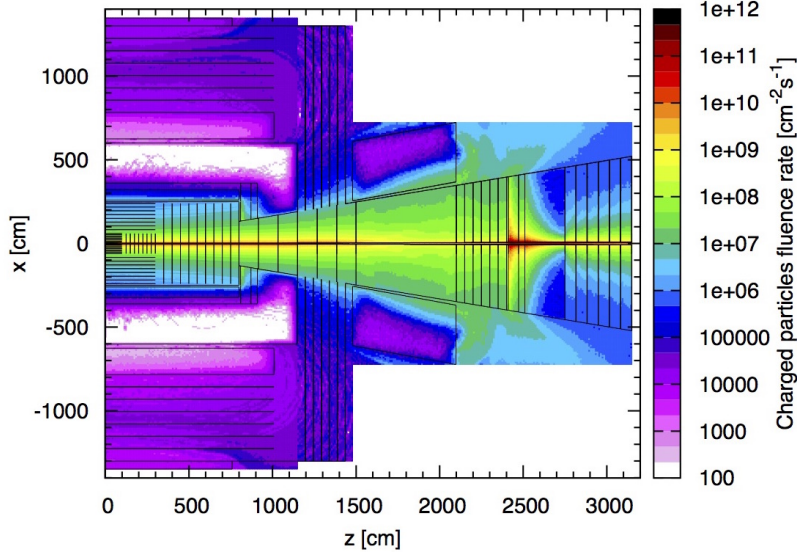


Fig. 3.13: Dipole option: charged particles flux for an instantaneous luminosity of  $30 \cdot 10^{34} \text{ cm}^{-2} \text{ s}^{-1}$ : top view. In the central region ( $z < 10.5 \text{ m}$ ) values are azimuthally averaged over 40 degrees around 0 (positive  $x$ ) and  $\pi$  (negative  $x$ ). In the forward region an average in the vertical direction around  $y = 0$  is done on a bin of 1 cm up to  $|x| = 0.6 \text{ m}$  and on a 10 cm bin for larger  $x$  values. The origin of the coordinate system corresponds to the nominal collision point.

The values in the barrel and outer endcap muon chambers are below 1 kGy. In the inner endcap chambers the dose reaches 1 kGy, due to the leakage from the gap between the barrel and the endcap calorimeters. The conical shielding between the beampipe and the forward muon spectrometer reduces the dose by almost a factor 50 and the maximum value is below 5 MGy for muon chambers at  $z > 20 \text{ m}$ , as can be seen in plot (b) of Fig. 3.12. The dose in the first chamber downstream of the calorimeters is higher and reaches 30 MGy.

Finally, the peak displacement, which can be seen comparing the three curves in plot (b) of Fig. 3.12, is due to the conical shape of the beampipe in the forward region.

### 3.2.4 Forward dipole option

Another proposed detector layout has two forward dipoles instead of the forward solenoids, as described in Section 1.2. The radiation values in the central part of the detector are very similar to the geometry with the forward solenoids. However, the presence of a dipole field affects the radiation levels in the external part of the detector and creates asymmetries.

These effects can be seen in Figs. 3.13 and 3.14, which show the charged particle flux distribution on the  $z - x$  plane at  $y = 0$  and on the  $z - y$  plane at  $x = 0$ , respectively for a detector option with forward dipoles as discussed in Ref. [29]. The distribution of charged particles is broader in the  $z - x$  plane, due to the effect of the dipole field directed along the  $y$  axis. This is also visible in the  $z - y$  plane, where the higher flux red line at  $y > 0$  between 14 and 17 m is due to electrons and positrons, which spiral around the magnetic field lines.

### 3.2.5 Detector material activation

A key radiation aspect related to the detector maintenance is the activation of the detector material and the related cool-down time, as indicated in Fig. 3.15. Towards the end of FCC-hh operation, having already collected a large fraction of the luminosity, the dose rate levels are around 1 mSv/h in the entire tracker volume after about one week of cooling time, and the values do not decrease significantly for one month

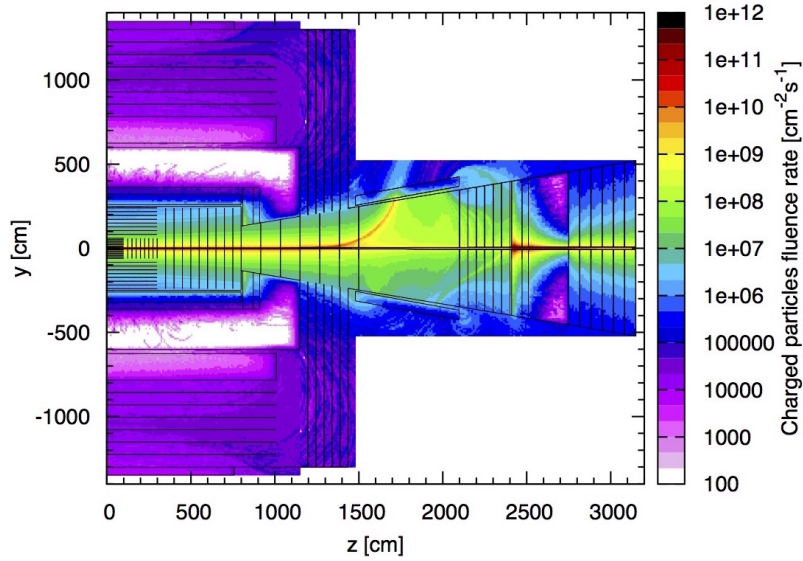


Fig. 3.14: Dipole option: charged particles flux for the forward dipole option for an instantaneous luminosity of  $30 \cdot 10^{34} \text{ cm}^{-2} \text{ s}^{-1}$ : lateral view. In the central region ( $z < 10.5 \text{ m}$ ), values are azimuthally averaged over 20 degrees around  $\frac{\pi}{2}$  (positive  $y$ ) and  $-\frac{\pi}{2}$  (negative  $y$ ). In the forward region an average in the horizontal direction around  $x=0$  is done on a bin of 1 cm up to  $|y| = 0.6 \text{ m}$  and on a 10 cm bin for larger  $y$  values.

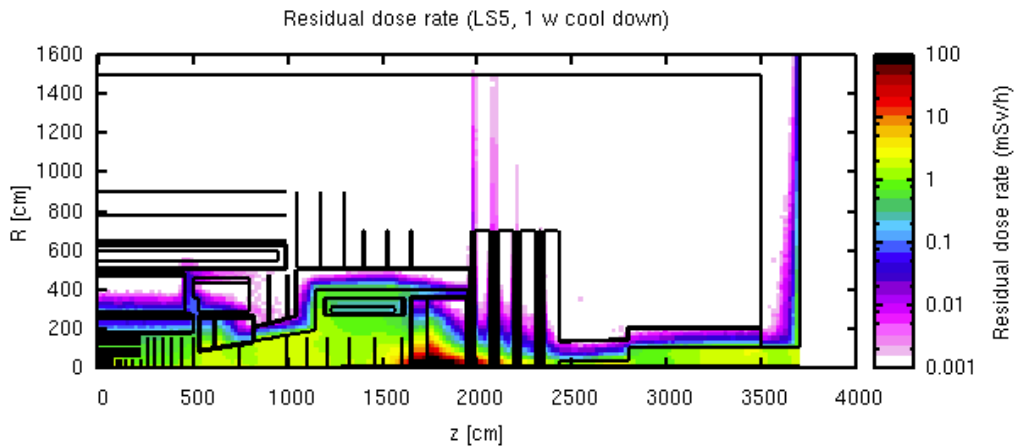


Fig. 3.15: Radiation dose rate after 1 week of cool-down towards the end of FCC-hh operation.

or one year of cooling time. This radiation originates mainly from the highly activated calorimeters. Consequently, the opening of the detector and the placement of shielding elements must, to a large extent, be automated, in order to allow access for maintenance and to limit the dose to personnel.



### 4.1 Introduction

In the realm of software we chose a very pragmatic approach to support the FCC studies, taking advantage of the existing software as much as possible.

The LHC experiments took the approach of having dedicated event data models, simulation and reconstruction software. While this diversity is definitely needed in some areas of the experiment software, it leads to some duplication of effort in other areas. The aim of the FCC software, in contrast, is to provide a framework to facilitate studies by all of the experiments envisioned for the three collider variants. This immediately generates some requirements for components of the framework:

- Flexible detector description for the different experimental setups.
- Event data model that can be adapted easily to accommodate different physics interests.
- Reconstruction software that performs well for both the high multiplicity events at FCC-hh and the precision measurements planned for FCC-ee.
- An analysis framework that is simple to use (outside of the full framework) and combines the performance of C++ with the flexibility of Python.

The concept of sharing some functionality was already proven to work in LHCb and ATLAS which use the same underlying event processing framework GAUDI [32]. GAUDI was therefore a natural choice as the framework for the FCC software (FCCSW).

### 4.2 Event data model

The event data model of the FCC study is shared between the various collider options and is implemented using the PODIO [33] library, choosing composition over complex inheritance relations. The choice of object definitions is inspired by experience from both the LHC experiments and the Linear Collider studies.

### 4.3 Full and fast simulation

The simulation package is an important part of the FCCSW software for both the detector and physics studies. It makes use of the external toolkits common for the HEP community, including DELPHES [34] for parametric simulation and GEANT4 [35–37] for both detailed (full) and parametric (fast) simulation.

The experiment independent event generation software is taken from the GAUSSINO package which is developed in collaboration with the LHCb experiment [38]. Also, the part of the simulation that can be experiment independent is shared between FCCSW and GAUSSINO.

### 4.3.1 Full simulation

Detailed simulation of the particles' passage through the detector is performed with GEANT4. The geometry description is provided by the DD4HEP toolkit [39], including the information about which volumes are sensitive to the particle passage and produce the signal that is passed to the reconstruction algorithms.

Due to the high pileup rates at FCC-hh, the detector simulation of the full event is however impractical. A more efficient use of computing resources is achieved by pre-simulating a sufficiently large pool of minimum bias events - specific to a given detector layout and beam configuration - and overlaying them after the simulation of the hard scatter event. FCCSW includes the necessary infrastructure to create and overlay background data (minimum bias events or beam background in the case of FCC-ee) from pools, randomising the input in order to minimise bias due to reuse of data.

#### 4.3.1.1 GEANT4 limitations

The electromagnetic physics of GEANT4 is already able to provide a reasonably accurate description of all the main physics processes relevant for the detector simulation of FCC-ee, FCC-eh and FCC-hh. The situation is different for the hadronic physics of GEANT4. Besides the well-known, unavoidable limitations of all the present hadronic models, due to the non-perturbative nature of strong interactions, there are also two aspects missing in the current GEANT4 simulations.

The first, and most important, is the lack of gluon-jet emissions in the hadronic interactions modelled by both hadronic string models of GEANT4, FRITIOF (FTF) and QUARK-GLUON-STRING (QGS) [35–37]. This means that for a hadron of (laboratory kinetic) energy above a few TeV, flying in a detector and having a strong interaction with a nucleus (more frequently in the calorimeter), all the secondary hadrons are produced by the fragmentation of strings formed by the constituent quarks of the projectile hadron and the participant nucleons of the target nucleus. There are no secondary hadrons produced by the fragmentation of gluons radiated by one of the quarks involved in the interaction. This simplified approach is sufficient at LHC, where single hadrons (in jets produced by beam collisions) rarely have energies above a TeV. But this is not the case for FCC-hh, where the most energetic jets can have constituent hadrons with higher energies than this: the strong interactions of these energetic hadrons in the detector are therefore not properly simulated by the current GEANT4 simulations. The impact of this limitation on the expected jet energy resolution for the most energetic jets at the FCC-hh detector is unknown. By interfacing GEANT4 with a cosmic-ray hadronic generator, such as EPOS [40], it will be possible to handle the simulation of hadronic interactions at very high energies, and then passing the secondary hadrons that are produced by this external generator back to GEANT4 to get a first estimate of the effect.

The second limitation of GEANT4 hadronic physics is the lack of hadronic interactions (elastic and inelastic) for charmed and bottom hadrons, as well as for tau leptons. Given the very short lifetimes of these particles, neglecting their hadronic interactions in a detector simulation is, in general, a very good approximation. However, highly boosted charmed and bottom hadrons as well as tau leptons may reach the beam pipe or the first layers of the tracker. GEANT4 currently only includes the electromagnetic interactions of these particles (essentially ionisation and multiple scattering for the charged ones). A possible extension of GEANT4 hadronic physics to cover the hadronic interactions of charmed and bottom hadrons as well as of tau leptons is under consideration. Both LHC-HL and FCC-hh may benefit from this extension, which however requires considerable effort.

### 4.3.2 Fast simulation

Full accuracy simulation is very detailed and takes into account all of the physics processes that the particles may undergo and therefore it consumes a lot of CPU time. At the early stage of the detector design and for different physics cases such accuracy is not needed. Therefore, the overall response of the



detector may be simulated in a parametric way.

Some physics studies may use the parametric simulation provided by DELPHES [34]. To extend the possible applications of the fast simulation, it is crucial to allow the interplay of both full and fast simulation within the same event, for instance as in the Integrated Simulation Framework (ISF) [41] developed in ATLAS. The different simulation types are mixed at the level of the event processing framework in ISF. However, it is possible to make use of the hooks provided by GEANT4 and to perform the simulation entirely within its framework, naturally mixing it with the full simulation where needed.

#### 4.3.2.1 DELPHES

DELPHES framework is used in HEP community for the parametric simulation with the general detector description used for the phenomenological studies. Given the detector resolutions and the event to simulate, it propagates the initial long-lived particles in the uniform magnetic field, smears their momenta and reconstructs leptons, jets and missing energy. A description of the latest developments in DELPHES can be found in the conference proceedings presented in Ref. [42].

#### 4.3.2.2 GEANT4

GEANT4 provides the tools to define the parameterisation and the trigger criteria. The parameterisation can only be performed in the defined volumes, for certain particles and if kinematic conditions are fulfilled. If fast simulation is not triggered, the standard full simulation of GEANT4 is performed.

The current implementation of the fast simulation models in FCCSW includes the model for the tracking detectors and the parameterisation of electromagnetic showers in the calorimeters. The parameterisation for the tracking detectors is performed by smearing the particle space-momentum coordinates and for calorimeters by reproducing the particle showers. The parameterisation may come from either external sources, or from the full simulation (which is detector-dependent but also more accurate).

The tracker resolutions may be derived from measurements of existing detectors or from various tools, TKLAYOUT [43] for instance, used in the CMS tracker performance studies. Regarding the calorimeters, the longitudinal and radial shower profiles can be parameterised using the GFLASH library [44]. Further details of the FCC simulation in GEANT4 can be found in the conference proceedings presented in Ref. [45].

### 4.4 Reconstruction software

The ATLAS tracking software was successfully used in production during LHC operation and has been improved over time to cope with the increasing track multiplicity due to increasing numbers of simultaneous events at the LHC [46]. Many parts of the software do not depend on the layout of the specific experiment. In a recent effort, ATLAS has extracted the generic components into a standalone package: A Common Tracking Software (ACTS). With first implementations of track seeding, extrapolation and fitting algorithms and an efficient tracking geometry description, ACTS can be used for the complete track reconstruction workflow. The details of the tracking software itself are described in Ref. [47]. This central piece of ATLAS reconstruction software is being adapted for tracking studies in the context of the FCC design study.

The integration of ACTS is eased by the geometry plugins of ACTS, which can automatically generate the specialised geometry description needed for the tracking procedure from sufficiently generic sources, such as the DD4HEP detector description used in FCCSW.

ACTS is currently in a testing phase and FCCSW is one of the early systems to use and adopt it. Integration into the FCC software framework is on-going but a first demonstrator exists.

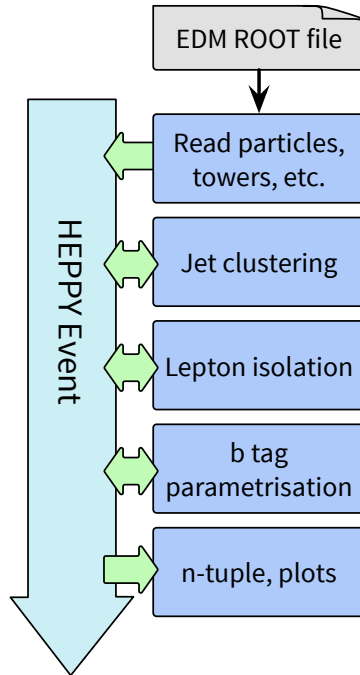


Fig. 4.1: Visualisation of a typical workflow in the High Energy Physics PYTHON analysis framework (HEPPY): The event data is translated and put into the HEPPY event, various modules are run that implement analysis or even reconstruction tasks.

## 4.5 Analysis framework

High Energy Physics with Python (HEPPY) is a modular Python-based framework for analysis of HEP collision events. It was originally developed in CMS and is re-used in the context of the FCC design study. Figure 4.1 illustrates a typical analysis workflow of an analysis performed with HEPPY.

The event processing is facilitated through a python configuration system similar to those of the CMS software or GAUDI. This configuration layer allows easy customisation of module properties without touching their implementation. As the illustration indicates, this enforces a modular approach where individual steps of analysis, such as selection or reconstruction algorithm prototypes are implemented in separate configurable modules. The HEPPY event that describes the collision event data is central to the event processing and information is passed to other modules by adding it to the event.

The HEPPY event is a data format that wraps the physics objects described in the experiment event data model. A first step for the converters implemented for the CMS and FCC event data format is to wrap the data in the HEPPY Python objects. Algorithms are then scheduled in a central event loop manager. As mentioned before, information exchange between algorithms is facilitated through reading from and writing to the event content.

Components of HEPPY are currently being ported to C++ to allow better integration into the main FCC event processing framework. This is being done in a staged approach and ported components are still usable via bindings automatically generated by the ROOT framework [48]. This allows a flexible and quick turn around in the prototyping phase and high performance in production.

The software framework for the FCC design study makes use of existing software packages that are experiment independent and leverages other packages, such as the LHCb simulation framework or the ATLAS tracking software. It has been demonstrated that they can be modified to factor out any experiment dependency. A novel approach to the implementation of an event data model which is generated from configuration files has been defined. This allows customisation, and enables parallelisation by supporting a corresponding data layout. This customisation makes it straight-forward to use outside



of the FCC software.

The simulation framework of LHCb was adapted to the use-case of the FCC design effort, implementing an integrated fast and full simulation. This allows the flexible adaptation of the level of detail of the simulation according to the needs of a given study. A switch between full and fast simulation can be based on various properties of particles or detectors which allows mixing of the two flavours in the same event.

The FCC software makes use of existing software solutions, working together with the LHC community on further abstraction from the experiment environment where needed. New contributions, such as the event data model library, are being developed with this abstraction in mind in order to ease sharing them across multiple experiments.

## 4.6 The FCC-hh detector parameterisation in DELPHES

### 4.6.1 Introduction

DELPHES is a framework for multipurpose detector fast-simulation [34]. Instead of simulating the time-consuming interactions of stable particles with matter (as done in Ref. [37] for example), DELPHES makes use of a parameterised detector response in the form of resolution functions and efficiencies. The DELPHES simulation includes a track propagation system embedded in a magnetic field, electromagnetic and hadron calorimeters, and a muon identification system. Physics objects which can be used for data analysis are then reconstructed from the simulated detector response. These include tracks and calorimeter deposits and high level objects such as isolated leptons, jets, taus, and missing energy. DELPHES also includes a simplistic particle-flow reconstruction that combines tracks and calorimeter information in an optimal way to form particle candidates. Such particles are then used as input for jet clustering, missing energy, and isolation variables. DELPHES also provides heavy flavour tagging and jet substructure algorithms. A detailed description of the DELPHES framework can be found in Ref. [34]. In the following we will focus on describing the key parameters of the FCC-hh detector implementation in DELPHES.

The FCC-hh DELPHES configuration can be found in the official DELPHES release [49] as well as in the FCC software webpage [50].

### 4.6.2 Tracking

The first step in DELPHES is the propagation of long-lived particles within a uniform axial magnetic field with  $B_z = 4$  T. The magnetic field is assumed to be localised in the inner tracker volume. In DELPHES only a single cylindrical volume can be defined as the propagation tracking volume. This differs from the actual tracker design of the FCC-hh detector (see Chapter 6), where central and forward trackers are defined with different radii and half-lengths. The magnetic field is assumed to be localised in the inner tracker volume, defined as cylinder of radius  $R_0 = 1.5$  m and an half-length  $Z_0 = 5$  m.

Charged particles have a user-defined probability to be reconstructed as tracks in the central tracking volume. The charged hadron tracking efficiencies for the FCC-hh detector are given in Table 4.1. It should be noted that since the reconstruction efficiencies are defined as a function of pseudo-rapidity, the (forward) tracker acceptance is equal to that of the full tracker, despite its shorter length.

A smearing of the norm and the direction of the charged particle momentum vector is applied at the stage of particle propagation. A momentum independent angular resolution of  $\sigma_\theta = 10^{-3}$  rad is assumed on tracks. This scale is compatible with the tracking angular resolution found in more detailed tracking studies. In addition, whenever two or more tracks fall within an angular separation  $\sigma_\theta$ , only the highest momentum track is reconstructed. This effect can result in an additional inefficiency to that shown in Table 4.1, and affects tracks in the core of highly boosted jets, as shown in Fig. 4.4 (left).

As an approximation, electrons and charged hadrons tracks are assumed to have an equal tracking performance. As discussed below in Section 4.6.4, the final electron objects are reconstructed by

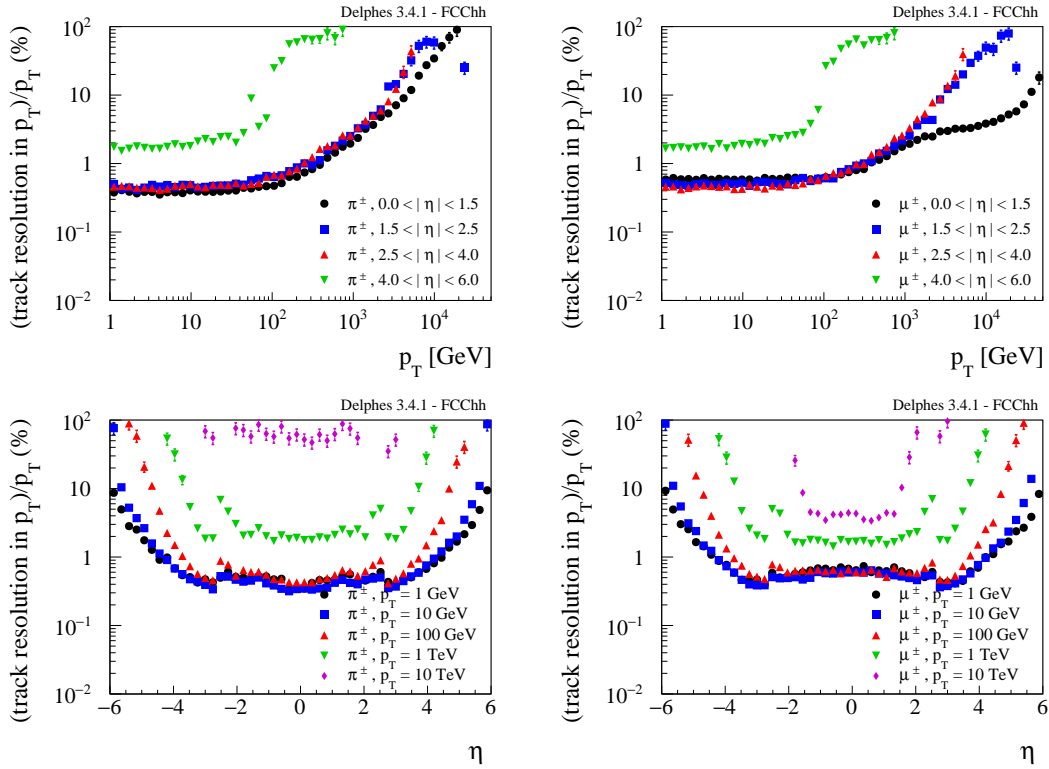


Fig. 4.2: Left: Charged hadron tracking  $p_T$  resolution as a function of  $p_T$  (top) and  $\eta$  (bottom). Right: Muon combined  $p_T$  resolution as a function of  $p_T$  (top) and  $\eta$  (bottom).

accounting for the calorimeter measurement, which provides a better performance at high energies. The muon resolution is, on the other hand, parameterised separately, and accounts for the combined measurement of the tracker and muon chambers. The  $p_T$  resolution of charged hadron (and electron) tracks and muons as a function of  $p_T$  and  $\eta$  is shown in Fig. 4.2. For example, the FCC-hh detector design allows for  $\sigma(p_T)/p_T \approx 20\%$  at  $p_T = 20$  TeV for central tracks as well as  $\sigma(p_T)/p_T \approx 5\%$  for  $p_T = 20$  TeV respectively.

Table 4.1: Tracking efficiency as a function of  $p_T$  and  $|\eta|$  for charged hadrons.

	$ \eta  < 2.5$	$2.5 <  \eta  < 4.0$	$4.0 <  \eta  < 6.0$	$ \eta  > 6.0$
$p_T < 0.5$ GeV	0%	0%	0%	0%
$0.5 < p_T < 1.0$ GeV	90%	85%	80%	0%
$p_T > 1.0$ GeV	95%	90%	85%	0%

### 4.6.3 Calorimetry

After their propagation in the magnetic field, long-lived particles reach the calorimeters. The electromagnetic calorimeter, ECAL, is responsible for measuring the energy of electrons and photons, while the HCAL measures the energy of charged and neutral hadrons. In DELPHES, the calorimeters have a finite lateral segmentation in pseudo-rapidity and azimuthal angle ( $\eta, \phi$ ) and no longitudinal segmentation. The transverse segmentation of the FCC-hh calorimeters assumed is given in Table 4.2. The coordinate of the resulting calorimeter energy deposit, the tower, is randomly smeared across the cell.

The resolutions of ECAL and HCAL are parameterised as a function of the particle energy and the

Table 4.2: Lateral segmentation in  $(\eta, \phi)$  (rad) of the electromagnetic and hadronic calorimeter.

	$ \eta  < 2.5$	$2.5 <  \eta  < 6.0$
ECAL	0.01	0.025
HCAL	0.025	0.05

pseudo-rapidity:

$$\left(\frac{\sigma}{E}\right)^2 = \left(\frac{S(\eta)}{\sqrt{E}}\right)^2 + C(\eta)^2, \quad (4.1)$$

where  $S$  and  $C$  are the *stochastic* and *constant* terms respectively. The electromagnetic and hadronic energy deposits are independently smeared by a log-normal distribution. For simplicity, it is assumed that electromagnetic particles such as electrons, photons and neutral pions (if undecayed by the Monte Carlo event generator) deposit their energy exclusively in the ECAL. Likewise, long-lived hadrons (such as charged pions, kaons, protons etc.) only deposit energy in HCAL and muons do not leave any energy deposit in the calorimeters. The values of  $S$  and  $C$  adopted for the FCC-hh calorimeters are summarised in Table 4.3. A complete description of FCC-hh calorimetry requirements can be found in Chapter 7 and Ref. [51]. We simply point out here the fine lateral segmentation (in Table 4.2) and the small constant terms (Table 4.3) are key for efficient reconstruction of jets with a transverse boost as high as 20 TeV.

Table 4.3: Resolution parameters of the electromagnetic and hadronic calorimeters as a function of  $|\eta|$ .  $S$  and  $C$  are respectively the *stochastic* and *constant* terms. The functional form for the energy resolution assumed is given in Eq. (4.1).

	$ \eta  < 1.7$	$1.7 <  \eta  < 4.0$	$4.0 <  \eta  < 6.0$
$S_{\text{ECAL}}$	10%	10%	30%
$C_{\text{ECAL}}$	0.7%	0.7%	3.5%
$S_{\text{HCAL}}$	50%	60%	100%
$C_{\text{HCAL}}$	3%	3%	10%

#### 4.6.4 Particle-flow

The philosophy of the particle-flow approach is to use a maximum amount of information provided by the various sub-detectors for reconstructing the event. This modus operandi has been adopted by some experimental collaborations (see for example Ref. [52]) and depends on the specificity of the experimental device. In DELPHES the particle-flow event reconstruction is based on a simplified approach that uses the tracks and the calorimeter towers as input.

If the momentum resolution of the tracking system is better than the energy resolution of calorimeters (typically for momenta below some threshold), it is convenient to measure the charged particles momenta using the tracking information. At high energy it is the other way round, calorimeters provide a better momentum measurement. The particle-flow algorithm exploits this complementarity to provide the best possible single charged particle measurement — the *particle-flow tracks*. These contain electron, muons and charged hadrons. The comparison of a pure tracking (calorimetric) measurement and the output particle-flow algorithm for charged hadrons and electrons is shown in Fig. 4.3 (left and centre). Thanks to the excellent tracking resolution assumed for the FCC-hh detector, the particle-flow electron

(charged hadron) resolution is dominated up to  $E = 500$  GeV ( $E = 2$  TeV) by the tracker. At higher energies the measurement is mainly driven by calorimeters.

If a significant energy deposit from a neutral particle which exceeds that of a charged particle is detected in a given calorimeter tower, *particle-flow photons* or *particle-flow neutral hadrons* are formed. Together with the *particle-flow tracks*, they form the (generically labelled) *particle-flow candidates* collection and are used as an input for electrons, muons and photons identification and isolation, as well as jets and missing transverse energy. The performance of jets using particle-flow input as opposed to calorimeter towers is shown in Fig. 4.3 (right). Again, a substantial improvement of the whole energy range can be observed by using particle-flow reconstruction. We note that this expected improvement obtained with the particle-flow is predicted by DELPHES. Studies performed with full-simulation are discussed in Chapter 7 and are found to be in good agreement with the pure calorimetric jet response. We stress however, that only a fully fledged particle-flow algorithm based on full-simulation will predict the ultimate jet performance under FCC-hh conditions.

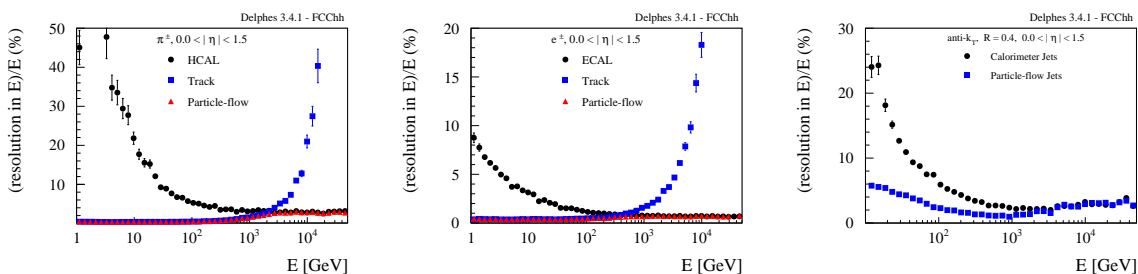


Fig. 4.3: Particle-flow performance as a function of energy compared to standalone tracking and calorimeter reconstruction for charged hadrons (left), electrons (centre) and jets (right).

#### 4.6.5 Object identification

#### 4.6.6 Leptons and photons

In DELPHES, a lepton (electron or muon) from the *particle-flow tracks* collection, or a photon from the *particle-flow photon* collection has a probability of being identified. For charged particles the identification efficiency is applied on top of the tracking efficiency discussed in the previous section. The identification efficiencies assumed for the FCC-hh detector are summarised in Tables 4.4, 4.5 and 4.6. The isolation variable for leptons and photons is computed by DELPHES as:

$$I = \frac{\sum_{i \neq p}^{\Delta R < R, p_T(i) > p_T^{min}} p_T(i)}{p_T(P)}, \quad (4.2)$$

where the sum runs over the full list of *particle-flow candidates* within a cone  $R$  excluding the particle under consideration.

Table 4.4: Identification efficiency for electrons as a function of  $p_T$  and  $|\eta|$ .

	$ \eta  < 2.5$	$2.5 <  \eta  < 4.0$	$4.0 <  \eta  < 6.0$	$ \eta  > 6.0$
$p_T < 4$ GeV	0%	0%	0%	0%
$p_T > 4$ GeV	95%	90%	85%	0%

Table 4.5: Identification efficiency for muons as a function of  $p_T$  and  $|\eta|$ .

	$ \eta  < 2.5$	$2.5 <  \eta  < 4.0$	$4.0 <  \eta  < 6.0$	$ \eta  > 6.0$
$p_T < 4 \text{ GeV}$	0%	0%	0%	0%
$p_T > 4 \text{ GeV}$	99%	99%	99%	0%

Table 4.6: Identification efficiency for photons as a function of  $p_T$  and  $|\eta|$ .

	$ \eta  < 2.5$	$2.5 <  \eta  < 4.0$	$4.0 <  \eta  < 6.0$	$ \eta  > 6.0$
$1 < p_T < 5 \text{ GeV}$	70%	60%	50%	50%
$5 < p_T < 10 \text{ GeV}$	85%	80%	70%	70%
$p_T > 10 \text{ GeV}$	95%	90%	80%	80%

#### 4.6.7 Jets and missing energy

The missing transverse energy  $p_T^{\text{miss}}$  is computed as the magnitude of the total transverse momentum carried by the full list of reconstructed particle-flow candidates. The DELPHES framework integrates the FASTJET package [53], allowing jet reconstruction with the most popular jet clustering algorithms. In the FCC-hh detector configuration jet collections using the anti- $k_t$  algorithm [54] are provided with several jet clustering R parameters ( $R = 0.2, 0.4, 0.8, 1.5$ ). As mentioned earlier, several jet collections are formed using several different input objects such as tracks (*Track-jets*), calorimeter (*Calo-jets*) and particle-flow candidates (*PF-jets*).

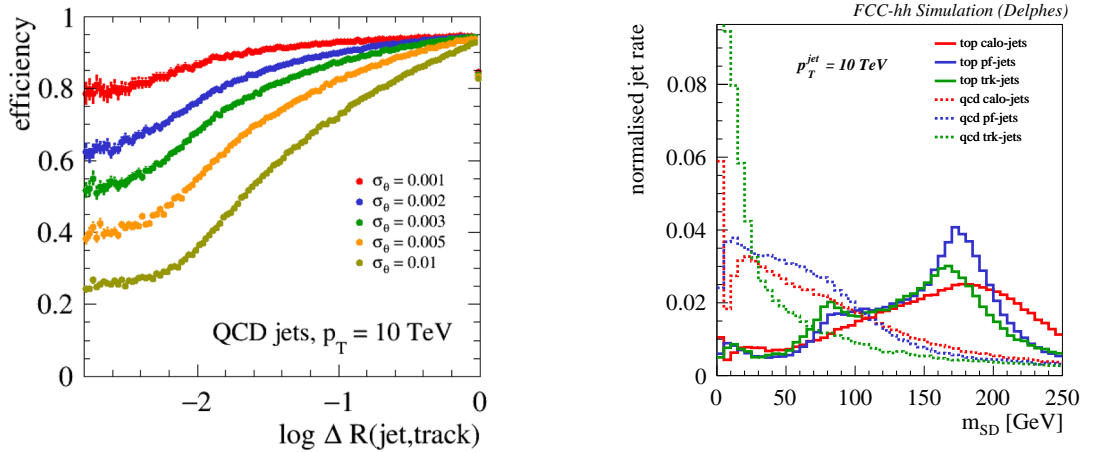


Fig. 4.4: Left: Track reconstruction efficiency inside highly QCD boosted jets as function of the angular distance between the track and the centre of the jet. Right: Reconstructed jet mass of highly boosted top and QCD jets using respectively as input to the jet clustering algorithm tracks, calorimeters towers or particle-flow candidates.

Common jet shape observables used for jet substructure analysis such as N-subjettiness [55] and the soft-dropped mass [56] are computed on-the-fly and stored in the output jet collections. This large number of jet collections (with varying R-parameter and input collections) is needed for physics analyses that feature highly boosted hadronic jets in the final states, spanning over more than one order of magnitude in energy range (e.g.  $Z' \rightarrow t\bar{t}$  searches). As an illustration, the reconstructed soft-dropped

mass for top and QCD jets with  $p_T = 10$  TeV and  $R = 0.2$  is shown in Fig. 4.4 (right). Thanks to the superior tracker segmentation, we find *Track-jets* perform better in terms of QCD background rejection despite the slightly worse jet mass resolution.

#### 4.6.7.1 Heavy-flavour tagging

The identification of jets that result from  $\tau$  decays or the hadronisation of heavy flavour quarks – typically b or c quarks – typically involves the input from tracking information, such as vertex displacement or low level detector input such as hit multiplicity [23]. Such information is not available as a default in DELPHES. Instead, a purely parametric approach based on Monte-Carlo generator information is used. The probability to be identified as b or  $\tau$  depends on user-defined parameterisations of the b and  $\tau$  tagging efficiency. The user can also specify a mis-tagging efficiency parameterisation, that is, the probability that a particle other than b or  $\tau$  be wrongly identified as a b or a  $\tau$ . The parameterisations of the b and  $\tau$  tagging efficiencies in the FCC-hh detector and their respective mis-identification rates from QCD jets are given in Tables 4.7 and 4.8.

Table 4.7: b-tagging efficiencies and light mistag rates as a function of  $p_T$  and  $|\eta|$ .

	$ \eta  < 2.5$	$2.5 <  \eta  < 4.0$	$4.0 <  \eta  < 6.0$
b-tagging efficiency			
$30 < p_T < 15000$ GeV	$(1 - p_T [\text{TeV}]/15) \cdot 85\%$	$(1 - p_T [\text{TeV}]/15) \cdot 64\%$	0%
$p_T > 15000$ GeV	0%	0%	0%
c-mistag efficiency			
$30 < p_T < 15000$ GeV	$(1 - p_T [\text{TeV}]/15) \cdot 5\%$	$(1 - p_T [\text{TeV}]/15) \cdot 3\%$	0%
$p_T > 15000$ GeV	0%	0%	0%
light mistag efficiency			
$30 < p_T < 15000$ GeV	$(1 - p_T [\text{TeV}]/15) \cdot 1\%$	$(1 - p_T [\text{TeV}]/15) \cdot 0.75\%$	0%
$p_T > 15000$ GeV	0%	0%	0%

Table 4.8:  $\tau$ -tagging efficiencies and light mistag rates as a function of  $p_T$  and  $|\eta|$ .

	$ \eta  < 2.5$	$2.5 <  \eta  < 4.0$	$4.0 <  \eta  < 6.0$
$\tau$ -tagging efficiency			
$30 < p_T < 15000$ GeV	$(1 - p_T [\text{TeV}]/30) \cdot 60\%$	$(1 - p_T [\text{TeV}]/30) \cdot 40\%$	0%
$p_T > 15000$ GeV	0%	0%	0%
QCD mistag efficiency			
$30 < p_T < 15000$ GeV	$(1 - p_T [\text{TeV}]/30) \cdot 1\%$	$(1 - p_T [\text{TeV}]/30) \cdot 0.75\%$	0%
$p_T > 15000$ GeV	0%	0%	0%
electron mistag efficiency			
$30 < p_T < 15000$ GeV	$(1 - p_T [\text{TeV}]/30) \cdot 0.5\%$	$(1 - p_T [\text{TeV}]/30) \cdot 0.3\%$	0%
$p_T > 15000$ GeV	0%	0%	0%

#### **4.6.8 Conclusion and discussion**

The FCC-hh baseline detector has been parameterised in DELPHES. This detector configuration has been used to study a list of benchmark physics analyses described in Chapter 2. We stress that pile-up simulation was not included in this FCC-hh detector description because an accurate description of such effects on reconstructed quantities requires more detailed studies. However, we note that only the nominal detector assumption has been presented here. In many analyses that are discussed Chapter 10, deviations from the baseline detector assumptions have been tested in order to explore the impact on the sensitivity of the various measurements, including possible indirect effects of the pile-up on specific observables.





# Magnet systems

---

## 5.1 Introduction

A general purpose experiment is proposed to probe 100 TeV proton-proton collisions provided by the Future Circular Collider, FCC-hh. An essential part of the experiment is the superconducting magnet system, providing the bending power required for the momentum measurements of the particles escaping from the collision. During the conceptual design phase of the project, several options for the arrangement of the coils which generate the magnetic field were studied. This finally evolved to the design for the reference detector presented here which was selected on the basis of its technical feasibility, relative simplicity, robustness and affordability. It comprises a central solenoid providing magnetic field for the inner detector in combination with two forward solenoids supplying magnetic field over a large angular range [57, 58]. It is not planned to have additional active shielding coils or a passive field return yoke for shielding purposes and providing additional magnetic field for the outer layer muon spectrometer. The magnetic (stray) field of the main solenoid in this area is regarded as being sufficient for these purposes. Since the magnet is positioned in a cavern some 350 m below the surface, the magnetic field at the surface remains comfortably below safety limits of 0.5 mT. Consequently, since shielding is not required for either operational or safety reasons, the magnet system is not shielded.

### 5.1.1 Outline

The FCC-hh detector magnet system comprises a central solenoid to provide an axial magnetic field of 4 T at the centre of the inner detector tracking volume. The reference detector has a solenoid with 10 m free bore enclosing an inner detector and calorimeters. Therefore, magnetic field is generated in both the inner tracker and calorimeter volumes and consequently there is a relatively large stored energy. Two forward solenoids, located on either side of the main central solenoid, are introduced to provide 3.2 T and bending power for particles escaping from the interaction point at low angles to the beam pipe in the forward and backward directions. An alternative design based on forward dipole magnets is also presented. The integral of the magnetic field for this dipole option is 4 Tm in the forward region. The technology for conductors and coil windings relies heavily on the experience gained with the ATLAS and CMS magnet systems [59–64] featuring indirectly cooled pure aluminum stabilised superconducting Nb-Ti Rutherford cables [65–67]. A concise summary of detector design, including magnet system is included in the FCC CDR summary volumes [1–3]. This document provides more technical details at the level of a conceptual design. A technical design report (TDR) is planned as the next step.

### 5.1.2 Requirements

The following aspects of the requirements which the magnet system has to fulfil are highlighted below:

1. **Magnetic field.** The magnetic field at the centre of the main solenoid is 4 T in axial direction, while the magnetic field at the centre of the forward solenoids is 3.2 T. The field is completely symmetric axially, except near the current leads on top of the solenoid. The peak magnetic field on the conductor is 4.5 T at  $z = 0$ . The pseudorapidity is defined as a function of the polar angle  $\theta$ :  $\eta = -\ln\left(\tan\left(\frac{\theta}{2}\right)\right)$ . The particle production is constant as a function of rapidity; therefore, the use of pseudorapidity is preferred over the polar angle. The main role of the detector magnet is to provide the required bending power over a wide range of pseudorapidity which necessitates the introduction of forward magnet systems in addition to the main solenoid.
2. **Polarity of the magnetic field.** The experimental setup is rotationally symmetric except in areas used for powering, cooling, readout and other service lines. It is also fully symmetric in the  $z = 0$  plane. In order to check for any front-back asymmetries in the detector, the polarities of the magnetic field in main solenoid and forward solenoids can be reversed a few times.
3. **Integration of the magnet and detector systems.** The main solenoid which is the largest single part of the experiment, to a large extent determines the cavern and shaft dimensions as well as the detector installation schemes. The installation scenario requires the axis of the main solenoid to be vertical when it is lowered into the cavern so that the diameter of the shaft is minimised. After lowering into the cavern, it is rotated to its horizontal position. The size and weight of the main solenoid directly affect the sizes of access shaft and experimental cavern, the lifting capacity of the cranes and also cryogenic cooling requirements. The main solenoid's cryostat provides structural support for the various detectors installed inside (calorimeters, inner tracker) and outside (muon system) the solenoid.
4. **Material properties and impact on physics.** Cryostats and force transfer points of main and forward solenoids need to be mechanically strong enough to sustain the huge magnetic forces between main and forward solenoids. The design has a conduction cooled cold mass at 4.5 K, which implies the use of highly conducting pure aluminium to achieve sufficient conductor thermal-electromagnetic stability and also a sufficiently large Minimum Quench Energy (MQE). Since the solenoid is positioned around the calorimeters, the material budget is not the most important design parameter since all measurable particles except muons will be stopped by the calorimeters and the impact on muon trajectories is minimal due to the muon's low cross-section. However, in the case of using the more aggressive design of positioning the main solenoid inside the calorimeters directly surrounding the inner tracker, the material budget becomes the key design parameter. Cryostat walls and cold mass must then be as thin and radiation transparent as possible leading to mandatory use of pure aluminium for conductor stabiliser and advanced structural aluminium for the cryostat [68, 69]. A design of an ultra-thin and radiation transparent solenoid has also been included in the study.
5. **Quench protection and recovery.** The magnet system must feature maximum reliability and have maximum operational margins in terms of thermo-electromagnetic stability, current sharing temperature and hotspot temperature after quench. Having sufficient margins in the operational parameters is essential to guarantee long-term stable operation. The quench recovery time has to be acceptably short in view of the very high stored energy of the magnet systems. A robust quench protection system has to deal with fast dumps. Since the magnet system comprises three magnets with large mutual forces which are not-thermally linked, the protection scheme has to cope with specific failure modes including asymmetric quenches. Appropriate slow and fast discharge schemes have to be in place.
6. **Tooling and Support structures.** Transport is a critical area because lowering, turning and handling the 10-m diameter main solenoid in the cavern, requires special tooling. The in-cryostat cold mass support structure connecting the vacuum vessel, radiation shield and cold mass requires special attention. Gravitational aspects, fault scenarios and seismic effects as well as de-centring of magnetic forces have to be evaluated.

7. **Alignment.** The solenoids generate a non-uniform magnetic field and the positions of the magnetic centres need to be known very precisely. The position of the cold mass inside the cryostat can change during several of the steps during installation and operation. The size and position of the cold masses change due to thermal contraction during cool down to 4.5 K. The position of the cold masses inside the cryostat is controlled by the cold mass supports i.e. tie-rods, and the relative position of the three solenoids is controlled through axial force transfer points. Magnetic field mapping measurements of the three solenoids will confirm the final positions.
8. **Radiation tolerance and degradation of material.** Only small numbers of high energy particles will reach the main solenoid, since the calorimeters provide shielding. The radiation level will still be low for the ultra-thin and transparent solenoid positioned inside the calorimeters and no serious radiation damage affecting magnet design is expected.
9. **Cryogenic cooling power, liquid helium supply and power converters.** Cold mass cooling of the three solenoids is based on the well-known and robust thermosiphon cooling schemes presently used for the ATLAS and CMS Solenoids. However, in view of the depth of the caverns, it is advantageous to position the liquifier cold boxes, compressors and associated equipment on the surface, thereby minimising interventions in the cavern. High-pressure helium gas lines at the 25 K level will go into the cavern feeding a local relatively cold box where liquefaction takes place. The magnets are connected electrically to the power converters on the surface through high-temperature superconducting bus bars which are integrated with the cryogenic feed lines.
10. **Operation, monitoring and control.** The operational lifetime of a large experiment like that for FCC-hh can easily be more than 25 years and even 35 years when on-surface testing, installation and commissioning is included. The operation of the infrastructure including magnet system is practically uninterrupted with preventive maintenance, some repair and improvement work being performed in short technical stops and longer shutdown periods. The magnet system is the largest component of the experiment it is not expected to be upgraded or replaced. It is of utmost importance that the system is robust and can operate without major interventions by specialists. Procedures for stable operation during physics data taking, as well as those for startup, shutdown and restart after slow and fast magnet discharges need to be in place and suitable for non-expert operators. Cool-down and warming up of cold masses have to be homogeneous, i.e. slow enough to avoid risky thermal stress and strain in coil windings and other cold masses. Ramping up to the nominal current has to be performed within three to five hours. The electrical circuit must be designed such that fault operations are avoided, in view of the huge Lorentz forces between main and forward magnets. Amongst other parameters, monitoring systems will probe currents, voltages, pressures, temperatures, quench detectors, stress and strain, position, magnetic field, water and helium flows. Monitoring is continuous and data are recorded and stored by the magnet control system for offline and historical analyses. Alarms and other threshold settings are automatically controlled and they trigger remote interventions under strict access control for experts when needed.
11. **Safety.** Depending on the locations for construction and tests, international legislation concerning quality assurance and safety aspects have to be considered. For on-site installation and operation, CERN rules are in place, which typically follow the strictest of EU or Swiss rules. Since the conceptual design does not include demonstration models or prototypes, safety aspects will be addressed later in the technical design report.

### 5.1.3 Evolution of the design

From the start of the conceptual design study to the moment of publishing this report, several options for the magnet system were explored, proposed, rejected, upgraded, changed and simplified. An obvious starting point is to use existing large systems, like CMS and ATLAS, as an example. However, having a

magnetic return yoke, leads to an undesired large mass of roughly 120 kt, which has serious consequences for the cavern floor, installation, opening and closing and further handling of the system. Therefore a development of the CMS design has not been considered. Also a toroid system, similar to ATLAS, but larger, was not considered, but due to cost rather than technical limitations. First rough cost estimates for an ATLAS+ design indicated that the magnet system alone would cost about one billion euros [70]. The baseline magnet system has thus gradually evolved into a system that is technically feasible to build, affordable and which meets the physics requirements. Overviews of the ongoing work were presented regularly, starting with the FCC Kick-Off meeting early 2014 [71, 72] and followed by many international conferences [70, 73–79] and the annual FCC weeks [58, 80–84]. This is complemented by several publications in peer-reviewed journals and publications in conference proceedings [75, 85–89, 89, 90]. A full description of the baseline magnet system and a comprehensive overview of the evolution is given in [57].

## 5.2 Main solenoid with forward solenoids (Configuration used for the reference detector)

The magnet system for the reference detector consists of three superconducting solenoids. The main solenoid generates a magnetic field of 4 T in a free 10 m diameter bore over a length of 20 m. The forward solenoids, positioned at either side of the main solenoid, augment the magnetic field in the forward regions to 3.2 T. The combined stored magnetic energy of this assembly is 13.8 GJ. The mass of the main solenoid, including cold mass and cryostat adds up to just under 2 kt, while the forward cold masses and cryostats add up to 80 t per magnet.

Figure 5.1a shows the complete experiment including magnet system, inner detector, calorimeters and muon detection systems. The central tracker and calorimeters are placed inside the bore of the main solenoid, while forward trackers are placed inside the bore of the forward solenoids, and forward calorimeters are placed just behind the forward magnets when seen from the interaction point. The muon spectrometer forms the outermost shell of the experiment and extends at the far ends in the forward directions. Figure 5.1b shows the bare coil windings packs without support cylinder, cryostat and detectors.

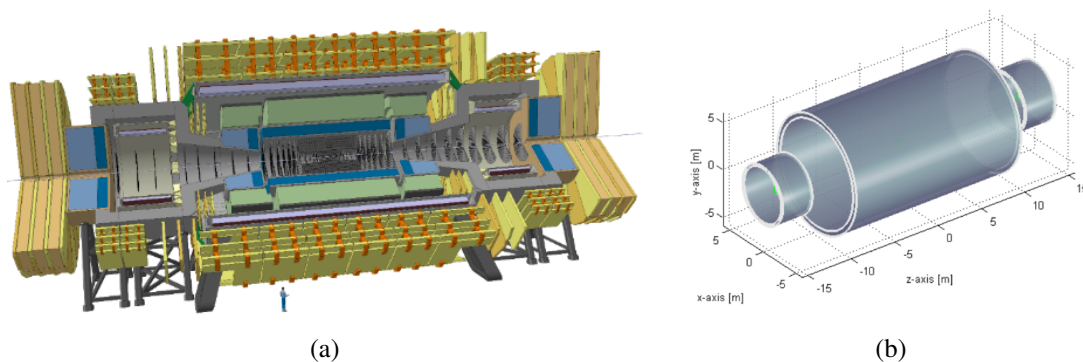


Fig. 5.1: (a) Overview of the entire FCC-hh experiment including magnet systems, trackers and calorimeters. (b) Bare coil windings layout of the 4 T central solenoid with two 3.2 T forward solenoids.

There are two possible layout configurations for solenoids in collider experiments. Both can be found in the present LHC experiments. In CMS, a wide bore solenoid is positioned around the central tracker and calorimeters. Since these two detectors are positioned inside the bore of the solenoid, the cryostat has to provide significant structural rigidity [64]. In ATLAS on the other hand, a much smaller solenoid is positioned in a common cryostat with the liquid argon calorimeter, in between the central tracker and the calorimeters. This solution is feasible provided the solenoid is as thin and light as possible, i.e. as radiation transparent as technically possible in order to have minimum impact on the energy

measurements [59–63]. For the FCC-hh reference detector the conservative design of using a wide bore solenoid around the calorimeters was adopted but without a magnetic return yoke.

Conflicting aspects need to be taken into consideration when choosing one of the above-mentioned designs. Obviously, magnetic field is not useful in the calorimeter, but is required in the central tracker to allow momentum measurements. A solenoid positioned around the calorimeters is thus much larger in size and stored energy than is strictly required, using much more material and roughly doubling the cost. Also magnet service systems for cryogenics, vacuum, power, safety and controls are more complex and expensive. Moreover, infrastructure and equipment for installation is more demanding. On the other hand, a small solenoid inside the calorimeters will, to some extent, have a negative impact on the physics performance. Particles created in the collision point fly through the layers of inner tracker and must pass through the solenoid’s cold mass and cryostat before reaching the calorimeters. This implies that the interactions which take place in the magnet cause the particles to lose energy which affects their trajectories and thus their position and angle in the calorimeter. Minimising this requires cold mass and cryostat to be as thin and as radiation transparent as possible, which determines the minimum values of radiation length and interaction length. As a rule of thumb the material budget of the solenoid should not exceed one radiation length, i.e.  $X_0 \leq 1$ .

The turns of a solenoid attract each other and two or more separated but magnetically aligned solenoids will attract each other as well. Effectively, due to their close proximity to the main solenoid, the smaller forward solenoids will experience a large net force of about 60 MN per solenoid towards the interaction point. In detail, the force depends on the magnetic material properties of the muon absorber disks in the forward region. The force on the forward magnets is slightly higher when non-magnetic material is used, 62 MN, whereas if magnetic steel is used, the net force drops to 58 MN. In the latter case a large force of  $\sim 9$  MN is also present on the absorber disks themselves. In the baseline layout these forces are transferred to the radiation shield surrounding the forward solenoids and spokes are used to transfer the forces again to the main solenoid cryostat. Using magnetic material for the muon absorber disks allows a toroidal magnetic field to be created by strategically placing windings on the iron. The latter, which require a modest number of ampere-turns, are not in the baseline design.

### 5.2.1 Magnetic field configuration in detector and magnetic stray field in service cavern

The magnetic field map of the baseline magnet system is shown in Fig. 5.2. The background colour indicates the absolute value of the magnetic field, while the arrows indicate the local direction of the magnetic field. Contour lines are also shown (at 4, 3, 2, 1, 0.5, 0.4, . . . 0.002, 0.001 T).

Since there is no magnetic return yoke, the magnetic field stretches out over a fairly large distance. The stray magnetic field, however, is not considered an important restriction. The experiment cavern for the FCC-hh experiment is some 350 m below surface and the service cavern with magnetic field-sensitive-equipment is located with a distance of 50 m between closest walls. The 5 mT level is reached at an axial distance of about 70 m and at a radial distance of 52 m from the IP. Figure 5.3 shows the magnetic field as a function of distance from the IP, both in the longitudinal direction (along  $z$ -axis) and in the radial direction on a linear and logarithmic scale. It shows that the stray magnetic field at the location of the service cavern is not an issue, since it is located at a radial distance of 66 to 96 m from the beamline. An intensive study was performed to investigate the behaviour of the stray magnetic field when the service cavern is positioned much closer to the experimental cavern, only separated by a thick concrete wall of some 10 m, similar to the present CMS cavern layout [64]. No feasible solutions were found for reducing the stray magnetic field to reasonable levels inside the service caverns without using huge amounts of magnetic material to shield the service cavern. A cost estimate for this shielding material amounts to several tens of millions of Euros.



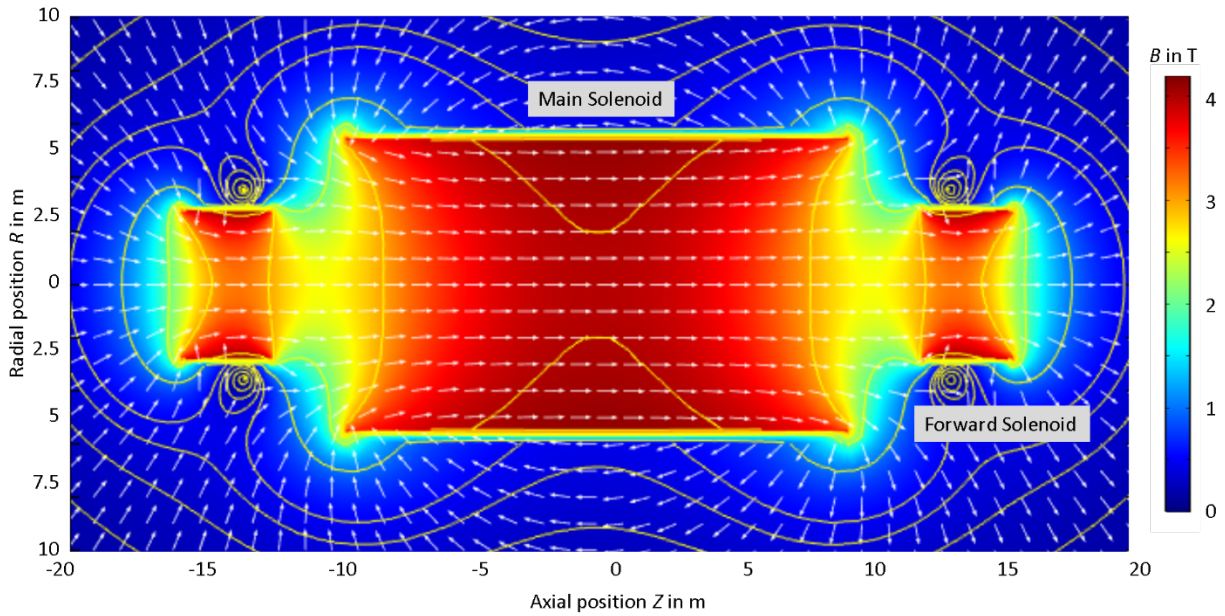


Fig. 5.2: Magnetic field map of the central solenoid of 4 T with a smaller solenoid at either forward side providing a 3.2 T magnetic field on the experiment's main axis.

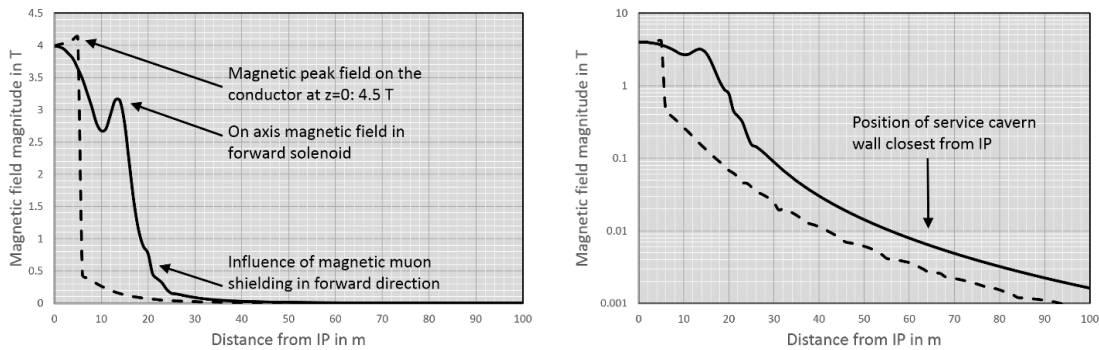


Fig. 5.3: Magnitude of the magnetic field as a function of distance from IP: along the  $z$ -axis (full line) and in radial direction (dashed), both on a linear (left) and logarithmic scale (right).

## 5.2.2 Main solenoid

The main solenoid has a length of 20 m and a free bore diameter of 10 m. This makes it the largest superconducting solenoid and it has a stored energy of 12.5 GJ, which is about a factor five to eight larger than CMS and ATLAS which feature 2.7 and 1.6 GJ, respectively. The operational parameters are summarised in Table 5.1.

### 5.2.2.1 Main solenoid cold mass

The cold mass consists of several layers of aluminium stabilised Rutherford-type cables. The cold mass is kept at 4.5 K by conduction cooling with liquid helium flowing through a web of cooling pipes attached to the aluminium alloy support cylinder present for mechanical purposes and to reduce the cold mass hot spot temperature after a quench. The main parameters of the cold mass are summarised in Table 5.2. The radial thickness of the cold mass is restricted by the space available in the cryostat. For the main solenoid the inner radius of the cold mass is determined by the inner radius of the cryostat, the thickness

Table 5.1: Main solenoid operational parameters.

Parameter	Value
Magnetic field at interaction point IP (T)	4.000 (total) / 3.953 (main solenoid only)
Operating current (kA)	30.0
Total magnet system self-inductance (H)	30.7
Main solenoid self-inductance (H)	27.7
Mutual inductance of main and forward solenoids (H)	0.29
Total stored energy (GJ)	13.8
Main solenoid stored energy (GJ)	12.5
Peak magnetic field on main solenoid conductor (T)	4.48
Operating temperature (K)	4.5

of the inner shell, the space for the radiation shield, suspension tie rods, and multi-layer insulation. The length of the cold mass is determined by similar arguments. The free parameter to increase the overall cross-sectional area of the cold mass is the outer diameter. The cross-sectional area of the cold mass follows from the magnetic field required at the IP as a certain number of ampere-turns are required to generate the 4 T design field. The stored energy per unit mass is chosen according to mechanical and quench protection considerations and consequently the overall cross-sectional area required follows. By fixing the operating current at 30 kA for quench protection and magnet charging reasons, the number of coil turns is fixed and the dimensions of the conductor can be chosen. The ramp rate is limited by the properties of the power supply, the resistive voltage drop over the current leads and joints and the inductance of the magnets. Either fixed voltage or fixed power are standard operating conditions of the power supply, leading to charging times of several hours. A rough estimate gives a ramp rate of  $15 \text{ V} / 30 \text{ H} = 0.5 \text{ A/s}$ , thus leading to a charging time of 60000 seconds, or about 17 hours, if a 15 V fixed voltage power supply is used.

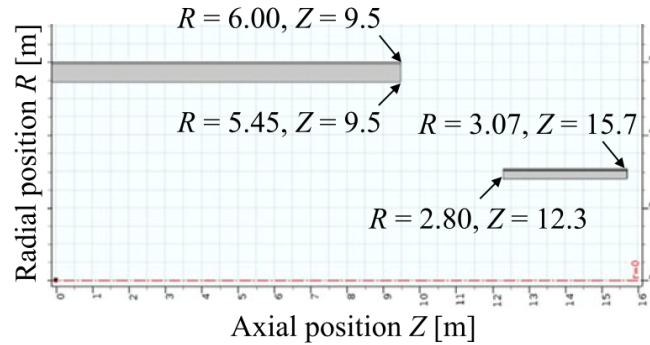


Fig. 5.4: Main solenoid and forward solenoids cold mass geometry (fully symmetric in azimuthal direction). The eight conductor layers in the main solenoid are 0.50 m thick in total, while the support cylinder is 50 mm thick. For the forward solenoids, the six conductor layers are 0.23 m thick in total, and the support cylinder is 40 mm thick.

### 5.2.2.2 Main solenoid superconductor

The superconductor used is NbTi because of its low cost and convenience. The proven technology for conductors in conduction cooled coil windings of large-scale detector magnets, with most recent examples CMS and ATLAS magnets, is a conductor comprising Ni doped pure aluminium stabilised Ruther-

Table 5.2: Main solenoid cold mass parameters.

Parameter	Value
Cold mass length (m)	18.937
Cold mass inner radius (m)	5.450
Cold mass outer radius (m)	6.000
Cold mass thickness (mm)	550
Support cylinder thickness (mm)	50
Cold mass volume (m <sup>3</sup> )	375
Number of conductor layers	8
Number of turns	290
Mass of NbTi, Cu, glass/resin, Al-alloy, <b>total</b> cold mass (t)	18, 26, 20, 1003, <b>1067</b>
Energy over mass density (kJ/kg)	12.1

ford cable formed from NbTi/Cu strands and when necessary, high-strength aluminium reinforcement to take up Lorentz forces on the solenoid body. The Ni doped pure aluminium mechanically reinforces the structure, conducts heat well, provides thermal stability and gives a sufficiently large minimum quench energy (MQE), thereby reducing the risk of quench. It is also providing a parallel path for the current in the case of a quench, thereby strongly reducing Joule heating, and drastically limiting the hotspot temperature. From a cost-perspective, aluminium is favourable to copper and it is superior in terms of conductivity. In addition, aluminium has the lowest density of all practicable metals, facilitating a light cold mass which has a positive impact on the support structure and tooling for installation.

Since the aluminium stabiliser fulfils several roles, various properties need optimisation in parallel. The electrical and thermal conductivities are mainly determined by the behaviour of the electrons in the material and therefore they can be improved simultaneously. However, to improve the mechanical properties the quantity of precipitates in the aluminium is important. Unfortunately, alloys with better electrical and thermal properties have less optimal mechanical properties and vice versa. By carefully choosing the composition of the alloy, the specifications can be met. The ATLAS central solenoid conductor is a pioneering example of using an optimised nickel-doped aluminium. The CMS conductor design followed a different strategy in which a strong 6000 series aluminium alloy is welded to the high-purity aluminium stabiliser in which the Rutherford-type NbTi/Cu cable is embedded. Electrical and thermal properties are in this case determined by the high-purity aluminium, whilst the mechanical properties are determined by the high yield stress aluminium alloy. A COMSOL Multiphysics simulation showed that coupled magnetic-mechanical behaviour results in a peak Von Mises stress of about 100 MPa in the coil windings of both main and forward solenoids. In the numerical model, the aluminium is in the elastic regime and dominates the mechanical behaviour. The elastic modulus of the glass/resin insulation is considered negligible. With a safety factor of 1.5, a feasible yield strength of about 150 MPa is obtained for the conductor [57].

Taking the arguments above into consideration, a functional conductor which satisfies the requirements can be defined. Note that there are many options for shaping the conductor so what is presented here is only a first design. Combinations of the number of turns per layer and the number of layers which respect the number of ampere-turns required to achieve 4 T, yield practical dimensions of the conductor. The final choice is a compromise of two conflicting arguments. Since cooling of the cold mass is through conduction and the helium pipes are attached to the outside of the support cylinder, the number of thermal barriers towards the inner layer of conductors must be minimised. Since each conductor is insulated with a 0.5 mm thick layer of glass reinforced epoxy resin, the total number of layers must be minimised. The opposing argument concerns the local peak magnetic field in the conductor. If the Rutherford cables have their flat side parallel to the main magnetic field, the peak field on the Rutherford-type cable is lower



than if the cable is positioned transversely. Therefore parallel placement is favourable in terms of conductor temperature margin, however, for this the conductor needs to be larger, following the shape of the Rutherford cable. Then there are fewer turns possible per layer and more conductor layers are required to achieve the same ampere-turns, which implies more insulation layers present and thus a higher thermal gradient. The conductor size-option proposed here is listed in Table 5.3 and visualised in Fig. 5.5.

Table 5.3: Design parameters of the first proposal for the conductor of the main solenoid.

Parameter	Value
Conductor width including insulation (mm)	65.3
Conductor thickness including insulation (mm)	62.5
Conductor glass/resin insulation thickness (mm)	0.5
Rutherford cable width (mm)	30 (20×1.5)
Rutherford cable thickness (mm)	3 (2×1.5)
Number of strands in cable	40
Strand diameter (mm)	1.5
Strand composition, NbTi to Cu ratio	1:1
Conductor length (km)	83
Current density in NbTi (A/mm <sup>2</sup> )	849
Current density in Rutherford cable (A/mm <sup>2</sup> )	424 (333 including voids)
Current density in conductor (A/mm <sup>2</sup> )	7.35
Current sharing temperature (K)	6.5
Temperature margin (K)	2.0

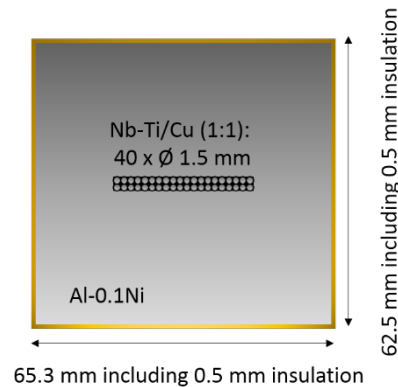


Fig. 5.5: Proposed conductor dimensions and composition of the main solenoid, comprising Ni-doped pure aluminium stabiliser and reinforcing material, embedding a 40 strands NbTi/Cu Rutherford cable.

### 5.2.2.3 Main solenoid cryostat

The cryostat of the main solenoid serves two main functions: firstly, to maintain the thermal insulating vacuum, and secondly, to support the relatively light inner detector and heavy calorimeters inside its bore. Use of a high yield strength stainless steel (304L) is an obvious choice to minimise the total amount of material and space it occupies. The cold mass suspension system, in the form of tie rods, requires a strong but low thermal conductivity metal like  $Ti_6Al_4V$  featuring a very high stress limit of 880 MPa. The dimensions of shells, flanges and tie rods were determined in an iterative approach and optimised while respecting a mechanical safety factor of 1.5 for all elements. The load case for the

ANSYS simulation considered the mass of the calorimeters inside the bore (5.5 kt); gravity; a seismic load in all directions of 0.15g; pressure difference between vacuum inside and atmospheric pressure outside; and the net Lorentz forces on the solenoids taking into account a 10 mm positioning error in axial and radial directions.

The main parameters of the cryostat design are summarised in Table 5.4 and Fig. 5.6 shows the cryostat and position of cold mass suspension tie rods. The results of the static analysis were fed into a linear buckling analysis which showed that the buckling load factor of the first failure mode exceeds five.

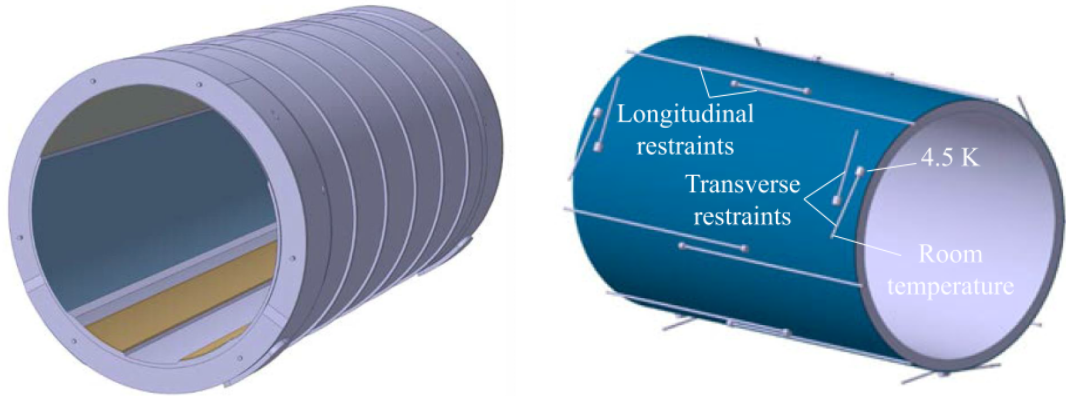


Fig. 5.6: Main solenoid vacuum vessel and schematic representation of the positions of the cold mass suspension tie rods.

In addition to the size, the cryogenic heat load on the thermal shield and cold mass are needed to be able to dimension the cryogenic plant correctly. The heat loads are summarised in Table 5.5.

Table 5.4: Main solenoid cryostat parameters of the vacuum vessel, suspension tie rods, and radiation shield.

Parameter	Value
Vacuum vessel length (m)	20
Vacuum vessel inner radius (m)	5
Vacuum vessel outer radius (m)	6.4
Vacuum vessel overall thickness (mm)	1400
Vacuum vessel outer shell thickness (mm)	55
Vacuum vessel inner shell thickness (mm)	90
Vacuum vessel flange thickness (mm)	107
Vacuum vessel mass (kt)	875
Radiation shield thickness (mm)	5
Radiation shield mass (t)	20.4
Suspension tie rods diameter (mm)	60
Number of longitudinal tie rods	12
Number of transverse tie rods	12

### 5.2.3 Forward solenoids

The role of the forward solenoids is to extend the region with magnetic field, such that bending power is also guaranteed for particles moving almost parallel to the particle beam at large  $\eta$ . The main operational parameters are summarised in Table 5.6. The current and operational temperature are the same as for the main solenoid.

Table 5.5: Cryogenic heat loads on the thermal shield and cold mass of the main solenoid.

Component	Load
Radiation heat load on thermal shield at 50 K (W)	4380
Radiation heat load on cold mass at 4.5 K (W)	280
Conduction through tie rods on thermalisation points (W)	760
Conduction through tie rods on cold mass (W)	5.8
Total heat load on thermal shield (W)	5140
Total heat load on cold mass (W)	286

Table 5.6: Forward solenoid operational parameters.

Parameter	Value
Magnetic field on axis (T)	3.2
Operating current (kA)	30.0
Forward solenoid self-inductance (H)	1.86 (2×0.93)
Mutual inductance between main and forward solenoids (H)	0.29
Mutual inductance between Forward Solenoids (H)	0.001
Forward Solenoids stored energy (MJ)	840 (2×420)
	4.45
Operating temperature (K)	4.5

### 5.2.3.1 Cold mass

The cold mass design of the forward solenoids follows the same considerations as the main solenoid. The cold mass parameters are listed in Table 5.7.

Table 5.7: Forward solenoid cold mass parameters.

Parameter	Value
Cold mass length (m)	3.4
Cold mass inner radius (m)	2.8
Cold mass outer radius (m)	3.07
Cold mass thickness (mm)	270 (6* 38.3+40)
Axial position relative to IP (m)	12.3-15.7
Support cylinder thickness (mm)	40
Cold mass volume (m <sup>3</sup> )	
Number of layers	6
Number of turns	70
Ground insulation glass/resin composite thickness (mm)	2.0
Mass of NbTi, Cu, glass/resin insulation, Al-alloy, <b>total</b> (t)	1.6, 2.4, 1.3, 43.9, <b>49.2</b>
Energy over mass density (kJ/kg)	8.5

### 5.2.3.2 Superconductor

The design of the conductor for the forward solenoids follows the same arguments as for the main solenoid conductor. The conductor parameters are listed in Table 5.8.

Table 5.8: Main parameters of the proposed conductor of the forward solenoids.

Parameter	Value
Conductor width including insulation (mm)	48.6
Conductor thickness including insulation (mm)	38.3
Glass/resin conductor insulation thickness (mm)	0.5
Rutherford cable width (mm)	30 (20×1.5)
Rutherford cable thickness (mm)	3 (2×1.5)
Number of strands	40
Strand diameter (mm)	1.5
Strand composition (NbTi to Cu ratio)	1:1
Cable length (km)	15.4 (2×7.7)
Current density in NbTi ( $A/mm^2$ )	849
Current density in Rutherford cable ( $A/mm^2$ )	424 (333 including voids)
Current density in conductor ( $A/mm^2$ )	16.1
Current sharing temperature (K)	6.5
Temperature margin (K)	2.0

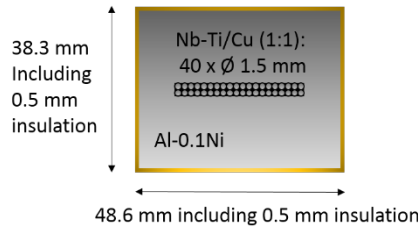


Fig. 5.7: Proposed conductor dimensions and composition of the Forward Solenoids.

### 5.2.3.3 Cryostat

The cryostat of the forward solenoids is mechanically less loaded by weight of detectors. The load on the bore tube is much less since it does not house the forward calorimeters, only the forward trackers, which have a mass of about 15 t. In this case, the strength of the vacuum vessel material is of less importance. However, the cryostat mass is an issue since it needs to be moved aside for detector opening and maintenance, so that it is possible to access the inner parts of the experiment. The aluminium alloy Al 5083-O is the preferred choice for this component because it is the most practical yet strong annealed aluminium alloy. While higher yield strength types exist in the six and seven thousand series, they are cold-worked and during local welding will anneal and are therefore less practical.

The same procedure for optimisation of the dimensions as for the main vacuum vessel was followed. In this case, the vacuum vessel is not symmetric, since large attractive forces of  $\sim 60$  MN between forward solenoids and main solenoid are present. The tie rods need to be positioned in specific spots to allow high force transfer, and are attached to the flange on the side far from the IP, such that the rods are always under tension. Consequently, the cryostat end flange needs to be much stiffer and therefore thicker than the flange on the IP side of the forward solenoids. For the forward solenoid vacuum vessel, the buckling load factor of the first failure mode also exceeds five. The heat loads on the thermal shield and cold mass for the forward solenoids are listed in Table 5.10.

Table 5.9: Forward Solenoid cryostat parameters including vacuum vessel, suspension tie rods, radiation shield.

Parameter	Value
Vacuum vessel length (m)	4
Vacuum vessel inner radius (m)	2.65
Vacuum vessel outer radius (m)	3.56
Vacuum vessel overall thickness (mm)	910
Vacuum vessel outer shell thickness (mm)	58
Vacuum vessel inner shell thickness (mm)	20
Vacuum vessel flange thickness – far from IP (mm)	200
Vacuum vessel flange thickness – close to IP (mm)	30
Axial position relative to IP (m)	11.97-16.20
Vacuum vessel mass (kt)	32 (including reinforcements and feet)
Radiation shield thickness (mm)	5
Radiation shield mass (t)	2.1 (0.9+1.0+2x0.1)
Suspension tie rods diameter – radial (mm)	25
Suspension tie rods diameter – axial (mm)	60
Number of longitudinal tie rods	9
Number of transverse tie rods	12

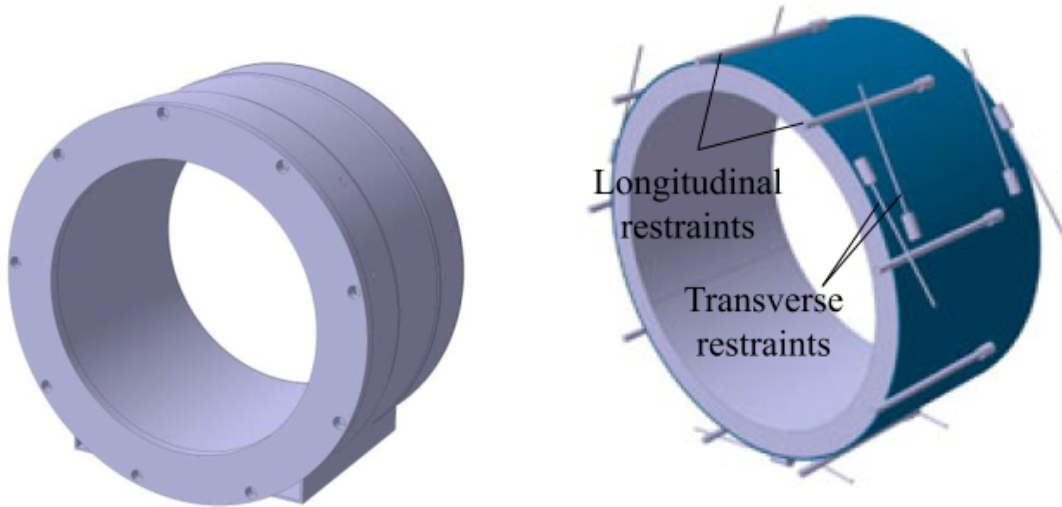


Fig. 5.8: Forward Solenoid vacuum vessel and schematic representation of the positions of the tie rods on the cold mass.

### 5.3 Electrical circuit, quench protection and controls

The electrical circuit for the baseline detector magnet is shown in Fig. 5.9. The main and two forward solenoids are connected in series and connected to a single power converter. This connection is not feasible in the case of main solenoid with forward dipole magnets since their operating currents are different. The solenoids also share a common slow-dump energy extraction system composed of a bank of resistors and diodes. The threshold voltage of the main solenoid's fast discharge diodes combined with the threshold voltage of the forward solenoid by-pass diodes, is sufficiently large to avoid conduction during the slow discharge mode. Note that in the scheme of Fig. 5.9 the diodes allow bidirectional

Table 5.10: Heat load on thermal shield and cold mass of the Forward Solenoids (per magnet).

Component	Load
Radiation heat load on thermal shield at 50 K (W)	525
Radiation heat load on cold mass at 4.5 K (W)	30
Conduction through tie rods at thermalisation points (W)	318
Conduction through tie rods to cold mass (W)	7.1
Total heat load on thermal shield at 50 K (W)	843
Total heat load on cold mass at 4.5 K (W)	37

current enabling bipolar powering of the magnets. Although the baseline design does not include this option, it should be considered for symmetry purposes.

In the case of a quench, a fast discharge is triggered by opening the fast dump current breaker. In fast discharge mode the main and forward solenoids are electrically decoupled by the parallel diodes, as shown in Fig. 5.9. Since the current density in the main and forward solenoids differ by more than a factor of two, most of the stored energy would be dissipated in the forward solenoids if the three magnets are not decoupled, which would lead to an excessive hot spot temperature. Due to the large difference in self-inductance, the main solenoid has a much longer time constant than the forward solenoids. If the fast dump breaker fails to open, the current will by-pass the forward systems via the parallel diodes.

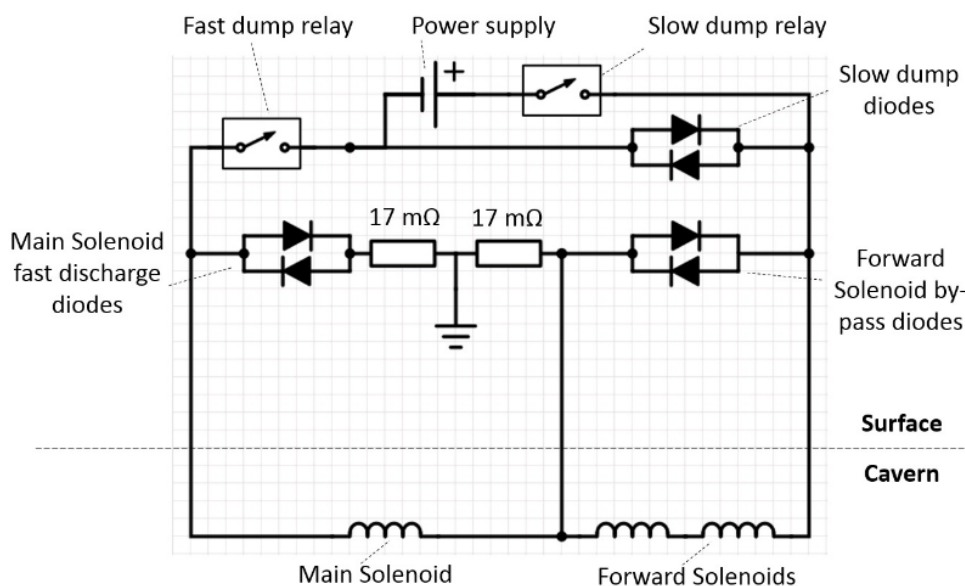


Fig. 5.9: Electrical circuit of the main and forward solenoids showing the common power converter, slow and fast dump breakers and the slow and fast dump resistor-diode units.

To provide easy and fast access for interventions and maintenance, it is planned to install the electrical circuit elements on the surface which will require a system of three bus bars of  $\sim 350$  m length running into the underground cavern. Two of the three leads will carry stationary current and are made of high temperature superconductor cooled with liquid nitrogen or cold return gas from the magnet system [57, 91]. The third bus bar is only active for a short time in the case of a fast dump and it is designed accordingly.

The quench behaviour of the magnets and the circuit described above was analysed [57] and it was found that a fast discharge results in a steep change of the magnet current and thus the magnetic field, causing eddy current loss induced heating in the normal conducting parts of the cold mass effectively

causing quench-back. To make sure that the stored energy is dissipated in a large fraction of the cold mass, thereby limiting the hot spot temperature, additional quench heaters are fired generating multiple normal zones in the coil windings. Fast energy extraction is implemented for the main solenoid, but not for the forward solenoids, see Fig. 5.9. The quench heaters cover the surface of at least nine turns in the main and six turns in the forward solenoids in the innermost layer.

The worst case scenario in which the main solenoid and one of the forward solenoids quench simultaneously was analysed and Fig. 5.10 and Table 5.11 show the results. In the case that both energy extraction and quench heaters fail to work, the peak temperature is still below 142 K in the main solenoid and below 133 K in the forward solenoid in which the quench originates. These numbers can be further reduced by passively increasing the axial quench velocity by introducing highly conductive aluminium strips glued to the inner layer of the cold masses.

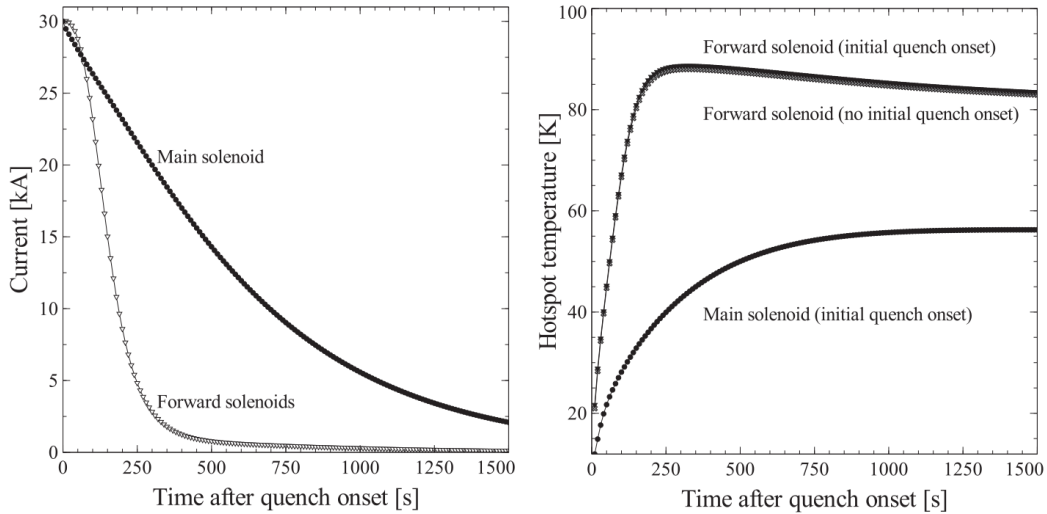


Fig. 5.10: Time dependent current decay during a well-protected quench, i.e. correct functioning of quench heaters and fast dump relay (left). Time dependent temperature evolution during the same quench (right).

Table 5.11: Quench behaviour: hot spot temperatures and voltages for regular and various fault scenarios.

Scenario	$T_{\max,\text{main}}$ (K)	$T_{\max,\text{forward}}$ (K)	Extracted energy (%)	$V_{\max,\text{main}}$ layer to layer (V)	$V_{\max,\text{main}}$ turn to ground (V)	$V_{\max,\text{forward}}$ turn to turn (V)
<b>Normal using quench heaters and energy extraction</b>	<b>56</b>	<b>89</b>	<b>73</b>	-	-	-
Failing quench heaters	60	138	73	-	-	-
Failing energy extraction relay	93	86	0	350	500	45
Worst case scenario: failing heaters & no extraction	142	133	0	-	-	-

#### 5.4 Main solenoid with forward dipole magnets (Alternative layout)

An alternative to the baseline of using a main solenoid and two forward solenoids to enhance the magnetic field for high-pseudorapidity particles, has been investigated. Since the magnetic field is almost



parallel for particles travelling at a low angle in the direction of the particle beam, the bending power is low. A perpendicular dipole field is more effective locally in the forward direction, rather than an almost parallel solenoidal field. One of the first proposals was to use force and torque balanced forward dipole magnets [87]. Simpler, lower risk and much more cost-effective designs were favoured over large, complex and more expensive magnet systems in the evolution towards the baseline system, as reported in Ref. [57]. Depending on the magnetic field in the solenoid, the momentum resolution in the case of three solenoids, can match the dipole case because tracking for the solenoid starts at the IP and extends along the entire trajectory. In the case of dipoles the transverse field is high, but it is only local and thus it is limited.

From a physics point of view, forward dipole magnets should not be excluded. The impact on the event analysis of a forward dipole field as opposed to a forward solenoid field has been investigated and is discussed elsewhere in this report. An optional design using forward dipoles which did not have a high impact on the overall layout of the experiment was developed. The dipole cold mass had to fit within the same envelope as the forward solenoid [90], see Fig. 5.11. A more detailed study is required to fully understand the impact of the forces and torques in the system. The largest change is in the mechanical design as the suspension tie rods and vacuum vessel walls have to be carefully designed to respect the envelope of the system. Also the supports of the dipole vacuum vessel on the main solenoid vacuum vessel as well as supports on the cavern floor have to be considered.

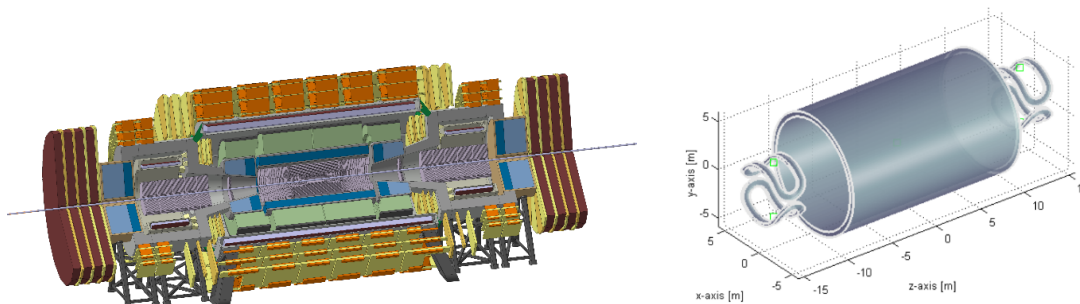


Fig. 5.11: (left) Overview of the baseline FCC-hh experiment including magnet systems, trackers and calorimeters. (right) Alternative: cold mass of central solenoid working together with two forward dipole magnets.

The choice of forward solenoids as the baseline is robust and based on strong technical arguments. The proposal of a magnet system with alternative forward dipoles is based on eventually improving the tracking performance for high-pseudorapidity particles. The proposed forward dipole magnets are unprecedented in dimension and stored energy, much more complex in construction and risky. Moreover, the azimuthal and rotational symmetry is lost and tracking is a challenge in the transfer zone between solenoid and dipole magnet.

#### 5.4.1 Magnetic field in the main solenoid—forward dipoles case

The magnetic field in the alternative design using forward dipole magnets is shown in Fig. 5.12. The magnetic field in the main solenoid does not change much between the baseline and alternative, but the magnetic field in the forward region changes drastically. In one of the forward directions, the magnetic field is pointed upwards, while in the other forward direction the magnetic field is pointing downwards, so that the net Lorentz force on the particle beam cancels out to zero.



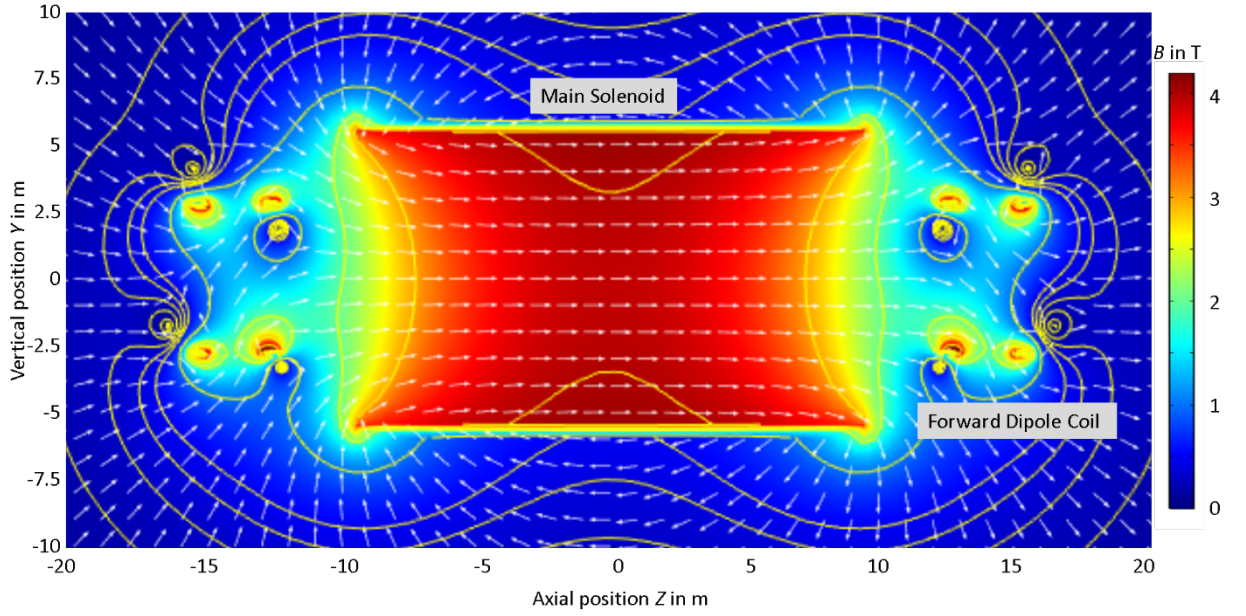


Fig. 5.12: Magnetic field map for a central solenoid of 4 T with a dipole magnet on either forward side, delivering a 4 Tm integrated field on axis.

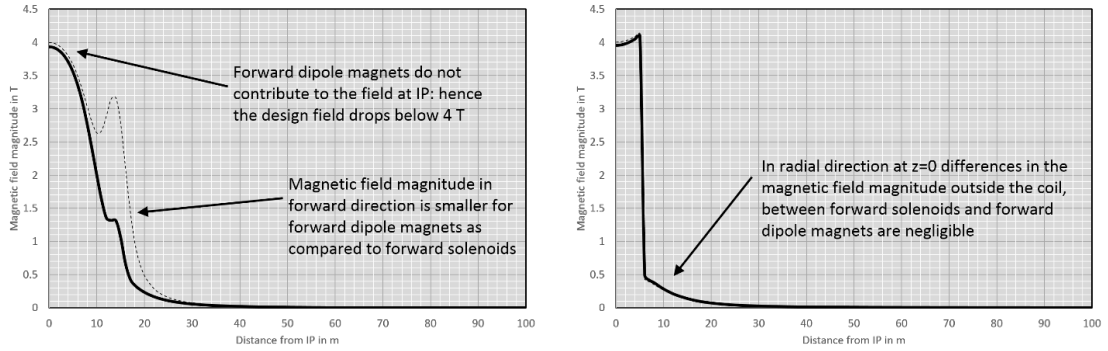


Fig. 5.13: Magnitude of the magnetic field as a function of distance from the IP, comparing forward solenoids and forward dipole magnets: along the  $z$ -axis (left) and in the radial direction (right). The magnetic field magnitude in the forward direction is much less for the forward dipole option, although the perpendicular component of the magnetic field for high- $\eta$  particles is much higher. In radial direction, there are almost no differences.

#### 5.4.2 Forward dipole magnets

Precise momentum measurements are required to reduce the error in the particle mass. The relative transverse momentum resolution is given by:

$$\frac{\sigma(p_T)}{p_T} = \frac{\sigma_x \cdot p_T}{0.3BL^2} \sqrt{\frac{720}{(N+4)}}$$

where  $B$  is the magnetic field in T,  $L$  the length of the particle track in the field in m,  $p_T$  the transverse momentum in kg.m/s and  $N$  the number of measurement points. It shows that the error in the transverse momentum can be reduced by either a more precise measurement (resolution of the detectors) or by increasing the double field integral  $BL^2$ , which is a direct measure for the sagitta of a particle track. Evidently, a higher magnetic field covering a larger volume is preferred.

If only the magnetic field of the main solenoid is considered, the absolute magnetic field integral for different pseudo-rapidities is shown in Fig. 5.14. It shows quantitatively the requirement for forward magnets: the integrated perpendicular magnetic field, and thus also the double integral of the perpendicular magnetic field, is very small for high-eta particles, since the magnetic field is pointing almost parallel to these trajectories.

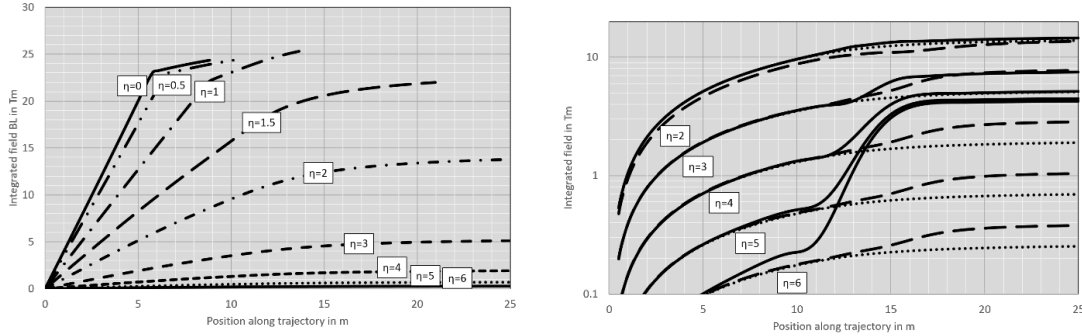


Fig. 5.14: (left) Integrated (absolute) magnetic field as a function of the position along the trajectories inside the volume covered by detectors if it is only the main solenoid generating the magnetic field. Since the detector is much longer than it is wide, high- $\eta$  tracks result in longer curves. (right) Impact of forward dipole magnets on the integrated magnetic field for various values of pseudo-rapidities.

The integrated magnetic field must be as high as possible for *all*  $\eta$  and therefore, especially in the forward region, there is a lot to gain and this can be achieved by introducing a perpendicular magnetic field generated by forward dipole magnets. An integrated magnetic field of 4 Tm for  $\eta$  between 4 and 6 is sufficient to significantly improve tracking in the forward region as is shown in Fig. 5.14 (right).

The operational parameters are summarised in Tab. 5.12. The current and current density of the forward dipole magnets is different to the main solenoid and the magnets require their own electrical circuit. This implies a more complex quench protection scheme as well, since currents and thus forces can change over time in either circuit. Forces will not only change in magnitude, but also in direction, asking for a specifically optimised mechanical structure as compared to the forward solenoid option. There is a net torque over the  $x$ -axis of some 57 MN.m and an upward force of 11 MN. Note that there must be no vertical component in the magnetic field integrated over the detector axis. Therefore, the current in the two forward dipole magnets is in opposite direction. The magnitude of the magnetic field as a function of distance from the IP is shown in Fig. 5.13. Compared to the all-solenoids baseline, there is still a left-right symmetry and forward-backward symmetry for magnetic field magnitude, not direction; but no top-bottom symmetry in either field magnitude or direction. If the magnetic field is swapped in the vertical plane, i.e. the forward dipoles are powered with the reverse polarity, the magnetic field points down, horizontal to the right and then up again. The force pattern will swap as well. There will be either a net force *down* on the set of forward dipole magnets and *up* on the main solenoid, or vice versa. In the first situation, the forward dipoles are pushed downwards, while the main solenoid wants to move upwards. This is the preferred situation, since the main solenoid is equipped with strong static feet, while the forward magnets always make use of a removable structure, which should contrarily also be easy to handle and relatively light and thus less strong. In addition, the main solenoid houses the calorimeters and the inner tracker and the mass of the calorimeters and the gravitational force acting upon them work in the correct direction.

### 5.4.3 Cold mass

The cold mass design of the dipole magnets is quite different compared to the forward solenoids due to its more complex shape and the large forces acting on the conductors. Stainless steel is used for the support

Table 5.12: Forward dipole magnet main operational parameters.

Parameter	Value
Transverse magnetic field on axis (T)	1.0
Integrated magnetic field along axis (Tm)	4.0
Operating current (kA)	16
Forward dipole magnet self-inductance (H)	1.66 (top 0.77, bottom 0.77, 2× mutual 0.06)
Mutual inductance main solenoid to forward dipole (H)	0 (top -0.05, bottom +0.05, canceling out)
Mutual inductance dipole to dipole (mH)	0.33
Stored magnetic energy (MJ)	213
Peak magnetic field on conductor (T)	5.9
Operating temperature (K)	4.5
Torque over x-axis (MNm)	57
Downward force (MN)	11

structure, which allows welding. Since the conductor mainly consists of copper and stainless steel which exhibit similar thermal contractions, high thermal stress due to cooling is avoided. The design is mostly inspired by the so-called Morpurgo dipole magnet operating at CERN on a test beam line in the North Area [92]. The main and forward solenoids make use of conduction cooling, which is only possible if the overall thermal conductivity of the materials in the cold mass is rather high like that of aluminium. When using stainless steel supports, the thermal conductivity is poor and conduction cooling is not an option. In addition, the conductors proposed for the forward dipole magnets are much smaller in cross-section and therefore the amount of insulation material in the cold mass is relatively high. Internal cooling is a proven technology in this case [92] and has a direct impact on the shape and dimensions of the conductor.

The support of the coil windings can be either done from inside and outside [75], or when using pre-compression from outside only [87]. The assembly procedure for the first method implies the use of a 50-mm thick stainless steel support cylinder. The coils are wound on mandrels, vacuum impregnated and transferred to this support cylinder. Cover plates of the same thickness, are then bolted or welded to create a tight enclosure. Inflated bladders are used to guarantee pre-compression on the coils thereby avoiding local cracks in epoxy and mitigating the risk of coil training.

The assembly procedure for the second method is based on the design of the W7X stellarator magnets [87]. In this case the coils are pre-compressed to avoid conductor movement. Instead of transferring the coils from mandrel to support cylinder, a stainless steel casing is placed over the coil and the coil is bolted to the main casing together with smaller supports. Welding guarantees proper mechanical connections. By heating the casing and filling the voids with a mixture of quartz and resin, the thermal shrinkage of the casing results in pre-compression of the coil windings. Both top and bottom half shells can be prepared separately and bolting and welding yields a rigid cold mass.

#### 5.4.4 Superconductor

The conductor has a different shape and dimensions to the conductors for the main and forward solenoids. Internal cooling of the forward dipoles is by forced helium flow through every turn of the coil using cable in conduit conductor. The concept is to have an inner cylinder acting as helium tube. NbTi strands are wound around a centre cooling and enclosed by two U-profiles when connected forming a conduit with a square cross-section, and insulated by a 0.5 mm thick layer of resin impregnated glass tape. The details of the conductor are presented in Fig. 5.15 and Tab. 5.14. Due to the relatively low stored energy compared to the main solenoid, the current density is much higher.

Table 5.13: Forward dipole magnet cold mass main specification.

Parameter	Value
Cold mass length (m)	3.40
Cold mass inner radius (m)	2.75
Cold mass outer radius (m)	3.08
Cold mass thickness (mm)	275
Axial stretch relative to IP (m)	12.3 to 15.7
Steel inner support cylinder thickness (mm)	50
Number of layers	11
Number of turns per layer	28
Cold mass parts: Nb-Ti, Cu, G10, steel, <b>total</b> (t)	2.2, 42.9, 0.53, 23.4, <b>69</b>
Stored energy over mass density (kJ/kg)	8.5

Table 5.14: Design parameters of the forward dipole magnets conductor.

Parameter	Value
Conductor width including insulation (mm)	25.0
Conductor thickness including insulation (mm)	25.0
Fiber reinforced epoxy insulation thickness (mm)	0.50
Inner diameter copper tube (mm)	13.7
Copper tube thickness (mm)	1.0
Outer diameter copper tube (mm)	15.7
Number of strands	36
Strand diameter (mm)	1.5
Strand composition, ratio NbTi to Cu	1:1
Radius semi-circle slot in -profile (mm)	9.35
Cable length (km)	23
Current density in NbTi ( $A/mm^2$ )	503
Mean current density in conductor ( $A/mm^2$ )	25.6
Current sharing temperature (K)	6.2
Temperature margin (K)	1.7

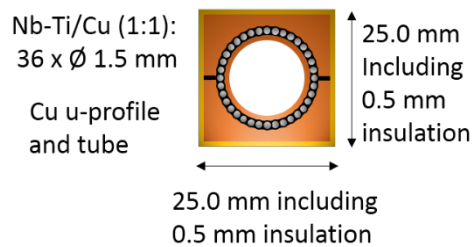


Fig. 5.15: Cross-section of the conductor for the forward dipole magnets.

#### 5.4.5 Cryostat

The cryostat for the dipole magnet is similar to that for the forward solenoids, but local reinforcements are required to deal with the large forces and torques. This will cause a mass increase as a result of locally thicker shells, flanges and tie rods with larger diameters. Eventually a stainless steel version may

be preferred.

## 5.5 Cryogenics

For the main and forward solenoids a thermosiphon cooling scheme, very well-known from the CMS and ATLAS solenoids, is used. Helium flows through cooling channels attached to the solenoid's support cylinder and heat is drained by conduction from the coil windings. The number of coil winding layers and the size and shape of the conductor are optimised for minimum thermal gradient. A main advantage of thermosiphon cooling is that the natural flow of coolant is guaranteed without using pumps. For the alternative forward dipole magnets case, forced flow helium cooling is necessary and pumps are required.

The concept of the cryogenic system for cooling of the superconducting magnets is ready but may be adjusted in due time [91]. Given the cryogenic requirements of operating temperature, heat load, cooling concept, operating current and total cold mass, it can be quickly established that a cryogenic system with moderate cooling capacity, complexity and size is sufficient. Secondly, the total cold mass is large and a long cool-down time is expected during the first cool down when only the cooling capacity required for nominal stationary thermal operation at 4.5 K is available. Thirdly, the position of the experimental cavern at about 300 m below the surface requires special attention concerning the transport of the cold helium between the cryoplant on the surface and the experiment cavern due to the fluid-static compression.

The cryogenic plant is installed on the surface and not underground as this facilitates interventions on critical installations like main and shield refrigerators. Underground space is precious, expensive and access is limited and time consuming. To avoid an accidental quench due to failure of the cooling systems and the need to re-cool and ramp the magnets, failure of any cryogenic sub-equipment must not lead to critical situations for the magnet. The cryogenic design must allow the operational current to be ramped up or down over a time span of several hours, even if mains or other standard service systems fail. To avoid time-consuming cool-down and structural fatigue due to thermal cycling, the cold masses are kept below 100 K for tens of years—over the whole lifetime of the experiment. The cryogenics concept of ATLAS is followed and two separate and independent refrigerators are installed: a shield refrigerator dedicated to cooling down and shield cooling, and a main refrigerator producing liquid helium for servicing the cold masses. In the case of failure of either unit, sufficient cooling capacity to keep the cold mass below 100 K is guaranteed.

High-pressure helium gas at 20 bar from the surface plant is sent down the shaft to the cavern where JT-liquefaction can take place in a buffer dewar from which helium is distributed to the main and forward magnets, each of which is equipped with a two-phase helium vessel. The amount of liquid is sufficient to guarantee cooling during a slow discharge of several hours. An additional reserve is required for the case of equipment or utility failures leading to additional downtime. Dimensions and helium inventory are summarised in Table 5.15 .

Table 5.15: Liquid helium storage in the experiment cavern.

	Quantity
Volume of phase separator for main solenoid (kL)	17
Mass of liquid helium in large phase separator (t)	1.6
Volume of phase separator for each of the forward solenoids (kL)	2.5
Mass of liquid helium in each of the small phase separators (t)	0.22

Keeping the cold mass temperature below 100 K is guaranteed when the thermal shield can stay at its nominal temperature, or when the main refrigerator has enough cooling capacity at 80 K when the shield is not cooled at all. Since the cold mass is huge and has a large heat capacity, the thermal inertia

of the system is large as well. Experience shows that such magnets can be kept below 120 K for three to four weeks without operating any refrigerator provided that the vacuum system is fully functional.

The capacity of the refrigerators not only depends on the heat loads in the magnet, but also on heat loads of flexible and rigid transfer lines, storage dewars and cryogenic valve boxes. A contingency factor of 1.5 is applied to cover uncertainties and safety factors. The required liquefaction capacity is summarised in Table 5.16.

Table 5.16: Capacity of main and shield refrigerators for the baseline magnet system.

	4.5 K main refrigerator (nominal)	4.5 K main refrigerator (re-liquefaction)	80 K shield refrigerator
Liquefaction (g/s)	2	12	-
4.5 K refrigeration (W)	610	610	-
20 K heat load (W)	80	80	-
Thermal shield load 50–75 K (kW)	0.90	0.90	11
Total equivalent load at 4.5 K (kW)	1	19	0.67
LN2 boost	NO	YES	NO

Cool down times can be estimated by making use of best estimates for the compressor mass flow and cooling capacity as a function of temperature as shown in Fig. 5.16 (left) leading to the cool down time indicated in the figure.

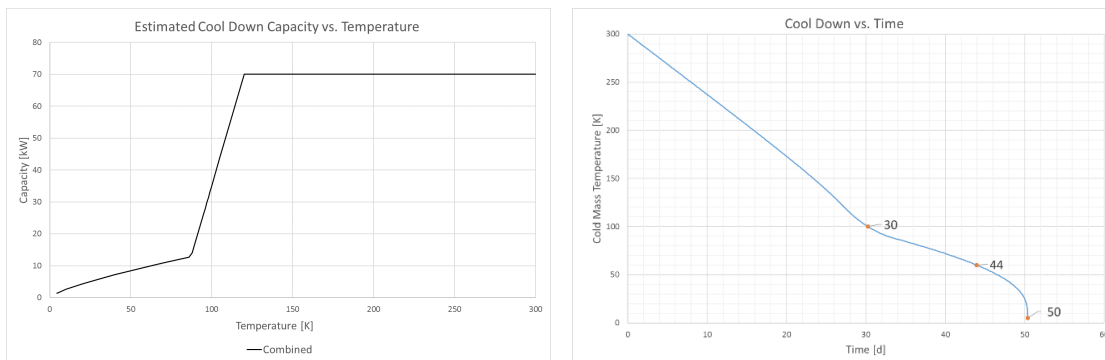


Fig. 5.16: Cool down capacity as a function of temperature (left) and cool down time (right).

Most parts of the cryogenic system and electrical circuit components for the magnet are installed on the surface. The following equipment is schematically represented in Fig. 5.17:

- Liquid nitrogen storage: two reservoirs of 25 kL each; 370 h autonomy on each tank for current lead cooling and equal to road trailer capacity;
- Gaseous helium storage: four tanks of 200 m<sup>3</sup> each, 2 t of helium in total;
- Common compressor station building: ambient-temperature helium compressors and spares;
- Liquid nitrogen pre-cooling unit: for initial cool down and boost;
- Upper cold box of split-design 4.5 K refrigerator: helium supply down to 20 K;
- Shield refrigerator cold box;
- Liquid nitrogen cooled current lead cryostat.

In the 300 m vertical shaft:



- 200 mm diameter chimney line housing high temperature superconducting bus bars connecting the vapour volume of the phase separator for the main solenoid to the current lead cryostat; vacuum insulated without thermal shield;
- 400 mm diameter transfer line linking the upper and lower cold boxes of the 4.5 K refrigerator; vacuum insulated and thermally shielded;
- 250 mm diameter transfer line with connecting the shield refrigerator to the thermal shield circuits in the experiment cavern.

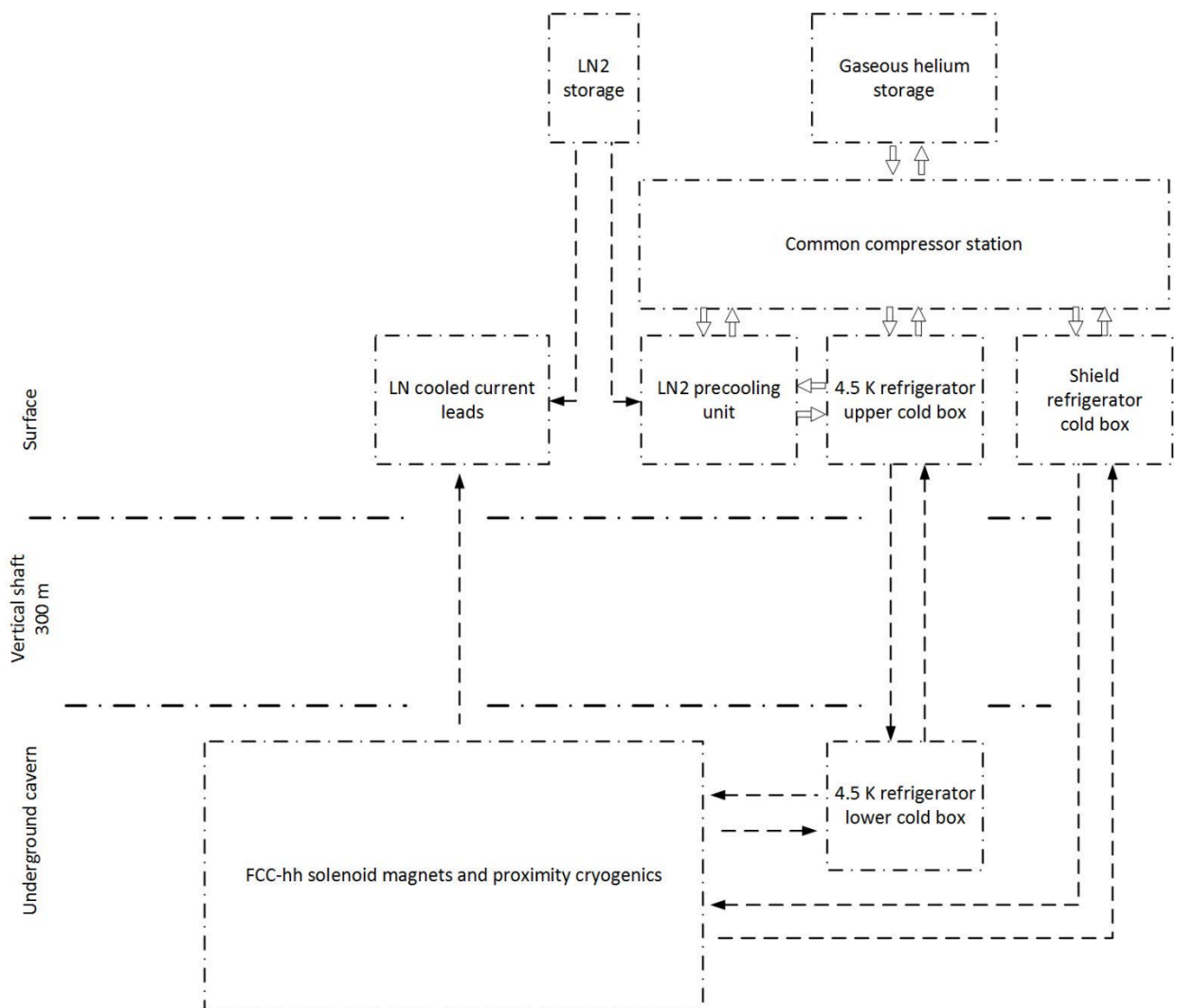


Fig. 5.17: Cryogenics layout showing parts installed on surface, lines running down the 300-m long shaft, and parts installed near the three solenoids.

The simplified flow diagram is shown in Fig. 5.18. The current bus bars transit through the main proximity phase separator, from the magnets up to the current lead cryostat at the surface level. This line carries all the helium vapour evaporated during magnet cooling and thus automatically cools the high temperature superconducting current leads. In the case of failure, cooling capacity reduces, heat load increases and therefore, helium flow cooling the leads increases, thereby guaranteeing stable behaviour.

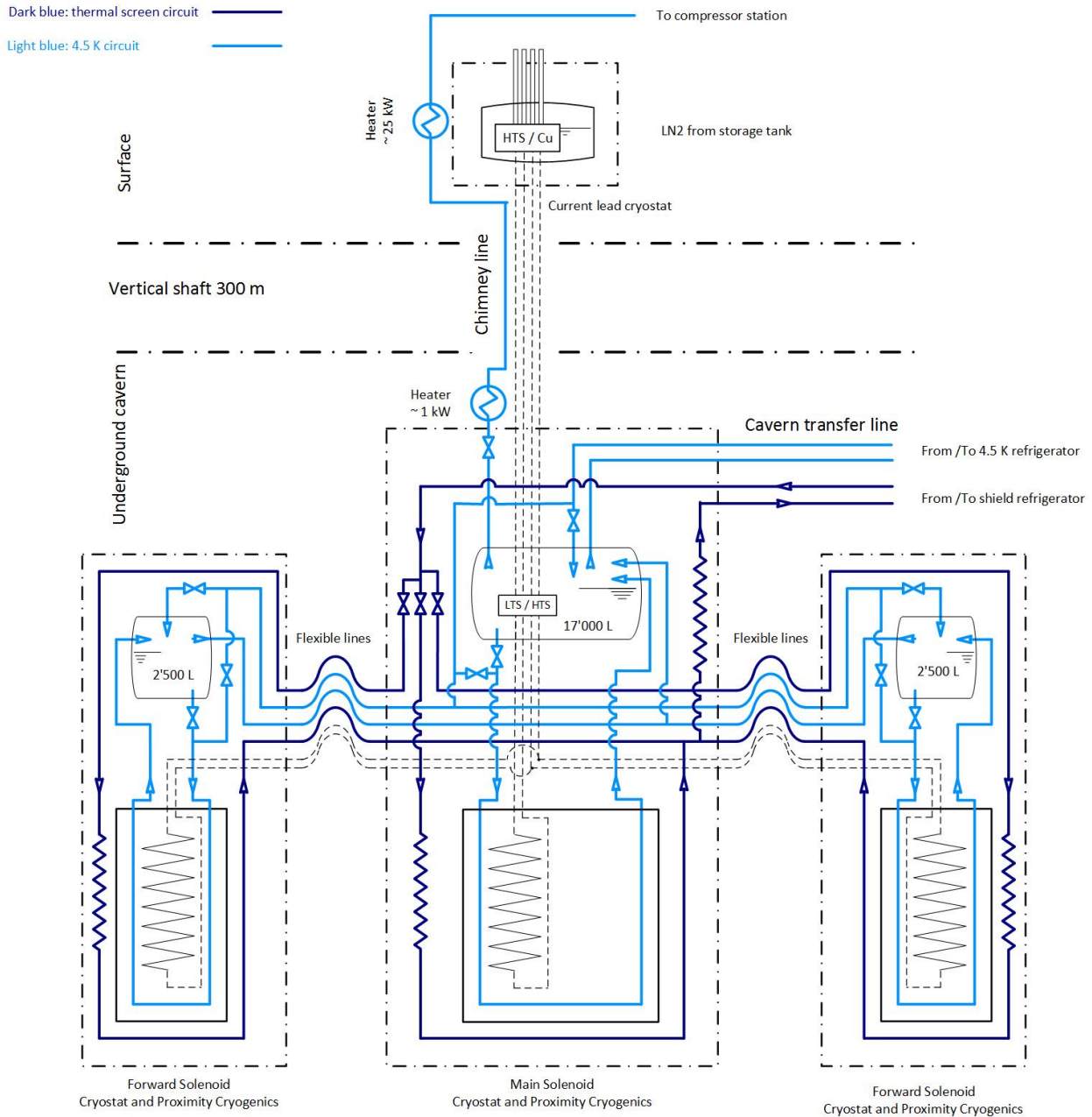


Fig. 5.18: Simplified helium flow diagram of the cryogenic installation for the baseline magnet system.

## 5.6 Magnet system installation, shielding and infrastructure

### 5.6.1 Main and side cavern

The return path of the magnetic flux has been an important design and cost consideration. When very precise momentum measurement of muons outside the main solenoid important, there must be sufficient magnetic field strength to deliver the bending power required. This can be achieved by directing the flux into the region directly surrounding the main solenoid. Flux return can be by a second, larger coil around the main solenoid, using a very large twin solenoid as was proposed in the early stage of the design [75]. Another option is to make use of a return yoke as in CMS for which however, a large amount of magnetic material is used. Studies showed that both of these options were bulky, heavy and most importantly, too expensive.



Since the experiment cavern is located some 300 m underground, a less concentrated stray field reaching out over larger distances is considered acceptable and sufficient for muon momentum measurements. It also has no negative impact on the environment since the stray field at the surface is far below the pacemaker limit of 0.5 mT. However, for auxiliary equipment like pumps, fans and moving parts in general, magnetic fields can cause problems. The general limit is  $\sim 5$  mT for rotary equipment and this is reached at a distance of 52 m from IP (see Fig. 5.3). The distance between the closest walls of the main and service caverns is 60 m (see Fig. 5.19) for civil engineering and cost reasons. This separation is favoured over the situation where the service cavern is located close to the experimental cavern for several reasons, but it also has some drawbacks. A few aspects are:

- If the service cavern is located close, the magnetic stray field is several tens of mT and massive magnetic shielding is required. Total shielding of the service cavern is not an option due to the large amount of magnetic material whereas local shielding may be, but the implementation is still cumbersome.
- If the caverns are close, the civil engineering is much more difficult, risky and costly. It is much easier to have two independent cavern structures connected by tunnels.
- The increased distance between service cavern and experiment cavern requires longer cables and transfer lines. The consequent signal delays need to be accounted for, but with present day technology, no significant problems are expected.
- The space requirements for detector and magnet systems installation and maintenance have determined the dimensions of the caverns and access shafts and these are presented in Fig. 5.20 and listed in Table 5.17.

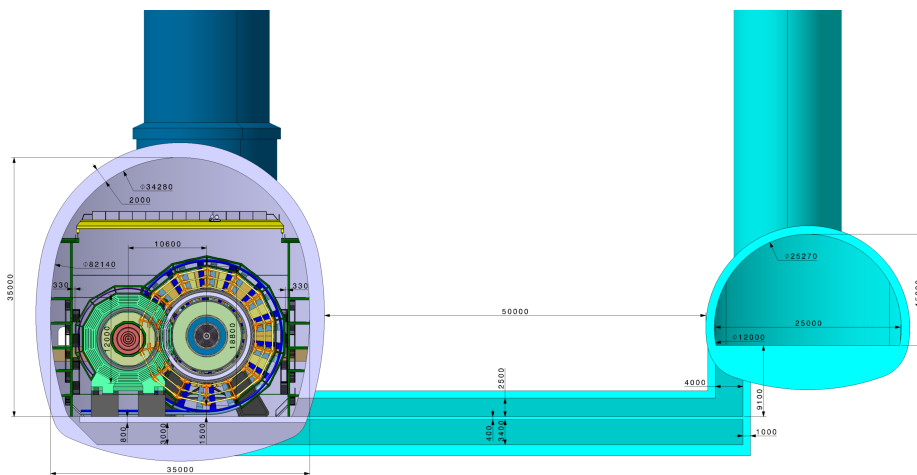


Fig. 5.19: Positions and cross-sectional dimensions of the experiment and service caverns.

## 5.6.2 Assembly and installation

Assembly and installation of the FCC-hh experiment and its magnet system need special attention. The logistics and infrastructure needed depend on the dimensions and weights of the various components. The main solenoid is the largest single sub-element and requires special handling.

The installation procedure developed has been visualised in a video [83]. It shows the main steps necessary to reach the final stage with the experiment operational. A few steps are illustrated in Fig. 5.21. Although the installation procedure will be developed further, currently the main steps planned are:

Table 5.17: Cavern and shaft dimensions determined by the installation and opening scenarios of the baseline detector and its magnet system.

Maximum length of experiment in open position (m)	66
Cavern size (L × W × H) (m <sup>3</sup> )	66 × 30 × 35
Main shaft diameter (m)	15
Secondary shaft diameter (m)	10
Main shaft crane requirement (kt)	3.0
Secondary shaft crane requirement (kt)	0.6

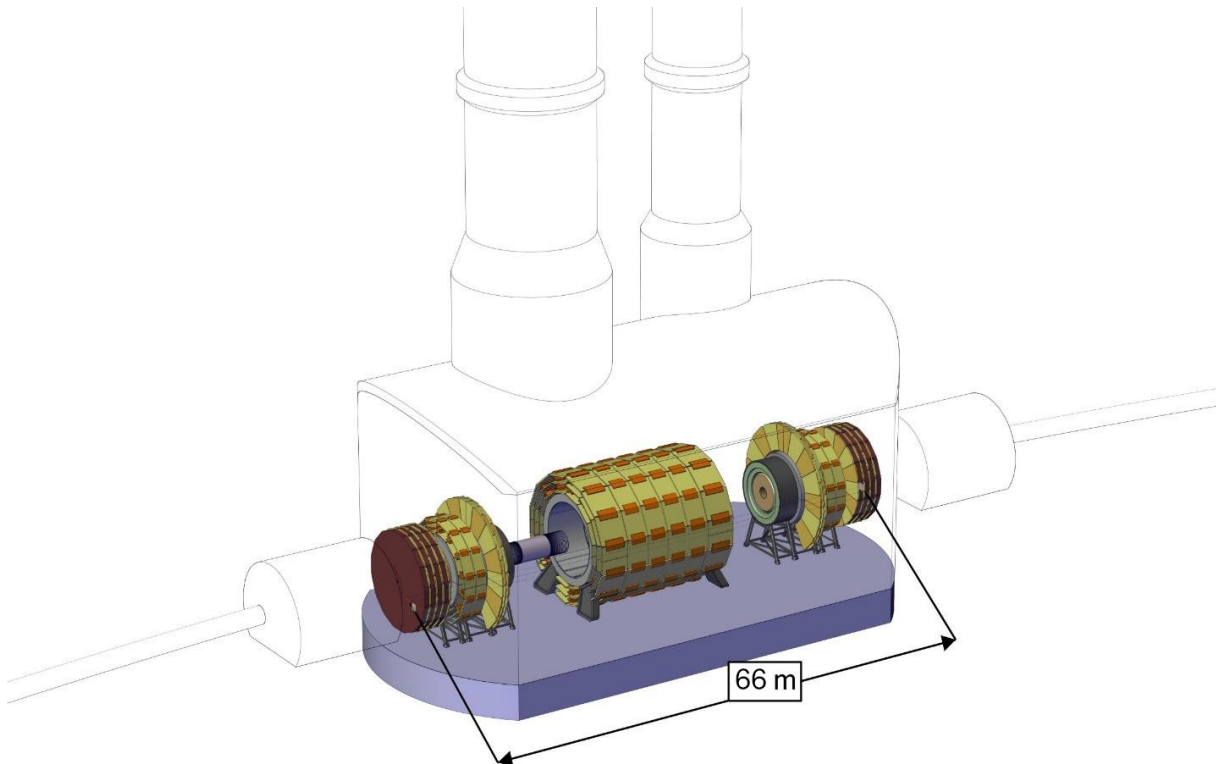


Fig. 5.20: Position of key components of the FCC-hh experiment during the proposed long opening scenario, when the maximum opening length is reached.

1. Installation of the central solenoid: tilted vertically and lowered through the main access shaft. Once in the experimental cavern, it is rotated to become horizontal and is placed on its feet;
2. Installation of the first HCAL module, together with the first ECAL module;
3. Installation of the central HCAL and ECAL modules;
4. Installation of the inner tracker and centre section of beam pipe;
5. Installation of the last HCAL module, together with the last ECAL module;
6. Installation of the forward tracker module inside the first and last ECAL modules;
7. Installation of the muon chambers system around the main solenoid;
8. Installation of the forward muon chambers, including massive magnetic shielding disks, located at the parking position, which is located axially away from IP to allow space for installation of the forward parts;

9. Installation of the forward solenoid support structure at either side of the main solenoid. The equipment is lowered via both access shafts. The forward components at one side of the main solenoid are installed through the main access shaft. The components installed via the secondary, off-axis shaft, are lowered and moved to their final position as a larger integrated structure. Not all components of both forward systems can be lowered via the main shaft, since the main solenoid and the other components which are already installed will block the passage to the other side of the experiment;
10. Installation of the bottom half of the massive radiation shield, surrounding the forward solenoids;
11. Installation of the forward solenoids on either side of the main solenoid;
12. Installation of the bottom half of the radiation shield nose;
13. Alignment of forward solenoids and main solenoid. Installation of the section of beam pipe which extends the central part up to the far end of the forward systems;
14. Installation of the forward trackers;
15. Installation of the top half of the radiation shield;
16. Installation of the top half of the radiation shield nose;
17. Installation of additional muon chambers in front of the radiation shield nose, seen from IP;
18. Installation of mechanical support structures called spokes that connect the forward vacuum vessels and the forward radiation shield to the vacuum vessel of the main solenoid;
19. Installation of additional muon chambers, closing the volume of the main system;
20. Installation of the forward ECAL support structure;
21. Installation of the bottom half of the ECAL radiation shield;
22. Installation of the forward ECALs;
23. Alignment of the off-axis ECAL, which was lowered through the secondary shaft;
24. Installation of the top half of the ECAL radiation shield;
25. Installation of the remaining muon chambers;
26. Movement and alignment of forward muon wheels to their final position.

Access to the inner components of the experiment is requested for repairs, replacements and upgrades. Short and long opening scenarios are proposed with the following steps for the short opening scenario:

1. Movement of the forward muon wheels, including detectors and shielding away from IP in the axial direction, i.e. to the parking position towards the end walls of the cavern;
2. Opening of the radiation shield, moving the forward ECALs with shielding and muon detectors away from IP in the axial direction;
3. Parking the muon chambers that are closing the main volume, so that access to the spokes connecting the forward vacuum vessel and shielding to the main vessel is available;
4. Movement of the forward solenoids away from the IP to near the parking position of the forward muon wheels and forward ECALs;
5. Installation of support structure for HCAL;
6. Movement of HCAL modules away from IP and to the top of the support structures;
7. Movement of HCAL and support structure towards the parking position of the forward solenoids;
8. The far ends of the forward muon wheels are now positioned about 70 m apart leaving about 5.5 m between the parked HCAL modules and the main solenoid.

For the long opening scenario, some additional steps are required:

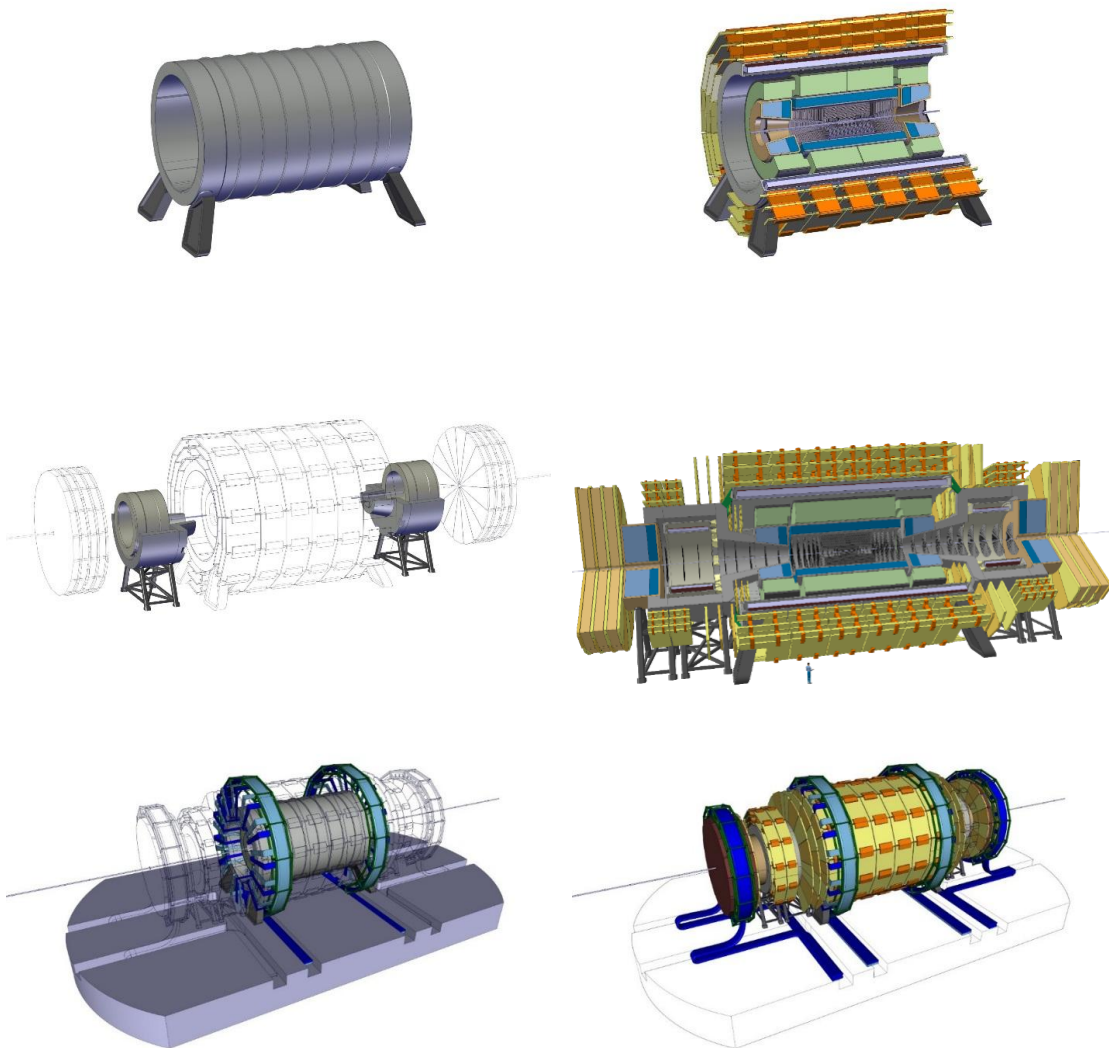


Fig. 5.21: Several installation steps are highlighted in the first two rows, from left to right: step 1, step 7, step 13, step 26. The bottom row shows how cables and services for the detectors inside the main solenoid are routed to the exterior of the detector and then to the service cavern. The forward detectors will make use of flexible chains positioned in trenches which only allow longitudinal movements.

1. Movement of the forward muon wheels, including detectors and shielding away from IP in the axial direction, i.e. to the parking position towards the end walls of the cavern;
2. Removal of the part of the beam pipe that has been liberated;
3. Opening of the radiation shield by moving the forward ECALs with shielding and muon detectors away from IP in the axial direction;
4. Removal of the part of the beam pipe that has been liberated;
5. Removal of the forward trackers if necessary;
6. Parking the muon chambers closing the main volume such that access is available to the spokes connecting the forward vacuum vessel and shielding to the main vessel;
7. Movement of the forward solenoids away from IP in the axial direction, to near the parking position of the forward muon wheels and forward ECALs;

8. Removal of the section of the beam pipe that is now accessible;
9. Removal of muon chambers on the top of the radiation shield nose;
10. Removal of top half of radiation shield nose;
11. Removal of tracker modules in forward direction;
12. Removal of muon chambers on the bottom of the radiation shield nose;
13. Installation of the support structure for HCAL;
14. Movement of HCAL modules away from IP to the top of the support structures;
15. Movement of HCAL and support structure towards the parking position of the forward solenoids;
16. Removal of another section of beam pipe;
17. Extraction of the inner trackers.

## 5.7 Alternative designs for the magnet system

During the design phase, several options for the magnet system were studied before converging on the baseline system comprising a main solenoid complemented with two forward solenoids, and the baseline alternative of using forward dipole magnets. The main technical disadvantages of the baseline design, though justified with good arguments with cost as the dominant aspect, is the limited bending power in forward direction, non-optimal use of the magnetic field and large stray field. The main drawbacks of the baseline alternative using dipole magnets are the presence of very large forces and torques between the main and forward magnets and high risk of failure since such wide bore dipole magnets have never been built.

Several alternative designs were proposed and partly engineered [57, 58, 93], and three of these are presented briefly here. Each one of them addresses one or more of the shortcomings of the baseline design, but obviously also have their own drawbacks and shortcomings mainly concerning complexity, risk and cost.

### 5.7.1 Actively shielded twin solenoid and forward dipoles

A very large 6 T, 12 m diameter free bore, twin solenoid was considered as baseline for quite some time, but was finally abandoned as being too large and too expensive with a price tag of roughly 900 MCHF [57]. However, a scaled down version with a 4 T main magnetic field and a 10 m diameter free bore, might still be an interesting alternative for the baseline. The main solenoid would in this case be very similar to the one described before, but there would be an additional outer shielding coil. This so-called twin solenoid comprising two solenoids oppositely powered, features magnetic shielding and concentrates the return flux from the main solenoid and therefore delivers comfortable magnetic field for precise muon momentum measurements beyond the outer skin of the main solenoid. An additional benefit would be the strongly reduced stray magnetic field, since the twin coil actively provides shielding for the main solenoid. For this design, force and torque balanced dipoles are an interesting feature. The main disadvantage of a force and torque balanced forward dipole magnet is its complexity. Several magnets with different operating currents and complex shapes are required to minimise forces and torques between the forward system and the main solenoids. The original large twin solenoid and in particular the force and torque balanced dipole magnets are presented in detail in Refs. [75] and [87], respectively. Fig. 5.22 shows the layout of the bare magnets, while Table 5.18 summarises their key parameters.

### 5.7.2 Iron yoke solenoid with forward dipole/toroid

Magnetic flux can also be collected and returned through a ferro-magnetic yoke, which is a proven concept demonstrated in the CMS experiment [64]. However, a massive amount of steel is required for this alternative. There were two different designs discussed in detail in Refs. [88] and [89]. The

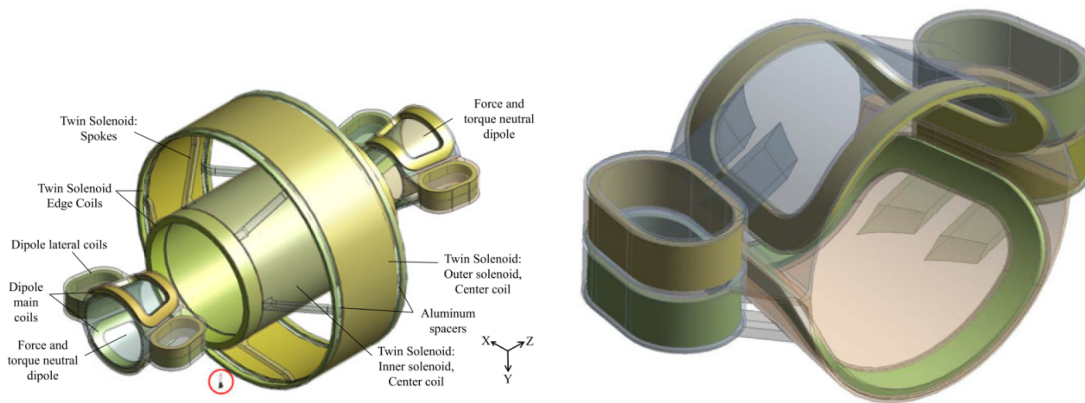


Fig. 5.22: Large 12 m free bore and 6 T twin solenoid with forward force and torque balanced dipole magnets (left). A more detailed view of 4 Tm integrated magnetic field forward dipole magnets, with compensation coils to avoid large net forces and torques (right).

Table 5.18: Main specification of the 4 T/10 m free bore twin solenoid with 4 Tm forward dipole magnets.

	<b>Twin solenoid</b>	<b>Balanced dipole</b>	<b>Unbalanced dipole</b>
Stored energy (GJ)	15	0.24	0.13
Operating current (kA)	47	16.6	16.6
Self-inductance (H)	14	1.7	1.0
Conductor length (km)	85	15	8
Cold mass (kt)	1.25	0.25	0.10
Vacuum vessel mass (kt)	1.40	0.15	0.18

first design, still based on the original 6 T, 12 m diameter free bore main solenoid, proposes a ‘minimum’ yoke comprising 23 kt of magnetic steel. The interesting aspect of this design is that in the forward region there are not only dipole magnets, but also toroidal magnets formed by magnetising steel disks. These are useful for precise muon measurements at the far ends of the experiment, making the magnetic elements in the experimental cavern stretch out over a length of 63 m. The dipole magnets deliver horizontal opposing magnetic fields on either side of the main solenoid. The conductor and quench back cylinder are of copper alloy rather than aluminium. An overview of the principle coil windings and yoke design is given in Fig. 5.23.

The second design makes use of the same idea for creating more bending power at the periphery of the main solenoid and reducing stray field. It evolved in such a way that a comparison to the baseline design can be made. In addition to being more expensive due to the introduction of large amounts of steel, the advantages are considered to be negligible. The general parameters of the minimal return yoke are summarised in Table 5.19, while Fig. 5.24a gives an overview of the baseline design equipped with a minimal yoke. The radiation shielding is made of magnetic carbon steel, rather than non-magnetic material as proposed in the baseline. A comparison of the magnetic field between the baseline and this minimal yoke design is shown in Fig. 5.24b [94].

### 5.7.3 Ultra-thin solenoid positioned inside the calorimeter

The baseline main solenoid can be regarded as a conventional solenoid that has been stretched a little. It encloses the calorimeters and therefore acts mechanically as support for the calorimeters and inner tracker. In addition to delivering a 4 T magnetic field in the inner tracker volume, it also generates mag-



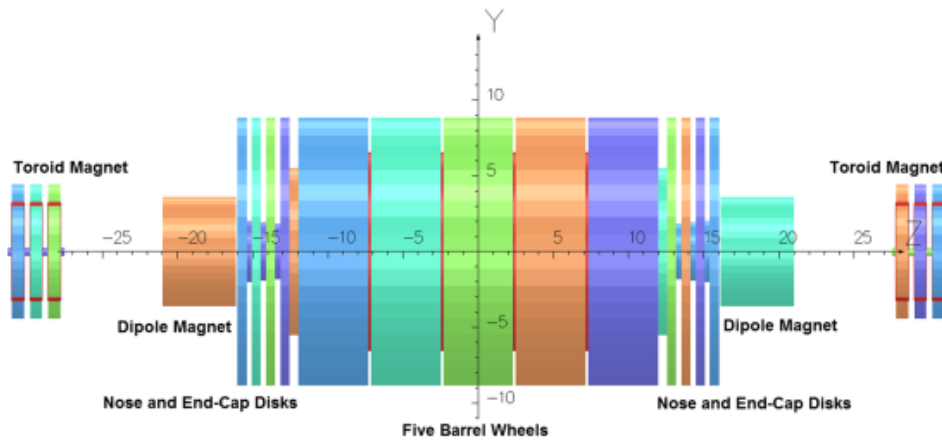


Fig. 5.23: Minimum yoke design for 4 T in 10 m free bore; overview of the magnetic elements with coils and magnetic yoke material.

Table 5.19: Parameters of the minimum yoke around the 4 T/10 m solenoid: endcap info is given for one side only.

Yoke properties	Barrel	End-Cap large	End-Cap small
Inner radius (m)	6.85	-	-
Outer radius (m)	8.85	8.85	7.0
Number of layers (-)	2	2	4
Axial width (m)	0.75	0.75	0.50 (1st), 0.75
Gap size (m)	0.50	0.50	0.50
Number of barrels (-)	5	-	-
Length per barrel (m)	3.9	-	-

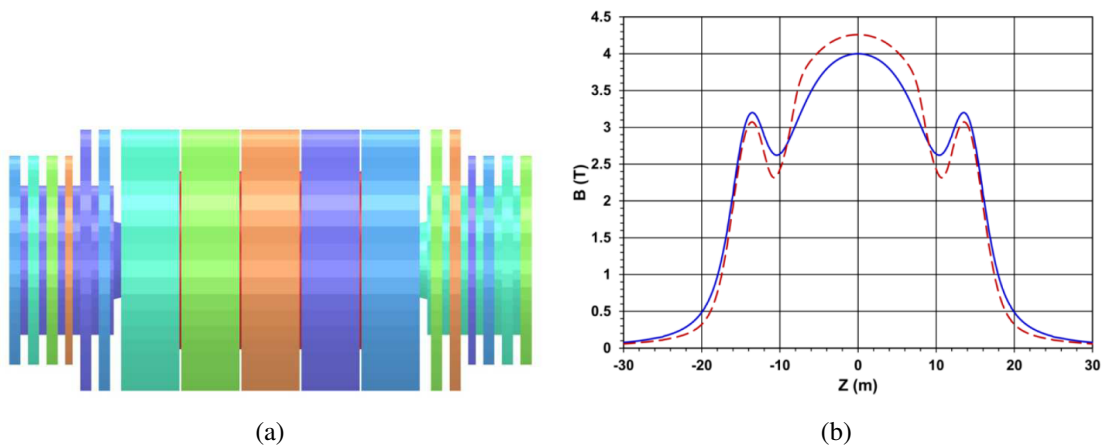


Fig. 5.24: Position of the steel yoke components as summarised in Tab. 5.19 and position of the main solenoid, forward solenoids and forward radiation shielding (left). Comparison of the magnetic field between 4 T/10 m baseline (solid line) and the one with minimum yoke (arced line).

netic field inside the calorimeter volume, where it is not used and not needed. Following this reasoning, a challenging ‘ultra-thin and radiation transparent’ solenoid enclosing the inner tracker only and thus

positioned inside the calorimeters, is an alternative. Due to its much smaller size and stored energy, the cost of such a solenoid can be reduced significantly, however, major developments are required to engineer it. Such an ultra-thin and transparent solenoid is proposed as the baseline magnet for the so-called IDEA experiment for an FCC-ee detector, however, in that case it only needs to generate 2 T [2, 95]. In the ATLAS experiment, a similar magnet is used, but there the solenoid shares its cryostat with the liquid argon calorimeter, hence avoiding the presence of additional layers of metallic cryostat walls between magnet cold mass and calorimeter. If a standalone magnet is positioned in its own cryostat, both cold mass and cryostat need to be as thin and radiation transparent as possible. A maximum radiation length  $X_0$  of 1 is the objective, which is very hard to achieve with the present technology for large coils and high magnetic field. Smaller transparent systems have been developed and successfully built for ATLAS [60–63].

For typical length-diameter aspect ratios of detector sub-systems, about 80% of the stored magnetic energy is present in the volume occupied by the calorimeters when the coil is positioned around the calorimeters where magnetic field is required. Obviously, by positioning the solenoid inside the calorimeters, significant savings can be achieved. Factors of about 4.2 in stored energy and 2.1 in cost are feasible for a small system like that proposed for FCC-ee [95]. A reduction in stored energy by a factor of 16 can be achieved with a 4 m free bore, 10 m long solenoid featuring 0.9 GJ stored energy, when replacing the FCC-hh baseline main solenoid. When using a small solenoid, bending power for muon tagging is still required and a minimum return yoke is proposed for this. A design with a 6 kt iron yoke, providing 1.2 Tm integrated magnetic field for muon measurements is presented in Ref. [57]. The concept of this system is shown in Fig. 5.25.

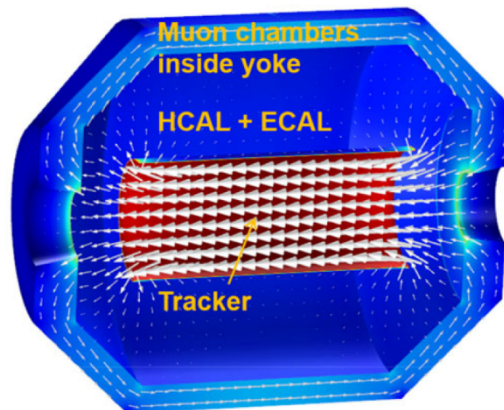


Fig. 5.25: Ultrathin solenoid concept: the superconducting magnet is placed in between the inner tracker and the calorimeters and an iron yoke is used to return the magnetic flux, also providing bending power for muon tagging and effectively reducing the stray field.

The drawback of having the magnet placed in front of the calorimeters is that particles emanating from the IP have to traverse the magnet before arriving in the calorimeters where precise energy measurements have to take place. By tunnelling through the magnet, scattering takes place and energy is lost which has a negative impact on detector performance. The total material budget of a magnet is composed of the cold mass and cryostat material and the radiation length has to be minimised. In the cold mass it can be minimised using high yield-strength superconductor. This has been proved to be possible, but only for small magnets generating low magnetic field. To guarantee safe quench behaviour, high peak temperature must be prevented and for a minimal cold mass, this implies that a maximum amount of energy has to be extracted, rather than being dissipated in the cold mass.

A self-supporting conductor makes use of the combined experience gained in ATLAS and CMS. Two different approaches were followed as ATLAS used a NbTi Rutherford type cable co-extruded in



aluminium reinforced by nickel micro-alloying, while CMS used pure aluminium around the Rutherford-type cable and edge electron beam welded reinforcements of a 6000 series aluminium alloy. Potentially, the way to make the ultra-high-strength conductor is to use nickel-doped aluminium around the Rutherford-type cable, further reinforced with a highest yield strength 7000 series aluminium alloy.

Besides a thin cold mass, the cryostat is to be minimised. Radiation shield and vacuum vessel walls are made as thin as possible. Options are using carbon fibre multi-layers or structured multi-layer materials instead of solid plate materials. Sandwiched corrugated plates or honeycombs are currently being produced.

Yet another development is to make use of extremely low thermally conducting insulation material instead of the standard technique of using a thick wall vacuum vessel, multi-layer insulation and a radiation shield. The new very light yet vacuum tight insulation material will provide structural support and be able to transfer forces as well. The vacuum sealing walls can then be reduced to thin foils as they do not have to withstand vacuum pressure.

## 5.8 Magnet R&D programme to complete the technical design report

Several design aspects require further work before preparing complete technical and manufacturing designs. The present conceptual design phase of the magnets is not appropriate for constructing a model coil to test various aspects. An R&D programme is therefore required in order to complete the technical design report (TDR). Some issues to be addressed are conductor development, powering and quench protection, coil winding pre-stressing, conduction cooling techniques and force transfer to the cryostat and neighbouring systems. Cryogenic issues concern the development of the 300 m long hybrid vertical transfer lines for transport of helium gas to the cavern in combination with superconducting bus bars.

For the ultra-thin and radiation transparent solenoids a thorough engineering effort is required in order to find the limits of high yield strength Al stabilised NbTi/Cu conductor and its cold mass technology. This will affect the feasibility of the concept of such a challenging magnet. Important issues are conductor development and its behaviour and integration in an ultra-thin cold mass. In this area material choices, Al welding and other production techniques are key [68]. Also key are the thermal and mechanical properties of advanced cryostats with unconventional structures and composite materials [69].

## 5.9 Conclusion and outlook

Several detector magnet layouts have been analysed regarding their feasibility for application in experiments for FCC-hh. The evolution towards the present CDR baseline design is strongly driven by requirements for simplification and cost reduction. A reduced magnetic field of 4 T in a 10 m free bore, as compared to the original 6 T in a 12 m bore; in combination with the suppression of magnetic shielding by a yoke or shielding coil, as well as a reduction of the number of sub-magnets, finally resulted in a solid and robust design which meets the physics requirements and budget constraints.

The baseline magnet system consists of a main superconducting solenoid providing 4.0 T central field in a 20 m long, 10 m diameter free bore, complemented by two forward solenoids each generating 3.2 T central field in a 4 m long, 5 m diameter free bore.

The main alternative design is to replace the forward solenoids with forward dipole magnets yielding more bending power for particles moving at low angles in the forward direction. The dipole magnets occupy the same space, but will provide a 1.3 T vertical field instead. However, large forces and torques need to be accommodated.

A safe quench protection design was demonstrated and no unforeseen technical problems were found. The cooling of the solenoid cold masses is based on the well-proven thermosiphon technique. Magnet powering components and the main part of the cryogenics plant are installed on the surface for easy maintenance. Only equipment with a long mean time between maintenance is installed in the

caverns. This concerns both the cryogenic system, controls and parts of the electrical circuit. Given the depth, this leads to the need for long vertical combined helium and superconducting current transfer lines.

The installation scenario of the magnet system has been developed. It has been demonstrated that, with the proposed size of cavern and access shafts, installation as well as short and long detector openings are feasible.

# Tracker and vertex detector

## 6.1 Overview and general challenges

The tracking system<sup>1</sup> has to provide high precision momentum measurements, track and vertex reconstruction, and flavour tagging under FCC-hh conditions. Compared to LHC, the FCC-hh energy and momentum reach will increase by approximately a factor of 7, which has to be reflected in the design of all detector subsystems. At the LHC experiments (cf. ATLAS [96] or CMS [97]) one of the driving requirements on tracker design was to measure track momenta of  $p_T = 1 \text{ TeV}/c$  particles with a precision:  $\delta p_T/p_T = 10 \%$ . To keep an equivalent performance but at the FCC-hh scale, the requirement is set one order of magnitude higher, to  $\delta p_T/p_T = 10 - 20 \%$  at  $p_T = 10 \text{ TeV}/c$ . Besides the key role of the tracker in high momentum spectroscopy, the detector needs to remain sensitive to low momentum particles, i.e. down to a few  $\text{GeV}/c$ , and thus provide non-degraded precision over a wide range of particle momenta—over nearly 4 orders of magnitude.

The high collision energies and new physics potential of FCC-hh necessitates a large  $\eta$ -coverage of the tracking system. All physics objects being ‘low’ mass compared to the 100 TeV collision energy will show a significant forward boost. In terms of pseudorapidity, such objects will be produced at higher  $\eta$  than at 14 TeV (LHC). As a motivation example, the forward jets produced by FCC-hh in a vector boson fusion event exhibit a distribution that peaks at  $\eta \approx 4.4$ , with a significant tail towards larger values (see Chapter 2 on Detector requirements from physics). Therefore, the main requirement for the tracking system is to provide precise tracking up to  $|\eta| = 4.0$  (cf.  $|\eta| < 2.5$  of the ATLAS [96] or CMS [97] experiments), and general tracking capability up to  $|\eta| = 6.0$ . High production energies at FCC-hh will also challenge the measurements of highly boosted objects: boosted  $\tau$  leptons, top quarks, W bosons or new physics objects. Their collimated decay products form a dense environment and thus pose stringent requirements on two-track separation, and correspondingly on the overall tracker granularity and geometry layout. Finally, efficient vertex reconstruction, i.e. primary or secondary vertexing, and b-, c-,  $\tau$ -tagging are essential for overall measurements precision.

The tracker and vertex detector need to be operated under a high number of p-p collisions per bunch crossing, i.e. pile-up. The nominal average pile-up level expected at FCC-hh is  $\mathcal{O}(1000)$  events. This is five to seven times (33 times) higher than expected at HL-LHC (LHC), cf.  $\mathcal{O}(140-200)$  ( $\mathcal{O}(30)$ ), respectively. However, the quantities typically used to classify minimum bias events: average particle  $p_T$ , total inelastic cross-section,  $\sigma_{\text{inel}}$ , or the number of charged particles per unit pseudorapidity increase by 30 – 40 % at FCC-hh with respect to the HL-LHC (see Table 3.1 in Introduction Chapter 3). This implies that the FCC-hh minimum bias events are expected to be very similar to those at HL-LHC, while the FCC-hh pile-up level may be critical for the design. Particularly challenging is a large line pile-up

<sup>1</sup>I.e. tracker and tracker innermost part (closest to the collision point), denoted further as a vertex detector.

density along the  $z$ -axis expected at FCC-hh,  $\langle \partial\mu/\partial z \rangle \approx 1$  p-p collision per 125  $\mu\text{m}$ . These experimental conditions will directly affect the tracker performance, and will pose a new level of requirements on detector/read-out technologies and overall detector read-out strategy (trigger system). In general, high detector occupancy, large data rates and challenging vertex/track reconstruction are expected, particularly in the innermost parts of the detector – the vertex detector. The focus in the reference design of the tracking system is therefore on the following features: sufficiently high detector granularity, precise spatial point resolution, ‘smart’ geometry layout and realistically low material budget. Similar to HL-LHC trends, extra timing resolution, in addition to accurate spatial point resolution, will be indispensable to enhance the signal-background discrimination power, and thus help the mitigation of pile-up effects.

Table 6.1: Expected radiation exposure: Dose in MGy and integrated particle fluence in 1 MeV neutron equivalent per  $\text{cm}^2$ , as simulated for the FCC-hh reference tracker layout (see details in Section 3.2). All values are for  $30 \text{ ab}^{-1}$  of p-p collisions at  $\sqrt{s} = 100 \text{ TeV}$ , assuming a total cross section,  $\sigma_{\text{pp}} = 108 \text{ mb}$ . Values are given for different positions in radius  $r$  and along  $z$ .

$r$ [mm]	$z$ [m]	Dose [MGy]	1 MeV neq. fluence [ $\text{cm}^{-2}$ ]
25	0	300	$5.5 \times 10^{17}$
25	5	407	$3.7 \times 10^{17}$
60	0	84	$1.3 \times 10^{17}$
100	0	42	$6.0 \times 10^{16}$
150	0	22	$3.3 \times 10^{16}$
270	0	8.8	$1.5 \times 10^{16}$
900	0	0.65	$3.3 \times 10^{15}$

Under FCC-hh conditions the detector and read-out technologies will be challenged by a very high radiation level and substantial long-term damage. Table 6.1 lists the total integrated dose (TID) and total integrated 1 MeV neutron equivalent fluence per  $\text{cm}^2$  expected after  $30 \text{ ab}^{-1}$  (as simulated in FLUKA—see Section 3.2 in Chapter 3). As a quantitative illustration of the environmental challenges, radiation tolerance of the technology required for the innermost vertex detector layer has been scaled from the LHC to FCC-hh conditions: an increase by a factor of  $\sim 23$  is expected from the LHC to HL-LHC, assuming that the CMS phase 2 upgrade first layer is positioned at  $r = 28 \text{ mm}$ , and by additional an factor of  $\sim 24$  from the HL-LHC to FCC-hh, assuming also that the FCC-hh first vertex detector layer is at  $r = 25 \text{ mm}$ . The uppermost limit on 1 MeV neutron equivalent fluence in the innermost layer rises then from  $\sim 1 \times 10^{15} \text{ cm}^{-2}$  at LHC, or  $\sim 2.3 \times 10^{16} \text{ cm}^{-2}$  at HL-LHC CMS phase 2 upgrade after  $3 \text{ ab}^{-1}$  [16], to  $\sim 5.5 \times 10^{17} \text{ cm}^{-2}$  at FCC-hh after  $30 \text{ ab}^{-1}$ . With the current limits on radiation hard technology, as assumed for the innermost vertex layer of the CMS phase 2 upgrade [16], the radial position of the FCC-hh innermost detectors would be limited to 270 mm from the interaction point – approximately a 10 times bigger radius than optimally required. (No assumption about regular replacement of the innermost tracker detectors during the operation was made in these evaluations). While technology will certainly advance in the coming years, it is evident that a significant R&D programme needs to be defined in order to develop such radiation hard technologies for the FCC-hh conditions. In the following sections, this important factor is not taken into account and it is assumed that the necessary progress can be achieved.

The reference concept of FCC-hh tracking system, as optimised by general design principles, together with the expected resolution of single track parameters, are introduced in Section 6.3. The corresponding key detector characteristics: geometry layout, detector hermeticity, material budget, non-uniformity of magnetic field, granularity, spatial point and time resolution, and their role in the overall detector design are discussed in individual sub-sections of Section 6.3. The tracking/vertexing perfor-

mance expected for the proposed reference detector system, and its layout modifications, are evaluated under FCC-hh conditions in Section 6.4. Expected data rates, detector occupancy and possible role of the tracker in the trigger system are addressed in Section 6.5. For completeness, the mathematical approaches applied and the software tools utilised are briefly explained in Section 6.2, the technical specification of reference layout geometry is summarised in Appendix 6.A. Further information on all aspects of the tracker design can be found in specific notes.

## 6.2 Mathematical approaches and software tools

There are several software (SW) tools and approaches being used throughout the tracker studies, each with a different level of detector description and track/vertex reconstruction complexity. These range from purely analytical or approximating approaches to full Monte Carlo simulation and sophisticated algorithms. The latter two represent the most realistic techniques, nevertheless, track and vertex reconstruction in an environment of  $\mathcal{O}(1000)$  pile-up events is an extremely challenging task, and, while the LHC experiments currently prepare for  $\mathcal{O}(140\text{--}200)$  pile-up events, coherent SW for the FCC-hh (FCCSW—see Chapter 4), is not yet available for the studies. To assess the performance of the tracking system from all necessary aspects, the functionality of FCC SW framework is therefore combined with other analytical or full simulation tools from other projects, namely CLIC [98], ATLAS and CMS experiments, or standalone SW tools are used, namely TKLAYOUT [99, 100], MATHEMATICA [101], PYTHIA 8 [102] and DELPHES [34].

### 6.2.1 Analytical, approximative and numerical approaches

The reference layout of FCC-hh tracking system, described in Section 6.3, is studied by an adapted version of TKLAYOUT [99, 100], a C++ toolkit, originally developed for geometrical layout studies and performance assessment of the CMS phase 2 tracker. For FCC-hh studies, this SW toolkit has been generalised (as a TKLAYOUT-LITE) and extended with new algorithms and mathematical approaches, e.g. analytical track propagator functionality and an estimator of track-to-vertex assignment capability in pile-up conditions. TKLAYOUT relies on building a 3D spatial model of tracking detectors together with a beam-pipe, and estimating a track covariance matrix by generalised least squares (GLS) method in a parabolic approximation. The only material effects being considered are multiple Coulomb scatterings and the effects of particle energy losses are currently ignored in TKLAYOUT. The reference magnetic field is approximated either by a constant 4 T uniform  $\vec{B}$  field or  $\vec{B}$  field variable in  $B_z$ , the component along the  $z$ -axis (N-parabola approximation). The evaluation of progressive track filtering capabilities, introduced in Section 6.4.1, follows the same principles, except that the track covariance matrix is evolved along the particle trajectory to the next measurement plane by an error propagation technique (calculated analytically in the parabolic approximation). In order to assess the full effects of a non-uniform magnetic field on the resolution of track parameters, the TKLAYOUT GLS method is implemented in MATHEMATICA [101] and the relevant covariance matrix is found numerically in the presence of a realistic  $\vec{B}$ -field map (interpolated on the spatial grid).

The ‘Track trigger’ study, described in Section 6.5.1 makes use of several SW tools, see details in Ref. [103]. Minimum bias events are simulated with PYTHIA8 and signal processes with PYTHIA8 interfaced to MADGRAPH [25]. Charged particle trajectories, emerging from Gaussian smeared vertices (beam-spot simulation), are propagated in a helix under a 4 T uniform magnetic field using the DELPHES [34] framework. The tracker geometry is assumed in the reference ‘flat’ layout (i.e. with no inclined detectors), except the seventh barrel layer which is substituted by the triplet trigger under study. The layers are further simplified as cylindrical surfaces and the coordinates of individual intersections with the charged particle tracks are considered as hits. Finally, track parameters are extracted with a circle fit in the  $r$ - $\varphi$  plane, and a straight line fit in the  $r$ - $z$  plane. To emulate the effects of detector resolution and multiple Coulomb scattering, Gaussian smearing is applied to the track parameters as estimated by TKLAYOUT-LITE.

## 6.2.2 CLIC software framework

The ‘Hit separation efficiency’ and ‘Hit-based b-tagging’ studies, described below in Sections 6.4.2 and 6.4.4, respectively, make use of the CLICDP software tools. The geometry description, defined using TKLAYOUT-LITE, is translated into the DD4HEP [39] format. Particle interactions with the detector are simulated using DDSIM [104], which is based on GEANT4 [35–37].

The ‘Tracking efficiency’ and ‘Track-based flavour tagging’ studies presented in Sections 6.4.2 and 6.4.4, respectively, require the full event reconstruction to be performed. For the purpose of these two studies only, a detector model based on the CLIC\_SiD detector [98] is used (more details can be found in Section 6.4.2). The simulation is performed using SLIC [105]. Charge deposition, drift and collection are not simulated, but their effects are emulated in the digitisation step. The simulated hit position is smeared, using a Gaussian distribution, according to the sensor single point resolution. Track reconstruction is performed using a set of `org.lcsim` [106] drivers detailed in [107]. Tracks and clusters are combined in a particle flow algorithm, PANDORAPFA [108, 109]. Primary and secondary vertices are reconstructed using the LCFIPLUS package [110]. The vertex reconstruction and flavour tagging is based on particle-flow objects. Flavour tagging is carried out using a multivariate analysis within the LCFIPLUS package, which uses boosted decision trees (BDT).

The studies performed using the CLIC SW do not include pile-up interactions as the framework is not designed for the reconstruction of events with the pile-up conditions expected at FCC-hh.

## 6.2.3 FCC software framework

The studies of ‘Expected occupancy and data rates’, described in Section 6.5.2, and ‘Track Parameters Resolution’, described in Section 6.3.4, have been carried out in the FCC SW framework. A common detector geometry description based on DD4hep is used within the framework: the reference tracker layout is designed in TKLAYOUT-LITE, exported to an XML format and translated into DD4HEP. Two different levels of geometry description are considered: simplified (a true 3D geometry projected to 2D surfaces, e.g. detector modules, with a correctly mapped material distribution) and detailed (full 3D). The simplified approach is used in fast simulation and track reconstruction, the detailed description is applied in full MC simulation by GEANT4. The FCC SW is designed as a chain of several simulation, reconstruction and analyses modules. The minimum bias events and signal processes are simulated by PYTHIA8 [102] in FCC SW, the particles generated are moved through the matter by FCC SW GEANT4 simulation [111]. To achieve a compromise between the performance and complexity, all pile-up interactions are simulated separately and overlaid with a hard-scattering process in GEANT4. To emulate a realistic detector response digitising and clustering are performed. The first emulates the detector response to ionising particles and photons, the latter searches for separate collections of neighbouring hit cells to estimate reconstructed hits. The digitisation procedure depends on the specific detector type; the definitive technologies are not yet defined for the FCC-hh tracking system, hence a purely geometric approach [112] is currently used. The clustering algorithm is based on connected-component labelling in sparse matrices, see the details in Ref. [112]. All hits are reconstructed by digitisation tools of the ‘A Common Tracking Software’ (ACTS) [113] package. The SW chain up to this point is used to make a complementary estimate of the tracker occupancy and data rates, the study of ‘Track parameters resolution’ requires a few additional steps: track seeding, pattern recognition and track fitting. In the current Monte Carlo study the pattern recognition is simplified based on Monte Carlo truth information and the Riemann fit [114] is applied as a track fitting algorithm. As the Riemann fit does not naturally account for the effects of multiple Coulomb scattering, the cross-check of results obtained with the TKLAYOUT-LITE estimates is only made for high momenta tracks.

For future studies, a cellular automaton seeding algorithm (TrickTrack package [114]) and A Common Tracking Software (ACTS [113] package) are being prepared. The track seeding, in particular, is a performance-critical step in both online and offline track reconstruction. The scaling with pileup events is typically combinatorial and thus the algorithm may represent a possible bottleneck in the overall re-



construction.

### 6.3 Reference layout and track parameter resolution

Geometrical constraints on the reference layout are illustrated in the detector overview, Fig. 3.1. The space for tracking is limited by the cylindrical beam-pipe inner radius,  $r > 20.8$  mm, and the central and forward ECAL outer radius and outermost  $z$ -position, respectively. The limits are due to requirements for large  $\eta$ -coverage, hermeticity and minimum space necessary for each sub-detector component. The barrel and end-cap ECALs are designed to cover the detector area up to  $|\eta| < 2.5$ , and thus restrict the tracker lever-arm available in the central region. In the barrel, the ECAL is cylindrical with the innermost part, a cryostat wall, at an inner radius of 1.7 m. In the end-cap, the ECAL encloses the central detector, thus affecting the tracker performance in the  $1.9 < |\eta| < 2.5$  range by decreasing the lever-arm available down to 53% at  $|\eta| = 2.5$ . Effectively, the reference tracking system is divided by the calorimeter into three separate parts with a different functionality: central, intermediate and forward. The central tracker is planned to provide high precision tracking and vertexing in the central part. Its outermost detector modules are positioned at  $r = 1.55$  m to leave a space between the tracker and ECAL cryostat wall for services, supports and cooling. The layout of the central tracker is closely related to the phase 2 upgrades of ATLAS and CMS tracking detectors. In contrast, the design of forward tracker is unusual. Due to its unconventional length it allows the extension of the full tracker lever-arm by more than one unit in pseudorapidity,  $1.9 < |\eta| < 3.0$ . The forward layout does not introduce any novel principles, except for the need to precisely align all detector modules over a very large distance. If it is combined with a dipole magnet, see magnet options in Section 5.4, the design of the forward tracker is closely related to the spectrometers of the present ALICE and LHCb experiments. The intermediate tracker is needed for efficient track reconstruction beyond  $|\eta| > 2.5$ . It connects the track segments reconstructed in the central and forward detectors by providing additional measurement points in the transition area. To conclude, the central tracker extends up to a distance of 5 m from the interaction point (IP) and the forward tracker up to a distance of 16 m from the IP, see Fig. 6.1.

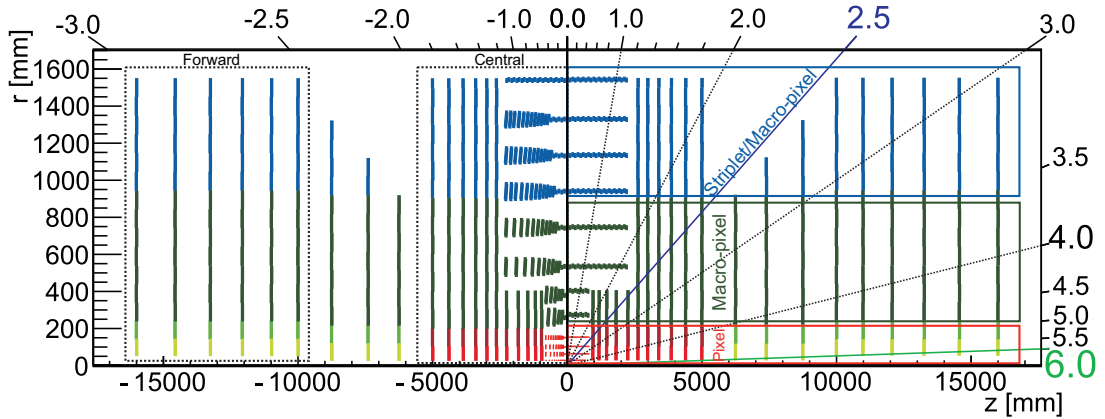


Fig. 6.1: A sketch of two quarters of reference tracker layout in  $r$ - $z$  view, comparing two detector layouts: tilted (left) and flat (right). The first follows the new HL-LHC trends – with detector modules being oriented perpendicularly to particles coming from the IP (and thus reducing the material traversed), the latter is based on a traditional design approach. Individual tracker regions are illustrated in the sketch: inner vertex detector (in red in the central region and green in the forward region), middle (in dark green) and outer tracker (in blue).

The reference layout is studied using two approaches: flat layout [115]—traditional with cylindrical barrel (BRL) layers and end-cap (EC) discs, and tilted/inclined layout [116]—novel, following the HL-LHC trends with inclined detectors along the  $z$ -axis. The latter has been widely applied in the phase 2 tracker upgrades of ATLAS and CMS. In essence, this approach aims to ‘optimally’ incline

modules to minimise the effect of their material on particles coming from the IP, namely in the transition region between the barrel and end-cap. In practice, this concept has its limitations as the IP (beam-spot) is not point-like and has finite dimensions. Further, to lessen the engineering complexity a common tilt angle is typically set for a group of modules. In the current design, two to three modules along  $z$  share the same tilt. Finally, with the inclined layout a more complex support structure, cooling and services routing are expected. Hence, the active silicon area and total material budget are expected to be smaller, but with a higher fraction of passive versus active material than in the flat layout. The total active silicon surface, as estimated by TKLAYOUT-LITE, amounts to  $430 \text{ m}^2$  for the flat geometry. The tilted layout is  $\sim 10\%$  smaller, amounting to  $391 \text{ m}^2$ . These numbers are to be compared to  $\sim 250 \text{ m}^2$  for the phase 2 trackers of ATLAS and CMS.

The key tracker parameters to be defined by reference design are the number  $N$  of measurement stations along  $r$  and  $z$ , the granularity in  $r$ - $\varphi$  and  $z(\text{BRL}) / r(\text{EC})$  directions, realistic material budget and hermetic layout structure with respect to the FCC-hh luminous region. As illustrated in Section 6.1, the radiation tolerance is another important aspect and hence, the technology/detector type suitable for various detector regions need to be specified. Three distinct areas based on the general radiation tolerance of related technologies are assumed: pixel, macro-pixel and strip/macro-pixel. The use of strips will mainly depend on the required resistance to combinatorial background (ghost hits) and the comparative costs of macro-pixel versus strip technology in the future. All these aspects together with the estimated momentum and impact parameter resolutions are discussed in the following subsections.

Finally, several important engineering details have not been realistically considered within the current design and they need to be addressed in the next design phase. Firstly, the current tracker layout does not assume any opening scenarios of the innermost parts, particularly in the context of the radiation levels expected and inevitable upgrades. The related layout changes will mostly affect the current design in the forward region, namely the end-cap and forward discs and correspondingly, the material budget due to different routing of services, necessary supports etc. Another aspect is the cylindrical beam-pipe; within the context of large tracking  $\eta$ -coverage, a more realistic beam-pipe design will be needed for the beam-pipe bellows and vacuum pumps.

### 6.3.1 Hermeticity and number of measurement layers/discs

The tracker layout is structured in a hierarchy of layers, ladders (rods) and detector modules in the BRL region, and discs, rings and detector modules in the EC region. Optimal positioning and overlaps of the modules are driven by general requirements for tracker hermeticity with respect to the luminous region. Additional constraints are determined by the minimum overlaps needed for alignment purposes—approximately 1 mm is assumed in the current layout. The dominant size of FCC-hh luminous region is along  $z$ -axis, see Table 1.1. It extends over tens of millimetres and thus affects the overall strategy for the hermetic layout. In  $r$ - $\varphi$ , the beam-spot is of the order of tens of micrometers and the effect is negligible. By assuming a Gaussian profile of the luminous region in  $z$ ,  $N(0, \sigma_z^{\text{lum}})$ , the typical approach to modules' positioning is as follows: the modules are required to provide sufficient overlaps and therefore to cover the luminous centre by  $\pm\Delta z$ , typically a few  $\sigma_z^{\text{lum}}$ . The current layout assumes coverage by  $\Delta z \approx 2\sigma_z^{\text{lum}}$  in a straight line limit. Closely following the CMS approach [16] using TKLAYOUT-LITE, a sketch to illustrate this concept of a generally inclined geometry is shown in Fig. 6.2.

Another layout aspect is a realistic choice of number of measurement layers/discs,  $N$ . In general, an increase in  $N$  leads to an increase in the number of measurement points and thus a decrease in the track propagation distance between individual hits. The latter is particularly important when assigning hits to a track candidate (see details in Section 6.4.1). In contrast, a higher  $N$  leads to a bigger material budget, and thus, a larger measurement uncertainty arising from the multiple Coulomb scattering. As can be illustrated in high  $N$  approximation by Gluckstern formulae [117, 118], the precision of the momentum measurement decreases with given  $N$  as  $1/\sqrt{N}$ , the material effect, in contrast, increases as  $\sqrt{N}$ . Their effects seem to be compensated, nevertheless, the effect of multiple scattering needs to be compared in



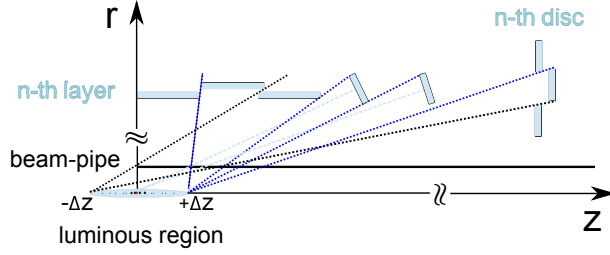


Fig. 6.2: An illustration of modules' positioning with overlaps, designed in a way that the tracker layout is hermetic with respect to the luminous region: in a flat, tilted barrel layer and end-cap disc.

a view of increasing material with higher  $\eta$ , unless an ideally inclined geometry is used. In the current design, the key requirement is to keep a layer-to-layer propagation distance at  $\eta = 0$  comparable to the phase 2 upgrades of CMS or ATLAS trackers. By considering the lever-arm of CMS phase 2 tracker,  $L \sim 1.15$  m, and the total number of barrel layers with at least 1 hit (neglecting the stubs' effect),  $N = 10$  [16], the FCC-hh tracker requires an additional 2 hits to fully cover its  $\sim 1.55$  m lever-arm with roughly the same propagation distances. In addition, the layer arrangement in the central tracker is as follows: 4 pixel barrel (BRL) layers in the innermost region (defined by seeding in dense FCC-hh environment, 3 + 1 back-up, and precise impact parameter resolution, see Section 6.3.2), 4 macro-pixel BRL layers in the intermediate region and 4 BRL triplet/macro-pixel layers in the outermost region. The large increase in the number of measurements in the forward region, see Fig. 6.3, follows directly from the requirements of a  $\pm 16$  m long tracker along  $z$  and sufficiently low track propagation distance between individual discs.

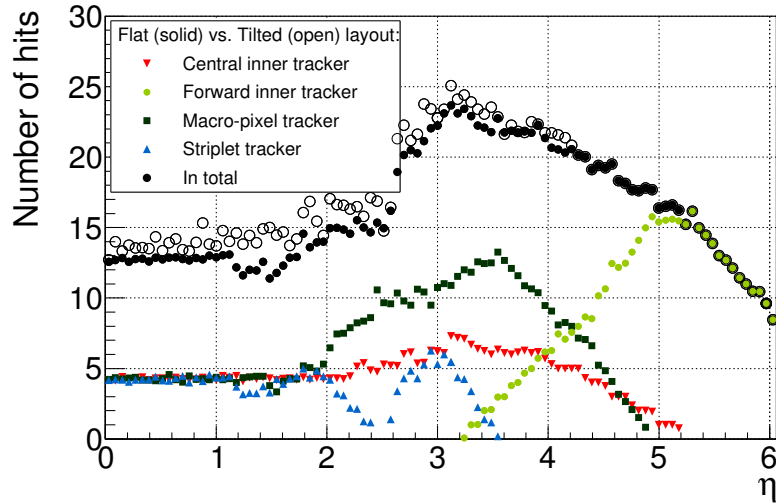


Fig. 6.3: An average number of hit layers/discs traversed by particles (i.e. with at least one hit), including the central inner tracker (red), forward inner tracker (light green), middle tracker (dark green) and outer tracker (blue), as well as the total cumulative distribution (black). The flat layout is shown in solid circles, the tilted layout in open circles. Particle trajectories are approximated by straight lines; effects of multiple Coulomb scattering and magnetic field are neglected.

### 6.3.2 Granularity

A final choice of granularity in  $r$ - $\varphi$  is mainly driven by the requirement on  $\delta p_T/p_T$  in the current design. By assuming a tracker layout with 1.55 m lever-arm and  $N = 12$  measurement layers, being positioned in a constant 4 T magnetic field, the signal point spatial resolution in a high momentum limit can be

directly derived from Eq. ( [117]):

$$\left. \frac{\delta p_T}{p_T} \right|_{\text{Res}} = \frac{\sigma_{r\varphi} |p_T|}{0.3BL^2} \sqrt{\frac{720}{(N+5)}} , \quad (6.1)$$

where  $p_T$ ,  $\sigma_{r\varphi}$ ,  $B$ , and  $L$  represent the transverse momentum in [GeV/c], sensor spatial resolution in  $r$ - $\varphi$  in [m], magnetic field in [T] and full tracker lever-arm in [m], respectively. The formula approximates the  $\delta p_T/p_T$  in a scenario with a constant magnetic field, and equal and equidistantly positioned tracker layers. To achieve the  $\delta p_T/p_T = 20\%$  at  $p_T = 10$  TeV/c, the spatial resolution should be on average  $\sigma_{r\varphi} \approx 9\ \mu\text{m}$ . There are other important aspects to be taken into account in addition to the requirement for momentum resolution. A sufficiently high granularity and reasonably low occupancy is required to avoid overlaps of individual hit clusters, created by different particles in a detector module. A general goal is to keep the occupancy  $\ll 1\%$  in all detectors. The dedicated study is addressed in Section 6.5.2. The granularity in  $r$ - $\varphi$ , particularly in the innermost layers, is also important for efficient tagging of displaced vertices via the impact parameter resolution in  $r$ - $\varphi$ ,  $\delta d_0$ . The final pitch,  $p$ , as obtained by analysing the tracker layout from all these aspects, is:  $p = 25\ \mu\text{m}$  in the first 4 innermost BRL layers and first innermost EC ring, and  $p = 100/3 \approx 33.3\ \mu\text{m}$  in the remaining layers and rings. Detectors with binary read-out are assumed in all studies, the single point resolution in  $r$ - $\varphi$  then reads  $\sim p/\sqrt{12}$  (neglecting a cluster size and charge sharing effects), i.e.  $\sim 7.5\ \mu\text{m}$  and  $\sim 9.5\ \mu\text{m}$ , respectively. For reader's convenience the reference granularity is summarised in Table 6.2 for both types of layouts: flat (top) and tilted (bottom).

Table 6.2: Summary of spatial dimensions (pitch values,  $p$ ) of detector read-out cells as optimised for different categories of sensors: inner vertex detector, middle and outer tracker, and two layouts: flat (top) [115] and tilted (bottom) [116], see also Appendix 6.A.

<b>Flat layout:</b>		
<b>Pixels (inner)</b>	<b>Macro-pixels (middle)</b>	<b>Striplets/Macro-pixels (outer)</b>
$25 \times 50\ \mu\text{m}^2$ (1–4th BRL)	$33.3 \times 400\ \mu\text{m}^2$	$33.3\ \mu\text{m} \times 50\ \text{mm}$ (BRL)
$25 \times 50\ \mu\text{m}^2$ (1st EC ring)		$33.3\ \mu\text{m} \times 10\ \text{mm}$ (EC)
$33.3 \times 100\ \mu\text{m}^2$ (2nd EC ring)		
$33.3 \times 400\ \mu\text{m}^2$ (3–4th EC ring)		
<b>Tilted layout:</b>		
$25 \times 50\ \mu\text{m}^2$ (1–4th BRL)	$33.3 \times 400\ \mu\text{m}^2$	$33.3\ \mu\text{m} \times 1.75\ \text{mm}$ (BRL)
$25 \times 50\ \mu\text{m}^2$ (1st EC ring)		$33.3\ \mu\text{m} \times 1.75\ \text{mm}$ (EC)
$33.3 \times 100\ \mu\text{m}^2$ (2nd EC ring)		$33.3\ \mu\text{m} \times 50\ \text{mm}$ (12th BRL layer)
$33.3 \times 400\ \mu\text{m}^2$ (3–4th EC ring)		

An optimal choice of granularity in  $z$  is more complex. A combination of several requirements need to be taken into account: a reasonably low detector occupancy  $\ll 1\%$ , efficient track reconstruction and sufficient two-track separation in boosted objects, as detailed in Sections 6.4.1 and 6.4.2. Another aspect is driven by the natural role of vertex detector granularity in the impact parameter resolution, and hence in efficiency of primary vertexing under FCC-hh pile-up conditions (see detailed results in Section 6.4.3). To discriminate a signal primary vertex from other pile-up vertices, the signal vertex needs to be first correctly reconstructed and then correctly selected (e.g. based on highest  $p_T$  sum). In the first step, a correct track to vertex assignment is the key. As pointed out in Section 6.3.1, the size of luminous region in  $r$ - $\varphi$  is approximately comparable to the spatial detector resolution, while in

$z$ -direction it extends over tens of millimetres. Therefore, only the impact parameter resolution in  $z$ ,  $\delta z_0$ , has enough discriminative power. It depends on  $z$ -granularity of the vertex detector, material being crossed by particles in the beam-pipe and innermost layers, and degrades with increasing  $\eta$  as [118]:

$$\delta z_0 \Big|_{\text{Res+MS}} \approx a_{\text{Res}} \oplus \frac{b_{\text{MS}}}{p_T} \cosh^{\frac{3}{2}} \eta \quad (6.2)$$

The material traversed affects the multiple scattering (MS) term as  $\sim \sqrt{\cosh \eta}$ , additional  $\sim \cosh \eta$  accounts for the MS error projection factor on the  $z$ -axis. Evidently, by tilting the modules the material effect of vertex detector can be minimised, while the beam-pipe material and projection factor can not be optimised by any layout modifications, see a schematic Fig. 6.4a. In Fig. 6.4b,  $\delta z_0$  resolution is shown for a reference tracker layout in an ideal configuration: with a zero material tracker and non-zero (realistic) material beam-pipe. As demonstrated, the discriminative power of  $\delta z_0$  decreases with increasing  $\eta$  and a new discriminative variable may be indispensable to mitigate the pile-up effects: a time-stamp per track, namely at higher  $\eta$  (cf. ATLAS phase 2 tracker design with timing detectors).

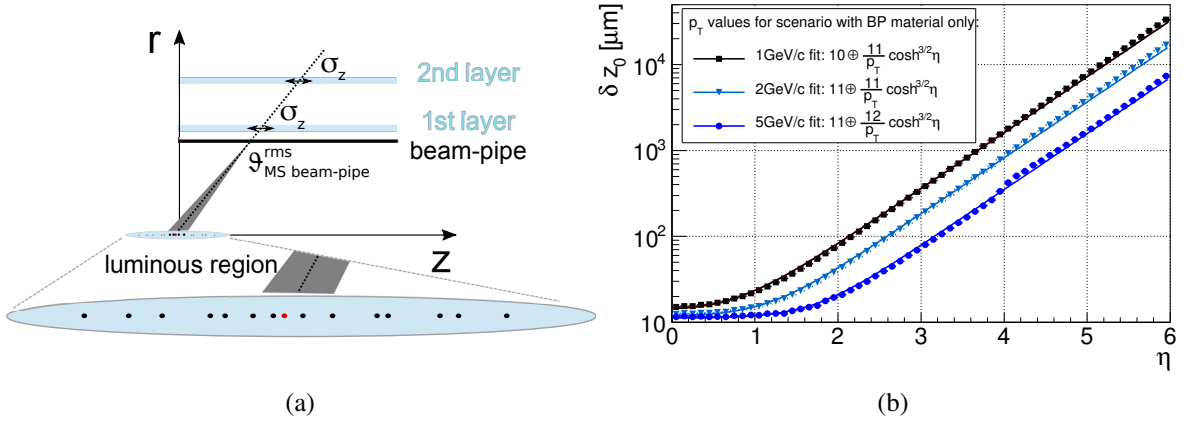


Fig. 6.4: A strict limit on vertexing performance in high pile-up environment entirely due to material budget of the beam-pipe and its radial position. On the left, (a) is a sketch illustrating the error propagation due to MS in the beam-pipe. On the right, (b) shows  $z_0$  resolution versus pseudorapidity in an ideal scenario with a material less ‘flat’ tracker; in this case the only source of MS is the beam-pipe. The  $\delta z_0$  curves are shown in the low  $p_T$  limit: 1 GeV/c (black), 2 GeV/c (azure blue) and 5 GeV/c (blue).

As shown in Eq. (6.1), the  $\delta p_T/p_T$  depends on  $r$ - $\varphi$  resolution in the global coordinate system. Assuming negligible effects from detector misalignment and tracking in a uniform magnetic field oriented in  $z$ , the detector modules in the BRL region in non-inclined geometries measure strictly  $r$ - $\varphi$  and  $z$  coordinates. That is to say that even after transformation of hit position errors along the track tangent to the global coordinate system, the global  $r$ - $\varphi$  measurement precision has no contribution from the local  $z$  error. In contrast, the EC disc modules in non-inclined geometries measure  $r$ - $\varphi$  and  $r$  coordinates, which both contribute their errors to the global  $r$ - $\varphi$  resolution after being transformed along the track tangent. This principle can be mathematically generalised for any inclined geometry [118]. Conceptually, that is the reason why the tilted layout requires a higher granularity in the local  $r/z$  coordinate than the flat layout.

Finally, a summary of the total number of read-out channels and total active silicon area, as expected for the granularity of two reference layouts, is given in Table 6.3. Compared to the LHC experiments, the large increase in the number of read-out channels, namely in the pixel region, is due to the requirement of a  $\pm 16$  m long tracker in  $z$ , and the necessary low occupancy and radiation tolerance of detector modules.

Table 6.3: Summary of total active silicon area in [m<sup>2</sup>] and number of read-out channels in [millions] for three categories (regions) of sensors: pixels (inner), macro-pixels (middle) and triplets/macro-pixels (outer), and two layouts: flat [115] (top) and tilted [116] (bottom), see also Appendix 6.A. Each number is shown as a sum of respective numbers of the central and forward tracker.

<b>Flat layout:</b>	Silicon area [m <sup>2</sup> ]	Number of read-out channels [M]
Pixels (inner)	6.5 + 3.1	4073.9 + 1387.1
Macro-pixels (middle)	82.4 + 50.6	6177.0 + 3787.4
Triplets/Macro-pixels (outer)	216.8 + 71.0	281.8 + 207.9
	<b>430 m<sup>2</sup></b>	<b>15915 M channels</b>
<b>Tilted layout:</b>		
Pixels (inner)	4.7 + 3.1	2692.6 + 1387.1
Macro-pixels (middle)	66.0 + 50.6	4947.0 + 3787.4
Triplets/Macro-pixels (outer)	195.3 + 71.0	2541.1 + 1205.9
	<b>391 m<sup>2</sup></b>	<b>16561 M channels</b>

### 6.3.3 Material budget

Another aspect of the reference detector design concerns a realistic description of the material budget. The tracking system opens up many challenges for future technologies, particularly due to very high radiation level in the innermost part, i.e. at  $r < 27$  cm, as shown in Table 6.1. Detector technologies intended for these innermost layers/rings remain completely open now and hence, the technologies for the LHC phase 2 upgrades can not be directly extrapolated to the current FCC-hh design. A more pragmatic approach is used instead. Each detector module is assumed to have a sandwich-like material structure in the ‘thickness’ dimension and uniformly distributed material in the remaining two dimensions. The corresponding sandwich material composition is simplified as: 20% Si, 42% C, 2% Cu, 6% Al and 30% plastic. To account for the accumulated effect of services and the cooling system being routed out from the detector, the corresponding material budget is increased, with respect to a perpendicular particle passage, in several steps with increasing radius: 1 % of an  $X_0$  per layer is assumed in the innermost BRL layers, 1.5 % per ring in the innermost two EC rings, 2 % per layer/ring in the macro-pixel and 2.5 % per layer/ring in the macro-pixel/triplet region. The accumulated effect of services along barrel staves is neglected in these assumptions. Such an assessment is very approximate and a more realistic model has to be taken into account in the next design phase, once there is a concrete idea for the technology.

The schematic map of material in  $X/X_0$  is shown in Fig. 6.5a, and the estimate of the overall material budget inside the tracking volume is presented in Fig. 6.5b. Two reference layouts are presented: the flat and tilted. The tilted geometry represents down to 50 % less material budget. Nevertheless, both designs have their advantages and disadvantages in terms of mechanical structure, cooling layout and services routing. For the tilted layout a more complex mechanical structure is expected. Additional material effects can be also expected from a future realistic design with tracker openings for the vertex detector upgrades.

### 6.3.4 Track parameter resolution

The tracker momentum resolution along  $\eta$  can be approximated by the square sum of two contributions: from detector spatial resolution that dominates at large  $p_T$  values, and multiple Coulomb scattering in the detector material that dominates at low  $p_T$  values. Both tracking limits, further denoted as ‘Res’ and ‘MS’, respectively, can be analytically assessed by the generalised Gluckstern formulae [117, 118] as:

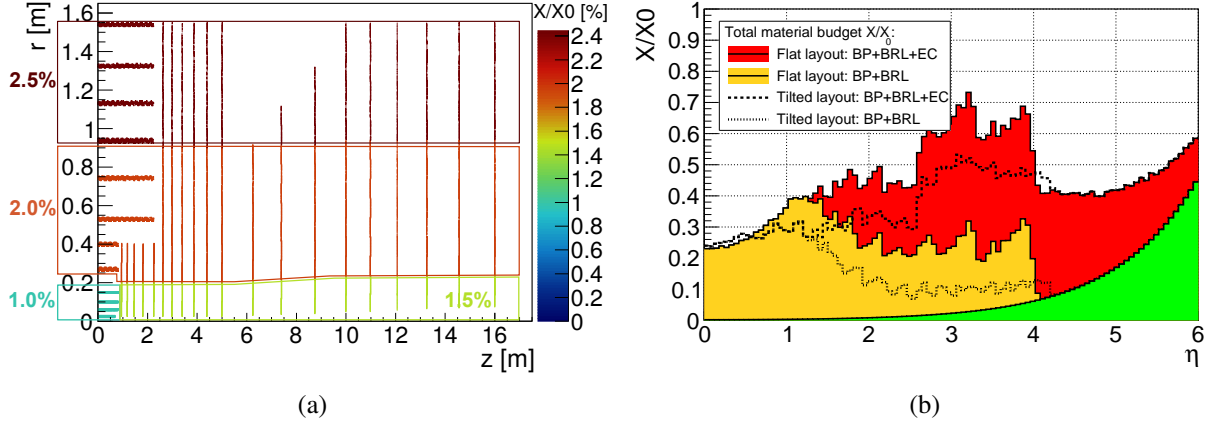


Fig. 6.5: Material budget of the tracker as estimated by TKLAYOUT in units of radiation lengths,  $X/X_0$ . On the left (a), a schematic map of the material for the flat layout is shown. Several regions with different material thicknesses in  $X/X_0$  per layer/disc are assumed to account for the accumulated effect of services: 1 % (central pixel), 1.5 % (forward pixel), 2.0 % (middle tracker) and 2.5 % (outer tracker). On the right (b), a total material scan,  $X/X_0$ , versus pseudorapidity,  $\eta$ , for both reference layouts is depicted: flat (solid lines) and tilted (dashed lines). The beam-pipe material, BRL and EC regions are shown in green, yellow and red, respectively.

$$\left. \frac{\delta p_T}{p_T} \right|_{\text{Res}} = \frac{\sigma_{r\varphi} |p_T|}{0.3BL^2} \sqrt{\frac{720N^3}{(N-1)(N+1)(N+2)(N+3)}} \quad (6.3)$$

$$\left. \frac{\delta p_T}{p_T} \right|_{\text{MS}} = \frac{13.6 \text{ MeV}/c}{0.3\beta BL} \frac{N}{\sqrt{(N+1)(N-1)}} \sqrt{\frac{x_{\text{tot}}}{X_0} \cosh \eta} \left[ 1 + 0.038 \ln \frac{x_{\text{tot}}/(N+1)}{X_0} \cosh \eta \right], \quad (6.4)$$

where  $p_T$ ,  $\sigma_{r\varphi}$ ,  $B$ ,  $L$ ,  $\beta$  and  $x_{\text{tot}}/X_0$  represent the transverse momentum in [GeV/c], sensor spatial resolution in  $r$ - $\varphi$  in [m], magnetic field in [T], full tracker lever-arm in [m], relativistic  $\beta = v/c$  factor and total detector material budget in radiation lengths, respectively. The formulae are derived for a scenario with a constant magnetic field, and  $N$  equal and equidistantly positioned tracking layers.

The final  $p_T$  resolution is estimated by GLS method [118] using MATHEMATICA and is shown in Fig. 6.6. The  $\delta p_T/p_T$  is calculated for the reference flat geometry, nevertheless both tracker layouts (flat and tilted) have proved to provide comparable momentum resolution in the whole  $p_T$  range studied. Two sets of curves are depicted: the solid and dashed curves, describing resolution in a reference solenoid  $B$ -field and alternative solenoid+dipole scenario, respectively. To validate these curves, the Gluckstern estimates from the above formulae are added to the plots: in high  $p_T = 10 \text{ TeV}/c$  and MS ( $p_T = 2 \text{ GeV}/c$ ) limits. They are evaluated by assuming a constant 4 T magnetic field and tracker with a 1.55 m lever-arm and an average spatial resolution  $\sigma_{r\varphi} \approx 9 \mu\text{m}$ . In the MS limit an average value of total material budget:  $x_{\text{tot}}/X_0 = 0.45$  at  $\eta = 0.0$  is considered. To assess the effects of additional material due to e.g. underestimated services, or lower material budget due to use of more advanced technologies, the value of  $x_{\text{tot}}/X_0$  in Eq. (6.4) is varied by  $\pm 50\%$ . In addition, the high  $p_T$  resolution curve ( $p_T = 1 \text{ TeV}/c$ ) is also validated by a Riemann fit using the FCC SW in a constant 4 T magnetic field [114]. As will be shown in Section 6.3.5, the difference between the Gluckstern/FCCSW curves and MATHEMATICA curves accounts for a difference between an ideal constant and realistic 4 T  $B$ -field exactly.

The results obtained for the reference solenoid magnetic field can be explained as follows. In the  $0 < |\eta| < 1.9$  region the tracking makes use of full spectrometer lever-arm,  $L = 1.55 \text{ m}$ , and the  $p_T$

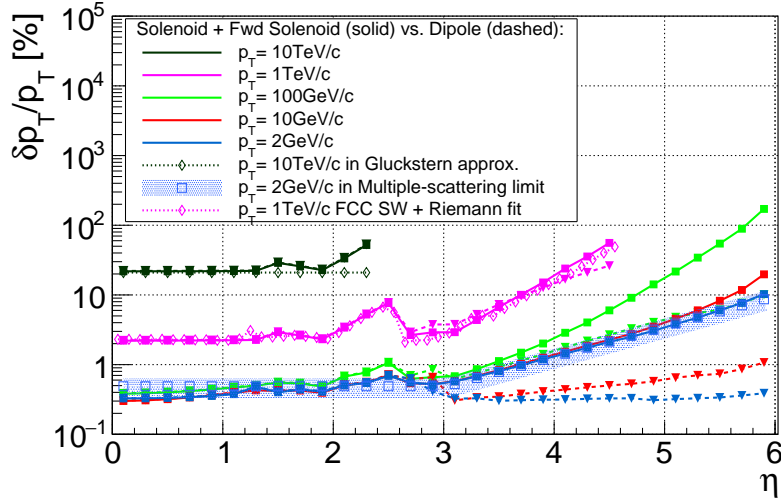


Fig. 6.6: Track  $\delta p_T/p_T$  in two scenarios: reference central + forward solenoid (solid curves, rectangles) and alternative central solenoid + dipole (dashed curves, triangles). For illustration, a high  $p_T$  limit curve (dotted with open diamonds) as well as low  $p_T$  MS limit curve (blue open rectangles with bands) are shown. 10 TeV/c and 1 TeV/c is calculated in a Gluckstern approximation [117, 118] and FCC SW by Riemann fit, respectively for a scenario with a constant 4 T magnetic field. The MS limit is calculated with an average total material budget at  $\eta = 0$ :  $x_{\text{tot}}/X_0 = 0.45 \pm 0.25$ .  $\delta p_T/p_T$  is shown for  $p_T = 10$  TeV/c (dark green), 1 TeV/c (magenta), 100 GeV/c (green), 10 GeV/c (red) and 2 GeV (azure blue).

resolution remains constant. The only exception is a small transition region between the BRL and EC. Beyond  $|\eta| > 1.9$  the spectrometer lever-arm decreases due to the presence of the end-cap calorimeter and the resolution degrades by up to a factor of 4 at  $|\eta| = 2.5$ . In the  $2.5 < |\eta| < 3.1$  region the full lever-arm is restored thanks to the forward tracker. Beyond this value the resolution starts degrading due to the continuous loss of lever-arm with an increasing pseudorapidity. At  $|\eta| \approx 3.7$ , the resolution is degraded to the same level as at  $|\eta| = 2.5$ . The forward tracker therefore increases the tracking acceptance by approximately one unit in  $\eta$ . An analysis for  $\delta p_T/p_T$  in  $B$ -field with a dipole magnet is explained in Section 6.3.5.

The impact point resolution is dominated by the spatial point resolution of the vertex detector at high  $p_T$  values, and material budget of the innermost layers and the beam-pipe at low  $p_T$  values. Its estimate for  $r$ - $\varphi$  direction,  $\delta d_0$ , can be expressed as [117, 118]:

$$\delta d_0 \Big|_{\text{res+MS}} \approx \sqrt{\sigma_{r\varphi}^2 + \left(\frac{13.6 \text{ MeV}/c}{\beta p_T}\right)^2 \left(\frac{t_{\text{BP}}}{X_{\text{BP}}} + \frac{t_0}{X_0}\right) r_0^2 \cosh \eta} \quad \text{for } r_0 \ll L \quad (6.5)$$

$$\approx a_{\text{res}} \oplus \frac{b_{\text{MS}} \cosh^{\frac{1}{2}} \eta}{p_T}, \quad (6.6)$$

where  $t_{\text{BP}}/X_{\text{BP}}$  and  $t_0/X_0$  is the thickness in radiation lengths of the beam-pipe and the first innermost layer, respectively,  $r_0$  stands for the radius of the first innermost layer, and the meaning of other parameters is the same as for the  $\delta p_T/p_T$  Gluckstern formulae. This analytical approximation neglects a minor effect of other measurement layers. The key outcome is in an explicit relation of how the  $\delta d_0$  depends on the low  $p_T$  limit of the vertex detector material budget and the track pseudorapidity. With increasing  $\eta$  the  $\delta d_0$  degrades as  $\sqrt{\cosh \eta}$  due to a combined effect of the material of the beam-pipe and the first measurement layer.

As discussed before (see Eq. (6.2)), the impact point resolution in  $z$  direction,  $\delta z_0$ , can be estimated



as [117, 118]:

$$\delta z_0 \Big|_{\text{res+MS}} \approx \sqrt{\sigma_z^2 + \left(\frac{13.6 \text{ MeV}/c}{\beta p_T}\right)^2 \left(\frac{t_{\text{BP}}}{X_{\text{BP}}} + \frac{t_0}{X_0}\right) r_0^2 \cosh^3 \eta} \quad \text{for } r_0 \ll L \quad (6.7)$$

$$\approx a_{\text{res}} \oplus \frac{b_{\text{MS}} \cos^{\frac{3}{2}} \eta}{p_T} \quad (6.8)$$

Similar to the case for the transverse direction, this  $\delta z_0$  approximative relation neglects the minor effect of other measurement layers. With increasing  $\eta$  the longitudinal impact parameter degrades as  $\cosh^{3/2} \eta$ .

The final performance is estimated by GLS method in TKLAYOUT for both tracker layouts: tilted and flat. The  $\delta d_0$  is depicted in Fig. 6.7a and  $\delta z_0$  in Fig. 6.7b. To cross-check the validity of the mathematical formalism applied, the Gluckstern curves in the MS limit above are added for the flat layout. The material budget of the innermost tracker layer is varied by  $\pm 50\%$  to estimate the potential effect of varying material budget. The first layer is positioned at  $r_0 = 25$  mm.

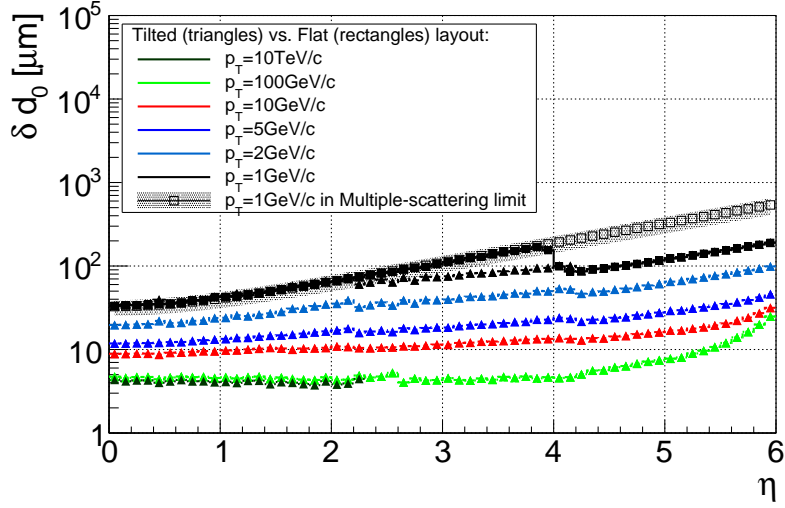
### 6.3.5 Effects of non-uniform magnetic field, dipole alternative

An FCC-hh detector magnet system has to provide bending power over a very large distance in  $z$ -direction. As described in Chapter 5, this is achieved in practice by a combination of two 4 T solenoids: central and forward. However, in the transition region between the two magnets the overall  $B$ -field uniformity is affected. As depicted in Fig. 6.8, the magnetic field manifests a variable  $B_z$  component in the tracker along the  $z$ -axis. In addition, the variability in  $B_z$  is compensated in a  $\varphi$  symmetric system by a non-zero radial component  $B_r$ , namely along  $z$ . The final  $B$ -field map of the two solenoid setup, together with a sketch of the reference tracking stations, is shown in Fig. 6.8a. The functional form of individual  $B$ -field components:  $B_z$  and  $B_r$ , as evaluated at  $r = 1.55$  m, is shown in Fig. 6.8b.

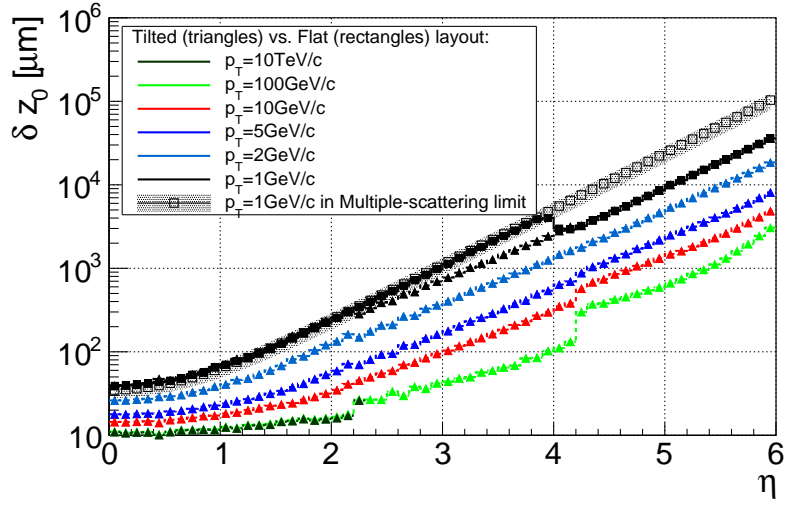
The effect of  $B$ -field non-uniformities on final  $\delta p_T/p_T$  is studied numerically by GLS method in MATHEMATICA. The  $p_T$  resolution is depicted relatively, i.e. as a ratio with respect to a  $p_T$  resolution in an ideal scenario with a 4 T uniform magnetic field. From the final results shown in Fig. 6.9, it can be directly concluded that the momentum resolution in the realistic solenoid  $B$ -field is negatively affected by its non-uniformities, namely beyond  $|\eta| > 2.5$ . Such conclusions can be well understood by following the  $\eta$ -lines in Fig. 6.8a. The non-uniformities of a realistic magnetic field occur mostly in the transition region between the two solenoids, and hence their major impact will be on the forward tracking, i.e. beyond  $|\eta| > 2.5$ . Compared to a scenario with an ideal 4 T uniform magnetic field, the final  $p_T$  resolution is at most 5 % worse at  $|\eta| = 2.5$  and up to 30 – 45 % worse in the remaining pseudorapidity region  $2.5 < |\eta| < 6.0$ . These effects can be also analysed by individual  $B$ -field components. The variations in  $B_z$  result in the  $p_T$  resolution deterioration by in maximum 25 to 35 % beyond  $|\eta| > 2.5$ . The presence of a non-zero  $B_r$  leads to an additional degradation of 10 %.

An alternative scenario assumes a combination of central solenoid and a dipole in the forward region. On one hand, this setup leads to a possible loss of  $r$ - $\varphi$  symmetry in the measurements. On the other, all tracks at very high pseudorapidity are almost parallel to the  $z$ -axis. The magnet system with a forward dipole has an ideal orientation to provide sufficient bending power for these tracks and  $p_T$  measurements. There are two limit cases of initial track conditions as illustrated in Fig. 6.10. The dipole  $B$ -field,  $B_{\text{dipole}}$ , is oriented either in  $x$ - $z$  projection (a) or  $y$ - $z$  projection (b). The corresponding initial track conditions are shown in the diagrams above the field maps: the total track momentum is oriented perpendicularly to  $B_{\text{dipole}}$  (a) or the longitudinal track component is oriented perpendicularly to  $B_{\text{dipole}}$  (b). In the first case, the radial granularity is important in momentum resolution measurements. That is in contrast to the solenoid case, where the  $r$ - $\varphi$  granularity is the key. In the latter case, the  $r$ - $\varphi$  granularity dominates. Hence, to provide precision momentum measurements for high  $\eta$  tracks





(a)



(b)

Fig. 6.7: Track impact parameter resolutions in  $r$ - $\varphi$ ,  $\delta d_0$  (a), and in  $z$ ,  $\delta z_0$  (b). Two sets of curves are depicted: for flat layout (solid curves, rectangles) and tilted layout (dashed curves, triangles);  $p_T = 10$  TeV/c (dark green), 100 GeV/c (green), 10 GeV/c (red), 5 GeV/c (blue), 2 GeV/c (azure blue) and 1 GeV/c (black). For illustration, a low  $p_T$  MS limit in a Gluckstern approximation [117, 118] is shown (black open rectangles with bands). It is calculated for a scenario with an ideal constant 4 T magnetic field and  $p_T = 1$  GeV/c. To estimate the effect of material budget, the  $t_0/X_0$  of the 1<sup>st</sup> layer is varied by  $\pm 50\%$  in the MS limit.

independently on the track azimuth angle,  $\varphi$ , at least two disc tracking stations positioned before and after the dipole have to be of the same granularity in both directions: the radial  $r$  and  $r$ - $\varphi$ .

By assuming a flat reference tracker layout with the last four outermost forward discs being pixelated, i.e. having the same granularity in  $r$  and  $r$ - $\varphi$ , the benefit of using the dipole magnet is huge at high  $\eta$ , see Fig. 6.11b. The improvement on  $\delta p_T/p_T$  starts from  $|\eta| > 3.5$  and is more significant towards the higher pseudorapidity values and lower  $p_T$ . As shown in absolute values in Fig. 6.6, for e.g.  $p_T = 1$  TeV/c the  $\delta p_T/p_T < 100\%$  in the whole tracker pseudorapidity range. A momentum resolution is shown for comparison for a non-pixelated case in Fig. 6.11a, i.e. the with reference layout EC discs. The  $r$ - $\varphi$  asymmetry in  $p_T$  measurements is then clearly visible. To conclude, the dipole in

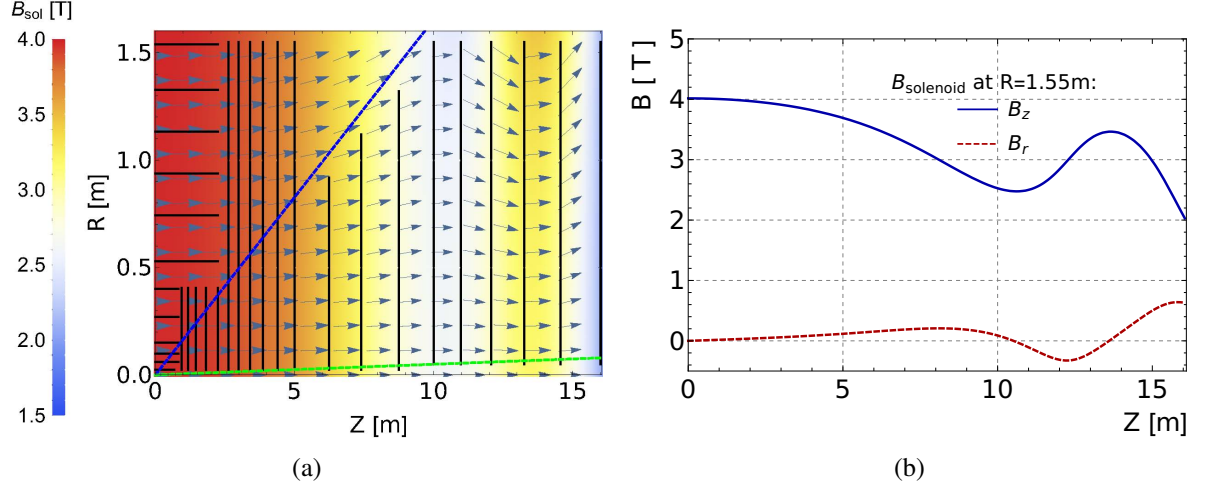


Fig. 6.8: Left (a): An  $r$ - $z$  projection of solenoid  $B$ -field map. For illustration, individual tracker layers/discs are sketched in black. The tracker envelope defined by  $\eta$ -lines at 2.5 and 6.0 is shown in blue and green, respectively. Right (b):  $B_z$  component (blue) and radial component  $B_r$  (red), as calculated at tracker maximum radius,  $r = 1.55$  m.

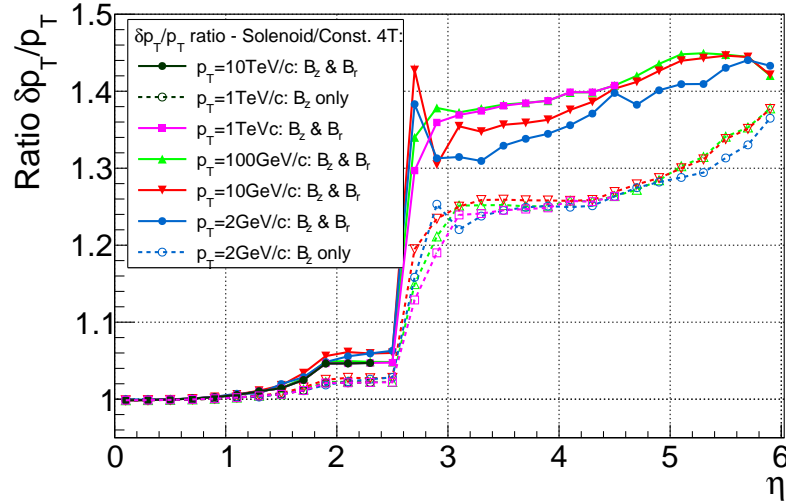


Fig. 6.9: Degradation of track  $\delta p_T/p_T$  along  $\eta$  due to non-uniformities of solenoid magnetic field. A ratio of  $p_T$  resolution is depicted: in a scenario with a 4 T solenoid  $B$ -field with respect to an ideal scenario with a constant 4 T  $B$ -field. Solid curves correspond to an accumulated effect of variable  $B_z$ , along  $z$ -direction, and a non-zero radial component  $B_r$ , along  $z$ -direction. Dashed curves reflect the non-uniformity effect along  $\eta$  arising from a variable  $B_z$  only.  $\delta p_T/p_T$  is shown for  $p_T = 10$  TeV/c (dark green), 1 TeV/c (magenta), 100 GeV/c (green), 10 GeV/c (red) and 2 GeV (azure blue).

combination with the pixelated tracking disc stations may almost restore the  $\varphi$  symmetry in track  $p_T$  measurements.

#### 6.4 Expected performance: vertexing, tracking and flavour tagging

The key aspect of the following studies is to evaluate the performance of the reference tracking system under FCC-hh experimental conditions. Two constraints are particularly significant for the layout considered: pile-up of 1000 events and a local dense physics environment in highly boosted objects.

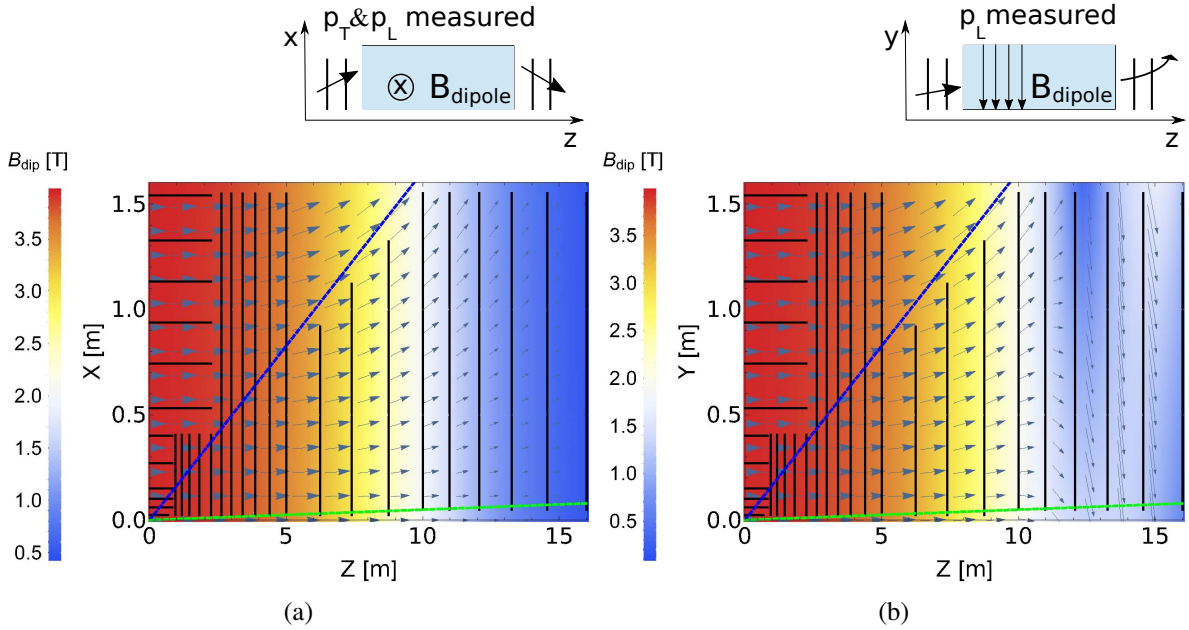


Fig. 6.10:  $x$ - $z$  projection of dipole  $B$ -field map is shown on the left (a),  $y$ - $z$  projection on the right (b). For illustration of tracking performance, an orientation of dominant component of the dipole magnetic field with respect to the tracker geometry is sketched above the field maps. Individual tracker layers/discs are depicted in black, the tracker envelope defined by  $\eta$ -lines at 2.5 and 6.0 is shown in blue and green, respectively.

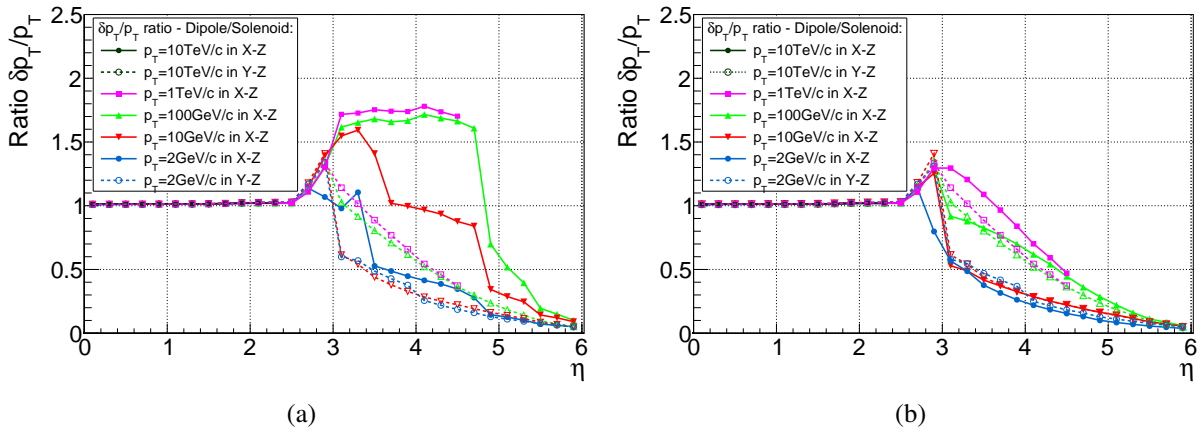


Fig. 6.11: An effect of dipole magnetic field in the forward region on track  $\delta p_T/p_T$ : a ratio of  $p_T$  resolution in a scenario with a dipole with respect to a scenario with a solenoid in the forward region. Due to dipole asymmetry two sets of curves are depicted: solid curves for tracks starting along  $x$ -axis at IP, and dashed curves for tracks starting along  $y$ -axis at IP.  $\delta p_T/p_T$  is shown for  $p_T = 10$  TeV/c (dark green), 1 TeV/c (magenta), 100 GeV/c (green), 10 GeV/c (red) and 2 GeV (azure blue). The left figure (a) shows the resolution for the flat layout. The right (b) for the flat layout with the last four outermost forward discs being pixelated, i.e. having the same fine granularity in  $r$  and  $r-\varphi$ .

The pile-up challenges the physics reconstruction by ‘contaminating’ a p-p hard scattering process with a large number of soft momentum charged particle tracks. The pile-up particles are produced approximately uniformly,  $dN_{\text{ch}}/d\eta \approx \text{const.}$  up to significantly high values in pseudorapidity,  $|\eta| \approx 4.0 - 5.0$  (see Fig. 23 in Ref. [15]). This production trend changes in higher  $\eta$  because of the phase space limits; consequently, the  $dN_{\text{ch}}/d\eta$  starts to fall off rapidly to zero. The corresponding  $p_{\text{T}}$  spectrum is relatively soft; the particles from pile-up collisions, dominated by soft QCD, are mostly produced in a sub-GeV/c range with an estimated mean value:  $\langle p_{\text{T}} \rangle \approx 0.7 \text{ GeV/c}$  (see Fig. 27 in Ref. [15]). In the presence of the detector 4 T magnetic field, the majority of such tracks will then stay confined in a radius of a few hundreds of millimetres around the beam axis. In addition, a real impact of the pile-up reduces significantly with increasing radial position  $r$ ; the particle density per unit area falls off approximately as  $\sim 1/r^2$ . Therefore, it can be expected that the pile-up will have the largest impact on the reconstruction steps which rely on detectors positioned relatively close to the beam-pipe. Then the major challenges arise for track finding (track seeding, pattern recognition and track filtering) and primary vertexing. The latter is additionally challenged by the line pile-up density expected along the  $z$ -axis:  $\langle \partial\mu/\partial z \rangle \approx 8$  vertices per mm (see Table 1.1). In the context of pile-up mitigation and the suggested reference inclined layout, the impact of the following parameters is found to be particularly important: propagation distances between individual measurement points, detector tilt, granularity and material budget.

The difficulties arising in track reconstruction of particles produced in local dense environments, such as cores of highly collimated jets of heavy flavour boosted objects, are of a different nature. These objects, being low mass compared to the FCC-hh energy reach, can be produced with a large forward boost and high momentum; the charged tracks of their decay products are close and hard to separate. In addition, regardless of the short lifetime, the particles like  $\tau$ -leptons and B-mesons can decay with a large lab-frame distance at a multi-TeV scale; e.g. a 5 TeV/c  $\tau$ -lepton (charged B-meson) will pass an average decay distance of  $\approx 245$  (465) mm in the tracker. Consequently, the reconstruction will have to rely on relatively distant measurements (in outer/forward detectors). All these challenges are addressed by analysing high-level objects reconstruction (hits/tracks separation efficiency) and heavy flavour identification. The following layout parameters are the key: overall tracker dimensions, number of measurement points and granularity.

#### 6.4.1 Progressive track filtering in pile-up and tilted layout

A realistic evaluation of tracking performance under nominal FCC-hh pile-up conditions requires a complex approach based on full simulation and sophisticated track reconstruction. However, to understand the tracking limits, this task can be studied fundamentally—by understanding the qualitative role of individual layout parameters throughout the track reconstruction. Apart from the track parameters resolution—see Section 6.3.4, the tracking performance can be quantified by two complementary variables: track reconstruction efficiency and fake-rate. Current experience from the ATLAS and CMS phase 2 upgrades [16, 119], with ‘similar’ tracking systems to those of the FCC-hh (namely in terms of material budget and spatial point resolution) indicates, that a requirement of approximately 10 hits per track will keep the fake-rate at an acceptable level under nominal HL-LHC pile-up conditions. In general, the fake tracks are mainly formed due to multiple Coulomb scattering (MS), which results in extra random hit combinations which are compatible with the signal track hypothesis. As pointed out in Fig. 6.5 in Section 6.3.3, the MS is dominated by the amount of material traversed within the detector and the propagation distances between individual measurement layers. In an ideal scenario with optimal pattern recognition the MS noise can be considered as automatically regulated by track fit, and the single remaining source for track reconstruction inefficiency can be attributed to particle nuclear interactions; therefore only the charged hadrons are expected to be reconstructed with a non-zero inefficiency in such a scenario. The material budget in units of interaction lengths,  $\lambda/\lambda_0$ , has been studied to illustrate the effect of layout geometr—see Fig. 6.12—all under an assumption limit of 10 hits per track from inside-out,

so that the fake-rate is kept under control. The result indicates that the reference tilted layout is superior to the flat layout in terms of nuclear interactions, namely in the barrel-endcap transition region.

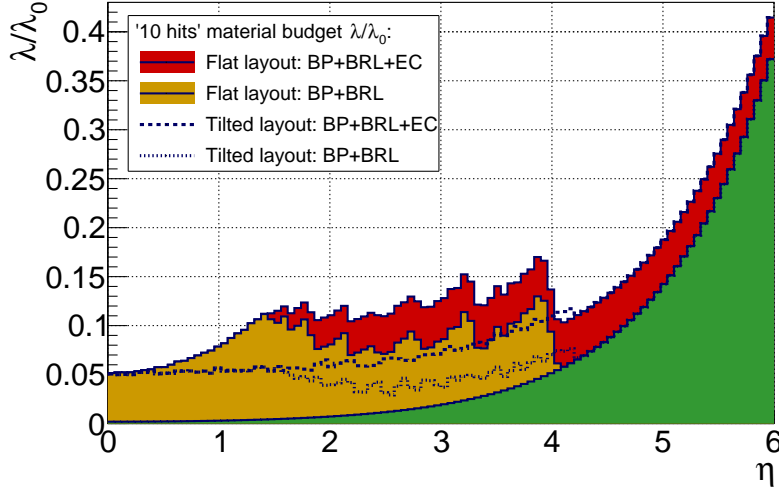


Fig. 6.12: A total material scan in units of nuclear interaction lengths,  $\lambda/\lambda_0$ , versus pseudorapidity,  $\eta$ , for both reference layouts: flat (solid lines) and tilted (dashed lines)—a limit of 10 hits per track (from inside-out) is assumed. The beam-pipe material, BRL and EC regions are shown in green, yellow and red, respectively.

To qualitatively address the role of individual layout parameters throughout the track reconstruction, namely in the given pile-up, low  $p_T$  limit and non-ideal pattern recognition case, a probabilistic approach to progressive track filtering has been applied. The goal is to identify the ‘weak spots’ in the designed layout, which may potentially affect the final performance, and to suggest the suitable changes to minimise them—finally leading to the reference tilted layout. The essence of the method can be described as follows: the errors (uncertainties) on track parameters, namely on their spatial components in  $r$ - $\varphi$  and  $z$ , are progressively propagated inside-out from the existing tracklet<sup>2</sup> to a new measurement point. At each filtering step, the errors on spatial track parameters define an error ellipse in the plane perpendicular to the track. After the ellipse is projected to the measurement plane, a decision is made whether a new hit is consistent with the tracklet at the required confidence level (CL). This method is illustrated in Fig. 6.13 and further details can be found in Ref. [118].

An accumulated probability  $p$  is defined in order to mathematically quantify the progressive track filtering performance. Let  $p_{\text{bkg\_95\%CL}}^i$  represents a signal-background merge probability, namely that at a given  $i$ -th measurement point (layer or ring) a true track hit (signal) is compromised by background hit at 95% CL. All layers/rings are assumed to be indexed by  $i$  in an increasing order, as being traversed by particle inside-out from the interaction region. To disentangle an algorithmic effect of seeding, a perfect track seed is assumed; at least the first 3 innermost layers/rings are therefore excluded from these calculations. The final product  $p$  of individual probability complements ( $1 - p_{\text{bkg\_95\%CL}}^i$ ) is evaluated for the complete set of tracker layers/rings traversed as:

$$p = \prod_{i=4}^N (1 - p_{\text{bkg\_95\%CL}}^i) \quad (6.9)$$

Within this process, the individual  $p_{\text{bkg\_95\%CL}}^i$  probabilities are used as ‘local’ quantifiers, i.e. to evaluate performance between individual layers/rings and to identify potential tracking ‘weak’ spots in the layout.

<sup>2</sup>A track segment consisting of a fraction of measured hits that evolves step-by-step, i.e. progressively, throughout the track filtering into a final track candidate.

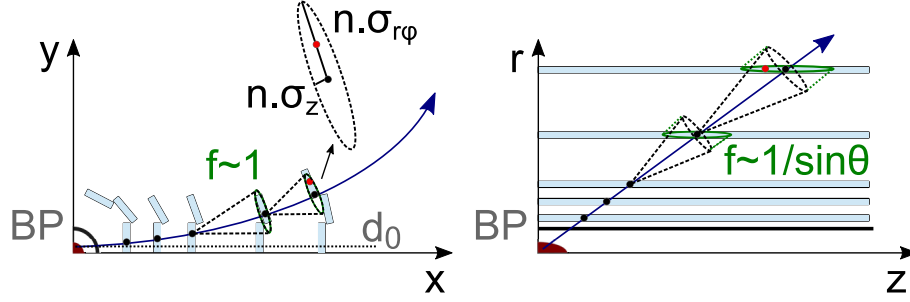


Fig. 6.13: A sketch of error propagation along true particle track (blue) in  $x$ - $y$  (left) and  $r$ - $z$  (right) projection planes. The luminous region is shown in dark red, beam-pipe (BP) in black, tracker geometry layout in azure blue and projected error ellipse in dark green. True hits (signal) are drawn in black and fake hits (background) in red.

As concrete examples: an unusually long propagation distance between  $(i - 1)$ -th and  $i$ -th measurement points or insufficiently high granularity at  $i$ -th measurement plane or large material budget of  $(i - 1)$ -th detector module have a direct impact on the area of error ellipse at certain  $\eta$ , and hence the  $p_{\text{bkg}_95\%CL}^i$ . To approximate the real spatial distribution of pile-up hits (background) a charged particle fluence map is used. This map has been estimated by FLUKA simulations and evaluated per 1000 p-p collisions at  $\sqrt{s} = 100$  TeV (see details in Chapter 3 - Section 3.2). All background hits are assumed to be uncorrelated, which neglects a positive reconstruction effect of using the pile-up tracklets in the signal track filtering. Nevertheless, such an approach can be considered as the worst case estimate.

To interpret and relate the  $p$  quantity to the realistic performance, this method is applied to two layouts under different experimental conditions: the reference FCC-hh tracker under nominal pile-up of 1000 events and the CMS phase 2 tracker (version: OT v3.6.5, IT v4.0.25 [16, 120]) under HL-LHC pile-up of 140 events. The tracking performance of the latter has been intensively studied and well demonstrated using full simulation [16]. The evaluation strategy is hence to calibrate the  $p$  first in the scenario with the CMS phase 2 layout under HL-LHC conditions. Then, the FCC-hh tracking system is modified, so that the progressive track filtering provides roughly the same performance, while the pile-up level and the detector layout change from the CMS phase 2 to FCC-hh scenario. As pointed out in Fig. 6.7 in Section 6.3.4, the track ‘spatial’ resolution degrades with the decreasing particle  $p_T$  due to material effects and multiple Coulomb scattering. Therefore the most critical is low  $p_T$  particle tracking—the benchmark value is set to  $p_T > 1$  GeV/c. As depicted in Fig. 6.14b, the worst performance of CMS phase 2 tracker for  $p_T = 1$  GeV/c tracks in 140 pile-up events is estimated as:  $p \approx 80\%$  at  $|\eta| \approx 1.5$ .

This value of  $p \approx 80\%$  is set as a benchmark for the progressive track filtering capabilities of the FCC-hh tracking system. The final results are depicted in Fig. 6.14a. Two sets of  $p_T$  curves are shown: one for the flat layout with the cylindrical barrel (BRL) region and end-cap (EC) discs, the other for the tilted layout with the inclined detector modules in the BRL-EC transition region, cf. the reference layouts in Fig. 6.1 in Section 6.3. The key layout parameters, which may lead to the degraded performance of low  $p_T$  tracking, are identified: material effects of non-inclined sensors in the BRL-EC transition region, granularity in  $z/r$  (BRL/EC), and layer-to-layer, layer-to-ring, ring-to-ring propagation distances. There are two main detector regions in the flat layout with significantly deteriorated performance: the BRL-EC transition region ( $0.5 < |\eta| < 2.5$ ) and the end-cap region at  $|\eta| \approx 3.0$ .

The degraded low  $p_T$  performance in the BRL-EC region can be mainly attributed to the material effects of non-inclined detector modules, and hence to effects of MS (and nuclear interactions). The driving design principle of the tilted layout is to minimise these effects on propagated errors, and thus to reduce the material crossed by charged particles in the detector. Nevertheless as illustrated in Fig. 6.13, the material effects are not the only contributions for the inclined tracks coming from the different physics objects (cf. the difference from collimated tracks in boosted objects). Due to the increasing projection



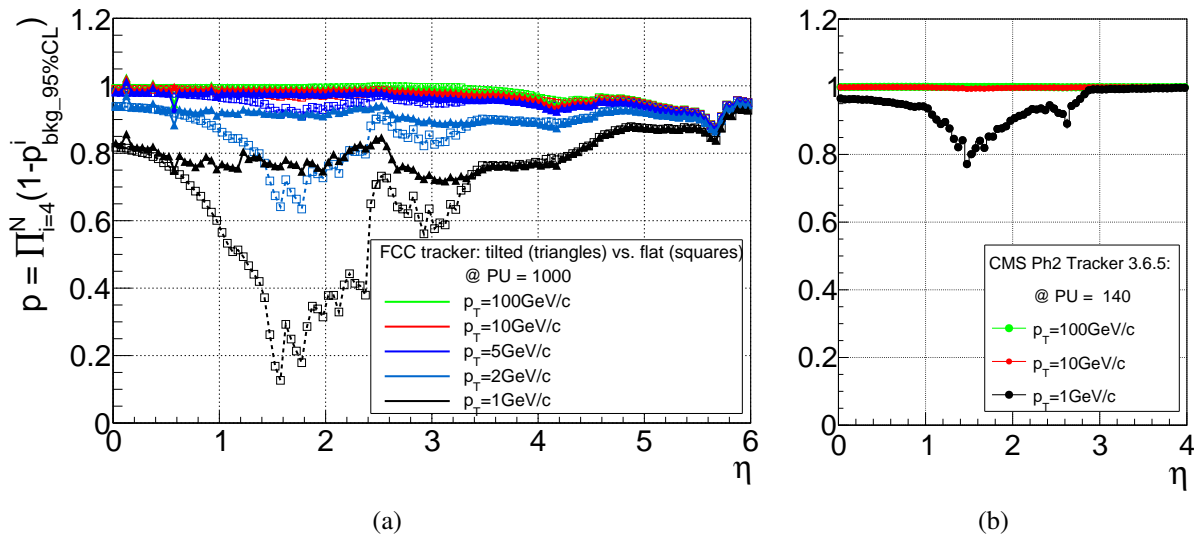


Fig. 6.14: Left (a): Progressive track filtering capabilities of FCC-hh tracking system, as studied by probabilistic approach for two layout geometries: flat (dashed curves, rectangles) and tilted (solid curves, triangles) at nominal pile-up  $\langle\mu\rangle = 1000$ . Right (b): A qualitative comparison to an HL-LHC scenario with nominal pile-up  $\langle\mu\rangle = 140$  and CMS phase 2 upgrade tracker geometry (OT v3.6.5, IT v4.0.25). The curves are depicted for following  $p_T$ : 1 GeV/c (black), 2 GeV/c (azure blue), 5 GeV/c (blue), 10 GeV/c (red) and 100 GeV/c (green).

in  $z$  with the higher  $\eta$ , the propagated track spatial resolution represents an additional limiting factor for the BRL. In  $z$  it scales with the pseudorapidity as  $\sim \cosh \eta$ , while in  $r$ - $\varphi$  it is  $\sim 1$ . Hence the layout with modules positioned perpendicularly to the tracks is in an ideal configuration. However, there are other constraints: first, to utilise the maximum tracker lever-arm the last BRL layer is designed as non-inclined. Second, the tilt angle of the first layer is a compromise between the positive outcome of the minimum material budget and the  $\delta d_0$  deterioration due to a varying radial position of individual measurement points. The tilt angle of the first FCC-hh layer is optimised to  $\vartheta_{\text{tilt}} \sim 10^\circ$ . Third, tracks are coming from the interaction region, which is an ellipse not a point. Finally, a common tilt angle is designed for a group of 2 – 3 modules to decrease the detector complexity. The detailed layout of the tilted tracker is shown in Fig. 6.15, the geometry parameters are given in Ref. [116] and Appendix 6.A.

The reduced performance in the EC region is due to the insufficient granularity of striplet detectors in the radial direction. As detailed in Section 6.3.2, the modules in inclined geometries measure the  $r$ - $\varphi$  and  $r$  coordinates locally, and they both may contribute to the measurement errors of global hit positions in  $r$ - $\varphi$  and  $z$ . The contribution of EC striplets to the tracking starts to dominate at  $|\eta| \approx 3.0$ , hence the observed effect. Based on the optimisation, the EC striplet pitch is set to 1.75 mm in the tilted layout instead of the 10 mm pitch as suggested for the flat layout. Table 6.2 in Section 6.3.2 summarises the pitch values for various detector categories.

Based on these studies, a minimum of 3 discs is suggested in the intermediate region between the central and forward tracker. Such a number is the minimum required to provide equidistant track measurements with sufficient propagation distances between the two main tracking systems, see Fig. 6.1.

#### 6.4.2 Tracking efficiency in boosted objects

The unprecedented collision energy at the FCC-hh implies that the particles in the final state can potentially have an unprecedented boost. Boosted objects produce dense environments that challenge track reconstruction and jet identification. Therefore, tracking performance within boosted objects may set



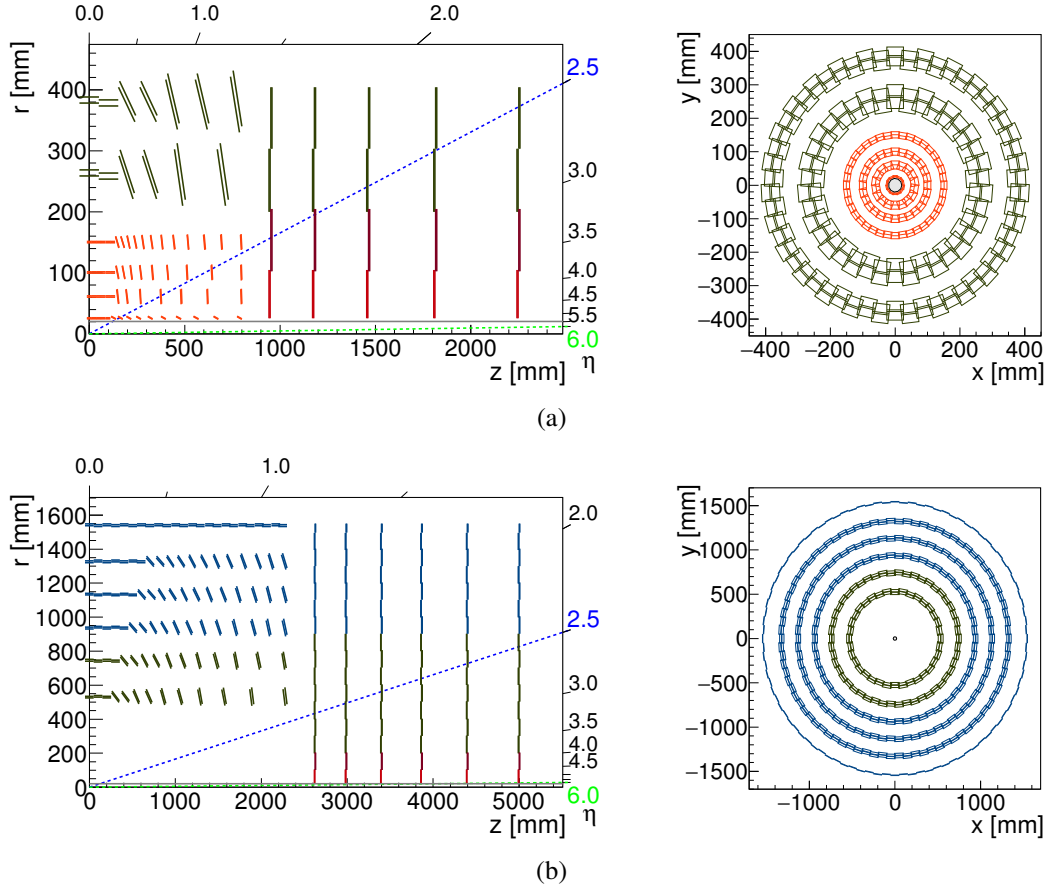


Fig. 6.15: Final reference layout of the central tracker with inclined detectors (tilted layout), as optimised by progressive track filtering. At the top (a) the inner tracker is shown:  $r$ - $z$  projection on the left and  $x$ - $y$  on the right. At the bottom (b) the outer tracker is depicted. The layout of forward region is identical in both geometries: flat and tilted. A ‘double module structure’ is used to schematically depict two neighbouring ladders in each tracker layer, see also Appendix 6.A.

additional constraints on the tracker geometry and define new requirements for the reconstruction algorithms needed at the TeV scale. In this section, tracking performance is evaluated in the long-lived objects which may suffer from the highest boost:  $\tau$ -leptons and B-hadrons. Two approaches are considered: the first is to evaluate the distance between hits from tracks close-by in a particular detector layer, and the second is to study the tracking efficiency and track purity within jets and b-jets. These studies assume the flat tracker layout configuration. A detailed description of both studies can be found in the dedicated notes [107, 121].

### Hit separation efficiency:

In general, in order to reconstruct and identify a multi-prong long-lived particle such as a 3-prong  $\tau$ -lepton decay or B-hadron decay, the individual decay products need to be reconstructed. The minimum number of hits required to reconstruct a track defines an acceptance to the displaced vertex reconstruction, i.e. a limit on the flight distance of the mother particle. It has been found that eight hits per track are required to keep the fake rate at a reasonable level [107] in the FCC-hh detector barrel region. Therefore, only the decay products of particles decaying before the 8<sup>th</sup> outermost layer traverse a sufficient number of sensors and can potentially be reconstructed. In the barrel region, the 8<sup>th</sup> outermost layer corresponds to the first macro-pixel layer and it is positioned at a radius of 27 cm. The decay vertex position for

central  $\tau$ -lepton ( $|\eta(\tau)| < 0.175$ ) and central ( $|\eta(b)| < 0.05$ ) B-hadron decays for different energies are shown in Figs. 6.16 and 6.17.

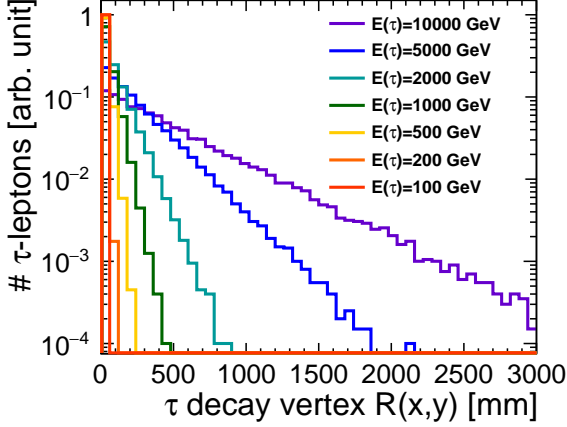


Fig. 6.16:  $\tau$ -lepton decay vertex position in the radial direction in central  $\tau^+\tau^-$  events for various  $\tau$ energies.

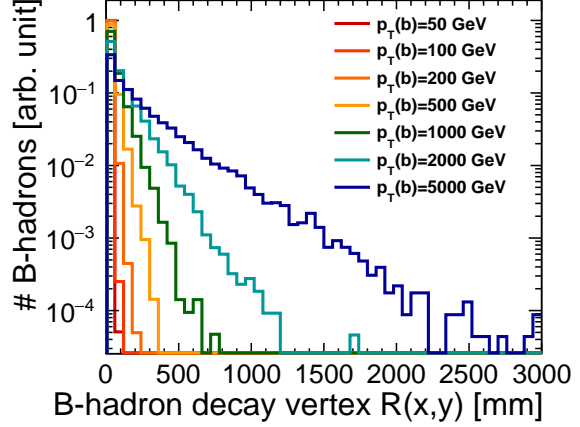


Fig. 6.17: B-hadron decay vertex position in the radial direction for different b-quark  $p_T$  values in central  $b\bar{b}$  events.

About 71% of B-hadrons in a  $p_T = 5$  TeV/c central jet, and about 68% of central  $\tau$ -leptons with  $E(\tau) = 5$  TeV decay before the first macro-pixel layer. Those which decay after that layer, are out of acceptance and their secondary vertex and daughter tracks cannot be reconstructed. This acceptance limit is most relevant in the barrel region, since the tracker is one order of magnitude larger in the  $z$ -direction than in the  $r$ -direction. In this study only the barrel part of the tracker detector is considered. Di- $\tau$  events containing central 3-prong  $\tau$ -leptons are simulated, as well as central  $b\bar{b}$  di-jet events.

For a track to be reconstructed, the particle needs to leave hits in at least eight layers, and all the eight hits must be unambiguously associated with the track. Hence, the hits must be separated enough in all the layers in order to produce different clusters. In this study it is assumed that, if the distance between two hits in a given layer is greater than twice the sensor pitch in either the  $r$ - $\varphi$  or the  $z$ -direction, the hits will form separate clusters. This approximation is valid for very central particles producing one-pixel clusters. For each event the closest pair of hits in a particular layer is selected, and their separation in the  $r$ - $\varphi$  and in the  $z$ -direction is calculated.

The ‘hit separation efficiency’ is defined as the fraction of closest pairs of hits, which form separate clusters in the 8<sup>th</sup> outermost layer. It is assumed that if the two particles can be separated on that layer, they can also be separated in the subsequent outer layers. This is because the granularity in  $r$ - $\varphi$  is the same in the eight outermost layers and, as shown in Fig. 6.18, the  $r$ - $\varphi$  granularity drives the hit separation efficiency. The hit separation efficiency is an estimation of the efficiency of reconstructing the tracks of all the decay products. This efficiency is calculated as a function of the single point resolution and for different energies of the mother particle. Digital readout is assumed throughout the tracker (as explained in Section 6.3) and therefore the single point resolution ( $\sigma$ ) is estimated from the detector pitch as:  $\sigma = \text{pitch}/\sqrt{12}$ .

Figure 6.18 shows the hit separation efficiency versus  $r$ - $\varphi$  and  $z$  single point resolution for events with 3-prong  $\tau$ -leptons of various energies. The 8<sup>th</sup> outermost layer has a default single point resolution of  $9.5 \times 115 \mu\text{m}^2$ . To understand the effect of the different granularities, the variations of  $r$ - $\varphi$  single point resolution are performed while keeping the  $z$  single point resolution at its default value, and vice-versa.

For events with low energy taus,  $E(\tau) < 100$  GeV, the hit separation efficiency is close to 100% and has a very weak dependence on the single point resolution. However, for high energy taus of  $E(\tau) >$

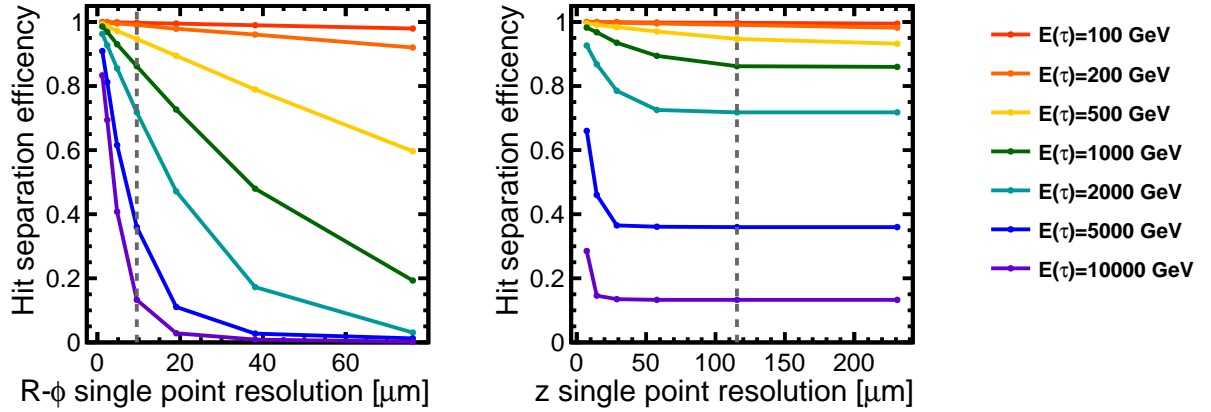


Fig. 6.18: Hit separation efficiency in central  $\tau^+\tau^-$  events for various  $\tau$  energies versus  $r$ - $\varphi$  (left) and  $z$  (right) single point resolution. The efficiency is defined as the fraction of closest pairs of hits in an event which form separate clusters in the 8<sup>th</sup> outermost layer (see text).

1 TeV, the efficiency rapidly drops with the increasing  $r$ - $\varphi$  pitch. When the sensor pitch in one direction is much smaller than in the other, it is much more likely that the hits are separated in the direction having the smallest pitch. This is the case for the sensors of the 8<sup>th</sup> outermost layer in the reference flat layout, which have more than ten times larger pitch in the  $z$  direction than in the  $r$ - $\varphi$  direction. Therefore the efficiency seems to have a stronger dependence on the resolution in  $r$ - $\varphi$  rather than in  $z$ . However, when the single point resolution in  $z$  is similar to the one in  $r$ - $\varphi$ , the separation in the  $z$ -direction does contribute significantly to the hit separation efficiency. Quantitatively, in only 36% of the events containing 3-prong  $\tau$  decays with  $E(\tau) = 5$  TeV it will be possible to reconstruct all the 3 tracks with the current granularity. The percentage may increase to over 60% if the pitch in the  $r$ - $\varphi$  direction is halved.

Figure 6.19 shows the same distributions for B-hadron decays. Only the hits from stable particles in the B-hadron decay chain are considered. Therefore, the hits produced by charged B- and C-hadrons are neglected in the calculations. The efficiency decreases with increasing jet  $p_T$  and degrading single point resolution. For energies above 1 TeV, a significant fraction of B- and C-hadrons reach the studied layer undecayed. Since they are not stable particles, the hits from their tracks are not considered. Therefore the undecayed B-hadrons do not enter the efficiency calculation, and the undecayed C-hadrons do not enter the ‘closest hit pair’ calculation. Thus the estimated efficiency may appear to be larger than for lower jet energies. For B-hadrons in jets of  $p_T = 5$  TeV/c, the probability that all the decay products are reconstructed is 72%, and may increase to 85% if the pitch in the  $r$ - $\varphi$  direction is halved.

To conclude, this study shows how the capability to reconstruct all the decay products of a long-lived particle decay rapidly decreases with increasing boost. This is partially due to the secondary vertex acceptance, which depends on the overall size of the tracker and number of layers. But it is also due to the hit separation, which depends on the detector granularity. It is found that even a small improvement in the  $r$ - $\varphi$  granularity provides a significant gain in the identification of the extremely boosted objects.

### Tracking efficiency:

The tracking efficiency performance has been estimated using the Linear Collider SW tools and a CLIC\_SiD-based detector. In the CLIC\_SiD-based detector model the CLIC\_SiD tracker is replaced with an adapted version of the FCC-hh barrel tracker. The barrel tracker has the same dimensions, geometrical layout and material budget as in the reference FCC-hh detector, except for the radii of the five outermost barrel layers, which are modified in order to fit inside the CLIC\_SiD calorimeter. The outermost tracker layer has a radius of 1.2 m, cf. 1.55 m radius of the reference layout, and the remaining four

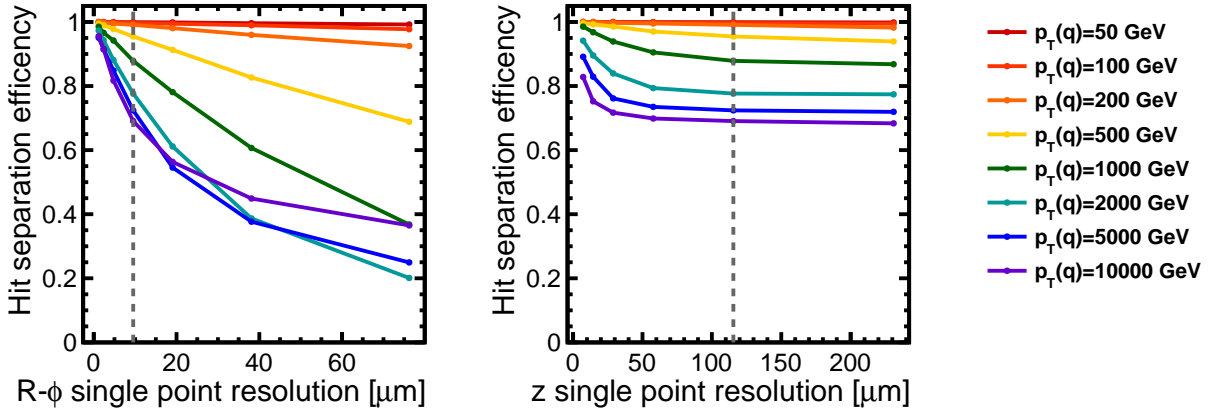


Fig. 6.19: Hit efficiency for  $b\bar{b}$  sample versus  $r$ - $\phi$  (left) and  $z$  (right) single point resolution. The efficiency is defined as the fraction of closest pairs of hits in an event which form separate clusters in the 8<sup>th</sup> outermost layer (see text).

tracker layers are positioned equidistantly within the available space.

The tracking efficiency is calculated in the barrel region using di-jet events in which the partons are required to be produced very centrally  $|\eta(q)| < 0.05$ . The efficiency is defined as the fraction of reconstructable MC particles that are associated with a reconstructed track. A reconstructable particle is defined as a stable MC particle with  $p_T > 1 \text{ GeV}/c$  and  $|\eta| < 0.175$ , leaving at least eight hits in the tracker. The purity is defined as the fraction of reconstructed tracks that are associated with a MC particle, i.e. the track contains at least 75% of the MC particle hits.

For tracks in di-jet events with  $p_T = 500 \text{ GeV}/c$  light-flavour (LF<sup>3</sup>) jets, the efficiency is 98.8% and the purity 99.4%. These values decrease for the  $p_T = 5 \text{ TeV}/c$  jets to 96.2% and 91.4% respectively. The decrease is mainly due to the highly collimated and high  $p_T$  tracks, which increase the probability to mis-assign the hits in pattern recognition. The b-jet tracks that come from the B-hadron decay chain have a lower efficiency of 79.8% due to the displaced decay of the B-hadron. When the decay is displaced, the daughters are produced closer to the detector layers, and therefore the separation between individual hits on the measurement layers decreases.

Figure 6.20 shows the distributions of angular distance ( $\Delta R^4$ ) between a reconstructable particle and its closest charged and stable MC particle for  $p_T = 500 \text{ GeV}/c$  jets 6.20a and  $p_T = 5 \text{ TeV}/c$  jets 6.20b. In addition, the tracking efficiency and track purity for those two energies are shown. The efficiency is depicted as a function of the angular distance between the reconstructable particle and its closest MC particle (as defined above). The purity is shown as a function of the angular distance between the reconstructed track and its closest track. The distributions and efficiencies are presented for both LF-jets, b-jets and also separately for the b-jet particles coming from the B-hadron decay chain, and the b-jet particles not coming from the B-hadron decay chain. It can be seen that, for the  $p_T = 500 \text{ GeV}/c$  jet sample, the efficiency and purity dependence on  $\Delta R$  is small. However, for the  $p_T = 5 \text{ TeV}/c$  di-jet events both the efficiency and the purity decrease by up to 20% when the closest particle is within  $\Delta R = 0.004$ . It is also clear from the  $\Delta R$  distribution that particles from B-hadron decays in the  $p_T = 5 \text{ TeV}/c$  sample are significantly more collimated than the other particles in the b-jet, since they carry a large fraction of the jet energy. Their tracking efficiency decreases for a larger range of  $\Delta R < 0.01$  because of the displaced production vertex. The efficiency for  $\Delta R < 0.002$ , where the reconstructable particle distribution

<sup>3</sup>jets from a gluon or an up-, down- or strange-quark

<sup>4</sup> $\Delta R \equiv \sqrt{\Delta\eta^2 + \Delta\phi^2}$

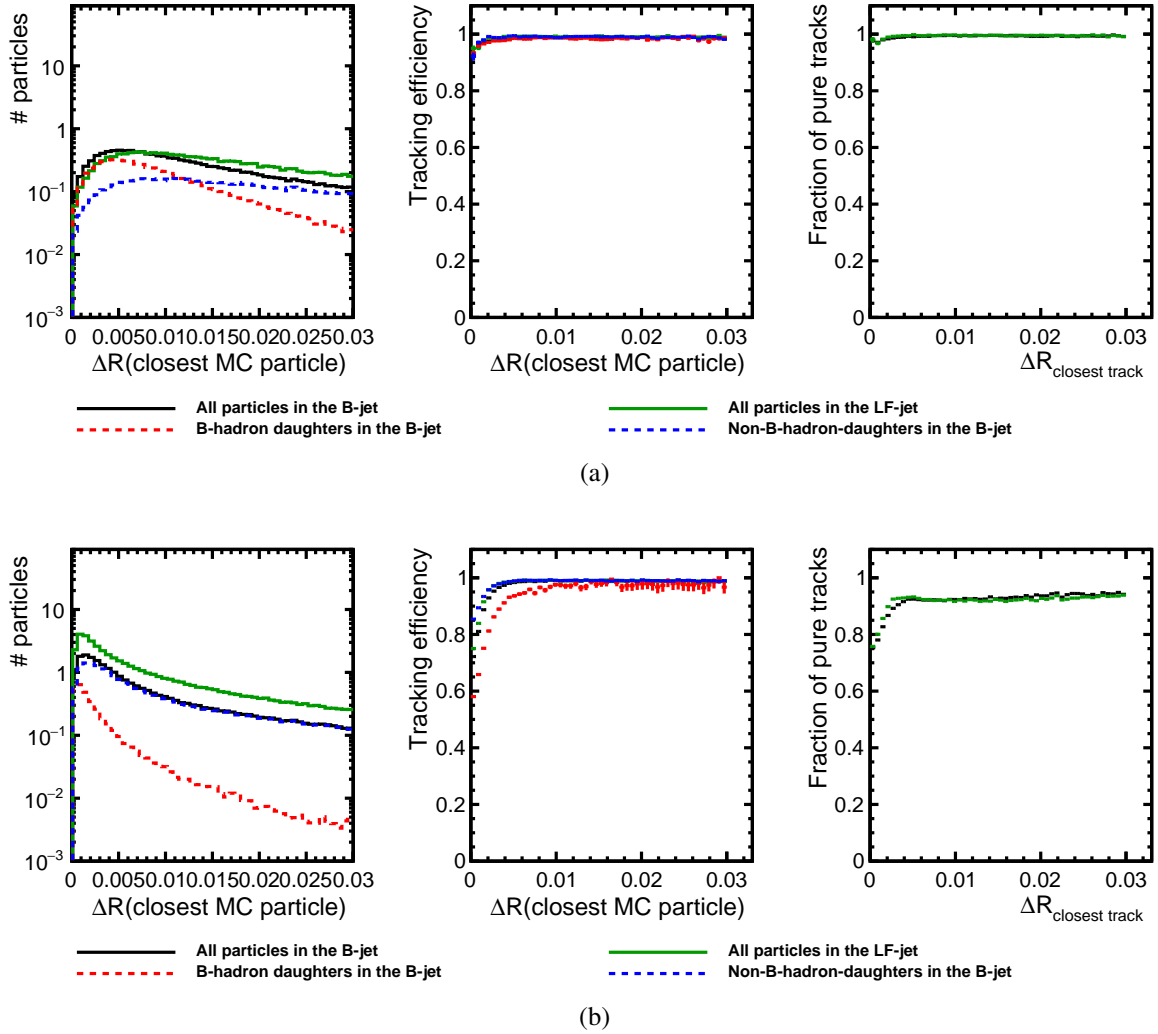


Fig. 6.20: Distribution of the  $\Delta R$  distance between a reconstructable particle and its closest MC particle (left), tracking efficiency versus this  $\Delta R$  (middle) and track purity versus the  $\Delta R$  between a reconstructed track and its closest track (right). Distributions are shown for particles with  $p_T > 1$  GeV/c and  $|\eta| < 0.175$  in the di-jet  $b\bar{b}$  and LF samples, and separately for the particles coming/not coming from the B-hadron decay chain. Figure a (top) shows the results for the  $p_T = 500$  GeV/c jet sample, and Fig. b (bottom) for the  $p_T = 5$  TeV/c jet sample.

peaks, has values between 60% and 80%.

Similarly, Fig. 6.21 shows the  $p_T$  distribution for reconstructable particles in  $p_T = 500$  GeV/c jets (Fig. 6.21a) and  $p_T = 5$  TeV/c jets (Fig. 6.21b). The efficiency is depicted as a function of the reconstructable particle  $p_T$ , and the purity is shown as a function of the reconstructed track  $p_T$ . The particles coming from a B-hadron decay have a significantly harder  $p_T$  distribution. The efficiency decreases at high  $p_T$ , especially in the  $p_T = 5$  TeV/c jet sample, since the high  $p_T$  particles correspond to the very central and collimated particles (particles with low  $\Delta R$  in Fig. 6.20). At  $p_T = 5$  TeV/c the purity of the tracks decreases with  $p_T$  as well, due to the hit mis-assignment in very dense environments.

To summarise, the tracking efficiency and purity for close-by tracks decreases significantly for highly boosted jets with very collimated tracks, and this effect is larger when the jet contains significantly displaced secondary vertices. Higher sensor granularity throughout the tracker or more sophisti-

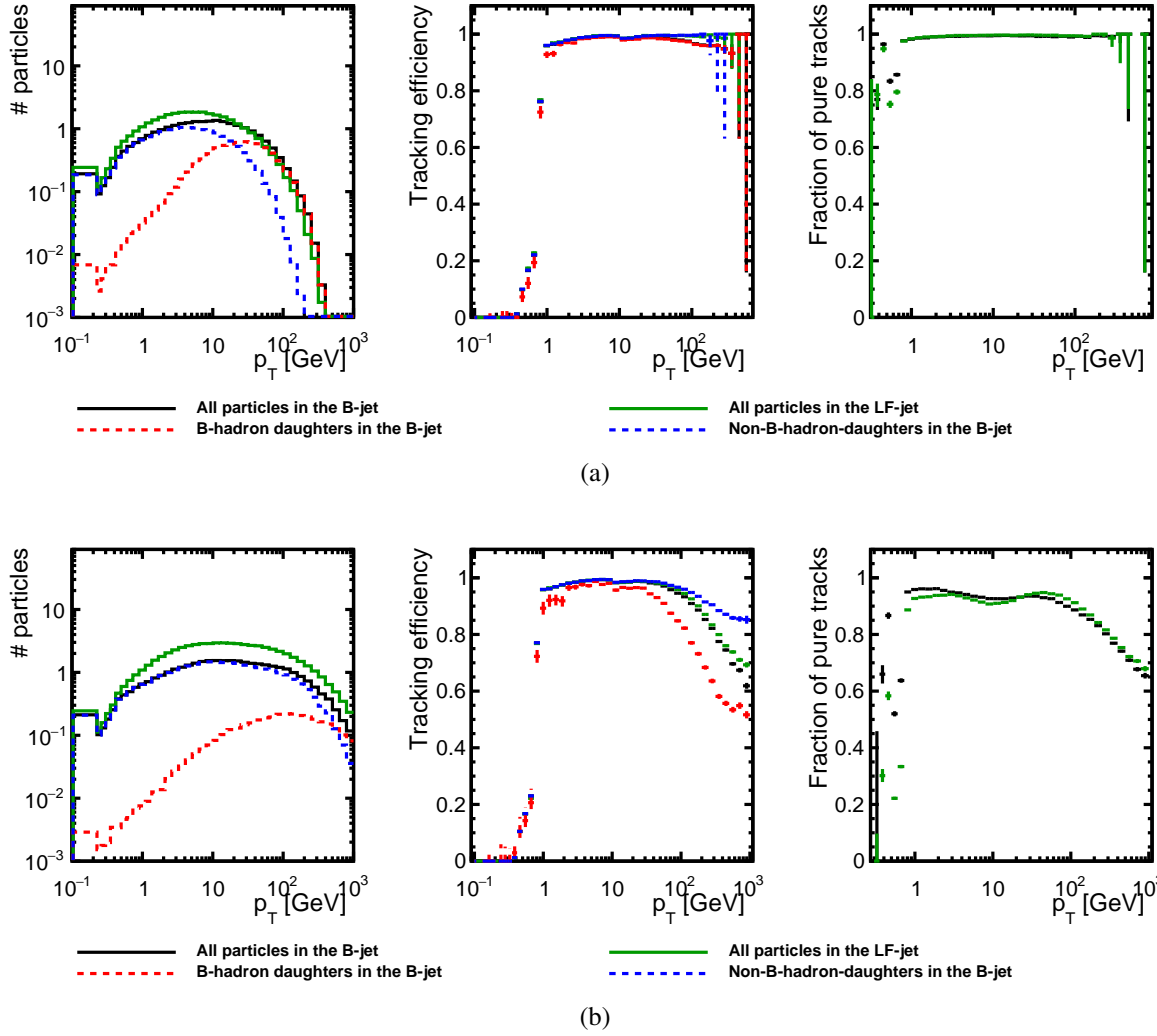


Fig. 6.21: Distribution of the reconstructable particle  $p_T$  (left), tracking efficiency versus reconstructable particle  $p_T$  (middle) and track purity versus reconstructed track  $p_T$  (right). Distributions are shown for particles with  $|\eta| < 0.175$  (the selection on the  $p_T$  is removed to produce this plot) in the di-jet  $b\bar{b}$  and LF samples, and separately for the particles coming/not coming from the B-hadron decay chain. **a** (top) shows the results for the  $p_T = 500$  GeV/c jet sample, and **b** (bottom) for the  $p_T = 5$  TeV/c jet sample.

cated clustering and tracking algorithms would be helpful to improve the performance. However, there exists an intrinsic limitation on tracking inside highly displaced and boosted objects, related to the large secondary vertex displacement.

### 6.4.3 Vertexing and pile-up mitigation by extra timing information

The challenges arising from the local space-time density of pile-up charged particle tracks and their production vertices generate the key limits on efficient primary vertex reconstruction at FCC-hh. A concept of ‘effective pile-up’ is applied to quantify these difficulties and define the corresponding requirements for detector layout. In general, to discriminate a hard scattering primary vertex (signal) from those produced by pile-up (background), the signal vertex needs first to be reconstructed and then correctly selected. The key for efficient reconstruction is a correct assignment of the relevant tracks to the primary vertex; the low  $p_T$  tracks are particularly challenging. As pointed out in Section 6.3.2, the main limiting



factor for tracks of a few GeV/c, being propagated to the interaction region (IR), is the multiple Coulomb scattering, namely in the beam-pipe and the first measurement layer; consequently, the track  $\delta z_0$  degrades with increasing  $\eta$  as illustrated in Fig. 6.4a in Section 6.3.2. The principal difficulties occur when more than one vertices are statistically consistent with the tracks being assigned, see Fig. 6.22. It is assumed that the signal primary vertex can be unambiguously found by a dedicated high level reconstruction algorithm, using e.g. high  $p_T$  tracks. The effective pile-up for additionally assigned tracks with given  $p_T$  is then defined as a number of pile-up vertices which are effectively contained within the track error ellipse propagated to the IR. Regarding the vertex selection, a reasonable discriminative power can be achieved by considering a different  $p_T$  spectrum of signal versus pile-up tracks. The pile-up is characteristic of a relatively soft  $p_T$  spectrum in contrast to the signal hard-scattering event; the choice of primary vertex based on the highest  $p_T$  sum is therefore generally efficient.

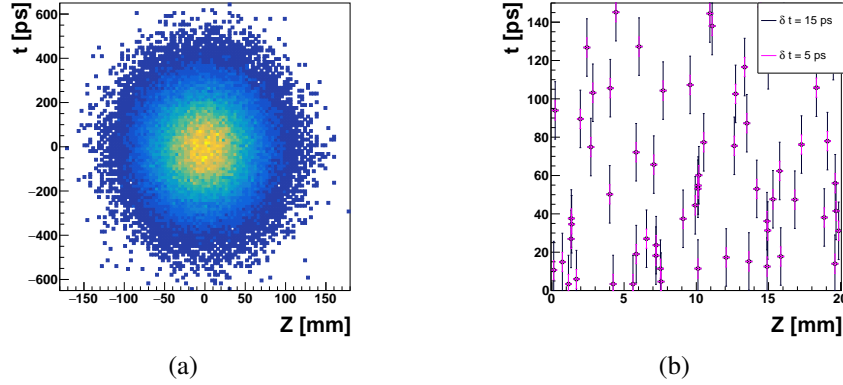


Fig. 6.22: Time and spatial distribution of pile-up vertices in FCC-hh luminous region (FCC SW simulation). Left (a): a 2D distribution of pile-up vertices in time and space. Right (b): a zoom-in with error bars, the  $\delta z_0 = 200 \mu\text{m}$  assumed corresponds to  $p_T = 1 \text{ GeV}/c$  at  $|\eta| = 2.0$ .

In a similar way to the approach applied in Section 6.4.1, the effective pile-up is quantified by a probabilistic method. The space-time track parameters resolution propagated to the IR define an error ellipse, with the surface area being estimated at 95 % CL – the term ‘error ellipse’ is defined statistically as an  $N$ -dimensional 95 % confidence interval; the dimension  $N$  stands for the number of discriminative variables used in the method. As detailed in Section 6.3, the spatial area of the error ellipse primarily depends on the beam-pipe and the first layer radial positions, their material budgets, the size of luminous region and the combination of propagation distance and error ellipse projection factor. As the beam-pipe radius,  $r_{\text{BP}} = 20 \text{ mm}$ , is constrained by the machine design, only the last three factors are analysed as a part of the vertex detector design. The size of luminous region in  $r$ - $\varphi$  is of the order of tens micrometers, while in  $z$  it extends over tens of millimetres; by assuming a Gaussian profile of colliding bunches with  $\sigma_z^{\text{bunch}} = 75 \text{ mm}$ , the region size in  $z$  can be approximately evaluated (neglecting effects of Piwinsky angles) as:  $\sigma_z^{\text{lum}} \approx \sigma_z^{\text{bunch}} / \sqrt{2} = 53 \text{ mm}$ . The strong discriminative power in track-to-vertex assignment is therefore expected only in  $z$ -direction, see Fig. 6.7; the  $\delta z_0$  will then function as a discriminant between the signal and pile-up vertices. The  $\delta z_0$  nevertheless degrades with increasing  $\eta$  as  $\cosh^{3/2} \eta$  (see Eq. (6.2)). In order to compensate for such a deterioration, an extra discriminative variable is indispensable – a track time-stamp information. As an explicit illustration, see the distribution of primary vertices within the FCC-hh luminous region in Fig. 6.22 (FCC SW simulation).

To interpret and relate the impact of effective pile-up to the realistic performance, the study is done for two layouts under different experimental conditions: the CMS phase 2 tracker (version: OT v3.6.5, IT v4.0.25 [16, 120]) in a scenario with  $\langle \mu \rangle = 140$  and the reference FCC-hh tilted tracker in a  $\langle \mu \rangle = 1000$  scenario. In both cases, the bunch profiles are assumed to be Gaussian with  $\sigma_z^{\text{bunch}} = 75 \text{ mm}$ , Piwinsky and time Piwinsky angles are estimated as:  $\Phi \approx 0.67$  and  $\Psi \approx 0.40$ , respectively [122]. These



quantities define the distribution of pile-up vertices in space,  $\partial\mu/\partial z$ , and time,  $\partial\mu/\partial t$ . As the final results demonstrate in Fig. 6.23, the effective pile-up extends from a few percent to several tens or even hundreds. Its meaning is purely statistical; for given  $p_T$  and  $\eta$  an effective pile-up of e.g. 0.1 illustrates, that the respective track being assigned to the primary signal vertex is compromised by one or more pile-up vertices in 10 % of all bunch crossing events. A number higher than one, e.g. 10, reflects that the given track is on average compromised by 10 pile-up vertices in every bunch crossing event. Therefore, the values significantly higher than 1 indicate that even by using high level reconstruction algorithms the primary vertexing may be very difficult.

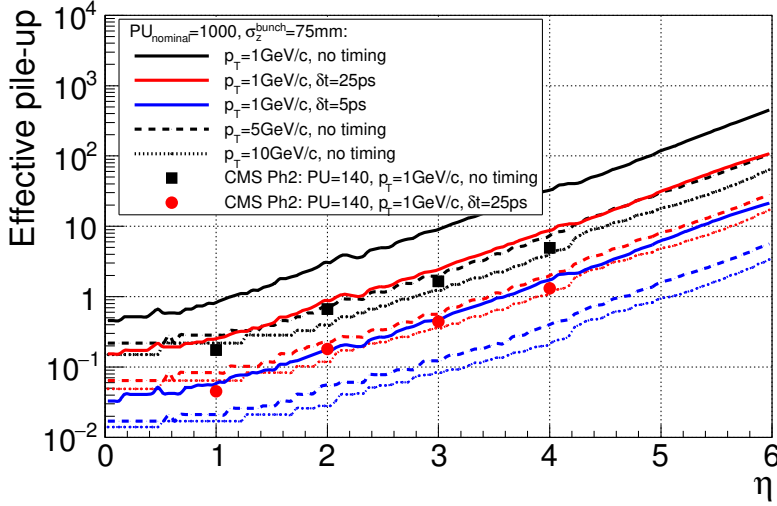


Fig. 6.23: Effective pile-up evaluated for the nominal pile-up of 1000 events, tracker in tilted geometry and the following track  $p_T$  values: 1 GeV/c (solid line), 5 GeV/c (dashed line) and 10 GeV/c (dotted line). Two options of primary vertexing are studied: 1D vertexing in  $z$  (black) and 2D vertexing in  $z$  and time. In 2D vertexing, the time resolution per track is set to:  $\delta t = 25$  ps (red) and  $\delta t = 5$  ps (blue). For reference, the effective pile-up for CMS phase 2 tracker (version: OT v3.6.5, IT v4.0.25) and nominal HL-LHC  $\langle\mu\rangle = 140$  is depicted:  $p_T = 1$  GeV/c with 1D vertexing (black rectangles),  $p_T = 1$  GeV/c with 2D vertexing and  $\delta t = 25$  ps (red circles).

In the scenario with CMS phase 2 tracker under HL-LHC conditions the effective pile-up is for low  $p_T = 1$  GeV/c tracks is on average 1.2 at the maximum CMS pseudorapidity  $|\eta| = 4.0$ . It is evaluated by considering 2D vertexing, combining the track  $\delta z_0$  and  $\delta t$  information; a timing resolution of  $\delta t = 25$  ps per track is assumed within this study. As demonstrated by full simulation in [16], vertexing and full reconstruction is feasible in such a scenario. In case of the tilted FCC-hh tracking system under nominal 1000 pile-up events, the 1D method (using  $\delta z_0$  information) leads to an effective pile-up of tens or even hundreds for low  $p_T$  tracks and high pseudorapidities  $|\eta| > 3.0$ . Hence, the 2D vertexing with additional time-stamp information seems essential. Yet, even by assuming a precise  $\delta t = 5 - 10$  ps per track the primary vertexing seems very challenging beyond  $|\eta| > 4.0$ .

In parallel to the layout modifications of the tracking system by adding the timing capabilities, there are other potential design options with a comparable pile-up mitigation effect. In the 2D vertexing the discriminative power in both  $t$  and  $z$  dimensions depends on the space-time difference distributions of the closest vertex pairs, as typically illustrated by  $\partial\mu/\partial z$  and  $\partial\mu/\partial t$  distributions. By modifying the bunch size in  $z$ , and thus extending the nominal 1000 pile-up events over a larger distance, the negative pile-up impact can be effectively decreased. Quantitatively, an increase in the bunch size by factor  $f$  leads to a decrease in the effective pile-up by  $f^2$ , i.e. in both  $t$  and  $z$  dimensions. The quadratic improvement represents the maximum achievable outcome under the assumption that the spatial and time distributions of the luminous region are strictly uncorrelated. The final result is shown in Fig. 6.24: an effective pile-

up versus  $\eta$  for  $p_T = 1$  GeV/c tracks. The individual curves demonstrate that increasing the bunch size in  $z$  from 75 mm to 150 mm leads to a positive effect similar to the relaxation of the requirement on track timing resolution from 5 ps to 25 ps per track.

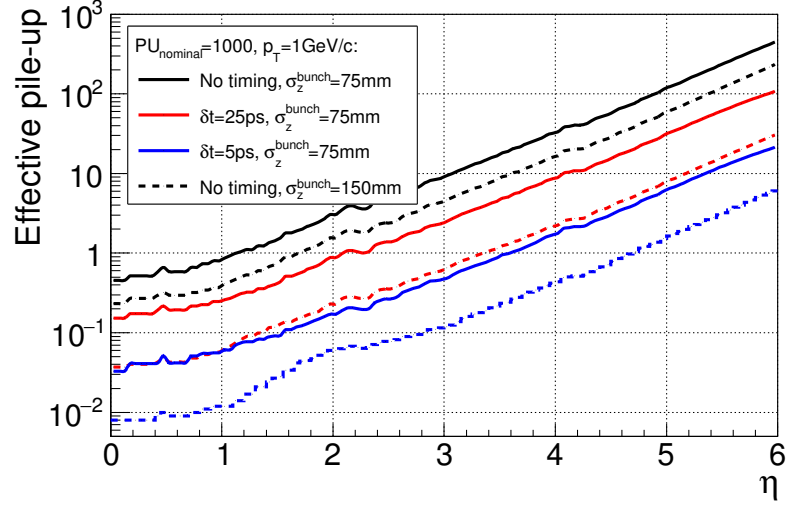


Fig. 6.24: Effective pile-up for tracker in tilted layout, nominal FCC-hh environment with  $\langle\mu\rangle = 1000$  and  $p_T = 1$  GeV/c. The effective pile-up is expressed as a function of time resolution per track:  $\delta t = 25$  ps (red),  $\delta t = 5$  ps (blue), 1D vertexing – no timing (black), and two bunch sizes in  $z$ : nominal  $\sigma_z^{\text{bunch}} = 75$  mm (solid lines) and increased  $\sigma_z^{\text{bunch}} = 150$  mm (dashed lines).

In order to cover the full FCC-hh detector acceptance  $|\eta| < 6.0$ , the combination of both approaches is suggested as beneficial for the future detector layout, i.e. the tracking system with timing measurement capabilities and the FCC-hh accelerator system providing a larger luminous region. In addition, the  $\delta t$  improves as  $1/\sqrt{N}$  with  $N$  being the number of timing measurements, hence there is no direct requirement implied by this study to have technology with an extreme 5 ps resolution; the tracking system with several layers/rings providing timing information can compensate for an extreme single measurement time resolution. The value of 5 ps is chosen in the study as an overall ‘hard’ limit arising from the limit on clock distribution. Finally, in comparison to the current ATLAS [96] or CMS [97] experiments, the FCC-hh tracking system is significantly larger in length. Therefore, an enlarged luminous region is not expected to have a significant negative impact on the overall detector hermeticity.

#### 6.4.4 Flavour tagging performance

Tagging heavy flavour jets will be extremely relevant in various aspects of the FCC-hh physics programme such as Higgs and top physics. In particular, tagging multi-TeV jets will be crucial for BSM searches such as  $Z' \rightarrow t\bar{t}$  or  $b\bar{b}$ , see Chapter 10, Section 10.3. Flavour tagging performance represents one of the main key drivers for the vertex detector design. In this section, two approaches to flavour tagging are studied: a traditional track-based tagger and a novel hit-based approach.

In the track-based approach the identification of heavy flavour jets is based on the impact parameters of the tracks in the jet, and on the identification of displaced secondary vertices compatible with the decay of a heavy flavour long-lived hadron. This approach requires the full event reconstruction: track reconstruction, calorimeter clustering, particle flow object reconstruction and identification, primary and secondary vertex reconstruction, etc. In this study the well understood CLIC\_SiD detector concept and software reconstruction chain (introduced in Section 6.2.2), which was used in the linear collider studies [98], is used to estimate the flavour tagging performance of the FCC-hh detector. The details on this study are documented in Ref. [107].

A new approach for tagging high energy b-jets without reconstructing tracks and secondary vertices has been suggested in Refs. [123, 124]. It exploits the fact that a long-lived particle decaying between two detector layers will cause the hit multiplicity to increase between those two layers. A hit-multiplicity-based tagger for FCC-hh is proposed and documented in Ref. [23]. It is based on a multivariate analysis (Boosted Decision Tree) using only the number of hits in different detector layers and in different concentric cones around the jet direction. The latter is implemented in order to exploit the differences in jet structure between heavy and light flavour jets.

The flavour tagging performance is evaluated in the barrel region using very central di-jet MC events of various energies and jet flavours. Three different jet flavours are considered:  $b\bar{b}$  events,  $c\bar{c}$  events and light-flavour (LF) events. The quark or gluon generated—before FSR—is required to have  $|\eta| < 0.05$  and to be within a narrow  $p_T$  range. For each flavour, five jet  $p_T$  samples are generated:  $p_T = 50$  GeV/c, 500 GeV/c, 1 TeV/c, 2 TeV/c and 5 TeV/c. The barrel region is where the reconstruction of highly boosted objects is most challenging in terms of secondary vertex reconstruction acceptance (as explained in Section 6.4.2). The forward jets will be most affected by the presence of pile-up interactions, which are not included in the simulation of the MC samples considered.

### Track-based flavour tagging:

Figure 6.25 shows the b-tagging efficiency evaluated against the LF background mis-identification efficiency for various  $p_T$  samples. For jets of  $p_T = 50$  GeV/c and  $p_T = 500$  GeV/c the background mis-identification is similar to that achieved in CLIC studies [125] for central jets of such  $p_T$ . For high  $p_T$  jets of 5 TeV/c the background mis-identification is worse than for  $p_T = 500$  GeV/c jets by more than one order of magnitude. This is because 30% of the B-hadron decays are out of acceptance in this sample, due to fact that the tracks of individual decay products do not traverse enough detector layers to be reconstructed. In addition, as seen in Section 6.4.2, even for the decays that are within acceptance, a significant fraction of the tracks used to reconstruct secondary vertices are not reconstructed or are badly reconstructed. This all has a direct impact on the flavour tagging performance. A similar decrease of b-tagging performance with increasing jet  $p_T$  is also seen at ATLAS [126].

C-tagging identification against LF jets is presented in Fig. 6.26. The performance is similar for the  $p_T = 50$  GeV/c and  $p_T = 500$  GeV/c samples, while for the 5 TeV/c sample the c-tagging performance is significantly worse. However, the difference is not as prominent—less than one order of magnitude in LF mis-identification efficiency—as for the case of b-tagging.

In b-tagging, the rejection of c-jets is an order of magnitude worse than the rejection of LF-jets for the  $p_T = 50$  GeV/c and  $p_T = 500$  GeV/c samples, as shown in Fig. 6.27. For the  $p_T = 5$  TeV/c sample the b- versus c-jet discrimination is very poor. The c-background mis-identification efficiency is 20% at 40% b-tagging efficiency. The c-tagging versus b-background performance, presented in Fig. 6.28, is very poor for all energies, the best performance being for the  $p_T = 500$  GeV/c sample.

To quantify how the vertex detector granularity affects the flavour tagging, variations of the vertex detector sensor pitch have been evaluated. Improving the detector granularity in the four innermost layers by e.g. using  $20 \times 20 \mu\text{m}^2$  pixel pitch instead of the reference  $25 \times 50 \mu\text{m}^2$ , results in an improvement of b- and c-tagging performance at low energies (jet  $p_T = 50$  GeV/c) by up to 40%. For higher energies the impact is less significant. However, decreasing the material budget in the four innermost layers by 50% leads to an improvement of the b-tagging performance by up to 70% (40%) for  $p_T = 50$  GeV/c ( $p_T = 5$  TeV/c) jets. The c-tagging performance improves by up to 40% for all jet energies.

### Hit-based b-tagging:

The hit multiplicity tagger results (described in detail in Ref. [23]) focus on multi-TeV jets since the performance of track-based taggers for such high  $p_T$  jets is limited and they can therefore benefit the most from this complementary approach. Figure 6.29 shows the b-tagging efficiency against LF mis-

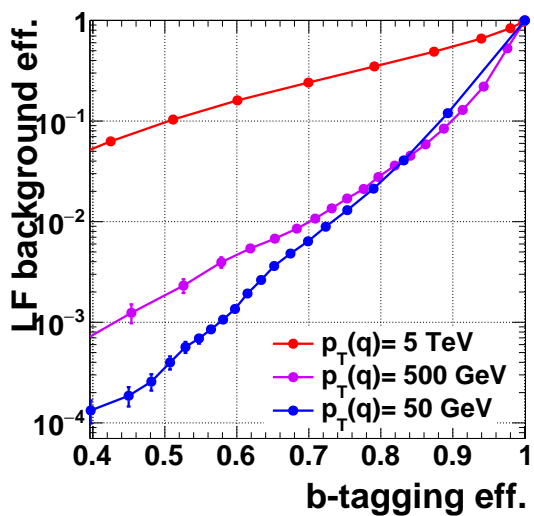


Fig. 6.25: b-tagging efficiency versus LF background mis-identification efficiency for various  $p_T$  samples.

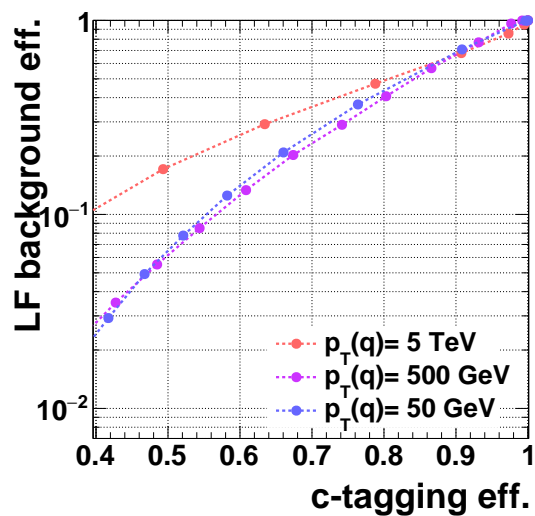


Fig. 6.26: c-tagging efficiency versus LF background mis-identification efficiency for various  $p_T$  samples.

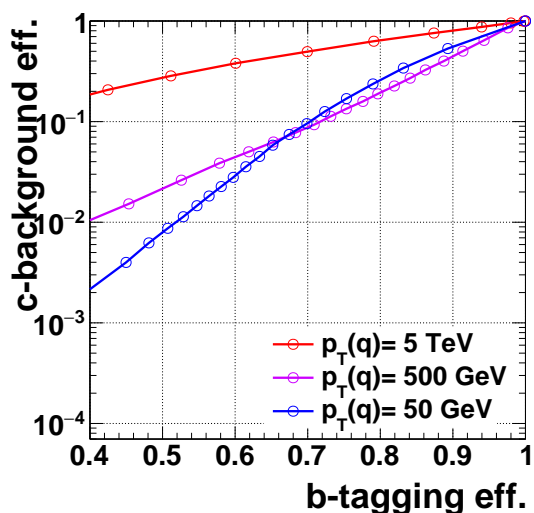


Fig. 6.27: b-tagging efficiency versus c-background mis-identification efficiency for various  $p_T$  samples.

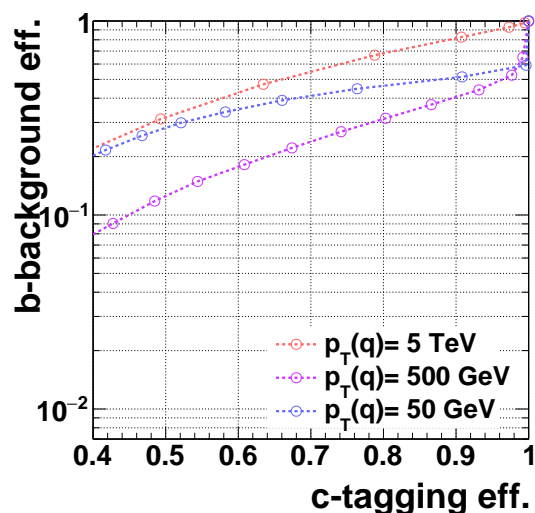


Fig. 6.28: c-tagging efficiency versus b-background mis-identification efficiency for various  $p_T$  samples.

identification probability for the  $p_T = 5 \text{ TeV}/c$  di-jet sample. It compares the performance obtained by using simulated hits, ‘SimHits’, and by using reconstructed hits, ‘RecoHits’. With SimHits the number of particles traversing the detector is counted, without taking into account the detector granularity. With RecoHits the effect of detector granularity is estimated ad hoc. The results show that by taking into account the detector granularity the background increases by about 20% to 50% depending on the b-tagging efficiency considered. Some variations of the detector granularity are studied, for instance improving the granularity of the four innermost layers (pixel layers) to  $20 \times 20 \mu\text{m}^2$ . This results in a recovery of about 20-30% of the background rejection, as extracted from the ‘RecoHit Granularity’ line in Fig. 6.29. If the sensors were able to distinguish between 0, 1, 2 or 3-or-more particles going through the same pixel (through analogue readout as in the ATLAS detector [127]), for example, it would be possible to recover

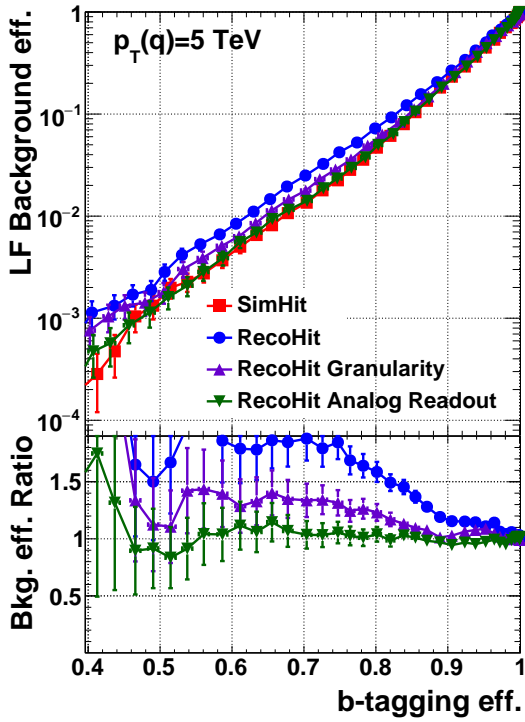


Fig. 6.29: b-tagging efficiency versus LF background mis-identification efficiency – comparison of the BDT classifier rejection power when considering simulated hits (red), and "reco" hits (as defined in the text) with default granularity (blue), improved granularity (violet) or default granularity with analogue readout (green).

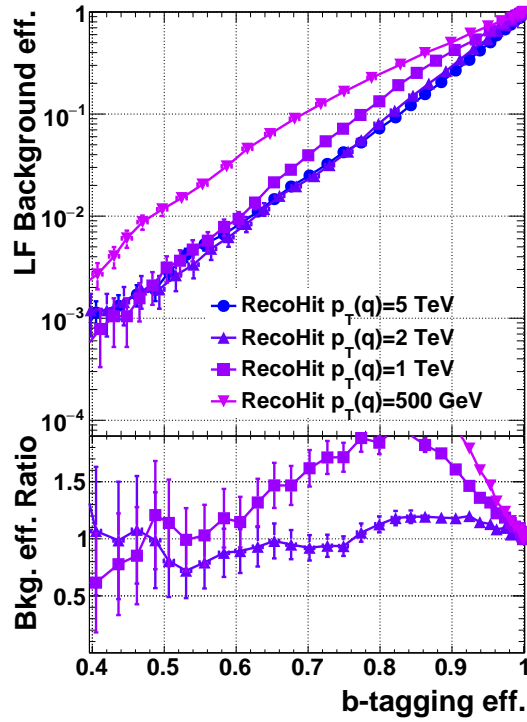


Fig. 6.30: b-tagging efficiency versus LF background mis-identification efficiency for various  $p_T$  samples, considering "reco" hits (as defined in the text).

the performance achieved by using simulated hits. Results are shown in the 'RecoHit Analog readout' line of Fig. 6.29.

The hit multiplicity tagger is optimised for each of the different jet  $p_T$  samples, and the performance results are presented in Fig. 6.30. In contrast to the track-based tagging approach, the performance improves with increasing jet energy. This is because, in this approach, having displaced decays taking place inside the tracker volume is advantageous for the flavour discrimination.

Pile-up interactions are not included in the simulation. However, it has been evaluated that for  $p_T = 5$  TeV/c jets the number of background hits from pile-up particles entering the cone defined around the jet direction is less than 1 in every detector layer. This is due to fact that multi-TeV jets are very narrow and the cone size defined is very small ( $\Delta R = 0.006$ ). Since the number of signal hits in the cone is on average between 5 and 10 in each layer, the pile-up hits are expected to have a limited impact on the flavour tagging performance for  $p_T = 5$  TeV/c jets. More details about this estimate can be found in Ref. [23].

The very displaced secondary vertices and very collimated tracks make the track-based approach a non-optimal method for flavour tagging multi-TeV jets. For such jets, an approach combining the information on the number of hits in each detector layer in a multivariate discriminator achieves a performance that is not only comparable but also superior to the discrimination power achieved by the track-based approach. Since the two methods are intrinsically complementary, the greatest benefit is expected to be

obtained by combining the two approaches. This combination—together with the effect of the expected pile-up interactions, noise, and the flavour tagging performance in the forward region—needs to be addressed in the future.

## 6.5 Triggering, occupancy and data rates

The increase in FCC-hh peak luminosity by a factor of 30 (6), compared to LHC (HL-LHC), results in significantly high radiation levels in the whole tracking system. These levels, which reach up to  $\approx 5.5 \times 10^{17} \text{ cm}^{-2}$  at  $r = 25 \text{ mm}$ , set the key limits on tracker technologies and requirements on detector radiation hardness (see the summary Table 6.1 with the tracker radiation exposure after  $30 \text{ ab}^{-1}$  in Section 6.1). The nominal FCC-hh pile-up of  $\mathcal{O}(1000)$  events, and associated charged particle density in the tracking layers/rings, defines additional hardware-related constraints, namely on detector granularity, required data read-out bandwidth, and overall triggering scheme. As pointed out in Section 6.4, the particle rate scales with the radius  $r$  as:  $\sim 1/r^2$ , hence the major impact will be expected on the detector technologies used in the innermost layers/rings, where the highest particle densities occur. Generally, sufficiently high detector granularity is important to reduce detector occupancy ( $\ll 1\%$ ), adequate data bandwidth is required to accommodate significantly larger data rates (cf. (HL)-LHC experiments [96, 97]), and the triggering scheme has to be well adapted to keep the trigger rate at an acceptable level without compromising FCC-hh physics potential. At the FCC-hh luminosity, the selection of interesting physics events becomes very challenging, particularly at the first trigger level (Level 1). It is not only because of the significant increase in particle rates, but also due to inefficiencies of the selection algorithms applied in the high pile-up environment, and due to hardware limits of the current read-out technologies, i.e. data bandwidth, trigger latency, on-chip logics versus tracker material budget, tracking performance, radiation hardness and overall cost.

Following the CMS phase 2 tracker upgrade [16] a concept of using track information within the Level 1 trigger (together with the calorimeters and/or muon triggers) seems strongly advantageous. It opens up the large potential to identify the primary vertices at the trigger level and hence may lessen the effects of pile-up interactions. The benefits of operating a track-trigger in a stand-alone mode is therefore being studied further and its impact on signal acceptances for a variety of physics processes under nominal pile-up conditions analysed (a detailed summary of this study is documented in Ref. [103]). Another conceptual solution is a direct read-out of tracker data into a High-Level Trigger (HLT) system. Although the latter approach can be considered as technically possible, the total data flows and necessary radiation hardness may be a significant challenge for the read-out technology – current, and even new technologies for optical data links being developed for the HL-LHC operation, are not sufficiently radiation hard [128]; moreover, due to high data rate densities, and consequently large number of optical links required for the innermost layers, the overall cost would be a significant additional factor. The read-out via electrical links is not a complementary solution either, as the material budget and necessary cooling infrastructure would have a significant impact on the overall tracking performance. To quantitatively evaluate the key challenges and specify requirements for the future R&D, the tracker occupancy and expected data rates have been evaluated for the reference tracker layouts (see details in the dedicated note [112]).

### 6.5.1 Track trigger

The general design of the track trigger involves reading out several tracking layers at the trigger level. To fully reconstruct a track, a minimum of three hits is needed—the basic design chosen for this study is therefore a ‘triplet’ of pixel layers inside the barrel region. Three measurement points provide enough redundancy to efficiently reduce the combinatorial background, they also combine the spatial resolution of individual layers to reconstruct the track position and direction with high precision. Note that other approaches exist, e.g. with a minimum of two doublets or even more complex solutions. However, to demonstrate the key idea, the approach with a triplet in the barrel region is chosen.



The optimal layout for this track trigger is to place the three layers at an average radius of 600 mm from the beam line, with a separation of 30 mm between layers. Such a large radius is required due to the constraint on the read-out rates, see Table 6.5 in Section 6.5.2, which is set to the approximate maximum rate achieved by the currently available technologies,  $\approx 1 \text{ Gb/s/cm}^2$ . Due to the large propagation distance between the track-trigger layers and the beam line, the track parameter uncertainties are relatively large when being extrapolated to the interaction region. However, the large radius has the benefit that tracks with  $p_T < 0.36 \text{ GeV}/c$  do not reach the triplet in the detector 4 T  $B$ -field. Such low  $p_T$  tracks are not of interest from a trigger perspective, and the  $p_T$  cut reduces the combinatorial complexity of reconstructing tracks. The triplet-spacing of 30 mm is chosen as a trade off between track parameter resolution and fake rate: a larger separation between triplet layers gives more fake tracks but better track parameter resolution, and vice versa. The triplet replaces the barrel layer at  $r = 600 \text{ mm}$  in the ‘flat tracker layout’, see Fig. 6.1 in Section 6.3; the layout of other layers/rings remains unchanged.

In order to reconstruct tracks, three hits are identified using geometrical constraints. They are chosen to provide good track reconstruction efficiency and a low fake rate. Essentially, tracks are required to form a straight line in the  $r$ - $z$  plane (within a given tolerance), made by one hit in each of the triplet layers and pointing towards the interaction region. In addition, an important constraint in  $r$ - $\phi$  plane is considered to reduce combinatorics: the hits are required to have a small  $\Delta\phi$  separation, referring to a  $\Delta\phi$  value of sufficiently low  $p_T$  tracks, e.g.  $2 \text{ GeV}/c$ , traversing the triplet in a 4 T magnetic field. Other constraints which are applied are summarised in Ref. [103]. Note that, although the effect of multiple scattering is taken into account throughout the triplet trigger optimisation, other material effects, such as energy loss, are currently ignored. The fake-rate rejection could be further improved by using time-stamp information at the trigger level, nevertheless, this advanced feature is not considered in the current study.

As explained in Section 6.4.3, the longitudinal impact parameter resolution  $\delta z_0$ , and the fractional  $p_T$  resolution of reconstructed tracks, are key to identifying the primary vertex. Both variables are shown in Fig. 6.31. For tracks with  $2 < p_T < 5 \text{ GeV}/c$  the  $\delta z_0$  ranges from 1–5 mm, depending on the track  $\eta$ . Given that the majority of vertices in the 1000 pile-up scenario will be separated by less than 1 mm from each other (the average vertex density is  $\langle \partial\mu/\partial z \rangle \approx 8$  per mm, see Table 1.1 in Chapter 1), no low- $p_T$  triplet tracks can be uniquely matched to a vertex. For higher  $p_T$  values the  $\delta z_0$  improves; for tracks with  $p_T > 10 \text{ GeV}/c$  the resolution ranges between 0.1–1.0 mm.

The reconstruction efficiency and fake rate are shown as a function of  $p_T$  in Fig. 6.32. The reconstruction efficiency is defined as the fraction of true particle tracks that reached the outermost triplet layer, and the fake rate is defined as the fraction of reconstructed tracks that do not match with their original true particle. The reconstruction efficiency is close to 100% for tracks of  $p_T \geq 2 \text{ GeV}/c$ , which is consistent with the  $\Delta\phi$  requirement applied to triplet hits. The excellent performance is a result of the simple pattern recognition, and of the fact that only three hits need be aligned. The fake rate displays a seemingly unusual feature: the fake rate increases, decreases and then increases again with increasing  $p_T$ . This can be understood as the convolution of the following factors:

- For true tracks, the  $p_T$  distribution falls off very sharply, whereas for fake tracks the distribution of  $p_T$  is more flat (fakes are made from random combinations of hits). Therefore a naive expectation of the fake rate increasing with higher track  $p_T$ .
- However, a combination of more stringent requirements (cuts) can be made on tracks with higher  $p_T$  to suppress the fake tracks. Hence the change in fake rate trend.

As previously mentioned, in the scenario with 1000 pile-up events the  $\delta z_0$  is not sufficient for tracks to be unambiguously assigned to a unique vertex, namely at higher  $\eta$  and in low  $p_T$  range. This results in a real challenge to identify the primary vertex (PV) and therefore to match tracks to it. However, at the trigger level the direct identification of PV is not necessary. Instead, an identification of a region in which the PV is contained is sufficient and can result in a dramatic reduction of pile-up effects. To identify this region, a sliding window algorithm is employed—it searches for the region along the



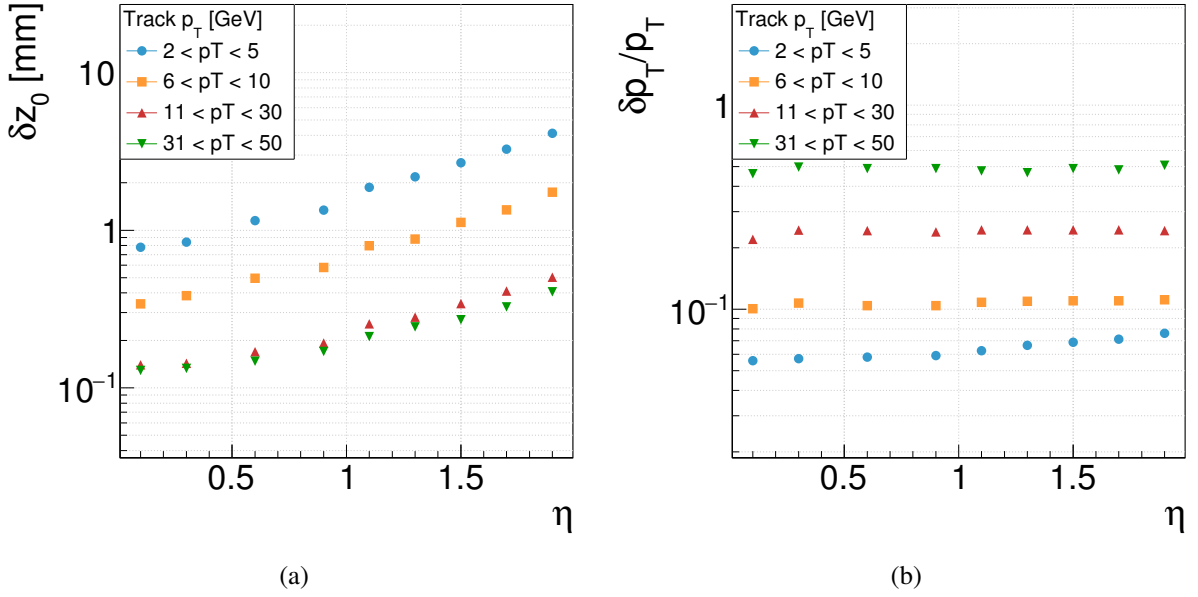


Fig. 6.31: Longitudinal impact parameter ( $z_0$ ) resolution (left) and fractional  $p_T$  resolution (right) for tracks reconstructed with only the triplet of tracking layers (at 600 mm from the beam-line and with a separation of 30 mm between each layer).

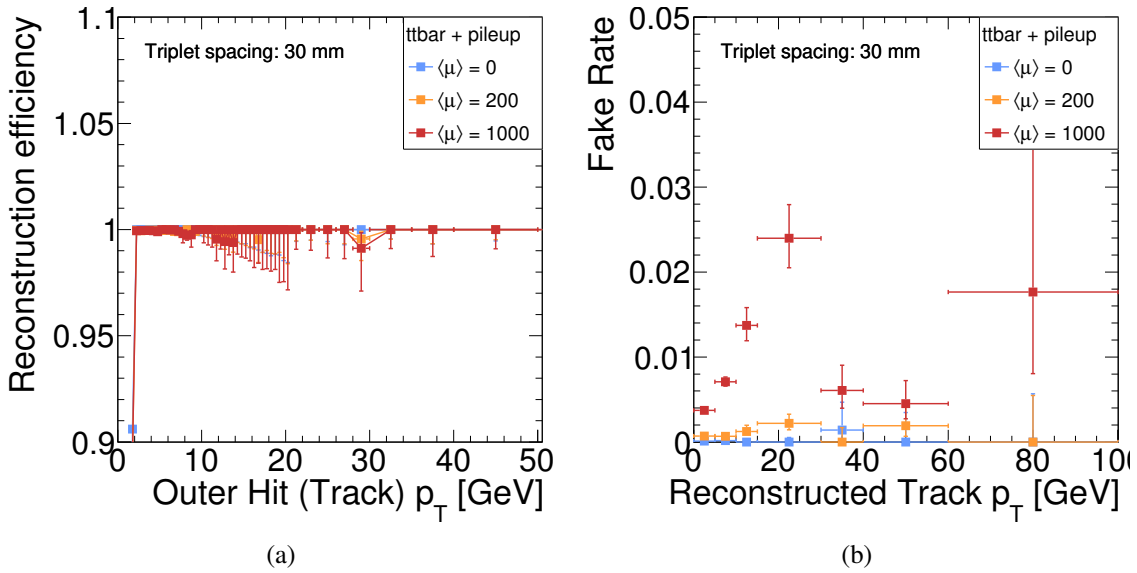


Fig. 6.32: The reconstruction efficiency (left) as a function of the true-track  $p_T$  (the  $p_T$  of the initial charged particle), and the fake rate (right) as a function of the reconstructed track  $p_T$ . Definitions of fake rate and efficiency are given in the text. The results are shown for  $t\bar{t}$  events with different pile-up conditions of: 0 (blue), 200 (orange) and 1000 (red) interactions per bunch crossing.

beam-line which has the largest  $\sum p_T^{\text{track}}$  associated to it. A window of length 1 mm is chosen (roughly matching the  $\delta z_0$  of low  $p_T$  tracks) and progressively moved along the beam-line in steps of 0.1 mm. The one with the largest  $\sum p_T^{\text{track}}$  is then defined as the *primary bin* (PB). In full simulation with a single  $t\bar{t}$  event overlaid with an average of 1000 pile-up vertices, this algorithm yields a PB which contains the true PV for 83% of events. The PB mis-identification is largely due to cases where the hard-scattering event is in the periphery of the vertex distribution, and  $\sum p_T^{\text{track}}$  may then be larger for a collection of many closely-spaced pile-up vertices near the core of the vertex distribution.

The effectiveness of the triplet as a trigger is described by the acceptance for a given rate, which is shown for HH and  $t\bar{t}$  events in Fig. 6.33. Distributions are presented for the highest- $p_T$  track in the event (Track 1) and the 3<sup>rd</sup>-highest  $p_T$  track in the event (Track 3). The leading track (a single high  $p_T$  track) is shown as this is the simplest object to trigger on, the 3<sup>rd</sup>-leading track is shown to give an example of a more complex strategy. The graphics compare the trigger rate if all tracks in the event are considered, with the trigger rate if only the tracks matched to the PB are considered. Fig. 6.33a shows that for events with the leading track having  $p_T \gtrsim 100$  GeV/c, the trigger rate from all tracks and those matched to the PB are equal. This indicates that in such cases the highest  $p_T$  track dominates the PB selection.

As a benchmark, a 100 kHz trigger rate is assumed, which is equivalent to the entire ATLAS Level-1 trigger readout rate during Run-2 operation [129]. Figures 6.33a and 6.33b show that the acceptance is less than 30%. However, the situation is improved when considering multi-track triggers. For the third-leading track (Figs. 6.33c and 6.33d), the signal acceptance for 100 kHz rate is approximately 50% when only tracks from the PB are used. In case the PB can not be identified and all tracks from all vertices have to be considered, then the acceptances become significantly worse, ranging from 10–15% for the third-leading track. This highlights the importance of being able to identify the primary bin. Finally, a more complex approach than tracks alone can be used for triggering. The tracks can be clustered into track-jets and used as multi-track-jet trigger. Similar acceptances of around 50% for a 100 kHz rate can be achieved for 3, 4 or 5 jets. Furthermore, one of the most powerful potential uses of tracking information is to identify tracks from the PV and match them to jets (or other objects) in the calorimeter, thereby reducing the impact of pileup on calorimeter or muon based triggers.

## 6.5.2 Expected occupancy and data rates

The evaluation of expected channel occupancy, data rates and data rate densities represent one of the important aspects of tracker design studies. To assess these characteristics quantitatively for the reference tracker layout, a detailed study based on PYTHIA8 and GEANT4 Monte-Carlo simulation tools has been carried out. As the definitive detector technology is not yet known (particularly for the innermost detector region), a simplistic—geometric—digitisation is used within this software framework (FCC SW). Therefore only the general, technology non-specific charge collection effects are taken into account. The digitisation procedure is followed by hit clusterisation (reconstruction) which is based on connected-component labelling; for details see FCC SW Section 6.2.3. The full SW chain is still limited in its functionality, and therefore only the layouts with non-inclined detector modules (flat geometry) can be studied. To understand the impact of earlier mentioned reference layout granularities, both configurations: ‘flat’ and ‘tilted’ are simulated in the flat geometry layout only, however.

The channel occupancy is calculated as a ratio of the number of read-out channels, activated by primary/secondary particles, to the corresponding total number of read-out channels on the detector module. As the hard-scattering proton-proton process occurs significantly less frequently than the soft QCD background, the level of channel occupancy is mostly driven by nominal pile-up of  $\mathcal{O}(1000)$  events. In general terms, the occupancy depends on cluster properties: cluster occupancy (i.e. density of clusters per unit area), cluster shape and size (i.e. the number of channels contributing to one cluster). The distribution of charged primary particles coming from the interaction region, see Fig. 6.34a), plays a major role in the spatial distribution of individual clusters. However, it is observed that the secondary particles produced within the tracker material make a substantial contribution too. The probability of

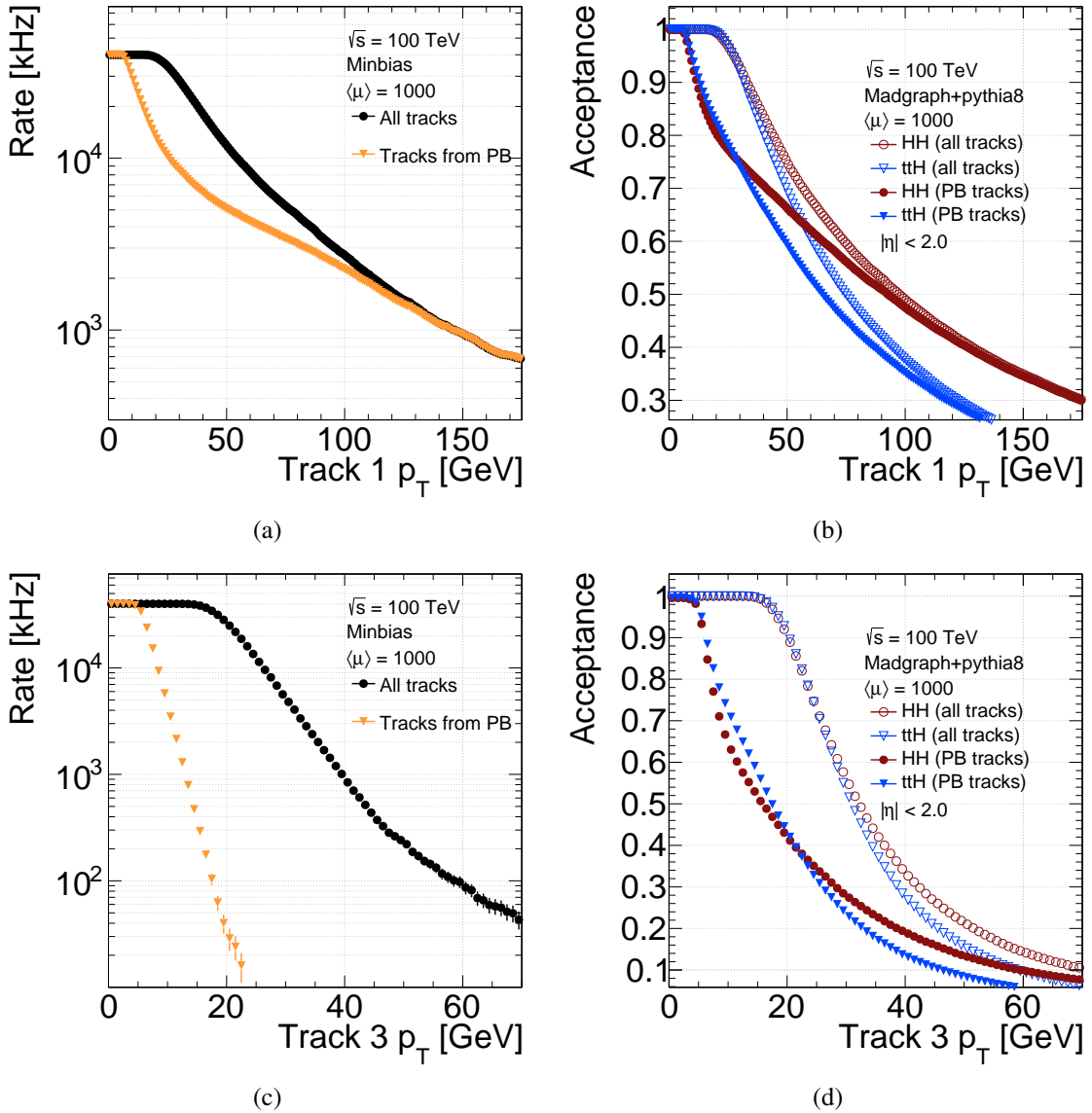
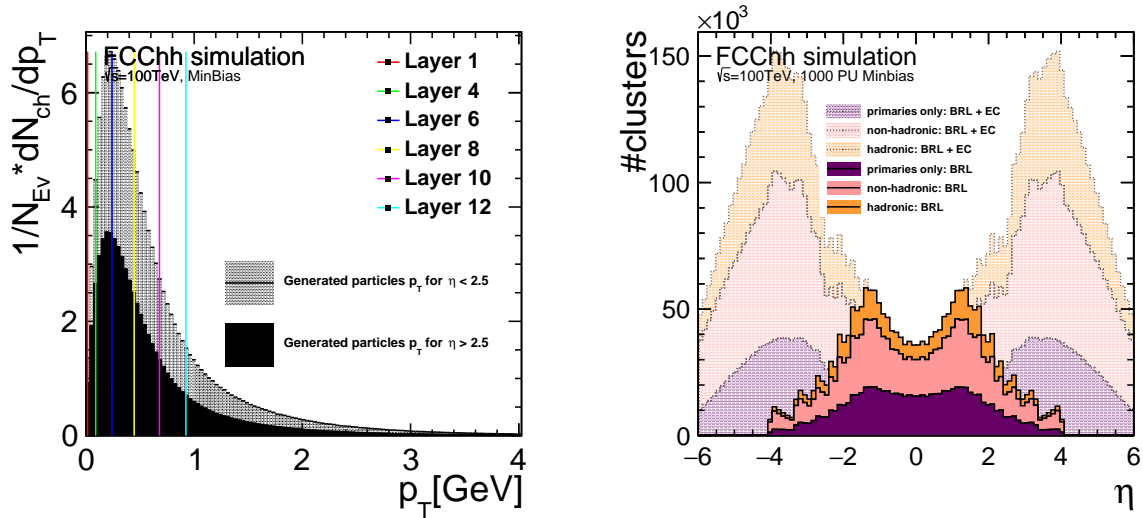


Fig. 6.33: Track trigger rates (left) and signal acceptances for HH and  $t\bar{t}H$  events (right). On the left plots, the black markers indicate the trigger rate if all tracks from an event are considered, whereas the orange markers indicate the rate if only tracks from the PB are used. Correspondingly on the right plots, the open markers indicate the acceptance if all tracks are used, and the filled markers indicate the acceptance only if tracks from the PB are used.

producing the secondaries increases with the amount of material traversed; this behaviour can be seen in Fig. 6.34b—the number of clusters are depicted separately for the barrel (BRL) and barrel + end-cap (BRL + EC) regions. Three different contributions are plotted versus pseudorapidity in this figure: the number of clusters from primary particles only (purple), from primary + secondary particles arising from non-hadronic interactions (pink), and from both non-hadronic and hadronic interactions (orange).

The cluster size depends on several factors: read-out granularity, active sensor thickness  $t$ , and particle trajectory incident angles with respect to the module surface (azimuthal  $\varphi$  and polar  $\vartheta$ ). For any cylindrical layer the cluster size in global  $z$ -direction rises approximately as  $\propto t / \tan \vartheta$  with increasing  $\vartheta$ , while in  $r$ - $\varphi$  direction the relation is more complex due to a dominant  $\vec{B}$ -field component along  $z$ . In general, the absolute value of  $r$ - $\varphi$  cluster size increases with larger radius and higher  $\eta$ ; however,



(a) The generated  $p_T$ -spectra (PYTHIA8—Monash tune) of charged particle tracks: two distributions are shown, assuming  $|\eta| < 2.5$  (dashed) and  $|\eta| > 2.5$  (solid). The coloured lines indicate the limit on  $p_T$  of particle tracks, necessary to reach the corresponding barrel layer, i.e. before they start curling back in the presence of the constant 4 T magnetic field.

(b) The distribution of number of clusters versus pseudorapidity, separately depicted for various contributions; from primary particles and primary plus secondary particles created in two types of interactions: hadronic and non-hadronic. Two sets of curves are shown: for barrel region (BRL) by solid curves, and superimposed barrel and end-cap regions (BRL + EC) by dashed curves.

Fig. 6.34: The PYTHIA8 generated charged particles  $p_T$ -spectrum (left) with  $\langle p_T \rangle = 0.64$  GeV/c, assuming  $\eta \in \langle 0; 6 \rangle$ . The number and composition of particle clusters (right).

the trend is less  $\eta$ -dependent for radially more distant layers. The explanation lies in a combination of two contributions: a relatively wide  $p_T$ -spectrum of primary particles, and the effect of traversing more material (with increased production of secondary particles at higher  $\eta$ ). By comparing the contribution to  $r$ - $\varphi$  clusters from ‘straight line’ tracks (i.e. high  $p_T$  particles) versus the contribution from ‘curling’ primary/secondary tracks (i.e. low  $p_T$  particles), the latter are observed to have a significantly lower impact in the innermost layers than the layers at higher radii (cf. 1<sup>st</sup> layer versus e.g. 12<sup>th</sup> layer in Fig. 6.34a). In addition, the  $p_T$ -spectrum is softer at higher  $\eta$ , and the low momentum looping particles tend to get accumulated in the forward region rather than the barrel region. Therefore, the 1D cluster size in  $r$ - $\varphi$  is dominated by the contribution from curling particles in middle/outer barrel layers and/or the edges of innermost barrel layers; the cluster size distribution of outermost layers also appears flatter than for the innermost layers. For illustration see Fig. 6.35a, where the cluster size is plotted in a global  $r$ - $\varphi$  coordinate versus  $\eta$  for a few BRL layers, namely the innermost layer (blue), 7<sup>th</sup> layer (green) and the outermost layer (red). By assuming an active silicon thickness of  $t = 100$   $\mu\text{m}$  its numerical value reaches  $\approx 4$ . In Fig. 6.35b the average 2D cluster-size is depicted against  $z$ -position of barrel modules. For the innermost layers the total cluster size increases with higher polar angle due to stronger material effects at higher  $z$ . In the middle/outer layers the  $z$ -granularity is significantly lower than in the pixel region (see the summary of tilted layout granularity in Table 6.2 in Section 6.3.2), and thus the 2D cluster size is dominated by  $r$ - $\varphi$  contribution in this region rather than material effects.

The average channel occupancy in the barrel region is displayed versus  $z$ -position of each module ring in Fig. 6.36a. The shape observed can be understood as a combination of two effects: an increasing cluster size (see Fig. 6.35b) and decreasing cluster occupancy with higher  $z$ . As pointed out in Section 6.4, the  $dN_{\text{ch}}/d\eta \approx \text{const.}$  up to  $|\eta| \approx 4.0 - 5.0$ , and hence the cluster occupancy in the barrel

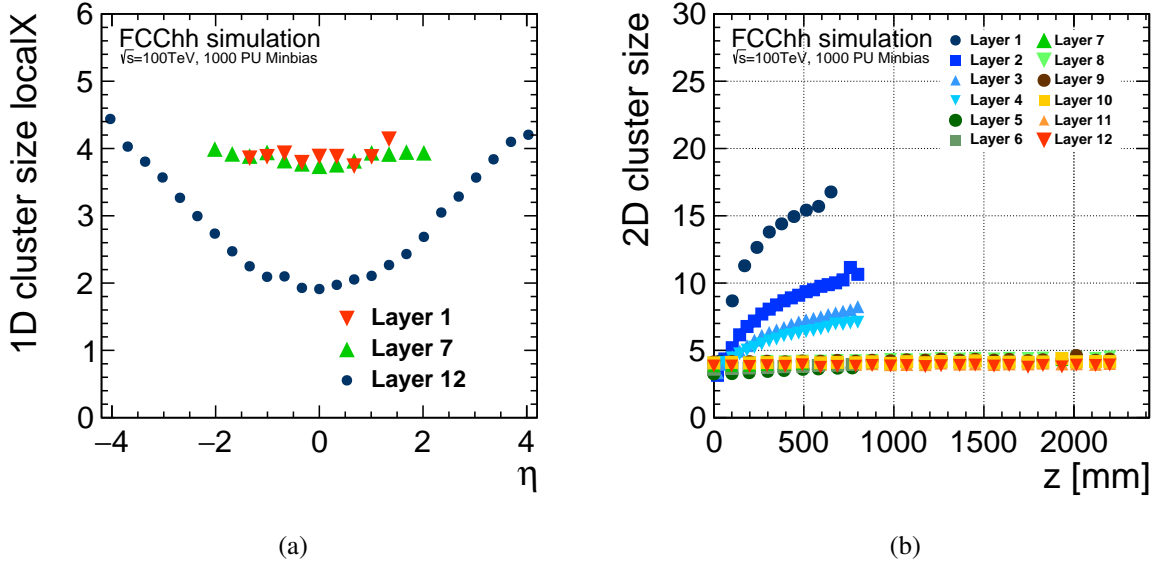


Fig. 6.35: 1D cluster-size (left) – in global  $r$ - $\varphi$  direction, i.e. local  $x$ -direction, depicted for three types of barrel detectors: pixel (1<sup>st</sup> layer - blue), macro-pixel (7<sup>th</sup> layer - green) and triplet (12<sup>th</sup> layer - red). 2D cluster-size versus  $\eta$  for each barrel layer (right). All curves are simulated for granularity of tilted tracker, arranged in a non-inclined layout.

region can be regarded as approximately constant over  $\eta$ . Since each module in the reference layout layer, positioned at radius  $r$ , covers a constant space in  $z$ , the corresponding  $\eta$ -coverage follows a decreasing trend:  $d\eta_{\text{ch}}/dz = \text{const.}/r \times 1/\cosh \eta$ . In the end-cap discs, the cluster size reaches its maximum value in the outer triplet/macro-pixel rings and decreases with lower radius due to smaller incident angle  $\vartheta$ . In contrast, the cluster density has its maximum value in the pixel region (close to the beam-pipe) and increases for the same ring with the increasing id of end-cap disc, mainly due to more material being traversed and higher production of secondary particles. The channel occupancy therefore rises mildly with increasing  $z$ -position, see Fig. 6.36b. In the case of the granularity optimised for a tilted layout, all occupancy numbers stay below 1% in all regions, except for the innermost barrel layer—its occupancy reaches up to 1.6%. In addition in the case of the granularity suggested for a flat layout, the occupancy reaches, up to 3% in the innermost triplet layer. The effect of insufficient granularity in the flat layout has been already observed for the scenario with nominal FCC-hh pile-up in Section 6.4.1, and the tilted layout has been optimised accordingly. Moreover, the channel occupancy in the BRL-EC transition region of a true tilted layout will be even lower due to the substantially lower material budget of inclined detector modules. The summary of calculated occupancy is given in Table 6.5. An energy threshold is required to activate a readout-channel, as for the case of the realistic read-out—within the study a threshold of 3.6 keV<sup>5</sup> is applied to demonstrate this effect; it reduces the occupancy by  $\approx 6 - 13\%$ .

The overall data read-out rates and corresponding densities are estimated using a simplified addressing scheme. As the binary read-out is assumed for the reference tracker layout, to evaluate the data rate quantities, 1 b per activated read-out channel times the number of bits to address this channel is assumed. In general, the read-out addressing depends on the module arrangement and their numbering scheme, i.e. the number of read-out channels, number of modules, number of layers/rings etc. To simplify the calculations the number of bits addressing the hit channel is evaluated as:  $n\text{Bits} = \log_2(n\text{Rows}) + \log_2(n\text{Columns})$ . The final data rates are then given as an integral over all modules in the region evaluated. By assuming a continuous read-out at 40 MHz bunch crossing rate, an upper

<sup>5</sup>3.6 keV corresponds to the production of 1000 electron-hole pairs in the silicon.

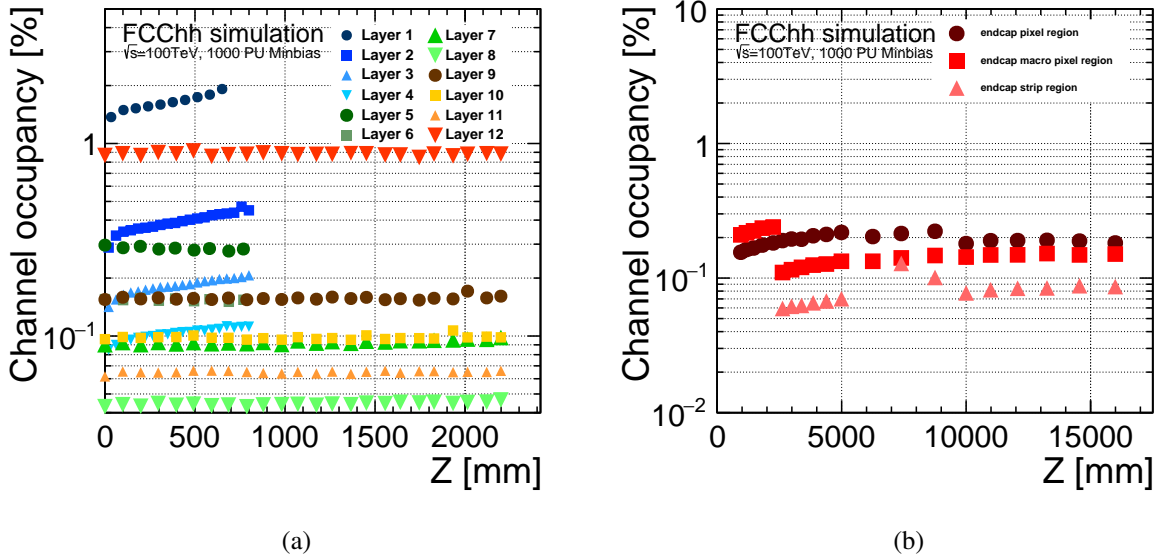


Fig. 6.36: The channel occupancy for each ring of the barrel layers along  $z$ -direction (left) and of the end-cap regions (right): pixel (circles), macro-pixels (squares) and triplets (triangles). All curves are simulated for granularity of tilted tracker, arranged in non-inclined layout.

limit for the FCC-hh scenario can be assessed. In Table 6.4 the data rates are evaluated for three different scenarios: flat layout, flat layout with electronics threshold of 3.6 keV applied and flat layout with tilted granularity. The total rate reaches up to 2740 TB/s for the flat layout scenario; by applying the electronics threshold cut the data rates are reduced by  $\approx 10\%$ . In the case of tilted granularity, the channel occupancy of the triplet region has been decreased (see Table 6.5), while the number of respective read-out channels increases (see Table 6.2 in Section 6.3.2); the total tracker data rate of 2830 TB/s is therefore slightly larger, see Table 6.5.

Table 6.4: Summary of total data rates as estimated for the three tracker regions: pixels (inner tracker), macro-pixels (middle tracker) and triplets/macro-pixels (outer tracker), as well as for different scenarios: Flat layout with/without energy threshold (3.6 keV to activate a pixel/triplet) and assuming tilted granularities (i.e. smaller triplet size). Each number is shown as a sum of the corresponding numbers of the central and forward tracker.

Data rates [TB/s]	Flat layout (no threshold)	with threshold	with tilted granularities
Pixels (inner)	1054.3 + 379.6	944.5 + 337.9	1056.3 + 380.2
Macro-pixels (middle)	559.2 + 423.1	515.4 + 391.4	560.3 + 423.8
Triplets/Macro-pixels (outer)	127.8 + 192.8	118.8 + 179.1	165.4 + 242.4
	<b>2737 TB/s</b>	<b>2487 TB/s</b>	<b>2828 TB/s</b>

In terms of tracker read-out, with its  $\approx 30$  M activated tracker channels and  $\approx 9$  M clusters per bunch crossing, the FCC-hh represents a very challenging environment. For the flat layout, the channel occupancy exceeds 1% in the first layer and in the triplet region; the latter has been avoided in the tilted design by reducing the triplet size. Moreover, the immense densities of data rates per unit area are of a particular concern in the innermost vertex detector layer and end-cap rings. The corresponding data rate density reaches a maximum at  $944 \text{ Gb/s/cm}^2$ . Therefore studies of the future technology-



Table 6.5: Summary of maximum fluence [ $\text{cm}^{-2}$ ], module occupancy, data size per bunch crossing [Mb/s], data rates [Tb/s] and data rate densities [Gb/s/ $\text{cm}^2$ ], as estimated for the nominal FCC-hh pile-up of 1000 events and tracker in flat layout.

<b>Barrel layer:</b>	<b>1</b>	<b>2</b>	<b>3</b>	<b>4</b>	<b>5</b>	<b>6</b>
Average radius [mm]	25	60	100	150	260	380
Maximum fluence [ $\text{cm}^{-2}$ ]	328.1	79.7	35.1	16.9	6.8	3.3
Module occupancy [%]	1.63	0.39	0.18	0.10	0.28	0.15
Data size per bunch crossing [Mb]	56.60	37.66	28.51	23.46	10.95	8.72
Data rate [Tb/s]	2263.1	1506.4	1140.3	938.5	438.0	348.6
Data rate density @ 40 MHz [Gb/s/ $\text{cm}^2$ ]	944.0	229.6	107.0	60.2	14.8	8.0
Data rate density @ 1 MHz [Gb/s/ $\text{cm}^2$ ]	23.6	5.7	2.7	1.5	0.4	0.2
	<b>7</b>	<b>8</b>	<b>9</b>	<b>10</b>	<b>11</b>	<b>12</b>
	530	742	937	1132	1327	1540
	1.9	0.83	0.46	0.26	0.16	0.13
	0.09	0.04	3.0	1.9	1.3	0.9
	835.5	537.8	331.3	249.0	192.8	109.5
	20.8875	13.445	8.2825	6.225	4.82	2.7375
	5.1	2.4	1.2	0.7	0.5	0.2
	0.1	...				

related optimisation as well as the layout studies of the tilted tracker need to be performed. The tilted layout with its inclined modules increases the cluster occupancy per module on one hand, but reduces the cluster size, material budget and overall number of detector modules in the BRL-EC transition area on the other. For details see the ATLAS upgrade studies in Refs. [130] (Chapter 3.4.) or [119] (Chapter 2.2.4.) or the CMS upgrade studies in Ref. [16] (Chapter 6.2.2.). Further reduction of cluster size, namely in  $r$ - $\varphi$  direction, can be achieved by optimising the rotation of detector modules in  $\varphi$ -direction. The corresponding Lorentz force will affect the deviation of charge carriers inside the active silicon, and so may help in the overall decrease of the cluster size. An additional lowering effect can be achieved by decreasing the material budget of silicon detectors—by using the technology of thinned down active sensors, such as monolithic silicon sensors, which nevertheless have to be sufficiently radiation hard to fulfil the challenging FCC-hh radiation requirements. There is an ongoing effort in this area by the CERN RD50 collaboration, which will be of an immense importance for the future projects like FCC-hh. The R&D effort in radiation hard read-out chips is addressed for the ATLAS and CMS experiments, and their upgrades for HL-LHC, in the same manner by the CERN RD53 collaboration.

## 6.A Technical specification of tracker layout

The following Tables: 6.6, 6.7, 6.8 (Barrel) and 6.9, 6.10 (End-cap) provide the detailed documentation of tracker layout parameters [115, 116], introduced in Section 6.3. Several types of detector modules are assumed – of various shapes, sizes, granularity; their summary is given in Tables<sup>6</sup>: 6.11 and 6.12.

<sup>6</sup>The parametric description of wedge-shaped pixel regions is only approximate and a more realistic design is expected.



Table 6.6: Barrel layers: Central Tracker in flat (v3.03) and tilted (v4.01) layouts. Subscripts: *min*, *max* and *avg* correspond to minimum, maximum and average position, respectively. A layer consists of several ladders (rods), a ladder of a set of modules, arranged in rings in the tilted layout.

<b>Inner tracker - flat layout:</b>							
<b>BRL Layer:</b>	1	2	3	4	5	6	<b>Total &lt;-z; +z&gt;</b>
$R_{avg}$ [mm]	25.0	60.0	100.0	150.0	270.0	400.0	
$R_{min}$ [mm]	23.3	58.3	98.3	148.3	261.1	391.1	
$R_{max}$ [mm]	27.5	63.0	102.5	152.3	280.1	409.7	
$Z_{min}$ [mm]	-685.0	-820.0	-820.0	-820.0	-820.0	-820.0	
$Z_{max}$ [mm]	+685.0	+820.0	+820.0	+820.0	+820.0	+820.0	
$N_{rods}$	14	16	26	38	34	50	
$N_{modules/rod}$	20	40	40	40	17	17	
$N_{modules}$	280	640	1040	1520	578	850	4908
<b>Outer tracker - flat layout:</b>							
<b>BRL Layer:</b>	7	8	9	10	11	12	<b>Total &lt;-z; +z&gt;</b>
$R_{avg}$ [mm]	530.0	742.4	937.2	1132.0	1326.7	1539.6	
$R_{min}$ [mm]	521.1	733.5	928.0	1122.7	1317.4	1530.3	
$R_{max}$ [mm]	541.4	753.1	947.9	1142.5	1337.0	1549.7	
$Z_{min}$ [mm]	-2250.0	-2250.0	-2250.0	-2250.0	-2250.0	-2250.0	
$Z_{max}$ [mm]	+2250.0	+2250.0	+2250.0	+2250.0	+2250.0	+2250.0	
$N_{rods}$	34	46	58	70	82	96	
$N_{modules/rod}$	47	47	47	47	47	47	
$N_{modules}$	1598	2162	2726	3290	3854	4512	18142
<b>Inner tracker - tilted layout:</b>							
<b>BRL Layer:</b>	1	2	3	4	5	6	<b>Total &lt;-z; +z&gt;</b>
$R_{avg}$ [mm]	25.7	60.0	100.0	150.0	260.0	380.0	
$R_{min}$ [mm]	22.9	46.7	86.7	136.8	207.8	328.7	
$R_{max}$ [mm]	29.7	74.4	114.0	163.7	313.2	432.1	
$Z_{min}$ [mm]	-800.0	-800.0	-800.0	-800.0	-728.7	-800.0	
$Z_{max}$ [mm]	+800.0	+800.0	+800.0	+800.0	+728.7	+800.0	
$N_{rods}$	14	18	28	40	38	54	
$N_{modules/rod}$	29	25	29	35	11	13	
$N_{modules}$	406	450	812	1400	418	702	4188
<b>Outer tracker - tilted layout:</b>							
<b>BRL Layer:</b>	7	8	9	10	11	12	<b>Total &lt;-z; +z&gt;</b>
$R_{avg}$ [mm]	530.0	742.4	937.3	1132.0	1326.8	1539.9	
$R_{min}$ [mm]	475.0	688.4	884.5	1080.8	1277.0	1530.6	
$R_{max}$ [mm]	587.1	798.0	991.3	1184.4	1377.4	1550.0	
$Z_{min}$ [mm]	-2300.0	-2290.7	-2300.0	-2300.0	-2300.0	-2299.6	
$Z_{max}$ [mm]	+2300.0	+2290.7	+2300.0	+2300.0	+2300.0	+2299.6	
$N_{rods}$	36	50	62	74	86	96	
$N_{modules/rod}$	25	29	33	35	37	47	
$N_{modules}$	900	1450	2046	2590	3182	4512	14680

Table 6.7: Barrel layers: detailed parameters of Inner Tracker in tilted (v4.01) layout.  $R_{\text{inner}}$  and  $R_{\text{outer}}$  describe the central radial position of inner and outer ladder ring module, respectively; inner/outer correspond to an even/odd or odd/even ladder ring module within the given barrel layer.

<b>Layer 1 Ring:</b>	1	2	3	4	5	6	7	8	9	10	11	12	13
$\vartheta_{\text{tilt}}$ [deg]	0.0	0.0	0.0	0.0	0.0	10.0	10.0	10.0	10.0	10.0	10.0	10.0	10.0
$R_{\text{inner}}$ [mm]	24.0	24.0	24.0	24.0	24.0	25.4	25.4	25.4	25.4	25.4	25.4	25.4	25.4
$R_{\text{outer}}$ [mm]	26.0	26.0	26.0	26.0	26.0	26.4	26.4	26.4	26.4	26.4	26.4	26.4	26.4
$ Z_{\text{avg}} $ [mm]	0.0	24.4	48.7	73.1	97.4	126.3	163.2	206.8	258.3	319.2	388.5	468.0	559.4
	14	15											
	10.0	10.0											
	25.4	25.4											
	26.4	26.4											
	664.2	787.4											
<b>Layer 2 Ring:</b>	1	2	3	4	5	6	7	8	9	10	11	12	13
$\vartheta_{\text{tilt}}$ [deg]	0.0	0.0	0.0	0.0	0.0	0.0	70.5	70.5	79.2	79.2	83.9	83.9	83.9
$R_{\text{inner}}$ [mm]	59.0	59.0	59.0	59.0	59.0	59.0	59.5	59.5	59.5	59.5	59.5	59.5	59.5
$R_{\text{outer}}$ [mm]	61.0	61.0	61.0	61.0	61.0	61.0	60.5	60.5	60.5	60.5	60.5	60.5	60.5
$ Z_{\text{avg}} $ [mm]	0.0	24.4	48.7	73.1	97.4	121.8	149.1	197.1	267.7	375.2	482.1	619.9	796.9
<b>Layer 3 Ring:</b>	1	2	3	4	5	6	7	8	9	10	11	12	13
$\vartheta_{\text{tilt}}$ [deg]	0.0	0.0	0.0	0.0	0.0	0.0	58.3	58.3	67.5	67.5	74.8	74.8	80.0
$R_{\text{inner}}$ [mm]	99.0	99.0	99.0	99.0	99.0	99.0	99.5	99.5	99.5	99.5	99.5	99.5	99.5
$R_{\text{outer}}$ [mm]	101.0	101.0	101.0	101.0	101.0	101.0	100.5	100.5	100.5	100.5	100.5	100.5	100.5
$ Z_{\text{avg}} $ [mm]	0.0	24.4	48.7	73.1	97.4	121.8	146.8	179.5	219.2	268.9	331.1	410.6	512.0
	14	15											
	80.0	84.0											
	99.5	99.5											
	100.5	100.5											
	642.6	796.9											
<b>Layer 4 Ring:</b>	1	2	3	4	5	6	7	8	9	10	11	12	13
$\vartheta_{\text{tilt}}$ [deg]	0.0	0.0	0.0	0.0	0.0	0.0	46.8	46.8	56.0	56.0	63.6	63.6	69.9
$R_{\text{inner}}$ [mm]	149.0	149.0	149.0	149.0	149.0	149.0	149.5	149.5	149.5	149.5	149.5	149.5	149.5
$R_{\text{outer}}$ [mm]	151.0	151.0	151.0	151.0	151.0	151.0	150.5	150.5	150.5	150.5	150.5	150.5	150.5
$ Z_{\text{avg}} $ [mm]	0.0	24.4	48.7	73.1	97.4	121.8	146.4	174.5	205.6	240.8	281.0	327.4	380.9
	14	15	16	17	18								
	69.9	74.9	74.9	78.6	78.6								
	149.5	149.5	149.5	149.5	149.5								
	150.5	150.5	150.5	150.5	150.5								
	443.7	517.1	603.6	693.4	796.1								
<b>Layer 5 Ring:</b>	1	2	3	4	5	6							
$\vartheta_{\text{tilt}}$ [deg]	0.0	0.0	43.9	43.9	65.5	65.5							
$R_{\text{inner}}$ [mm]	257.5	252.5	255.0	255.0	255.0	255.0							
$R_{\text{outer}}$ [mm]	267.5	262.5	265.0	265.0	265.0	265.0							
$ Z_{\text{avg}} $ [mm]	0.0	99.9	195.6	319.1	475.0	700.1							
<b>Layer 6 Ring:</b>	1	2	3	4	5	6	7						
$\vartheta_{\text{tilt}}$ [deg]	0.0	0.0	33.5	33.5	53.1	53.1	63.1						
$R_{\text{inner}}$ [mm]	377.5	372.5	375.0	375.0	375.0	375.0	375.0						
$R_{\text{outer}}$ [mm]	387.5	382.5	385.0	385.0	385.0	385.0	385.0						
$ Z_{\text{avg}} $ [mm]	0.0	100.7	198.6	310.7	436.1	591.8	770.2						

Table 6.8: Barrel layers: detailed parameters of Outer Tracker in tilted (v4.01) layout. The rings positioning of the 12<sup>th</sup> layer is not displayed as it follows the same layout as of the 12<sup>th</sup> barrel layer in flat configuration, cf. Table 6.6.  $R_{\text{inner}}$  and  $R_{\text{outer}}$  describe the central radial position of inner and outer ladder ring module, respectively.

<b>Layer 7 Ring:</b>	1	2	3	4	5	6	7	8	9	10	11
$\vartheta_{\text{tilt}}$ [deg]	0.0	0.0	0.0	34.1	34.1	49.2	49.2	60.8	60.8	69.5	69.5
$R_{\text{inner}}$ [mm]	522.5	527.5	522.5	525.0	525.0	525.0	525.0	525.0	525.0	525.0	525.0
$R_{\text{outer}}$ [mm]	532.5	537.5	532.5	535.0	535.0	535.0	535.0	535.0	535.0	535.0	535.0
$ Z_{\text{avg}} $ [mm]	0.0	101.8	202.0	303.7	419.4	545.2	691.4	857.6	1055.9	1287.6	1567.3
	12	13									
	75.6	75.6									
	525.0	525.0									
	535.0	535.0									
	1890.0	2276.2									
<b>Layer 8 Ring:</b>	1	2	3	4	5	6	7	8	9	10	11
$\vartheta_{\text{tilt}}$ [deg]	0.0	0.0	0.0	0.0	31.9	31.9	43.6	43.6	53.4	53.4	61.4
$R_{\text{inner}}$ [mm]	739.9	734.9	739.9	734.9	737.4	737.4	737.4	737.4	737.4	737.4	737.4
$R_{\text{outer}}$ [mm]	749.9	744.9	749.9	744.9	747.4	747.4	747.4	747.4	747.4	747.4	747.4
$ Z_{\text{avg}} $ [mm]	0.0	101.2	203.3	302.6	406.3	521.5	643.2	777.7	923.6	1087.5	1268.6
	12	13	14	15							
	61.4	67.9	67.9	71.3							
	737.4	737.4	737.4	737.4							
	747.4	747.4	747.4	747.4							
	1474.3	1704.4	1967.5	2265.1							
<b>Layer 9 Ring:</b>	1	2	3	4	5	6	7	8	9	10	11
$\vartheta_{\text{tilt}}$ [deg]	0.0	0.0	0.0	0.0	0.0	31.0	31.0	40.7	40.7	49.1	49.1
$R_{\text{inner}}$ [mm]	929.8	934.8	929.8	934.8	929.8	932.3	932.3	932.3	932.3	932.3	932.3
$R_{\text{outer}}$ [mm]	939.8	944.8	939.8	944.8	939.8	942.3	942.3	942.3	942.3	942.3	942.3
$ Z_{\text{avg}} $ [mm]	0.0	101.8	202.0	304.5	402.8	507.6	622.9	743.2	873.0	1010.9	1161.3
	12	13	14	15	16	17					
	56.4	56.4	62.4	62.4	66.7	66.7					
	932.3	932.3	932.3	932.3	932.3	932.3					
	942.3	942.3	942.3	942.3	942.3	942.3					
	1323.1	1501.1	1694.6	1909.0	2083.3	2272.0					
<b>Layer 10 Ring:</b>	1	2	3	4	5	6	7	8	9	10	11
$\vartheta_{\text{tilt}}$ [deg]	0.0	0.0	0.0	0.0	0.0	0.0	30.4	30.4	38.6	38.6	46.0
$R_{\text{inner}}$ [mm]	1129.5	1124.5	1129.5	1124.5	1129.5	1124.5	1127.0	1127.0	1127.0	1127.0	1127.0
$R_{\text{outer}}$ [mm]	1139.5	1134.5	1139.5	1134.5	1139.5	1134.5	1137.0	1137.0	1137.0	1137.0	1137.0
$ Z_{\text{avg}} $ [mm]	0.0	101.2	203.3	302.6	405.4	502.7	608.2	723.5	842.9	969.8	1102.7
	12	13	14	15	16	17	18				
	46.0	52.5	52.5	58.2	58.2	62.5	62.5				
	1127.0	1127.0	1127.0	1127.0	1127.0	1127.0	1127.0				
	1137.0	1137.0	1137.0	1137.0	1137.0	1137.0	1137.0				
	1245.3	1396.1	1558.9	1732.6	1921.0	2089.2	2269.8				
<b>Layer 11 Ring:</b>	1	2	3	4	5	6	7	8	9	10	11
$\vartheta_{\text{tilt}}$ [deg]	0.0	0.0	0.0	0.0	0.0	0.0	0.0	30.0	30.0	37.1	37.1
$R_{\text{inner}}$ [mm]	1319.3	1324.3	1319.3	1324.3	1319.3	1324.3	1319.3	1321.8	1321.8	1321.8	1321.8
$R_{\text{outer}}$ [mm]	1329.3	1334.3	1329.3	1334.3	1329.3	1334.3	1329.3	1331.8	1331.8	1331.8	1331.8
$ Z_{\text{avg}} $ [mm]	0.0	101.8	202.0	304.5	402.8	505.9	602.3	708.2	823.5	942.3	1067.2
	12	13	14	15	16	17	18	19			
	43.6	43.6	49.5	49.5	54.7	54.7	58.8	58.8			
	1321.8	1321.8	1321.8	1321.8	1321.8	1321.8	1321.8	1321.8			
	1331.8	1331.8	1331.8	1331.8	1331.8	1331.8	1331.8	1331.8			
	1197.1	1334.5	1478.5	1631.7	1793.2	1965.9	2112.5	2267.7			

Table 6.9: End-cap discs/rings of Central Tracker: with the same layout for flat and tilted geometry.

<b>Inner tracker:</b>								
<b>EC Disc:</b>	1	2	3	4	5	<b>Total &lt;-z; +z&gt;</b>		
$R_{\min}$ [mm]	25.0	25.0	25.0	25.0	25.0			
$R_{\max}$ [mm]	404.0	404.0	404.0	404.0	404.0			
$ Z_{\text{avg}} $ [mm]	950.0	1178.5	1462.0	1813.7	2250.0			
$ Z_{\min} $ [mm]	941.1	1169.6	1453.1	1804.8	2241.1			
$ Z_{\max} $ [mm]	958.9	1187.5	1471.0	1822.6	2258.9			
$N_{\text{rings}}$	4	4	4	4	4			
$N_{\text{modules/disc}}$	108	108	108	108	108	1080		
<b>EC Ring:</b>	1	2	3	4				
$R_{\min}$ [mm]	25.0	101.3	198.9	302.6				
$R_{\max}$ [mm]	104.7	204.6	303.4	404.0				
$N_{\text{modules/ring}}$	12	20	32	44				
<b>Outer tracker:</b>								
<b>EC Disc:</b>	1	2	3	4	5	6	<b>Total &lt;-z; +z&gt;</b>	
$R_{\min}$ [mm]	25.0	25.0	25.0	25.0	25.0	25.0		
$R_{\max}$ [mm]	1549.3	1549.3	1549.3	1549.3	1549.3	1549.3		
$ Z_{\text{avg}} $ [mm]	2625.0	2986.1	3396.8	3864.0	4395.4	5000.0		
$ Z_{\min} $ [mm]	2615.7	2976.8	3387.5	3854.7	4386.1	4990.7		
$ Z_{\max} $ [mm]	2634.3	2995.3	3406.1	3873.3	4404.7	5009.3		
$N_{\text{rings}}$	16	16	16	16	16	16		
$N_{\text{modules/disc}}$	948	948	948	948	948	948	11376	
<b>EC Ring:</b>	1	2	3	4	5	6	7	8
$R_{\min}$ [mm]	25.0	99.9	198.8	301.4	398.7	503.5	599.0	701.6
$R_{\max}$ [mm]	104.2	203.1	303.1	402.6	504.4	603.6	703.2	805.6
$N_{\text{modules/ring}}$	12	20	32	44	52	64	44	52
	9	10	11	12	13	14	15	16
	798.9	901.7	997.9	1100.9	1195.9	1299.1	1393.0	1496.4
	902.7	1005.4	1101.5	1204.4	1299.3	1402.4	1496.3	1549.3
	56	64	68	76	84	88	96	96

Table 6.10: End-cap discs/rings of Forward Tracker: with the same layout for flat and tilted geometry.

<b>Forward tracker:</b>										
<b>EC Disc:</b>	1	2	3							<b>Total (-z; +z)</b>
$R_{\min}$ [mm]	25.0	25.0	25.0							
$R_{\max}$ [mm]	918.6	1120.2	1321.5							
$ Z_{\text{avg}} $ [mm]	6250.0	7395.1	8750.0							
$ Z_{\min} $ [mm]	6241.1	7385.8	8740.7							
$ Z_{\max} $ [mm]	6258.9	7404.4	8759.3							
$N_{\text{rings}}$	9	11	13							
$N_{\text{modules/disc}}$	388	524	684							3192
<b>EC Ring:</b>	1	2	3	4	5	6	7	8	9	
$R_{\min}$ [mm]	25.0	115.8	215.5	315.6	414.4	514.4	612.5	714.8	814.7	
$R_{\max}$ [mm]	120.6	219.3	317.5	417.0	515.4	615.2	716.7	818.8	918.6	
$N_{\text{modules/ring}}$	12	20	32	44	56	64	48	52	60	
	10	11	12	13						
	1020.9	1120.2	1222.6	1321.5						
	64	72	76	84						
<b>EC Disc:</b>	4	5	6	7	8	9	<b>Total (-z; +z)</b>			
$R_{\min}$ [mm]	49.5	49.5	49.5	49.5	49.5	49.5				
$R_{\max}$ [mm]	1550.2	1550.2	1550.2	1550.2	1550.2	1550.2				
$ Z_{\text{avg}} $ [mm]	10000.0	10985.6	12068.4	13257.8	14564.5	16000.0				
$ Z_{\min} $ [mm]	9990.7	10976.3	12059.1	13248.5	14555.2	15990.7				
$ Z_{\max} $ [mm]	10009.3	10994.9	12077.6	13267.1	14573.8	16009.3				
$N_{\text{rings}}$	15	15	15	15	15	15				
$N_{\text{modules/disc}}$	868	868	868	868	868	868	10416			
<b>EC Ring:</b>	1	2	3	4	5	6	7	8	9	
$R_{\min}$ [mm]	49.5	139.1	238.2	337.8	436.7	536.3	637.3	739.4	840.0	
$R_{\max}$ [mm]	144.6	241.2	339.6	438.8	537.5	640.8	741.4	843.4	943.8	
$N_{\text{modules/ring}}$	12	24	36	48	56	40	48	52	60	
	10	11	12	13	14	15				
	1045.9	1146.1	1248.3	1348.2	1450.5	1550.2				
	68	72	80	84	92	96				

Table 6.11: Detector module parameters in barrel region – tilted layout.

<b>Detector modules - tilted:</b>					
<b>BRL Layers:</b>	$r-\varphi \times z$ dims [mm <sup>2</sup> ]	$X/X_0$ [%]	$N_{\text{ch}} \times r-\varphi$ pitch [ $\mu\text{m}$ ]	$N_{\text{ch}} \times z$ pitch [ $\mu\text{m}$ ]	$N_{\text{modules}}$
1	$12.8 \times 25.6$	1.0	$1 \times 512 \times 25$	$1 \times 512 \times 50$	406
2-4	$25.6 \times 25.6$	1.0	$2 \times 512 \times 25$	$1 \times 512 \times 50$	2662
5-6	$51.2 \times 102.4$	2.0	$3 \times 512 \times 33.3$	$1 \times 256 \times 400$	1120
7-8	$102.4 \times 102.4$	2.0	$6 \times 512 \times 33.3$	$1 \times 256 \times 400$	2350
9-11	$102.4 \times 102.4$	2.5	$6 \times 512 \times 33.3$	$1 \times 58 \times 1750$	7818
12	$102.4 \times 102.4$	2.5	$6 \times 512 \times 33.3$	$1 \times 2 \times 50000$	4512

Table 6.12: Detector module parameters in end-cap region – tilted layout. Different ring(s) layouts are used in the inner, outer and forward regions due to conical beam-pipe; two types of sensors are used: rectangular and wedge-shaped (denoted as  $w$ ); the  $d_{\text{wafer}}$  is an assumed wafer diameter, necessary to form the wedge-shaped sensors at average  $z$ -position of respective end-cap and of required radial length, for further details refer [99, 100].

<b>Detector modules - tilted:</b>					
<b>EC Rings – Inner:</b>	$d_{\text{wafer}}$ [mm]	$X/X_0$ [%]	$N_{\text{ch}} \times r\text{-}\varphi$ pitch [ $\mu\text{m}$ ]	$N_{\text{ch}} \times z$ pitch [ $\mu\text{m}$ ]	$N_{\text{modules}}$
1 ( $w$ )	86.2	1.5	$(2 \times 512 + 328) \times 25$	$(2 \times 512 + 498) \times 50$	120
2 ( $w$ )	113.0	1.5	$(2 \times 512 + 418) \times 33.3$	$(1 \times 512 + 495) \times 100$	200
3 ( $w$ )	114.8	2.0	$(2 \times 512 + 456) \times 33.3$	$258 \times 400$	320
4 ( $w$ )	112.6	2.0	$(2 \times 512 + 490) \times 33.3$	$251 \times 400$	440
<b>EC Rings – Outer:</b>	$d_{\text{wafer}}$ [mm]	$X/X_0$ [%]	$N_{\text{ch}} \times r\text{-}\varphi$ pitch [ $\mu\text{m}$ ]	$N_{\text{ch}} \times z$ pitch [ $\mu\text{m}$ ]	$N_{\text{modules}}$
1 ( $w$ )	86.2	1.5	$(2 \times 512 + 373) \times 25$	$(2 \times 512 + 483) \times 50$	144
2 ( $w$ )	113.0	1.5	$(2 \times 512 + 427) \times 33.3$	$(1 \times 512 + 493) \times 100$	240
3 ( $w$ )	114.8	2.0	$(2 \times 512 + 474) \times 33.3$	$257 \times 400$	384
4 ( $w$ )	112.6	2.0	$(2 \times 512 + 502) \times 33.3$	$250 \times 400$	528
5 ( $w$ )	118.6	2.0	$(3 \times 512 + 118) \times 33.3$	$262 \times 400$	624
6 ( $w$ )	113.7	2.0	$(3 \times 512 + 111) \times 33.3$	$249 \times 400$	768
	$r\text{-}\varphi \times z$ dims [ $\text{mm}^2$ ]	$X/X_0$ [%]	$N_{\text{ch}} \times r\text{-}\varphi$ pitch [ $\mu\text{m}$ ]	$N_{\text{ch}} \times z$ pitch [ $\mu\text{m}$ ]	$N_{\text{modules}}$
7-9	$102.4 \times 102.4$	2.0	$6 \times 512 \times 33.3$	$1 \times 256 \times 400$	1824
10-15	$102.4 \times 102.4$	2.5	$6 \times 512 \times 33.3$	$1 \times 58 \times 1750$	5712
16	$102.4 \times 52.0$	2.5	$6 \times 512 \times 33.3$	$1 \times 29 \times 1750$	1152
<b>EC Rings – iForward:</b>	$d_{\text{wafer}}$ [mm]	$X/X_0$ [%]	$N_{\text{ch}} \times r\text{-}\varphi$ pitch [ $\mu\text{m}$ ]	$N_{\text{ch}} \times z$ pitch [ $\mu\text{m}$ ]	$N_{\text{modules}}$
1 ( $w$ )	103.1	1.5	$(3 \times 512 + 146) \times 25$	$(3 \times 512 + 265) \times 50$	72
2 ( $w$ )	115.5	1.5	$(3 \times 512 + 107) \times 33.3$	$(1 \times 512 + 488) \times 100$	120
3 ( $w$ )	114.1	2.0	$(3 \times 512 + 76) \times 33.3$	$250 \times 400$	192
4 ( $w$ )	113.7	2.0	$(3 \times 512 + 66) \times 33.3$	$250 \times 400$	264
5 ( $w$ )	113.4	2.0	$(3 \times 512 + 57) \times 33.3$	$250 \times 400$	336
6 ( $w$ )	114.8	2.0	$(3 \times 512 + 153) \times 33.3$	$250 \times 400$	384
	$r\text{-}\varphi \times z$ dims [ $\text{mm}^2$ ]	$X/X_0$ [%]	$N_{\text{ch}} \times r\text{-}\varphi$ pitch [ $\mu\text{m}$ ]	$N_{\text{ch}} \times z$ pitch [ $\mu\text{m}$ ]	$N_{\text{modules}}$
7-9	$102.4 \times 102.4$	2.0	$6 \times 512 \times 33.3$	$1 \times 256 \times 400$	960
10-13	$102.4 \times 102.4$	2.5	$6 \times 512 \times 33.3$	$1 \times 58 \times 1750$	864
<b>EC Rings – Forward:</b>	$d_{\text{wafer}}$ [mm]	$X/X_0$ [%]	$N_{\text{ch}} \times r\text{-}\varphi$ pitch [ $\mu\text{m}$ ]	$N_{\text{ch}} \times z$ pitch [ $\mu\text{m}$ ]	$N_{\text{modules}}$
1 ( $w$ )	107.6	1.5	$(2 \times 512 + 373) \times 25$	$(2 \times 512 + 483) \times 50$	144
2 ( $w$ )	113.1	1.5	$(2 \times 512 + 427) \times 33.3$	$(1 \times 512 + 493) \times 100$	288
3 ( $w$ )	112.7	2.0	$(2 \times 512 + 474) \times 33.3$	$257 \times 400$	432
4 ( $w$ )	112.7	2.0	$(2 \times 512 + 502) \times 33.3$	$250 \times 400$	576
5 ( $w$ )	114.4	2.0	$(3 \times 512 + 118) \times 33.3$	$262 \times 400$	672
	$r\text{-}\varphi \times z$ dims [ $\text{mm}^2$ ]	$X/X_0$ [%]	$N_{\text{ch}} \times r\text{-}\varphi$ pitch [ $\mu\text{m}$ ]	$N_{\text{ch}} \times z$ pitch [ $\mu\text{m}$ ]	$N_{\text{modules}}$
6-9	$102.4 \times 102.4$	2.0	$6 \times 512 \times 33.3$	$1 \times 256 \times 400$	1824
10-15	$102.4 \times 102.4$	2.5	$6 \times 512 \times 33.3$	$1 \times 58 \times 1750$	5712





---

# Calorimetry

---

## 7.1 Introduction

### 7.1.1 Calorimetry at the FCC-hh

Calorimeters will play a crucial role in the exploitation of the full physics potential of the FCC-hh. Proton collisions at unprecedented centre-of-mass energies will produce particles with energies up to the multi-TeV range. Due to the statistical nature of the energy measurement in calorimeters, the energy resolution improves with energy, which makes them the ideal candidates for the measurement of particles with energies in the multi-TeV range. In addition, calorimeters produce fast signals and can be read out at the bunch-crossing frequency which makes them an ideal choice for a hardware trigger. In future collider experiments, the final 4-momentum measurement can be obtained by combining several sub-detectors. In particular, the tracker and the calorimeter measurements can be combined by using the *particle flow* technique [52], that is already in use at the LHC experiments. This technique requires highly granular calorimeters such as the HGCAL, planned for the CMS upgrade [131] or CALICE calorimeters [132] for future linear collider experiments. Furthermore, calorimeters are the basis for the missing  $E_T$  measurement and play an important role in particle identification, background and pile-up rejection. The ability to resolve collimated decay products from highly boosted objects sets constraints on the position resolution and a related pointing resolution, which will also help to identify the primary vertex for neutral particles such as photons. Last but not least, a time measurement with a resolution at the level of 30 ps could be used to reject energy deposits from particles of many other collision vertices at the same bunch crossing (in-time pile-up). All these properties call for a high resolution, and fine grain calorimeter systems with adequate time-measurement capabilities whilst the harsh radiation environment limits the choice of technologies.

The reference calorimeter system for the FCC-hh detector is composed of sampling calorimeters using liquid argon and scintillating tiles as active media. Liquid argon as an intrinsically radiation hard noble liquid is suitable for the FCC-hh radiation environment. The design of the scintillating tile calorimeter for the central hadronic calorimeter, allows very fine transverse segmentation and a good intrinsic energy resolution. A novel design of highly segmented liquid argon and tile calorimeters are presented below. An alternative option with a digital electromagnetic calorimeter is also discussed.

### 7.1.2 Calorimeter requirements

#### 7.1.2.1 *Benchmark physics channels and general requirement considerations*

Calorimeters for the next generation of high energy machines like FCC, will have to operate efficiently in a very broad energy range. Final states produced at a given characteristic energy scale  $Q$ , will be produced on average at higher rapidities at  $\sqrt{s} = 100$  TeV compared to  $\sqrt{s} = 14$  TeV. As an illustration

Fig. 7.1 (a) shows the highest lepton pseudo-rapidity  $\eta^{max}$ , for a gluon-gluon fusion produced Higgs decaying into four leptons for both 13 and 100 TeV p-p collisions. To reach 90 % fiducial acceptance in this channel, a detector coverage of  $|\eta| < 3.8(4.8)$  is needed for 13(100) TeV respectively. Figure 7.1 (b), shows the maximum jet pseudo-rapidity  $|\eta_j^{max}|$ , for a Vector-Boson-Fusion (VBF) produced Higgs. To reach 90 % fiducial acceptance for the forward jets, the pseudo-rapidity acceptance will need to be extended from  $|\eta| = 4.5$  to  $|\eta| = 6$ . This increase has strong consequences on the detector design, as the very shallow polar angle of  $0.28^\circ$  for  $|\eta| = 6$  requires the calorimeters to be very far out of the interaction region and/or very close to the beam pipe. As an example, if the forward calorimetry is located at 16.5 m in  $z$ , the calorimeter system must have an inner radius of 8.2 cm in order to comply with the  $|\eta| = 6$  acceptance requirement. Needless to say, in the calorimeter endcaps the radiation levels will be extremely high, e.g. the 1 MeV neutron equivalent fluence will be  $\approx 2 \cdot 10^{16} \text{ cm}^{-2}$  showing that radiation hardness will be a key requirement for such sub-detectors.

FCC-hh is possibly the only machine that can allow for a few percent level precision on the Higgs self coupling [17]. Since this process is very rare even at 100 TeV, the full integrated luminosity and an excellent calorimetry will be needed to achieve the few percent accuracy. One of the most promising channels for double Higgs production is  $HH \rightarrow bb\gamma\gamma$ —which heavily relies on the precise measurement of the photon energy and position, with an electromagnetic (EM) calorimeter, and the two b-quarks. Figure 7.2 (a) shows the precision at which the Higgs self coupling can be measured for Higgs mass resolutions of 1.3 and 2.9 GeV respectively. At the one sigma level, the error on the self coupling increases from 5 to 6 %, thus having an excellent di-photon mass resolution is absolutely essential.

The requirements are different for new high mass particles that would eventually decay to high energetic objects in the central part of detector. The energy resolution of the calorimeter can be parameterised according to

$$\frac{\sigma_E}{E} \approx \frac{a}{\sqrt{E}} \oplus \frac{b}{E} \oplus c \quad (7.1)$$

where  $a$  is the stochastic term<sup>1</sup> due to shower fluctuations and sampling,  $b$  is called the noise term due to electronic noise and pile-up and  $c$  stands for the constant term due to various effects including shower leakage, construction non-uniformities and cell to cell calibration variations and is the dominant term for highly energetic objects.

It has already been shown [20] that with a total interaction length of about  $11 \lambda$ , hadronic showers are sufficiently contained to reach the desired 3% constant term. As seen in Fig. 7.2 (b), if the mass resolution degrades, the discovery reach of a narrow resonance decaying to jets is strongly reduced, thus keeping the constant term at the 3 % level is important. Additionally, the calorimeter response has to be linear at the per-cent level over many orders of magnitude to extrapolate the absolute energy calibration with known resonances (e.g. Z or Higgs boson decays) to the multi-TeV range. This is important to limit systematic uncertainties on measured masses of high-mass resonances. In addition to good energy resolution and linearity, high granularity is relevant for efficiently reconstructing the high energetic unstable particles. For instance, decay products from a high  $p_T$  particle which decays, are collimated with a typical angular distance  $\Delta R \approx \frac{2m}{p_T}$ . Thus, in order to have the ability to disentangle the sub-structure inside such boosted objects, the granularity of the calorimeters (both, lateral and longitudinal) should be increased significantly with respect to the LHC experiments.

The high pile-up environment finally necessitates robust pile-up rejection. While the tracker will be the key instrument to assign particles to the correct primary vertex and hence allow the rejection of tracks from pile-up vertices, the ability to connect tracks to the correct primary vertex without using any timing information decreases significantly for rapidity of  $|\eta| \geq 3$ . It will therefore be essential to integrate a time measurement into the tracker and also into the calorimeters. Experience from simulations for the HL-LHC show that a time resolution of  $\mathcal{O}(30 \text{ ps})$  can reduce pile-up effectively by a factor of six

<sup>1</sup>The stochastic term is also called sampling term in sampling calorimeters.

(assuming a time distribution of primary vertices of 180 ns) [133]. In summary, key ingredients to be taken into account for the design of the calorimeter system are:

- excellent resolution and linearity of the response at the per-cent level from few GeVs up to multi-TeV particles
- acceptance up to  $|\eta| \leq 6$
- time measurement of showers of  $\mathcal{O}(30 \text{ ps})$ .
- high longitudinal and lateral segmentation

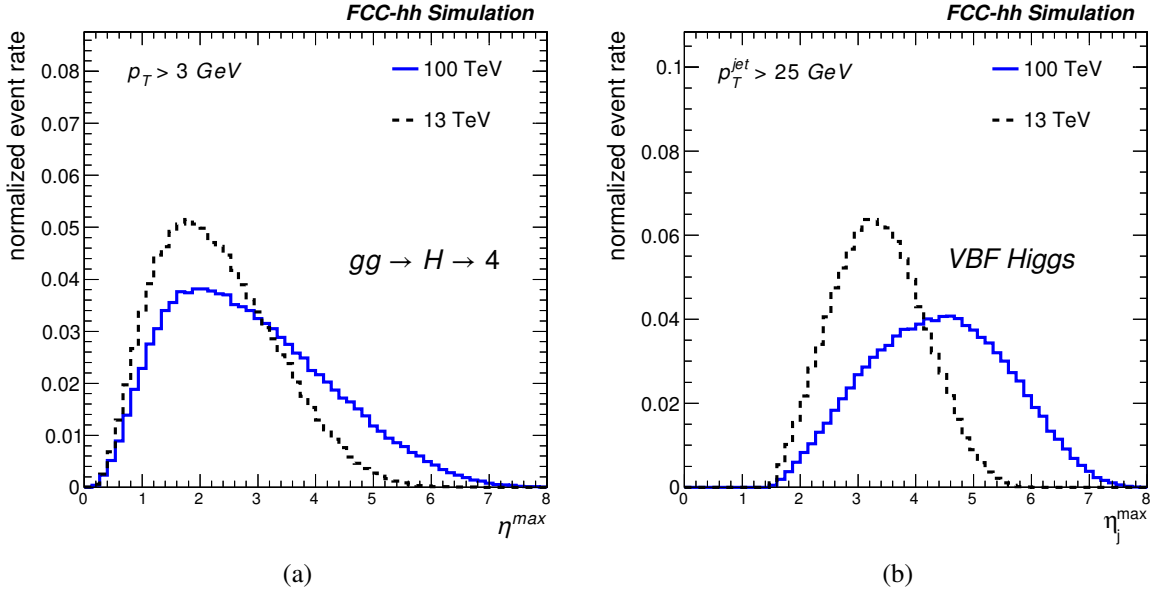


Fig. 7.1: Highest lepton pseudo-rapidity for gluon-gluon fusion Higgs decaying to 4 leptons (a) and maximum jet pseudo-rapidity for vector-boson fusion Higgs (b).

### 7.1.2.2 Requirements for electromagnetic calorimetry

**Energy resolution over the energy range 10-500 GeV:** An excellent energy resolution is necessary to achieve a mass resolution close to 1% for  $H \rightarrow \gamma\gamma$  and  $H \rightarrow 4e$  decays. This can only be achieved if the stochastic term of the electromagnetic energy resolution stays at a level of  $\sim 10\% \sqrt{\text{GeV}} / \sqrt{E}$  and the noise term is kept under control. The constant term should be smaller than 1% in order to have a better mass resolution than the intrinsic width of heavy  $Z'$  that occur in many models. The goal for the energy resolution in the region  $|\eta| \leq 4$  is

$$\frac{\sigma_E}{E} = \frac{10\% \sqrt{\text{GeV}}}{\sqrt{E}} \oplus \frac{0.3 \text{ GeV}}{E} \oplus 0.7\%, \quad (7.2)$$

neglecting the effect of pile-up. The expected average number of pile-up interactions  $\langle \mu \rangle = 200$  and  $\langle \mu \rangle = 1000$  for the FCC-hh baseline and ultimate scenarios, respectively, will lead to energy deposits from pile-up collisions on top of the hard scatter of interest. Due to the bipolar read-out of the calorimeters, in long bunch trains these energy deposits will cancel on average, however, due to fluctuations of the exact number of collisions in each bunch crossing and the statistical nature of their energy deposits this pile-up will lead to additional noise in the calorimeter, referred to as pile-up noise in the following. Without any pile-up rejection procedure, the noise term could increase at  $\langle \mu \rangle = 200$  and depending on

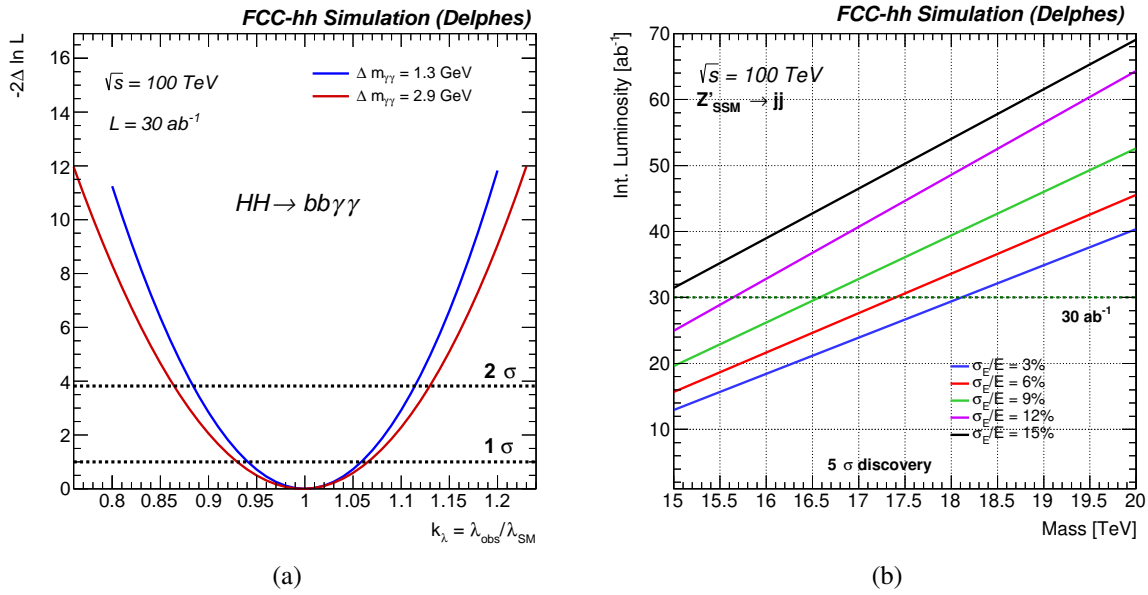


Fig. 7.2: Precision on the Higgs self coupling measurement in the  $bb\gamma\gamma$  channel (a), di-jet mass reach in the case of a narrow resonance (b).

the size of the cluster, by a factor of two to six. It is therefore obvious that the tracker and timing information will be needed to reduce the impact of pile-up. An expected azimuthal non-uniformity due to the detector geometry will contribute to a global constant term not larger than  $\sim 0.7\%$ .

**Rapidity coverage:** As previously mentioned, the very large increase in the centre-of-mass energy with respect to LHC leads to decay products at higher rapidity, thus an acceptance of up to  $|\eta| = 6$  is needed. High acceptance will be beneficial for detecting rare processes like double Higgs production and also for tagging vector boson fusion or scattering induced processes as well as single Higgs production where forward jets and event tagging capabilities are needed. At pseudorapidity  $4 < |\eta| < 6$ , the EM calorimeter will mainly be needed for jet reconstruction and forward jet tagging, missing transverse energy ( $E_T^{\text{miss}}$ ) measurement, and pile-up rejection.

**Dynamic range:** The dynamic range for each read-out cell is defined by the range between the lowest and the highest energy that the calorimeter should be able to measure. The lower limit is typically set to a value close to the electronics noise per cell (see Section 7.3.2.1), since such a choice allows the measurement of the noise and its auto-correlation by the calorimeter read-out. On top of that, the possibility of measuring the energy deposits of minimum ionising particles (MIPs) per cell or at least per longitudinal layer will be very beneficial for the layer calibration. The upper limit should be set close to the expected energy deposit per cell of electrons or photons from heavy resonances such as  $Z'$ ,  $W'$ , or Gravitons with masses up to 50 TeV. Taking into account these considerations a dynamic range of  $\sim 2$  MeV to  $\sim 100$  GeV ( $\sim 16$  bits) per cell will be necessary, depending on the exact cell position. Detailed simulation studies are required to understand the maximum energy deposit in one read-out cell or per layer.

**High segmentation and granularity:** High granularity in the calorimeters will be necessary for particle identification, background rejection, position measurement of showers, photon pointing, and the correct connection of tracks with calorimeter clusters, which is crucial for both, pile-up rejection and particle flow reconstruction techniques. Many of these aspects will be further developed in the performance chapter, Section 7.4.1, while in this section we introduce some of the most important aspects. At FCC, the boost of relatively light SM particles will be large, leading to very collimated decay products. The

calorimeters need to be able to resolve and reconstruct such highly boosted objects. To resolve boosted objects, a cell size of a fraction of a Molière radius of about  $\sim 2$  cm ( $R_M = 5.7$  cm in the EM calorimeter proposed in Section 7.2.2) is probably optimal. Simulations showed that below a certain cell size the separation of partial showers doesn't improve anymore. Efficient  $\gamma/\pi^0$  separation will require a layer (so-called strip layer) with very fine segmentation at the beginning of the shower. In addition, a large number of longitudinal layers, producing 3D images of the shower together with sophisticated analysis techniques, will allow efficient particle identification.

**Total thickness of at least 30 radiation lengths at  $\eta = 0$ :** The shower depths of electromagnetic showers increase with  $\propto \ln(E)$ . Longitudinal leakage of electromagnetic showers leads to a loss of resolution and also a deterioration of particle identification capabilities. Due to the higher particle energies with respect to LHC, the showers become longer and the calorimeter needs to be deeper to achieve  $\mathcal{O}(99\%)$  containment. Figure 7.3 shows that with a calorimeter depth of  $30 X_0$ , a containment of  $> 99\%$  can be achieved for particles  $\leq 1$  TeV.

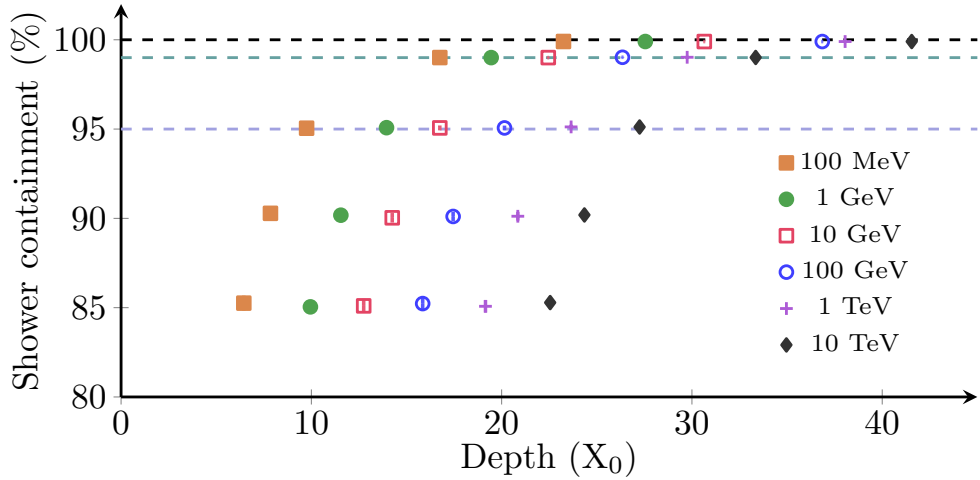


Fig. 7.3: Dependence of the electron shower containment on the calorimeter depth expressed in radiation lengths. The horizontal lines correspond to the shower containment of 95%, 99% and 100% respectively.

**Others:** In addition to what is listed above, excellent photon/jet, electron/jet and  $\tau$ /jet separation needs to be achieved. This is extremely important as very rare signals that will decay to electron/photon/ $\tau$  should be distinguishable from SM processes with jets in the final state. Moreover, some compressed SUSY models would benefit from identifying electrons with energies of a few GeVs only, long lived or highly ionising particles could give rise to peculiar signatures in the detector which are relevant for the design. Finally, it is also worth mentioning the need for excellent angular resolution.

### 7.1.2.3 Requirements for hadronic calorimetry

**Energy resolution over the energy range 20 GeV–10 TeV:** For hadronic calorimetry, the energy resolution requirements are set by the jet energy resolution required for the different  $\eta$  regions,

$$\frac{\sigma_{p_T}}{p_T} = \frac{50 - 60\% \sqrt{\text{GeV}}}{\sqrt{p_T}} \oplus 3\% \quad \text{for } |\eta| \leq 4, \quad (7.3)$$

$$\frac{\sigma_{p_T}}{p_T} = \frac{100\% \sqrt{\text{GeV}}}{\sqrt{p_T}} \oplus 10\% \quad \text{for } 4 < |\eta| < 6. \quad (7.4)$$

Such resolutions have been found adequate for providing jet and di-jet mass reconstruction as well as  $E_T^{\text{miss}}$ . A strong motivation for these performance goals is the discovery reach of heavy narrow resonances like a  $Z'$ , shown in Fig. 7.2, and tested for different jet energy resolutions ranging from 3-20%.

At these very high energies, the constant term of the calorimeter resolution dominates and it therefore has to be kept under control at  $< 3\%$ .

**Rapidity coverage:** As discussed for the electromagnetic calorimeters, and shown in the examples in Fig. 7.1, a coverage for up to  $|\eta| \leq 6$  is essential to enable jet measurements and tagging.

**High segmentation and granularity:** The two main criteria to take into account for the granularity and segmentation are boosted high  $p_T$  bosons or top quarks and pile-up mitigation. At FCC-hh, objects produced with momenta  $p_T$  of up to 15 TeV will have to be distinguishable from QCD jets. For example, the two quarks from a 5 TeV Z boson decay will only be separated by  $\Delta R \sim 0.03$ . Although the more granular electromagnetic calorimeter in front will help, the granularity of the hadronic calorimeter should also be of this order. The same arguments as for the electromagnetic calorimeter apply for pile-up mitigation and particle-flow techniques.

**Total thickness of at least 11 interaction lengths at  $\eta = 0$ :** As shown in Figs. 7.4a and 7.4b, a total (EM and hadronic) depth of about 11 interaction lengths ( $\lambda$ ) is required for sufficient shower containment compatible with a constant term of the energy resolution of about 3%. Another important aspect is the leakage into the muon system, which needs to be kept to a minimum to avoid fake muon triggers. Further studies are required to estimate this fake trigger rate, but the additional material of the solenoid between the hadronic calorimeter and the muon system will mostly eliminate this effect in the central region.

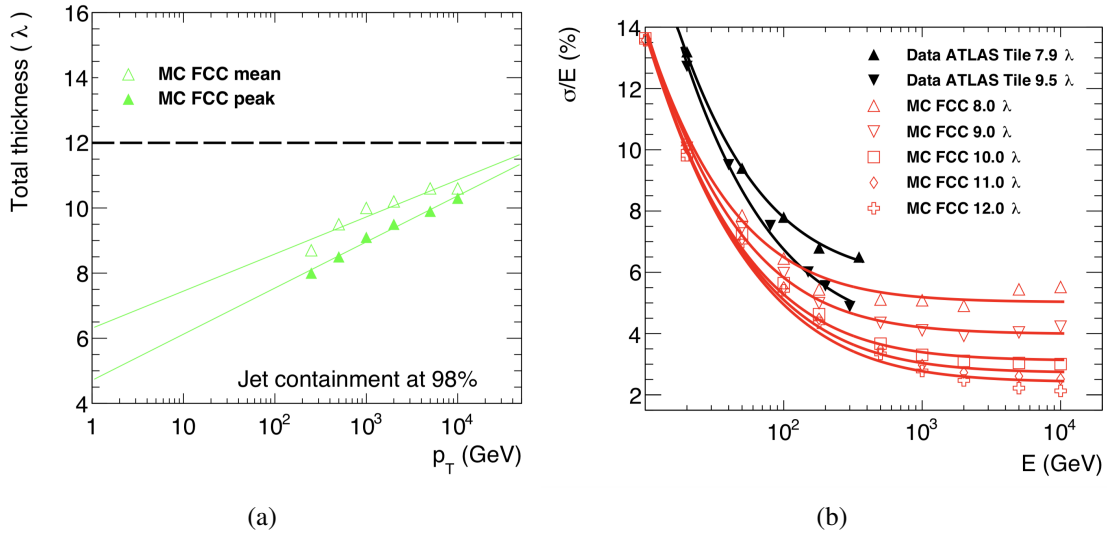


Fig. 7.4: (a) Calorimeter depth in interaction lengths  $\lambda$  for 98% jet containment as a function of jet  $p_T$ . Jets come from simulated  $Z' \rightarrow q\bar{q}$  events. Two methods, so-called ‘FCC mean’ (mean of the distribution of the total thicknesses) and ‘FCC peak’ (a mean of the Gaussian fit in the range of  $\pm 2\sigma$  around the maximum), are used for the evaluation: more details can be found in Ref. [20]. (b) Energy resolution for single pions as a function of the particle energy for the FCC-hh simulations compared to ATLAS data [20].

**Dynamic range:** The dynamic range necessary for the Barrel HCAL (HB) has been studied in full simulations of the FCC-hh detector, as proposed in Section 7.2.3. It has been found that a 10 TeV pion at  $\eta = 0.36$  deposits on average 100 – 500 MeV per cell in the hadronic calorimeter, with tails up to 2 TeV. The variation with the calorimeter depth, in terms of layers, is shown in Fig. 7.5a, where the different colours correspond to the radial layer sizes of 10, 15, and 25 cm. The radial layer size determines the cell size due to the perpendicular orientation of the scintillating tiles in the HB. The response to MIPs has been determined from a Landau-Gauss convoluted fit to the cell energy distribution, see details in Section 7.2.3.5, and features a most probable value (MPV) of 56 MeV per HCAL cell in the barrel



region. These numbers are given for the HB in full granularity configuration, and prove the sensitivity to MIPs for an estimated electronic noise per cell of  $\approx 10$  MeV (see Section 7.3.2.1). The required dynamic range of the HB cells has been determined to be 10 MeV to 10 GeV, for a minimum hit cell rate  $> 1\%$  (see Fig. 7.5b). However, this estimate from single MIPs and 10 TeV pions only supports the performance results shown for hadrons and jets, and will need further evaluation from additional studies including e.g. rare decays. The dynamic range necessary for the performances presented in this document, corresponds to a 10 bit readout. Similar studies have to be performed for the endcap and forward hadronic calorimeters, where the hit rates are higher, but cell sizes and sampling fractions are much smaller.

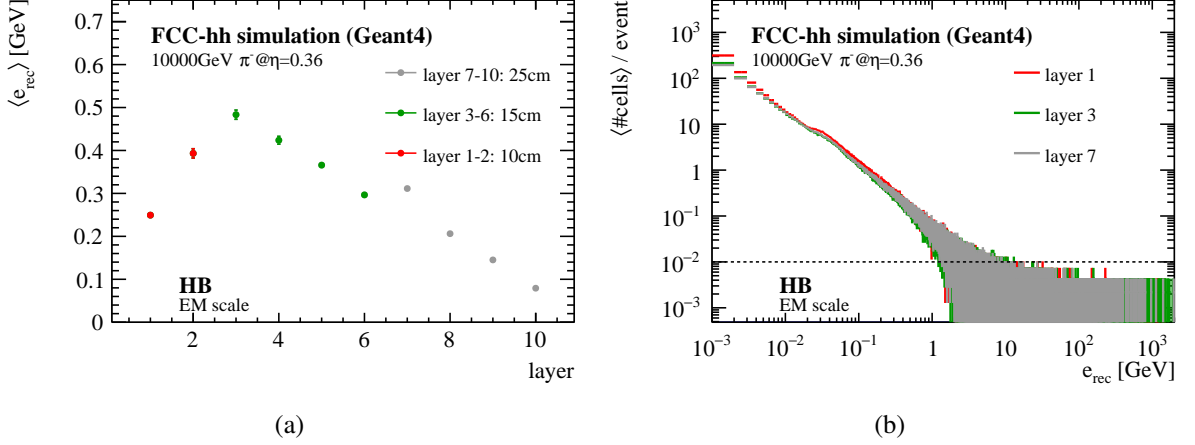


Fig. 7.5: (a) Average energy deposited by 10 TeV hadron in the hadronic barrel (HB) calorimeter cells. (b) The cell energy distributions per HB layer.

**Others:** Another important aspect for the hadronic calorimetry is the energy calibration (see Section 7.2.3.4) and a good linearity of the response. As already mentioned in Section 7.1.2, good timing resolution is expected to help in dealing with high pile-up. Excellent jet identification and measurement in the full acceptance, very good di-jet mass resolution, forward jet tagging capabilities and  $E_T^{\text{miss}}$  reconstruction will therefore be required and are mostly addressed in Section 7.4.5.

## 7.2 Layout of the calorimeter system

### 7.2.1 Overview and reminder of FCC-hh detector environment

The layout of the calorimeter system of the reference FCC-hh detector has been driven by the following requirements:

- Use of technologies that withstand the high radiation environment.
- Under these constraints have the best possible conventional calorimetry to ensure the best possible standalone energy measurement.
- Use of technologies that can achieve a timing resolution of  $< 100$  ps.
- High transverse and longitudinal granularity to optimise the combination with the tracker to enable particle flow techniques and use of 4D imaging for sophisticated particle ID and pile-up rejection algorithms.

In this section we will introduce the calorimeter system of the FCC-hh reference detector, which is a possible implementation aimed at demonstrating that the performance requirements can be achieved. In Section 7.4 we will then show its performance and discuss the optimisations that have led to this design and which further improvements could be achieved.



The overview of the calorimeter system of the reference FCC-hh detector is shown in Fig. 7.6. It consists of a central and extended barrel, two endcaps, and two forward calorimeters, with the dimensions given in Table 7.1. The sub-systems and the corresponding acronyms are shown in Fig. 7.7. The central barrels and the endcaps are immersed in the magnetic field of the main solenoid of  $\sim 4$  T. Due to the high integrated luminosity goals and high collision rates at the FCC-hh, the radiation environment in the detector is very challenging. The expected radiation dose and 1 MeV neutron equivalent fluence (NIEL) is presented in Table 7.1 for an integrated luminosity of  $30 \text{ ab}^{-1}$ . These unprecedented radiation requirements, especially in the forward region, call for radiation hard technologies and front-end electronics that can be placed behind the calorimeters in areas of reduced radiation exposure. The material budget of the reference detector is described in the following sections and is shown graphically in Figures 7.8a and 7.8b.

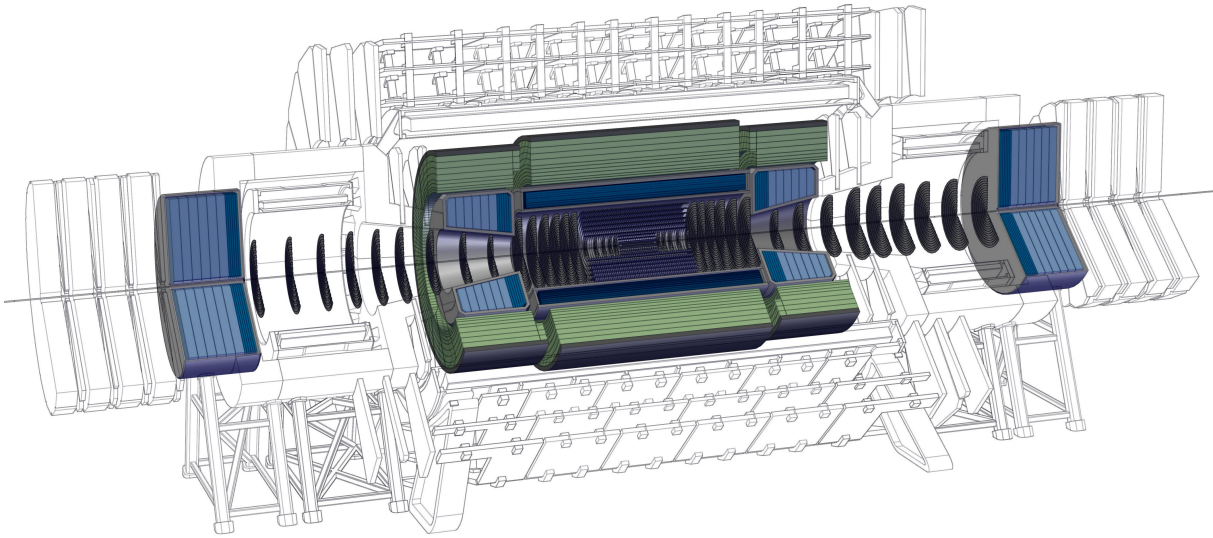


Fig. 7.6: Calorimetry of the reference FCC-hh detector.

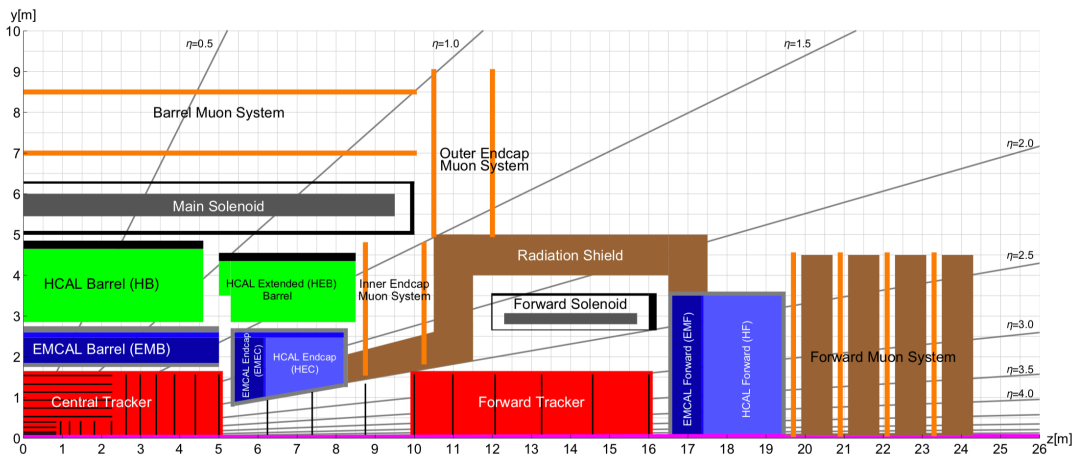


Fig. 7.7: Longitudinal cross-section of the FCC-hh reference detector [3].

Liquid argon (LAr) was chosen as the active material for the electromagnetic calorimetry due to its intrinsic radiation hardness (provided LAr impurities can be kept low)<sup>2</sup>. As the radiation levels increase

<sup>2</sup>Experience from the ATLAS LAr calorimeter shows that purity levels down to 0.3 ppm oxygen equivalent are possible to

Table 7.1: Dimensions of the envelopes for the calorimeter sub-systems (including some space for services) and the maximum radiation load at inner radii (total ionising dose is estimated for  $30 \text{ ab}^{-1}$ ). The abbreviations used in the first column are explained in the text.

Unit	$R_{\min}$ m	$R_{\max}$ m	$z$ coverage m	$\eta$ coverage	Dose MGy	1 MeV $n_{\text{eq}}$ fluence $\times 10^{15} \text{ cm}^{-2}$
EMB	1.75	2.75	$ z  < 5$	$ \eta  < 1.67$	0.1	5
EMEC	0.82–0.96	2.7	$5.3 <  z  < 6.05$	$1.48 <  \eta  < 2.50$	1	30
EMF	0.062–0.065	3.6	$16.5 <  z  < 17.15$	$2.26 <  \eta  < 6.0$	5000	5000
HB	2.85	4.89	$ z  < 4.6$	$ \eta  < 1.26$	0.006	0.3
HEB	2.85	4.59	$4.5 <  z  < 8.3$	$0.94 <  \eta  < 1.81$	0.008	0.3
HEC	0.96–1.32	2.7	$6.05 <  z  < 8.3$	$1.59 <  \eta  < 2.50$	1	20
HF	0.065–0.077	3.6	$17.15 <  z  < 19.5$	$2.29 <  \eta  < 6.0$	5000	5000

with pseudo-rapidity and in the vicinity of the beam-pipe, the hadronic calorimeters in the endcaps and in the forward region also use the liquid argon technology. There are lead/steel absorbers (2.0 mm thick) for the barrel (EMB) and endcap (EMEC) electromagnetic calorimeters. Tungsten is an interesting option for the absorbers due to its smaller Molière radius and hence smaller clusters, which could reduce the impact of pile-up by up to a factor  $\sim 1.5$ . The LAr based hadronic endcap (HEC) and forward calorimeter (EMF, HF) have copper absorbers, following the example of the ATLAS forward calorimeters [134]. The hadronic calorimeters in the central part of the detector (hadronic barrel, HB, hadronic extended barrel HEB) are based on scintillating plastic tiles within an absorber structure consisting of steel and lead. The baseline detectors for the liquid argon calorimeters are described in detail in Section 7.2.2 and the hadronic scintillator calorimeter is described in Section 7.2.3.

The proposed longitudinal and transverse granularity for the reference system is summarised in Table 7.2. The strip layer is introduced to allow an efficient  $\gamma/\pi^0$  separation. The segmentation in the strip layer is  $\Delta\eta \approx 0.0025$  (two photons originating from a decay of a 50 GeV  $\pi^0$  are separated by  $\Delta R \approx 0.005$ ). Overall, the granularity is  $2 - 4\times$  higher in each dimension ( $\eta - \phi - layer$ ) compared to the calorimeters in the ATLAS experiment.

Table 7.2: Depth and proposed granularity of the FCC-hh reference calorimeter.

	material	minimal depth		granularity		# channels ( $10^6$ )
		$\#X_0$	$\#\lambda$	$\Delta\eta$	$\Delta\phi$	
EMB	LAr/Pb	26.5	1.5	0.01 (0.0025 in strip layer)	0.009 (0.018 in some layers)	8 $\sim 1.7$
EMEC	LAr/Pb	45	1.8	0.01 (0.0025 in strip layer)	0.009 (0.018 in some layers)	6 $\sim 0.6$
EMF	LAr/Cu	30	2.8	0.025	0.025	6 $\sim 0.1$
HB	Sci/Pb/steel	136	9.4	0.025	0.025	10 $\sim 0.2$
HEB	Sci/Pb/steel	141	9.8	0.025	0.025	8 $\sim 0.1$
HEC	LAr/Cu	119	11.3	0.025	0.025	6 $\sim 0.5$
HF	LAr/Cu	145	13.5	0.025	0.025	6 $\sim 0.1$

As explained in Section 7.1.2.2, the increase of the centre-of-mass collision energy results in higher transverse momenta of the particles produced. Therefore, the required depth of the electromagnetic calorimeter is  $\sim 30 X_0$ , and of  $\sim 11 \lambda$  for the full EM + hadronic calorimeters. The thickness of the achieve if all materials used inside the cryostat are carefully chosen.

reference detector as a function of pseudo-rapidity in units of radiation length and interaction length is shown in Figs. 7.8a and 7.8b respectively. The thickness is measured including all inactive materials of the detector, as well as the tracker and the beam-pipe. At  $\eta = 0$  the total depth of the EMB calorimeter is  $\sim 29.5 X_0$ . It increases with pseudorapidity (up to  $|\eta| = 1.5$ ) as particles traverse the detector with a smaller angle with respect to the beam-pipe (and cryostat). Material in front of the electromagnetic calorimeter is presented in Fig. 7.41b and discussed in Section 7.4.1.1.1. For the endcap (EMEC) and the forward electromagnetic calorimeter (EMF) the depth is above  $30 X_0$ . Including the hadronic calorimeters (HB, HEB, HEC and HF), a total depth in terms of interaction lengths of  $> 11\lambda$  is achieved over the full rapidity range.

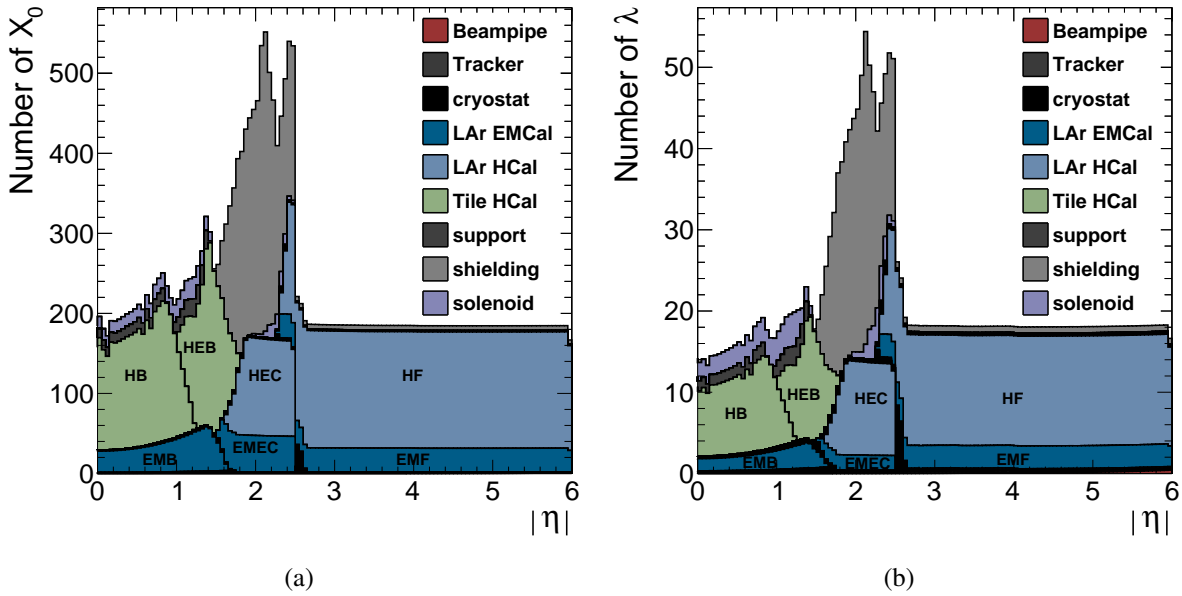


Fig. 7.8: Material budget of the reference detector expressed in units of (a) radiation length and (b) nuclear interaction length. The amount of material is measured from the interaction region (centre of the detector) to the outer boundary of the calorimeter. The spike at  $|\eta| = 2.5$  corresponds to the inner wall of the cryostat of the endcap. The colour code is the same as in Fig. 7.6.

## 7.2.2 Liquid argon calorimeters

Liquid argon (LAr) calorimetry has been proven to provide excellent electromagnetic energy measurements, with high resolution, linearity and uniformity of the response, high stability and ease of calibration. Additionally, it is an intrinsically radiation hard material that can be used in the detectors with high particle fluence rates and high ionising radiation doses. LAr-based calorimetry is successfully operating in ATLAS experiment [96, 134]. It has been chosen for the FCC-hh reference detector as a baseline technology for the electromagnetic calorimetry and also, due to the high radiation dose expected, for the hadronic calorimeters at pseudo-rapidities of  $> 1.4$ .

The electromagnetic barrel calorimeter is located within a 10 m long and 1 m thick double-vessel cylindrical cryostat, with an inner radius of 1.75 m, covering the pseudorapidity range  $|\eta| < 1.5$ . The length is dictated by the length of the central tracker, which provides full lever arm for momentum spectroscopy for pseudorapidity up to  $|\eta| < 2$ . The calorimeter endcaps are located next to the barrel, starting at  $|z| = 5.3$  m, and are 3 m thick (along the beam axis). They are positioned closer to the beam axis, with the active volume spanning up to  $|\eta| = 2.5$ , housed in two double-vessel cryostats. The forward detector is localised far from the centre of the detector, from  $|z| = 16.5$  m to  $|z| = 19.5$  m.

In order to cover pseudorapidity up to  $|\eta| = 6$ , the inner radius of the forward calorimeter must be  $r = 8.2$  cm, which leaves little space for the cryostat and the beam pipe but is regarded as feasible<sup>3</sup>.

### 7.2.2.1 Barrel

#### 7.2.2.1.1 Geometry layout

As explained above, it has been attempted to adapt LAr calorimetry to high granularity read-out. For the moment, cell sizes as described in Table 7.2 are planned for the various parts of the calorimeter. To achieve this granularity a design as depicted in Fig. 7.9 has been chosen. Straight lead/steel absorbers are interleaved with LAr gaps and straight electrodes with HV and read-out pads forming a cylinder of 192 cm (257 cm) inner (outer) radius respectively. The increase of the longitudinal segmentation (compared to the accordion ATLAS LAr calorimeter [134] with three-layer kapton electrodes) is possible thanks to the use of multi-layer electrodes realised as straight printed circuit boards (PCB). Therefore the electrodes as well as the absorber plates are arranged radially, but azimuthally inclined by 50 degrees with respect to the radial direction as shown in Fig. 7.9. This ensures readout capabilities of the electrodes via cables arranged at the inner and outer wall of the cryostat together with a high sampling frequency. The inclination of the plates also provides a uniform response in  $\varphi$  down to a few GeV for incoming particles. Together with honeycomb spacers defining the exact width of the LAr gap, this relatively simple structure should lead to a high mechanical precision and hence small impact on the energy resolution and uniformity. However, the LAr gaps in this design increase radially (opening angle with the calorimeter depth), leading to a sampling fraction which changes with depth. The shower profile will be measured for each shower due to the longitudinal layers and the energy calibration will correctly handle the non uniform sampling fraction. As described in Section 7.2.2.1.2, with eight longitudinal layers or more, the effect on the energy resolution is negligible. In the current simulation, the electrodes and absorbers are assumed to be single piece. However, due to mechanical and fabrication constraints, both absorbers and electrodes will have to be divided into pieces (in  $z$  or projected in  $\eta$ ), forming distinct detector wheels, which can be manufactured separately. Strong outer rings<sup>4</sup> together with spacers at the inner and outer radius will hold the electrodes and absorbers in place with high precision. A detailed engineering design is needed to produce these wheels with the required precision<sup>5</sup>.

The thickness of the active detector is 650 mm and it is composed of 1408 absorber plates which are inclined to the radial direction by  $50^\circ$ . Each absorber is 980 mm wide, 9.9 m long<sup>6</sup> and 2 mm thick. The absorbers are composed of a sandwich of lead (1.4 mm thick) with steel sheets on both sides (0.2 mm thick) to yield a flat and conducting surface glued with 0.1 mm epoxy impregnated fabric (preg). Steel increases the mechanical strength, ensures the uniformity of the surface, and serves as a second HV electrode for the electric field in the liquid argon gap needed for the ionisation charge drift. Between two absorbers there are two liquid argon gaps of  $2 \times 1.15$  mm at the inner radius and  $2 \times 3.09$  mm at the outer detector radius. The gaps are separated by a 1.2 mm thick electrode. Two of these double gaps are read-out together, forming a  $\varphi$  cell. That gives  $\varphi$  granularity of  $2\pi/704 = 0.009$ . The segmentation in  $\eta$  and depth (layers) is formed by cells on the readout electrode. The granularity in pseudorapidity is 0.0025 in the second (strip) layer, and 0.01 in the remaining 7 layers<sup>7</sup>. The fine segmentation in the strip layer is needed for a good  $\gamma/\pi^0$  separation. The thickness of the first layer is 4.5 times smaller (Fig. 7.10a) as the signal from this layer is used to correct for the energy deposited in the upstream material, as described in

<sup>3</sup>In ATLAS the forward calorimeter's inner radius is 7.2 cm [134].

<sup>4</sup>To avoid additional material in front of the active calorimeter, the main mechanical structure must sit at the outside radius.

<sup>5</sup>Note, that for a uniformity of  $\sim 0.7\%$  the absorber width and also the LAr gap width needs to be controlled at that level (at least for the sum of all absorbers and gaps in one cluster). A precision of  $\mathcal{O}(10\ \mu\text{m})$  will therefore be necessary. Such a precision was achieved for the ATLAS LAr calorimeter (see [134]). Non-uniformities can also be corrected using in-situ calibration with  $Z \rightarrow e^+e^-$  events.

<sup>6</sup>As mentioned above, how to best divide the detector in  $z$  or  $\eta$  has to be studied.

<sup>7</sup>Some of the simulations in the performance section are done for a granularity of 0.01 in all layers.

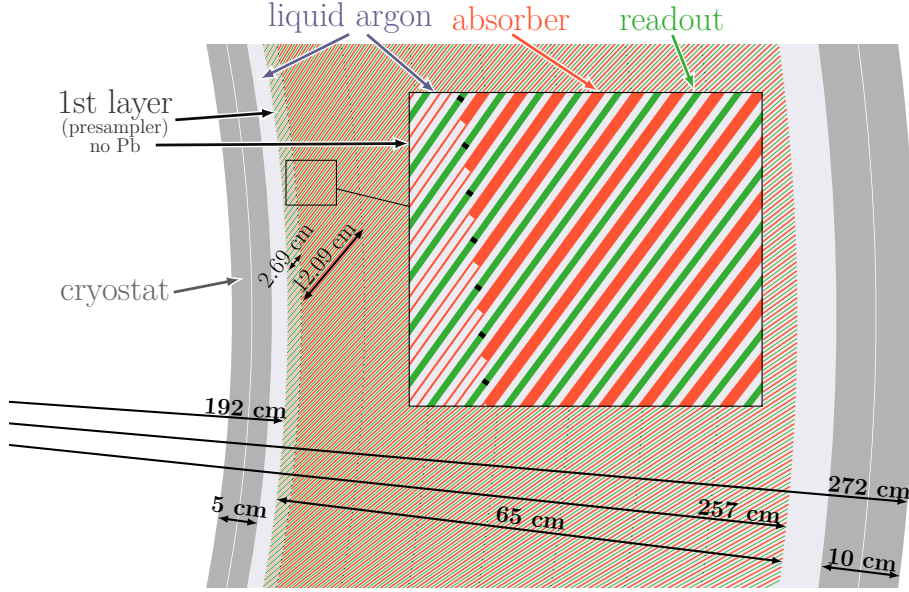


Fig. 7.9: The cross section of the electromagnetic barrel calorimeter.

Section 7.4.1.1.1. To achieve a  $\varphi$ -uniform response of this first layer, the absorbers do not contain lead in the middle to form a ‘LAr-only’ presampler layer.

The electrodes will be implemented as multi-layer PCBs ( $\epsilon_r = 4$ ) and the following seven layers from the outside to the inside are:

- Two outside HV layers that produce a  $\sim 1$  kV/mm electric field in the LAr gaps. Due to the changing LAr-gap width, there will be several depths of HV channel. In order to limit the current and possible damage during discharges and to decouple these layers from the read-out, they need to be protected by  $\mathcal{O}(10$  k $\Omega$ ) HV resistors.
- Two read-out layers with printed signal pads of the size of the desired read-out channels at a distance of  $h_{\text{HV}} = 100$   $\mu\text{m}$  from the HV layers. A schematic view of the read-out layer of the electrodes is presented in Fig. 7.10a. The radial depth of the layers is the same for the whole barrel (i.e. for pseudorapidity ranging from 0 to 1.5): a first layer of 20 mm and then seven 90 mm deep layers. This creates large difference in the thickness of layers expressed in the units of a radiation length (for particles originating near the interaction point). This may be addressed in the future by decreasing the thickness of layers as the pseudorapidity increases, so that measurements of the shower evolution are more uniform for different pseudorapidity values.
- Two grounded shielding layers at  $h_m = 285$   $\mu\text{m}$  inside the read-out layer to shield the signal pads from the signal traces. The width of these shields has been assumed to be  $w_s = 250$   $\mu\text{m}$  for the noise calculations in Section 7.3.2.1, but will need to be optimised to keep cross-talk from the signal pads to the signal traces low ( $< 0.1\%$ ). Larger shields, however, will translate into larger cell capacitance to ground and hence larger noise.
- One layer with  $w = 127$   $\mu\text{m}$  wide and  $t = 35$   $\mu\text{m}$  thick signal traces that are connected with vias to each of the signal pads. The signal traces together with the shielding layers should form transmission lines with an impedance in the range of  $25 \Omega \leq Z \leq 50 \Omega$ . For  $Z = 50 \Omega$  the distance of the signal traces and the shields has to be  $h_s \sim 170$   $\mu\text{m}$ <sup>8</sup>.

<sup>8</sup>The following approximation for a strip line between two ground shields has been used (see Ref. [135]):

$$Z[\Omega] = \frac{60}{\sqrt{\epsilon_r}} \log \frac{1.9(2h_s + t)}{0.8w_t + t} .$$



Figure 7.10b shows a cross section of such a read-out electrode for an impedance of  $Z = 50 \Omega$ . The middle layer used for the extraction of the signal to the front or back of the detector are sketched in Fig. 7.11a and 7.11b respectively.

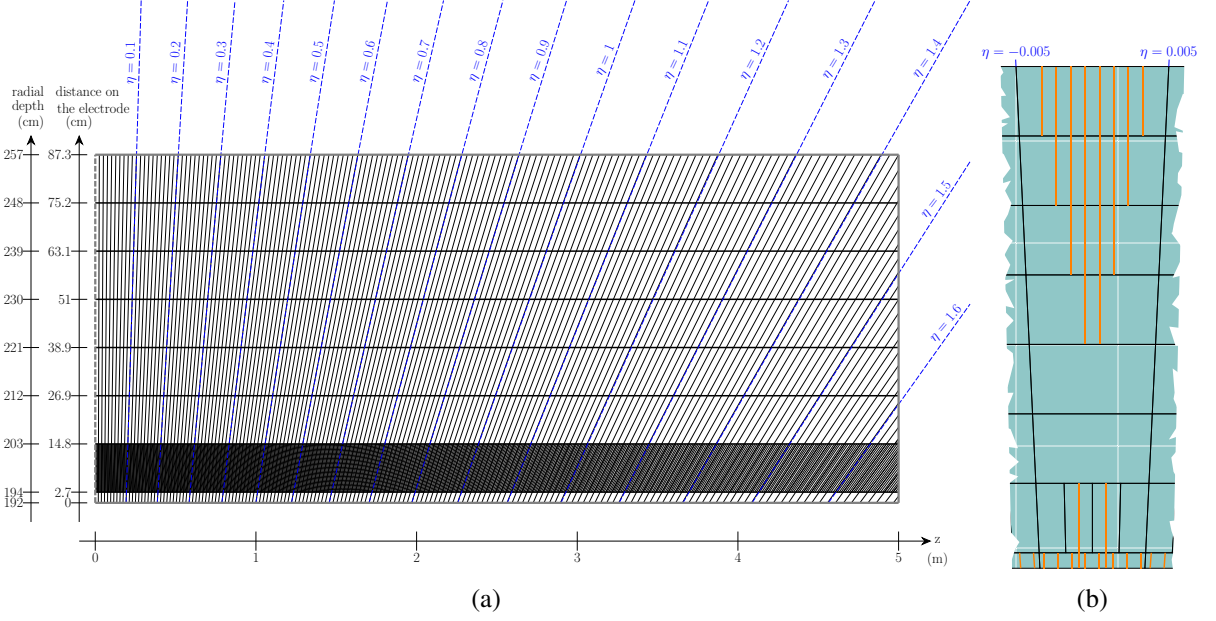


Fig. 7.10: Read-out PCB: **(a)**: Read-out electrode and cell segmentation on one electrode longitudinally (8 layers) and in pseudorapidity. The first layer is 4.5 times smaller than the rest for the correction described in Section 7.4.1.1.1. The cell size in pseudorapidity is  $\Delta\eta = 0.01$  in all layers except for the second (strip layer), where it is equal to  $\Delta\eta = 0.0025$ . **(b)**: Top view of the signal pads and the signal traces and shields from each layer. The signals are extracted to the front for the first three layers, and to the back of the detector for the remaining five layers.

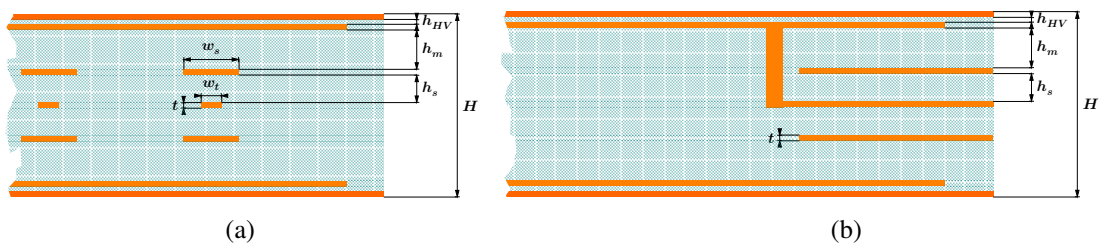


Fig. 7.11: Cross-sections of the read-out PCB: **(a)**: Cross-section perpendicular to the signal traces: High voltage layers create an electric field in the liquid argon gap of the detector. The signal pads, located in the layer below, collect the ionisation signal which is extracted to either back or front of the electrode by the signal traces. In between the pads and the traces there is a layer of shields that minimise the cross talk from the pads to the signal traces connected to different pads. **(b)**: Cross-section parallel to the signal traces: One signal pad is connected to a signal trace by vias inside the PCB.

Since the electronic noise of a calorimeter cell is proportional to its capacitance, how much the cell capacitance increases due to the shields inside the PCBs was checked. The capacitance of the signal pads to the shields  $C_s$  are in parallel to the capacitance of the LAr gap  $C_d = \epsilon_{\text{LAr}}\epsilon_0 A/d$  of width  $d$  and area  $A$  ( $\epsilon_{\text{LAr}} = 1.5$ ), and therefore needs to be added to the total cell capacitance. An approximation for

the capacitance of a microstrip line<sup>9</sup> summed to the gap capacitance  $C_d$  yields read-out cell capacitance (4 LAr gaps per read-out cell) of  $C_{\text{cell}}$  ranging from 100 pF to 500 pF at  $\eta = 0$  and up to 1000 pF at  $\eta = 1.5$ . Such a cell capacitance is similar to the cells of the ATLAS LAr calorimeter, although their size is much smaller. The calculation of the capacitance for the barrel detector is described in Section 7.3.2.1 and it is also explained how realistic electronic noise values for each cell are estimated and used for the performance simulation.

### 7.2.2.1.2 Optimisation of longitudinal layers

Due to the increase of the LAr gap with radius, the sampling fraction changes with depth. Fluctuations of the shower depth would therefore immediately translate into different reconstructed energies and hence a degraded resolution. The energy reconstruction must therefore take this into account and apply a corrected sampling fraction to energy deposits at different depths. Figure 7.12 and Table 7.3 show the energy resolution of electrons using different number of longitudinal layers with different sampling fractions. The values of the sampling fraction are extracted from the simulation by comparing the deposits in the active and the passive materials. Calibration of the shower energy using only one sampling fraction value leads to a high constant term  $c = 2\%$ . Using at least 8 longitudinal layers significantly improves the resolution ( $c = 0.6\%$ ). Therefore 8 layers are chosen for the FCC-hh EMB calorimeter. Dividing it into more layers does not significantly improve the resolution, whereas it would increase the number of read-out channels significantly.

Table 7.3: Energy resolution of electrons for different numbers of layers of equal thickness used for the cell energy calibration. The geometry layout used in this study assumed  $30^\circ$  inclination angle of absorber and readout plates from the radial direction (at the inner radius).

Number of layers	$a$ ( $\sqrt{\text{GeV}}$ )	$c$
1	$8.4\% \pm 0.7\%$	$2.03\% \pm 0.05\%$
2	$9.9\% \pm 0.5\%$	$1.35\% \pm 0.03\%$
3	$7.9\% \pm 0.3\%$	$1.02\% \pm 0.03\%$
4	$6.9\% \pm 0.3\%$	$0.71\% \pm 0.02\%$
8	$6.4\% \pm 0.2\%$	$0.56\% \pm 0.02\%$
15	$6.1\% \pm 0.2\%$	$0.51\% \pm 0.02\%$
30	$6.2\% \pm 0.2\%$	$0.46\% \pm 0.02\%$

The values of the sampling fractions obtained for each of the 8 detector layers in the current detector setup are presented in Fig. 7.13. The thickness of the first layer (presampler) is a factor of 4.5 smaller than other layers in order to provide an input to the correction for the energy deposited in the material in front of the detector, as explained in Section 7.4.1.1.1. Results for 50, 100 and 200 GeV electrons have been found to be similar and have been averaged. These values have been used for all performance simulations shown in this document. However, as also performed in ATLAS, an MVA based recalibration using shower depth and shower shape variables could be considered for the reconstructed clusters in order to improve the energy measurement further.

<sup>9</sup>The following approximation for a microstrip line on top of one ground shield has been used (see Ref. [135]):

$$C_s [\text{pF}/\text{cm}] = \frac{0.26(\varepsilon_r + 1.41)}{\log \frac{5.98h_m}{0.8w_s + t}} .$$



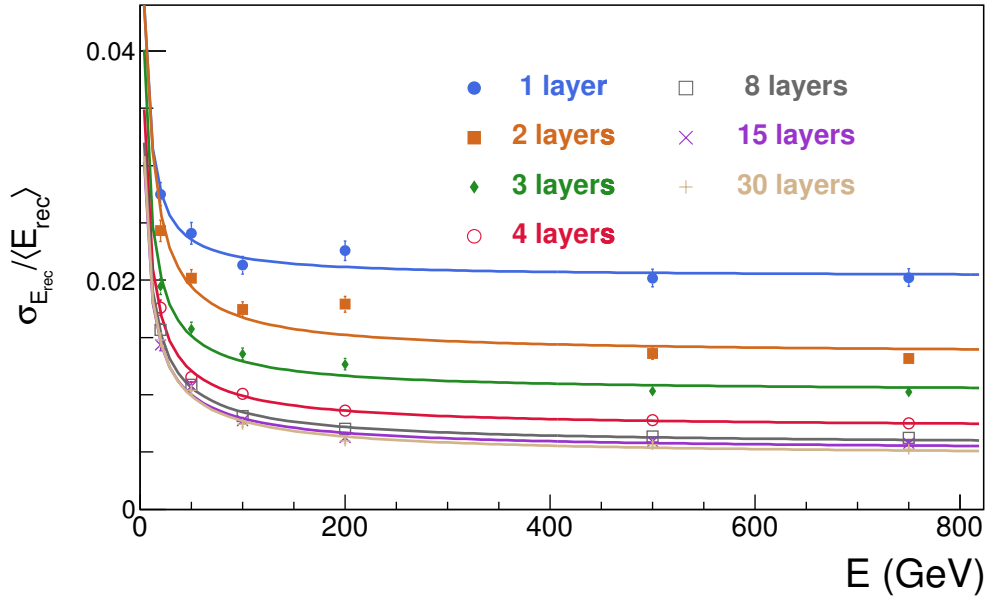


Fig. 7.12: Energy resolution of electrons for different number of longitudinal layers used for cell energy calibration. The geometry layout used in this study assumed  $30^\circ$  inclination angle of absorber and readout plates from the radial direction (at the inner radius). Furthermore, it was performed without the tracker in front and the cryostat in order to compare only the effect of calibration on the energy resolution. The barrel was divided into layers of identical thickness. Sampling and constant terms are listed in Tab. 7.3.

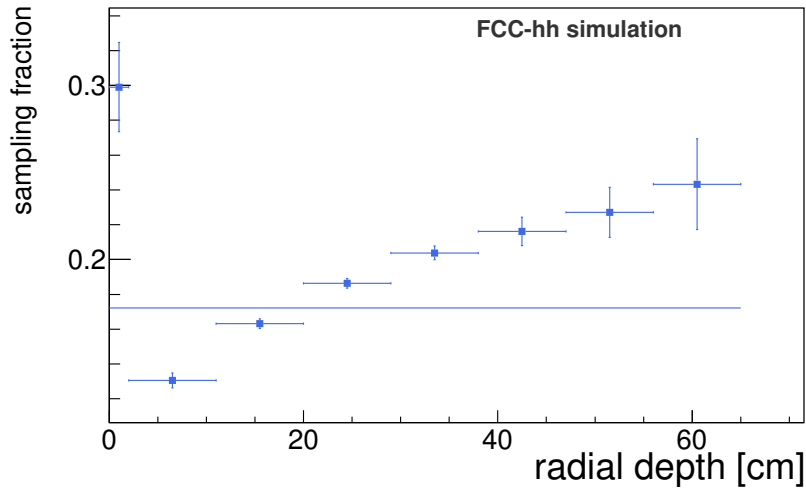


Fig. 7.13: Average sampling fraction ( $E = 50\text{--}200$  GeV) calculated from the energy deposited by electrons in each of the 8 layers of the detector. The horizontal line represents the average sampling fraction, obtained without longitudinal segmentation.

## 7.2.2.2 Endcap calorimeters

### 7.2.2.2.1 Geometry layout

Due to the radiation load, both the electromagnetic (EMEC) and the hadronic calorimeters (HEC) in the endcaps use liquid argon as the active medium. Both calorimeters share an endcap cryostat. The endcaps are located on both sides of the central barrel, from  $|z| = 5.3$  m to  $|z| = 8.3$  m. The outer radius of the endcaps is  $r = 2.7$  m, similar to the electromagnetic barrel calorimeter. The inner radius changes with  $|z|$  leading to a conical inner bore of the cryostat, allowing the active detector volume to

cover a pseudorapidity region up to  $|\eta| = 2.5$ . The cross section through the upper half of one endcap is presented in Fig. 7.14. The segmentation used in the simulation is summarised in Table 7.2 and follows the segmentation of the barrel region.

The layout of the detector is again inspired by the ATLAS calorimeters, but in the electromagnetic endcaps it also uses parallel discs of absorbers and readout electrodes instead of accordion-shaped electrodes and absorbers. The material and thickness of the absorbers differ for the electromagnetic and the hadronic part. The electromagnetic calorimeter is made of 1.5 mm thick lead discs, glued inside steel sleeves as described in detail for the barrel in Section 7.2.2.1. Between two absorbers, there are two liquid argon gaps,  $2 \times 0.5$  mm thick. The readout electrode, implemented as a seven-layer PCB as described in Section 7.2.2.1, is positioned in between the LAr gaps, providing the HV for the drift field inside the gap, and housing the read-out pads and signal traces for the read-out. The thickness of the drift gap is less than in the ATLAS detector (which has a 2.16 mm gap) because of the larger particle densities expected at FCC-hh which would lead to space-charge inside the drift gaps. The hadronic part of the detector uses copper as passive material, with 40 mm thick discs and  $2 \times 1.5$  mm liquid argon gaps. The thickness of the read-out electrode PCB is 1.2 mm, as in the barrel detector. The read-out electrodes are rather large disk-shaped panels in that design. A re-partitioning into smaller size electrodes will need to be studied as well as the exact layout of the signal traces inside the PCBs, to avoid the traces being too long which could lead to an attenuation of the signal.

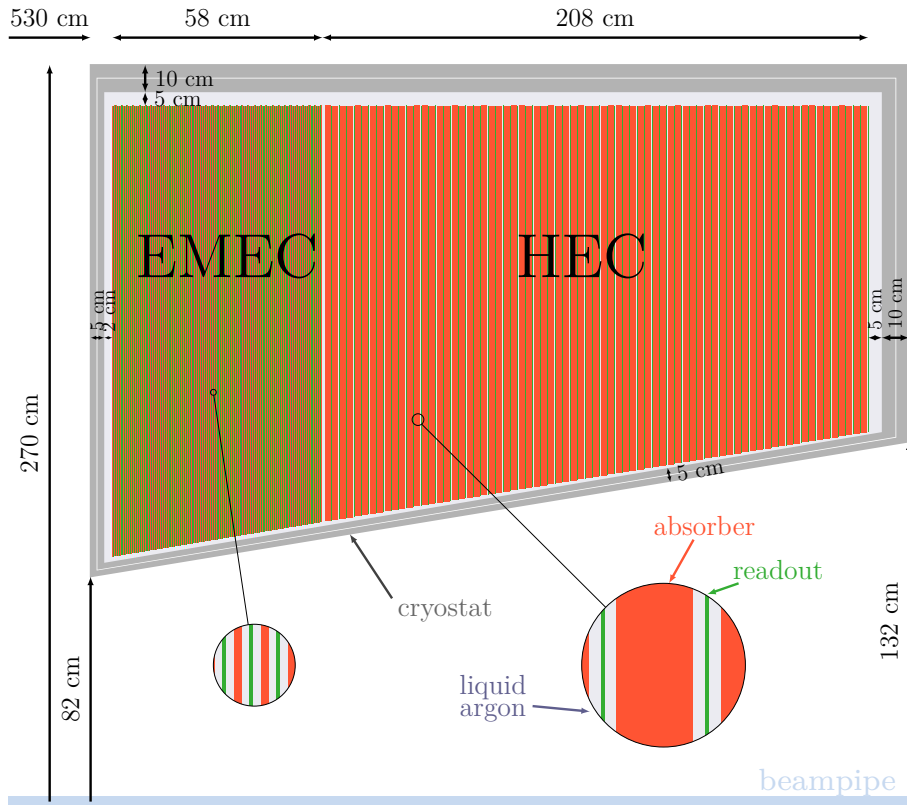


Fig. 7.14: Cross section of the calorimeter endcap. EM indicates the electromagnetic calorimeter, H the hadronic part. They differ in terms of the thickness and material of the absorber plates.

The ratio of active to passive material in this detector is constant, therefore the energy calibration could be performed using one calibration constant. The sampling fraction is equal to  $f_{\text{sampl}} = 0.072$  for the electromagnetic endcap and  $f_{\text{sampl}} = 0.030$  for the hadronic endcap.

### 7.2.2.3 Forward calorimeters

#### 7.2.2.3.1 Geometry layout

As shown in Table 7.1 the forward calorimeters (EMF and HF) will have to withstand an unprecedented integrated ionising radiation dose of up to 5000 MGy and a 1 MeV neutron equivalent fluence of  $5 \times 10^{18} \text{ cm}^{-2}$ . This goes far beyond the specifications of any currently operating detector system, e.g. the forward calorimetry at HL-LHC will experience 1 MeV neutron equivalent fluence of up to  $3 \times 10^{17} \text{ cm}^{-2}$ . Some ATLAS calorimeter components were tested up to such fluence and the results are summarised in Section 2.5 of Ref. [136]. However, it is rather difficult to extrapolate by an additional factor of 15 from existing experience. Very careful irradiation studies will therefore be needed to qualify all the materials used for these detectors. As LAr calorimetry is based on a liquid active material, we believe that it has the best chance to withstand this hostile radiation environment. The proposed layout of the forward detector is similar to the layout of the calorimeter endcaps, with the dimensions adapted as presented in Fig. 7.15. The forward calorimeter is positioned far from the centre of the detector, from  $|z| = 16.5 \text{ m}$  to  $|z| = 19.5 \text{ m}$ . The outer radius is  $r = 3.6 \text{ m}$ , while the inner radius of the cryostat is just outside the beam-pipe ( $r \approx 5 \text{ cm}$ ), so that the active volume of the detector covers the region up to  $|\eta| = 6$  ( $r \approx 8.2 \text{ cm}$  for  $|z| = 16.5$ ). The segmentation used in the simulation is summarised in Table 7.2 and it follows the granularity of the hadronic barrel for both the electromagnetic and hadronic detectors.

The absorbers are proposed to be copper for the forward region in both parts of the calorimeter (EMF and HF). In order to avoid ion build-up due to large energy densities, the thickness of LAr gap is reduced to 0.1 mm. The thickness of the absorber discs in the electromagnetic part is 0.9 mm in order to keep the sampling fraction similar to that in the ATLAS forward detector. In the hadronic part, the copper discs are 40 mm thick. Such a design of parallel plates could turn out to be difficult to implement due to the large discs. An alternative design—inspired by the ATLAS forward calorimeter—could consist of copper rods inside a copper matrix forming a 100  $\mu\text{m}$  drift gap in between. The values of the sampling fraction for the electromagnetic and hadronic forward calorimeters are equal to  $f_{\text{sampl}} = 0.0033$  and  $f_{\text{sampl}} = 0.00083$ , respectively.

#### 7.2.2.4 Cryostats

These calorimeters will be housed in the five different cryostats that can be seen in Fig. 7.6. The barrel EM calorimeter sits inside a 10 m long cylindrical barrel cryostat (internal volume of  $\sim 110 \text{ m}^3$ ), the EM endcaps and hadronic endcaps are housed in two cylindrical endcap cryostats with a conical inner bore (internal volume of  $\sim 50 \text{ m}^3$  each) and the forward calorimeters will be located inside two cylindrical forward cryostats (internal volume of  $\sim 110 \text{ m}^3$  each). Very similar, though slightly smaller cryostats were designed for the ATLAS LAr calorimeters. They are built as double-vessel aluminium cryostats (see Ref. [134]). It is very likely that a similar design, scaled to the new dimensions, could be used for the FCC-hh LAr calorimeters. However, R&D has started within the CERN EP R&D programme, to develop a cryostat with the necessary mechanical properties and lowest possible material budget of the inner bore. The outer vessels of the barrel and endcap cryostats will be situated between the EM calorimeter and the hadronic calorimeter, and therefore should also be kept thin to ensure that even lower energetic particles will reach the hadronic calorimeter despite the strong magnetic field.

The barrel calorimeter is immersed in a 10 m long cylindrical cryostat with an inner bore of 185 cm radius and an outer radius of 272 cm, that has to support the  $\sim 350$  tons of the barrel calorimeter (including  $\sim 275$  tons of absorber material) immersed in a LAr bath of  $75 \text{ m}^3$  weighing  $\sim 100$  tons. To minimise the material upstream of the EM calorimeter, the inner bore of this cryostat needs to be as thin as possible in terms of radiation lengths. In the simulation the two vessels of the cryostat have been assumed to be  $2 \times 25 \text{ mm}$  thick aluminium in the inner bore, and  $2 \times 50 \text{ mm}$  aluminium at the outer detector radius. Space between the active detector and the cryostat is filled with liquid argon and is reserved for the necessary services.

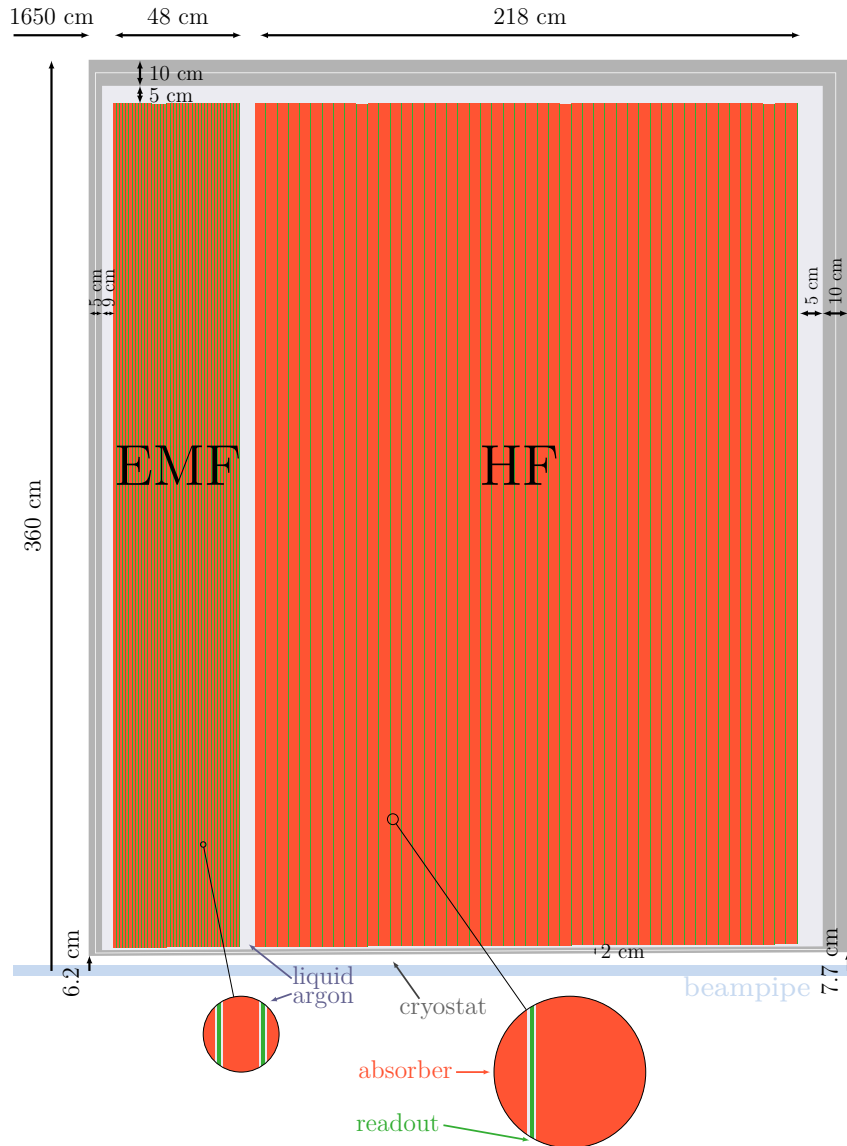


Fig. 7.15: The cross section view of the forward calorimeter. EMF indicates the electromagnetic calorimeter, and HF the hadronic part. They differ in terms of the thickness of the absorber.

The two endcap cryostats (see Fig. 7.14) have also been assumed to have  $2 \times 25$  mm thick aluminium front and inner bore walls and thicker walls behind the calorimeters. The cryostats for the forward calorimeters have been assumed to have a very thin inner bore walls to allow space for the beam pipe (see Fig. 7.15). A detailed engineering design needs to be performed for all of these cryostats taking into account the huge load they have to support.

### 7.2.2.5 Cryostat feedthroughs

The number of read-out channels of the LAr calorimeters described above is not yet fixed, but needs to be optimised after detailed simulations evaluating the granularity needed for pile-up rejection, particle identification and particle flow techniques. However, we anticipate that the number of channels will strongly increase in comparison to current noble liquid detectors (e.g. ATLAS LAr calorimeter, 183 000 channels). Assuming a granularity as summarised in Table 7.2, signals of  $\sim 2$  million channels will have to be fed out of the five cryostats. Whereas e.g. in ATLAS the density of signal cables at the

feed-through flange is about 6–7 per cm<sup>2</sup> (ATLAS is using glass sealed gold pin carriers), values of up to 20–50 signals per cm<sup>2</sup> need to be achieved to accommodate the higher number of read-out channels. New ways of sealing these cables have to be studied. Epoxy based sealing technologies exist, also seals of strip lines using solder, or feeding the signals through sealed PCBs can be done. All these technologies will need to be developed further to achieve the cable density and reliability required for 20 years of operation. An R&D project has been started to survey existing techniques, to design and construct test feed-throughs with promising techniques and to further optimise these techniques. Close collaboration with industry and interested laboratories will be very important. Cold tests and electrical tests of these test-feed-throughs have to be carried out to check their cryogenic reliability and electrical properties. The signal feed-throughs of the barrel cryostat will sit at both ends of the cryostat (highest  $|z|$ ) on the outer warm vessel and will lead the signals into read-out boxes with read-out electronics that will be located in the gap between the hadronic barrel (HB) and extended barrel (HEB). The feed-throughs on the endcap cryostats could be located on the forward wall of the endcap cryostats at the largest possible radius. The feedthroughs of the forward cryostats could be located on the outer radius.

As well as the signal feedthroughs, there will be at least two HV feedthroughs per cryostat, bringing the HV for the drift gaps into the cryostats. The proximity of the cryogenic system will also use several cryogenics feedthroughs per cryostat for controlling and monitoring cryostat operation.

#### 7.2.2.6 Read-out electronics

Particles crossing the LAr filled drift gap will ionise the argon atoms. Due to the high electric field ( $\sim 1$  kV/mm) the electrons will immediately be separated from the Ar ions and both will start to drift inside the electric field. This drift of charges will induce triangular current signals in the read-out pads of the electrodes dominated by drift of the electrons (typical drift time of  $\sim 200$  ns/mm<sup>10</sup>).

Based on various considerations, in particular maintainability and long-term reliability in the strong radiation environment of FCC-hh, it is planned to have all active read-out electronics located outside the cryostats. ATLAS has chosen this approach for the EM calorimeter and has proved that excellent noise performance can be reached despite the long cable connections from the detector cell outside the cryostat to the preamplifier. In ATLAS the signal to noise ratio of a muon (MIP) in the second (first) calorimeter layer in ATLAS is  $\sim 7$  ( $\sim 3$ ) [137], respectively. It should be noted that measurement of the response to muons per layer is extremely useful to inter-calibrate the different longitudinal layers independently from the exact knowledge of the material in front of the calorimeter. In the proposed calorimeter design the signal-to-noise ratio of muons per layer will degrade due to longer cables (stronger attenuation), and smaller longitudinal layer dimensions, however due to PCB electrodes, comparable cell capacitances to those of ATLAS could be achieved. The read-out electronics will be located in boxes mounted directly on the read-out feedthroughs. The signals will be guided on transmission lines through the read-out electrode PCBs and then on coaxial cables from the detector to the feedthroughs. The impedances  $Z$  of the transmission lines must accurately match the preamplifier input impedance  $Z_{\text{pa}}$  that defines the preamplifier time constant  $\tau_{\text{pa}} = C_{\text{cell}}Z_{\text{pa}}$ , with  $C_{\text{cell}}$  being the cell capacitance. As described in Section 7.2.2.1 transmission lines in the range of  $25 \Omega \leq Z \leq 50 \Omega$  seem adapted for the cell capacitance expected.

Like in ATLAS, bipolar shaping seems to be the optimal choice [134]. Due to the signal shape that has a zero net area, the average signal in any read-out cell is also zero except for settling effects at the beginning of bunch trains. Pile-up signals from the same bunch crossing and pile-up from previous bunch crossings will therefore cancel to zero on average. However, due to the statistical nature of the proton collisions, the particles created and their energy deposits inside the calorimeter, pile-up will induce fluctuations of the baseline that can best be described as pile-up noise. Section 7.3.2.2 will describe how this pile-up noise was estimated for the FCC-hh simulations.

<sup>10</sup>The exact drift time will depend on the LAr temperature, the exact field and the gap width.

The shaping time will need to be optimised taking into consideration the electronics noise, which decreases with higher shaping time, and the pile-up noise, which increases with higher shaping time. Also, the series noise contribution from the additional capacitance of the long transmission lines of impedance  $Z$  can only be neglected if  $C_{\text{cell}}Z \gg \tau_{\text{sh}}$ . For ATLAS and a pile-up of  $\langle\mu\rangle = 25$  an optimum around  $\tau_{\text{sh}} = 45$  ns was found [134], but due to the much higher peak pile-up expected at FCC-hh and the constraint mentioned above, the best choice will likely be at lower values. For the simulation results presented, we assumed that a similar shaping as in ATLAS could be achieved. The shaped signals will be digitally sampled with the bunch crossing frequency (40 MHz) or twice this frequency, within a dynamic range of 16 bits and sent via optical links into the counting room. There, these data can be used as input to the hardware trigger and will, after a positive trigger decision, be written to disk.

With this architecture, which has also been chosen for the HL-LHC upgrade of the ATLAS LAr calorimeters [136], the full history of energy deposits is available in the counting room and therefore could be used to actively subtract the impact of out-of-time pile-up from preceding bunch crossings. Signal reconstruction algorithms based on this idea are currently being developed and tested for HL-LHC [136].

Since a precise time measurement of energy deposits inside the calorimeter will be essential to reduce impact of pile-up, the design of the read-out electronics will need to take into account the precise timing requirements at the 30 ps level. In comparison, the ATLAS LAr calorimeter achieves a timing resolution of  $\mathcal{O}(65)$  ps for high energetic clusters. The timing resolution is discussed in more detail in Section 7.4.1.4.

## 7.2.3 Scintillator tile calorimeters

### 7.2.3.1 Hadronic barrel and extended barrel

Based on the reduced radiation requirements behind the EM barrel calorimeters and on cost and performance considerations, a hadronic calorimeter based on scintillating tiles is proposed for the barrel (HB) and extended barrels (HEB) of the FCC-hh reference detector. The calorimeter design has been inspired by the ATLAS Tile Calorimeter [138].

The hadronic ‘tile’ calorimeter is a sampling calorimeter using stainless steel, lead and scintillating plastic tiles, with a ratio between volumes of 3.3:1.3:1. The choice of mixing different absorber materials will be further discussed in Section 7.2.3.5. The central barrel and two extended barrels are divided into 128 modules in the  $\phi$  direction. The modules have 10 and 8 longitudinal layers in the central barrel and extended barrels respectively. The geometry of the barrel module is sketched in Fig. 7.16 and a summary of the main dimensions and parameters is given in Tables 7.1, 7.2 and 7.4. Each module contains two scintillating tiles per longitudinal layer, which will be separated by a reflective material and read out into two separate silicon photomultipliers (SiPMs) by 1mm diameter wavelength shifting (WLS) fibres. This increases the granularity in  $\phi$  by a factor of two to  $\Delta\phi = 2\pi/256 \approx 0.025$ . The orientation of the scintillating tiles perpendicular to the beam line, in combination with wavelength-shifting fibre readout, allows almost seamless azimuthal calorimeter coverage. For fibre transport and cross-talk suppression between tiles, plastic profiles similar to those shown in Fig. 7.17a and 7.17b will be integrated along the outer sides of each module. A module consists of 0.5 cm thick master stainless steel plates, lead spacers of 0.4 cm thickness, and 0.3 cm thick scintillating tiles, as illustrated in Fig. 7.16. These tiles are 6.9 cm to 11.3 cm in length, and 10, to 15, to 25 cm in height, increasing with the radius and layer. The sequence of scintillator and Pb tiles repeats with the layer radius, see the zoom in Fig. 7.16. The granularity provided by a one-to-one readout of scintillator tile and SiPM results in a  $\eta$  granularity of less than 0.006. However, a granularity of 0.025 is expected to be sufficient and thus is the default choice and the merging of the individual SiPM signals that form one cell will be done at the read-out level. Simulation studies of the angular resolution support this choice, and are discussed in detail in Section 7.4.2.2.3.

The extended barrel consists of two parts, with only the second part covering the full radial space

of 1.74 m. The first part is only 30 cm long (along beam direction), which ensures that there is enough space for the supports of the cryogenics system needed for the LAr calorimeter in front. The gap between the barrel and the extended barrel could have additional instrumentation of thin scintillator counters to partially recover the performance in a region occupied by services and electronics of the electromagnetic calorimeter. The WLS fibre readout not only ensures optimal space usage of active and absorber material and thus very homogenous calorimeter response, but allows the readout electronics to sit at the outer radius, in an area of moderate radiation levels. These reduced radiation levels at the outer radius lie within the tolerances for current technologies of readout electronics and SiPMs. An additional advantage is the easy access to the electronics, which allows for upgrades in maintenance periods.

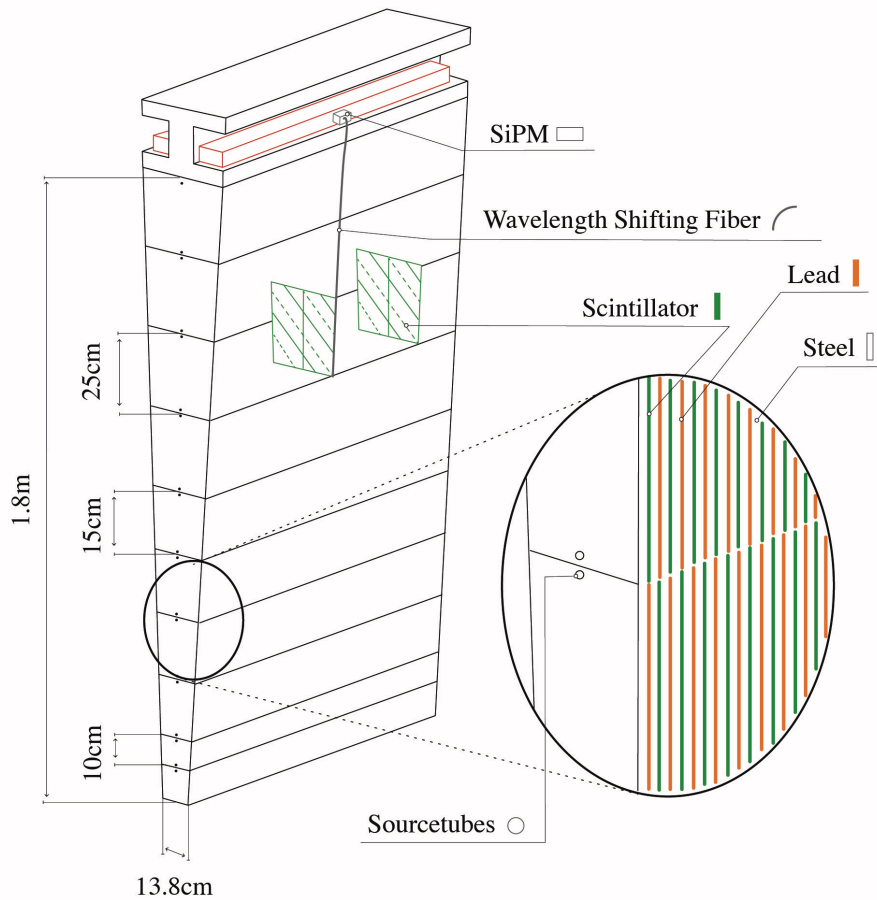


Fig. 7.16: Schematic of one module of the hadronic barrel Tile calorimeter. The optical components (the two scintillating tiles per layer, wavelength shifting fibre and the SiPM) are shown. The tubes designed for a movable radiation source (for details about the calibration system see Sec. 7.2.3.4) are also sketched.

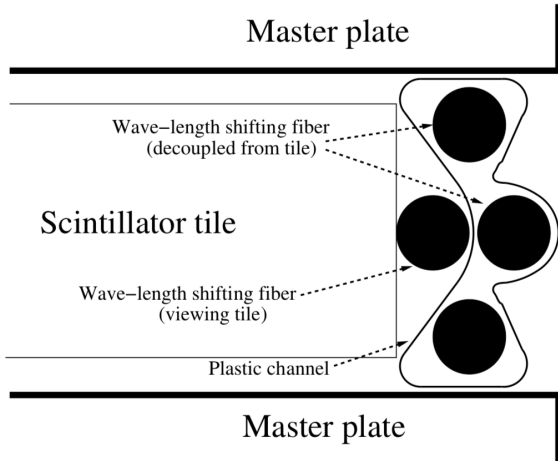
### 7.2.3.2 Mechanics

The mechanical structure has been designed and found to be mechanically feasible to construct. A cut through of the barrel and extended barrel structure is displayed in Fig. 7.18a. The outer steel structure housing the readout electronics and yielding mechanical support is shown in red in Fig. 7.18b. These studies include an estimate of the total weight of the whole calorimeter, which includes the scintillating

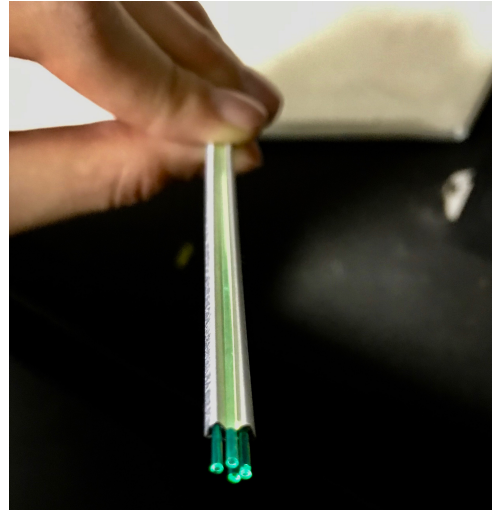


Table 7.4: Summary of tile calorimeter specifications: granularity, longitudinal layers in the barrel (HB) and extended barrel (HEB), and nuclear interaction length.

Granularity	Long. layers HB (HEB)	$\langle\lambda\rangle$ [cm]	$\#\lambda$ ( $\eta = 0$ )
Default: $\Delta\eta = 0.025$ , $\Delta\phi = 0.025$	10 (8)	21.68	8.3
Full: $\Delta\eta < 0.006$ , $\Delta\phi = 0.025$			



(a)



(b)

Fig. 7.17: (a) Schematic of profile to connect WLS fibres with scintillating plastic tiles and transport towards outer radius. [138] (b) Picture of fibre filled plastic profile as used in the ATLAS TileCal.

tiles as well as the outer steel support structures. In total the HB and HEB will weigh approximately 4.4 kt, see Table 7.5. The central barrel consists of 128 modules of 21 t each, weighing in total 2.7 kt.

### 7.2.3.3 Light collection, readout and electronics

The incredibly challenging environment of 100 TeV centre-of-mass proton collisions every 25 ns with up to  $\langle\mu\rangle = 1000$  collisions per bunch-crossing, sets stringent requirements on the sensitive material as well as the signal readout devices and electronics. The maximum radiation dose to be expected in the HB region is 8 kGy for the scintillating plastic tiles and WLS fibres, see Table 7.1. Ongoing R&D on radiation hard scintillator for the upgrades of the LHC experiments show promising results and prove that these technologies will be able to withstand the radiation levels expected at the FCC-hh [139].

The scintillation light guided through the WLS fibre is read out by silicon photomultipliers (SiPMs), which are matrices of single-photon avalanche diodes operated in Geiger mode. These devices allow single photon detection, and achieve photon detection efficiencies (PDEs) between 20 and 60%. Each scintillating tile will be connected via a WLS fiber to one SiPM. The single SiPMs will be arranged within arrays on PCBs, digitised, summed and sent via optical links to the counting room where they can be used for the hardware trigger and, after a positive trigger decision, will be written to disk.

The radiation levels expected at the outer radius of the hadronic barrel are of the order of  $10^{11}/\text{cm}^2$  1 MeV neutron equivalent fluence. The resulting damage to the silicon substrate and the effect on the dark count rate, leakage current, over voltage, and PDE has been studied in the context of the CMS

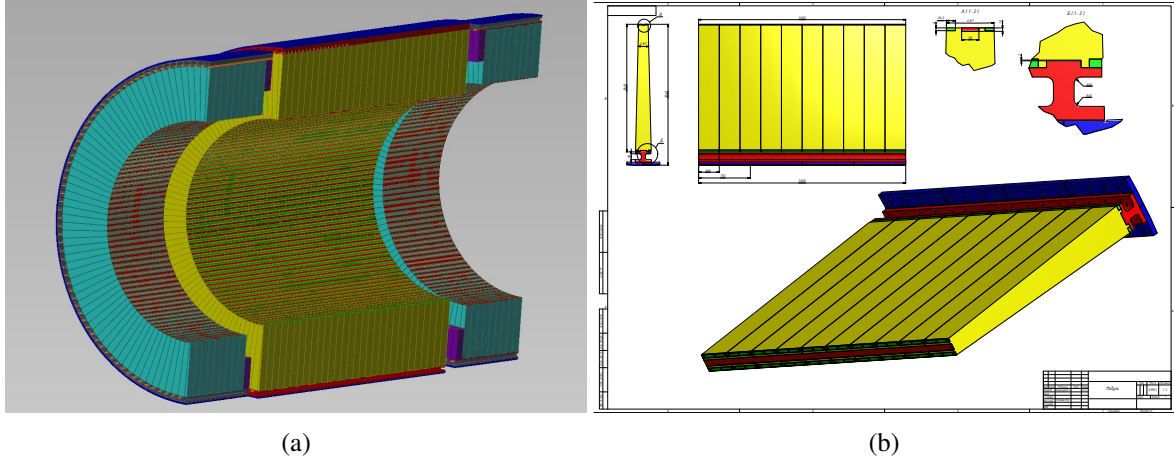


Fig. 7.18: Technical drawings of the hadronic barrel (HB) and extended barrel (HEB). (a) Half of full calorimeter, with the division of the HEB in part 1 (purple) and part 2 (turquoise). (b) Detailed view of one HB module.

Table 7.5: Summary of dimensions and total weight of the HB and HEB; one HB module weighing  $\sim 21$  t.

	Material	Volume [m <sup>3</sup> ]	Weight [t]
	Pb	76.5	845
	Scintillator	57.4	59
	Steel plates	193.8	1521
	Steel support	39.1	307
<b>HB</b>			<b>2732</b>
	Pb	22.8	258
	Scintillator	17.0	18
	Steel plates	57.8	453
	Steel support	13.8	108
<b>1 <math>\times</math> HEB</b>			<b>837</b>
<b>Total</b>			<b>4406</b>

hadronic calorimeter upgrade for the HL-LHC and proven to function up to  $2.2 \times 10^{14}$  n/cm<sup>2</sup> [140]. Nonetheless, the strong temperature dependence of these devices will require either temperature control or cooling and precise temperature monitoring.

First tests have started at the single channel level, focusing so far on the response of the optical components used in the ATLAS tile calorimeter: scintillating tiles made of polystyrene doped with 1.5% pTp and 0.04% POPOP and double cladding Y11 wavelength-shifting fibres from Kuraray [141].

Tiles were cut to the dimensions of the first and tenth FCC-hh HB layer. These tiles are then coupled to WLS fibres of the required length by contact with one tile edge, and wrapped in tyvek® [142], to enhance light collection efficiency. The right-angled trapezoid surface of the tested tiles is scanned using a Sr<sup>90</sup> source mounted on a 2D stage. These tests focused on the response uniformity, fibre coupling, fibre length and wrapping options. The attenuation length of the WLS fibres is  $> 2$  m, thus acceptable for the transport of the light produced in the first HB layer tiles at the inner-most radius. With the scintilla-

tion light collected by the WLS fibre of 1 mm diameter on one side of the tile, as planned for the FCC-hh TileCal modules, the WLS fibres are connected by simple contact to a  $1 \times 1 \text{ mm}^2$  multi-pixel photon counter (MPPC)<sup>11</sup>. The SiPM output signals are integrated over  $\sim 1 \text{ ms}$ , and read out with a multimeter. Different wrapping materials and configurations have been studied, ranging from simple back-reflection on a WLS fibre plastic profile (shown in Fig. 7.17b) on the opposite tile edge, up to full tyvek wrapping. Figure 7.19a shows the measured response over the full tile area with a spread in response of  $< 5 \%$  (including a reflective material on the opposite tile edge to the readout fibre). The attenuation length  $L_{\text{att}}$  of the tile is determined from the fit of the response  $\langle S/N \rangle$  to an exponential function  $I_0 \cdot \exp(-\Delta x/L_{\text{att}})$ , as a function of the distance from the readout tile edge  $\Delta x$ , see Fig. 7.20. The response height is measured in a quantity related to the signal to noise ratio, by the normalisation of the measured charges to the measurement points outside the tile volume. The attenuation length in case of layer #1 and fully wrapped tile reaches 90 cm, with a S/N ratio of about 6.7. These results are comparable with previous measurements using the standard ATLAS Tile PMT readout. The distributions of the response for the different tile configurations are displayed in Fig. 7.19b, and the mean values, as well as the widths, are summarised for both tile types in Table 7.6.

Table 7.6: Summary of uniformity tests for different tile configurations for tile sizes in the first (#1) and last (#10) HB layer. Profile stands for back-reflection on a WLS fibre plastic profile on the opposite tile edge.

	FCC tile #1				FCC tile #10			
	rms/mean	$\sigma/\mu$	$L_{\text{att}}$	$I_0$	rms/mean	$\sigma/\mu$	$L_{\text{att}}$	$I_0$
unit	%	%	cm		%	%	cm	
Naked tile	6.5	6.7	33	4.5	7.6	6.3	41	4.3
Naked tile + profile	4.5	4	52	5.9	-	-	-	-
tyvek + profile	3.9	3.1	66	6.6	-	-	-	-
Full tyvek	3.2	2.7	90	6.7	4.4	3.8	74	6.9

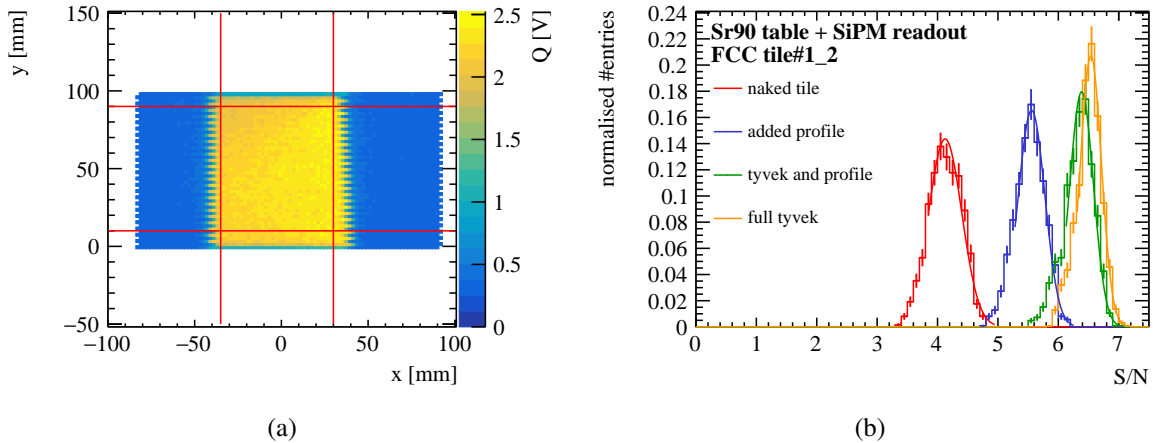


Fig. 7.19: (a) 2D scan of FCC tile at the inner most radius, wrapped in tyvek, and read out with a WLS fibre on the right side. The red lines indicate the area cut used for (b) the response distributions for different tile configurations. The curves correspond to Gaussian fits within a range of  $-1/ + 2 \sigma$ .

<sup>11</sup>Taken from Hamamatsu, type S12571-015C, [www.hamamatsu.com](http://www.hamamatsu.com).

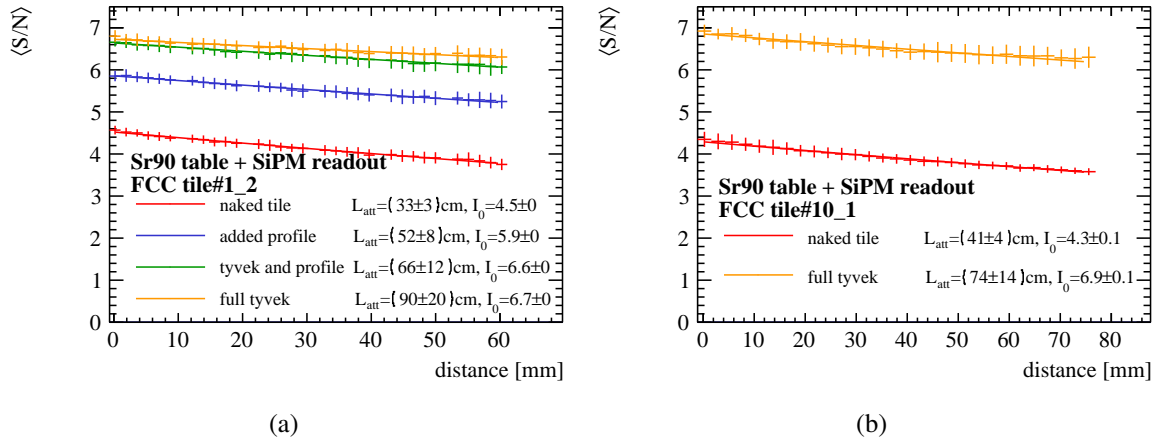


Fig. 7.20: The mean S/N ratio as a function of the distance to the readout tile edge of (a) a tile sized for the inner radius, and (b) a tile at the outer-most radius. The tile attenuation length was obtained through an exponential fit in each case. Error bars correspond to the rms of the response measured on a grid covering the surface of the tile.

While it is not yet possible to estimate the exact characteristics of the optical materials and SiPMs for the final detector, these preliminary tests are very encouraging and clearly indicate the usefulness of a campaign to optimise the design of various aspects of the optics system.

### 7.2.3.4 Calibration systems

#### 7.2.3.4.1 Caesium calibration

The caesium calibration system could be based on a movable  $^{137}\text{Cs}$   $\gamma$  source ( $E_\gamma = 661.7 \text{ keV}$ ) that is moved through the calorimeter body via source tubes penetrating all scintillators of a module (see source tubes in Fig. 7.16). The individual channel response to the energy deposits is used to equalise the global response and calibrate the calorimeter to the electromagnetic scale. ATLAS is successfully using this technique and achieves a precision of 0.5% [143].

#### 7.2.3.4.2 SiPM characterisation and calibration

The SiPMs will be characterised before being connected to the WLS fibres to determine the breakdown voltage, gain, and response-temperature coefficients. At the start, the operating voltage will be adjusted to equalise the response of all the cells. The inter-calibration of cells will be done with the caesium calibration system, while a fraction of the modules should be tested both with the caesium source and in testbeams (with electron and muon beams) to settle the absolute electromagnetic scale. The variations over time, to account for temperature variations, ageing and radiation damage will be monitored with the caesium calibration system. To monitor and calibrate the stability of the SiPMs a calibration system using LEDs or lasers injecting light into some fibres will be implemented. Together with the caesium calibration this will allow the variations of SiPMs from the optics system (tile and fibres) to be disentangled.

First measurements of the light yield for cosmic muons have proved the sensitivity and determined the expected response of the FCC hadronic barrel calorimeter to MIPs. Figure 7.21 shows the response of the smallest and largest FCC tile in first and tenth layer attached to 0.45 and 1.8 m long WLS fibre and read out by a SiPM (as described in Section 7.2.3.3). The measured light yield results in 5 to 7 photo-electrons per MIP. Additionally, it has been shown that cosmic muon runs can be used for calibrations of the SiPM gain due to the small responses within the range of a few photo-electrons. The single photon

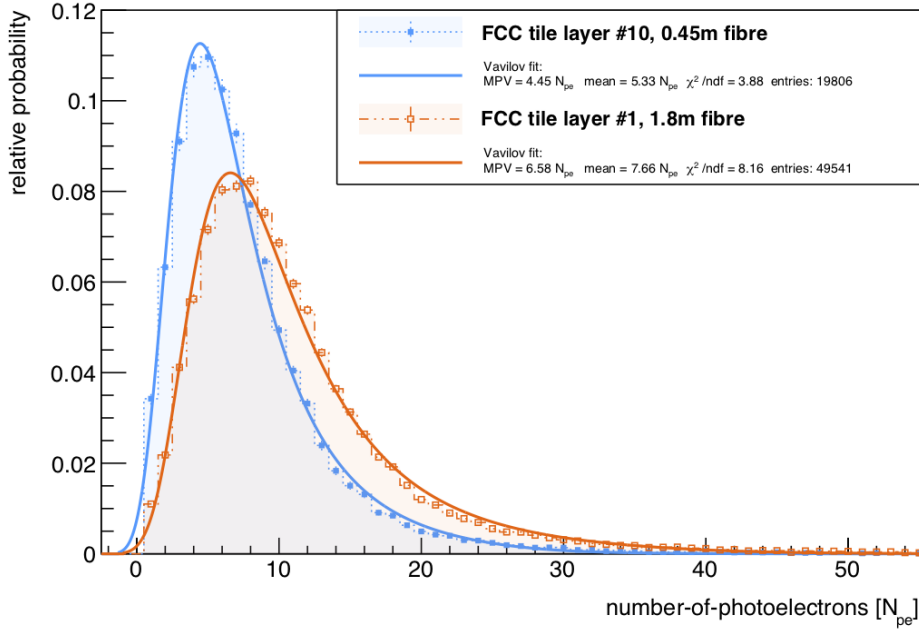


Fig. 7.21: Energy loss distribution of cosmic muons in the smallest and largest FCC-hh tile corresponding to inner-most and outer-most layer radius. The tiles were wrapped in tyvek and connected through 0.45 and 1.80 m long WLS fibres.

spectrum for  $\sim 230\,000$  events is shown in Figure 7.22. The spectrum is fitted with a generalised poisson function and enables the extraction of the gain from the distances between the peaks [144].

### 7.2.3.5 Optimisation of absorber materials

Even though the overall design follows the ATLAS scintillator-steel calorimeter, the FCC-hh HB and HEB use an absorber structure consisting of a major stainless steel structure (*masters*) with additional lead tiles (*spacers*), while keeping the absorber dimensions and thus the volume fractions the same. The partial replacement of stainless steel with lead absorbers, resulting in a calorimeter closer to compensation, aims to improve the hadronic performance in terms of linearity and resolution. The expected slight decrease of total calorimeter thickness in terms of nuclear interaction lengths  $\lambda$  and consequently poor containment of hadronic showers has been evaluated. The impact on the calorimeter depth (in units of  $\lambda$  and  $X_0$ ) has been studied for three absorber scenarios: full Steel (Sci:Steel with a ratio of 1:4.7), Pb mixture (Sci:Pb:Steel with a ratio of 1:1.3:3.3) and full Pb (Sci:Pb with a ratio of 1:4.7), see Fig. 7.23a and 7.23b. Whereas the decrease of depth in terms of interaction lengths is small, the increase in terms of radiation lengths is rather dramatic when adding more Pb. While this is not a problem for the calorimetry performance, this is a source of an increased amount of multiple scattering of the muons before reaching the muon system.

The depth in nuclear interaction lengths ( $\lambda$ ) needed to contain jets and hadronic showers up to 98% can be parameterised with a function similar to the one shown in Fig. 7.4a and the impact of the absorber choice on the jet and pion energies contained can be estimated by

$$E^{98\%} = \exp\left(\frac{\lambda - b}{a}\right), \quad (7.5)$$

with parameters  $a_{\text{jet}} = 0.495$ ,  $b_{\text{jet}} = 6.3$  for jets and  $a_{\pi^+} = 0.64$ ,  $b_{\pi^+} = 5.4$  for single pions, see Ref. [20]. Furthermore, the energy is estimated with an additional  $2\lambda$  of the EMB in front (see Sec. 7.2.2)

pulse-height spectrum - Hamamatsu S13360-1325CS

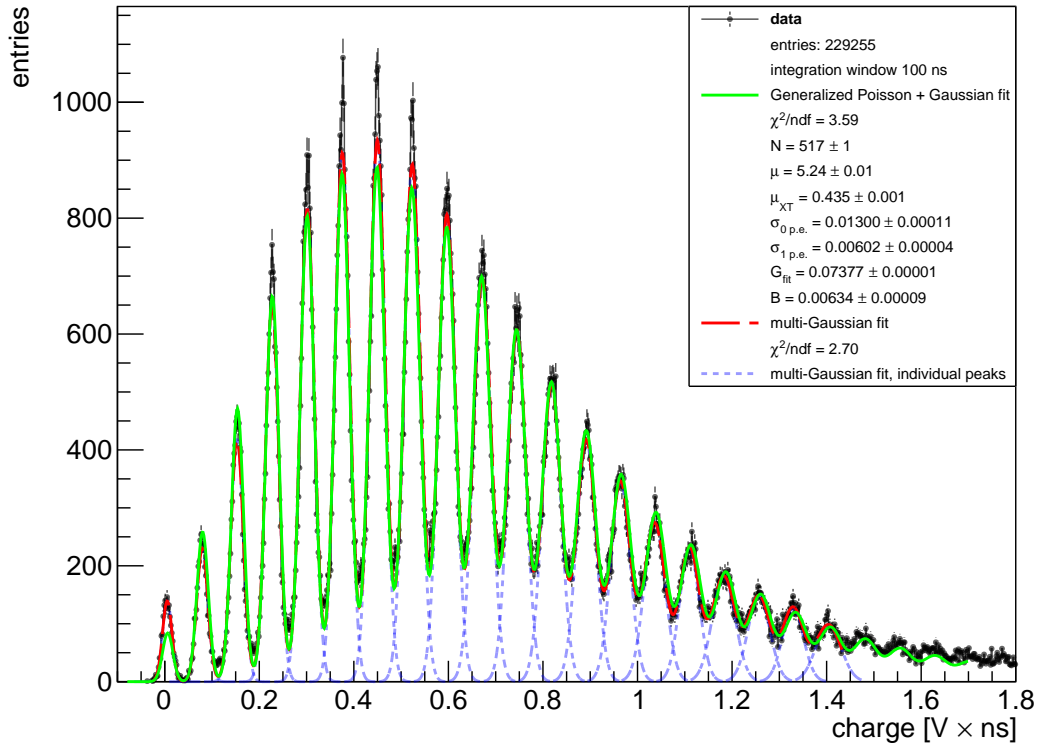


Fig. 7.22: Single photon spectrum of 230 thousand cosmic muon events in FCC-hh tiles in different configurations [144]. The green line corresponds to a generalised poisson fit.

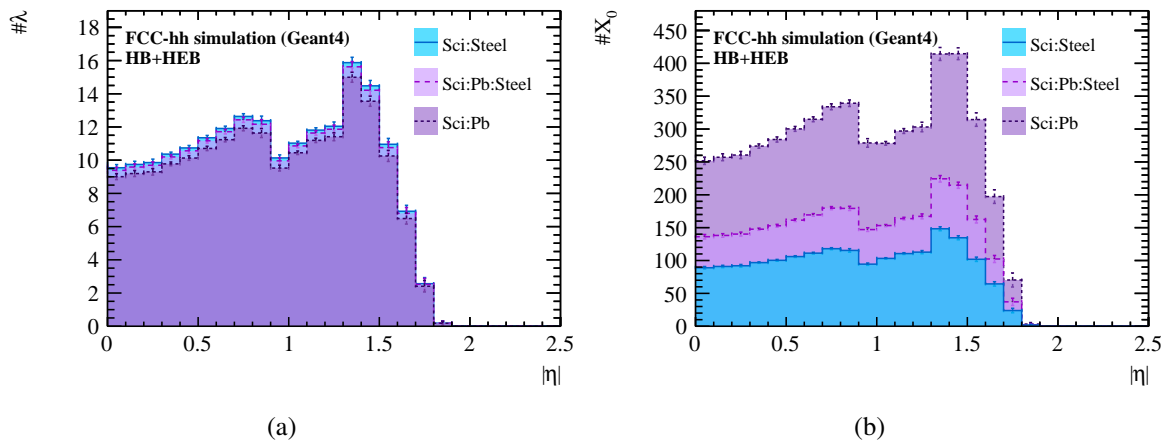


Fig. 7.23: Depth of the hadronic scintillator tile calorimeter as a function of  $\eta$  in nuclear interaction lengths (a) and radiation lengths (b). Shown is the impact of the material choice for full Steel:Sci, Steel:Pb:Sci mix and full Pb:Sci option. The material of the outer support structure is included.

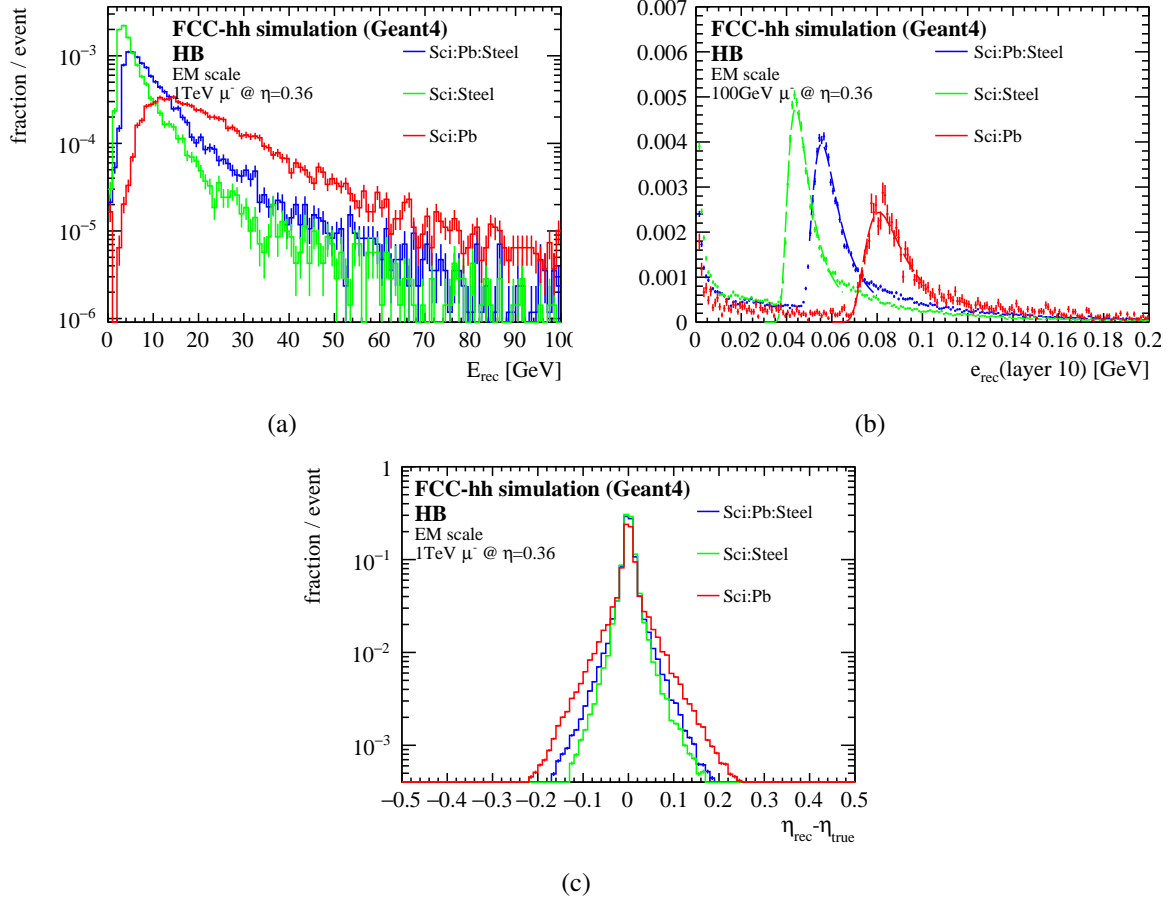


Fig. 7.24: Total energy loss (a), energy deposit per tile in last HB layer 10 (b), and angular distribution (c) of 100 GeV and 1 TeV muons in three HB absorber options.

and the resulting values are summarised for the three absorber scenarios in Table 7.7. As expected, it shows the strong increase of calorimeter depth in terms of radiation lengths with an increased amount of Pb absorbers (second column). This increase however, not only affects hadronic showers, but strongly impacts traversing muons which will experience increased multiple scattering, deteriorating the accuracy of the momentum measurement. The resulting effect on the muons' energy loss and angular distributions is shown in Fig. 7.24a, 7.24b, and 7.24c. The peak total energy loss of muons in the three scenarios is summarised in the fourth column of Table 7.7. Figure 7.24b shows the expected energy per cell in the last HB layer (layer 10) for 100 GeV muons. The most probable value of the energy measured ranges from 40 to 80 MeV, which is well above the expected electronic noise per cell of 10 MeV showing the calorimeter's sensitivity to MIPs.

The jet and hadronic shower containment is less affected by the proportion of lead due to the rather moderate decrease in depth in terms of nuclear interaction lengths with higher Pb content (third column). However, the detector response to hadronic showers is strongly affected by the higher atomic number of lead compared to iron, which suppresses the response to the electromagnetic component of the shower. Thus the intrinsic non-compensation  $e/h > 1$ , due to the partially invisible deposits of the hadronic shower components, can be brought closer to compensation. The effect of an  $e/h$  ratio closer to 1 (closer to compensation) can be seen in an improved energy resolution and linearity as shown in Fig. 7.26b. It should be pointed out that the constant term is better for the Sci:Pb:Steel option despite the reduced shower containment.



An example of the true energy deposited for electrons of 100 GeV is presented in Fig. 7.25a as a function of pseudo-rapidity. The dip around  $\eta = 1.2$  originates from the gap between the hadronic barrel and the extended barrel. The dependence of the sampling fraction on the incident angle  $\eta$  is given in Fig. 7.25b, and is determined for electron energies ranging from 10 to 1000 GeV. The modulation is due to the orientation of the tiles which is perpendicular to the beam axis and a distance of 18 mm between two adjacent tiles, but this is of no concern because most of the hadronic particles will start to generate showers in the electromagnetic calorimeter. The response for single pions in the HB standalone has been tested for the same  $\eta$  range, and the modulation has been found to be negligibly small. The resolution of single hadron energy is always shown in the following for an incident angle of  $\eta = 0.36$  to ensure that the response is unaffected by the geometry of the calorimeter. As discussed above, fluctuations in the response at  $\eta = 0$  are expected due to the perpendicular orientation of the absorber-scintillator structure.

Table 7.7: Summary of major parameters for three different absorber scenarios of the Tile HB/HEB.

	$\#X_0$ (active) $\eta = 0$	$\#\lambda$ (active) $\eta = 0$	$E_{\text{peak}}^\mu$ $\eta = 0.36$	$f_{\text{sampl}}$	$E_{\text{jets}}^{98\%}$	$E_{\pi^+}^{98\%}$
unit			GeV	%	TeV	TeV
Sci:Steel (B=4 T)	89 (78)	9.5 (8.4)	4	$3.14 \pm 0.01$ $3.22 \pm 0.01$	4.2	2.5
Sci:Pb:Steel (B=4 T)	136 (123)	9.4 (8.3)	5	$2.49 \pm 0.01$ $2.55 \pm 0.01$	3.1	2.1
Sci:Pb (B=4 T)	252 (242)	9.0 (7.9)	14	$1.75 \pm 0.01$	1.4	1.1

The energy deposited  $E_{\text{dep}}$  is calibrated to the electromagnetic (EM) scale:

$$E_{\text{rec}} = \frac{E_{\text{dep}}}{f_{\text{sampl}}} \quad (7.6)$$

with  $f_{\text{sampl}} = 2.55\%$  (3.22% for Sci:Steel) in a magnetic field of 4 T as shown in Table 7.7. The sampling fractions have been determined from simulations of electrons with energies from 20 GeV to 1 TeV within a pseudo-rapidity range of  $0.35 \leq \eta \leq 0.37$ . The uncertainties in  $f_{\text{sampl}}$  are determined as the standard deviation over the full energy range. To determine the mean response and resolution of the calorimeters, the  $E_{\text{rec}}$  distributions are fitted with a Gaussian in the range of  $\pm 2\sigma$  around the mean of the Gaussian. An example is shown in Fig. 7.26a.

The  $e/h$  ratio has been determined from a fit to the ratio of the mean calorimeter response to the true particle energy  $\langle E_{\text{rec}} \rangle / E_{\text{true}}$  as a function of energy (see the top plot in Fig. 7.26b). A perfectly linear and compensated calorimeter would make this curve flat at around 1 over the full energy range. The response shows values between 0.85 and 0.95 (0.95 and 0.98) for Sci:Steel and Sci:Pb:Steel respectively. This change in the response depends on the electromagnetic fraction, increasing with the pion energy. The linearity can be described with the formula [145]:

$$\frac{\langle E_{\text{rec}} \rangle}{E_{\text{true}}} = (1 - F_{\text{h}}) + F_{\text{h}} \times \left( \frac{e}{h} \right)^{-1}, \quad (7.7)$$

where the energy dependent hadronic fraction in a hadronic shower is written as

$$F_{\text{h}} = \frac{E^{k-1}}{E_0}, \quad (7.8)$$

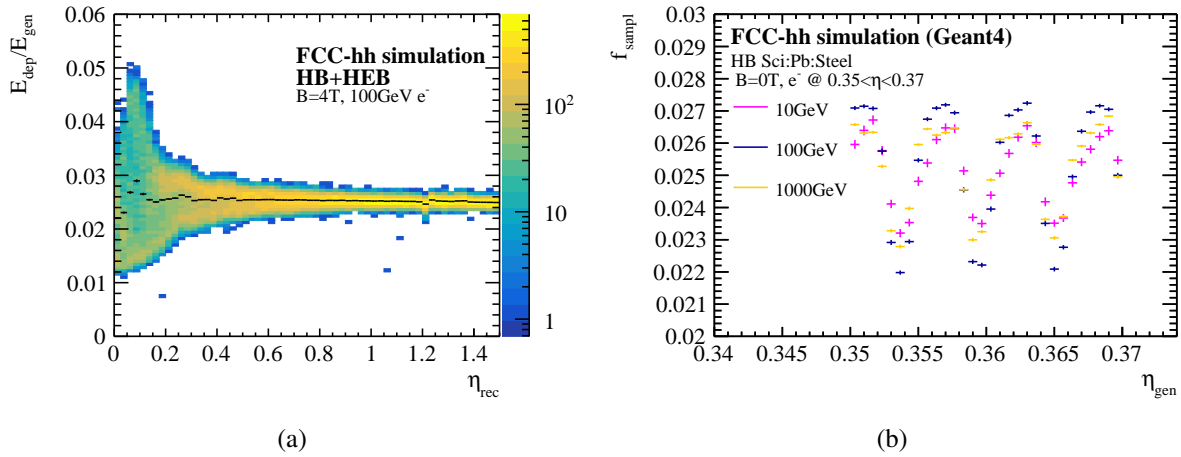


Fig. 7.25: (a) Response to 100 GeV electrons over the full  $\eta$  range of the HB. (b) Response modulations in the scintillating tiles as a function of  $\eta$ , in absence of a magnetic field.

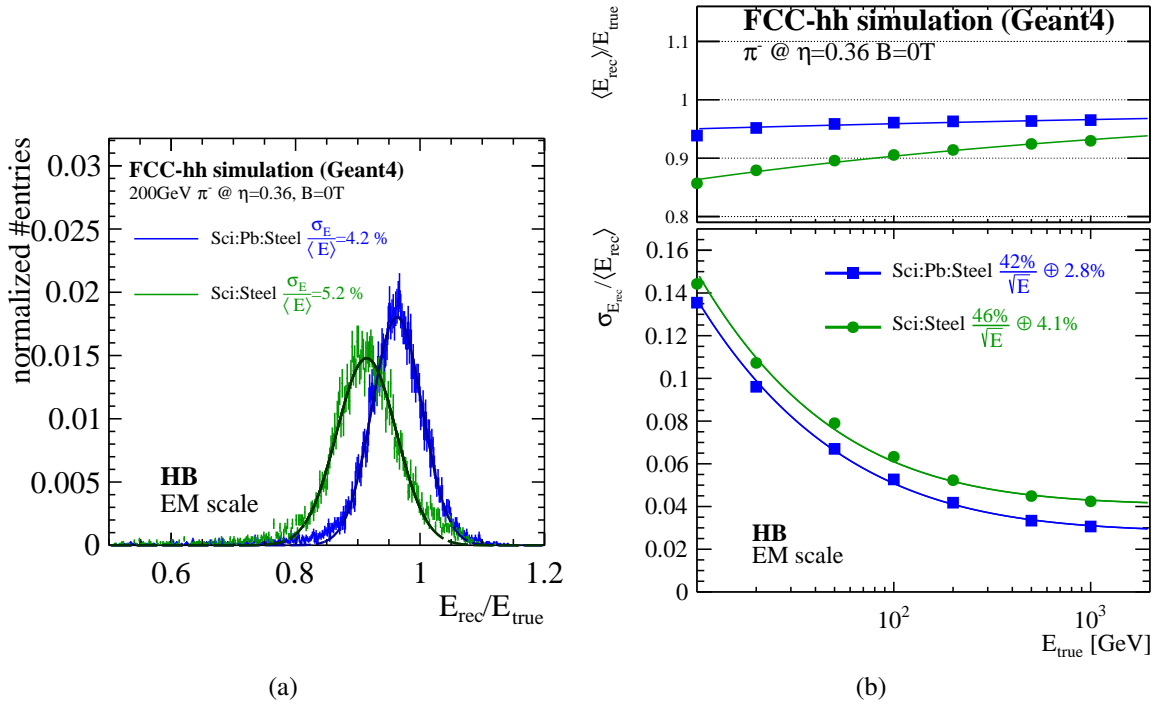


Fig. 7.26: (a) Reconstructed energy distributions for 200 GeV pion showers, where the curves show the Gaussian fit. (b) Single pion energy resolution (bottom) and linearity (top) for the FCC-hh HB for particles at  $\eta = 0.36$  in an energy range of 10 GeV to 1 TeV. The resolution is compared to the ATLAS-type design with a Sci:Steel ratio of 1:4.7.

with a fixed value of  $E_0 = 1$  GeV. The fits to the linearity are shown as straight lines in Fig. 7.26b, and the  $e/h$  ratios extracted are listed in Table 7.8.

Table 7.8: Summary of the resolution and linearity fit parameters in Fig. 7.26b.

	$e/h$	k	Resolution $\pi^- @ \eta = 0.36$
Sci:Steel	$1.24 \pm 0.01$	$0.849 \pm 0.002$	$46\%/\sqrt{E} \oplus 4.1\%$
Sci:Pb:Steel	$1.06 \pm 0.01$	$0.917 \pm 0.004$	$42\%/\sqrt{E} \oplus 2.8\%$

The excellent single pion energy resolution, as well as the improved linearity due to the  $e/h$  ratio close to 1, motivates the choice of the Sci:Pb:Steel mixture as the reference design for the hadronic scintillator calorimeters.

### 7.3 Software implementation

The detector simulation studies presented in this and the following section are performed within FCC-hh software framework (FCCSW) [146]. The geometry description is implemented using the DD4HEP toolkit [147]. GEANT4 [37] is used for the simulation of particle transport through the detectors. In this section we describe the reconstruction methods of particle energies in the detectors, introduced in Section 7.2. The handling of electronics and pileup noise will also be discussed.

#### 7.3.1 Digitisation and reconstruction

Particles traversing the detector material produce particle showers and deposit their energy. Calorimeters proposed for FCC-hh experiments are sampling calorimeters, where only a fraction of the energy ( $f_{\text{sampl}}$ ) is deposited inside the active material, and only these deposits are used for the energy reconstruction. In order to account for the energy deposited in the passive material, a calibration is made using the equation

$$E_{\text{cell}} = \frac{E_{\text{deposited}}}{f_{\text{sampl}}} . \quad (7.9)$$

Values of the sampling fraction depend on the calorimeter. For the EMB the sampling fraction depends on the layer of the detector and is described in Section 7.2.2.1.2. For the other calorimeter parts only one sampling fraction value is used as the ratio of the passive to active material is constant. The sampling fraction is estimated using a simulation registering energy deposits in both the active and the passive material and then calculating the fraction of energy inside the active material. These energy deposits then lead to a current signal in the LAr-based calorimeter or a light signal in the tile calorimeter which gets amplified, shaped and digitised. However, these steps are missing in the energy reconstruction at the moment and will need to be implemented later on<sup>12</sup>. The digitisation does not include any signal modelling of the readout systems. However, the saturation of the light output of scintillator materials used in the hadronic calorimeter in the barrel is included following Birk's law [148].

In addition to the simulated energy deposit, the readout from each calorimeter cell will be affected by electronic noise. We assume uncorrelated Gaussian noise for each read-out channel, with a mean centred around zero and a standard deviation estimated from prior experience, see Section 7.3.2 for a description of how the electronic noise is implemented.

<sup>12</sup>Note that the widening LAr gap with depth in the EMB will lead to different drift fields across the LAr gaps and hence different current responses for energy deposits depending on their depth. This effect decreases the effect of an increasing sampling fraction with depth. We therefore believe that neglecting this effect does not artificially improve the simulated energy resolution.

### 7.3.1.1 Clustering

In order to reconstruct the energy deposited by single particles in the calorimeters, clusters of read-out cells are created and summed. There are two types of reconstructions implemented in FCCSW, the main difference being the resulting final cluster shapes: the sliding window algorithm produces clusters of a fixed size (in  $\Delta\eta \times \Delta\varphi$ ) and a constant size in radius  $r$ . Alternatively topological clustering starts with a seed cell and then adds adjacent cells according to their energy deposits to form a cluster. As a result, each reconstructed cluster has a different shape. The sliding window algorithm can be used for both analogue and digital calorimeters. In the latter the number of hits in a read-out pad are used, instead of the energy. The sliding window algorithm is used for the reconstruction of photons and electrons, whereas the topological clustering is optimised for the reconstruction of hadrons and jets. Both clustering algorithms are based on the standard calorimeter reconstruction algorithms used at the ATLAS experiment [149, 150].

#### 7.3.1.1.1 Sliding window algorithm

The sliding window algorithm considers the calorimeter as a two-dimensional grid in  $\eta$ - $\varphi$  space, neglecting the longitudinal segmentation of the calorimeter. There are  $N_\eta \times N_\varphi$  elements building this space, each of size  $\Delta\eta^{\text{tower}} \times \Delta\varphi^{\text{tower}}$ . The energy of each tower is the sum of energies deposited in all cells within the tower.

First, the grid of towers is scanned for local maxima: A window of a fixed size  $N_\eta^{\text{seed}} \times N_\varphi^{\text{seed}}$  (in units of  $\Delta\eta^{\text{tower}} \times \Delta\varphi^{\text{tower}}$ ) is moved across the grid, as depicted in Fig. 7.27, so that each tower is once in the middle of the window. Since the windows are symmetric around the central tower, their sizes are expressed with an odd number of towers in each direction. If the sum of the transverse energy of towers within the window is a local maximum and is larger than the threshold  $E_T^{\text{threshold}}$ , a pre-cluster is created. The size of the seeding window and the threshold energy are optimised to achieve the best efficiency of finding pre-clusters while reducing the fake rate.

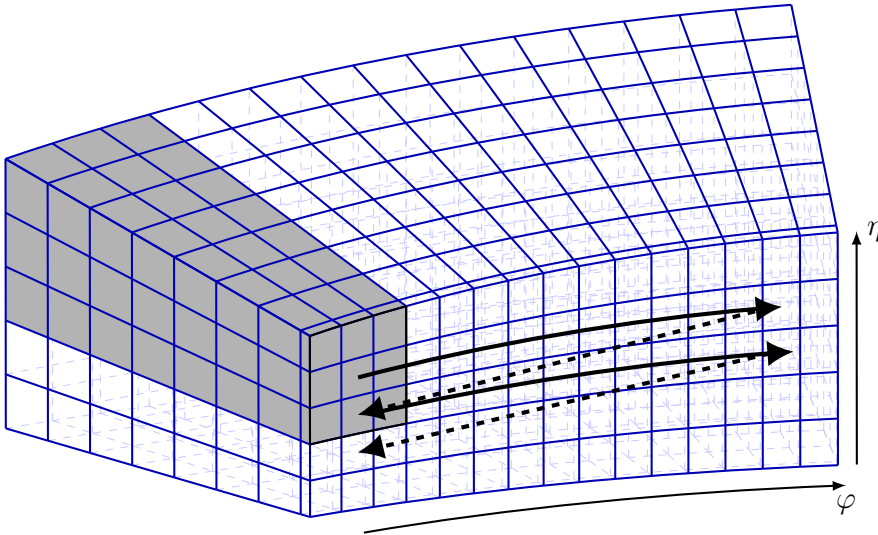


Fig. 7.27: An illustration of the basic concept of the sliding window algorithm. A window of fixed size (here  $N_\eta^{\text{seed}} \times N_\varphi^{\text{seed}} = 3 \times 3$ ) is moved across the tower grid.

The position of a pre-cluster is calculated as the energy-weighted average of the  $\eta$  and  $\varphi$  positions of the centre of cells within the fixed-sized window. The window for the position calculation may have different (smaller) size  $N_\eta^{\text{pos}} \times N_\varphi^{\text{pos}}$  than the seeding window in order to mitigate the effect of noise. The exact position in pseudo-rapidity is corrected afterwards, as described in Section 7.4.1.1.2.

In the next step the overlapping pre-clusters are removed and only the most energetic one is kept. A final cluster is built of all cells located within a fixed size window  $N_{\eta}^{\text{fin}} \times N_{\varphi}^{\text{fin}}$  around the tower containing the calculated position of the pre-cluster. This window needs to be large enough to contain most of the shower, thus limiting the effect of the lateral shower leakage. However, the more cells contained in the cluster, the higher the noise contribution. Therefore, the final shape of the cluster is elliptic, reducing the number of cells containing mostly noise contribution. The final cluster shape is shown in Fig. 7.28.

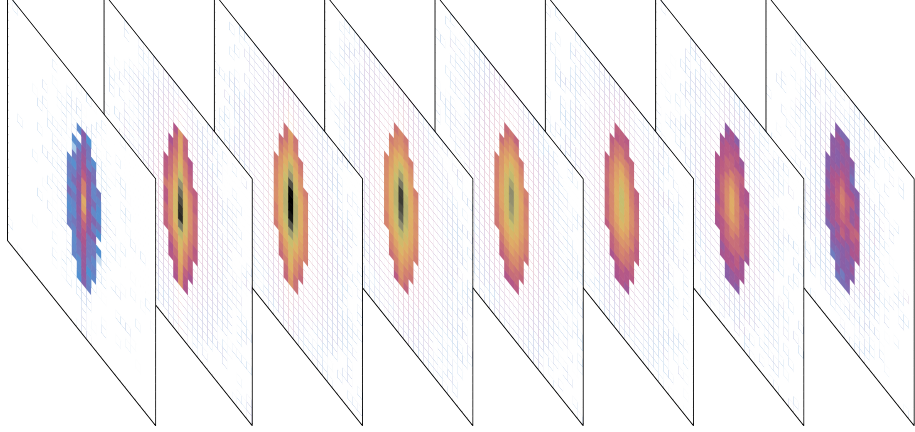


Fig. 7.28: The shape of a reconstructed shower created by a 50 GeV photon in the EMB at  $\eta = 0$ . Each projection represents one calorimeter layer. The energy is collected for all layers from the cells within an ellipse whose axes are defined by the final reconstruction window ( $N_{\eta}^{\text{fin}} \times N_{\varphi}^{\text{fin}} = 7 \times 19$  for no pile-up).

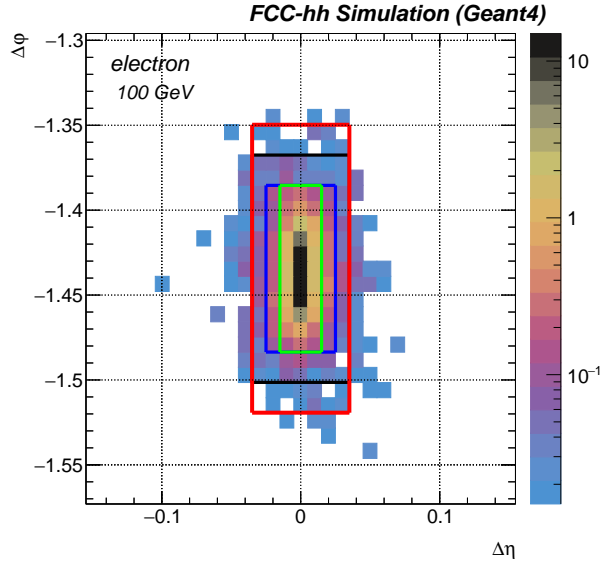


Fig. 7.29: Transverse profile of the shower created by a 100 GeV electron. All towers in which an electron deposited energy are included (without the detector noise). The reconstructed cluster is formed from the cells inside the red window ( $N_{\eta}^{\text{fin}} \times N_{\varphi}^{\text{fin}} = 7 \times 19$ ). The black window corresponds to the seeding window ( $N_{\eta}^{\text{seed}} \times N_{\varphi}^{\text{seed}} = 7 \times 15$ ), and the green corresponds to the window used to calculate the position ( $N_{\eta}^{\text{pos}} \times N_{\varphi}^{\text{pos}} = 3 \times 11$ ). The blue window represents the area from where the overlapping pre-clusters are removed ( $N_{\eta}^{\text{seed}} \times N_{\varphi}^{\text{seed}} = 5 \times 11$ ),

Results for window sizes as indicated in Table 7.9 are presented in Section 7.4.1. The transverse profile of a shower of a 100 GeV electron can be seen in Fig. 7.29. An example of the sliding-window

size ( $\Delta\eta^{\text{fin}} \times \Delta\varphi^{\text{fin}} = 0.07 \times 0.17 \Rightarrow N_{\eta}^{\text{fin}} \times N_{\varphi}^{\text{fin}} = 7 \times 19$ ) is indicated with a red line. In order to mitigate the effect of noise, the size of that window is decreased in the presence of pile-up.

Table 7.9: Parameters used in the sliding window reconstruction for different pile-up scenarios. The final cluster is of an elliptic shape and the size represents the axes of an ellipse.

$\langle\mu\rangle$	$E_T^{\text{threshold}}$	$N_{\eta}^{\text{seed}} \times N_{\varphi}^{\text{seed}}$	$N_{\eta}^{\text{pos}} \times N_{\varphi}^{\text{pos}}$	$N_{\eta}^{\text{fin}} \times N_{\varphi}^{\text{fin}}$
0				$7 \times 19$
200	3 GeV	$7 \times 15$	$3 \times 11$	$3 \times 9$
1000				$3 \times 9$

Figure 7.30a presents the energy resolution for 50 GeV photons in the EMB as a function of the transverse size of the reconstructed cluster for three pile-up scenarios:  $\langle\mu\rangle = 0, 200, 1000$ . Without the presence of pile-up, the energy resolution saturates for clusters larger than  $\Delta\eta \times \Delta\varphi = 0.004$ . Not enough energy is collected for smaller clusters hence the degradation due to a larger sampling term. For pile-up of  $\langle\mu\rangle = 200$  the noise originating from simultaneous collisions degrades the energy resolution for large clusters. This effect is even more prominent for  $\langle\mu\rangle = 1000$ . The minimum between the two degrading effects (increased sampling term for small clusters and noise term for large clusters) is located around 0.0025 (0.002) for  $\langle\mu\rangle = 200(1000)$ . Therefore the final cluster size used for reconstruction in pile-up environment has been chosen to be a window of  $\Delta\eta \times \Delta\varphi = 0.0023$  which corresponds to  $N_{\eta}^{\text{fin}} \times N_{\varphi}^{\text{fin}} = 3 \times 9$  in units of tower size. The improvement of the energy resolution for  $\langle\mu\rangle = 1000$  can be seen in Fig. 7.30b, where the noise term has been reduced by more than 50% from  $b = 3$  GeV to  $b = 1.4$  GeV.

### 7.3.1.1.2 Topological clustering

This clustering algorithm builds so-called topo-clusters from topologically connected calorimeter cells. The algorithm explores the spatial distribution of cell signals in all three dimensions to connect neighbouring cells, thus reconstructing the energies and directions of the incoming particles. The collection of cells into topologically connected cell signals is an attempt to extract significant energy deposits by particles and reject signals coming from electronic noise or fluctuations due to pile-up. The logic of this algorithm follows ATLAS topo-clustering [150].

Topo-clusters created in the FCC-hh calorimeters are not expected to contain all cells with signals created by a single particle, but rather fractional responses of particle (sub-)showers dependent on the spatial separation. The main observable controlling the building of topo-clusters is the cell significance  $\xi_{\text{cell}}$  which is defined as the absolute value of the ratio of the cell signal to the expected noise in this cell,

$$\xi_{\text{cell}} = \left| \frac{E_{\text{cell}}}{\sigma_{\text{cell}}^{\text{noise}}} \right|. \quad (7.10)$$

To avoid positive biases all thresholds are applied on absolute values. The cluster formation starts with a highly significant seed cell that has a significance of  $\xi_{\text{cell}} \geq S$ ,  $S$  being a tunable parameter. In the next step, the seed cells are ordered by energy and a proto-cluster is created per seed. Starting with the highest energy proto-cluster, the next cell neighbours are added if their cell significances  $\xi_{\text{cell}}$  are larger than a parameter  $N$ , while the newly added cells become the next seed cells of that cluster. This step is repeated until no more neighbouring cells pass the required criterion  $\xi_{\text{cell}} \geq N$ . In this way the cluster growth is controlled by the threshold  $N$ . Finally, the cell collection is finalised by adding all neighbours (of cells collected up to this point) that display a cell significance  $\xi_{\text{cell}}$  larger  $P$ . In the FCC-hh calorimeters the neighbours are defined in 3D. Hence, all cells sharing a border or a corner within their own or a nearby layer are neighbours. Additionally, neighbours across sub-calorimeters are defined. This is done for the

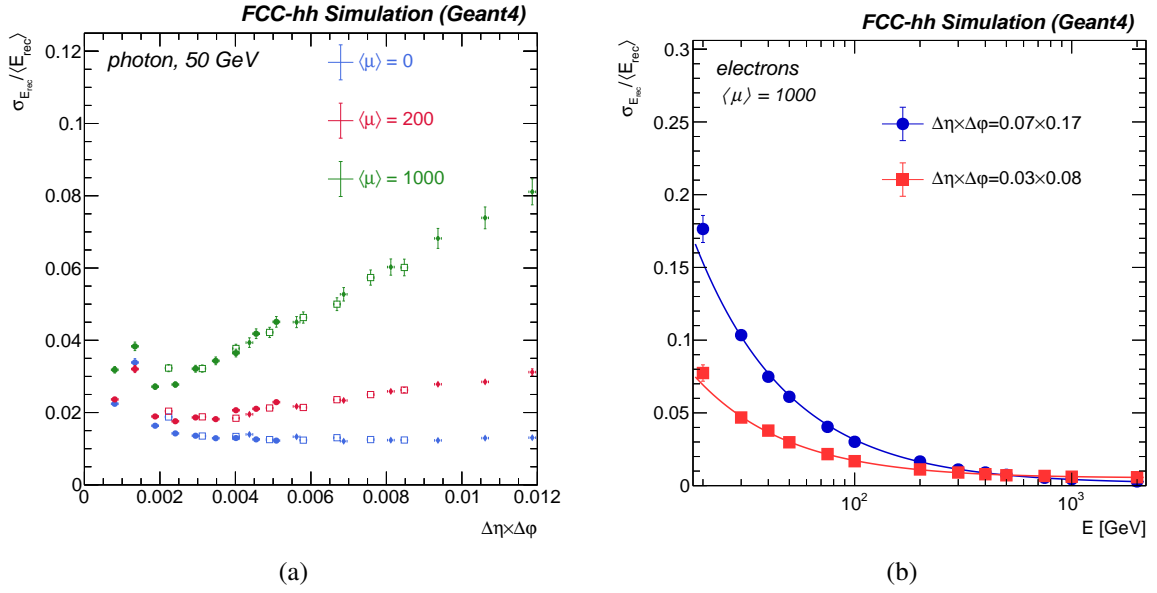


Fig. 7.30: Energy resolution **(a)** for 50 GeV photons as a function of the size of the reconstructed cluster. A no pile-up environment (blue symbols) and a pile-up environment  $\langle \mu \rangle = 200$ , 1000 (red, green) are presented. Different markers correspond to different cluster widths measured in  $\Delta\eta$ :  $N_{\eta}^{fin} = 3$  (full circles),  $N_{\eta}^{fin} = 5$  (hollow squares),  $N_{\eta}^{fin} = 7$  (full diamonds).; **(b)** Energy resolution for electrons in the presence of pile-up  $\langle \mu \rangle = 1000$ . The blue circles correspond to a larger window ( $\Delta\eta \times \Delta\phi = 0.07 \times 0.17$ ), and the red squares a smaller window ( $\Delta\eta \times \Delta\phi = 0.03 \times 0.08$ ). The resolution can be fitted to  $\frac{\sigma_E}{E} = \frac{10\%}{\sqrt{E(\text{GeV})}} \oplus \frac{b}{E} \oplus 0.5\%$ , where  $b = 3$  GeV and  $b = 1.4$  GeV for larger and smaller windows, respectively.

EMB and HB by adding the cells in the first HB layer with a distance in  $\varphi$  of  $\leq \frac{1}{2} (\Delta\phi_{EMB} + \Delta\phi_{HB})$  and of  $\leq \frac{1}{2} (\Delta\eta_{EMB} + \Delta\eta_{HB})$  in  $\eta$  to the list of neighbours to the last EMB layer cells. The clusters are characterised by a core of cells with highly significant signals, surrounded by an envelope of cells with less significant signals. The types of clustered cells are shown as 1, 2 and 3 corresponding to their significances above thresholds  $S$ ,  $N$  and  $P$  in Fig. 7.31.

In each event, cluster IDs are assigned, counting from 0 for each proto-cluster. These cluster IDs allow a clear classification of clustered cells. Before assigning a cell to a proto-cluster, it is checked whether the cell already belongs to another cluster with a different ID. If a cell already belongs to another cluster, and its significance is above  $N$  or  $P$ , the two clusters are merged. For the particular case of  $N$  or  $P$  equal 0, the clusters stay separate and the cell is assigned to the cluster with higher energy. The mechanism of cluster merging allows for clusters with more than one seed cell. The cluster ID of the cells in all EMB and HB layers is shown in Fig. 7.32 for an event of a 100 GeV  $\pi^-$  shower at  $\eta = 0.36$ .

The default configuration of  $S = 4$ ,  $N = 2$ , and  $P = 0$ , has been optimised for single charged hadrons on test-beam data of ATLAS calorimeter prototypes, and has proven good performance in LHC Run 1 data [150]. Additionally, the thresholds have been tested in FCCSW and optimised for different pile-up scenarios, see Section 7.4.2.2.1. An example of the noise suppression power of the algorithm is shown in Fig. 7.33, which illustrates the cell selection that reduced the number of cells by three orders of magnitude after topo-clustering for minimum bias events with electronic noise in the EMB and HB calorimeters (see more on the noise modelling in FCCSW in Section 7.3.2).



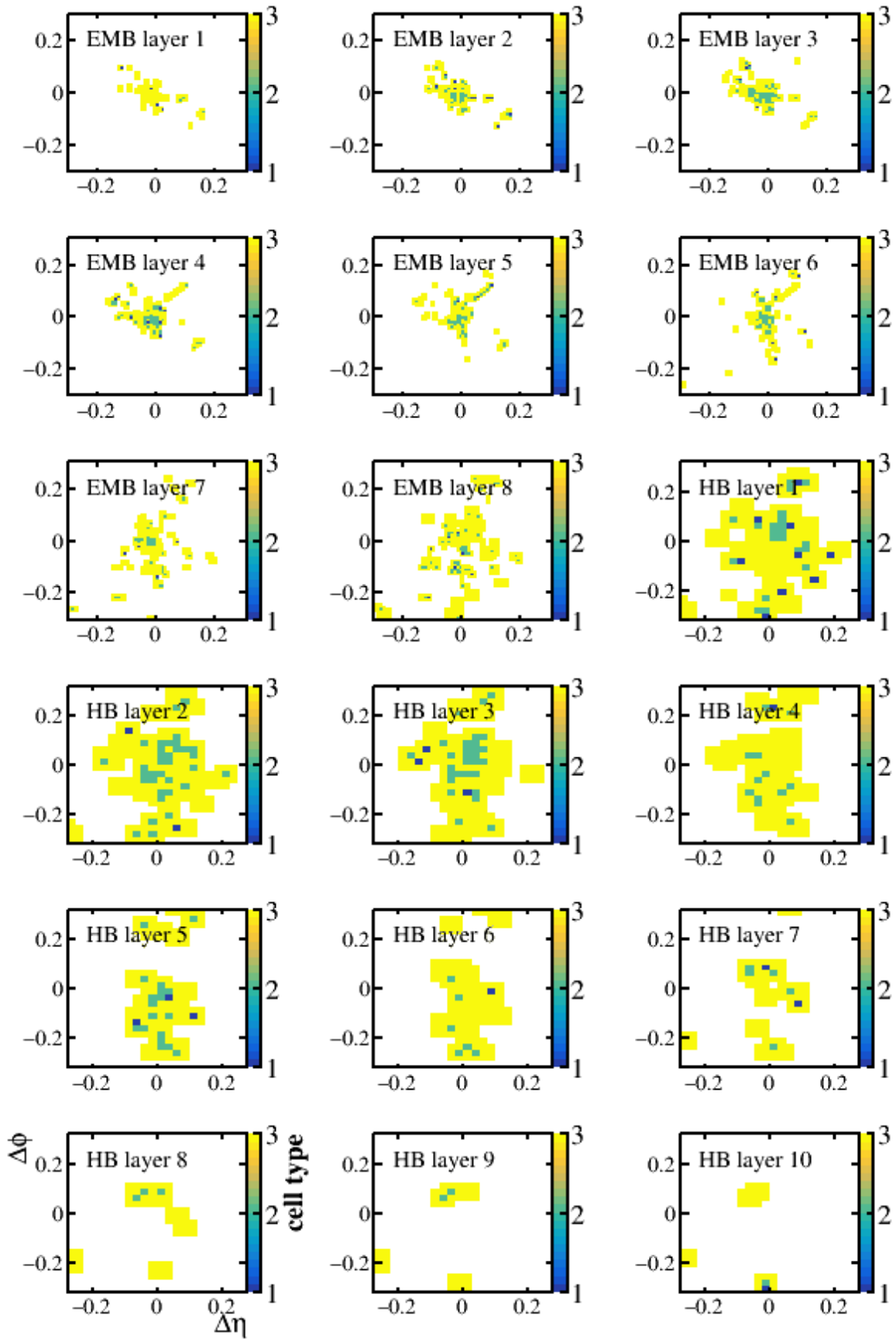


Fig. 7.31: Cell types of seeds (blue), neighbours (green), and last iteration cell (yellow) shown in  $\Delta\eta = \eta_{\text{cell}} - \eta_{\text{gen}}$  and  $\Delta\phi = \phi_{\text{cell}} - \phi_{\text{gen}}$ , for topo-cluster of a 100 GeV  $\pi^-$  shower per layer in the combined EMB+HB system at  $\eta_{\text{gen}} = 0.36$  with electronics noise.

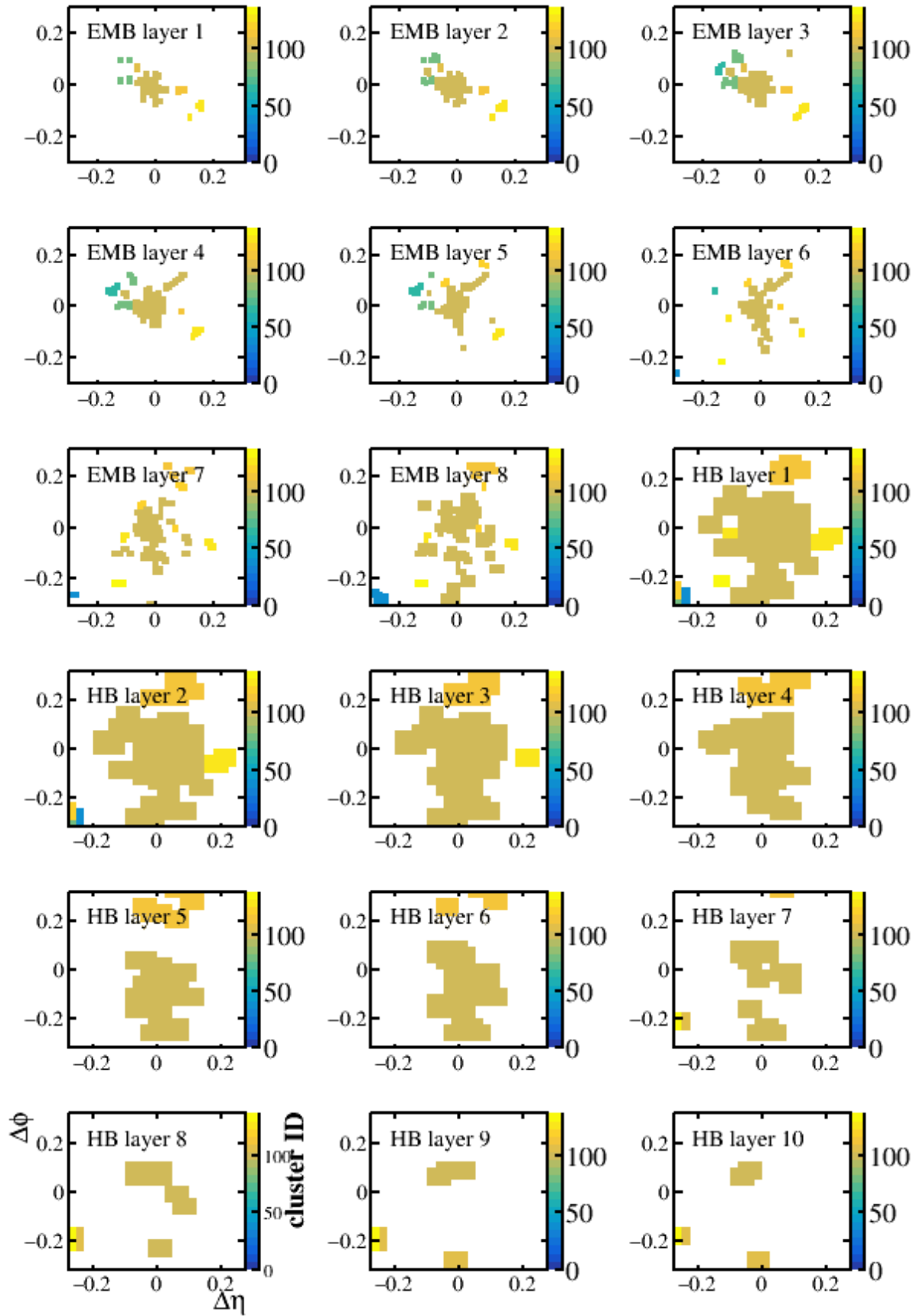


Fig. 7.32: Cluster ID of cells, shown in  $\Delta\eta = \eta_{\text{cell}} - \eta_{\text{gen}}$  and  $\Delta\phi = \phi_{\text{cell}} - \phi_{\text{gen}}$ , for topo-cluster of the same 100 GeV  $\pi^-$  shower as in Fig. 7.31.

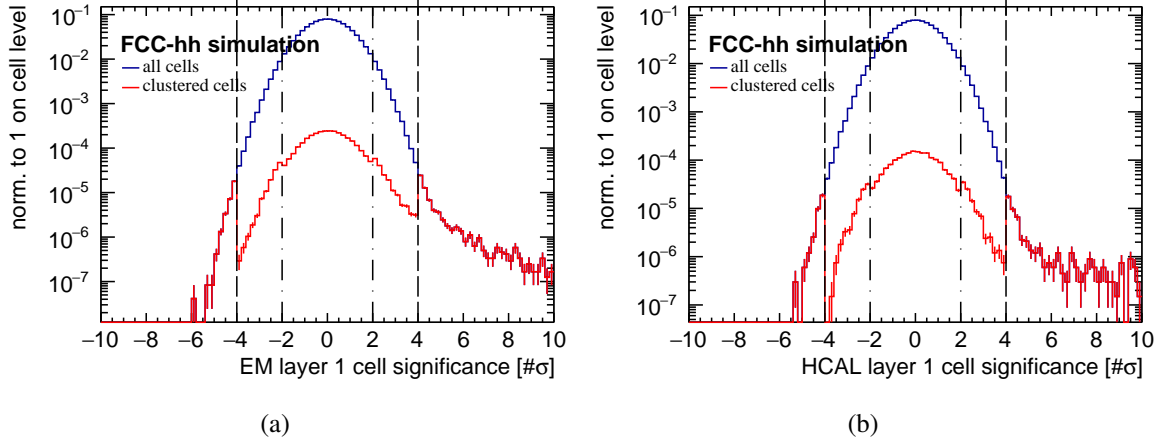


Fig. 7.33: Cell significances of 100 minimum bias events before (blue) and after (red) topo-clustering in the first EMB layer (a) and the first HB layer (b).

### 7.3.1.2 Jet reconstruction

The jet reconstruction is based on the anti- $k_T$  algorithm using the FASTJET software package [53, 54]. This algorithm is based on the distances  $d_{i,j}$  between entities, which in our case are calorimeter cells or cluster

$$d_{i,j} = \min \left( 1/p_{Ti}^2, 1/p_{Tj}^2 \right) \frac{\Delta R_{ij}^2}{R^2} , \quad (7.11)$$

with  $\Delta R_{ij}^2 = (\eta_i - \eta_j)^2 + (\phi_i - \phi_j)^2$  and  $p_T$ ,  $\eta_i$  and  $\phi_i$  being the transverse momentum, rapidity and azimuth of particle  $i$ , respectively,  $R$  is the parameter of the algorithm. The algorithm proceeds by identifying the smallest of the distances  $d_{i,j}$  and recombining entities  $i$  and  $j$ , while calling  $i$  a jet and removing  $B$  from the list of entities if it is  $d_{i,j} = d_{i,B}$  with

$$d_{i,B} = p_{Ti}^{2p} , \quad (7.12)$$

where  $p = -1$  for the anti- $k_T$  algorithm. The distances are recalculated and the procedure repeated until no entities are left. Following the example of ATLAS, the default jet parameter  $R$  is set to  $R = 0.4$ , if not stated differently.

### 7.3.2 Noise

Each read-out channel will be affected by electronic noise due to series and parallel noise of the read-out electronics. On top of that, energy deposits from particles coming from pile-up collisions will add to the energy deposits of the collision of interest, the hard scatter<sup>13</sup>. In-time pile-up will increase the energy deposits, whereas—depending on the read-out electronics—out-of-time pile-up from prior bunch crossings might reduce the cell signals due to negative signal undershoots (see also the discussion in Section 7.2.2.6). In case of bipolar shaping the in-time and out-of-time pile-up contribution will cancel on average (for infinite bunch trains). However, due to the stochastic nature of pile-up there will be fluctuations that will be referred to in the following as pile-up noise. If one neglects significant correlations between different cells, pile-up noise can be treated very similarly to electronic noise.

<sup>13</sup>The following terminology will be used in this section: The proton collision of interest is called the hard scatter emerging from the primary vertex, whereas other (minimum bias) collisions occurring during the same (prior) bunch crossing(s) are called in-time (out-of-time) pile-up collisions, respectively.

### 7.3.2.1 Electronic noise

In order to obtain realistic simulation results, especially for topological clustering, it is necessary to assume values of electronic noise for each read-out channel. In the following sections we will explain how these realistic noise estimates were obtained for the FCC-hh LAr calorimeter and the hadronic tile calorimeter.

#### 7.3.2.1.1 LAr calorimeter

In order to estimate realistic noise levels for the FCC-hh LAr calorimeters without a detailed design of the read-out electrodes, the transmission lines, the signal feed-throughs and the read-out electronics, it is assumed that an extrapolation from the ATLAS calorimeter middle layer can be made. Empirical formulae are used to calculate the capacitances of the FCC read-out cells. The conversion factor which translates the capacitance into the electronic noise is estimated using measurements performed with the ATLAS LAr calorimeter. A correction due to different sampling fractions in ATLAS and FCC-hh LAr calorimeters has to be considered. The correction factor between a cell electronic noise and its capacitance ( $\sigma_{\text{noise}}/C_{\text{cell}}$ ) is extracted using values from ATLAS [151], yielding  $0.04 \text{ MeV/pF} \times f_{\text{sampl}}^{\text{ATLAS}}/f_{\text{sampl}}^{\text{FCC-hh}}$ , where  $f_{\text{sampl}}^{\text{ATLAS}} = 0.18$  is the sampling fraction of the ATLAS LAr calorimeter and  $f_{\text{sampl}}^{\text{FCC-hh}}$  the depth dependent sampling fraction of the FCC-hh LAr calorimeter (see Fig. 7.13). The extrapolation from ATLAS neglects the fact that an optimisation of the read-out electronics in terms of noise will have to be performed for FCC-hh. This will likely lead to shorter preamplifier rise and shaping times than those used in ATLAS. It is also neglected that the signal attenuation inside the read-out PCBs and along the (longer) transmission lines might lead to slightly higher noise values at FCC-hh. However, we believe that the following estimates predict the actual electronic noise within an accuracy of about a factor 2.

As described in Section 7.2.2.1, the capacitance of the read-out cells is composed of the LAr-gap capacitance  $C_d = \varepsilon_{\text{LAr}}\varepsilon_0 A/d$  for a LAr gap of width  $d$  and an area  $A$  ( $\varepsilon_{\text{LAr}} = 1.5$ ) and the capacitance  $C_s$  of the read-out pads to the signal shields of width  $w_s = 250 \mu\text{m}$  traversing below the pads inside the PCB (distance  $h_m = 285 \mu\text{m}$ ) and shielding the signal traces from the read-out pads (see Figs. 7.10b, 7.11a and 7.11b).

For each cell, the capacitance between the signal shields and the read-out pads  $C_s$  depends on the length of the shield and the number of signal traces that are passing below each read-out pad. In order to minimise that number, cells from the first and second detector layer will be read out via the front of the detector, while the rest will be read out via the back (see Fig. 7.10b). The resulting capacitance of read-out cells  $C_{\text{cell}}$  in all layers as a function of pseudorapidity is presented in Fig. 7.34.

Assuming the above mentioned conversion factor  $\sigma_{\text{noise}}/C_{\text{cell}}$ , we obtain values of electronic noise per cell as presented in Fig. 7.35. This electronic noise is assumed to be uncorrelated between cells.<sup>14</sup> The electronic noise of clusters can therefore be calculated by the quadratic sum of the noise in individual cells. For a cluster of size  $\Delta\eta \times \Delta\varphi = 0.07 \times 0.17$  this yields  $\sigma_{\text{noise}} \approx 300 \text{ MeV}$  at  $\eta = 0$ .

As discussed, this estimation of the electronic noise in the LAr calorimeter is very preliminary and is based on many approximations and assumptions. A detailed design and simulation of the full read-out chain will have to be carried out in order to obtain more reliable results.

#### 7.3.2.1.2 Tile calorimeter

The electronic noise in the tile calorimeter will be dominated by electronic noise of the SiPMs read-out electronics. Due to the strong dependence on the missing design details in the SiPM readout chain, in the following a conservative assumption is used based on estimations for the HL-LHC upgrade of the

<sup>14</sup>During the design of the read-out electrodes, feed-throughs and read-out electronics, the correlated noise contribution and cross-talk needs to be simulated in detail and kept to an absolute minimum. A cross-talk between neighbouring strip cells of  $\leq 7\%$  has been achieved in ATLAS.

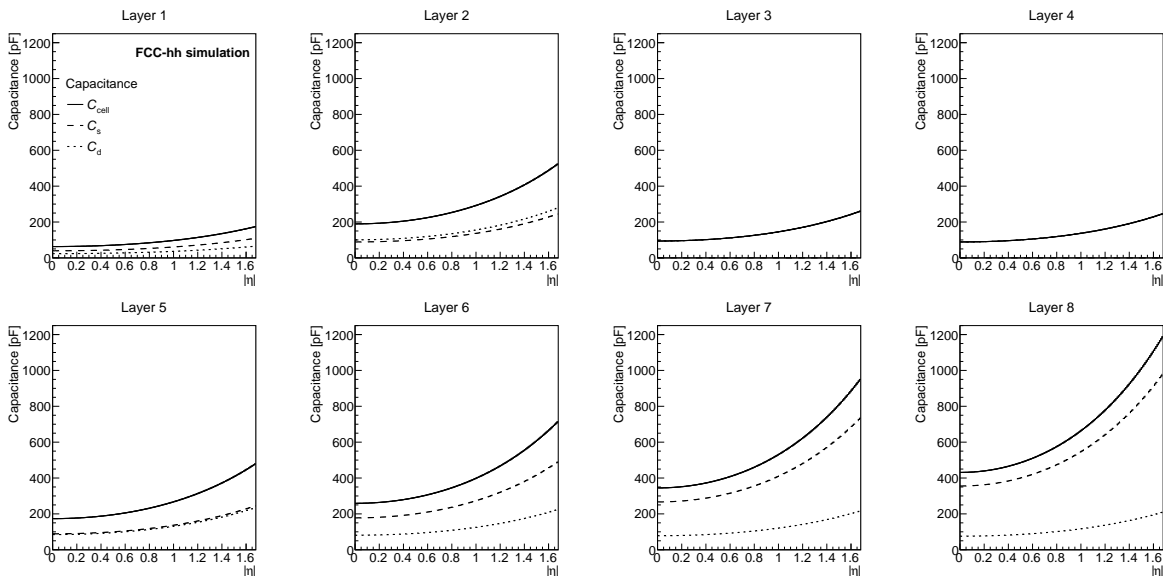


Fig. 7.34: Capacitance  $C_{\text{cell}}$ ,  $C_s$  and  $C_d$  calculated for each longitudinal layer of the EMB as a function of pseudorapidity. The signal pads of the first three layers are read out via traces leading to the inner radius of the calorimeter and all other layers via the outer radius, as depicted in Fig. 7.10b. Here a granularity of  $\Delta\eta \times \Delta\varphi = 0.01 \times 0.009$  is assumed for all layers.

read-out electronics of the ATLAS tile calorimeter, that assumes 10-15 MeV per read-out channel on the EM scale. We therefore add uncorrelated random Gaussian noise of 10 MeV on the EM scale for each read-out cell. Additional effects due to the dark count rate, cross talk, after pulses, and saturation of pixels of the SiPM are not included in the simulation because all of these effects vary strongly between SiPM types and manufacturers, and have been greatly improved over the past years.

### 7.3.2.2 Pile-up noise

Energy deposits of particles from simultaneous collisions in the same bunch crossing will create a background to the energy deposits of the hard scatter collision of interest. These pile-up energy deposits will create a bias to the energy measurement. This positive bias can be reduced by using bi-polar shaping, as discussed in Section 7.2.2.6 and proposed for the calorimeters of the reference detector, whereas fluctuations of these pile-up energy deposits will remain. We call these fluctuations pile-up noise. This noise is usually composed of the energy deposits from the same bunch crossing (the in-time pile-up) and those from prior bunch crossings (the out-of-time pile-up) creating negative contributions through the signal undershoots. In case of signal collection and shaping times smaller than the time between two bunch crossings ( $< 25$  ns)—as is the case for Si sensors—out-of-time pile-up will not influence the energy measurement, but the bias and fluctuations of the in-time pile-up will remain. For our case of longer signal collection and shaping times it is also possible to minimise the impact of out-of-time pile-up. Due to the known history of energy deposits from prior bunch-crossings, the out-of-time pile-up can be unfolded from the measurement of the current bunch crossing. Such an approach has been studied in detail and demonstrated for the ATLAS LAr Calorimeter HL-LHC upgrade [136].

In-time pile-up can be reduced by using energy deposit timing information and rejecting those deposits which are not consistent with the time-of-flight of particles from the primary vertex. It is also possible to reject pile-up deposits if they can be attributed to a charged particle track reconstructed with the tracker that does not originate at the primary vertex. Such techniques will need to be developed and studied to exploit the full physics potential of an FCC-hh experiment.

In the following we assume that the out-of-time pile-up can be corrected for, but estimate the full

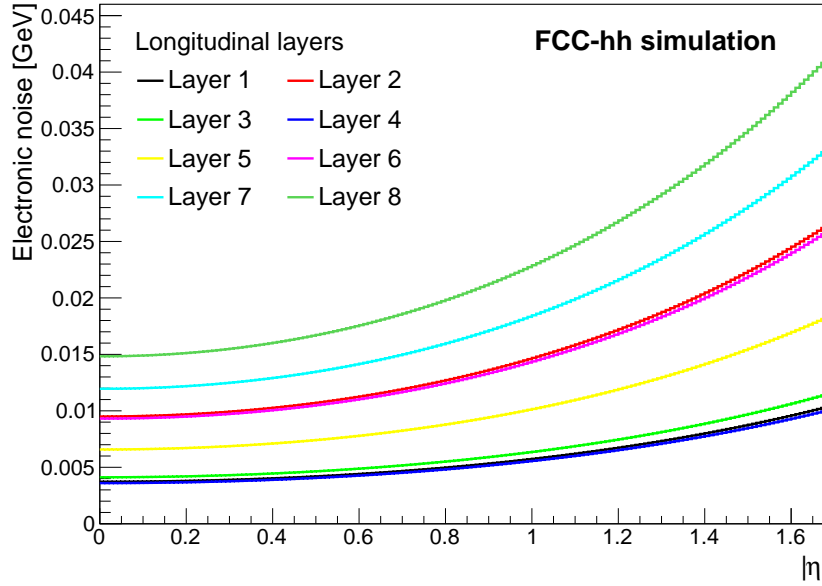


Fig. 7.35: Estimated electronic noise per cell for each longitudinal layer of the EMB as a function of pseudorapidity.

in-time pile-up noise contribution (without any of the above mentioned corrections).

#### 7.3.2.2.1 LAr calorimeter

The ATLAS detector with its planned updates for the HL-LHC proves that LAr calorimetry can provide excellent energy measurement even in a high pile-up environment [136].

In order to estimate the in-time pile-up, a sample of minimum bias events has been simulated with the PYTHIA8 [102] event generator. The electronic noise was switched off for these special simulations with a single pile-up collision per event. The energy distribution for a single calorimeter cell is presented in Fig. 7.36. The standard deviation of the energy distribution is used to quantify the fluctuations caused by the pile-up collisions, i.e. the pile-up noise.

The size of the sample was not large enough to overlay hundreds of pile-up collisions per event. Therefore the standard deviation obtained with one minimum bias collision per event has been scaled with  $\sqrt{\langle\mu\rangle}$ , where  $\langle\mu\rangle$  is the desired average number of simultaneous collisions per bunch crossing. It has been checked with simulation that this scaling yields the correct values. In order to increase the sample size, azimuthal symmetry is assumed.

Pile-up noise is correlated between neighbouring cells, and therefore cannot be treated in the same way as the electronic noise which is modelled on a cell-by-cell basis. The impact of pile-up has been studied for the two clustering algorithms separately. The first approach is used for the EM calorimeters and is relatively straight forward for fixed-size clusters as used in the sliding window algorithm, where all clusters consist of the same number of cells. Instead of looking at the individual cell, the noise in a cluster of dimensions  $\Delta\eta \times \Delta\varphi$  is studied, assuming same size in all longitudinal layers. As expected, a clear dependence on the cluster size is found, which is presented in Fig. 7.37a (squares) for  $\langle\mu\rangle = 200$ . This dependence on cluster size can be parameterised in bins of pseudorapidity using

$$\sigma = p_0 \cdot (\Delta\eta \times \Delta\varphi)^{p_1} \quad (7.13)$$

where  $p_0$  and  $p_1$  are the two fit parameters and  $\Delta\eta$  and  $\Delta\varphi$  the cluster dimensions in  $\eta$  and  $\varphi$ , respectively.

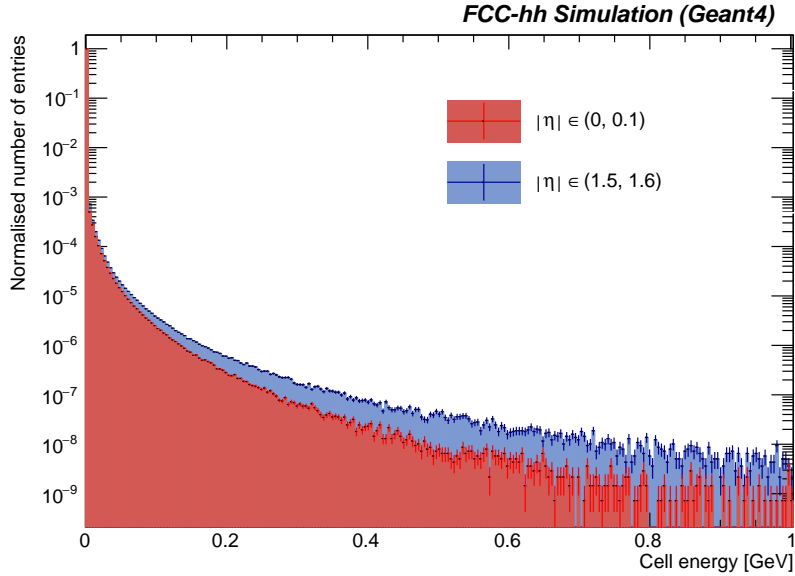


Fig. 7.36: Energy distribution in calorimeter cells of size  $\Delta\eta \times \Delta\varphi = 0.01 \times 0.009$  in the third calorimeter layer within  $|\eta|$  range between 0 and 0.1 (red) and for  $|\eta| \in (1.5, 1.6)$  (blue).

Figure 7.37a also shows the result obtained (filled circles) if the pile-up noise in cells of  $\Delta\eta \times \Delta\varphi = 0.01 \times 0.009$  is summed up quadratically (no correlation assumed,  $p_1 = 1/2$ ) as well as the case (open circles) of summing the pile-up noise linearly (assuming fully correlated pile-up noise,  $p_1 = 1$ ). As presented in Fig. 7.37b  $p_0$  depends on pseudorapidity, while parameter  $p_1$  is constant,  $p_1 = 0.66 \pm 0.01$  in our case. Using these noise parameterisations, pile-up studies with different window sizes can be performed.

The pile-up noise dependence on pseudo-rapidity for  $\langle\mu\rangle = 200$  and 1000 for clusters with a sliding window size of  $\Delta\eta \times \Delta\varphi = 0.07 \times 0.17$  is presented in Fig. 7.38. As can be seen, a large pile-up noise rising in  $\eta$  from 3.5 GeV to 6.5 GeV for  $\langle\mu\rangle = 1000$  is obtained. This result suggests that it will be crucial to further optimise cluster sizes and especially make them smaller in the first calorimeter layers and to use timing information and the tracker measurement to reject more pile-up energy deposits. Nevertheless, these values have been used in the performance section to smear the cluster energies of sliding window clusters.

### 7.3.2.2.2 Combined LAr and tile calorimeter

The situation becomes more difficult for clusters of variable size and dispersion like topo-cluster. Due to the different cluster volumes and centre of gravity in all three dimensions a simple scaling as presented above does not work. Instead, the performance within a realistic pile-up scenario is studied by the overlay of minimum bias events on top of the hard scatter event, with the topological clustering applying energy thresholds using the expected noise level per cell (electronic noise and pile-up noise quadratically summed) within the cluster formation. However, before the topo-clustering is run, the mean cell energy is corrected for the mean noise per cell, determined from the merged, corresponding number of minimum bias events. The mean cell energies are shown for the EMB and hadronic calorimeter HB per layer and as a function of  $\eta$  in Fig. 7.39a and 7.39b. The cell noise for each tile of the HB shows the expected decreasing noise levels with increasing  $\eta$ , while the HB with  $\Delta\eta = 0.025$  segmentation increases the noise due to the merging of up to 7 tiles per cell for higher pseudo-rapidity. Within the topo-cluster algorithm, the cell significance is determined from the expected noise levels. The pile-up noise is estimated by the standard deviation of the cell energy distributions, one example is shown in Fig. 7.36. The noise levels,



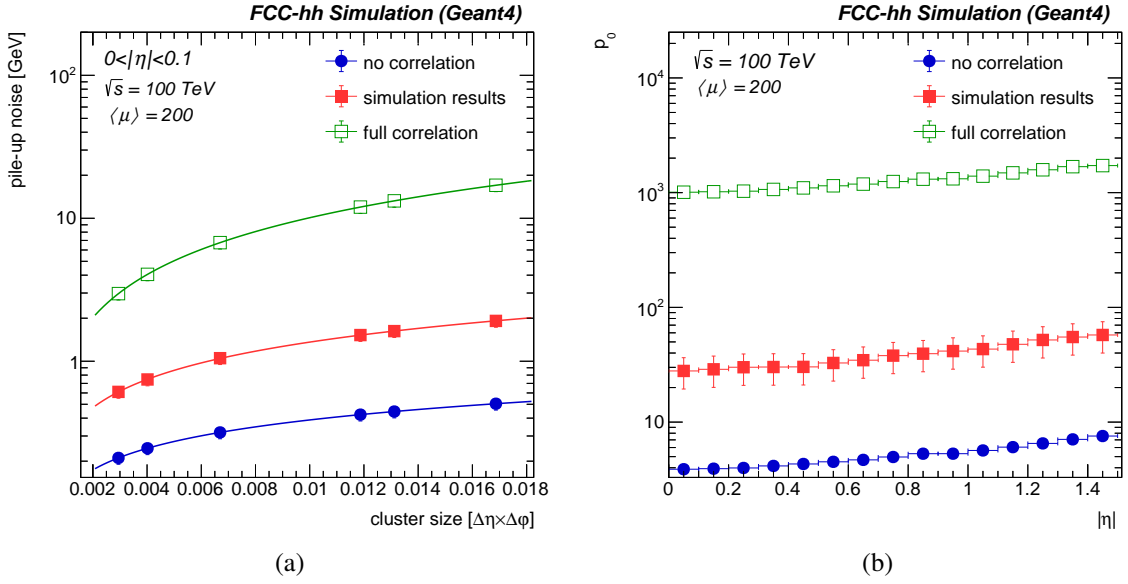


Fig. 7.37: (a): Cluster noise as a function of cluster size in terms of  $\Delta\eta \times \Delta\phi$  for clusters in the EM calorimeters within  $|\eta| < 0.1$ . The full squares show the minimum bias simulation result, whereas the filled circles show the quadratic sum of pile-up noise of individual cells (no correlation) and the open squares show the linear sum of individual cells (full correlation). (b): Parameter  $p_0$  as a function of  $\eta$  using the parametrisation of Eq. (7.13) for all three cases shown in (a).

determined from merged minimum bias events, are shown for the pile-up scenario of 1000 collisions per bunch crossing in Fig. 7.40. The impact of pile-up noise on the energy reconstruction of hadronic showers is presented and discussed in Section 7.4.2.2.4.

### 7.3.3 Reconstruction and identification using deep neural networks

In addition to the more conventional reconstruction algorithms presented above, the use of deep neural networks (DNNs) was also tried for particle identification and energy reconstruction in an attempt to make use of the high granularity of the proposed calorimeter system. In this section the implementation of these DNNs is described, the results will be presented in Section 7.4.2.1.2.

In the last decade, significant advances have been made with respect to the design and application of DNNs. These were enabled by new algorithms, and also by developments in computing hardware, such as the capabilities of graphics processor units (GPUs) to compute thousands of operations in parallel. Their architecture, in principle consisting of a set of matrix multiplications, and the dedicated hardware can make these networks very fast, so that they are also well suited for triggering applications.

In contrast to boosted decision trees (BDTs), which are widely used in high energy physics and can be interpreted as shallow neural networks, DNNs allow the exploitation of the structure and symmetries of the input data and can therefore process a large input dimensionality. In this context, the sensor signals from the calorimeters can be interpreted as 3-dimensional energy images. Based on these images, DNN-based energy reconstruction and identification of electrons, photons, muons, charged and neutral pions are studied.

The particles are generated at  $\phi = 0$  and  $\eta = 0.36$  with a flat energy spectrum between 10 and 1000 GeV. The image is centred using the mean energy deposits of the particle in the barrel calorimeters. For the EMB,  $34 \times 34 \times 8$  pixels are defined in  $\eta$ ,  $\phi$ , and layer number, which corresponds to about  $\Delta\eta = 0.34$  and  $\Delta\phi = 0.31$  given the EMB granularity. For the HB, the energy deposits of the sensors

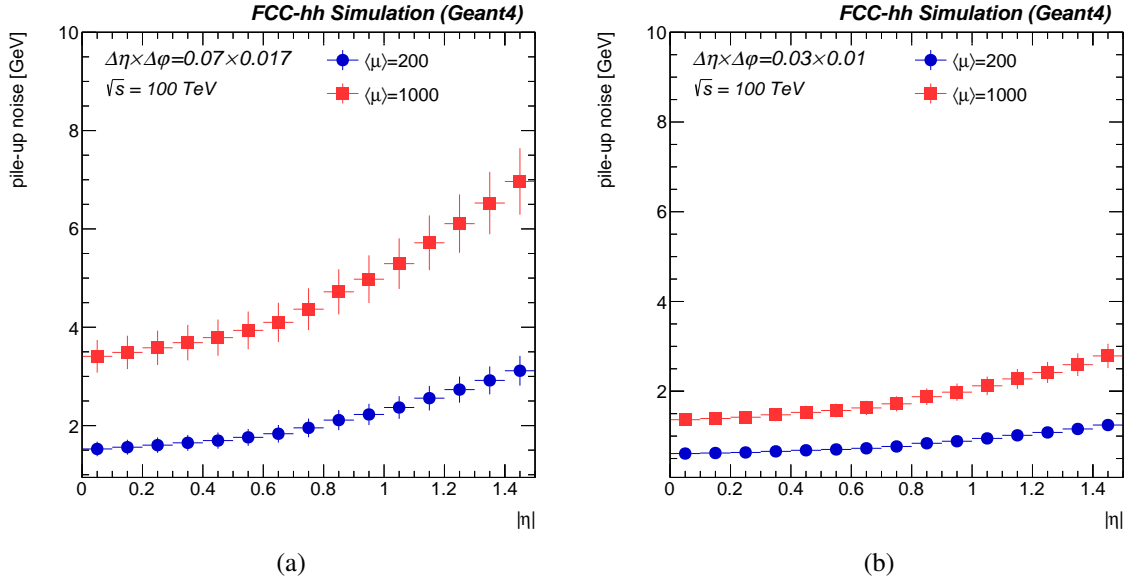


Fig. 7.38: Pile-up noise estimated for electromagnetic barrel (EMB) for two scenarios:  $\langle\mu\rangle = 200$  (blue circles) and  $\langle\mu\rangle = 1000$  (red squares) for cluster of size (a)  $\Delta\eta \times \Delta\phi = 0.07 \times 0.17$  and (b)  $\Delta\eta \times \Delta\phi = 0.03 \times 0.1$ .

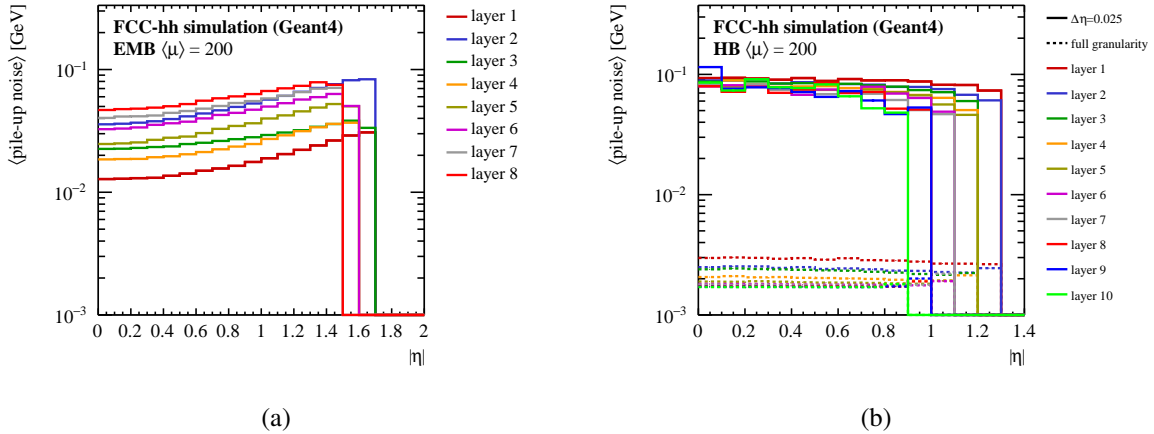


Fig. 7.39: Mean energy deposit per cell for  $\langle\mu\rangle = 200$  in (a) the EMB, and (b) the HB. The values per scintillating tile in the HB is shown in dashed lines.

are considered in  $17 \times 17 \times 10$  pixels, corresponding to a similar area with  $\Delta\eta = 0.43$  and  $\Delta\phi = 0.42$ . These energy deposits are superimposed with energy deposits from 0, 200, or 1000 pile-up interactions. The total sample for the particle identification contains about 1 M events, with equal contributions from all particles. For the energy reconstruction, only charged pions are considered with a total sample size of 1.2 M events. For performance evaluation, a separate dataset is used in both cases to avoid possible biases from overtraining.

For both energy reconstruction and identification, the DNN architecture is mostly based on convolutional neural networks [152–157]. For the identification network, the first convolutional layer consists of 8 filters with a kernel size of  $5 \times 5 \times 5$  pixels. In case of the EMB image, strides of  $2 \times 2 \times 1$  are used, such that the output corresponds to  $17 \times 17 \times 8$  pixels, which allows merging of the EMB and HB images along the layer dimension without information loss. The combined calorimeter image is fed through two

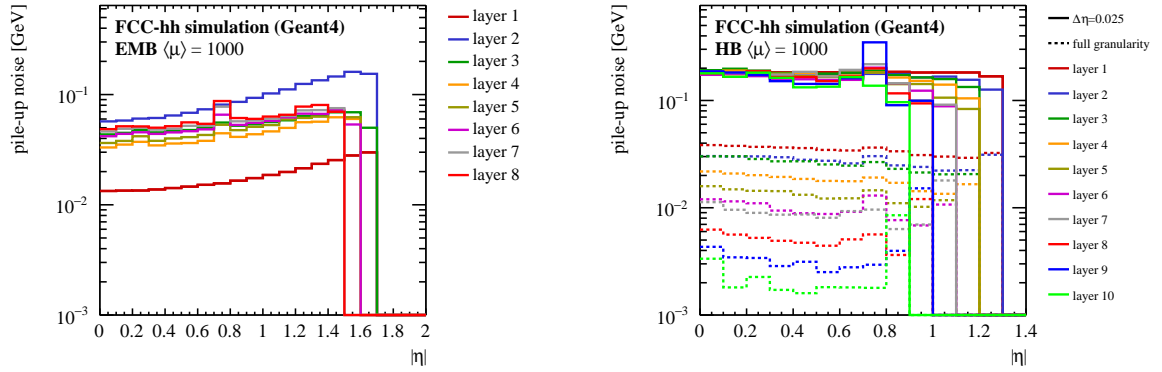


Fig. 7.40: Pile-up noise level per cell for  $\langle\mu\rangle = 1000$  in (a) the EMB, and (b) the HB. The noise per scintillating tile in the HB is shown in dashed lines.

paths of convolutional layers. One path is dedicated to muons, only considering the innermost  $7 \times 7$  pixels in  $\eta$ ,  $\phi$  which consists of two layers. The other path consists of five layers and covers the full image. Both paths are merged and then fed through two dense layers with 128 or 32 nodes, respectively. The final network output is configured as a multi-classifier with five output nodes, each corresponding to the predicted probability of the signature stemming from an electron, photon, muon, or charged or neutral pion. The network contains 250k free parameters in total.

The energy reconstruction network architecture is based on the concept that convolutional layers are used to locally determine the sum of the cell energies and a topology based correction to it. The architecture is inspired by the ResNet [158] model: in total four blocks with convolutional layers are used before their output is passed on to dense layers. Each block consists of one convolutional layer with a kernel size that equals the strides size and parallel additional layers with a larger kernel size, in the following referred to as direct layer and correction layers, respectively. Within the direct layer, the first filter is set to sum the first feature per pixel, while the other filters contain trainable weights. The correction path consists of three sequential convolutional layers with larger kernel sizes and more filters. The corresponding weights are trainable and initialised with low values. The last of these layers has the same kernel size and strides as the direct layer, such that its output is added as a small correction. Before the four blocks, common for EMB and HB, both images are fed through one direct layer without an additional correction path. For the EMB part, this layer is used to reduce the size to  $17 \times 17 \times 8$  pixels such that it can be merged with the HB image along the calorimeter layer dimension for further processing. Finally, the output is fed through three dense layers with 64, 12, and 1 nodes. An additional multiplicative offset correction is trained using this output fed into a wide dense layer. The typical number of filters for the direct and correction layers is between 16 and 32, kernel sizes do not exceed 30 pixels, such that the total number of free parameters in the model is 130k.

The technical implementation is done in KERAS [159] using TENSORFLOW [160] as the backend. The minimisation is performed using the ADAM [161] optimiser. For the identification, the cross entropy loss is minimised, for the energy determination, a Huber loss [162] is applied. The loss is modified, such that it follows

$$L = \frac{(E_p - E)^2}{E - 8 \text{ GeV}} \quad (7.14)$$

for  $L < 0.2$  and grows linearly with the same slope as at  $L = 0.2$  with  $E_p - E$ . Here,  $E$  is the energy of the generated particle and  $E_p$  the predicted energy by the network. The additional constant term in the denominator introduces an additional focus on the reconstruction of low energetic particles.

## 7.4 Performance

### 7.4.1 Electrons and photons

#### 7.4.1.1 Reconstruction of $e/\gamma$ -objects

As explained in Section 7.3.1, the energy deposits of particles showering inside the calorimeter need to be summed into clusters to reflect a first, uncorrected estimate of the energy of those particles. The primary algorithm used for electrons and photons (often also called  $e/\gamma$ -objects) is the sliding window algorithm (see Section 7.3.1.1.1). As described, it scans a two-dimensional grid of calorimeter cells in pseudorapidity and in azimuth, looking for local maxima. Around the local maximum a cluster of fixed size in  $\Delta\eta$  and  $\Delta\varphi$  is formed. The energy of this cluster is a sum of the energies of all cells within the cluster. The position in  $\eta$  and  $\varphi$  is calculated as the energy-weighted mean of the individual cell positions. The corrections outlined in the following section are applied to these quantities to improve precision. The cluster energy is corrected for the energy lost in the material in front of the detector, mainly the cryostat. The so-called upstream material correction will be discussed in Section 7.4.1.1.1. As explained in Section 7.4.1.1.2, logarithmic weights of energy are used to improve the position resolution.

Reconstructed clusters take into account the effect of electronics noise in each cell of the detector and pile-up noise is added to the cluster energy.

##### 7.4.1.1.1 Upstream material correction

In high energy physics experiments particles coming from the interaction point have to traverse a significant amount of material before reaching the calorimeter (beam pipe, inner tracker, services,...). Upstream material in typical experiments ranges at  $\eta = 0$  from  $0.5 X_0$ , as realised in the CMS experiment to  $3 X_0$  in the ATLAS experiment where the EM calorimeter sits inside a cryostat behind the solenoid coil. For the FCC-hh reference detector we expect a value between these two, since the calorimeter is located inside the solenoid coil, but—due to the cryogenic temperatures necessary for LAr—will sit inside a cryostat. The amount of material expected in front of the active LAr calorimeter is presented in Fig. 7.41a, showing values below or around  $2 X_0$  for most of the pseudorapidity apart from the transition regions between EMB and EMEC and between EMEC and EMF. In the EMB the amount of material increases with  $\eta$  due to flatter angle of incoming particles with respect to the cryostat walls. Since particles will lose energy and start the electromagnetic cascade in this un-instrumented material in front of the active calorimeter, the energy measurement has to be corrected for this lost energy. If no correction is applied, the energy resolution, will degrade as a function of the material traversed upstream as can be seen in Fig. 7.42. It presents the degradation for the  $30^\circ$  inclination of the absorbers, but the same applies for a larger inclination (this optimisation brought the constant term down, leaving the sampling term unchanged). The constant term is almost independent of material, whereas the sampling term increases rapidly for upstream material thicknesses larger than one radiation length.

The energy deposited in the upstream material fluctuates and cannot be corrected for globally. However, for single particle showers, there is a strong correlation between the energy detected in the first calorimeter layer and the energy deposited upstream. This linear relationship is shown in Fig. 7.41b and can be used to estimate the energy lost upstream  $E_{\text{upstream}}$  as a function of the energy measured in the first calorimeter layer  $E_{\text{firstLayer}}$ . Equation (7.15) shows the parameterisation that has been used, the two parameters  $P_0$  and  $P_1$  are functions of the cluster energy  $E_{\text{cluster}}$  and  $|\eta|$ .

$$E_{\text{upstream}} = P_0(E_{\text{cluster}}, |\eta|) + P_1(E_{\text{cluster}}, |\eta|) \cdot E_{\text{firstLayer}} \quad (7.15)$$

The energy dependence of parameters  $P_0$  and  $P_1$  for  $\eta = 0$  is presented in Fig. 7.43a. This dependence can again be parameterised using simple functions of the cluster energy  $E_{\text{cluster}}$  as shown in Eq. (7.16) for  $P_0$  and Eq. (7.17) for  $P_1$ . These functions were chosen to fit the data obtained best.

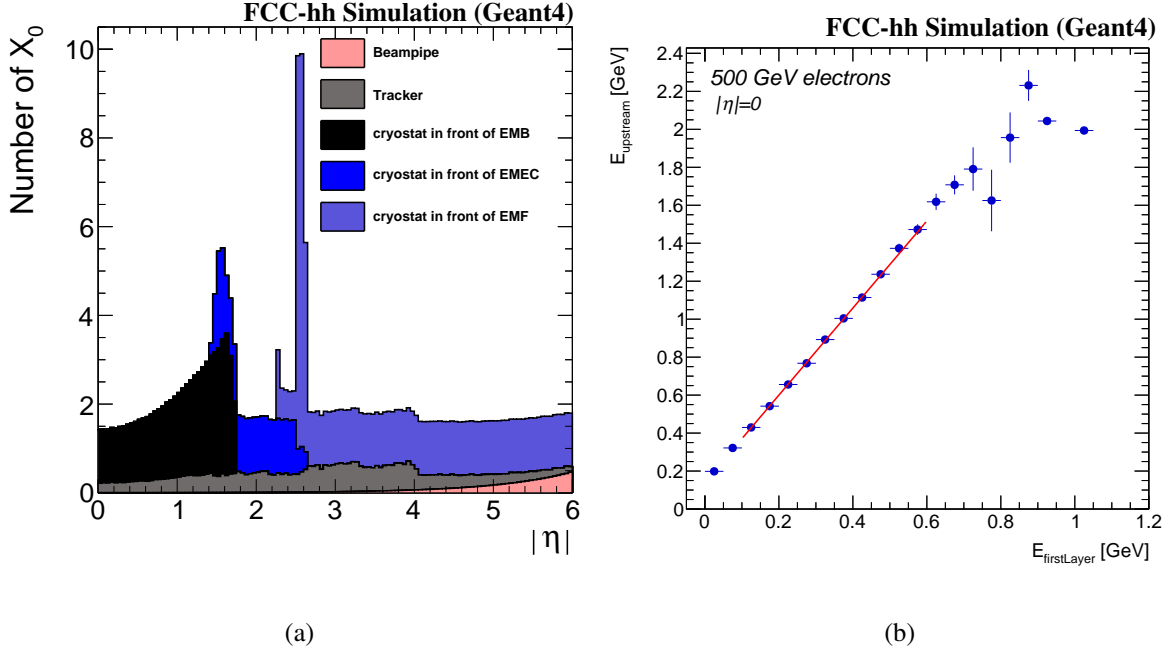


Fig. 7.41: Left (a): Material in front of the calorimeter expressed in units of radiation length, measured from the centre of the detector to the outer boundary of the LAr calorimeter. The ‘spike’ at  $|\eta| = 2.5$  corresponds to the wall at the inner bore of the endcap cryostat. Right (b): Linear correlation between the material upstream and the energy deposited in the first calorimeter layer, for 500 GeV electrons and  $|\eta| = 0.25$ . The parameterisation shown in Eq. (7.15) is used.

$$P_0 = P_{00}(|\eta|) + P_{01}(|\eta|) \cdot E_{\text{cluster}} \quad (7.16)$$

$$P_1 = P_{10}(|\eta|) + \frac{P_{11}(|\eta|)}{\sqrt{E_{\text{cluster}}}} \quad (7.17)$$

Since the amount of upstream material varies strongly with pseudorapidity (see Fig. 7.41a), the parameters  $P_{00}$ ,  $P_{01}$ ,  $P_{10}$ , and  $P_{11}$  are all extracted for several  $|\eta|$  values (every  $\Delta\eta = 0.25$ ). The energy of reconstructed electrons is then calculated as the sum of the energy deposited in the calorimeter  $E_{\text{cluster}}$  and the estimated energy lost upstream  $E_{\text{upstream}}$  according to Eq. (7.18):

$$E = E_{\text{upstream}} + E_{\text{cluster}} \quad (7.18)$$

$$E_{\text{cluster}} = \sum_{\text{deposits}} E_{\text{deposit}} \cdot f_{\text{sampl}}^{\text{layer}}$$

$$E_{\text{upstream}} = P_{00} + P_{01} \cdot E_{\text{cluster}} + \left( P_{10} + \frac{P_{11}}{\sqrt{E_{\text{cluster}}}} \right) \cdot E_{\text{firstLayer}} \quad .$$

The effect of the corrections on the energy resolution for electrons at  $|\eta| = 0$  is presented in Fig. 7.43b. The sampling term of the energy resolution improves significantly. Note also the improvement in response linearity. The corrected energy resolution for electrons impinging the calorimeter at different pseudorapidities is presented in Table 7.10b. As can be seen, the upstream energy correction achieves very good results and ensures excellent electron resolution for all pseudorapidities studied.

This upstream material correction is inspired by the corrections done for the ATLAS LAr calorimeter [163]. The same procedure should be repeated for photons as a function of their conversion radius as well as extended into the other detector parts, the EMEC and the EMF.

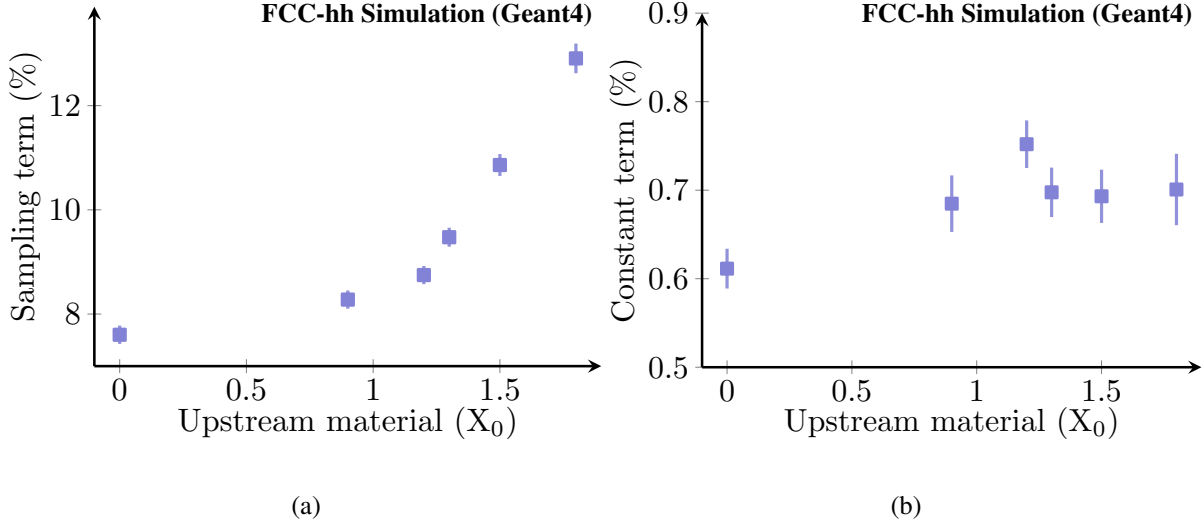


Fig. 7.42: Dependence of the electron energy resolution on the amount of upstream material expressed in terms of sampling term  $a$  (left plot, (a)) and constant term  $c$  (right plot, (b)) for the parameterisation of the energy resolution  $\frac{\sigma_E}{E} = \frac{a}{\sqrt{E}} \oplus c$ . This study was done for an absorber inclination of  $30^\circ$ .

Table 7.10a shows the sampling term  $a$  and constant term  $c$  of the energy resolution for several values of pseudorapidity before (a) and after (b) correction. Especially at higher  $\eta$  (more upstream material) a large improvement is obtained confirming the efficiency of the upstream material correction proposed above.

Table 7.10: Energy resolution of electrons for different pseudorapidity values. **(a)** No correction is applied. **(b)** The correction for upstream material improves the energy resolution. The results presented refer to the geometry with an inclination angle of  $30^\circ$  for the absorber and readout plates.

$\eta$	$a$ ( $\sqrt{\text{GeV}}$ )	$c$	$\eta$	$a$ ( $\sqrt{\text{GeV}}$ )	$c$
0	$8.7\% \pm 0.1\%$	$0.64\% \pm 0.01\%$	0	$6.9\% \pm 0.1\%$	$0.60\% \pm 0.01\%$
0.25	$8.9\% \pm 0.2\%$	$0.62\% \pm 0.01\%$	0.25	$6.5\% \pm 0.2\%$	$0.58\% \pm 0.01\%$
0.5	$9.2\% \pm 0.3\%$	$0.59\% \pm 0.01\%$	0.5	$6.6\% \pm 0.2\%$	$0.53\% \pm 0.01\%$
0.75	$10.5\% \pm 0.3\%$	$0.53\% \pm 0.02\%$	0.75	$7.5\% \pm 0.3\%$	$0.41\% \pm 0.01\%$
1	$12.3\% \pm 0.3\%$	$0.50\% \pm 0.03\%$	1	$8.5\% \pm 0.3\%$	$0.24\% \pm 0.02\%$

(a)

(b)

#### 7.4.1.1.2 Pseudorapidity correction

The most straightforward method to calculate the pseudorapidity of an incident particle showering in the calorimeter is to calculate the centre of gravity of the shower (7.19), where  $\eta_i$  is the pseudorapidity of cell  $i$  and  $E_i$  is energy deposited in that cell.

$$\eta_{\text{rec}} = \frac{\sum_i E_i \eta_i}{\sum_i E_i} \quad (7.19)$$

The result of this position calculation for 50 GeV electrons is presented in Fig. 7.44a. It can be seen that there are systematic differences between the calculated and generated pseudorapidity of the particles as a function of pseudorapidity. This ‘S-shaped’ difference can be minimised by taking advantage of

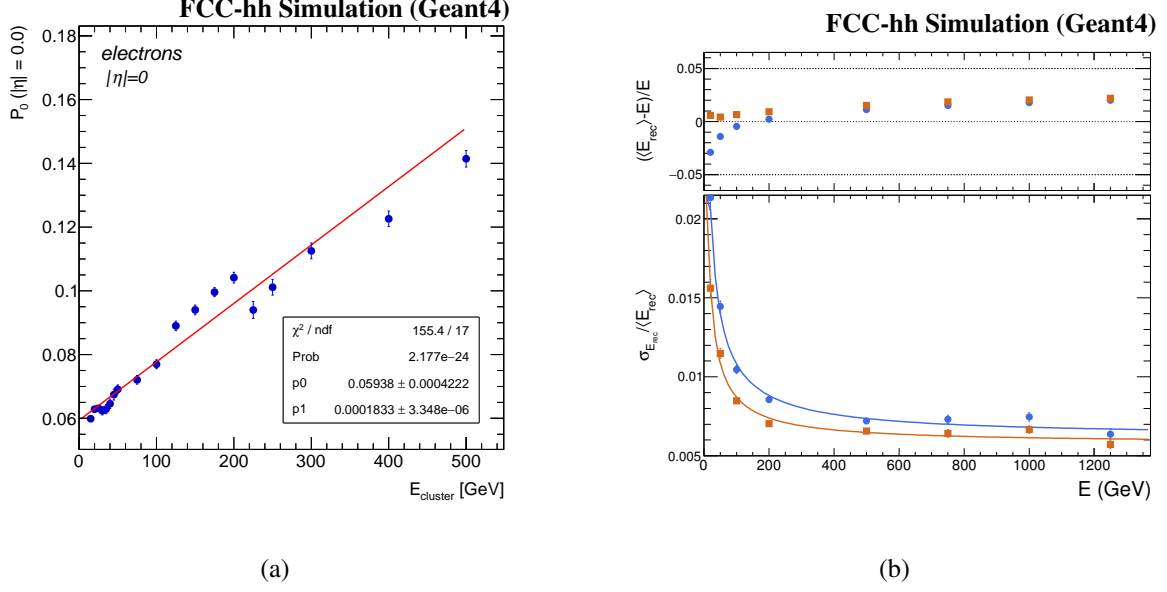


Fig. 7.43: (a) Parameter  $P_0$  of Eq. (7.15) as a function of initial particle energy for  $|\eta| = 0$ .  $P_0$  is described with Eq. (7.16). In the legend  $p_0$  corresponds to  $P_{00}$  and  $p_1$  to  $P_{01}$ . (b) Energy resolution of electrons at  $|\eta| = 0$ . The effect of the upstream material correction is presented (blue circles: no correction, orange squares: correction). The results presented refer to the geometry with an inclination angle of  $30^\circ$  for the absorber and readout plates.

the exponential transverse profile of the shower and using the logarithms of cell energies as weights, as shown in Eq. (7.20).  $E_{\text{layer}}$  is the energy deposited in the given layer,  $w_0^{\text{layer}}$  is a parameter that needs to be carefully chosen.

$$\eta_{\text{rec}}^{\text{layer}} = \frac{\sum_i w_i \eta_i}{\sum_i w_i}, \text{ where}$$

$$w_i = \max(0, w_0^{\text{layer}} + \log \frac{E_i}{E_{\text{layer}}}). \quad (7.20)$$

The parameter  $w_0$  is optimised for each layer in order to minimise the position resolution. Effectively,  $w_0$  defines a threshold of the fraction of energy deposited per layer which a cell must exceed to be included in the calculation. It thereby adjusts the relative importance of the tails of the shower transverse profile: for  $w_0 \rightarrow \infty$  all cells are weighted equally, and for too small  $w_0$  only few cells dominate in the calculation, making it position-sensitive again. The position resolution for 50 GeV photons for different values of  $w_0$  is presented in Fig. 7.45. It can be seen, that  $w_0 = 5$  is very close to the optimum in all layers apart from the first layer which has little energy deposited. A large improvement due to the fine segmentation of the second layer is also visible (resolution for both  $\Delta\eta = 0.01$  and  $\Delta\eta = 0.0025$  in the second layer is presented).

Finally, particle position  $\eta_{\text{rec}}$  is calculated as the weighted mean of the layer positions. The weight could for instance, be energy deposited in the given layer (analogously to Eq. 7.19). The calculation of the pseudorapidity using these parameters significantly mitigates the ‘S-shaped’ systematic differences as can be seen in Fig. 7.44b. In order to improve further the pseudorapidity resolution as a function of energy, instead of energy, resolution in a given layer could be used. This approach, however, requires a prior knowledge about the particle resolution. It has been presented in the results summarised in Section 7.4.1.3.



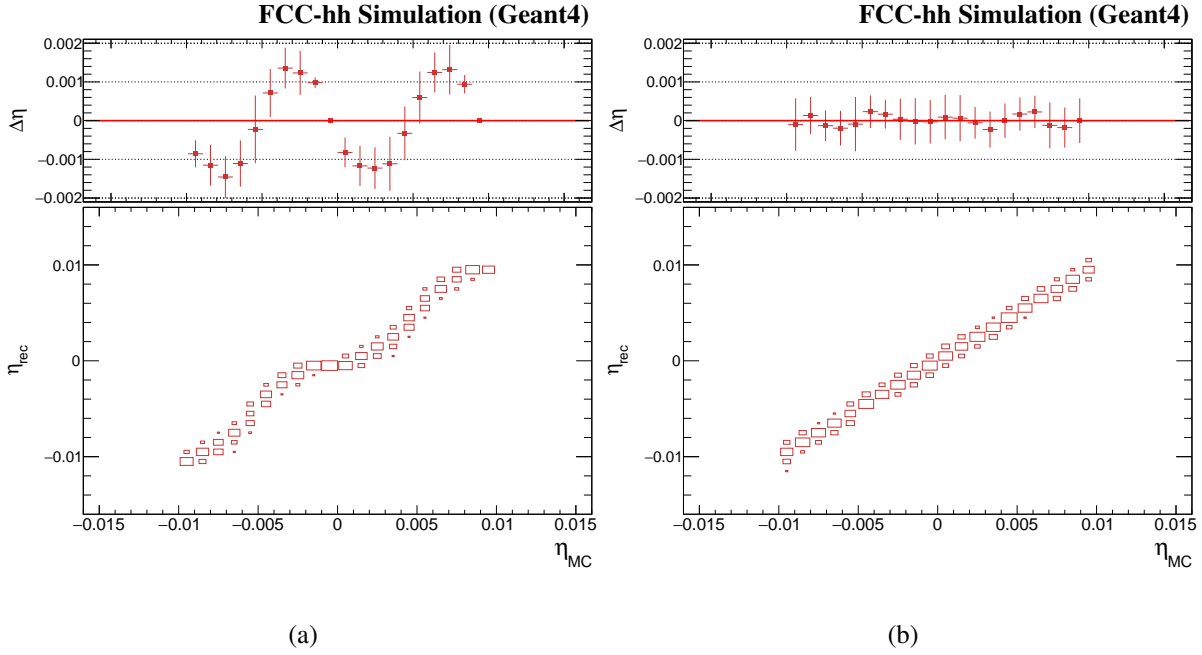


Fig. 7.44: Reconstructed pseudorapidity  $\eta_{\text{rec}}$  as a function of the incident pseudorapidity  $\eta_{\text{MC}}$ . The top plots represent the difference  $\Delta\eta$  between both values. The pseudorapidity is reconstructed (a) using energy weighting, Eq. (7.19), and (b) logarithmic weighting according to Eq. (7.20). One cell in the detector spans from  $\eta = -0.005$  to  $\eta = 0.005$ .

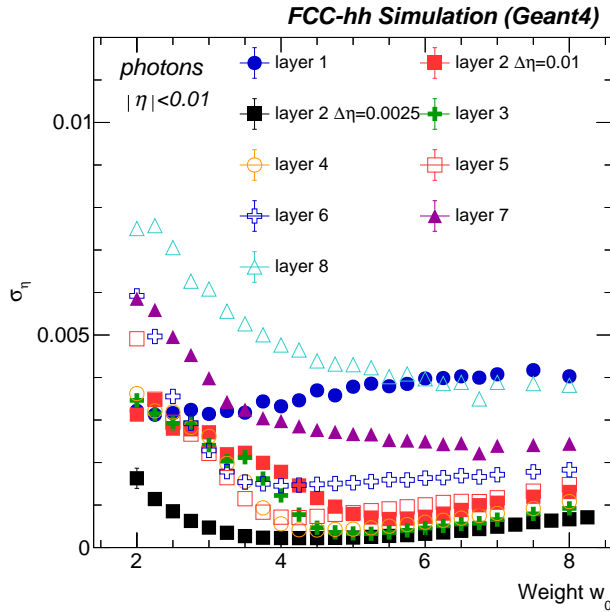


Fig. 7.45: Dependence of the pseudorapidity resolution on the weight parameter  $w_0$  for 50 GeV photons. A resolution is shown for each of the detector layers. The minimum of the pseudorapidity resolution determines the choice of the weight parameter  $w_0$ . A value of  $w_0 = 5$  is very close to the optimum for all layers and was chosen in this study. The segmentation of all layers used here is  $\Delta\eta = 0.01$ , with the exception of the second layer where both  $\Delta\eta = 0.01$  (red full squares) and  $\Delta\eta = 0.0025$  (black squares) are presented.

### 7.4.1.2 Energy resolution and linearity

The energy resolution of a calorimeter can be parameterised using Eq. (7.1) with  $a$  as the sampling term,  $c$  as the constant term and  $b$  as the noise term.

Energy resolution for single electrons for all calorimeter sub-systems is presented in Fig. 7.46. These results do not take into account either electronic or pile-up noise ( $b = 0$  for the fit with Eq. (7.1)). A similar performance is achieved for the barrel ( $\eta = 0$ ) and for the endcaps ( $|\eta| = 2$ ), with the sampling term equal to  $a = 8.2\%$  for the barrel and  $a = 7.6\%$  for the endcaps. The constant term is  $c = 0.15\%$  for the barrel due to the increasing thickness of liquid argon gap, and is equal to 0 for the endcaps, where the ratio of liquid argon to absorber is constant. The energy resolution obtained matches the design goal resolution of  $\frac{\sigma_E}{\langle E \rangle} = \frac{10\%}{\sqrt{E(\text{GeV})}} \oplus 0.7\%$  Eq. (7.2). In the forward region for  $|\eta| > 4$  sampling term of the energy resolution increases to  $a = 23\%$  due to the decrease of the ratio of liquid argon to absorber.

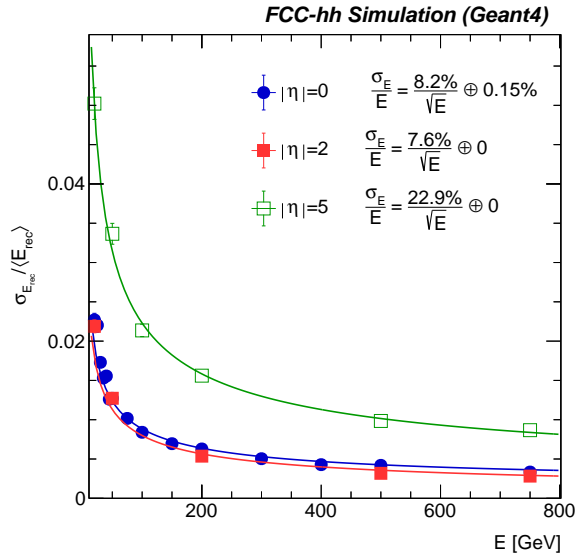


Fig. 7.46: Energy resolution of response for electrons in the barrel ( $\eta = 0$ ), endcaps ( $|\eta| = 2$ ) and forward detector ( $|\eta| = 5$ ).

Figure 7.47 presents energy resolution and linearity of single photons and electrons in the barrel detector for no pile-up environment, with the electronic noise included. The energy resolution obtained is similar for photons and electrons. The sampling and constant terms of the energy resolution are fixed to the values obtained without presence of electronic noise, and the noise term  $b = 0.3$  GeV matches the estimation of the noise level per cluster that is described in Section 7.3.2.1.1. The same correction factors are applied in the reconstruction of both particles: the upstream material correction and the response scaling. The upstream material correction parameters are extracted from the simulation of electrons and lead to the overestimation of the energy deposited by low-energetic photons as can be seen in the linearity plot. Regarding the energy scaling factor, the cluster energy is scaled with an energy-independent factor of  $1/0.96$  to compensate for energy deposited outside of the reconstructed cluster. This factor has been extracted from the response of 100 GeV photons.

In the presence of pile-up, the energy resolution deteriorates. For the sliding window reconstruction with the elliptic window of size  $\Delta\eta \times \Delta\varphi = 0.03 \times 0.08$  the noise term increases to  $b = 0.65$  GeV for  $\langle\mu\rangle = 200$  and  $b = 1.31$  GeV for  $\langle\mu\rangle = 1000$ , as can be seen in Fig. 7.48a. It has a direct impact on the width of the invariant mass peak for Higgs decaying to two photons generated with PYTHIA8. Using the current reconstruction with sliding window and calculating invariant mass for all pairs of electromagnetic clusters with energy above  $E_\gamma > 30$  GeV (no particle identification and no isolation cuts), the width of the invariant mass peak is 1.3% in a no pile-up environment, as can be seen in Fig. 7.48b.

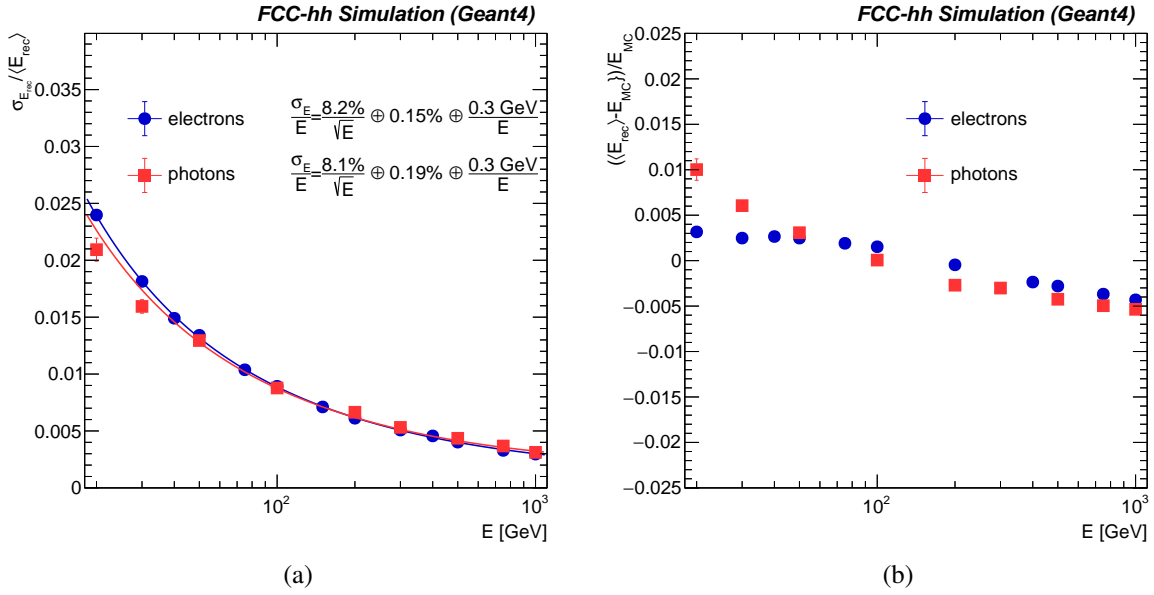


Fig. 7.47: (a) Energy resolution and (b) linearity of response for single electrons and photons in the barrel ( $\eta = 0$ ) for a no pile-up environment. The same correction factors are applied in reconstruction of both particles.

The width increases to 1.9% in the presence of pile-up  $\langle \mu \rangle = 200$  and to 2.3% for  $\langle \mu \rangle = 1000$ . These results show the importance of the pile-up mitigation. First of all, information from calorimeters should be complemented with information from tracking detectors. This should allow the estimation of the contribution from the charged particles from the pile-up events thus reducing the contribution of the energy deposited in calorimeters originating from the pile-up events. It is important to note that for physics analysis where Higgs bosons with high transverse momenta are considered, the mass resolution improves, as can be seen in Fig. 7.49. For pile-up  $\langle \mu \rangle = 1000$  mass resolution improves from 2.3% for an inclusive sample to 2.1% for the transverse cut  $p_T^H > 100$  GeV and further to 1.8% for  $p_T^H > 200$  GeV.

### 7.4.1.3 Position resolution

Using logarithmic weights and the optimisation described in Section 7.4.1.1.2 leads to a pseudorapidity resolution as presented in Fig. 7.50a. The position resolution can be described with Eq. (7.21), where energy  $E$  is expressed in GeV and parameters  $a$  and  $c$  for simulation of photons summarised in Table 7.11. The layer combined measurement is calculated according to Eq. (7.22), where  $i$  indicates the layers of the detector used in the combined calculation. Two layers that yield the best pseudorapidity resolution are the second layer (finely segmented) and the third one (usually containing the shower maximum). The combined  $\eta$  measurement obtained with these layers ( $i = 2, 3$ ) results in an improvement of  $\eta$  resolution. Further improvement is obtained for photons with energies above 50 GeV once all layers ( $i = 1, \dots, 8$ ) are used. For low energetic particles, which deposit most of the energy in the first three (four) layers, the resolution degrades and it is more beneficial to only use those layers in the  $\eta$  position calculation.

$$\sigma = \frac{a}{\sqrt{E}} \oplus c \quad (7.21)$$

$$\eta = \frac{\sum_i \eta_i \cdot \sigma_i^{-1}}{\sum_i \sigma_i^{-1}} \quad (7.22)$$

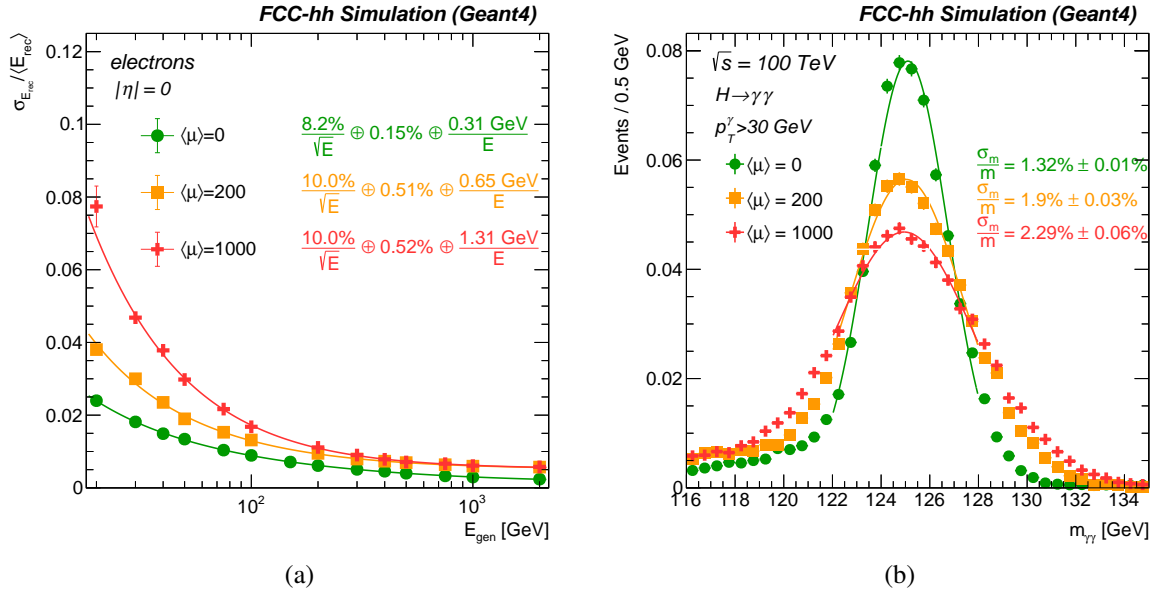


Fig. 7.48: **(a)** Energy resolution of single electrons for different levels of pile-up at  $\eta = 0$ . The no pile-up configuration uses a cluster size of  $\Delta\eta \times \Delta\phi = 0.07 \times 0.17$  whereas in presence of pile-up the optimised cluster size is  $\Delta\eta \times \Delta\phi = 0.03 \times 0.08$ . **(b)** Effect of pile-up on the Higgs invariant mass distribution by selecting two electromagnetic clusters with  $p_T^\gamma > 30$  GeV.

Table 7.11: Summary of the pseudorapidity resolution presented in Fig. 7.50a. It includes two layers with the best resolution: second (finely segmented) and third (usually containing the shower maximum), as well as combined measurements of those two layers and combined measurement of all EMB layers.

Layer	a ( $\cdot 10^{-3}$ )	c ( $\cdot 10^{-3}$ )
2	1.34	0.14
3	1.82	0.23
2+3	1.21	0.13
All	1.36	0.10

Resolution of the azimuthal angle  $\varphi$  for photons and electrons is presented in Fig. 7.50b. The results obtained for photons are  $\sigma_\varphi = \left( \frac{3.76}{\sqrt{E}} \oplus 0.22 \right) \cdot 10^{-3}$ , and for electrons  $\sigma_\varphi = \left( \frac{4.39}{\sqrt{E}} \oplus 0.18 \right) \cdot 10^{-3}$ . For low energetic electrons a clear degradation is observed due to presence of the magnetic field.

#### 7.4.1.4 Timing resolution

As described in Section 7.1.2, the exact measurement of the time of arrival of particles at the calorimeter will be very necessary to help mitigate pile-up. Since the expected number of proton collisions every bunch crossing (up to 1000) will not happen simultaneously, but, depending on the exact beam parameters, will take place in a time window of 50 to 500 ps, a time measurement with  $\mathcal{O}(30)$  ps resolution could help to reduce pile-up substantially by rejecting all particles where the arrival time is not compatible with the time of the primary vertex. Such a timing measurement in front of the calorimeters is planned to be introduced for HL-LHC for both ATLAS [164] and CMS [165]. Since the measurement is performed before showers develop, single charged particles will be measured and each track from the inner tracker will get its time tag.

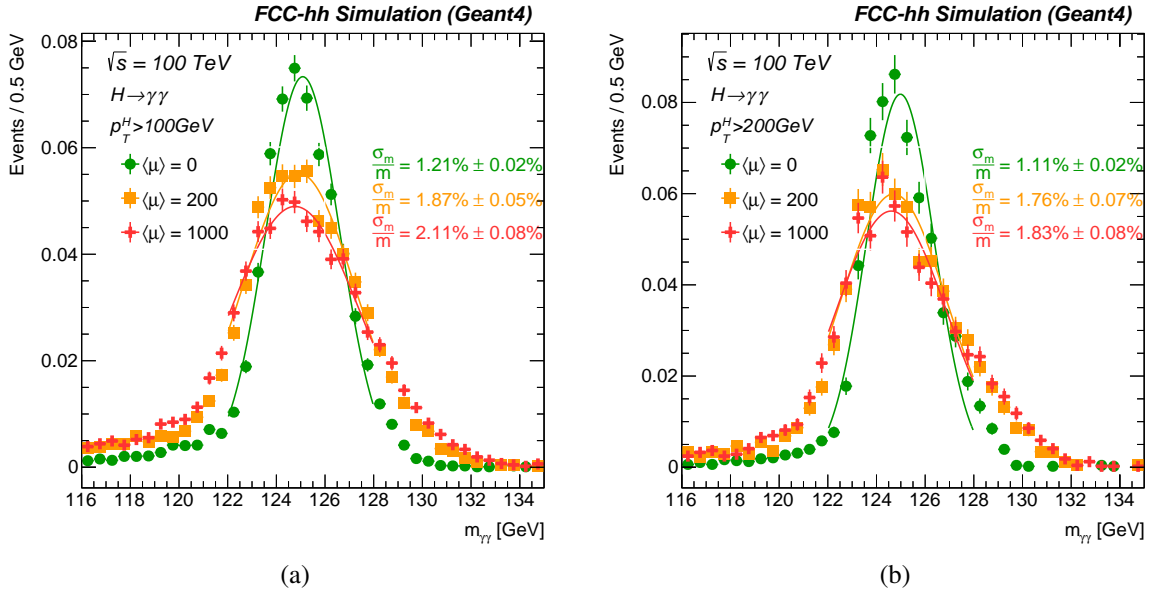


Fig. 7.49: Higgs invariant mass distribution by selecting two electromagnetic clusters with  $p_T^\gamma > 30$  GeV in a no pile-up environment, for  $\langle \mu \rangle = 200$  and  $\langle \mu \rangle = 1000$ . An additional cut is applied on the transverse momentum of the reconstructed Higgs, improving the mass resolution: (a)  $p_T^H > 100$  GeV, and (b)  $p_T^H > 200$  GeV.

A timing measurement inside the calorimeter could, in addition, supply timing information for neutral particles, that would help to identify the primary vertex for e.g.  $H \rightarrow \gamma\gamma$  events as planned for the HL-LHC upgrade of CMS [166]. The high granularity will help to obtain separate clusters for each incoming particle and keep merging of clusters at a minimal level. A time tag for each calorimeter cluster would then be a strong handle to reject energy deposits coming from pile-up vertices. Furthermore, within merged clusters the timing measurement of single cells could be used to disentangle parts of the cluster containing energy deposits of different particles. On top of that, the timing information could also be used to obtain higher connection efficiency between tracks and calorimeter clusters. Again, a timing resolution of  $\mathcal{O}(30)$  ps per cluster would be a good target for an FCC-hh calorimeter.

The timing resolution of an LAr calorimeter will depend on the signal rise time of the ionisation signal after preamplification and shaping and the electronic noise. The signal rise time will be determined by the time constants of the preamplifier (defined by the product of the preamplifier's input impedance and the cell capacitance, see Section 7.2.2.1) and the shaper, as well as the signal amplitude. Whereas the electronic noise depends mainly on the signal attenuation along the signal traces and read-out cables, and the cell capacitance. The ATLAS LAr calorimeter was not optimised for a timing measurement, it nevertheless achieves a timing resolution of  $\mathcal{O}(65)$  ps for high energetic clusters. It is expected that a careful optimisation of all parameters will allow a more precise time measurement of the proposed FCC-hh LAr calorimeter.

## 7.4.2 Hadronic showers

The 100 TeV proton-proton collisions inside the FCC-hh detector will produce jets with transverse momenta of up to 50 TeV. In such jets 10% of the hadrons are expected to have an energy of at least 1 TeV [20]. Thus a precise hadron energy measurement up to very high energies is essential for several key physics channels. The single hadron reconstruction is a crucial first step towards the full jet performance.

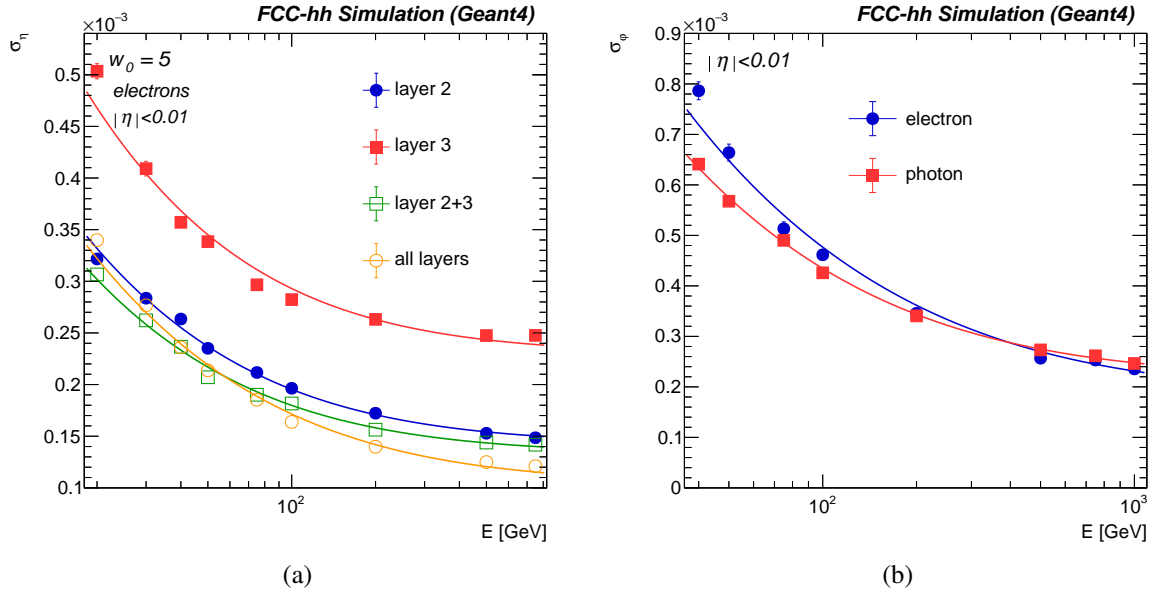


Fig. 7.50: (a) Pseudorapidity resolution for the two best calorimeter layers: second (red full circles) and third (blue full squares), as well as combined measurements of those two layers (green hollow squares) and from all EMB layers (yellow hollow circles). (b) Azimuthal angle resolution for electrons (blue circles) and photons (red squares).

#### 7.4.2.1 Reconstruction at the cell level

The reconstruction of hadrons in the central barrel region has to combine the energy deposits in the EMB and HB. This can be done simply by summing up all deposits on EM scale. However, this leads to sub-optimal results due to the different hadronic energy scales of the two calorimeters (different  $e/h$  ratios), and due to the significant energy loss between the calorimeters in the passive material of the LAr cryostat. To recover the energy losses, the correlation between the energy in the cryostat and the energy deposits in the last EMB and first HB layer can be used as depicted in Fig. 7.51. The energy reconstruction performed in this subsection is done without yet considering the electronics noise.

##### 7.4.2.1.1 Benchmark method

The so-called benchmark method has been developed for ATLAS test-beam measurements. It applies a correction for the energy lost between EMB and HB and calibrates the energy deposits to the hadronic scale. The total energy is reconstructed as following

$$E_{\text{rec}}^{\text{bench}} = E_{\text{EMB}}^{\text{EM}} \cdot p_0 + E_{\text{HB}}^{\text{had}} + p_1 \cdot \sqrt{\left| E_{\text{last layer}}^{\text{EMB}} \cdot p_0 \cdot E_{\text{first layer}}^{\text{HB}} \right|} + p_2 \cdot \left( E_{\text{EMB}}^{\text{EM}} \cdot p_0 \right)^2 \quad . \quad (7.23)$$

The first term,  $E_{\text{EMB}}^{\text{EM}}$ , is the energy sum in the electromagnetic barrel calorimeter. This energy is by default calibrated to EM scale and thus needs to be corrected by the first parameter  $p_0$ . The second term,  $E_{\text{HB}}^{\text{had}}$ , is the energy sum in the hadronic calorimeter which is calibrated to the hadronic scale using a constant scaling of  $f_{\text{hadronic}} = 2.4\%$  instead of the sampling fraction. This value has been determined for the HB using a linear fit, similar to the determination of the EM fraction, but comparing the mean pion instead of electron response to the true particle energy. The third term determines and corrects the amount of energy lost between EMB and HB as a function of  $\sqrt{\left| E_{\text{last layer}}^{\text{EMB}} \cdot p_0 \cdot E_{\text{first layer}}^{\text{HB}} \right|}$ , and the fourth term is a correction for the non-compensation of the EMB.

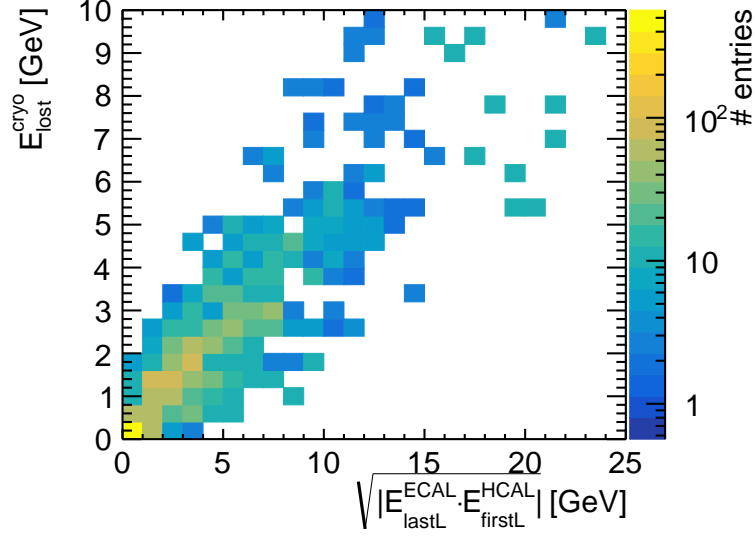


Fig. 7.51: Correlation of the energy loss of a pion in the LAr cryostat between the EMB and the HB, and the geometric mean of the energy deposited in the last EMB and first HB layer.

The parameters  $p_0$ ,  $p_1$ , and  $p_2$  are determined minimising  $\xi^2 = \sum_i \frac{(E_{\text{true}}^i - E_{\text{rec}}^{\text{bench},i})^2}{E_{\text{true}}^i}$  with a sample simulation set of 2,000 pion events with energies of 10, 100, 1000, and 10000 GeV each. Due to the energy dependence of hadronic shower shapes, and the constant parameters  $p_0$ ,  $p_1$ , and  $p_2$ , a non-linearity of up to 10% remains. In a last step this non-linearity is corrected, using a simple power law fit to the response. Thus, the final energy is measured following:

$$E_{\text{rec}}^{\text{final}} = \left( \frac{E_{\text{rec}}^{\text{bench}} - p_3}{p_4} \right)^{1/p_5}, \quad (7.24)$$

which is valid for particle energies between 10 GeV and 1 TeV.

The reconstruction parameters are summarised in Table 7.12. The resulting energy resolution and linearity obtained from the sum over all cells without considering electronics noise, with and without magnetic field are shown in Fig. 7.52. After the response correction, a linearity at the level of one percent is obtained.

Table 7.12: Benchmark parameters for single pions, determined at  $\eta = 0.36$ .

B [T]	$p_0$	$p_1$	$p_2$ [1/GeV]	$p_3$ [GeV]	$p_4$	$1/p_5$
0	$1.062 \pm 0.001$	$0.659 \pm 0.005$	$-(6.31 \pm 0.16) \times 10^{-6}$	-0.83	0.9834	0.9973
4	$0.996 \pm 0.002$	$0.565 \pm 0.006$	$-(7.42 \pm 0.22) \times 10^{-6}$	-0.92	0.9697	0.9956

The single pion energy resolution of the FCC-hh combined calorimeter system results in a stochastic term of 44% without magnetic field and 48% with magnetic field respectively and a constant term of approximately 2%, well inside the requirements described in Section 7.1.2.

#### 7.4.2.1.2 Comparison to energy reconstruction using deep neural networks

Deep neural networks can bring benefits for the energy reconstruction particularly for hadronic showers. As described in Section 7.3.3, a part of the energy reconstruction network is designed in similar way



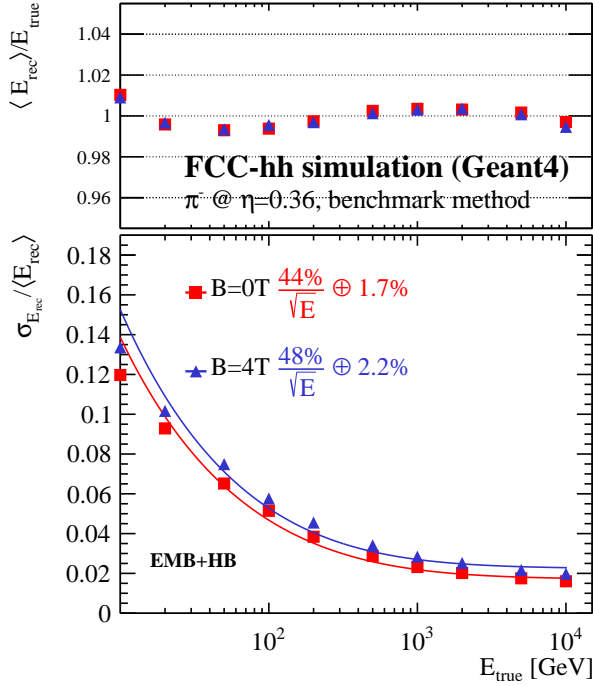


Fig. 7.52: Energy resolution (bottom) and linearity (top) for single  $\pi^-$  at  $\eta = 0.36$  using the benchmark reconstruction on all barrel calorimeter cells. The electronic noise is not considered here.

to an object identification network in computer vision. Therefore, parts of the shower can be identified on an event-by-event basis, such as e.g. the EM fraction, provided sufficiently granular information is available. As a result, the energy resolution can potentially be much better than for simpler approaches such as the benchmark method described in the previous section. An example of the energy distributions after applying the DNN (green circles) and benchmark method (blue triangles) to 200 GeV pion showers in the presence of the magnetic field, is shown in Fig. 7.53a. The better performance of the DNN is evident. As shown in the top plot of Fig. 7.53b, the response is very linear between 20 and 1,000 GeV, and the resolution (bottom plot) is strongly improved compared to the results obtained with the benchmark method. The DNN reconstruction achieves a stochastic term of 37% and the constant term of 1%. It should be noted that these results are obtained with calorimetry information only (no tracker information), without electronics noise and without pile-up. It is expected that this approach can also be applied for more realistic assumptions of noise and pile-up and will profit from additional information from the tracker.

#### 7.4.2.1.3 Including electronic noise at the cell level reconstruction

Realistic estimates of the expected electronic noise have been added to the cells of the EMB and HB calorimeters. To test the impact on the single pion energy resolution, the cells included have been limited to a range within a cone in  $\eta$  and  $\phi$  of radius  $R = \sqrt{(\Delta\eta)^2 + (\Delta\phi)^2}$  with  $\Delta\eta = \eta_{\text{cell}} - \eta_{\text{true}}$ ,  $\Delta\phi = \phi_{\text{cell}} - \phi_{\text{true}}$ . The expected noise contribution  $\sigma_{\text{noise}}$  to the single particle resolution is estimated by adding the noise contributions per cell in quadrature. The number of cells within the cone, the noise in EMB and HB, and the total noise for different cone radii are summarised in Table 7.13. In the following, the cone radius has been chosen to contain 98% of the single pion energy over the full energy range, see Fig. 7.54, and found to be 0.3/0.4 for B = 0/4 T, respectively.

The impact of the cone selection on the single pion energy resolution has been studied and is summarised in Fig. 7.55. The FCC-hh resolutions obtained are given for B = 0 T and compared to ATLAS testbeam results [167]. The benchmark method was also used by ATLAS in the combined testbeam

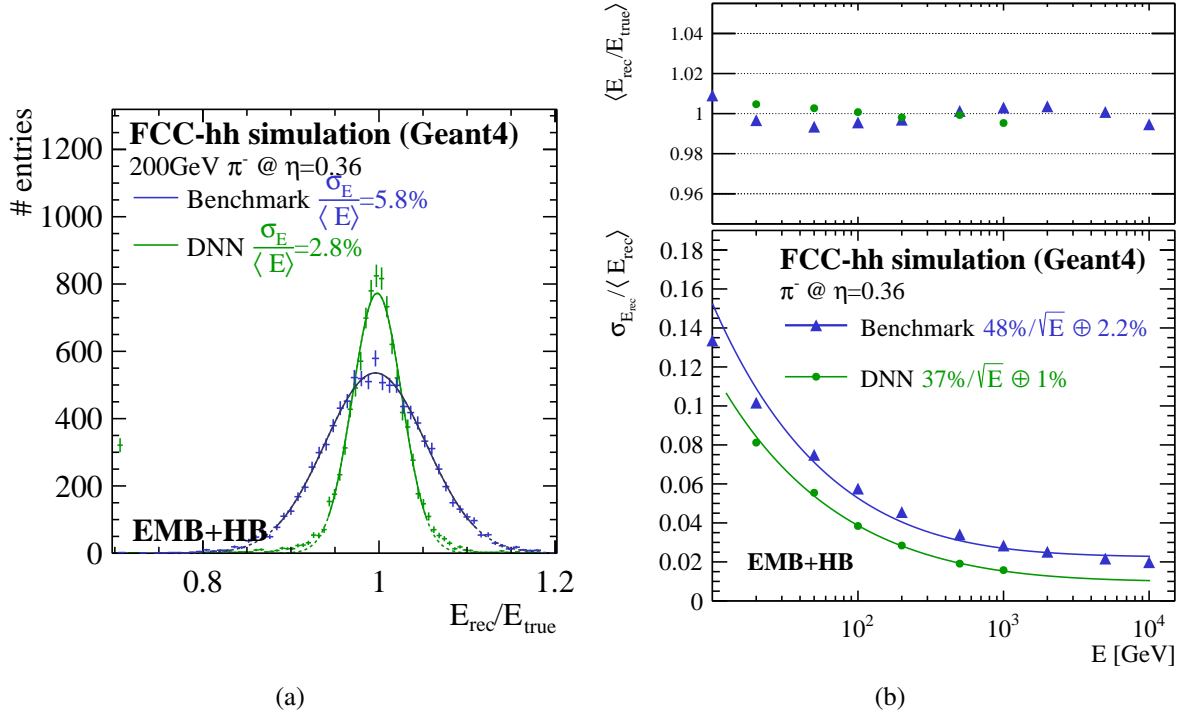


Fig. 7.53: (a) Energy distributions, (b) resolution and linearity for charged pions using the DNN (green) and benchmark (blue) energy reconstruction, with the magnetic field of 4 Tesla applied.

Table 7.13: Summary of the noise expected for different cone radii, thus different number of cells around  $\eta = 0.36$ .

Cone/window	EMB $\langle \text{noise} \rangle / \text{cell}$ [MeV]	HB $\langle \text{noise} \rangle / \text{cell}$ [MeV]	EMB cells [#]	HB cells [#]	EMB noise [GeV]	HB noise [GeV]
$R < 0.40$	3.5-40	10	45 080 <b>53 230</b>	8 150	2.05 <b>2.24</b>	0.90
$R < 0.30$	3.5-40	10	25 344 <b>29 954</b>	4 610	1.52 <b>1.66</b>	0.68
$R < 0.17$	3.5-40	10	8,088 <b>9 568</b>	1480	0.86 <b>0.94</b>	0.38
$0.34 \times 0.34$ (DNN)	3.5-40	10	41 344 <b>48 634</b>	7 290	1.98 <b>2.15</b>	0.84

for the energy combination of an electromagnetic liquid argon accordion calorimeter and a hadronic scintillating-tile calorimeter, however featuring a different ratio of active to passive absorber material with a Sci:Fe ratio of 1:4.7. The cone size of  $R = 0.17$  corresponds approximately to the selection used in the analysis of the ATLAS testbeam. The parameters of the energy resolution are listed in Table 7.14 for different cone sizes, that correspond to different lateral shower containments  $C_{20 \text{ GeV}}$  (values for 20 GeV pions). Figure 7.55 shows that the FCC setup achieves a better resolution than the ATLAS testbeam over the full energy range. An improvement with respect to ATLAS is expected due to the optimised absorber of the HB. However, part of the difference has to be attributed to the fact that testbeam measurements are compared to simulations assuming perfect calibration and uniformity of the calorimeter response.

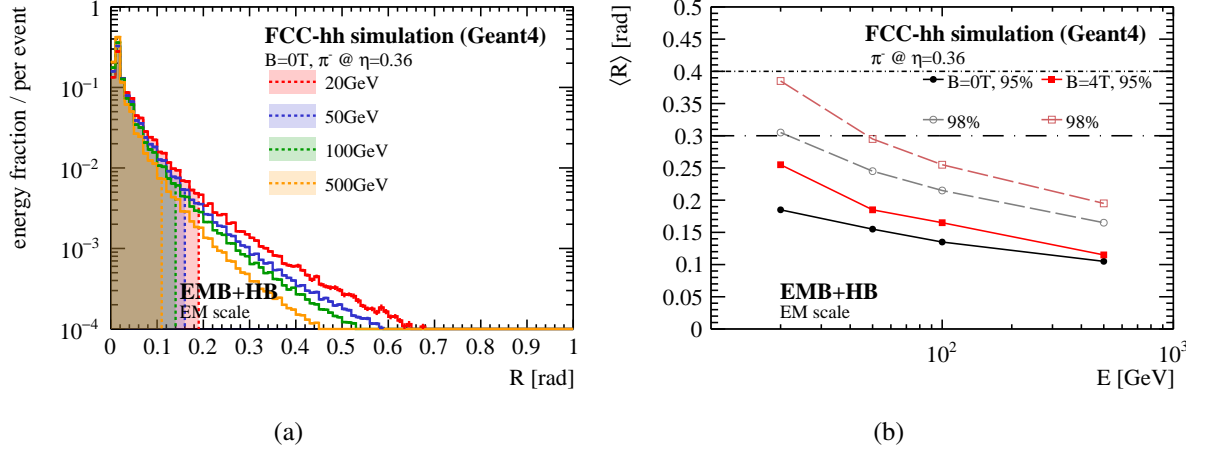


Fig. 7.54: a) Energy fractions of 20-500 GeV pions within  $R$  in the EMB + HB on the EM scale. Filled area corresponds to 95% containment. Lateral containment of 95, and 98% of pion showers in the EMB + HB as a function of the particle energy.

Table 7.14: Impact of selection cut in  $R$  on the stochastic  $a$ , noise  $b$ , and constant term  $c$  for benchmark reconstruction on cell level. The lateral shower containment, corresponding to the different cone sizes, is given for 20 GeV pions as  $C_{20\text{ GeV}}$ .

$R$ [rad]	B [T]	$C_{20\text{ GeV}}$ [%]	$a$ [% $\sqrt{\text{GeV}}$ ]	$b$ [GeV]	$c$ [%]
0.3	0	98	55.6	1.66	1.7
0.17	0	95	64.5	0.94	1.9
0.4	4	98	59.9	2.24	2.3
0.3	4	95	61.8	1.66	2.3
0.17	4	92	74.1	0.94	2.6

#### 7.4.2.2 Performance of topological cell clustering algorithm

An example of one pion shower, after topo-clustering is presented in Fig. 7.56 and visualises the use of the calorimeters granularity as well as the effective noise suppression by the reconstruction algorithm. The electronic noise is always included in the case of the reconstruction using the topo-clustering algorithm.

In the following, clusters within a cone around the particles generated with a radius

$$R = \sqrt{\left(\eta_{\text{rec}}^{\text{cluster}} - \eta_{\text{true}}\right)^2 + \left(\phi_{\text{rec}}^{\text{cluster}} - \phi_{\text{true}}\right)^2} \quad (7.25)$$

are summed up. This cut on the radius is different to the cell selection, previously introduced in Section 7.4.2.1, since the cluster positions are based on the centre of gravity of the cells contained, thus the cells can extend the selection cone. This selection criterion is used to substitute the missing information from the tracker, which would effectively preselect a certain calorimeter area to match the track with calorimeter cluster. This will be crucial, especially in the high pile-up environment.

##### 7.4.2.2.1 Optimisation of the topo-clustering algorithm

The thresholds of the topological clustering algorithm, introduced in Section 7.3.1.1.2, are optimised for single pions on the EM scale.

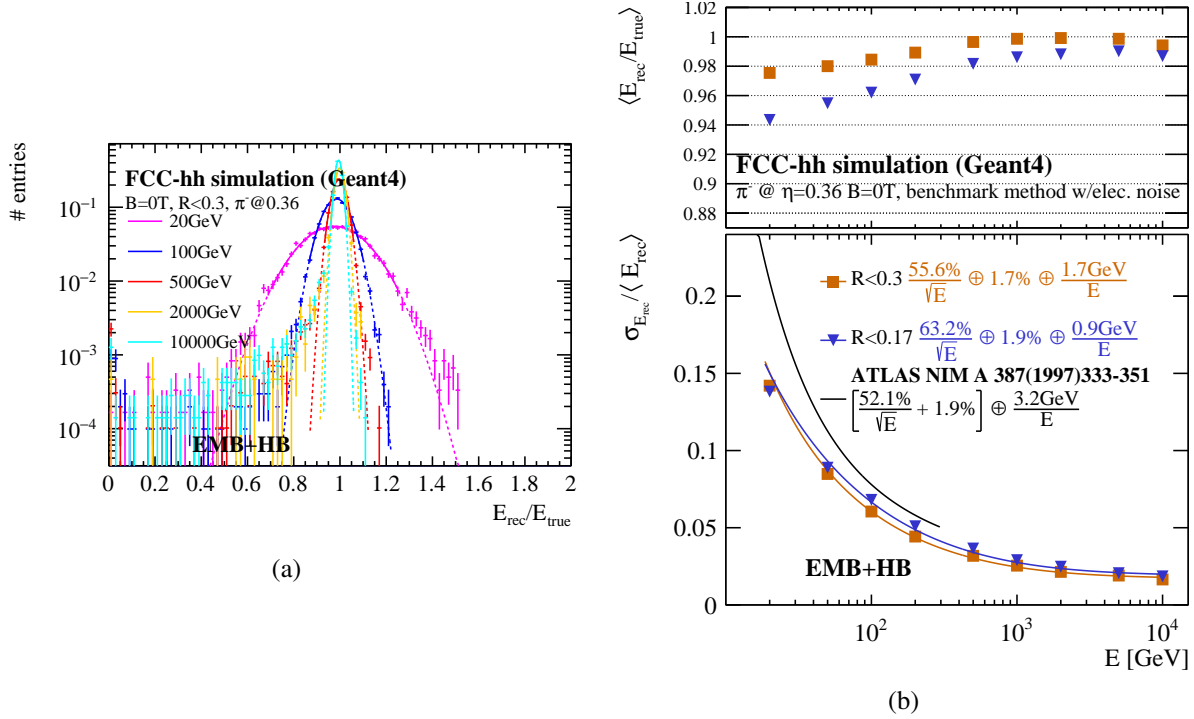


Fig. 7.55: Left plot (a): Energy distributions for a cone cut of  $R < 0.3$ . Right plot (b): The energy resolution of pions at  $\eta = 0.36$ , with  $B = 0\text{T}$  is shown for 98%, and 95% lateral shower containment, corresponding to  $R < 0.3$  and  $0.17$  respectively. The combined performance of EMB + HB is compared to ATLAS testbeam results [167].

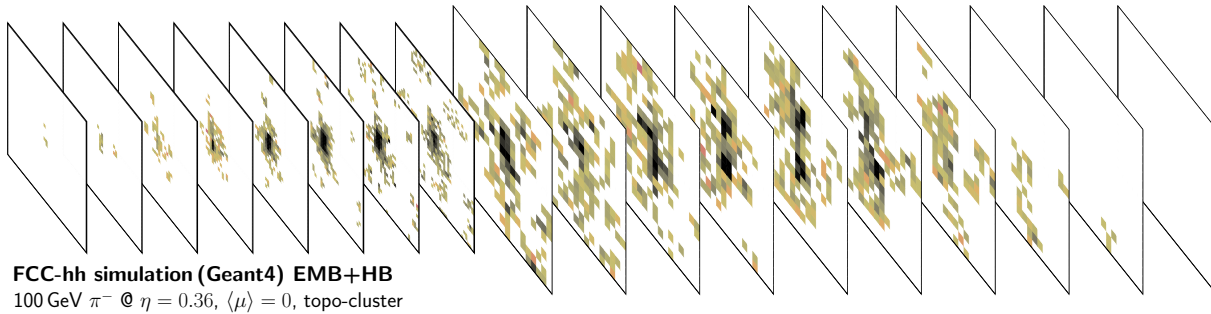


Fig. 7.56: The energy deposited per calorimeter layer of single 100 GeV pion shower in the EMB + HB. The colour code visualises the amount of energy per calorimeter cell on a log scale.

The linearity of the response and the energy resolution curves for different parameters of the topo-clustering algorithm were tested. The results without any cut on  $R$  and those obtained when applying a cut of  $R < 0.4$  around the barycentre of the topo-cluster were compared, see Fig. 7.57a and 7.57b, respectively. The difference between various thresholds is obvious at low energies only, the different values are in good agreement in the high energy regime, as expected. The thresholds  $S = 4$  (seed threshold),  $N = 2$  (threshold for neighbours) and  $P = 0$  (final step), noted in units of  $\sigma_{\text{noise}}$ , are found to be optimal. These parameters result in a good linearity as well as energy resolution for both cases— with and without the cut on the radius, and they are consistent with the choices made by the ATLAS collaboration [150].

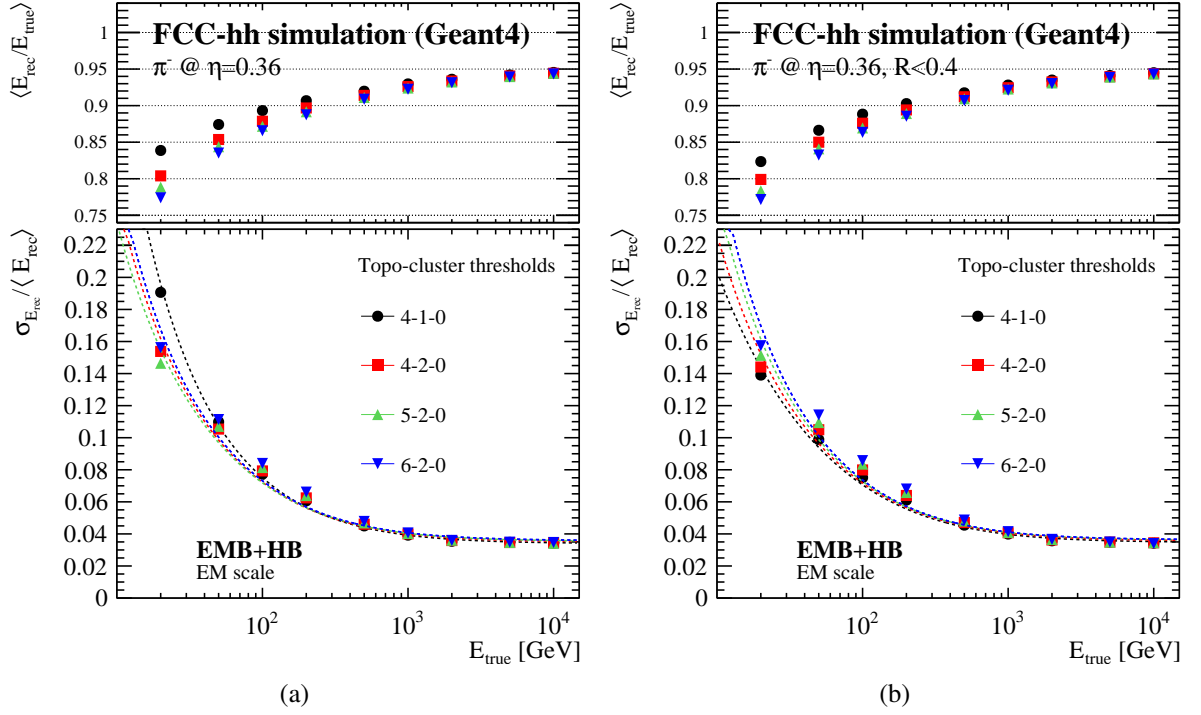


Fig. 7.57: Energy resolution and linearity of pion showers at the EM scale for different thresholds of the topo-clustering algorithm with (a) no cut on R applied and (b) with cut  $R < 0.4$  on the barycentre of the topo-cluster.

#### 7.4.2.2.2 Calibration of topo-cluster

The clusters are built of cells which have been calibrated to the EM scale, nevertheless, the performance can be improved if a correction for the lost energy within the LAr cryostat is included. To correct for the energy lost between EMB and HB, as described in Section 7.4.2.1.1, a calibration is applied using the energy deposited in the last EMB and first HB layer as a measure of the energy deposited in the cryostat. The benchmark correction on a topo-cluster is based on the clustered cells, whereas the total energy per event is given by the sum over all clusters:

$$E_{\text{rec}}^{\text{topo-cluster}} = \sum_i^{\text{cluster}} E_i \quad , \quad (7.26)$$

with cluster energies  $E_i$

$$E_i = \sum_j^{\text{cells}} E_{\text{EMB},j}^{\text{EM}} \cdot p_0 + \sum_j^{\text{cells}} E_{\text{HB},j}^{\text{had}} + p_1 \cdot \sqrt{|E_{\text{last layer}}^{\text{EM}} \cdot p_0 \cdot E_{\text{first layer}}^{\text{HB}}|} + p_2 \cdot \left( \sum_j^{\text{cells}} E_{\text{EMB},j}^{\text{EM}} \cdot p_0 \right)^2 \quad . \quad (7.27)$$

The parameters  $p_0$ ,  $p_1$  and  $p_2$  are determined on the cell level, and the performance has been validated. Further tests have been performed to allow for an energy dependence of parameters  $p_0$ ,  $p_1$  and  $p_2$ . However, only little further improvement was achieved. Therefore in the following, the simplest approach without energy dependence was used.

The impact of the cluster calibration on the reconstructed energy can be seen in Fig. 7.58. The linearity as well as the resolution is improved over the full energy range. In comparison to the performance obtained when adding up all cells, the improvement due to the decreased number of cells is most pronounced at 20 GeV.

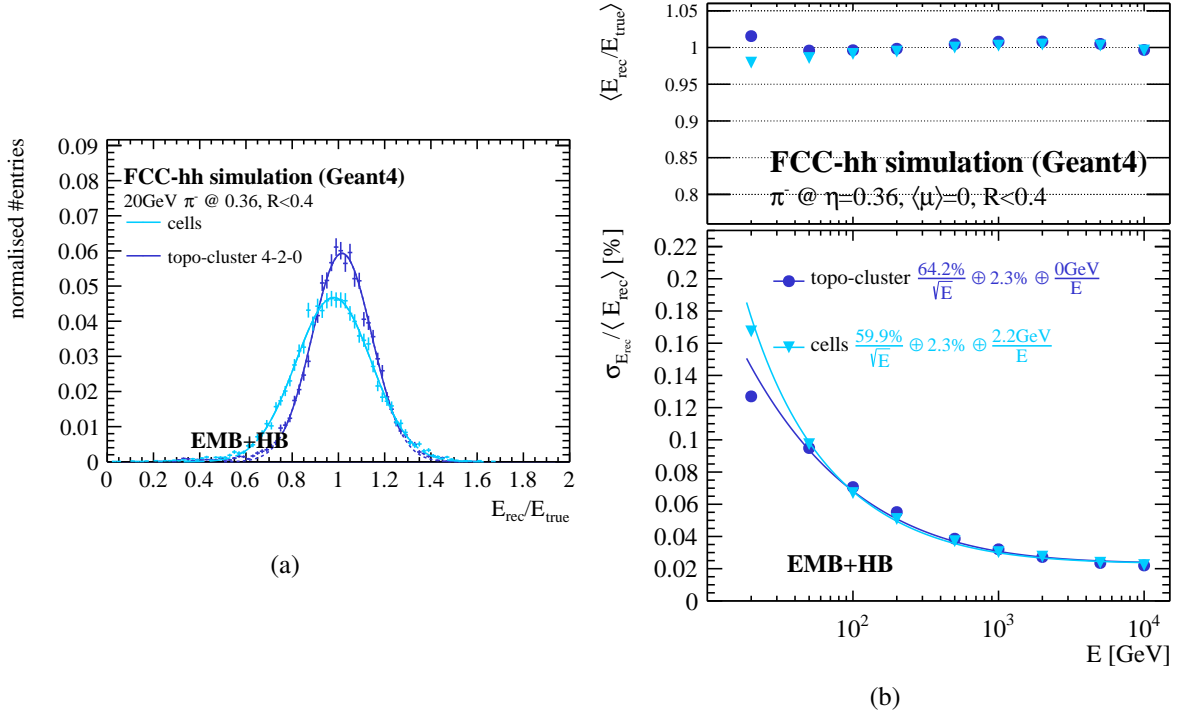


Fig. 7.58: Energy distributions of single pions (a) when adding up all cells with  $R < 0.4$  and after topo-clustering, both including the benchmark corrections. (b) The energy resolution and linearity of pion showers in full EMB + HB simulations at  $\eta = 0.36$ . The resolution is obtained from topo-cluster with 4-2-0 thresholds within  $R < 0.4$ . Again, the values with and without topo-cluster are shown.

#### 7.4.2.2.3 Angular resolutions and impact of HB granularity

The highest HB granularity in  $\eta$  of  $\Delta\eta < 0.006$  could be obtained if each scintillating tile is read out separately. However, to reduce the number of readout channels and thus cost, several scintillating tiles will be summed together resulting in an effective granularity of  $\Delta\eta = 0.025$ . In this way the number of effective readout channels is reduced from 1 305 600 to 226 307, still providing a five times higher granularity than the current ATLAS tile calorimeter [138]. The effect on the angular resolution for single pions is discussed in the following, while the angular resolutions for jets is shown in Section 7.4.5.

As shown in Fig. 7.59b, the  $\eta$ -resolution for single pions falls steeply with energy and improves up to 15% if the full granularity of the HB is exploited. Figure 7.60b shows the angular resolution for the two HB granularities as a function of the generated particle rapidity. The position resolution decreases for the default HB granularity, and increases for the full HB granularity with increasing  $\eta$ . These tendencies can be explained by the increasing sampling fraction in the EMB. The HB granularity of  $\Delta\eta < 0.006$  in the full granularity configuration is finer than the granularity of the EMB with  $\Delta\eta = 0.01$ , thus the larger the shower fraction in the EMB, the worse the resolution and vice versa. In the case of a broader HB segmentation of 0.025, the larger energy fraction in the EMB improves the resolution.

To determine whether the full granularity at scintillator level should be exploited, further studies including particle flow algorithms and particle ID algorithms will be needed. Additional studies are also needed to evaluate the impact of the very high pile-up environment and the power of the high granularity for pile-up suppression.

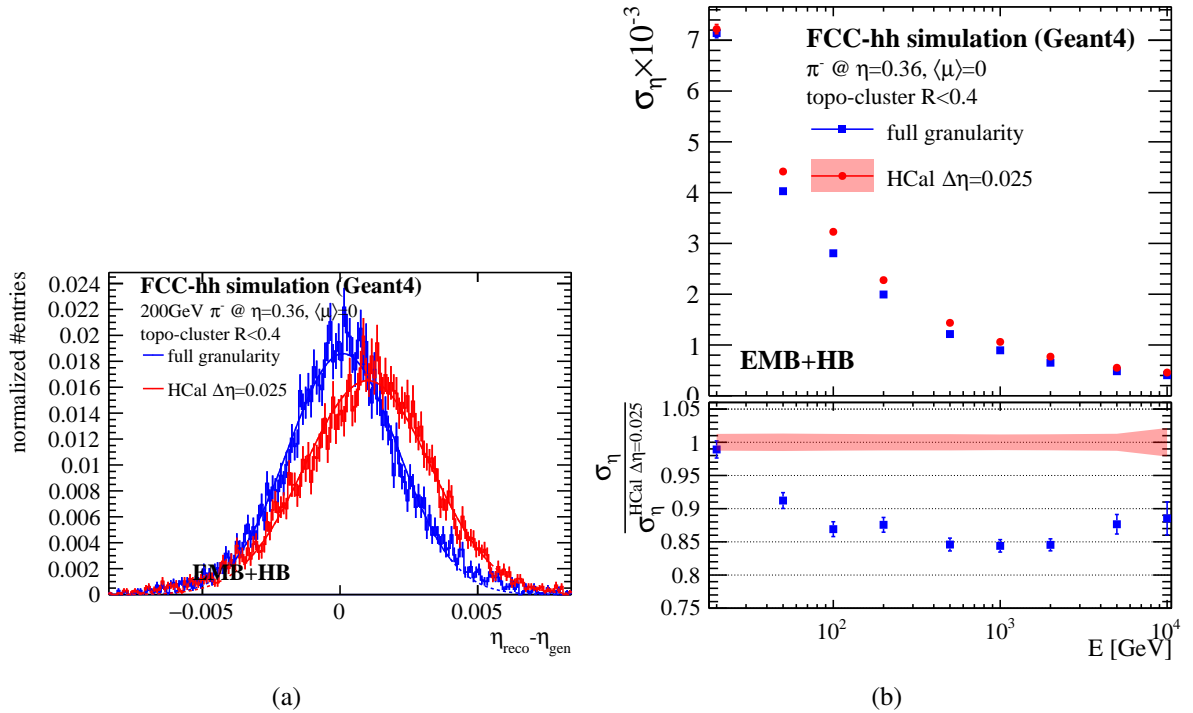


Fig. 7.59: (a) Difference between reconstructed and generated  $\eta$  for topo-cluster within  $R < 0.4$  for 200 GeV pions generated at  $\eta = 0.36$ , shown for the finest possible HB granularity of  $\Delta\eta < 0.006$  (full granularity, blue) compared to the baseline granularity of the HB ( $\Delta\eta = 0.025$ , red). (b) Impact of the HB granularity on the  $\eta$  resolution for single pions.

#### 7.4.2.2.4 Energy reconstruction of single hadrons in a high pile-up environment

To determine the performance of the topo-cluster algorithm, 200 simulated minimum bias events are overlaid to mimic a realistic pile-up environment. It is expected that—due to the bipolar shaping—the out-of-time pile-up will on average compensate the positive energy deposit due to in-time pile-up. Therefore, due to the fact that out-of-time pile-up is not included, the mean energy deposit per calorimeter cell is shifted to positive values. In order to emulate the effect of out-of-time pile-up, the mean value is therefore corrected<sup>15</sup> and shifted back to 0, see also Section 7.3.2.2. However, due to the very steep energy spectrum and small cell sizes this correction is relatively small with maximum shifts by 25 and 9 MeV for  $\langle\mu\rangle = 200$  of the EMB and HB cell energies, respectively. The expected noise per cell, which is needed to determine the cell’s significance, is estimated by the quadratic sum of the pile-up and the electronic noise contribution. The pile-up noise contributions are estimated as the RMS of the energy distribution of 200 and 1000 minimum bias events per cell, above the respective electronics noise level, as also described in Section 7.3.2.2. The energy reconstruction within the high pile-up environment is particularly challenging for low energetic particles, due to the number of pile-up clusters with energies of up to multiple hundreds of GeV (topo-cluster in 4-2-0 mode, on EM scale) for  $\langle\mu\rangle = 200$ . Figure 7.61a shows the energy distribution for topo-cluster (EM scale) for events with 200 collisions per bunch crossing ( $\langle\mu\rangle = 200$ ) and Fig. 7.61b shows the corresponding number of clusters that are built from 200 minimum bias events in the full EM and hadronic barrel calorimeters.

The linearity and energy resolution for different thresholds at the EM scale with an in-time pile-up of  $\langle\mu\rangle = 200$  are shown in Fig. 7.62. To reduce the effect of pile-up, a cylindrical region with  $R < 0.3$

<sup>15</sup>It should be noted that this approach does not include the impact of out-of-time pile-up on the event-to-event fluctuations due to energy deposits in previous bunch-crossings. An event-to-event correction of the out-of-time pile-up through the application of advanced filtering algorithms using the full event history is being studied for the HL-LHC upgrades.



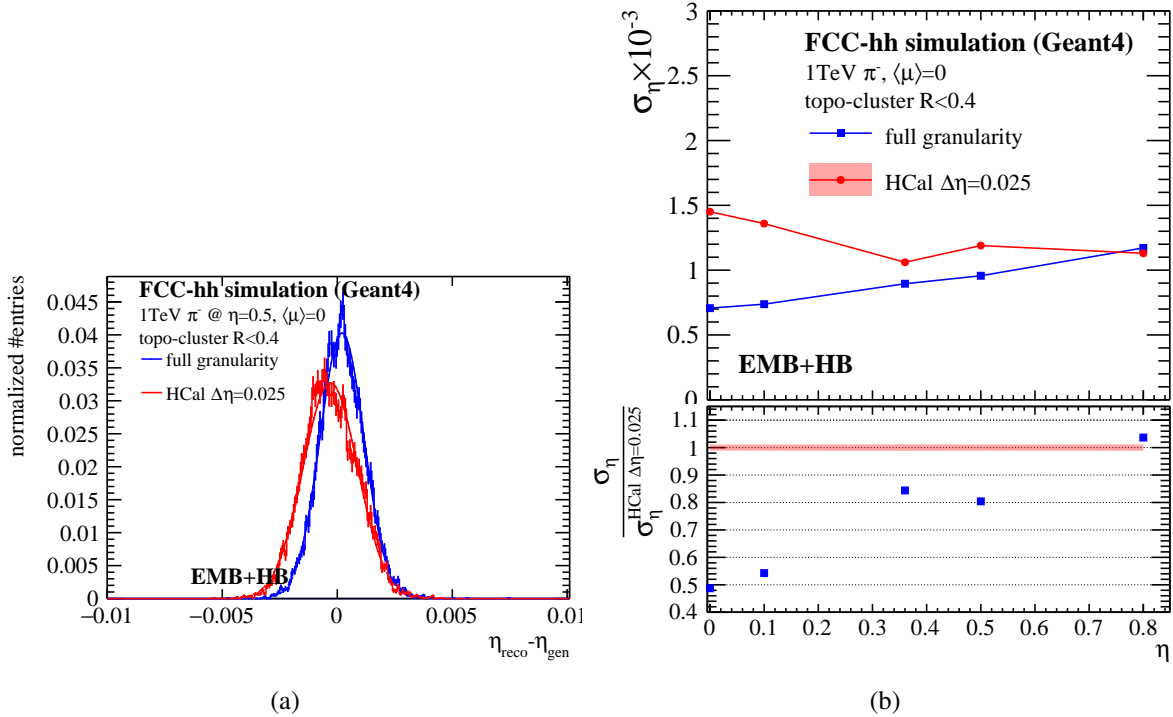


Fig. 7.60: (a) Difference between reconstructed and generated  $\eta$  for topo-cluster within  $R < 0.4$  for 1 TeV pions generated at  $\eta = 0.5$ , shown for the finest possible HB granularity of  $\Delta\eta < 0.006$  (full granularity, blue) compared to the baseline granularity of the HB ( $\Delta\eta = 0.025$ , red). (b) Angular resolution as a function of  $\eta$  for 1 TeV pions, shown for the full HB granularity (blue) compared to the baseline granularity of the HB (red).

around the barycentre of the topo-cluster is used to calculate the energy. The linearity of the energy response is heavily degraded, the ratio of the reconstructed and true energy exceeds 2.5 for 20 GeV pions. This result demonstrates that an energy reconstruction at  $\langle\mu\rangle = 200$  needs to incorporate pile-up suppression techniques. The comparison to the energy resolution without pile-up (solid line) shows the strong impact on the performance for  $\langle\mu\rangle = 200$ , up to high energies of 5 TeV. It is obvious that such high pile-up cannot be handled with a simple clustering algorithm alone, but more sophisticated rejection techniques and the information from the tracker will be needed for an accurate energy measurement of the products of the hard scatter. It was not possible to develop such techniques in the scope of this study. Figure 7.62 shows that a small improvement can be achieved by optimising the thresholds of the topo-cluster algorithm. The thresholds  $S = 6$ ,  $N = 2$  and  $P = 0$  are chosen for the following plots.

The energy resolution for single pions and 200 pile-up events after topo-cluster reconstruction, including a simple calibration as described in Section 7.4.2.2.2, is shown in Fig. 7.63a. A strong degradation of the resolution is observed especially at energies below 500 GeV, which increases the stochastic term from 70 to 125%. Additionally, the linearity cannot be ensured in this scenario due to the addition of pure pile-up clusters, see top plot in Fig. 7.63a. Due to the bad linearity below 50 GeV, the resolution fit does not include the low energy points. The topo-cluster algorithm alone is not able to reject pile-up, which illustrates the need for either smart cluster energy correction like the jet-area-based offset correction [168], or particle flow algorithms that match the particle tracks in the tracker to the calorimeter clusters [169]. The effect of pile-up on the number of clusters and the number of clustered cells is shown in Fig. 7.64. It is observed that the total number of clusters is increased by one order of magnitude moving from  $\langle\mu\rangle = 0$  to 200. The energy spectra of these topo-cluster in  $\langle\mu\rangle = 200$  range from 0 to 260 GeV and include up to 12 000 cells.

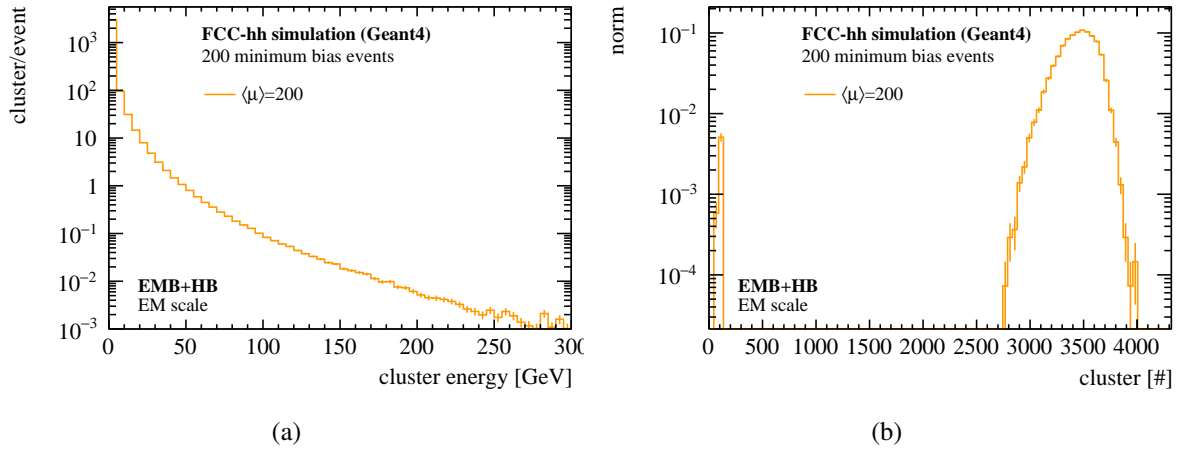


Fig. 7.61: (a) Energy distribution and (b) the number of topo-cluster for events with 200 collisions per bunch crossing ( $\langle\mu\rangle = 200$ ), on the EM scale, and 4-2-0 topo-cluster threshold configuration.

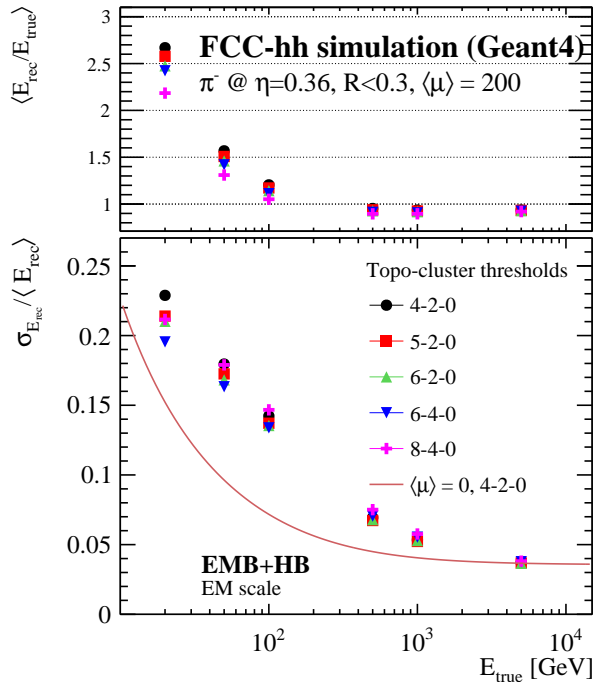


Fig. 7.62: Energy resolution and linearity of pion showers at the EM scale for different thresholds of the topo-clustering algorithm at  $\langle\mu\rangle = 200$  with a cut of  $R < 0.3$  around the barycentre of the topo-cluster. The solid line corresponds to the resolution curve for the default threshold (4-2-0) without pile-up. Configurations with  $P = 1$  were also tried, but showed no difference from cases with  $P = 0$ , and are therefore not shown in the plot.

The comparison of the resolution with the results of the DNN for  $\langle\mu\rangle = 200$  is shown in Fig. 7.63b. As expected, the DNN is able to reconstruct the particle energy with a much better linearity, and an energy resolution of 46% in the stochastic and 1.8% constant term is achieved. However, it needs to be mentioned, that electronic noise is not included in this case. The effect can be estimated by adding another 2.15 GeV in quadrature to the noise term of the original fit, see the dashed blue line in Fig. 7.63b. The noise value has been determined from cells within a window of  $\Delta\eta \times \Delta\phi = 0.34 \times 0.34$ , see the bottom row in Table 7.13.

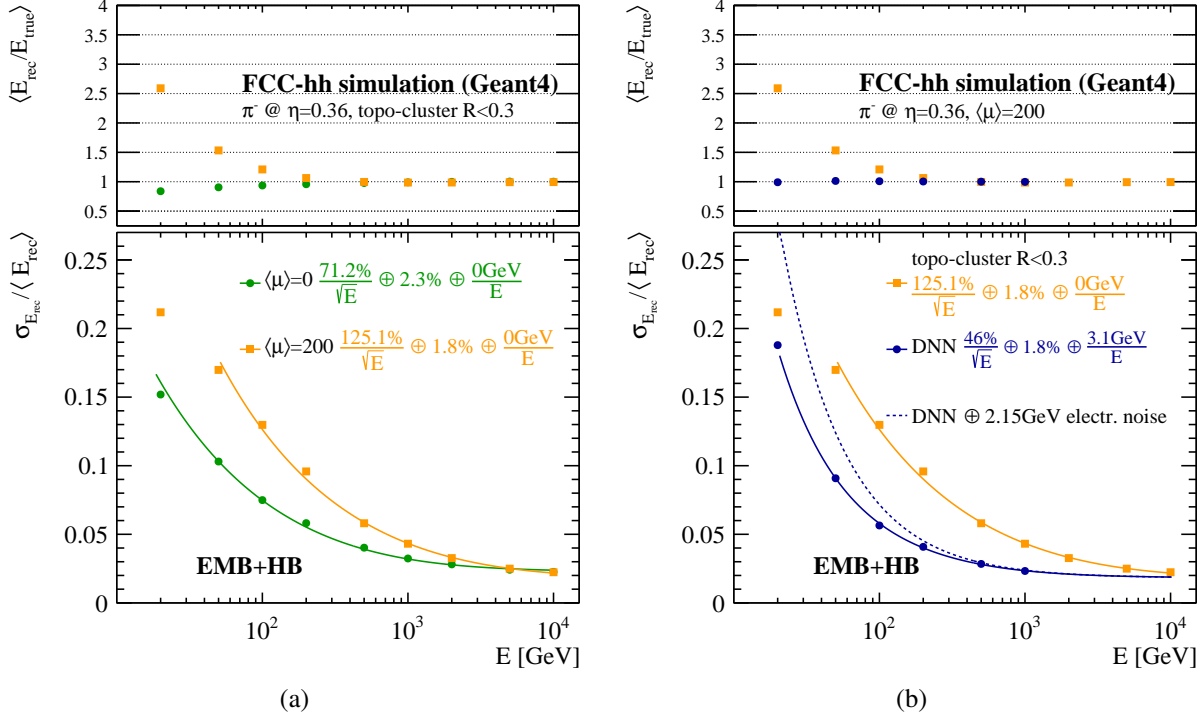


Fig. 7.63: (a) Energy resolution and linearity of pion showers at  $\eta = 0.36$  for pile-up of  $\langle \mu \rangle = 0/200$ . The resolution is obtained after topo-clustering in 4-2-0/6-2-0 mode after calibration, with  $R < 0.3$ , and (b) compared for  $\langle \mu \rangle = 200$  to the performance of the deep neural network (DNN).

The impact of  $\langle \mu \rangle = 1000$  in-time pile-up on the hadron performance has been tested as well. However, as the results for  $\langle \mu \rangle = 200$  already show, more sophisticated algorithms are needed to reject and suppress the pile-up events and contributions, respectively. A first step towards improving the topo-cluster algorithm has been recently developed [170].

### 7.4.3 Pion and photon identification using multivariate analysis (MVA) techniques

In the following, the ability to distinguish single photons from  $\pi^0$  mesons in the EMB of the FCC-hh detector is tested. This is an important property to be considered for optimising the design of the detector as it is key for the reduction of the background of the important  $H \rightarrow \gamma\gamma$  decay. Due to the small mass of the  $\pi^0$ , the two photons coming from a  $\pi^0 \rightarrow \gamma\gamma$  decay are very close to each other and therefore can be misidentified as a single photon. With sufficiently fine granular calorimetry, however, it is possible to detect the separation between the two photons and therefore distinguish the  $\pi^0$  signal from a single  $\gamma$  signal. In this study we analyse the  $\pi^0$  rejection in the EMB for transverse momenta  $p_T \in [10 - 80]$  GeV at  $|\eta| = 0$ .

#### 7.4.3.1 Methodology

##### 7.4.3.1.1 Monte Carlo simulations

The single particle simulations of  $\pi^0$  and  $\gamma$  in the EMB were produced without considering pile-up or electronic noise. The number of events analysed for every data point was at least  $(1 \pm 0.05) \times 10^5$  for each particle in order to minimise random fluctuations. The following geometries were explored:

1. The simplest geometry with cell size  $\Delta\eta = 0.01$  and  $\Delta\phi = 0.009$  in all layers.
2. The EMB layout with cell size  $\Delta\eta = 0.0025$  and  $\Delta\phi = 0.009$  in the 2<sup>nd</sup> layer and  $\Delta\eta = 0.01$  in all other layers.

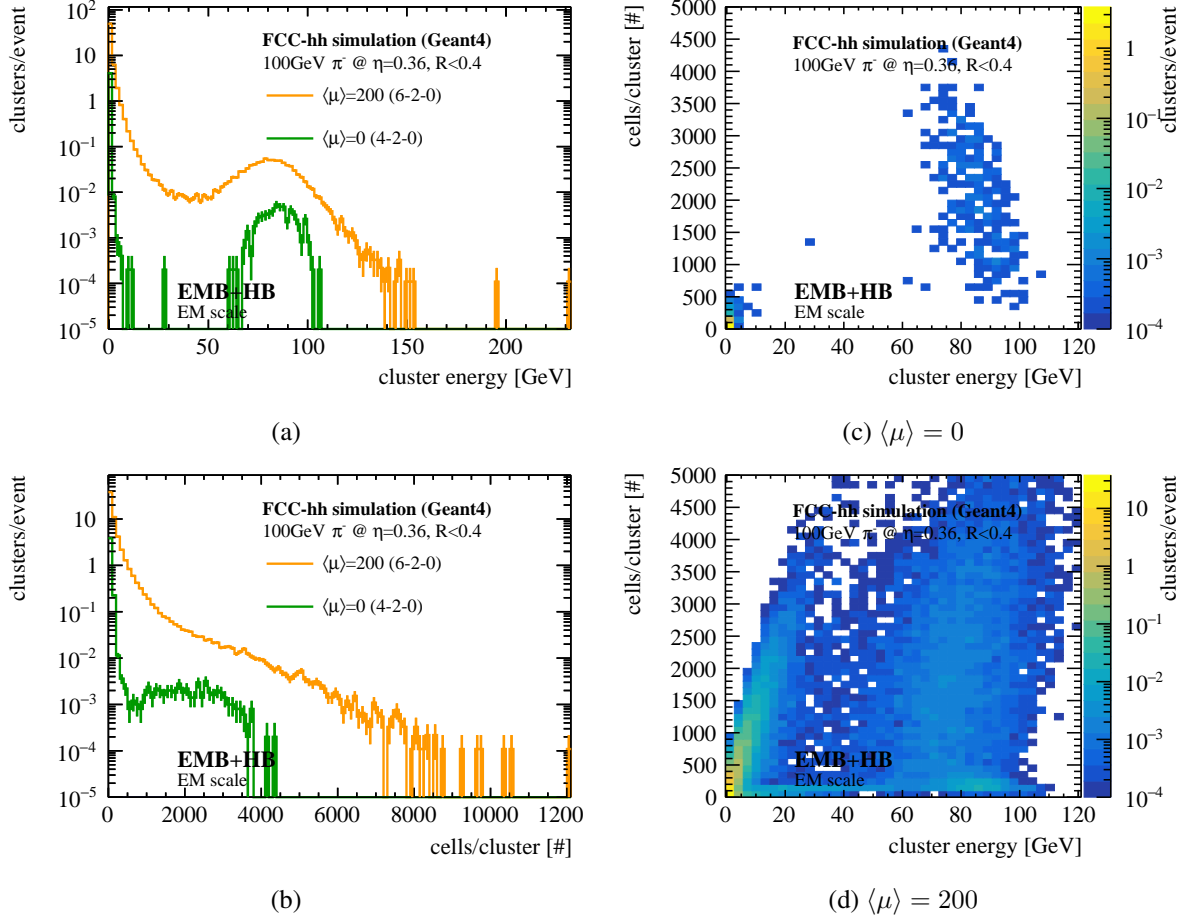


Fig. 7.64: (a) Cluster energies and (b) number of cells per cluster for 100 GeV pion showers at  $\eta = 0.36$ , in EMB + HB for  $\langle\mu\rangle = 0$  and 200. (c) and (d) show the strong increase in the total number of topoclusters, and their energy distribution.

3. Geometry 1 with the 2<sup>nd</sup> layer split in half (in longitudinal direction) while combining the 7<sup>th</sup> and 8<sup>th</sup> layers to maintain a constant number of readout channels.
4. Geometry 2 with the now 4<sup>th</sup> layer (layer 3 in geometry 1) also halved while combining the new 6<sup>th</sup> and 7<sup>th</sup> layers (layers 5, 6, 7 and 8 in geometry 1).
5. Geometry 4 with also finer segmentation in  $\phi$ ,  $\Delta\phi = 0.0045$  in all layers, which effectively doubles the number of layers in the  $\phi$  direction.

The individual characteristics of all analysed data sets are summarised in Table 7.15 and the layer structure for all geometries is illustrated on Fig. 7.65.

#### 7.4.3.1.2 Discriminating variables

The energy and cell data from the single particle simulations was then used to calculate a set of variables that are expected to distinguish between  $\pi^0$  and  $\gamma$  energy deposits. These are inspired by the previous study done on  $\gamma/\pi^0$  separation in the 1<sup>st</sup> compartment of the ATLAS EMB and adjusted to accommodate more layers provided by the FCC detector. The variables are defined as follows:

1.  $E_{\max}$  - Maximal cell energy deposit for all the cells of the second layer.
2.  $E_{2^{\text{nd}}_{\max}}$  - A second energy maximum separate from  $E_{\max}$  by at least one cell.

Table 7.15: Properties of the data sets used in the analysis. The segmentation in pseudo-rapidity is set to  $\Delta\eta = 0.0025$  only in the second layer for samples 2 to 5. The "used layer" refers to the number of longitudinal layers used

	$p_T$ [GeV]	# used layer	$\eta$	$\Delta\eta^*$	$\Delta\phi$
Sample 1	10 to 50	3	0	0.01	0.009
Sample 2	10 to 50	3	0	0.0025	0.009
Sample 3	10 to 50	4	0	0.0025	0.009
Sample 4	10 to 80	5	0	0.0025	0.009
Sample 5	10 to 80	5	0	0.0025	0.0045

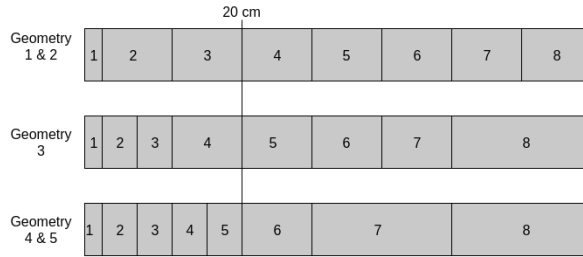


Fig. 7.65: Schematic of the distribution of EMB layers in the different geometries that were analysed.

3.  $E_{\text{ocore}}$  - Fraction of energy deposited outside the shower's centre where  $E(\pm n)$  is the energy deposited in  $\pm n$  cells around the cell with the maximal energy deposit:

$$E_{\text{ocore}} = \frac{E(\pm n) - E(\pm 1)}{E(\pm 1)} \quad (7.28)$$

with  $n = 3$

4.  $E_{\text{dmax}}$  - Difference between the second energy maximum and the minimal energy deposit in the valley between the maximal energy deposit and the second energy maximum:

$$E_{\text{dmax}} = E_{2^{\text{nd}}_{\text{max}}} - E_{\text{min}} \quad (7.29)$$

5.  $W_{nst}$  - The shower width summed over  $n$  central cells along  $\eta$  that are within  $\pm 1$  of the  $\phi$  coordinate of the maximal energy deposit.  $st$  stands for strips as the nomenclature originates from ATLAS where energy was summed over  $n$  strip cells. In Eq. (7.30)  $i$  denotes the cell number and  $i_{\text{max}}$  the cell with the maximal energy deposit. It is always computed in the same layer.

$$W_{nst} = \frac{\sum E_i \cdot (i - i_{\text{max}})^2}{\sum E_i} \quad (7.30)$$

6.  $E_{nT}$  - Energy deposited in the  $n^{\text{th}}$  layer divided by the total energy  $E_T$  deposited in the EMB:

$$E_{nT} = \frac{E_n}{E_T} \quad (7.31)$$

7.  $E_{n1}$  - Energy deposited in the  $n^{\text{th}}$  layer divided by the total energy deposited in the 1<sup>st</sup> layer of the EMB.

$$E_{n1} = \frac{E_n}{E_1} \quad (7.32)$$

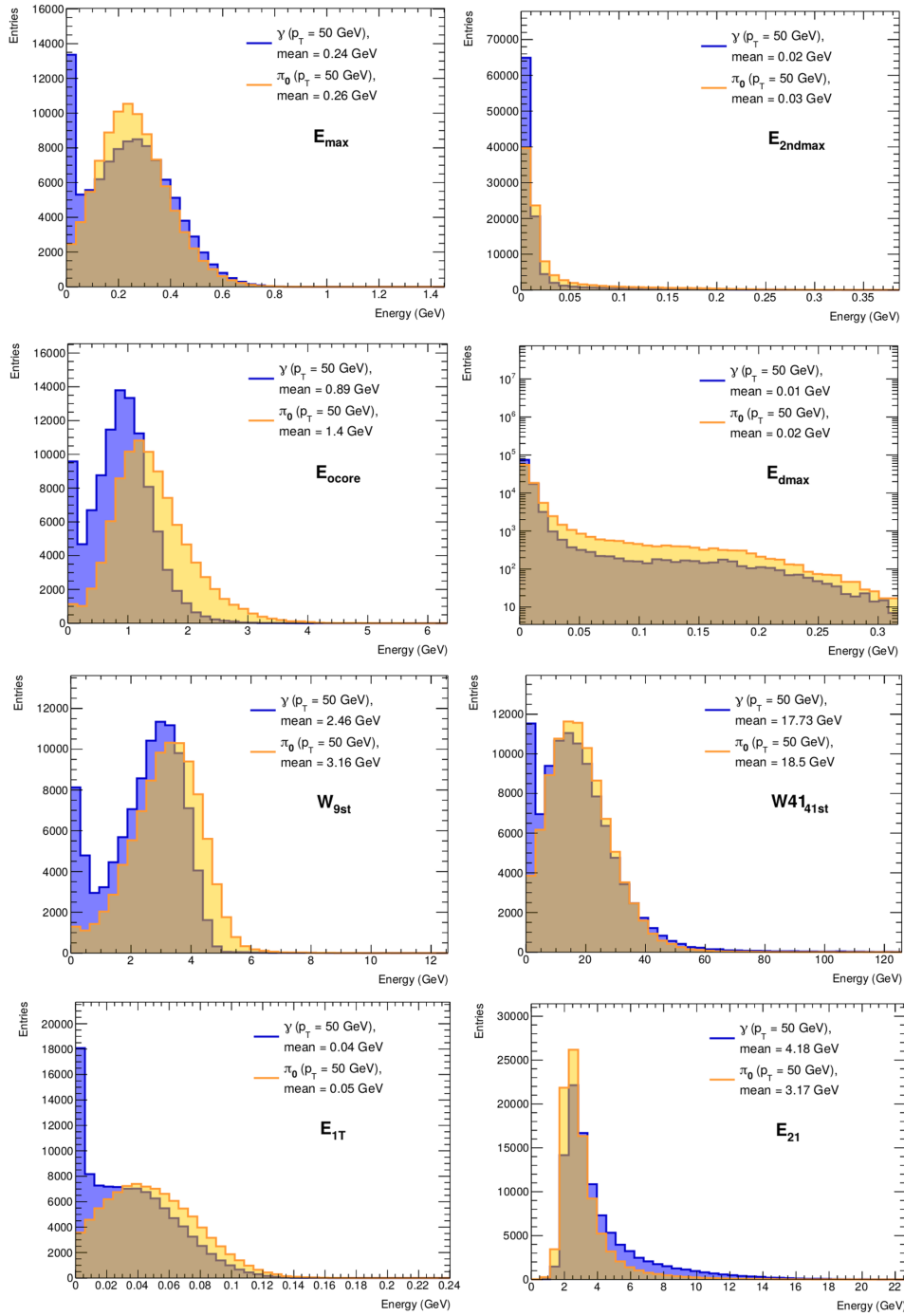


Fig. 7.66: Distributions of discriminating variables for both  $\gamma$  and  $\pi^0$  with  $p_T = 50$  GeV and  $\eta = 0$ . No pile-up or electronic noise is included.

The shower width was calculated twice in each layer, using a low and high number of cells to sum over.  $E_{nT}$  and  $E_{n1}$  were calculated for all layers but other variables were capped at 20 cm depth in the EMB since the energy considered here is low and the particles do not penetrate too far. The corresponding final layer can be seen in Fig. 7.65. Also, because of the varying properties of the calorimeter layers such as finer granulation in  $\eta$  in the 2<sup>nd</sup> layer, the variables were adjusted for each layer individually to obtain the best discrimination. For example, the shower width in the 1<sup>st</sup> layer was summed over 9 and 41 cells whereas it was summed over 3 and 21 cells in other layers. Figure 7.66 shows the distributions of the discriminating variables calculated for the 1<sup>st</sup> layer of sample 5.

#### 7.4.3.1.3 Multivariate data analysis

The multivariate classification using the discrimination variables was done using the boosted decision tree (BDT) algorithm of TMVA. This takes repeated decisions on every single variable individually until a criterion is fulfilled and this creates multiple regions in the phase space which are classified as either signal ( $\gamma$ ) or background ( $\pi^0$ ). Half of the simulated events are used for training the analysis methods and obtaining the importance of each variable in distinguishing between the events i.e. how often they were used to split decision tree nodes. The other half of events is then analysed with the trained BDT. From this the  $\pi^0$  rejection factor,  $R_\pi$ , is calculated using Eq. (7.33), where  $B$  is the fraction of  $\pi^0$ s rejected at a given  $\gamma$  signal efficiency.

$$R_\pi = \frac{1}{1 - B} \quad (7.33)$$

#### 7.4.3.1.4 Optimal geometry

The different geometries of the EMB that were tested are laid out in Section 7.4.3.1.1. All of these were investigated to find highest  $\pi^0$  rejection for the same calorimeter depth of 20 cm. For sample 3 the 2<sup>nd</sup> layer was halved and for samples 4 and 5 also the 3<sup>rd</sup> layer was halved therefore these contain more data and variables and are expected to perform better. Figure 7.67 shows the  $\pi^0$  rejection obtained with each geometry at various  $p_T$  for a 90% single photon reconstruction efficiency.

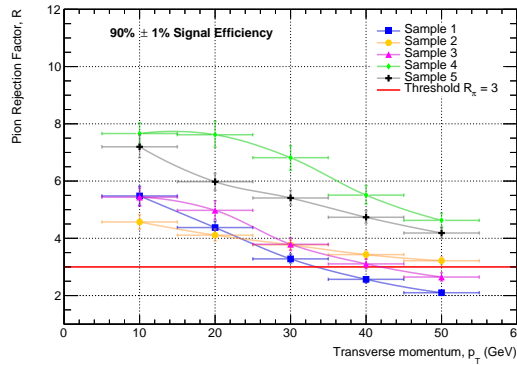


Fig. 7.67:  $\pi^0$  rejection of all samples at  $p_T$  up to 50 GeV for a signal efficiency of 90%. The threshold value for the  $\pi^0$  rejection factor is 3.

There is significant improvement in  $\pi^0$  rejection at  $p_T > 40$  GeV when fine segmentation in  $\eta$  is introduced in the 2<sup>nd</sup> layer. This effect alone increases the rejection above the threshold value as is shown by the yellow line on Fig. 7.67 which describes the baseline geometry of the FCC EMB. The best choice of geometry is #4 or #5 with finer segmentation in  $\phi$  also. These both performed similarly and produced  $R_\pi > 4$  at 50 GeV while other geometries were close to  $R_\pi = 3$  at this energy but geometry



#5 was chosen for the rest of the study because it contains more information and has the potential to be better at higher energies. The variables were calculated identically for samples 4 and 5 which could be the reason in the low performance of geometry #5 and could be improved by adjusting the number of  $\phi$  bins when calculating each variable. For example, the shower width is calculated by summing over 3 bins in  $\phi$  in both cases but for geometry #5 this will contain fewer hits. Therefore, more optimisation needs to be done to get the full  $\pi^0$  rejection potential from finer segmentation in  $\phi$  but this preliminary study shows that there does not appear to be much to gain in this  $p_T$  range.

Sample 5 uses the highest granularity and up to 45 variables may be considered for the analysis. However, to improve calculation time some variables were removed from subsequent analysis while maintaining the largest possible  $\pi^0$  rejection at higher energies. These were chosen based on their separating power and correlation with other variables at  $p_T \geq 50$  GeV. Figure 7.68 shows how the  $\pi^0$  rejection factor changes when trained with different numbers of variables. The separating power of each variable changes with the energy as the  $\pi^0$  decay kinematics become different. Table 7.16 shows the ranking of variables based on their separating power at 10 GeV and 80 GeV.

Table 7.16: The top 15 discriminating variables ranked by their method specific separating power at different  $p_T$  for sample 5.

Rank	Variable	Variable	Variable
	$p_T = 10$ GeV	$p_T = 50$ GeV	$p_T = 80$ GeV
1	$W_{3st}$ (layer 3)	$W_{3st}$ (layer 3)	$W_{3st}$ (layer 3)
2	$W_{3st}$ (layer 2)	$W_{3st}$ (layer 2)	$E_{ocore}$ (layer 1)
3	$E_{max}$ (layer 2)	$E_{max}$ (layer 1)	$E_{max}$ (layer 1)
4	$E_{max}$ (layer 3)	$E_{ocore}$ (layer 1)	$W_{3st}$ (layer 2)
5	$E_{3T}$	$E_{max}$ (layer 2)	$W_{3st}$ (layer 4)
6	$W_{21st}$ (layer 3)	$W_{3st}$ (layer 4)	$E_{max}$ (layer 2)
7	$W_{3st}$ (layer 4)	$E_{max}$ (layer 3)	$E_{max}$ (layer 3)
8	$E_{max}$ (layer 1)	$E_{4T}$	$E_{ocore}$ (layer 2)
9	$E_{ocore}$ (layer 1)	$E_{ocore}$	$E_{1T}$
10	$W_{21st}$ (layer 2)	$W_{9st}$ (layer 1)	$W_{9st}$ (layer 1)
11	$E_{1T}$	$E_{8T}$	$E_{3T}$
12	$E_{8T}$	$E_{21}$	$E_{5T}$
13	$E_{dmax}$ (layer 1)	$e_{01}$	$E_{8T}$
14	$E_{2T}$	$E_{max-104}$	$E_{21}$
15	$E_{ocore}$ (layer 3)	$E_{max-100}$	$E_{max}$ (layer 4)

In the subsequent analysis the number of discriminating variables is lowered to 15 as this produces a similar result to 45 variables but in a shorter time. The difference is most prominent at lower energies (10–40 GeV) and negligible at higher energies (50–80 GeV). Since the  $\pi^0$  rejection factor is very high at the lower energy region and although  $\pi^0$  rejection is crucial at lower energies as well, this effect can be ignored because the rejection is large regardless. It is possible to optimise the training at every simulated  $p_T$  point to obtain a better overall rejection. From Table 7.16 it is apparent that the variables have different separating power at different  $p_T$  when comparing the most important variables at  $p_T = 10$  GeV and  $p_T = 80$  GeV. Adjusting the variables for training of each data set will improve the results obtained in this study since only the top 15 variables at  $p_T = 50$  GeV are considered for training at every  $p_T$ .

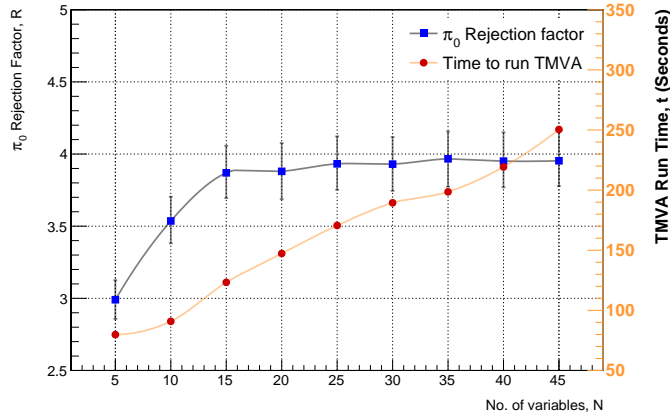


Fig. 7.68:  $\pi^0$  rejection calculated at 50 GeV and 90% signal efficiency for different numbers of discriminating variables, chosen based on their separating power and correlation. The right axis shows the time needed for training the BDT.

### 7.4.3.2 $\pi^0$ rejection

The  $\pi^0$  rejection for transverse momenta  $10 \leq p_T \leq 80$  GeV at pseudorapidity  $\eta = 0$  was investigated using sample 5 for  $\pi^0 \rightarrow \gamma\gamma$  events. It was found that a  $\pi^0$  rejection factor above 3 can be obtained for up to  $p_T = 75$  GeV in this regime, see Fig. 7.69. This result along with the one shown on Fig. 7.67 suggests that there is reason to further investigate finer segmentation in  $\phi$ . In this analysis,  $\Delta\phi = 0.0045$  for all layers was assumed in geometry #5, but it is likely to be sufficient to have  $\Delta\phi = 0.0045$  in one or two layers only while maintaining a similar performance in terms of  $\pi^0$  rejection. The best segmentation would have to be optimised with simulations. The number of discriminating variables is increased compared to the previous study done on the ATLAS EMB because of multiple layers and higher granularity in the detector. The  $\pi^0$  rejection factor obtained here is significantly improved as a result of this. The mean value over all  $p_T$  was found to be  $R_\pi = 3.58 \pm 0.16$  without pile-up which is considerably higher than the  $R_\pi = 2.82 \pm 0.19$  found in ATLAS for  $p_T \in [20 - 75]$ . It is important to note the difference in the number of events analysed in each study, the statistics here are much higher ( $\mathcal{O}(10^5)$  vs  $\mathcal{O}(10^3)$  events) which gives a more accurate but possibly lower rejection value.

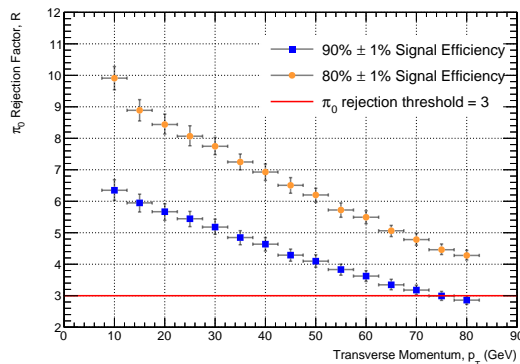


Fig. 7.69:  $\pi^0$  rejection factor of sample 5 calculated for  $p_T$  from 10 to 80 GeV in steps of 5 GeV with 80% and 90% signal efficiencies.

#### 7.4.4 DNN based particle identification at $\langle\mu\rangle = 1000$

Pattern recognition is a strong domain of DNNs, which are trained to discriminate between individual patterns by exploiting symmetries of the problem such as translation invariance. Similar techniques are used to separate individual particles from pile-up and identify them using calorimeter information by interpreting the showers as 3-dimensional images, as described in Section 7.3.3. Individual DNNs are trained for 0 and 1000 pile-up, each discriminating simultaneously between electrons, photons, muons, charged and neutral pions.

As shown in Fig. 7.70, the discrimination between muons and charged pions is excellent using calorimeter information only, even with 1000 pile-up. Without pile-up or when discriminating against electromagnetic showers, the performance shown here is further exceeded. The mild energy dependence is less pronounced without pile-up.

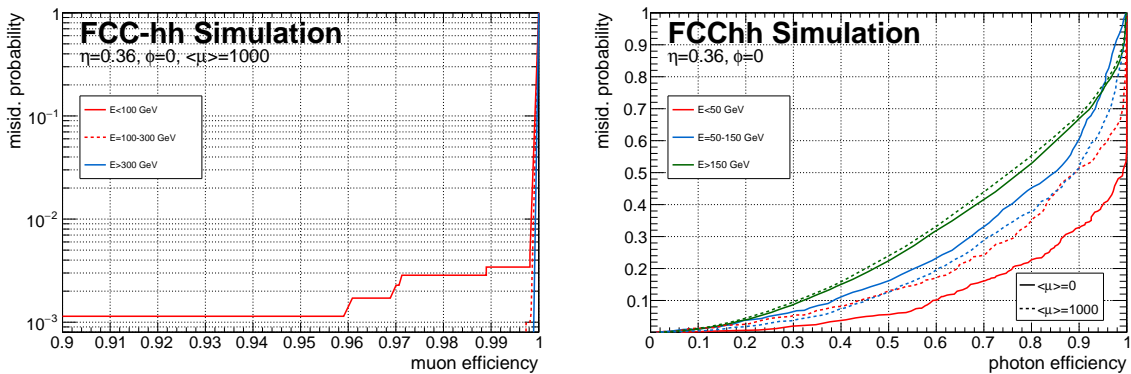


Fig. 7.70: Discrimination of muons from charged pions (left) and photons (right) from neutral pions for different particle energies and pile-up conditions.

An important ingredient for the identification of photons is their separation from neutral pions that decay into two non-prompt photons, as discussed in the previous section, leaving two electromagnetic showers in the calorimeter. With increasing energy, these two showers merge, making the distinction between prompt photons and neutral pions even more challenging. In addition, energy deposits from pile-up make it harder to separate the showers. As shown in Fig. 7.70, this also applies to the DNN based identification. Photons with energies below 50 GeV can be disentangled well from neutral pions in particular without pile-up. For pile-up and higher energies, the discrimination power decreases, which could only be mitigated by a higher EMB granularity and requires further investigations. It has to be mentioned that the simulation samples used featured the basic EMB geometry, which has been named as sample 1 in Sec. 7.4.3.1.1. Thus the TMVA study displays better performance without pile-up and the optimised EMB geometry of sample 4 and 5.

#### 7.4.5 Jets

Hadronising quarks form particle jets and produce hadronic and electromagnetic cascades in the calorimeters. The main components of these jets are photons, hadrons and marginally leptons that share the primary quarks' momentum. The jet content in the number of particles and particle energy is shown in Fig. 7.71a. While only  $\sim 60\%$  of the particles within a jet are hadrons, they carry around 75% of the total energy. The other 25% of the energy is carried by photons, which are measured in the EM calorimeter<sup>16</sup>.

The fraction of the total transverse momentum carried by charged single hadrons within these jets is shown in Fig. 7.71b. These fractions correspond to the particles in the FCC-hh reference detector that do not reach the calorimeters but instead curl up within the tracking system due to the 4 T magnetic field.

<sup>16</sup>It should be noted that the fractional energies are dependent on the energy of the jet.

The minimum  $p_T^{\min}$  necessary is estimated to

$$p_T^{\min} = 0.3 \cdot 4 \text{ T} \cdot r_0, \quad (7.34)$$

with  $r_0$  corresponding to the radial distance of the second barrel ECal layer from the interaction point of 1.97 m at  $\eta = 0$ .

This corresponds to a minimum of  $p_T > 2.4 \text{ GeV}$  to reach the calorimeter in the presence of a 4 T magnetic field. Thus the jet performance in the presence of a 4 T magnetic field is expected to be seriously impacted by this effect if the calorimeter system alone is used, without any tracker information. Therefore, the performance of the calorimeter system is shown in the following without the magnetic field. Future studies are planned to combine the tracking information with the calorimeter clusters using particle flow algorithms.

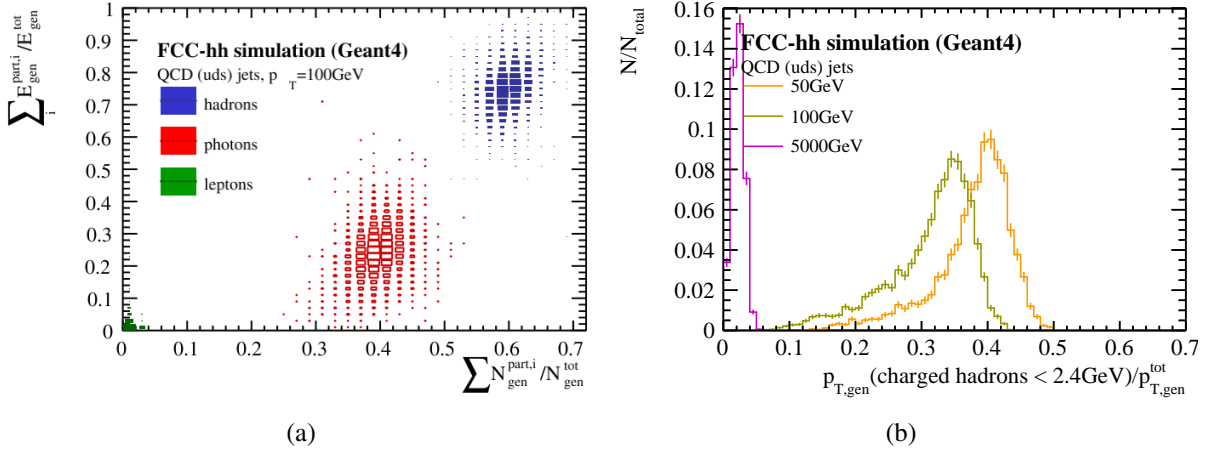


Fig. 7.71: (a) Particle and energy fraction of hadrons, leptons, and photons within QCD jets of  $p_T = 100 \text{ GeV}$ . (b) Fraction of charged hadrons with  $p_T < 2.4 \text{ GeV}$  in jets of transverse momenta  $p_{T,\text{gen}} = 50, 100, \text{ and } 5000 \text{ GeV}$ .

The jet reconstruction of the FCC-hh calorimeter system is based on the standard anti- $k_T$  algorithm described in Section 7.3.1.2, which uses topological clusters as input.

#### 7.4.5.1 Jet energy resolution and energy scale

In the following, the jet  $p_T$  resolution, in the absence of magnetic field, is shown for di-jet events of up, down and strange quarks with transverse momenta of 20 GeV to 10 TeV. The jets are measured in the FCC-hh barrel calorimeters using so-called ‘calibrated’ topo-clusters that are calibrated to the hadronic scale if they contain cells in the HB, or cells in both the EMB and HB. Additionally, the calibration corrects for the lost energies within the LAr cryostat between the EM calorimeter and the HCAL, see more details in Section 7.4.2.2. To determine the performance, in addition to the *rec*-jets built from clusters, the jet reconstruction is also run on stable, final-state, generated particles which represent the so-called *truth/generated*-jets. For the determination of the resolution, the reconstructed and truth jets are matched within a distance of  $R < 0.3$ . In the case of the reconstructed jets, only the two leading jets with the highest transverse momentum are selected and considered for the  $p_T^{\text{rec}} / p_T^{\text{gen}}$  distributions. The momentum resolution is determined in 16  $p_T$  bins, and an example of one distribution and the corresponding Gaussian fit within  $\pm 2\sigma$  is shown in Figure 7.72a and 7.72b.

Without B-field, the FCC-hh barrel calorimeters alone achieve a jet energy resolution with a constant term  $< 2\%$ , see Fig. 7.73b. Further development of reconstruction techniques like particle-flow algorithms, are expected to improve the jet energy measurement in the medium and low  $p_T$  range by using tracking information for jet constituents. Due to the large spread of particles for the case of  $B = 4 \text{ T}$ ,

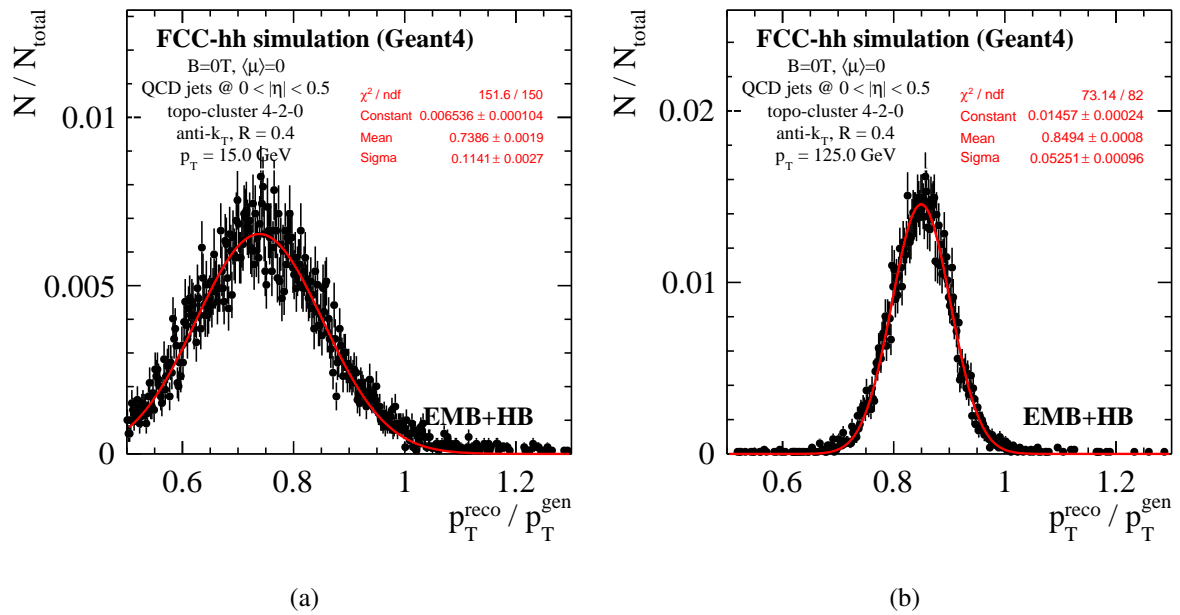


Fig. 7.72: Jet  $p_T$  distributions for (a) 15 and (b) 125 GeV jets. Reconstructed from topo-cluster in 4-2-0 mode after calibration, using the jet clustering algorithm for  $\langle\mu\rangle = 0$ .

a combined reconstruction of jets with the tracker is compulsory. Even without the B-field a non-linearity of the mean transverse momentum of up to 25% at low  $p_T$  remains after the simplistic topo-cluster energy reconstruction as shown in Fig. 7.73a.

The average energy response to jets is presented in Fig. 7.74a, which shows a constant response in pseudo-rapidity for the central barrel of the FCC-hh calorimeters. In a next step, a method to correct the jet energy scale, as done for the ATLAS experiment [171], could be applied using a numerical inversion procedure similar to the second step of the benchmark method. The centre of gravity of the reconstructed jets has been tested along  $\eta_{\text{gen}}$ , see Fig. 7.74b, which shows a slight bias towards smaller  $\eta_{\text{rec}}$  for increasing pseudo-rapidity. However, this effect is at the sub-percent level.

#### 7.4.5.2 Angular resolutions

First tests of the chosen angular segmentation of the EM and hadronic calorimeters have started. One adjustment made for optimising the separation of photons and  $\pi^0$  by a highly segmented 2nd ECal layer (see Section 7.4.3). The impact of the full  $\eta$  granularity of the HB has been tested with single pions in Section 7.4.2.2.3, and an improvement in the angular resolution of up to 15% was determined. However, this comes with the cost of a 6 times higher number of readout channels.

The  $\eta$  granularity of the HB has been tested on di-jet events and the precision on which the jet angle can be measured. The results are presented in Fig. 7.75a and 7.75b for the pseudo-rapidity and the azimuthal angle, respectively. The precision determined of  $< 0.01$  in both  $\eta$  and  $\phi$ , lies well below the HCAL granularity of 0.025 for jet  $p_T$  larger than 40 GeV. This indicates that the intrinsic calorimeter segmentations is still being exceeded by the combination of cells. However, a further increase of the  $\eta$  granularity of the HB does not improve the jet angular resolution significantly: this supports the choice for the reference detector design. Studies of the cell granularity of the hadronic calorimeter, optimised for jet sub-structure variable, have shown similar results [22] and support the chosen granularity of  $\Delta\eta \times \Delta\phi = 0.025 \times 0.025$  for the hadronic calorimeter. Including more sophisticated jet reconstruction techniques like particle flow algorithms or DNNs could, however, be more sensitive to the granularity

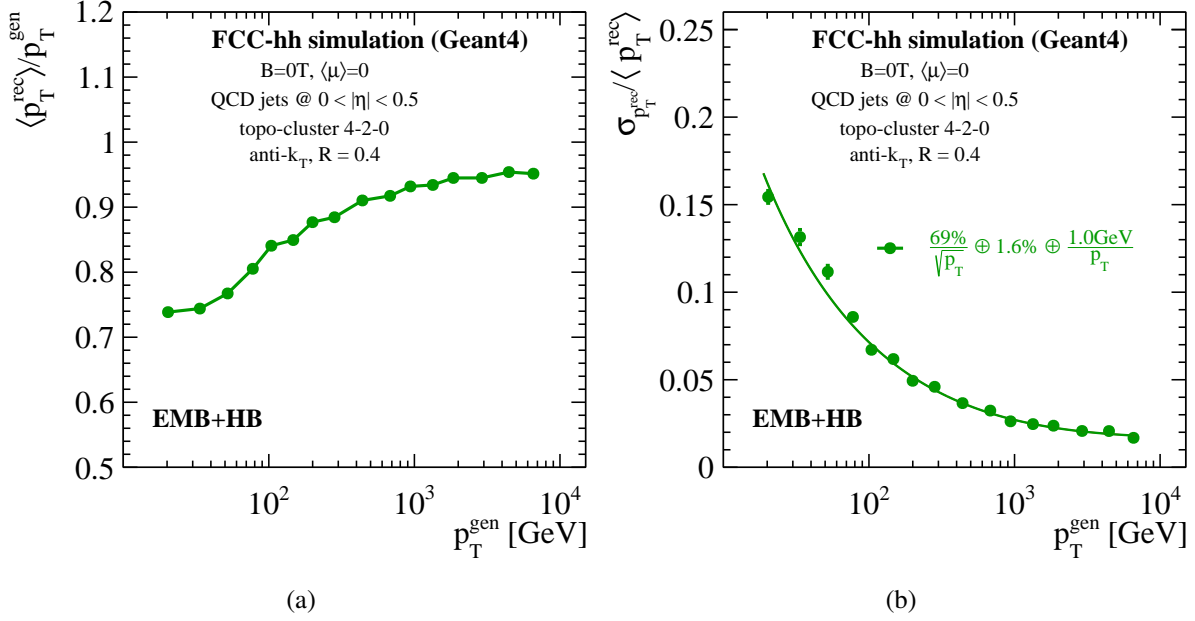


Fig. 7.73: Jet  $p_T$  (a) response and (b) resolution after topo-cluster reconstruction in 4-2-0 mode after calibration, using the jet clustering algorithm for  $\langle\mu\rangle = 0$ .

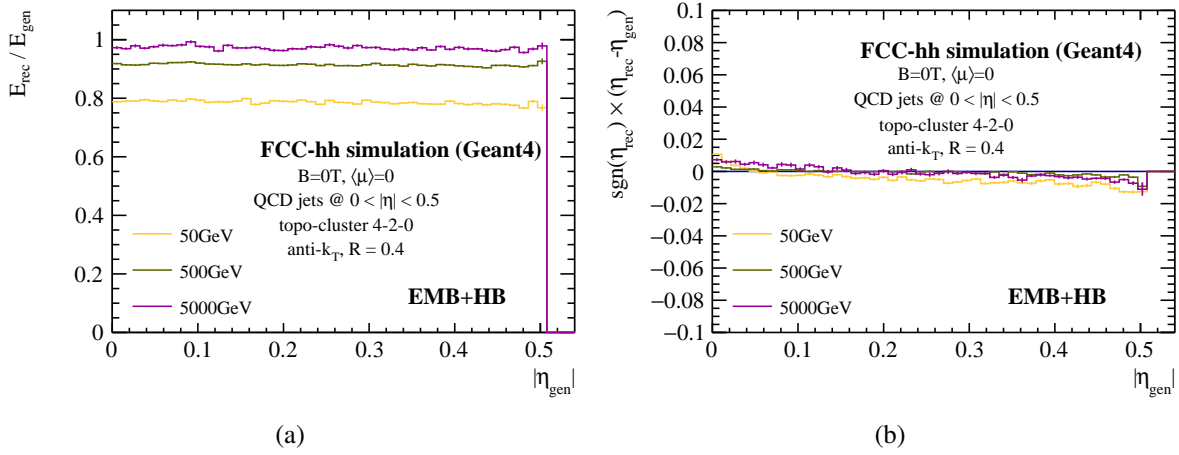


Fig. 7.74: (a) Average energy response as a function of the pseudo-rapidity of the jets with  $p_T$  50, 500, and 5000 GeV. (b) The signed difference of  $\eta_{\text{gen}}$  and  $\eta_{\text{rec}}$ .

and thus point in another direction.

### 7.4.5.3 Outlook

#### 7.4.5.3.1 Pile-up jet identification

Pile-up interactions can affect the global event reconstruction in many ways. In extreme pile-up regimes ( $PU > 200$ ), random associations of low energy showers can fake prompt jets, especially in the forward region of the detector where large amounts of energy are deposited. This can have large effects on measurements of processes that feature the presence of forward jets such as vector boson fusion Higgs production. Pile-up jets can be disentangled from prompt jets by exploiting the difference in the longitudinal and transverse energy profile. In Fig. 7.76 (left) the energy of the jet per layer normalised to the

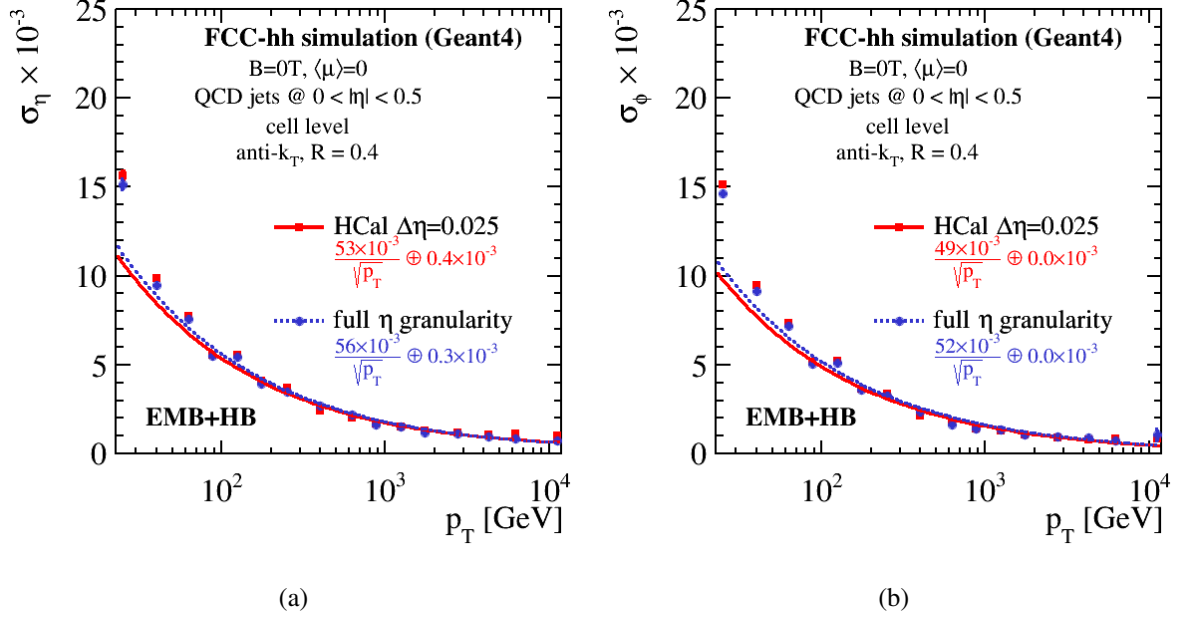


Fig. 7.75: Angular resolution in pseudo-rapidity  $\eta$  and azimuthal angle  $\phi$  for jets up to  $|\eta| < 0.5$ . The red curve shows the results on cell level with the HB tiles merged in  $\Delta\eta = 0.025$ , and the blue points/curves show the resolution obtained with ultimate HB granularity of  $\Delta\eta < 0.006$ .

total jet energy is shown as a function of the layer number. It can be seen clearly that a large fraction of the energy is deposited in the first layers for pile-up jets. The explanation is that pile-up jets feature a uniform soft energy distribution among their constituents that penetrate a few layers of the calorimeter, as opposed to a prompt QCD jet that is typically made up of fewer and harder long lived hadrons. Similarly the transverse energy profile, integrated over all layers of the ECAL and HCAL subdetectors can be seen in Fig. 7.76 (centre and right respectively). Prompt jets concentrate their deposited energy on a well-defined centre whereas pile-up jets feature a uniform diffuse transverse energy profile. Having such handles, provided by a high longitudinal and transverse segmentation at our disposal will clearly improve the identification of pile-up jets. Finally we note that an optimal pile-up rejection can be performed with the so-called particle flow approach [52] that aims at combining optimally calorimetric and tracking information into single particle candidates. Since particle-flow relies on extrapolating and matching reconstructed tracks to calorimeter deposits, it is clear that in order to achieve an optimal performance with such an approach, the highest possible transverse and longitudinal granularity should be aimed for.

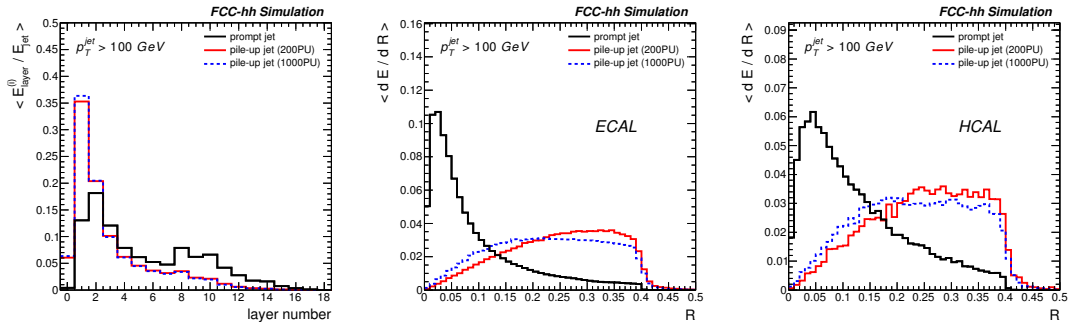


Fig. 7.76: Left: Transverse energy deposited by QCD jets and by jets reconstructed from pile-up as a function of calorimeter layer. Centre/Right: Radial profile of QCD jets and jets made from pile-up in the EMB (centre) and in the HB (right).



### 7.4.5.3.2 Boosted objects, substructure

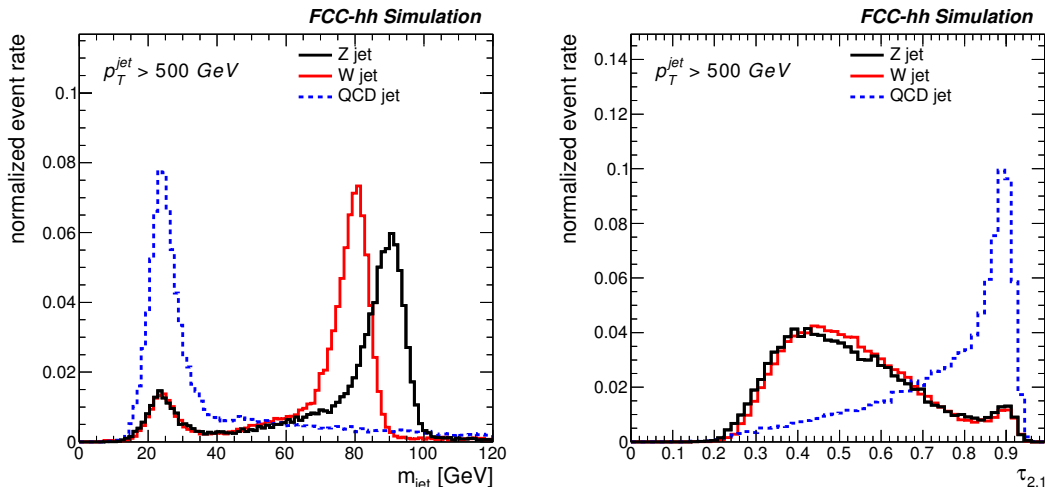


Fig. 7.77: Distributions of the jet mass (left) and  $\tau_{2,1}$  (right) for boosted W, Z and QCD jets with  $p_T > 500$  GeV.

The impact of a high lateral segmentation can be seen on observables that are sensitive to the angular separation in jets. The mass of a highly boosted jet depends both on the energy and the angular separation of hadrons and can be used for such an investigation. Another useful variable is the N-subjettiness ratio  $\tau_{2,1}$ . A detailed description of this complex observable can be found in Ref. [55]. We simply point out that this variable is also built from the energy-momentum vector of the jet constituents. It is expected to peak at values close to 0 if the jet features a 2-prong structure (such as W, Z of Higgs jets) and close to 1 if the jet substructure is one prong-like. Jets are reconstructed with the anti- $k_T$  algorithm [54] with  $R=0.2$  directly from calorimeter hits. No magnetic field was applied in the simulation implying that charged and neutral hadrons are treated equally and no pile-up was assumed. In Fig. 7.77 (left) we show the reconstructed jet mass for W, Z and QCD with  $p_T = 500$  GeV. A good separation between QCD and  $V=W,Z$  jets can be observed, as well as decent discrimination between W and Z bosons. In Fig. 7.77 (right) we show the  $\tau_{2,1}$  variable. Although it is difficult to discriminate between W and Z jets with  $\tau_{2,1}$  (both feature a 2-prong structure), it is clear that this observable provides a handle against background QCD jets. It should be noted that this preliminary study does not make use of tracking, which is expected to provide additional angular separation power for jets, especially in combination with calorimetric information using the particle-flow approach. In such a paradigm, high (transverse) granularity is indeed crucial in order to uniquely assign tracks to calorimeter deposits.

## 7.5 Alternative technology for the EM barrel calorimeter

### 7.5.1 Silicon tungsten calorimeter

In addition to the LAr baseline, the feasibility of a sampling electromagnetic calorimeter using silicon as the sensitive layer and tungsten as the absorber (SiW) has been studied for the FCC-hh. Two distinct readout modes have been investigated: a conventional analogue readout Si calorimeter such as those proposed for the ILD electromagnetic calorimeter within CALICE [172], and the CMS HGCal [131]; and an ultra granular digital electromagnetic calorimeter that counts the number of particles in a shower, rather than the energy they deposit, first investigated by the SPiDeR collaboration [173] and later adopted as a potential technology for the ALICE FoCal [174].

Current developments in Depleted MAPS have demonstrated a radiation tolerance of at least  $10^{15}$   $n_{eq}/cm^2$  [175] and it is assumed that the required radiation tolerance in the ECAL barrel (as stated

in Table 7.1) will be achieved in the timescales of the project. However, the radiation tolerance required in the forward regions at the FCC-hh are an order of magnitude higher, and as such, we do not envisage the use of silicon in these regions of the calorimeter. The silicon based electromagnetic calorimeter barrel consists of five modules in  $z$ , each with eight staves arranged in an octagonal configuration as shown in Fig 7.78. Each staff is segmented longitudinally into 50 layers of alternating silicon and  $0.6 X_0$  of absorbing material to achieve the necessary calorimeter depth of  $30 X_0$ . Tungsten, with a radiation length of 3.5 mm, was chosen as the absorbing material for two main reasons: firstly, its Molière radius of 9.3 mm leads to compact electromagnetic showers and allows better separation of nearby showers and pile-up events; and secondly, the calorimeter itself can be much more compact, reducing the size and cost of all the detector components outside of it. An air gap of 3 mm for services was included between each alternating pair of silicon and tungsten. The silicon electromagnetic calorimeter operates at room temperature and as such, there is no need for a cryostat that would introduce additional passive material in front of the calorimeter systems.

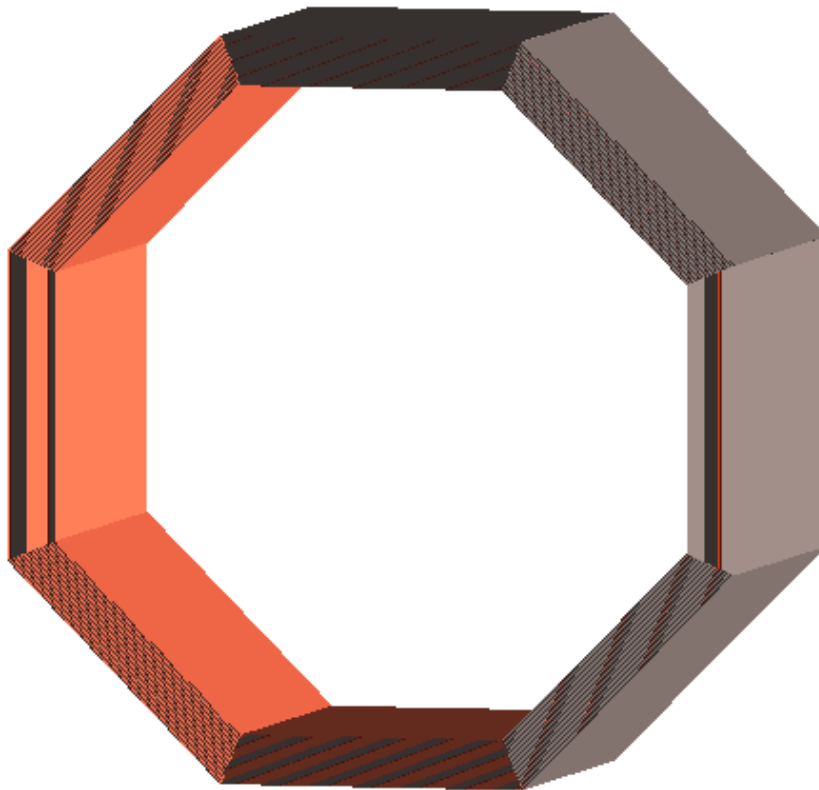


Fig. 7.78: The cross section of the silicon electromagnetic barrel calorimeter. The centre of each of the eight staves was fixed to the inner radius of the baseline design to ensure the calorimeter remained within the required envelope.

#### 7.5.1.1 Analogue readout

For the analogue variant of the SiW, a layer of  $300 \mu\text{m}$  silicon is assumed. This value is consistent with the pad detectors used for CALICE and the CMS HGCal and leads to a sampling fraction,  $f_{\text{sampl}} = 5.3 \times 10^{-3}$ . The silicon is divided into  $5 \times 5 \text{ mm}^2$  pads, leading to  $\sim 10^8$  readout channels. As the

main focus of these studies was the digital readout, the analogue calorimeter has a simplistic clustering algorithm to find the total energy of the shower as there has been no consideration of pile-up removal. However, as the granularity of the analogue and digital readouts (following reconfiguration from pixels to pads) are both  $5 \times 5 \text{ mm}^2$ , and as detailed below, the digital case allows excellent suppression of pile-up events, and it can be assumed that the same will be possible for the analogue silicon ECAL.

### 7.5.1.2 Digital readout

The basic premise of the digital electromagnetic calorimeter (DECal) is to count the number of particles in the shower rather than the energy they deposit. The currently envisaged DECal pixels only register one hit even if multiple particles pass through the given pixel. Therefore, the DECal begins to saturate should more than one particle traverse each pixel per readout cycle. In order to prevent this situation even in the very dense shower cores, the cells must be very small. A cell size of  $50 \times 50 \mu\text{m}^2$  was therefore used for previous studies for the International Large Detector (ILD) at the ILC [176]. CMOS Monolithic Active Pixel Sensors (MAPS) are proposed to achieve a calorimeter with the required granularity. Each pixel of a MAPS contains the required readout electronics, can be read out at every 25 ns bunch crossing and, due to recent developments, can withstand the radiation levels expected in the FCC-hh barrel region (see Table 7.1). A typical cross section of a MAPS device is shown in Fig. 7.79. When a MIP traverses the sensor, the energy deposited liberates electron-hole pairs in the epitaxial layer which diffuse (or drift in the case of depleted MAPS) to the collection electrodes.

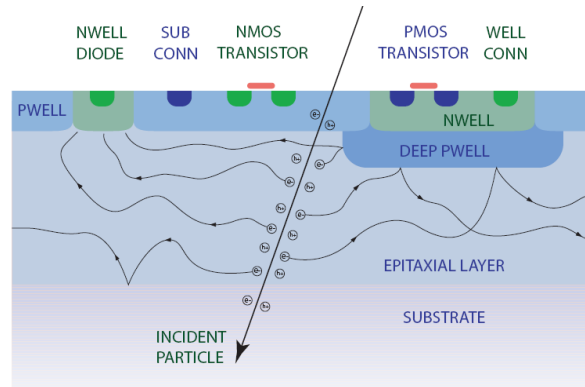


Fig. 7.79: The cross section of a typical MAPS device, taken from Ref. [177].

The studies in this document assume an  $18 \mu\text{m}$  epitaxial thickness, on a substrate of  $300 \mu\text{m}$ . The  $50 \times 50 \mu\text{m}^2$  pitch pixels are summed into  $5 \times 5 \text{ mm}^2$  pads to reduce the data rate. A depleted MAPS device, capable of collecting all the charge within the pixel and summing the number of pixels in the pad within 25 ns has been designed, fabricated and tested for the proposed FCC-hh DECal [178].

## 7.5.2 Software implementation

### 7.5.2.1 Hit generation and digitisation

Both of the SiW geometries are implemented and scored in the simulation at the same time to allow for direct comparisons to be made between the two technologies. Each layer of the calorimeter consists of an  $18 \mu\text{m}$  silicon epitaxial sensitive volume, used for scoring the digital hits, and a  $300 \mu\text{m}$  silicon substrate for scoring the analogue deposits. A 2.1 mm thick tungsten absorber is located directly after the two silicon layers, followed by a 3 mm air gap. The standard 4 T field is used for all studies and the inner radii of the first layer is consistent with the baseline design. In the first instance both the epitaxial and substrate layers are segmented in to  $50 \times 50 \mu\text{m}^2$  pixels to allow a single detector object to score all energy deposits. The energy deposits are then filtered depending on the analysis stream as presented schematically in Fig. 7.80. For the analogue SiW, all the energy deposits which occur within the substrate

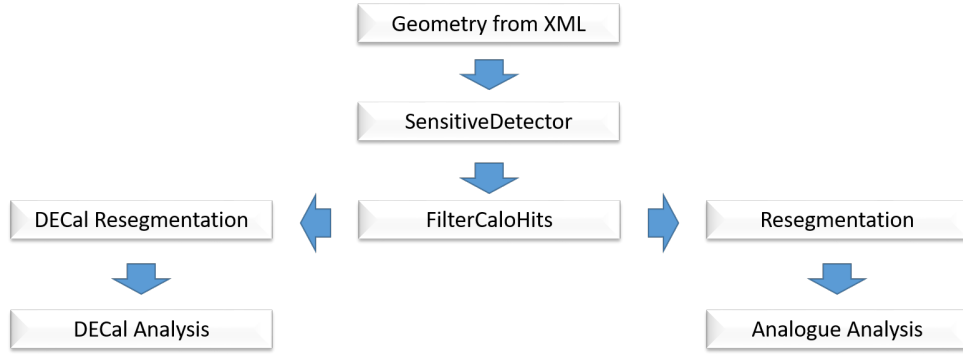


Fig. 7.80: The workflow of the SiW calorimeter system as implemented in FCCSW

are selected, the pixels are grouped into  $5 \times 5 \text{ mm}^2$  pads, the energy deposited in all pixels in a pad are summed together, and finally all pads which contain an energy deposit are summed to yield the total energy deposited in an event. For these studies, there is no threshold applied to the analogue case and all energy deposits are combined. This makes the analogue results optimistic due to the electronic noise anticipated with a  $5 \times 5 \text{ mm}^2$  pad [131]. The DECal analysis flow begins by selecting the hits which occur in the epitaxial layer and summing the energy deposits in each pixel and applying a threshold of 480 electrons to each pixel (corresponding to a  $6\sigma$  noise cut in the DECal reconfigurable MAPS sensor device level simulations). The pixels which remain after thresholding are then reconfigured and resegmented in to  $5 \times 5 \text{ mm}^2$  pads and the number of pixels above threshold in each pad, and the mean  $\eta$  and  $\phi$  are found. The sum of all pixels in all pads is then found to yield the signal in the calorimeter.

### 7.5.2.2 Noise and pile-up

In the DECal there are approximately  $10^{12}$  pixels covering the barrel region, each with an estimated noise level of 80 electrons prior to irradiation from simulation and measurements of the new reconfigurable DECal sensor [178]. An MIP traversing  $18 \mu\text{m}$  of silicon has a most probable energy deposit of 1400 electrons. Applying a threshold of 480 electrons maintains an excellent particle detection efficiency and yields a probability of a pixel firing due to noise of  $10^{-8}$  which translates to  $10^4$  pixels firing every bunch crossing. As these are caused by random noise fluctuations they will be evenly distributed, with a low hit density throughout the barrel region and are easily mitigated by searching for clusters. The electronic noise is generated in the simulations on an event by event basis by randomly generating  $10^4$  pixel addresses and merging these with the pixel addresses prior to the reconfiguration of the sensor into pads. Whilst this creates an excess of pixels in a shower, the fraction is negligible due to the low hit density and can thus be ignored in these studies.

A larger and altogether more difficult source of noise hits to identify and remove arises from pile-up events. Whilst most of the additional hits will be caused by low energy particles which can be easily mitigated in the same way as the random noise hits, the presence of high energy particles which cause dense showers in the calorimeter will require additional information from other detector sub-systems to fully remove. The energy deposits for pile-up events were generated on a single pile-up event basis and then randomly selected and merged with the signal and the electronic noise pixels, before thresholds were applied. In these studies, we remove these dense secondary showers by requiring that the pad corresponding to the cluster seed (described in the following section) has at least 30 pixels that are above threshold. Distributions of the maximum pad occupancy for 20 GeV electrons, and for 140 pile-up and 1000 pile-up events can be seen in Fig. 7.81. Whilst it is clear that a higher cut value will remove a greater proportion of the pile-up clusters, the cut has been optimised for maximum efficiency for 20 GeV electron showers.

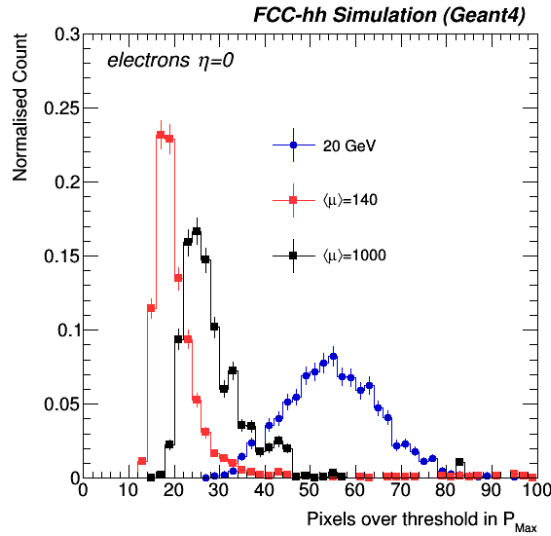


Fig. 7.81: The maximum number of pixel hits per pad for different levels of pile-up and 20 GeV electrons.

### 7.5.2.3 DECal clustering

The DECal clustering algorithm is a modified version of the sliding window algorithm as detailed in Section 7.3.1.1.1. The entire barrel region is scanned for the  $5 \times 5 \text{ mm}^2$  pad containing the most pixels above threshold,  $\text{Pad}_{\text{max}}$ , which is then used as the cluster seed. The mean  $\eta$  and mean  $\phi$  of all pixels in  $\text{Pad}_{\text{max}}$  are calculated, and  $\Delta\eta$ ,  $\Delta\phi$  found for all hits in the barrel relative to these values. The total number of pixels above threshold in a cone originating from the interaction point, is summed for each layer. The mean value of  $\text{Pad}_{\text{max}}$  with no pile-up, increases with incident particle energy due to a larger particle density in the shower core. This relationship has been parameterised with a second order polynomial which allows a first estimate of the incident energy to be made. Using the first estimate of energy, the cone width, in  $\eta$ , and  $\phi$  is then extracted from a second parameterisation of the shower width versus incident particle energy. Typical values for a 100 GeV shower are  $\Delta\eta = 0.020$ ,  $\Delta\phi = 0.015$ , which highlights the compactness of the showers due to the use of tungsten as the absorber.

Figure 7.82 shows the number of pixels over threshold in the entire DECal for just the signal, signal with 140 minimum bias events, and signal with 1000 minimum bias events both before and after clustering has been applied. It is clear that a huge fraction of the pile-up is removed by using the clustering. There is a finite number of events where the cluster seed is associated with a pile-up event, for completeness of this study these events are included in the final sample. However, these should be removed with more sophisticated analyses using other detector components and particle flow algorithms. The fraction of pixels in a cluster originating from pile-up events rises to 9% for a 20 GeV electron in the presence of 1000 minimum bias events. These pixels cannot be removed as it is not possible to determine whether a pixel is over threshold due to the signal, electronic noise, pile-up interactions, or a combination of the three. However, this fraction quickly falls to the percent level for showers of electrons greater than 100 GeV.

### 7.5.2.4 Non-linearity corrections

In an ideal calorimeter the response as a function of incident energy should be linear. As highlighted in Fig. 7.82 the response of the DECal becomes non linear for energies above 300 GeV. This is due to the particle density in these showers being greater than 1 particle / pixel and yielding an under counting by the DECal. To correct for this a second order polynomial is used to convert the number of pixels in an

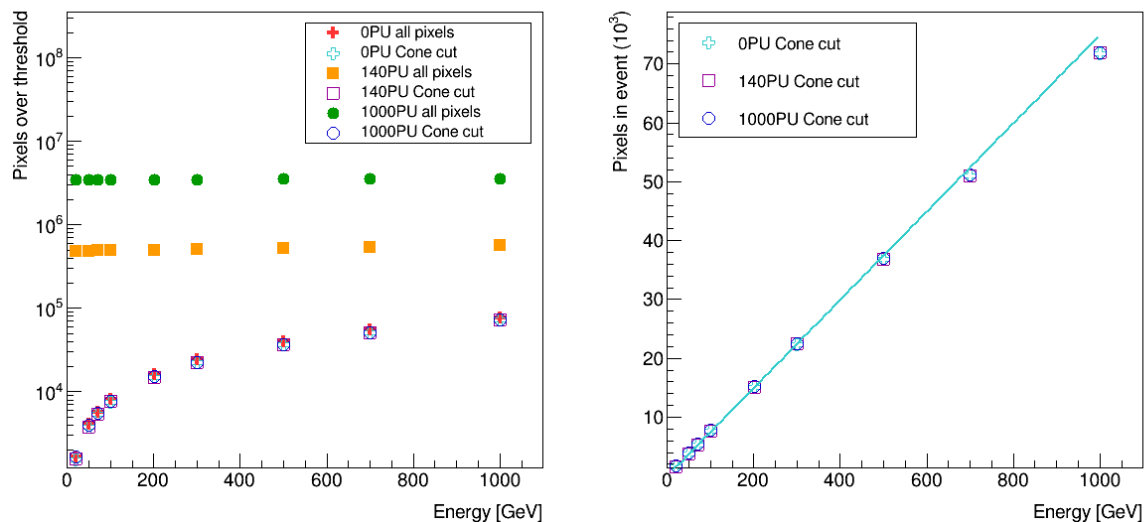


Fig. 7.82: The mean total number of pixels over threshold in an event for the different pile-up scenarios both before and after clustering (a) and only after clustering to highlight the performance (b).

event to the incident energy. Interestingly, the addition of the air gap for services between the absorbing and silicon of the next layer improves the linearity of the DECal. This is in part due to the showers having a greater distance over which they develop before reaching the next layer. Counter-intuitively the number of pixels recorded in an event with an increasing air gap decreases rather than increasing as one would expect from the increased inter particle separation in the shower. This is due to very low energy particles exiting the tungsten layer which in the presence of a magnetic field do not reach the silicon layer when they are separated by the air gap. The behaviour and implication of these low energy particles need further study for the DECal concept.

A further non-linear correction which needs to be applied for the DECal is the number of pixels as a function of  $\eta$ . In a conventional calorimeter, as the angle of the incident particle increases, so does the distance that the particle traverses in both the absorber and sampling material. In the DECal, there is no increase to the signal as a function of angle as we are counting pixels over threshold rather than the sum of all energy deposits. This effect has been studied previously for the ILC and is a small effect along the majority of the barrel; the current studies focus on  $\eta = 0$  so the impact is negligible.

### 7.5.3 Performance

#### 7.5.3.1 Comparison in the absence of pile-up

Single electron showers were simulated in the absence of pile-up for the detector geometry detailed in the previous sections, for both the analogue and DECal read out methods. This allows a direct comparison to be made between the modalities and not the reconstruction methods. The linearity of response for the two modalities can be seen in Fig. 7.83. The non-linearity of the DECal above 300 GeV can be clearly seen, with a non-linearity of 2.5% observed at 700 GeV. Below this point, where the calorimeter is not saturating, the linearity is excellent as is the performance in the analogue case. Table 7.17 highlights the resolution for 20 GeV, 100 GeV, 500 GeV, and 1000 GeV electrons for both the analogue and DECal. The DECal has a total energy resolution of 1.1% for a 1000 GeV electron compared to 0.8% for the analogue case. The bottom of the table displays the results of fits of the resolution function Eq. (7.1).

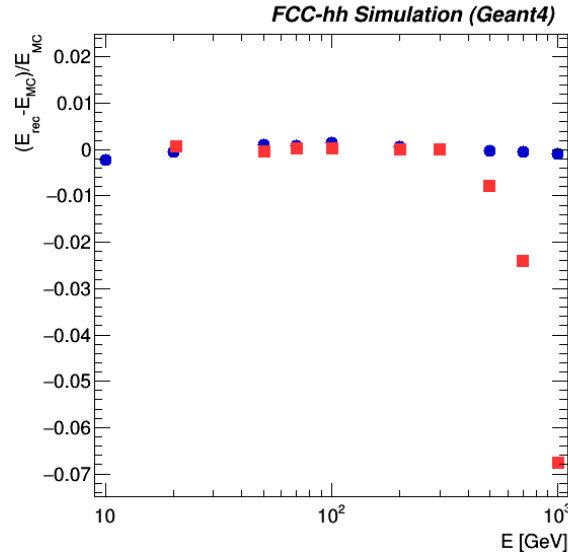


Fig. 7.83: The linearity of response for single electrons in the barrel ( $\eta = 0$ ) for the analogue SiW ECal (blue dots) and the DECal (red squares) in the absence of any pile-up.

Table 7.17: The total energy resolution for the DECal and analogue readout for various energies of interest at the FCC-hh. The bottom part of the table lists the fit parameters  $a$ ,  $b$  and  $c$  determining the stochastic term, the noise term and the constant term of the energy resolution as defined in Eq. 7.1.

Energy [GeV]	Analogue $\langle\mu\rangle=0$	DECal $\langle\mu\rangle=0$	DECal $\langle\mu\rangle=140$	DECal $\langle\mu\rangle=1,000$
20	0.042	0.041	0.043	0.058
100	0.019	0.020	0.021	0.023
500	0.009	0.012	0.012	0.012
1000	0.008	0.011	0.011	0.011
$a$ [% $\sqrt{\text{GeV}}$ ]	17.9	17.0	17.9	17.9
$b$ [GeV]	0.249	0.231	0.249	0.808
$c$ [%]	0.47	0.98	0.97	0.96

### 7.5.3.2 Impact of pile-up on DECal

The impact on performance of the DECal for two pile-up configurations,  $\langle\mu\rangle=140$  and  $\langle\mu\rangle=1000$ , was investigated. It should be noted that the clustering algorithm is now applied. At higher energies, the fraction of pile-up hits remaining after clustering is small compared to the very dense showers and as such the energy resolution tends to the same value. However, at lower energies the remaining fraction becomes significant and the resolution degrades with pile-up. At 20 GeV, 9% of all pixels over threshold originate from pile-up. As can be seen in Tab. 7.17, the addition of pile-up deteriorates the stochastic term and the noise term. The total energy resolution is shown in Table 7.17 for each scenario. Interestingly, the linearity of the calorimeter at higher energies appears to improve for higher pile-up. It should be noted that this cannot be the case and is an artefact arising from an increased number of pile-up hits at lower energies causing a distortion to the regime in which we fit.



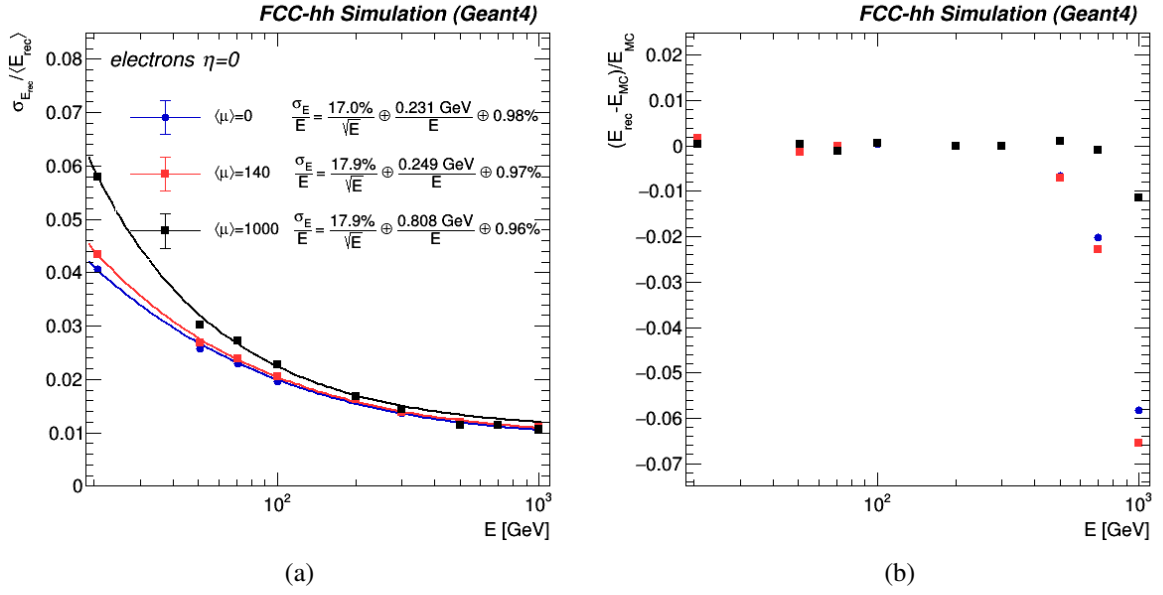


Fig. 7.84: Single electron DECal energy resolution (a) and linearity (b) for  $\langle\mu\rangle=0$ ,  $\langle\mu\rangle=140$ , and  $\langle\mu\rangle=1000$ .

#### 7.5.4 Discussion

The energy resolution presented here of  $\sim 17\% \sqrt{\text{GeV}}/\sqrt{E}$  for the FCC-hh SiW ECAL are consistent with previous studies in CALICE and for the CMS HGCal. It has been shown that the DECal concept holds for showers up to 300 GeV before the saturation of multiple particles traversing a single pixel becomes significant. Therefore, the impact on the physics from the use of the DECal is heavily dependant on the processes involved and beyond the scope of these studies. The performance of the DECal pixel assumed for these studies matches that of the prototype reconfigurable CMOS MAPS for outer tracking and calorimetry described in Ref. [178]. Reduced noise and additional functionality to cope with multiple hits in a pixel to extend the linearity regime would be easily realised in future versions of the chip.

The LAr baseline offers improved energy resolution compared to either of the SiW options. However, the intrinsic standalone energy resolution of the ECAL is not the only parameter for consideration in future detectors. Detectors that utilise particle flow algorithms (PFA) will offer improved performance as the detector sub-system best suited for measuring each particle type is used. An essential aspect of PFA is the granularity and longitudinal segmentation of the detectors. The SiW options offer an improvement over the LAr for both of these and as such could offer improved PFA performance. In addition, the granularity of the SiW options are capable of measuring the internal structure of the denser showers induced in the tungsten and therefore are expected to offer increased  $\pi^0$  discrimination from single photons and better  $\tau$  identification. In these studies the most basic reconstruction has been used for the DECal where the total number of pixels corresponds directly to the energy of the particle. However, the ultra high granularity and large number of longitudinal layers of the DECal would also allow complex pattern recognition to be implemented to measure the energy. One such study using the number of pixels and ratio of these per layer was able to improve the linear response of the DECal [179].

The SiW options would operate at room temperature and as such would not require a cryostat, not only would this reduce the complexity of the design and the amount of material traversed before the calorimeters, but the inner radius of the calorimeter systems could also be reduced. The use of tungsten as the absorbing material significantly reduces the depth of the ECAL and therefore reduces the size of all the sub systems outside of the ECAL. It is anticipated that the cost of silicon detector systems will

undergo significant reductions on the envisaged timescales before the FCC-hh construction begins, and whilst tungsten is expensive, the combination of silicon and smaller radii of external detector components promises significant cost saving benefits for the detector as a whole.

Finally, a hybrid approach, using a very high granularity pre-shower detector complemented by a more conventional energy measuring calorimeter, may offer an alternative optimisation but at the cost of a higher radial space required for the calorimeter and subsequent cost increases for outer sub-detectors and magnet system.

## 7.6 Summary and outlook

The goal of the international FCC study was to develop a conceptual design of a future circular collider including possible experiments to exploit its full physics potential, in time to serve as an input for the update of the European Strategy for Particle Physics that started in 2019. The Conceptual Design Report (CDR) that appeared in four volumes, with the third volume describing a possible hadron collider [3], FCC-hh, summarises the results of this study.

In order to demonstrate that the full physics potential of such a hadron collider could be exploited, a conceptual design of a possible FCC-hh experiment was developed. Many studies were conducted, that led to the short summary in Ref. [3]. This chapter has presented the details of those studies conducted to develop the conceptual design of the calorimeter system and explains the reasoning behind the various design decisions that have been made. In general, the main focus was to demonstrate the feasibility of a calorimeter system that could fulfil the physics requirements which are briefly outlined at the beginning. Beyond that, some promising alternative technologies are also described, but it goes without saying, that other designs to realise such an FCC-hh calorimeter system might exist.

The general strategy has been followed:

- determine a calorimeter concept from a pen and paper detector, and develop a possible design of a calorimeter system for FCC-hh (see Section 7.2);
- implement this conceptual calorimeter system into a realistic simulation of a realistic FCC-hh experiment (see Section 7.3) and
- evaluate if the performance of such a calorimeter system would meet the expected performances (see Section 7.4).

Whereas final state particles in a future FCC-hh experiment will be identified and measured by combining the information of several detectors, the main focus was to evaluate the standalone performance of the calorimeter system. As demonstrated in Section 7.4.1, most required performance benchmarks for electromagnetic showers even at highest expected pile-up can be achieved by a standalone measurement in the proposed electromagnetic calorimeter, based on LAr as active material with lead-steel absorbers. Nevertheless, a combination with measurements in the tracker will further improve this performance, mainly through pile-up suppression. For the hadronic calorimeter a sampling ‘tile’ calorimeter, with scintillating tiles and passive stainless steel and lead absorbers, is proposed for the barrel and extended barrel, and an LAr/Cu calorimeter for the forward region. The performance for hadrons and jets, discussed in detail in Sections 7.4.2 and 7.4.5 respectively, shows that the proposed calorimeter system achieves very good results at low pile-up and without magnetic field, but will have to be combined with the inner tracker by particle flow and pile-up suppression algorithms to achieve the required performance with a 4 T magnetic field and highest pile-up regime. In a nutshell, it has been shown that the proposed calorimeter concept performs as expected, but only a combination with the inner tracker will achieve the ultimate performance in the highest pile-up scenario. The high granularity of the proposed calorimeter system will facilitate this combination with the inner tracker through the use of particle flow and will provide 3D imaging information for machine learning algorithms that will be used for energy reconstruction, particle ID and pile-up suppression.

A promising alternative technology, inspired by the on-going R&D for the upgrades of the current LHC detectors, based on Si sensors as the active material (digital or analogue read-out) and tungsten absorber plates is presented in Section 7.5. This detector technology focuses even more on facilitating the combination with the inner tracker by even higher lateral granularity and more longitudinal layers, while accepting a slightly worse standalone performance for electromagnetic showers.

Future studies will be needed to determine the best solution from amongst all of the calorimeter concepts described. Additional R&D in two main directions will be crucial to prepare these concepts for more technical designs:

- R&D on the detector concepts, technical designs and prototyping to demonstrate that the predicted performance can be achieved.
- Further development of the FCC software towards a fully functional particle-flow algorithm to combine the tracker and the calorimeter measurements to evaluate the necessary granularity of the calorimeter system.



# Muon system

## 8.1 Introduction

The considerations for the muon system have a significant impact on the overall detector design. When the LHC detectors were designed, it was still unclear whether precision tracking close to the IP would be possible, so significant emphasis was put on the standalone performance of muon systems. The ATLAS detector therefore uses a large air core toroid magnet system for excellent standalone muon momentum spectroscopy up to  $|\eta|=2.5$  with a multiple scattering resolution limit of about 2.5% and around 10% resolution at  $p_T=1$  TeV/c. The standalone muon performance of CMS shows about 8% resolution at the multiple scattering limit and 20% resolution at  $p_T=1$  TeV/c in the central region, with a significant performance decrease at large  $p_T$  in the endcaps. However, the CMS detector shows better performance than ATLAS for the combined muon momentum resolution by also using the tracker information (except for very high  $p_T$  muons in the end-cap region). Since there is little doubt today that large scale silicon trackers will be core parts of future detectors, the emphasis on standalone muon performance is less pronounced and the focus should be on the aspects of muon trigger and muon identification.

## 8.2 Momentum measurement

There are three possibilities for measuring the muon momentum with the FCC-hh reference detector, as shown in Fig. 8.1:

- Momentum measurement with the tracker. The muon system is just used as a muon identifier.
- Standalone momentum measurement. The momentum is determined by measurement of the angle under which the muon exits the calorimeter and assuming that the muon originates from the primary collision.
- Combined momentum measurement. Using the central tracker together with a position measurement in the muon system.

Figure 8.2a shows the performance of these three measurement techniques for different values of the position resolution in the muon system. Standalone performance is provided by the angular difference between track angle in the muon system and the radial line connecting to the FCC beam axis. The limit of the standalone resolution due to multiple scattering in the calorimeters is around 4%. Assuming a position resolution of 50  $\mu\text{m}$  per station in the muon system, a combined muon momentum resolution of 6% is found even for momenta as high as 10 TeV/c. Figure 8.2b shows the standalone muon momentum resolution as a function of  $\eta$ . It can be seen that at  $\eta=2.5$  the multiple scattering limits the momentum resolution to about 28%. Beyond  $\eta=2.5$  in the forward region, the momentum resolution is beyond 100%, so the forward muon system using the forward solenoid can only provide muon identification but

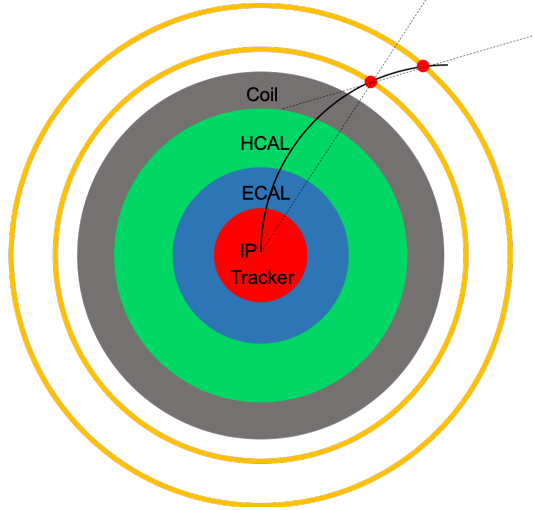


Fig. 8.1: Different possibilities for measurement of the muon momentum. In the tracker, in the muon system only and by combining the measurements.

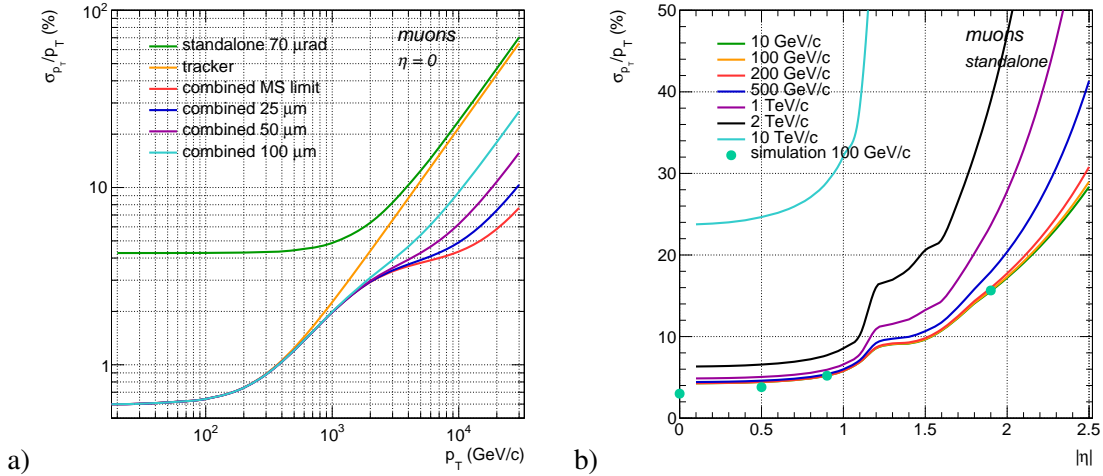


Fig. 8.2: a) Muon momentum resolution at  $\eta=0$ ; b) Muon standalone momentum resolution as a function of  $\eta$  of different muon momenta.

no standalone muon trigger capabilities. If a standalone muon trigger for  $\eta > 2.5$  were needed, as applied in the LHCb and ALICE experiments, one has to use dipole magnets in the forward region.

### 8.3 Muon rates

Neglecting energy loss, muons of  $p_T = 4 \text{ GeV}/c$  would just make it into the muon system and muons of  $p_T = 5.5 \text{ GeV}/c$  would exit the solenoid coil at  $45^\circ$ . The energy loss of  $3\text{--}4 \text{ GeV}$  in the calorimeters will result in a  $p_T$  cutoff around  $6\text{--}7 \text{ GeV}/c$ . Figure 8.3a shows the differential cross-sections for muons from  $c$ ,  $b$ ,  $W$ ,  $Z$  and  $t$  decays assuming a lower  $p_T$  cutoff of  $5 \text{ GeV}/c$ . The muon rate is dominated by  $c$  and  $b$  decays with cross-sections of  $\approx 100 \mu\text{b}$  each. The total differential cross-section for muons of  $p_T > 5 \text{ GeV}/c$   $\sigma_{\mu 5} \approx 200 \mu\text{b}$  therefore results in a muon flux of  $\mathcal{L} \times \sigma_{\mu 5} / (2\pi r^2)$  in the muon system, which evaluates to about  $20 \text{ Hz}/\text{cm}^2$  in the first muon stations at  $r = 650 \text{ cm}$  for the peak luminosity. The

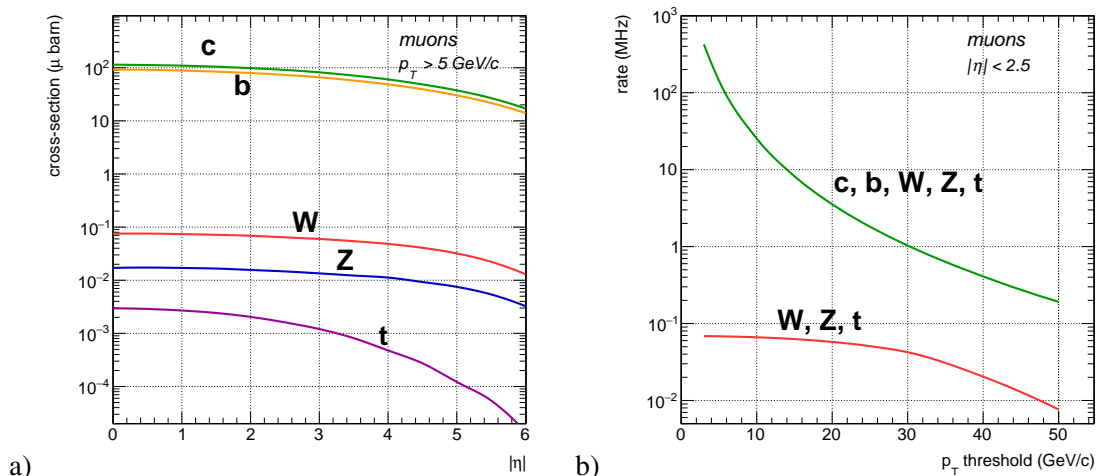


Fig. 8.3: a) Differential cross-section for muons with  $p_T > 5 \text{ GeV}/c$  [180]. b) Rate of muons inside  $|\eta| < 2.5$  including all muons and only those from W, Z, t.

additional rate from punch-through still has to be evaluated, but it is clear that the charged particle count rate of about  $500 \text{ Hz}/\text{cm}^2$  due to high energy photons will dominate the rate in the muon system. The total rate of muons above a given threshold inside an acceptance of  $|\eta| < 2.5$  is shown in Fig. 8.3b, together with the muon rate from W, Z, t decays only. The total muon rate is above 20 MHz for a  $p_T$  threshold of 10 GeV/c and a single muon trigger with this threshold will therefore not provide any selectivity. The rate of muons from W, Z, t on the other hand, always stays below 100 kHz for any threshold. Since muons from c and b decays are always accompanied by jets, the determination of muon isolation at the first trigger level is a key item for selectivity.

Including a safety factor of 2.5, the charged particle rates amount to  $1.25 \text{ kHz}/\text{cm}^2$  in the barrel and outer endcap muon system and rise up to  $25 \text{ kHz}/\text{cm}^2$  in the inner part of the inner endcap muon system. In the forward muon system the rates range from 25 to  $250 \text{ kHz}/\text{cm}^2$ . It is therefore concluded that technologies planned to be used at the HL-LHC, like the sMDTs from the ATLAS experiment with a diameter of 15 mm are, suitable for the barrel and endcap regions. An arrangement of  $2 \times 4$  layers of sMDTs at a distance of 1.4 m constructed as one mechanical object can provide an angular resolution of  $60 \mu\text{rad}$  and spatial resolution of  $40 \mu\text{m}$  and therefore fulfil the requirements. A total area of  $1150 \text{ m}^2$  with about 250 MDT chambers would consist of 260 k tubes and would therefore represent an efficient implementation of the muon system. The points in Fig.8.2b) show a GEANT simulation of the reference detector with such an arrangement. An additional layer of thin-gap RPCs with 1 mm gas gap could provide 0.5 ns time resolution if needed.

## 8.4 Simulation of the standalone performance

A study of muon detector performance is presented based on a gas-based muon detector similar to the one currently operating in the ATLAS experiment at the LHC, arranged to be consistent with the layout shown in Fig. 3.1. The study focuses on the expected performance of muon reconstruction and identification, triggering capability as well as the evaluation of expected background from hadronic interactions.



### 8.4.1 Momentum reconstruction

The muon momentum is reconstructed by translating the azimuthal angle  $\phi$  measured with the muon detector to the transverse momentum  $p_T$  using the relation:

$$p_T = 0.3B\rho \quad (8.1)$$

and

$$\cos(\pi/2 - \phi) = R/(2\rho) \quad (8.2)$$

where  $\rho$  is the curvature of the muon track and  $B$  is the magnitude of the  $B$ -field, under the assumption of a constant  $B$ -field of 4 Tesla within the radius  $R = 6$  m. The muon track is reconstructed by a straight-line fit to the average hit positions in the four layers, for each of the barrel and endcap detectors, and extrapolating the fit to the point where the reconstructed muon exits from the  $B$ -field. Only hits created by the injected muons (identified with GEANT information) are used in the reconstruction. The azimuthal angle between the extrapolated line and the line connecting the detector centre and the point of the muon exit is used for the momentum measurement. The extrapolation used in this approach could introduce a bias to the measured momentum scale and this effect is accounted for by the calibration procedure described later. The momentum reconstruction scheme is illustrated in Fig. 8.4.

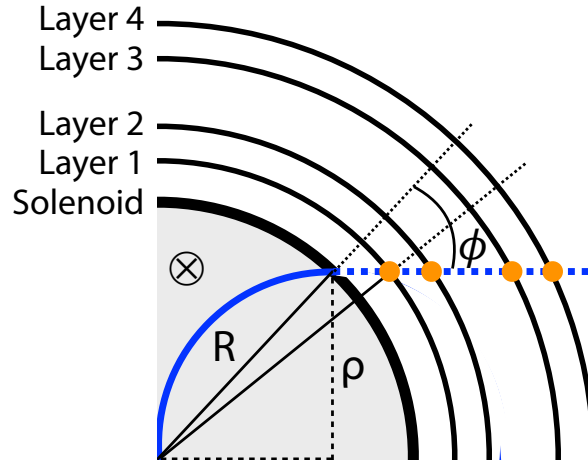


Fig. 8.4: Muon momentum reconstruction scheme used in this analysis. A constant  $B$ -field of 4 Tesla in the  $z$  direction is assumed inside the solenoid. The average hit position per layer (orange circles) is used for a straight-line fit and extrapolation to measure the angle  $\phi$  for each muon event.

Figure 8.5 shows the reconstructed  $p_T$  distributions for the generator-level muons of  $p_T = 10, 100$  and  $500$  GeV injected at different  $\eta$  positions from 0 to 1.8. The small offset of about 2–3 GeV with respect to the injected momentum of 10 GeV is attributed to the minimum-ionising energy loss due to interaction with the material preceding the muon detector. The relative  $p_T$  resolution of reconstructed muons as a function of muon  $\eta$  is shown in Fig. 8.6 for the  $p_T$  range between 10 and 1000 GeV.

Lowering the muon transverse momentum from 10 GeV, the reconstruction efficiency is expected to decrease significantly when the muon barely reaches the muon detector due to bending by the  $B$ -field. Figure 8.7 shows muon reconstruction efficiency as a function of generator-level muon  $p_T$  ( $p_T^{\mu(\text{truth})}$ ) between 3 and 10 GeV for different  $\eta$  positions. The muons with  $p_T > 7.5$  GeV are reconstructed more than about 90% of the time while those with  $p_T < 6.5$  GeV are hardly reconstructed in this  $\eta$  range.

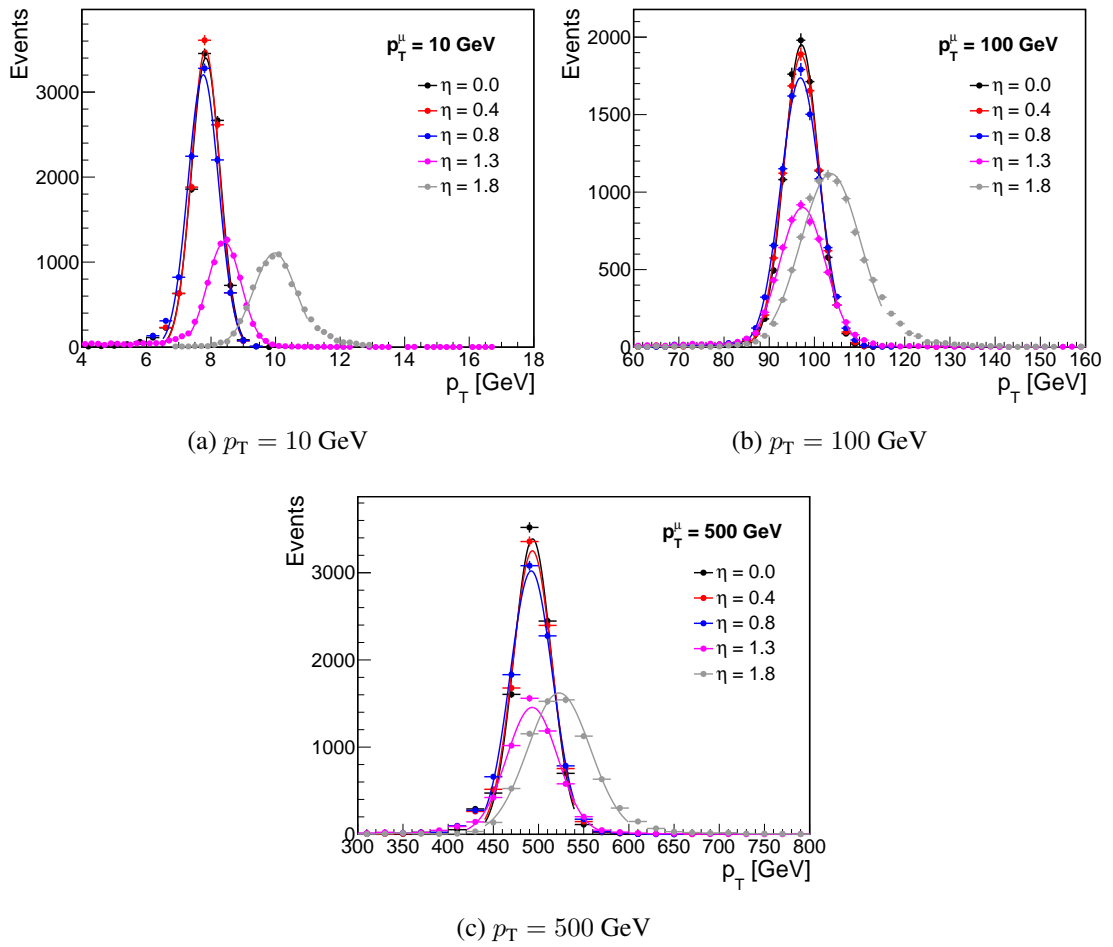


Fig. 8.5: Reconstructed muon  $p_T$  distributions for muons with the generator-level  $p_T$  at (a) 10, (b) 100 and (c) 500 GeV at different  $\eta$  values.

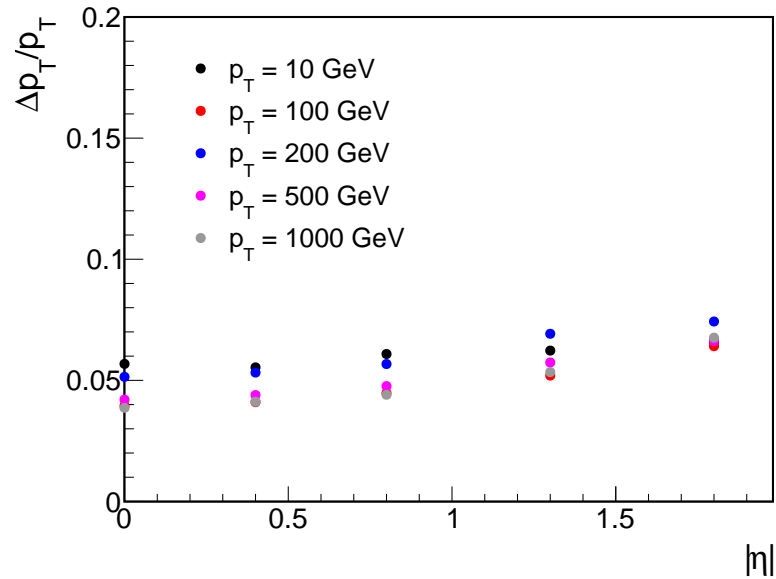


Fig. 8.6: Relative  $p_T$  resolution for reconstructed muon as a function of muon  $\eta$  for different generator-level  $p_T$  values between 10 and 1000 GeV.

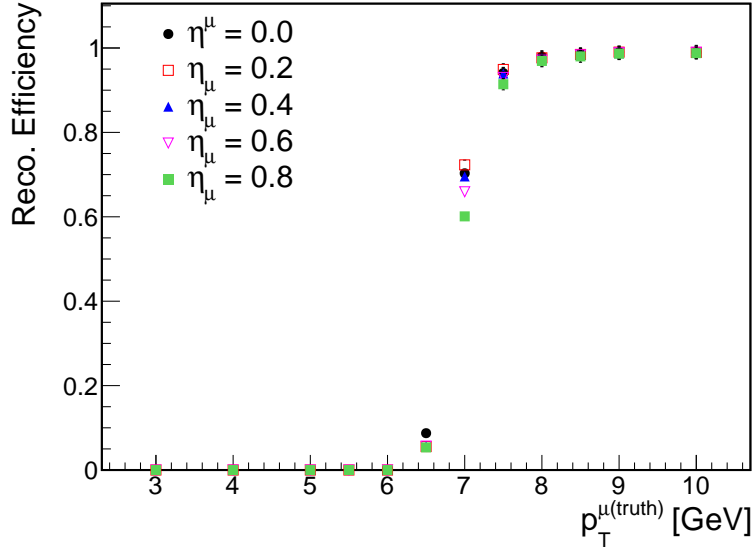


Fig. 8.7: Stand-alone muon reconstruction efficiency as a function of generator-level muon  $p_T$  at different  $\eta$  values between 0.0 and 0.8.

#### 8.4.2 Momentum calibration

The measured momentum scale varies with the position with respect to the straight-line fit where the angle of the muon track is measured. To reduce the position dependence, a simple calibration procedure exploiting the correlation between the true muon energy and detector observables is adopted. The calibration is done by using either simulation or data, depending on how the correct momentum scale is obtained. For the simulation-based calibration, the generator-level muon energy is used as described below. For the data-based calibration, this could be switched to the muon momentum measured using the inner tracker.

The detector observable could, for example, be the angle  $\Delta\phi$  between the fit to the muon layer hits and the straight line drawn from the detector centre to the innermost or outermost muon layer hits, or the transverse distance  $\Delta L$  between the individual layer hits and the position where the straight line between the detector centre and the outermost muon layer hits, as shown in Fig. 8.8. Figure 8.9 shows two-dimensional correlation between the inverse of the muon  $p_T^{\mu(\text{truth})}$  ranging between 10 and 100 GeV and the  $\Delta\phi$  measured at the first and fourth layers or the  $\Delta L$  measured at the second and third layers of the muon detector. Performing a second-order polynomial fit to the mean values as a function of  $1/p_T^{\mu(\text{truth})}$ , the mapping between the detector observables and the true momentum scale can be extracted. In order to evaluate the resolution of reconstructed muon momentum, this mapping is applied to  $\Delta\phi$  or  $\Delta L$  values measured from a statistically independent set of simulation samples with the same  $p_T^{\mu(\text{truth})}$  range. The resolution is defined here as a root-mean-square of the deviation from unity of the ratio of the inverse of the calibrated reconstructed  $p_T$  to the inverse of the  $p_T^{\mu(\text{truth})}$  for each sample. Figure 8.10 shows the result, indicating that a typical momentum resolution of about 10% is obtained for the measurement of  $\Delta\phi$  angles at the  $p_T$  range of 10–100 GeV. The worse resolution for the  $\Delta L$  measurement at the third layer is qualitatively understood to be due to a limited lever-arm between the third and fourth layers.

#### 8.4.3 Triggering

The trigger capability of muon detectors is studied with the stand-alone muon reconstruction using the angle measured with the muon detector. Producing single muon events with the generator-level  $p_T$  ranging from 5 to 35 GeV in bins of 0.5–2 GeV at different  $\eta$  positions, the muon  $p_T$  is reconstructed for each

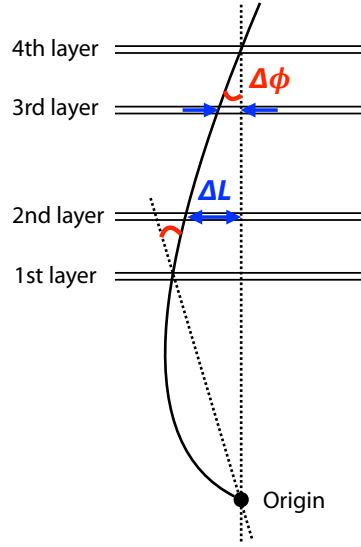


Fig. 8.8: Detector observables (e.g.  $\Delta\phi$  or  $\Delta L$ ) that could be used to calibrate the muon momentum scale. The dashed lines connect the detector centre and the positions of muon hits in the first or fourth layers, and are used together with the muon trajectory (solid curve) to measure the angle  $\Delta\phi$ .

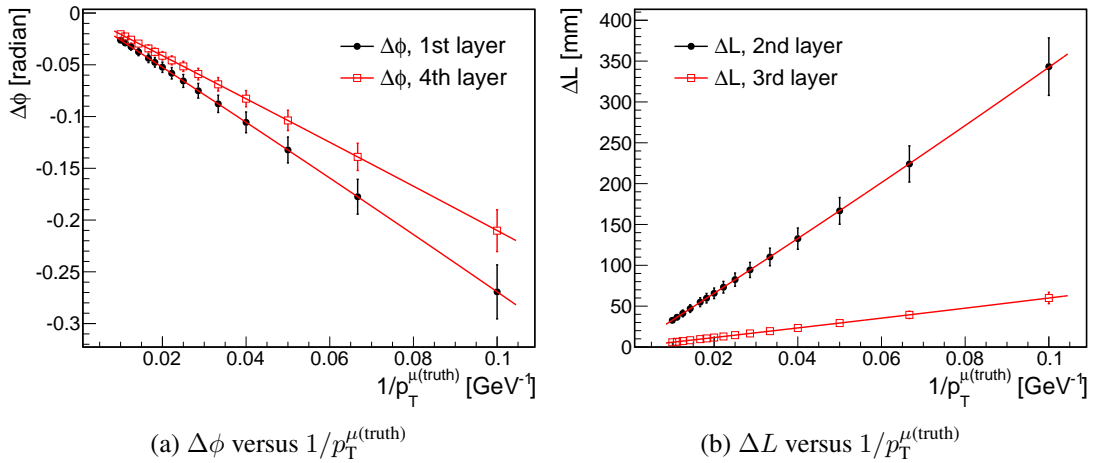


Fig. 8.9: (a) Two dimensional correlation between  $\Delta\phi$  or (b)  $\Delta L$  measured at the muon detector and the inverse of the generator-level muon  $p_T$  in the range between 10 and 100 GeV. Each curve on the distribution represents a second-order polynomial fit to extract the mapping between the observable and the true muon momentum used in the calibration.

sample using the angle as previously described. Given the measured  $p_T$  spectra, nearly full ( $> 95\%$ ) trigger efficiency can be achieved for muons with generator-level  $p_T$  of 10, 20 and 30 GeV by applying the cut on the reconstructed-level  $p_T$  at 6, 16 and 25 GeV, respectively for  $|\eta| < 0.8$ . The trigger efficiencies as a function of the generator-level muon  $p_T$  with the reconstructed-level  $p_T$  cuts of 6, 16 and 25 GeV are shown in Fig. 8.11.

#### 8.4.4 Contribution from hadronic interaction background

The primary interest of the muon detector is to identify and reconstruct muons produced in the decay of electroweak gauge bosons. However, it is important to evaluate the contribution from non-prompt muon sources, e.g. muons produced from the decay of heavy flavour hadrons, or hadronic background such

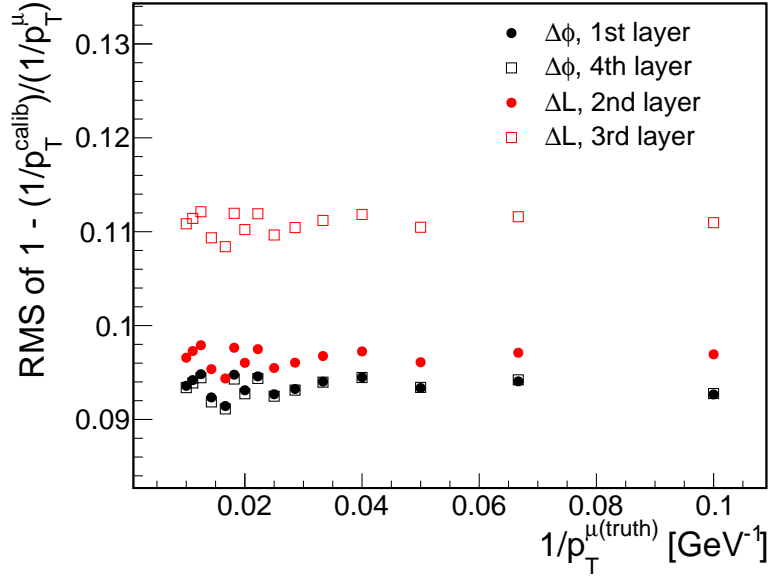


Fig. 8.10: Reconstructed muon momentum resolution, defined as a root-mean-square of the deviation from unity of the ratio of the inverse of the calibrated reconstructed  $p_T$  to the inverse of the  $p_T^{\mu(\text{truth})}$ , as a function of  $1/p_T^{\mu(\text{truth})}$  for the range between 10 and 100 GeV. The measurement is performed using the angles  $\Delta\phi$  at the first and fourth layers or the transverse distance  $\Delta L$  at the second and third layers of the muon detector.

as high- $p_T$  particles punching through the region with less calorimeter material. Such contributions will have a direct impact on the event rate triggered by the activity in the muon detector.

In order to assess these contributions in the current detector design, dijet events are produced using PYTHIA8 and the activity in the muon detector is studied. Two samples of dijet events are generated in  $2 \rightarrow 2$  hard scattering processes; the first sample with gluons and all flavor quarks as outgoing partons (referred to as inclusive jet sample) and the second one with only  $b$ - and  $c$ -quarks as outgoing partons (referred to as HF jet sample). For both samples at least one outgoing quark or gluon is required to have  $\hat{p}_T > 10$  GeV,  $90 < \hat{p}_T < 110$  GeV or  $900 < \hat{p}_T < 1100$  GeV to study jet  $p_T$  dependence. Jets are reconstructed at the generator level from all stable particles excluding neutrinos using the FASTJET package, and any simulation-level hits in the muon detector are associated to jets with the requirement of  $\Delta R < 0.4$  around the jet axis. As seen in Fig. 8.12, about 2 (3)%, 8 (10)% and 30 (20)% of inclusive (HF) jets have associated hits in the muon detector for dijets with  $\hat{p}_T > 10$  GeV,  $90 < \hat{p}_T < 110$  GeV and  $900 < \hat{p}_T < 1100$  GeV, respectively, with the relative fraction increasing from the barrel to the endcap region. The relative fraction becomes highest at  $\eta$  around 1.7 presumably due to less material before the muon detector, as indicated in the reduced muon energy loss as well. For dijets with  $\hat{p}_T > 10$  GeV ( $90 < \hat{p}_T < 110$  GeV,  $900 < \hat{p}_T < 1100$  GeV), about 13, (40, 12)% of HF jets with muon detector hits contains a generator-level muon within  $\Delta R = 0.4$  around the jets while this fraction is only 2 (8, 5)% for the inclusive jets. For  $\sim 1$  TeV jets, the contribution from real muons to muon detector hits is relatively reduced compared to the lower  $p_T$  jets of  $\sim 100$  GeV.

From Fig. 8.12, approximately 49M HF jets (per  $\text{pb}^{-1}$ ) with  $\hat{p}_T > 10$  GeV and  $|\eta| < 2.5$  have hits in the muon detector, out of which 6.5M HF jets contain generator-level muons. Assuming the peak luminosity of  $3 \times 10^{35} \text{ cm}^{-2}\text{s}^{-1}$  at the FCC-hh, this corresponds to a jet rate of approximately 15 (2.0) MHz for all HF jets (HF jets with real muons) at  $\hat{p}_T > 10$  GeV. The HF jet rate of 2.0 MHz will be subject to the isolation requirements investigated below.

The muons in jets are surrounded by other hadronic activity, so these muons are expected to be

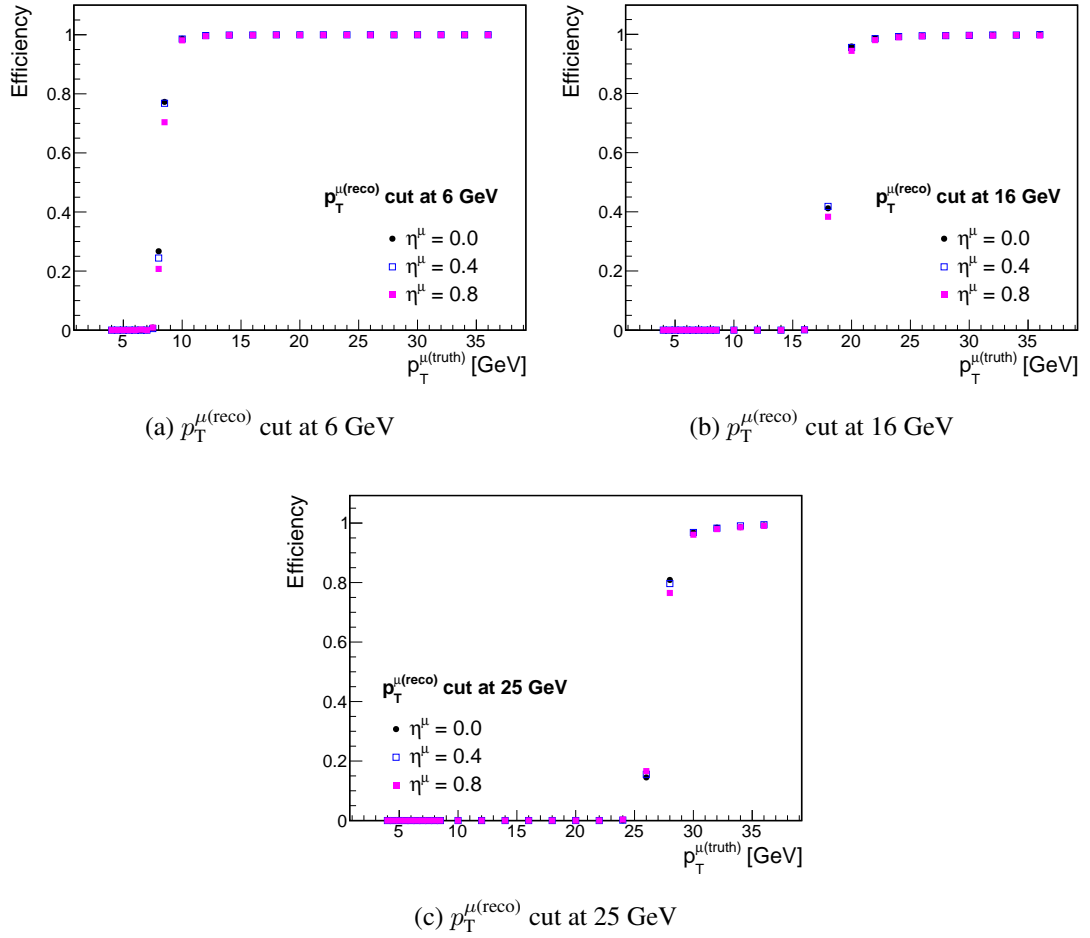


Fig. 8.11: Trigger efficiency for stand-alone muon reconstruction as a function of generator-level muon  $p_T$  at different  $\eta$  values. The efficiency is shown after the reconstructed muon  $p_T$  is required to be larger than (a) 6, (b) 16 and (c) 25 GeV, which corresponds to a full ( $> 95\%$ ) trigger efficiency at the generator-level  $p_T$  of (a) 10, (b) 20 and (c) 30 GeV and above.

reduced significantly with some isolation requirement. Figure 8.13 shows  $p_T$  and relative ‘isolation’ distributions of the generator-level muons found inside HF jets with  $|\eta| < 2$  in events with  $90 < \hat{p}_T < 110$  GeV. Here the relative isolation is defined as the ratio of the scalar  $p_T$  sum of charged particles with  $p_T > 1$  GeV associated with HF jets within  $\Delta R = 0.4$  around the jet axis, excluding the muon itself, to the  $p_T$  of the muon. As expected, the muons inside HF jets have large associated activity, resulting in a significant reduction in rate if a certain isolation condition is required. If the relative isolation is required to be less than 10%, the muon contribution from HF jets is reduced to the level of 1%.

The inclusive jet rates with muon detector hits are examined further for the barrel ( $|\eta| < 1.0$ ), inner endcap ( $1.5 < |\eta| < 2.5$ ) and outer endcap ( $1.0 < |\eta| < 1.5$ ) regions separately. For jets with  $\hat{p}_T > 10$  GeV, the average number of hits registered within  $\Delta R < 0.4$  of jets is translated to the number of hits per  $\eta$ - $\phi$  area in each detector station, approximately 35–45 with the statistical uncertainty of about 4 in the barrel region, about 35 with the uncertainty of  $\sim 2$  in the inner endcap and 25–40 with the uncertainty of 5 in the outer endcap regions. Convoluting them with the rates of jets with hits in each of the three detector components (Fig. 8.12), the hit rates per  $\eta$ - $\phi$  are estimated to be around a few GHz up to 10–20 GHz as shown in Table 8.1.

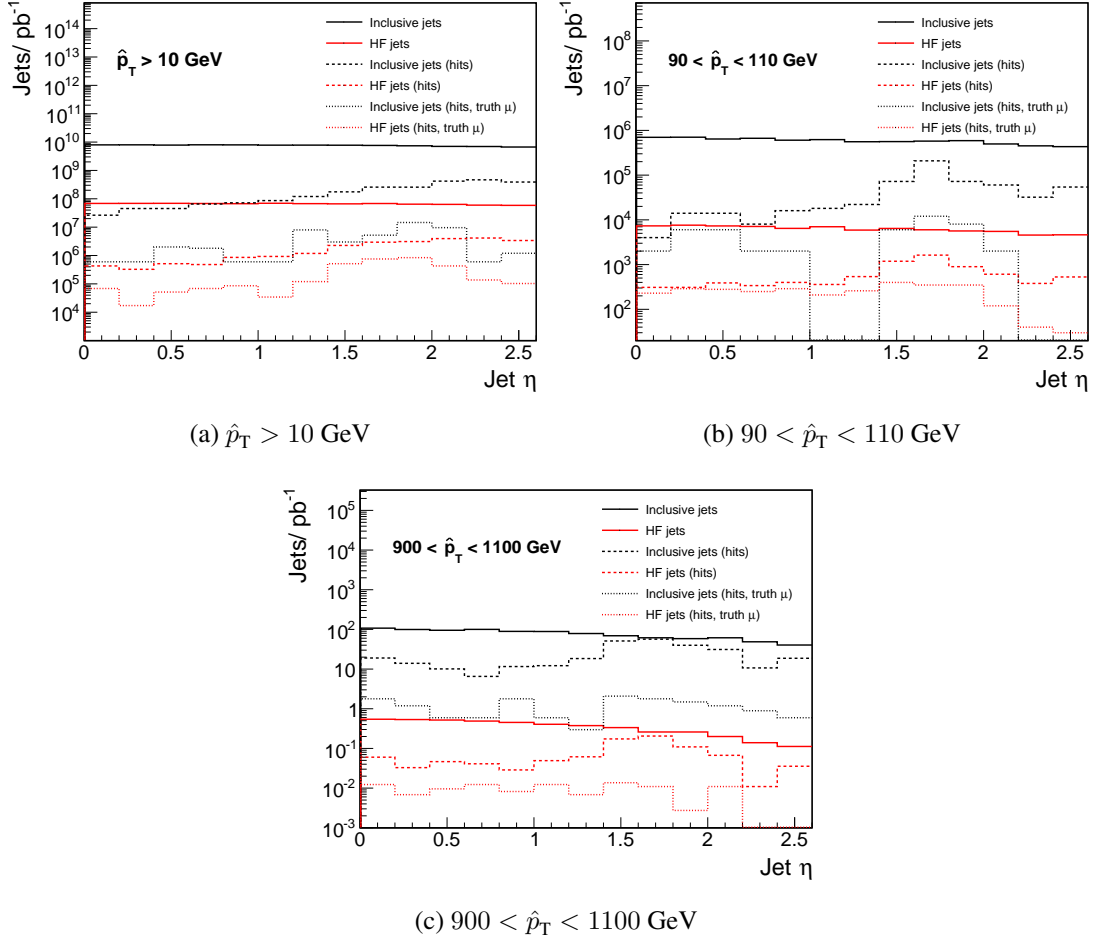


Fig. 8.12: Jet  $\eta$  distributions within  $0 < \eta < 2.5$  for inclusive (black histograms) and HF (red histograms) jets in dijet events with  $\hat{p}_T$  in the range (a)  $\hat{p}_T > 10 \text{ GeV}$ , (b)  $90 < \hat{p}_T < 110 \text{ GeV}$  and (c)  $900 < \hat{p}_T < 1100 \text{ GeV}$ . All the distributions are normalised to the integrated luminosity of  $1 \text{ pb}^{-1}$ . The solid histograms show the distributions for all jets while the dashed histograms show only those with simulation hits in the muon detector. The dotted histograms show the distributions for only those with simulation hits and generator-level muons inside the jet.

Table 8.1: Rates of inclusive jets with muon detector hits and associated hits registered per  $\eta$ - $\phi$  area in the barrel and endcap muon detectors at an instantaneous luminosity of  $3 \times 10^{35} \text{ cm}^{-2} \text{ s}^{-1}$ . Inclusive jets with  $\hat{p}_T > 10 \text{ GeV}$  are considered.

Detector Station #	$ \eta $	Jet rate [MHz]				Hit rate per $\eta$ - $\phi$ area [GHz]			
		1	2	3	4	1	2	3	4
Barrel	$< 1.0$	110	103	92	103	4.7	4.5	3.3	3.5
Inner Endcap	$1.5 - 2.5$	240	217	733	555	8.1	7.7	26.4	19.7
Outer Endcap	$1.0 - 1.5$	71	31	30	29	2.8	1.1	0.79	0.81



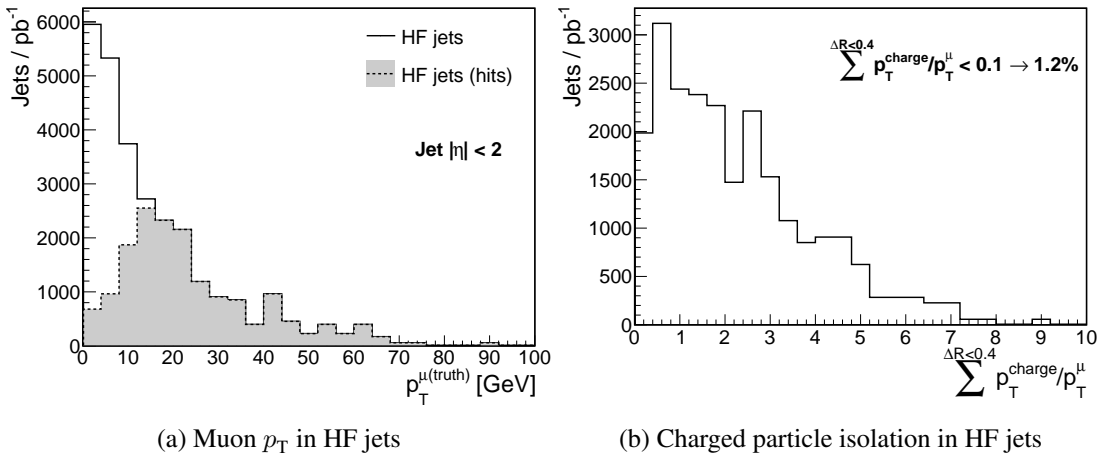


Fig. 8.13: (a) Generator-level muon  $p_T$  distributions for all HF jets (solid histogram) and HF jets with the muon detector hits (shaded histogram) in dijet events with  $90 < \hat{p}_T < 110$  GeV. The HF jets with  $|\eta| < 2$  are selected. (b) Relative isolation distribution calculated from charged particles within the HF jet, as described in the text. Pile-up is not taken into account in this study, but is assumed to be suppressed to a large extent by requiring that all tracks are associated with the primary vertex.



# Trigger/DAQ

## 9.1 The FCC-hh trigger challenge

Figure 9.1 shows how the cross-sections for typical SM processes increase from 14 to 100 TeV and the rates of typical processes are given in Table 3.1. In addition, the factor six increase in peak luminosity from HL-LHC to FCC-hh results in an average pile-up increase from 135 to 1000 that has to be taken into account. Since the  $b\bar{b}$  cross-section is only 50 times smaller than the inelastic pp cross-section, on average there will be 20  $b\bar{b}$  pairs in a single bunch crossing. One will also find 3 jets with  $p_T > 50$  GeV in a single bunch crossing. The rates for a few standard model processes are shown in Table 7.1. Around 400 kHz of Ws, 120 kHz of Zs, 40 kHz of W to leptons and 4 kHz of Z to leptons will be produced at the FCC-hh. The ratio of photons with  $p_T > 50$  GeV to jets with  $p_T > 50$  GeV is of the order of  $10^{-4}$ , similar to LHC, so to avoid increasing the rate of fake photon triggers due to jets, the discrimination between jets and photons on the trigger must reach levels of  $10^{-5}$ .

The increased granularity and acceptance of the FCC-hh reference detector will result in about 250 TByte/s of data for calorimetry and muon system, about 10 times more than the ATLAS and CMS Phase-II scenarios. It is highly likely that it will be possible to digitise and read this data volume at the full bunch-crossing rate by the time of detector construction. The question remains whether the data rate of almost 2 PB/s from the tracker can also be read out at the full bunch crossing rate or whether calorimeter, muon and possible coarse tracker information allow a first level trigger to be formed, reducing the tracker readout rate to the few MHz level, without the loss of important physics. Even if the optical link technology for full tracker readout were available and affordable, sufficient radiation hardness of devices and infrastructure constraints from power and cooling might be prohibitive.

## 9.2 State of the art

In this section we review the trigger and data acquisition challenges at LHC and HL-LHC, and discuss the systems currently employed by CMS and ATLAS to meet these challenges.

During LHC Run 2, both ATLAS and CMS use a Level-1 trigger (L1) followed by a software based higher level trigger (HLT). The L1 trigger is implemented largely using custom FPGA processors, and use reduced granularity of the calorimeter and muon systems to reduce the event rate to  $\sim 100$  kHz, within a latency of  $\sim 3 \mu\text{s}$ . The HLT is implemented using off-the-shelf computing devices further reducing the event rate to around  $\sim 1$  kHz. The event size for both detectors is  $\sim 2$  MB, giving a total data rate for offline storage and analysis of  $\sim 2$  GB/s.

For HL-LHC, the detectors will be upgraded and the event size for both detectors will increase to  $\sim 5$  MB. This corresponds to a total data production of  $\sim 200$  TB/s at the 40 MHz bunch-crossing frequency. The transfer of such a data rate is technically possible, requiring 150 000–300 000 rad-hard

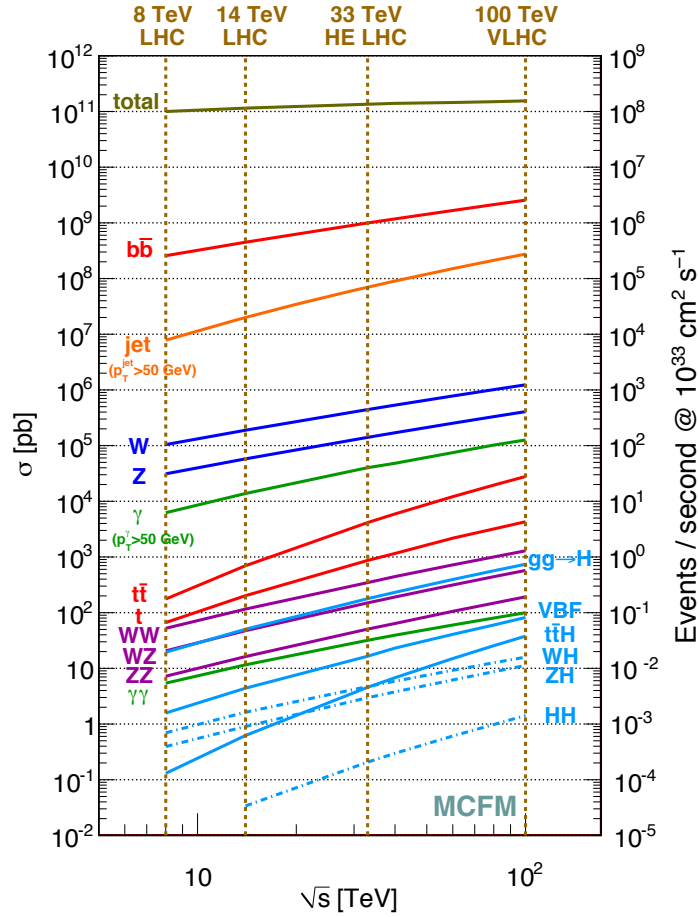


Fig. 9.1: Cross-section for various processes as a function of  $\sqrt{s}$ , from the authors of Ref. [181].

optical links, developed for HL-LHC. However, the power and cooling required would introduce significant material into the inner detectors, seriously degrading performance. For both detectors it is therefore planned hardware triggers to reduce the rate of data transferred off-detector. ATLAS will operate an L0 trigger using calorimeter and muon data to reduce the rate to  $\sim 1$  MHz with a latency of  $\sim 10 \mu\text{s}$ , at which point the tracker will be readout [182]. Tracks will then be reconstructed using a fast associative memory based system, allowing the L1 trigger to reduce the rate to  $\sim 100$  kHz for processing by HLT. CMS plans a single L1 hardware trigger, with a latency of  $\sim 12 \mu\text{s}$  and an output rate of  $\sim 750$ – $1000$  kHz [183]. Tracks will be reconstructed at the full bunch-crossing rate of 40 MHz, by making use of coincidences between closely-spaced layers of silicon to construct track ‘stubs’ on detector, from tracks with  $p_T \gtrsim 2$ – $3$  GeV. These will be used to reconstruct tracks in an FPGA-based track trigger for inclusion in the L1 trigger. The resulting off-detector data rates are  $\sim 30$  TB/s for ATLAS and  $\sim 50$  TB/s for CMS. The HLT system, in both cases, will reduce the event rate to  $\sim 10$ – $20$  kHz.

The large FPGAs and high-speed optical links planned for HL-LHC allow increasingly sophisticated reconstruction techniques at L1. CMS plans to perform a particle-flow based reconstruction at L1 [183], and recent progress with employing Machine-Learning techniques in FPGAs [184] will likely see this used widely at the HL-LHC and beyond.

### 9.3 Extrapolating CMS trigger rates to 100 TeV

Trigger rates are highly dependent on detector effects, in particular resolution, as well as details of the trigger processing system. Prediction of trigger rates, a priori, is challenging, and requires full simulation of the detector and trigger. To understand the order of magnitude of the challenge, we developed a fast simulation to estimate rates of the CMS Phase-1 single jet, muon and electron/photon triggers at  $\sqrt{s} = 100$  TeV. The trigger performance is parameterised in terms of the efficiency and resolution of the trigger to find these objects. We first compute the rate of objects identified by the trigger, from the product of the true object rate and the trigger efficiency, as a function of object  $p_T$ . We then compute the trigger rate from a convolution of the true object rate and the  $p_T$  resolution of objects identified by the trigger. Finally, any residual difference between the trigger rates estimated with the fast simulation and the full simulation are encapsulated in a scaling factor, which is of the order of 1. True object rates were calculated using PYTHIA8. The trigger object efficiency and  $p_T$  resolution were computed using the CMS full simulation, by matching trigger objects to true objects in  $\Delta R$ . In addition, muon triggers due to in-flight decays of long-lived particles, such as pions, are parameterised by considering the probability that a proton-proton interaction will produce such a muon, and their momentum distribution. The parameterised simulation is used to compute the probability that a single proton-proton interaction will pass the trigger selection. To take pile-up effects into account, the probability is first rescaled by pile-up, and the result used to compute trigger rates. This method does not allow taking into account a complex combinatoric pile-up effect. However, to first order this effect is not dominant for single-object trigger rates for the thresholds we are interested in.

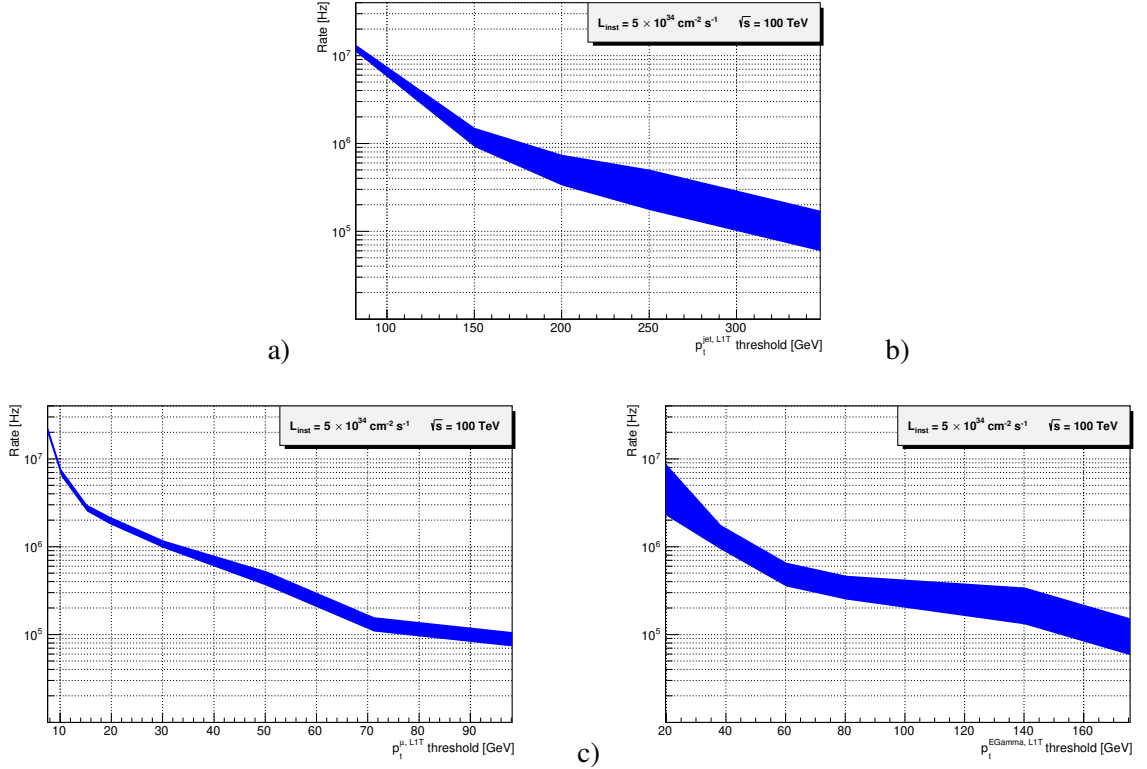


Fig. 9.2: Estimated rates of a) single jet, b) muon and c) electron/photon triggers as a function of  $p_T$  threshold, at  $\sqrt{s} = 100$  TeV and  $\mathcal{L} = 5 \times 10^{34} \text{ cm}^{-2} \text{ s}^{-1}$ .

The results of the fast simulation for a luminosity of  $\mathcal{L} = 5 \times 10^{34} \text{ cm}^{-2} \text{ s}^{-1}$  are presented in Fig. 9.2. We assume a total L1 trigger rate of 1 MHz at FCC-hh, and that single object triggers are allocated the same fraction of bandwidth as in CMS Run 2 ( $\sim 10\%$ ). The  $p_T$  thresholds required to

maintain single muon, jet and electron/photon triggers within the allocated 100 kHz at FCC-hh are 78, 300 and 150 GeV, respectively. At the full FCC-hh luminosity of  $\mathcal{L} = 3 \times 10^{35} \text{ cm}^{-2} \text{ s}^{-1}$  these rates are even a factor 6 larger and these thresholds would lead to a 6 MHz L1 rate. It is clear that more sophisticated algorithms using higher granularity must be developed for the FCC-hh in order to arrive at a few MHz L1 rate without loss of interesting physics.

#### 9.4 Track trigger studies

As shown in the tracking chapter, a triplet of tracking layers at a radius of 600 mm with layer separation of 30 mm can provide a track trigger that retains 50% of the HH and ttH signals at a trigger rate of only 100 kHz at the highest luminosity with pile-up of 1000. This is evidence that tracking can provide enough selectivity if calorimetry and muon measurements are not sufficient. About half of the tracker data originate from the region of  $< 200$  mm from the beampipe, where hit densities are enormous, radiation levels very high and material budget has to be very low for excellent vertex tracking. It is therefore conceivable to assume 40 MHz readout, for the tracking layers at radii  $> 200$  mm for a high performance track trigger, and to read out the vertex tracker at a lower rate.

---

# FCC-hh physics benchmark studies

---

## 10.1 Introduction

The FCC-hh has an extremely rich physics programme, ranging from precision Standard Model (SM) measurements, to direct searches for physics beyond the SM (BSM). The latter can include high mass resonances (decaying into leptons ( $\ell = e, \mu$ ),  $\tau$ 's, light/heavy quarks or gauge bosons), weakly or strongly coupled supersymmetry (SUSY) and dark matter (DM). Such searches often involve very massive states decaying to SM particles with high transverse momentum and subsequently decaying into highly collimated clusters or jets. These high energy particles are useful benchmarks for exploring the limitations of the detectors, such as the angular separation and energy resolution. SM measurements include studying the interactions of the Higgs boson with SM particles, in particular its self-interaction, as well as a rich programme including topics such as top physics, flavour physics and QCD.

Here we summarise a selected set of physics benchmark studies intended to characterise the capabilities of the FCC-hh machine and detectors. The assumptions made in terms of the baseline detector performance are discussed in other chapters. In many studies, we varied the assumptions to probe the dependence on those assumptions. For example, we found in the context of the  $Z'$  search that the mass reach is equivalent between electrons and muons, indicating that the muon momentum resolution is optimal. In the VBS study, we found that the detector acceptance in  $\eta$  plays a critical role in driving the sensitivity. The disappearing-track study indicates the dramatic improvement that could be provided by a timing detector. Almost all studies will benefit from a further reduction in the size of systematic uncertainties, which will certainly arise in due time from reliable data-driven direct determinations of backgrounds and systematics, from novel analysis techniques, and from improved theoretical modeling. We also assume that new methods can be developed to reduce the luminosity uncertainty. In many studies, the role of the ‘ultra-boosted’ regime is highlighted, which requires new reconstruction techniques extending the capabilities of those used at the LHC.

All studies were performed using simulation. Monte Carlo samples were generated with the MG5\_aMC@NLO 2.5.2 [185] package, showered and hadronised with PYTHIA 8.230 [102]. The detector simulation has been performed with the fast simulation tool DELPHES 3.4.2 [34] using the reference FCC-hh detector parameterisation. In many studies, further study with full simulation will be required to fully assess the impact from pile up.

This Chapter is divided into two main sections. Section 10.2 discusses studies probing the Higgs boson and electroweak symmetry breaking, while Section 10.3 discusses searches for new physics. A more complete review of the full physics potential of FCC-hh, including its heavy ion programme, can be found in Refs. [1, 186].



## 10.2 Higgs and electroweak symmetry breaking

### 10.2.1 Higgs properties

Following the discovery of the Higgs particle [187, 188], the scalar sector of the SM, in particular the Higgs couplings to SM particles, has only been probed with limited precision. Higgs measurements involving rare decays, such as  $H \rightarrow \mu^+ \mu^-$  or  $H \rightarrow Z\gamma$  will be statistically limited even at the high-luminosity LHC (HL-LHC) [189, 190]. Measurements, such as Higgs couplings to photons or gauge bosons, performed for instance in the decays  $H \rightarrow \gamma\gamma$  and  $H \rightarrow ZZ^* \rightarrow 4\ell$ , will benefit from very large statistics at the HL-LHC and will become systematically limited [189, 190]. At  $\sqrt{s} = 100$  TeV, the Higgs production rate increases by a factor 15 for gluon-fusion production (ggF) with respect to  $\sqrt{s} = 14$  TeV, and up to a factor 55 for associated production with a  $t\bar{t}$  pair (ttH). With a total integrated luminosity of  $\mathcal{L} = 30 \text{ ab}^{-1}$  at the FCC-hh, we expect  $\mathcal{O}(100)$  increase in the number of Higgs events compared to HL-LHC, leading to an overall reduction of  $\mathcal{O}(10)$  of statistical uncertainty in Higgs-related measurements. Abundant statistics can be exploited by explicitly selecting phase space regions where systematic uncertainties are small and better understood, thereby trading high statistics for low systematics. This theme will be exploited throughout this chapter, by focussing on the following subset of Higgs decay channels:  $H \rightarrow ZZ^* \rightarrow 4\ell$ ,  $H \rightarrow \gamma\gamma$ ,  $H \rightarrow \mu^+ \mu^-$  and  $H \rightarrow Z\gamma \rightarrow \ell^+ \ell^- \gamma$ , where  $\ell = e, \mu$ .

Table 10.1: Upper row: Cross sections at  $\sqrt{s} = 100$  TeV for the production of a SM Higgs boson in the gluon fusion (ggF), vector boson fusion (VBF), top pair associated (ttH) and Higgs-strahlung (VH) production modes. Lower row: Expected number of Higgs bosons produced with an integrated luminosity of  $30 \text{ ab}^{-1}$  [5].

	ggF	VBF	ttH	VH
$\sigma(\text{pb})$	802	69	33	27
$N(\sqrt{s} = 100 \text{ TeV}, 30 \text{ ab}^{-1})$	$25 \times 10^9$	$2.5 \times 10^9$	$10^9$	$7.5 \times 10^8$

**Signal** The following production modes are considered: gluon fusion production (ggF), vector boson fusion (VBF), top pair associated production (ttH) and Higgs-strahlung (VH). The cross-sections and the expected number of events expected with an integrated luminosity of  $30 \text{ ab}^{-1}$  at  $\sqrt{s} = 100$  TeV are summarised in Table 10.1. Higgs events were generated at leading order (LO) with up to two additional MLM-merged jets [191]. All diagrams considered are at tree level except for the ggF mode, which was generated including the full  $m_t$  dependence. The yields after inclusive K-factors accounting for current calculations have been applied, are summarised in Table 10.2. The Higgs decay branching fractions have been taken from [192] and the following values were used:

- $\text{BR}(H \rightarrow \gamma\gamma) = 2.27 \times 10^{-3}$
- $\text{BR}(H \rightarrow 4\ell) = 1.25 \times 10^{-4}$
- $\text{BR}(H \rightarrow \mu^+ \mu^-) = 2.17 \times 10^{-4}$
- $\text{BR}(H \rightarrow \ell^+ \ell^- \gamma) = 1.03 \times 10^{-4}$ .

Table 10.2: Expected number of Higgs produced in each decay channel for various Higgs transverse momentum thresholds with an integrated luminosity of  $30 \text{ ab}^{-1}$ .

	$H \rightarrow \gamma\gamma$	$H \rightarrow 4\ell$	$H \rightarrow \mu^+\mu^-$	$H \rightarrow \ell^+\ell^-\gamma$
$p_T(H) > 0 \text{ GeV}$	$50 \times 10^6$	$3 \times 10^6$	$5 \times 10^6$	$2.5 \times 10^6$
$p_T(H) > 200 \text{ GeV}$	$900 \times 10^3$	$50 \times 10^3$	$90 \times 10^3$	$40 \times 10^3$
$p_T(H) > 500 \text{ GeV}$	$100 \times 10^3$	$6 \times 10^3$	$10 \times 10^3$	$5 \times 10^3$
$p_T(H) > 1 \text{ TeV}$	4000	250	400	200

**Backgrounds** In the  $H \rightarrow \gamma\gamma$  channel the irreducible background of QCD di-photon production is considered including: a large tree level  $q\bar{q} \rightarrow \gamma\gamma$  component, generated with up to two additional merged jets, and a smaller loop-induced component,  $g\bar{g} \rightarrow \gamma\gamma$ , generated with up to one additional merged jet. The background was generated with the following requirements:  $p_T^\gamma > 30 \text{ GeV}$ ,  $|\eta^\gamma| < 5$  and  $50 < m_{\gamma\gamma} < 200 \text{ GeV}$ . The LO cross sections are  $\sigma(q\bar{q} \rightarrow \gamma\gamma) = 615 \text{ pb}$  and  $\sigma(g\bar{g} \rightarrow \gamma\gamma) = 25 \text{ pb}$  respectively. A conservative K-factor of 2 is applied to both contributions.

In the  $H \rightarrow ZZ^* \rightarrow 4\ell$  channel, only the (dominant) continuum  $4\ell$  background is considered. It was generated at tree-level, with up to one extra merged jet and with  $p_T^\ell > 4 \text{ GeV}$ ,  $|\eta^\ell| < 5$  and  $50 < m_{4\ell} < 200 \text{ GeV}$ . The cross section is found to be 62 fb, including  $K=1.6$ , assumed equal to the inclusive  $ZZ$  production K-factor at  $\sqrt{s} = 100 \text{ TeV}$  [15].

In the  $H \rightarrow \mu^+\mu^-$  and  $H \rightarrow Z\gamma$  channels the continuum  $\mu\mu$  and  $\ell^+\ell^-\gamma$  backgrounds were generated at tree-level, up to one extra merged jet and with  $p_T^{\ell,\gamma} > 20 \text{ GeV}$ ,  $|\eta^{\ell,\gamma}| < 5$  and  $50 < m_{\mu\mu}(m_{\ell\ell\gamma}) < 200 \text{ GeV}$ . The cross-section for these processes are  $\sigma(\mu\mu) = 200 \text{ pb}$ , with  $K=1.2$  assumed equal to the Drell-Yan production K-factor, and  $\sigma(\ell^+\ell^-\gamma) = 2 \text{ pb}$  with  $K=1.5$ .

Contributions from object mis-identification (fakes) were neglected. The  $H \rightarrow \gamma\gamma$  channel, where the light jets in the  $\gamma$ +jets background (mostly coming from  $\pi^0$  in jets) can be mis-identified as photons, could potentially have a significant fake contribution. At the current LHC experiments, after applying all identification and isolation criteria, the fake background contribution constitutes at most 25% of the total background. We therefore assume this contribution to be included in our conservative K-factor.

**Proposed measurements** The results are expressed in terms of precision on the signal strength defined as  $\mu = \sigma_{\text{obs}}/\sigma_{\text{SM}}$  or equivalently on the branching fraction of  $\text{BR}(H \rightarrow X)$ . For the channels considered here, the Higgs decay products are visible in the detector and thus the invariant mass can be reconstructed. The analyses focus on phase spaces where the impact of systematic uncertainties tied to reconstruction efficiencies is small.

A key observable is the transverse momentum of the Higgs,  $p_T(H)$ , where for large values of  $p_T(H)$  the signal-to-background ratio considerably improves.

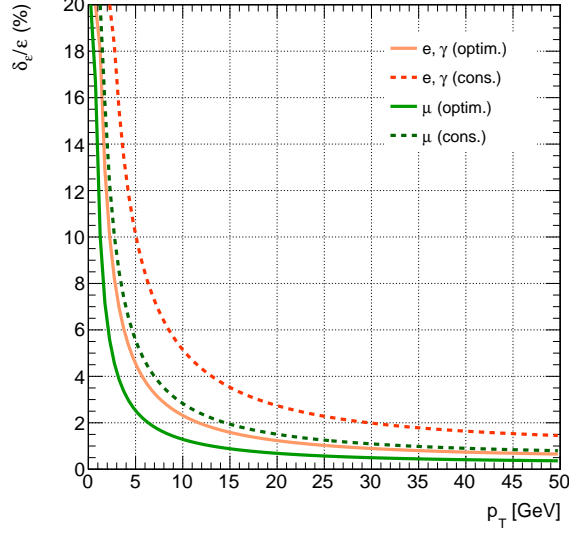


Fig. 10.1: The uncertainty on the reconstruction efficiency of electrons, photons and muons as a function of transverse momentum. An optimistic (solid) and a conservative (dashed) scenario are considered.

Table 10.3: Summary of the event selection criteria used for each channel

$H \rightarrow \gamma\gamma$	$H \rightarrow 4\ell$	$H \rightarrow \mu^+\mu^-$	$H \rightarrow \ell^+\ell^-\gamma$
$p_T^{\max}(\gamma) > 30 \text{ GeV}$ $p_T^{\min}(\gamma) > 25 \text{ GeV}$	$p_T^{(1)}(\ell) > 20 \text{ GeV}$ $p_T^{(2)}(\ell) > 10 \text{ GeV}$ $p_T^{(3)}(\ell) > 7 \text{ GeV}$ $p_T^{(4)}(\ell) > 5 \text{ GeV}$	$p_T^{\max}(\mu) > 20 \text{ GeV}$ $p_T^{\min}(\mu) > 20 \text{ GeV}$	$p_T^{\max}(\ell) > 20 \text{ GeV}$ $p_T^{\min}(\ell) > 20 \text{ GeV}$ $p_T(\gamma) > 15 \text{ GeV}$
$ \eta(\gamma)  < 4$	$ \eta(\ell)  < 4$	$ \eta(\mu)  < 4$	$ \eta(\ell, \gamma)  < 4$
rel.Iso( $\gamma$ ) < 0.15	rel.Iso( $\ell$ ) < 0.4	rel.Iso( $\mu$ ) < 0.4	rel.Iso( $\gamma$ ) < 0.15 rel.Iso( $\ell$ ) < 0.4
	$m_{\ell\ell}^{(1)} \in [40, 120] \text{ GeV}$ $m_{\ell\ell}^{(2)} \in [12, 120] \text{ GeV}$		$m_{\ell\ell} \in [75, 105] \text{ GeV}$
$ m_{\gamma\gamma} - m_H  < 2.5 \text{ GeV}$	$ m_{4\ell} - m_H  < 2.5 \text{ GeV}$	$ m_{\mu\mu} - m_H  < 1 \text{ GeV}$	$ m_{\ell\ell\gamma} - m_H  < 2.5 \text{ GeV}$

**Event selection and signal extraction** Only minimal optimisation of the selection has been performed. Acceptance cuts for isolated electrons, muons and photons aimed at maximising the signal to background (S/B) ratio are applied, followed by the requirement that the invariant mass constructed from the Higgs decay candidates be compatible with  $m_H = 125 \text{ GeV}$ . The relative isolation is computed using the momentum sum of particle-flow candidates [52] inside a cone of size  $R = 0.3$  around the reconstructed particle (excluding the particle itself) divided by the particle  $p_T$ .

The event selection for the  $H \rightarrow \gamma\gamma$  and  $H \rightarrow \mu^+\mu^-$  requires at least two isolated photons or opposite sign muons. For the  $H \rightarrow ZZ^* \rightarrow 4\ell$  channel, at least four leptons with two opposite sign and same flavour pair are required. One pair is required to have kinematics compatible with an on-shell Z decay, while the other is allowed to be largely off-shell with a small  $m_{\ell\ell}$ . For the  $H \rightarrow Z\gamma \rightarrow \ell^+\ell^-\gamma$  channel, an isolated photon and only one opposite sign and same flavour pair compatible with an on-shell

Z decay is allowed. Further details of the event selection can be found in Table 10.3. The Higgs invariant mass distributions used for signal extraction are shown in Figs. 10.2 and 10.3 (left).

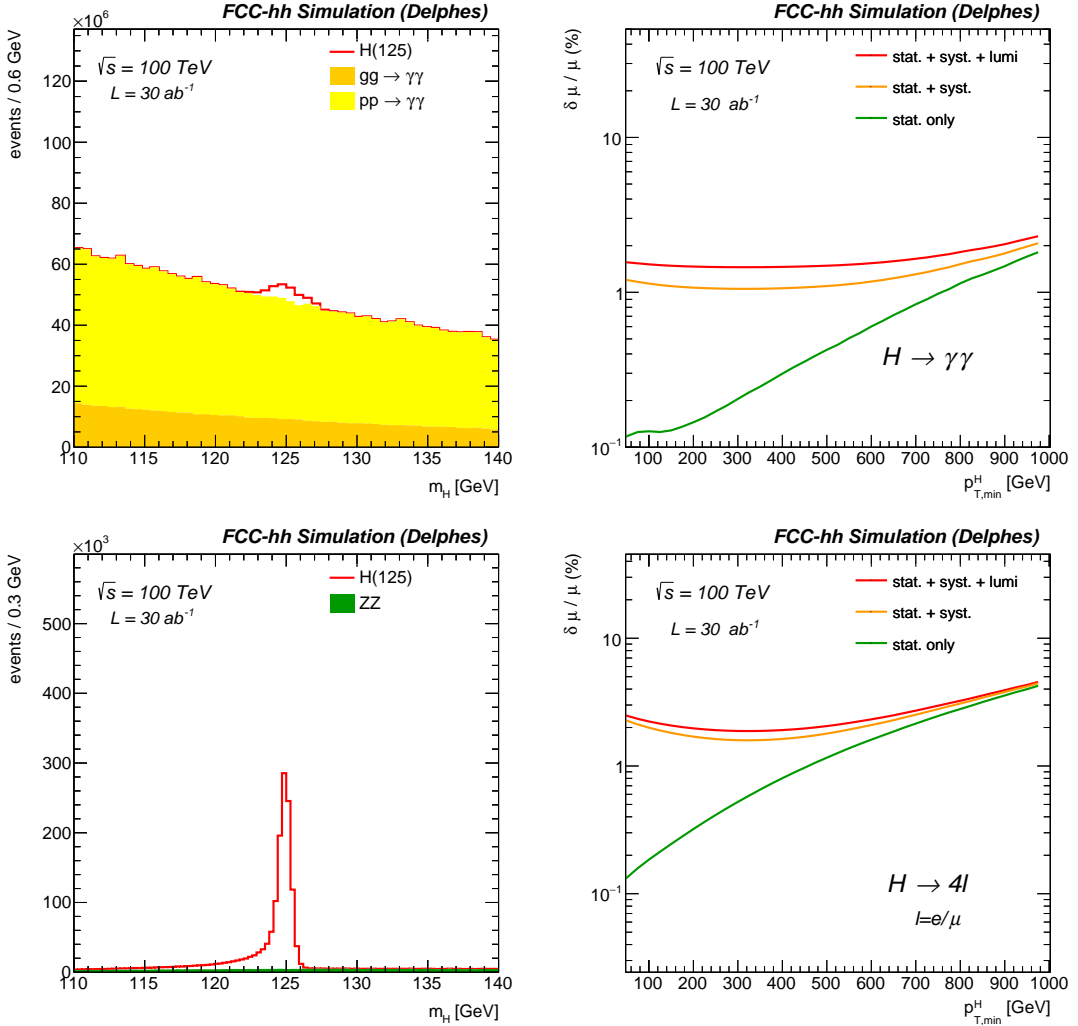


Fig. 10.2: Left: Invariant mass spectrum of the reconstructed Higgs candidate in the  $H \rightarrow \mu^+ \mu^-$  (top) and  $H \rightarrow 4\ell$  (bottom) channels, for signal and backgrounds. Right: Expected precision on the signal strength (defined as  $\mu = \sigma_{\text{obs}}/\sigma_{\text{SM}}$ ) as a function of the minimal requirement on the Higgs reconstructed transverse momentum obtained in the  $H \rightarrow \mu^+ \mu^-$  (top) and  $H \rightarrow 4\ell$  (bottom) channels. The expected precision is given for three scenarios where various assumptions on the uncertainties are made: only statistical uncertainties are included (stat-only), statistical and systematics on the object reconstruction efficiencies (stat. + syst), and statistical, systematics on the object reconstruction efficiencies, and luminosity systematics of  $\delta\mathcal{L} \approx 1\%$  (stat + syst + lumi).

**Systematic uncertainties** Typically at hadron colliders the ultimate precision of cross-section measurements is limited by systematic uncertainties on the production cross section  $\sigma_{\text{prod}}$  and the integrated luminosity  $\mathcal{L}$ . The current uncertainty on the Higgs production cross section is  $\sim 3\%$  [193], dominated by uncertainties on the parton distribution function,  $\alpha_S$  and scale uncertainties. We assume that improvements in the theoretical predictions within the timescale of the FCC will be  $\delta\sigma_{\text{prod}} < 1\%$ . Typical LHC analyses have luminosity uncertainties of  $\delta\mathcal{L} \approx 2.5\%$  [194], here we assume that novel techniques can improve this systematics to  $\delta\mathcal{L} \approx 1\%$ .

Systematic uncertainties also enter due to object reconstruction efficiencies. The uncertainties for

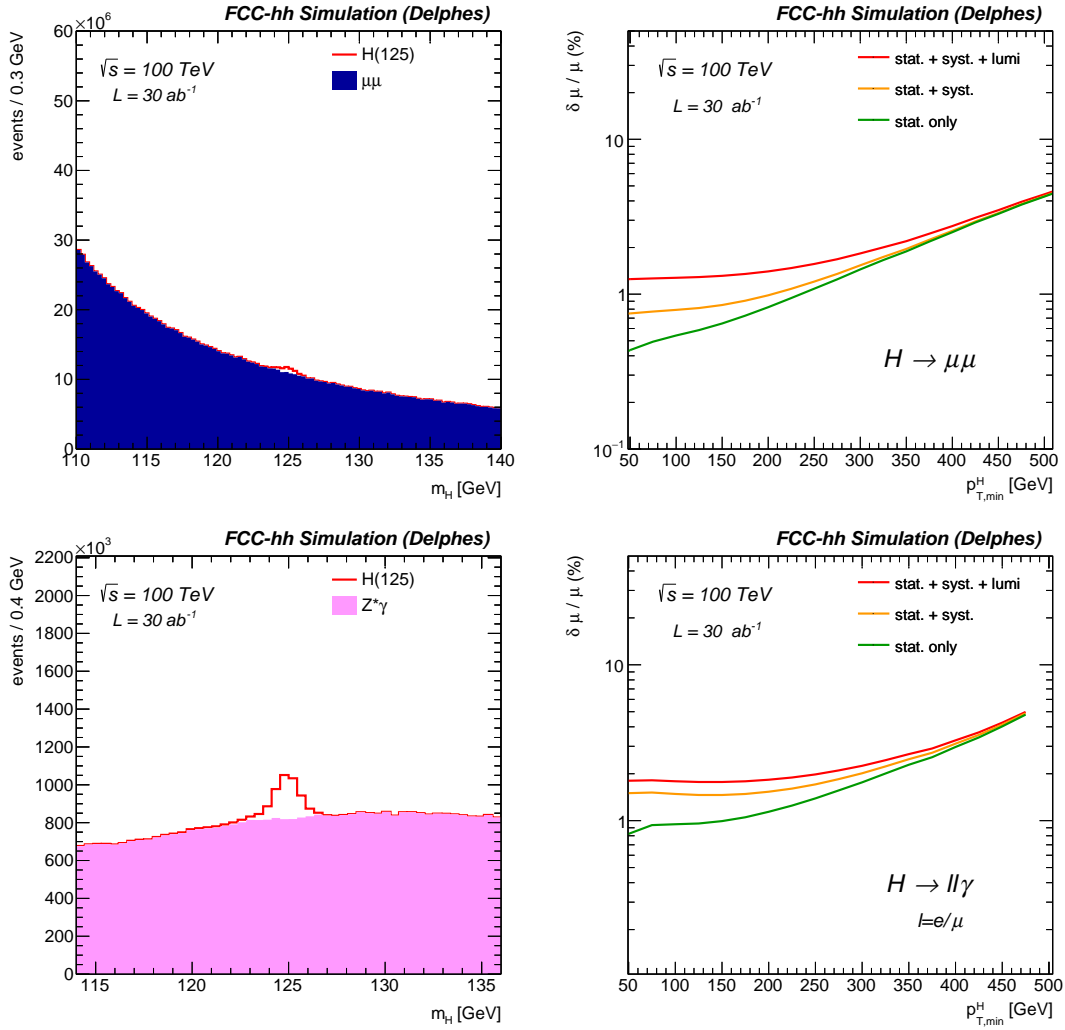


Fig. 10.3: Left: Invariant mass spectrum of the reconstructed Higgs candidate in the  $H \rightarrow \mu^+\mu^-$  (top) and  $H \rightarrow \ell^+\ell^-\gamma$  (bottom) channels, for signal and backgrounds. Right: Expected precision on the signal strength (defined as  $\mu = \sigma_{\text{obs}}/\sigma_{\text{SM}}$ ) as a function of the minimal requirement on the Higgs reconstructed transverse momentum obtained in the  $H \rightarrow \mu^+\mu^-$  (top) and  $H \rightarrow \ell^+\ell^-\gamma$  (bottom) channels. Three scenarios where various assumptions on the uncertainties are shown: only statistical uncertainties are included (stat-only), statistical and systematics on the object reconstruction efficiencies (stat. + syst), and statistical, systematics on the object reconstruction efficiencies, and luminosity measurement systematics of  $\delta\mathcal{L} \approx 1\%$  (stat + syst + lumi).

single muon, electron and photon are shown in Fig. 10.1. A conservative and an optimistic scenario are considered. For example, at asymptotically high momenta  $\delta_\epsilon(e, \gamma) = 0.5\%$  and  $\delta_\epsilon(\mu) = 0.25\%$  for the optimistic and  $\delta_\epsilon(e, \gamma) = 1.0\%$  and  $\delta_\epsilon(\mu) = 0.50\%$  for the conservative scenarios, respectively. We assume that the uncertainties for electrons and photons are equal and fully correlated, but uncorrelated to those for the muons.

The normalisation of the backgrounds for all channels is determined from control regions defined away from the Higgs mass peak. Given the large statistics in these sidebands, we therefore assume  $\delta_B$  to be negligible.

**Individual channel results** The expected precision on the signal strength (defined as  $\mu = \sigma_{\text{obs}}/\sigma_{\text{SM}}$ ) is given in Figs. 10.2 (right) and 10.3 (right) as a function of the minimal requirement on the Higgs reconstructed transverse momentum obtained in the  $H \rightarrow \gamma\gamma$ ,  $H \rightarrow 4\ell$ ,  $H \rightarrow \mu^+\mu^-$  and  $H \rightarrow \ell^+\ell^-\gamma$  channels. The expected precision is given for three scenarios where various assumptions on the uncertainties are made: only statistical uncertainties are included (stat-only), statistical plus systematic uncertainties on the object reconstruction efficiencies (stat. + syst), and statistical plus systematics on the object reconstruction efficiencies and luminosity  $\delta\mathcal{L} = 1\%$  (stat + syst + lumi). When considering statistical uncertainty only, the expected  $\delta\mu/\mu$  is below 1% up to  $p_T(H) = 200\text{GeV}$  in all channels. When including systematic uncertainties, in particular those related to reconstruction efficiencies,  $\delta\mu/\mu$  reaches a minimum for a given  $p_T^{\text{min}}(H)$ . This is because the systematic uncertainty dominates over statistical uncertainty at low momenta, whereas the opposite occurs at high momenta. There is no explicit minimum for the  $H \rightarrow \mu^+\mu^-$  channel, because statistical and systematic uncertainties are already comparable at low  $p_T(H)$ . In all channels, the precision is in the range  $\delta\mu/\mu \sim 1\text{-}2\%$ .

**Combined results and discussion** The results presented in the previous sections can be combined into ratios of couplings, or equivalently ratios of branching fractions. Given that the fiducial regions for the single channel measurements are defined as function of  $p_T(H)$ , we assume that the relative contributions of production rates across the various channels are preserved. Therefore, the theoretical uncertainties on the production mechanisms, as well as the luminosity uncertainty, cancel out in  $\text{BR}(H \rightarrow X)/\text{BR}(H \rightarrow Y)$  ratios. The precision on such ratios is thus determined by statistics and by efficiency uncertainties. Moreover, in specific ratios such as  $\text{BR}(H \rightarrow \mu^+\mu^-)/\text{BR}(H \rightarrow 4\mu)$ ,  $\text{BR}(H \rightarrow \gamma\gamma)/\text{BR}(H \rightarrow 2e2\mu)$  or  $\text{BR}(H \rightarrow \mu\mu\gamma)/\text{BR}(H \rightarrow 4\mu)$ , the reconstruction efficiency uncertainties partially cancel. The cancellation is complete when the uncertainties on the objects are fully correlated (e.g. if the same object appears in the numerator and denominator) and if the kinematics are similar. The expected precision for four such ratios is shown in Fig.10.4 as a function of the requirement on  $p_T(H)$ . The expected precision is given for three scenarios where various assumptions on the uncertainties are made: only statistical uncertainties are included (stat-only), statistical and optimistic (conservative) systematics on the object reconstruction efficiencies. Roughly, the maximum precision is respectively  $\approx 1\%$  ( $2\%$ ) for optimistic (conservative) assumptions. At the FCC-ee,  $\text{BR}(H \rightarrow ZZ^*)$  can be measured with a precision of  $\approx 0.1\%$ . Provided that such measurement becomes available before FCC-hh data taking, relative measurements that involve the  $H \rightarrow ZZ^*$  coupling in the denominator can be converted to absolute measurements of the branching fraction involved in the numerator.

## 10.2.2 ttH production

The top Yukawa coupling  $y_t$  is particularly important in the Standard Model. In contrast to other Yukawa couplings that are measured by studying Higgs decay rates, the best direct sensitivity can be obtained via the ttH production mechanism. The ttH production mode was recently observed at the LHC [195, 196]. Due to the small production rate (only 1% among the Higgs bosons produced at the LHC are produced via ttH),  $y_t$  is expected to be measured with a precision of  $\approx 5\%$  by the end of HL-LHC programme [189, 190]. Given the large  $Q^2$  of the ttH production mode, the cross section increases by a factor  $\approx 60$  from  $\sqrt{s} = 14\text{ TeV}$  to  $\sqrt{s} = 100\text{ TeV}$ . There are a number of Higgs decay channels that can be used to study ttH production, including  $H \rightarrow \gamma\gamma$ ,  $H \rightarrow b\bar{b}$  and decays to leptons. Here we study the case of ttH,  $H \rightarrow b\bar{b}$  (boosted) following the approach of Ref. [197].

### 10.2.2.1 ttH, $H \rightarrow b\bar{b}$ (boosted)

**Introduction** Following the approach proposed in Ref. [197], the ratio  $\sigma_{\text{ttH}}/\sigma_{\text{ttZ}}$  in the  $H \rightarrow b\bar{b}$  and  $Z \rightarrow b\bar{b}$  decay modes can be predicted reliably, due to the similarity between the diagrams and energy scales for ttH and ttZ production: the theoretical uncertainties largely cancel in the ratio [197]. Most

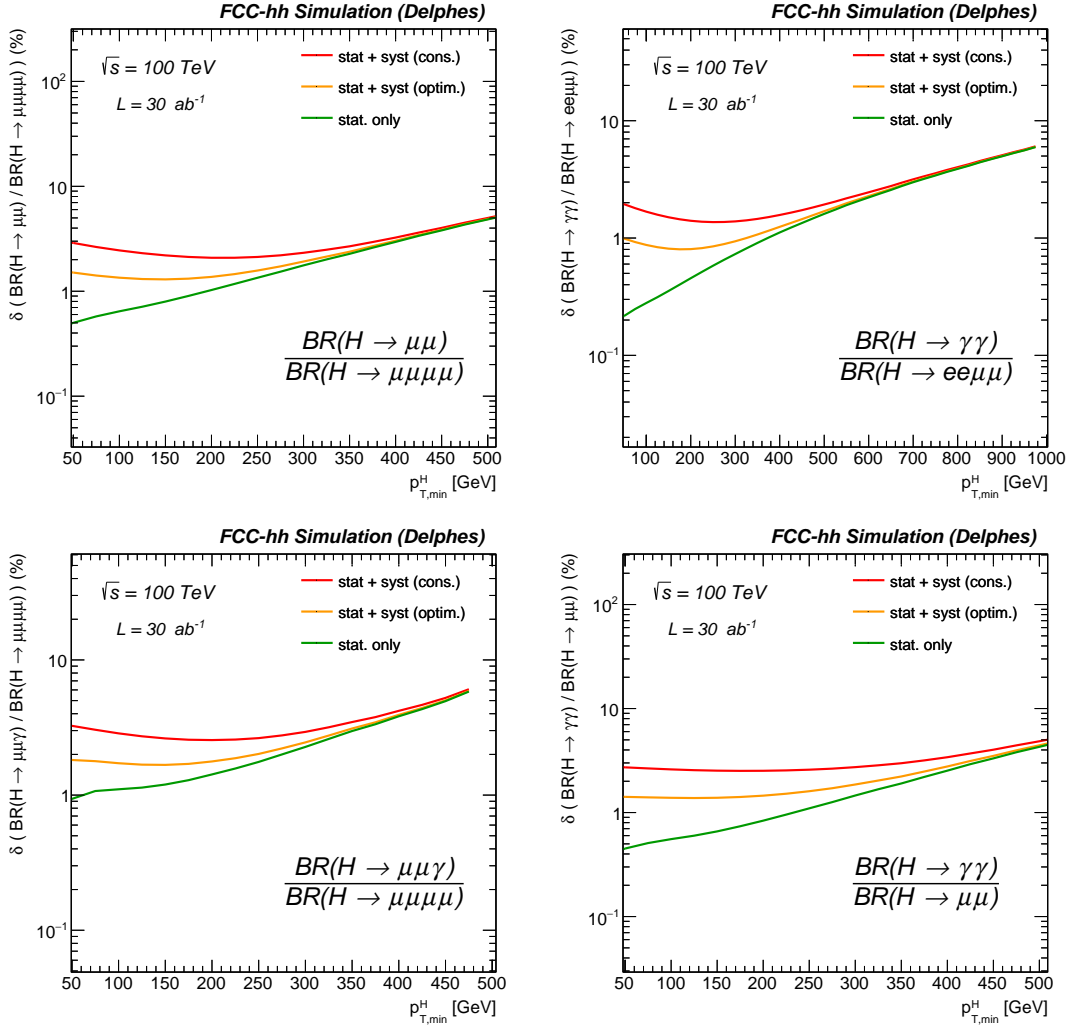


Fig. 10.4: Expected precision on the ratio  $BR(H \rightarrow \mu^+ \mu^-) / BR(H \rightarrow 4\mu)$  (top left),  $BR(H \rightarrow \gamma\gamma) / BR(H \rightarrow 2e2\mu)$  (top right),  $BR(H \rightarrow \mu\mu\gamma) / BR(H \rightarrow 4\mu)$  (bottom left) and  $BR(H \rightarrow \gamma\gamma) / BR(H \rightarrow \mu^+ \mu^-)$  (bottom right) as a function of the minimal requirement on the Higgs reconstructed transverse momentum. The expected precision is given for three scenarios where various assumptions on the uncertainties are made: only statistical uncertainties are included (stat-only), statistical and optimistic (conservative) systematics on the object reconstruction efficiencies. All the uncertainties on the production, both theoretical and from luminosity, cancel in the ratio.

experimental uncertainties, such as the luminosity uncertainty and uncertainties on the event selection due to similar kinematics will likewise, to a large extent, cancel.

One top is required to decay leptonically; the other hadronically, and the Higgs decays to a  $b\bar{b}$  pair. The combinatorial backgrounds are reduced by focussing on the ‘boosted topology’, where the Higgs boson is produced with large transverse momentum. The final state has one high  $p_T$  lepton, two large radius jets that contain the hadronic top and Higgs decay products, and an additional heavy flavour jet and missing energy.

**Monte Carlo Events** The  $t\bar{t}H$  and  $t\bar{t}Z$  samples were generated at LO with up to one extra merged jet. NLO cross sections of  $\sigma_{t\bar{t}H} = 34$  pb [5] and  $\sigma_{t\bar{t}Z} = 64.2$  pb [15] were used. The  $t\bar{t} + \text{jets}$  background was generated at LO in two separate components: the reducible  $t\bar{t} + \text{jet}$  contribution in the



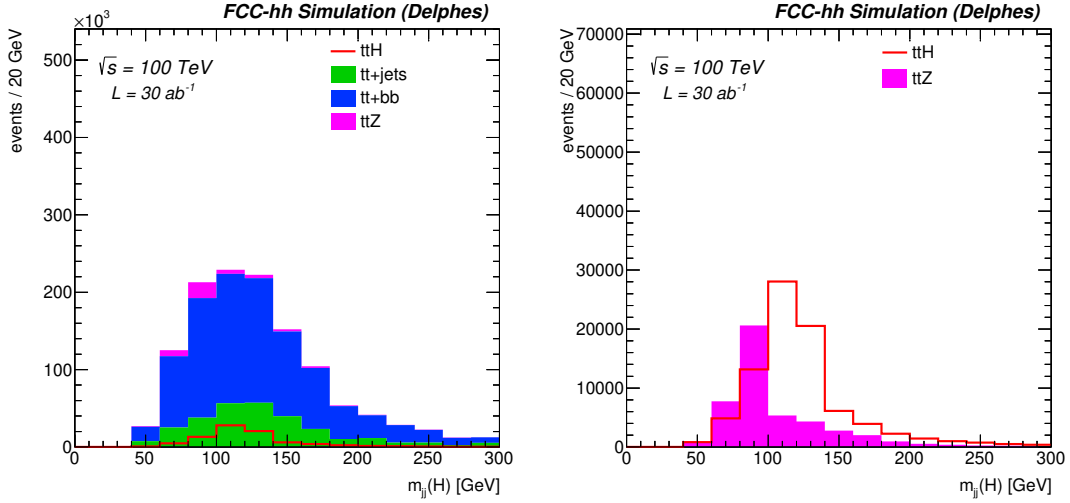


Fig. 10.5: Invariant mass the di-jet pair forming the Higgs candidate including all backgrounds (left) and after (perfect) background subtraction as input for measuring the ttH/ttZ fraction (right).

4-flavour (4F) scheme and the  $t\bar{t}b\bar{b}$  irreducible contribution. Both components were generated with a  $p_T^{\bar{t}t} > 150$  GeV requirement. In order to account for higher order corrections a K-factor ( $K=1.4$ ) was derived from inclusive  $t\bar{t}$  production and has been applied. The final cross sections are  $\sigma_{t\bar{t}+jet} = 6.75$  nb and  $\sigma_{t\bar{t}b\bar{b}} = 120$  pb. The W+jets background is estimated to be negligible, and is not considered.

**Event selection** Jets are clustered from particle-flow candidates with the anti- $k_T$  algorithm [54] with a radius parameter  $R=1.5$ . A large fraction of the Higgs and top decay products are included in the jet, hence the denomination ‘fat jets’. Events are first pre-selected by requiring at least two central fat jets with  $p_T^j > 250$  GeV and  $|\eta^j| < 3.0$  that contain at least two subjets with  $R=0.4$ , and at least one central isolated lepton with  $p_T^\ell > 25$  GeV and  $|\eta^\ell| < 3.0$ .

The fat-jets containing the smallest and largest number of sub-jets are labeled as the ‘Higgs-jet’ and ‘Top-jet’ respectively. If the number of sub-jets is equal, the fat-jets are ranked according to the soft-dropped mass  $m_{SD}$  [56] and the fat-jet with the smallest (largest)  $m_{SD}$  is labeled the Higgs-(Top)-jet.

Fat jets containing the Higgs or top decay products will feature two-prong or three-prong structures, in contrast to QCD jets from the  $t\bar{t}$  +jets background that feature a small subjet multiplicity. The difference in the 2 versus 1 prong hypotheses of a jet is exploited with the  $\tau_{2,1}$  observable [55] and used to further increase the signal purity in Higgs-jet candidates. Similarly a  $\tau_{3,2}$  selection can exploit the difference in the 3 versus 2 or fewer sub-jets hypotheses. The Top-jet candidate is required to pass the criteria  $120 < m_{SD}^{\text{top}} < 250$  GeV and  $\tau_{3,2} < 0.8$  while the Higgs-jet is only required to pass the  $\tau_{2,1} < 0.6$  selection. Given that  $m_{SD}^H$  is used for the signal extraction, no selection is applied on this observable. Finally, in order to further reject the large  $t\bar{t}$  + jet background, at least 4 b-tagged jets are required.

**Signal extraction and results** The ttH and the ttZ contributions are simultaneously extracted by fitting the dijet invariant mass spectrum shown in Figure 10.5. Our signal model is a linear combination of ttH and ttZ templates where the ttH and ttZ yields are the parameters of interest. The  $t\bar{t}$  + jet and  $t\bar{t}b\bar{b}$  backgrounds yields are measured with a negligible statistical uncertainty from a control sample defined by the  $m_{bb} > 200$  GeV event selection criterion. A potentially large bias on  $\alpha = N(\text{ttH})/N(\text{ttZ})$  can originate from the modelling of the background shape under the mass peaks. Given that a control sample to measure the  $t\bar{t}b\bar{b}$  shape is not trivial to construct, we take the background shape from Monte Carlo. We estimate the effect on  $\alpha$  induced by the uncertainty on the background shape by convoluting

the background distribution with a linear function ( $f(m_{bb}) = \lambda * m_{bb} + \beta$ ). A  $\pm X\%$  variation on the shape is defined such that the background yield at  $m_{bb} = 125$  GeV is varied by  $\pm X\%$  and such that the yield at  $m_{bb} = 100$  GeV is left unchanged. Such shape variations induce a systematic error on  $N(ttH)/N(ttZ)$  of  $\delta\alpha < 1\%$ . We can then write  $N(ttH)/N(ttZ) = 1.90 \pm 0.02$  (stat.)  $\pm 0.03$  (syst.) that leads to an overall precision on the Yukawa coupling of  $\delta y_t/y_t \approx 1\%$ , assuming that the theoretical prediction on  $N(ttH)/N(ttZ)$  (inclusive and differential) will have similar precision [15]. Luminosity and selection efficiencies uncertainties almost entirely cancel due to the very similar kinematics of the ttH and the ttZ processes.

### 10.2.3 Measurement of di-Higgs production

The Higgs boson is an essential part of the SM and responsible for electroweak symmetry breaking. The SM predicts that the Higgs boson interacts with itself at tree-level: the Higgs self-coupling. A precise measurement of the Higgs self-coupling  $\lambda$  probes the shape of the Higgs potential near our vacuum and could provide insights about the electro-weak phase transition (EWPT). The non-resonant production of pairs of Higgs boson occurs either via the self-coupling or via quark-loops with Yukawa-type interactions as illustrated in Fig. 10.6. The production cross section for pairs of Higgs bosons is very small in the SM, yet it can be significantly enhanced by physics beyond the SM. At  $\sqrt{s} = 100$  TeV, the di-Higgs boson production cross section in gluon fusion is  $\sigma_{gg \rightarrow HH} \approx 1.5$  pb and the tri-Higgs boson production cross section is only 5 fb, therefore the latter is expected to be extremely challenging even at the FCC.

The Higgs self-coupling can be probed via a number of different Higgs boson decay channels. Given the small cross section, typically at least one of the Higgs bosons is required to decay to a pair of b-quarks. Here, we consider five channels:  $HH \rightarrow bb\gamma\gamma$ ,  $HH \rightarrow bb\tau\tau$ ,  $HH \rightarrow 4b$ ,  $HH \rightarrow bbZZ(4\ell)$  and  $HH \rightarrow bbWW$ . The first three channels give the largest sensitivity, and their study has been presented in great detail in Ref. [6]. The sensitivity of the 4b (boosted) final state is discussed in Ref. [17]. Here only a short summary of the key findings is presented.

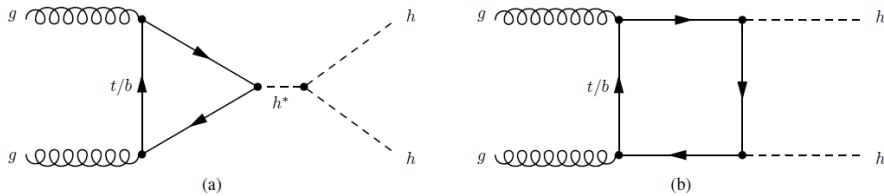


Fig. 10.6: Leading order Feynman diagrams for non-resonant production of Higgs boson pairs in the Standard Model through (a) the Higgs boson self-coupling and (b) the top-box diagram.

The FCC-hh detector simulation framework is discussed in Section 4.3.2.1. For the study of the  $HH \rightarrow bb\gamma\gamma$ ,  $HH \rightarrow bb\tau\tau$  and  $HH \rightarrow 4b$  channels, three different parameterisation scenarios for the performance and the systematics were selected, in order to assess the potential impact on the self-coupling measurement of varying levels of performance degradation due to pile-up:

- scenario I: optimistic – target detector performance, similar to Run 2 LHC conditions
- scenario II: realistic – intermediate detector performance
- scenario III: conservative – pessimistic detector performance, assuming extrapolated HL-LHC performance using present-day algorithms

The assumptions on the performance of various physics objects for each baseline scenario, presented for a reference value of  $p_T$  for each object set at 50 GeV, are summarised in Table 10.4. Table 10.5 lists the systematic uncertainties assumed.

Table 10.4: Performance of physics objects for the various scenarios. Objects efficiencies and mistag rates are given for a representative  $p_T \approx 50$  GeV. For b and  $\tau$ -tagging (and their respective mistag rates) numbers for two different working points are given (Medium and Tight).

Parameterisation	Scenario I	Scenario II	Scenario III
b-jet ID eff.	82–65%	80–63%	78–60%
b-jet c mistag	15–3%	15–3%	15–3%
b-jet l mistag	1–0.1%	1–0.1%	1–0.1%
$\tau$ -jet ID eff	80–70%	78–67%	75–65%
$\tau$ -jet mistag (jet)	2–1%	2–1%	2–1%
$\tau$ -jet mistag (ele)	0.1–0.04%	0.1–0.04%	0.1–0.04%
$\gamma$ ID eff.	90%	90%	90%
jet $\rightarrow \gamma$ eff.	0.1%	0.2%	0.4%
$m_{\gamma\gamma}$ resolution [GeV]	1.2	1.8	2.9
$m_{bb}$ resolution [GeV]	10	15	20

Table 10.5: Summary of the sources of systematic uncertainties in the 3 scenarios. The last column indicates the processes that are affected by the corresponding source of uncertainty. For each given object (b-jet,  $\tau$ -jet,  $\gamma$ , lepton), the quoted uncertainty on reconstruction and identification efficiency is applied as many times as the object appears in the final-state.

Uncertainty source	Scenario I	Scenario II	Scenario III	Processes
b-jet ID eff. /b-jet	0.5%	1%	2%	single H, HH, ZZ
$\tau$ -jet ID eff. / $\tau$	1%	2.5%	5%	single H, HH, ZZ
$\gamma$ ID eff. / $\gamma$	0.5%	1%	2%	single H, HH
$\ell = e-\mu$ ID efficiency	0.5%	1%	2%	single H, HH, ZZ
Luminosity	0.5%	1%	2%	single H, HH, ZZ
Theoretical cross section	0.5%	1%	1.5%	single H, HH, ZZ

### 10.2.3.1 $HH \rightarrow bb\gamma\gamma$

The  $bb\gamma\gamma$  decay mode has been singled out as the *golden* channel despite the small branching ratio ( $BR = 0.25\%$ ) because the clear signature of two photons and two b-jets in the final state allow the large background rates to be controlled. The main backgrounds are  $\gamma\gamma$ +jets,  $\gamma$ +jets (with at least one jet being mis-identified as a photon) and single  $H \rightarrow \gamma\gamma$  production. A complete description of the Monte Carlo event generation for signals and backgrounds is given in Ref. [6].

**Event selection and signal extraction** Events are required to contain at least two isolated photons and two b-tagged jets. Jets are clustered using particle-flow candidates with the anti- $k_T$  algorithm with radius parameter  $R = 0.4$ . We required  $p_T(\gamma, b) > 30$  GeV and  $|\eta(\gamma, b)| < 4.0$ , and the leading photon and b-jet are further required to have  $p_T(\gamma, b) > 35$  GeV. The Higgs candidates are formed from the two jets and photons with highest  $p_T(\gamma, b)$ . In order to exploit the kinematic differences between signal and background to the maximum, a boosted decision tree (BDT) is trained using kinematic information relative to all reconstructed objects in the event. Separate trainings are performed for single-Higgs and QCD backgrounds, due to the different discriminating power with respect to the di-photon invariant mass. This leads to two different discriminants,  $BDT_H$  and  $BDT_{QCD}$ .

Table 10.6: Expected precision at 68% CL on the di-Higgs production signal strength and Higgs self coupling using the  $b\bar{b}\gamma\gamma$  channel at the FCC-hh with  $30 \text{ ab}^{-1}$ . The symmetrised value  $\delta = (\delta^+ + \delta^-)/2$  is given in %.

	@68% CL	Scenario I	Scenario II	Scenario III
$\delta_\mu$	stat only	2.5	3.6	5.6
	stat + syst	2.8	4.4	7.5
$\delta_{\kappa_\lambda}$	stat only	3.4	4.8	7.4
	stat + syst	3.8	5.9	10.0

**Results and discussion** The expected precision on the signal strength  $\mu = \sigma/\sigma_{\text{SM}}$  and on the self-coupling modifier  $\kappa_\lambda$  are obtained from a 2-dimensional fit of the (BDT<sub>H</sub>, BDT<sub>QCD</sub>) output. The results are shown in Fig. 10.7. The various lines correspond to the different scenarios described in Table 10.4. From Fig. 10.7 one can extract the symmetrised 68% and 95% confidence intervals for the various scenarios. The expected precision for  $b\bar{b}\gamma\gamma$  is summarised in Table 10.6 for each of these assumptions. Depending on the scenario assumed, the Higgs self-coupling can be measured with a precision of 3.8-10% at 68% C.L using the  $b\bar{b}\gamma\gamma$  channel alone. We note that the precision achievable is largely dependent on the assumptions on the detector configuration and the systematic uncertainties. Such a result needs to be compared against the precision of  $\delta_{\kappa_\lambda} = 3.4\text{--}7.4\%$ , obtained using statistical uncertainties alone.

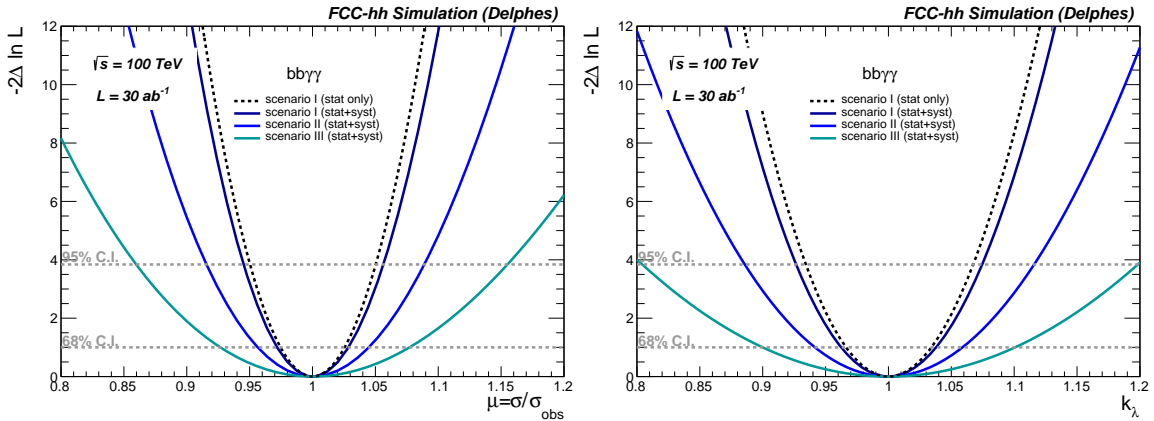


Fig. 10.7: Expected negative log-Likelihood scan as a function of the signal strength  $\mu = \sigma/\sigma_{\text{SM}}$  (a) and trilinear self-coupling modifier  $\kappa_\lambda$  (b) in the  $b\bar{b}\gamma\gamma$  channel. The various lines correspond to the different systematic uncertainty assumptions summarised in Table 10.5. The black dashed line shows the likelihood profile when only the statistical uncertainty is included under scenario I.

### 10.2.3.2 $HH \rightarrow b\bar{b}\tau\tau$

The  $b\bar{b}\tau\tau$  channel is very attractive thanks to the large branching fraction (7.3%) and the relatively clean final state. As opposed to the  $b\bar{b}\gamma\gamma$  channel, the  $HH \rightarrow b\bar{b}\tau\tau$  decay cannot be fully reconstructed due to the presence of  $\tau$  neutrinos in the final state. We consider mainly two channels here: the fully hadronic final state  $b\bar{b}\tau_h\tau_h$ , and the semi-leptonic one,  $b\bar{b}\tau_h\tau_\ell$  ( $\ell = e, \mu$ ).

Several backgrounds affect the  $b\bar{b}\tau\tau$  final state, in particular QCD and  $t\bar{t}$ . QCD is a background mainly for the  $b\bar{b}\tau_h\tau_h$  decay channel, but we verified that it can be suppressed entirely, thanks to the absence of prompt missing energy in QCD events. Moreover, analyses using CMS data [198] show

that QCD is overall a subdominant background at the LHC, and negligible in the signal region. As a result, recent CMS Phase II projections neglect this background altogether [199]. In order of decreasing magnitude, the largest backgrounds are  $Z/\gamma^*$ +jets, single Higgs, ttV and ttVV, where  $V = W, Z$ .

**Event selection and results** Events are required to contain at least two b-jets with  $p_T(b) > 30$  GeV and  $|\eta(b)| < 3$ . We require two, or more, b-jets, in order not to suppress the ttHH signal contribution. For the  $b\bar{b}\tau_h\tau_l$  final state the presence is required of exactly one isolated ( $I_{\text{rel}} < 0.1$ ) lepton  $\ell = e, \mu$  with  $pp_T(\ell) > 25$  GeV and  $|\eta(\ell)| < 3$  and at least one hadronically tagged  $\tau$ -jet with  $p_T(\tau_h) > 45$  GeV and  $|\eta(\tau_h)| < 3$ . For the  $b\bar{b}\tau_h\tau_l$  final state, we require at least two hadronically tagged  $\tau$ -jet with  $p_T(\tau_h) > 45$  GeV and  $|\eta(\tau_h)| < 3.0$ . The hadronic  $\tau$  is identified according to the ‘Tight’ criterion defined in Table 10.4. This ensures a highly efficient rejection of the QCD background (at the cost of a smaller  $\tau_h$  efficiency) which strengthens the solidity of our assumption of neglecting the QCD background altogether. In what follows we refer to a  $\tau$ -candidate as the lepton  $\ell = e, \mu$  or the  $\tau$ -jet. In particular the  $\tau$  4-momentum is defined as the sum of the 4-momenta of the visible  $\tau$  decay products. In order to exploit the kinematic differences between the signal and the dominant  $t\bar{t}$  background to the maximum, a multivariate BDT discriminant is built from of the main kinematic properties of the final-state objects.

The precision expected on the signal strength and the Higgs self-coupling are derived from a maximum likelihood fit on the BDT observable, as described in Ref. [6]. The  $b\bar{b}\tau_h\tau_h$  and  $b\bar{b}\tau_h\tau_l$  channels are considered separately with their relative set of systematic uncertainties and then combined assuming a 100% correlation on equal sources of uncertainties among the two channels. The combined expected precision on the  $b\bar{b}\tau\tau$  channel is shown in Fig. 10.8. The various lines correspond to the different scenarios described earlier. From the figure one can extract the 68% and 95% confidence intervals for the various assumptions for systematics. Depending on the scenario assumed, using the  $b\bar{b}\tau\tau$  channel, the Higgs pair signal strength and Higgs self-coupling can be measured with a precision of  $\delta\mu = 5.8\text{--}7.9\%$  and  $\delta\kappa_\lambda = 9.8\text{--}13.8\%$  respectively at 68% C.L. Despite the large signal event rate in the  $b\bar{b}\tau\tau$  channel, the sensitivity is limited by the large background. Therefore, the  $b\bar{b}\tau\tau$  channel is statistically dominated at the FCC-hh, and the precision achievable is only moderately dependent on the assumptions for the systematic uncertainties. We note that Ref. [200] quotes a precision of  $\delta\kappa_\lambda = 13\%$  using the resolved semi-leptonic final state, which is consistent with the result presented here of  $\delta\kappa_\lambda = 14\text{--}18\%$ . The same study shows that further precision can be obtained using the boosted topology, which has not been considered here.

### 10.2.3.3 $HH \rightarrow 4b$

The  $HH \rightarrow b\bar{b}b\bar{b}$  decay mode has the largest branching fraction among all possible Higgs-pair decays. Despite the presence of soft neutrinos from semi-leptonic b decays (that may impact negatively the reconstructed hadronic Higgs-mass resolution), the Higgs decays into b-jets can be fully reconstructed. However, due to the fully hadronic nature of this decay mode, this channel suffers from very large QCD backgrounds and hence features a relatively small S/B. Moreover, a combinatorial ambiguity affects the possibility to correctly associate the four b-jets to the two parent Higgs candidates.

We mainly consider the case where the Higgs candidates are only moderately boosted, leading to four fully resolved b-jets. The boosted analysis, where the Higgs candidates are sufficiently boosted to decay into a single large radius jet [201, 202], provides less sensitivity to the self-coupling measurement and was discussed in previous studies [17, 200]. The main backgrounds to this final state are QCD and  $t\bar{t}$ , followed by  $Z \rightarrow b\bar{b}$ , single-Higgs production and ZZ. A complete description of the Monte Carlo event generation for signals and backgrounds is given in Ref. [6].

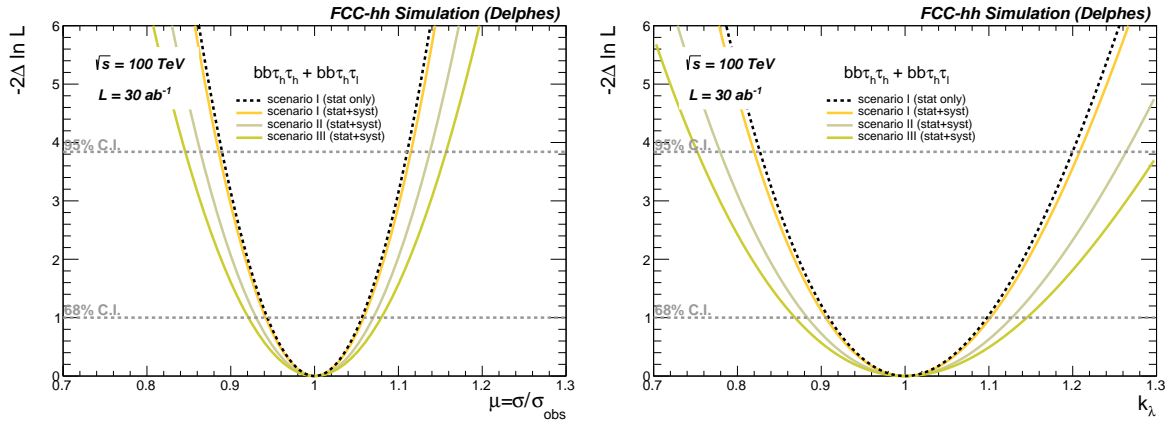


Fig. 10.8: Expected negative log-Likelihood scan as a function of the signal strength  $\mu$  (left) and trilinear self-coupling modifier  $\kappa_\lambda$  (right) in the  $b\bar{b}\tau\tau$  channel (combination of the  $b\bar{b}\tau_h\tau_h$  and  $b\bar{b}\tau_h\tau_l$  channels). The various lines correspond to the different systematic uncertainty assumptions summarised in Table 10.5. The black dashed line shows the likelihood profile when only the statistical uncertainty is included under scenario I.

Table 10.7: Expected precision at 68% CL on the di-Higgs production cross-section and Higgs self coupling using the  $b\bar{b}\tau\tau$  channel at the FCC-hh with  $30 \text{ ab}^{-1}$ . The symmetrised value  $\delta = (\delta^+ + \delta^-)/2$  is given in %.

	@68% CL	Scenario I	Scenario II	Scenario III
$\delta_\mu(b\bar{b}\tau_h\tau_h)$	stat only	8.7	10.7	10.9
	stat + syst	9.0	11.1	11.6
$\delta_{\kappa_\lambda}(b\bar{b}\tau_h\tau_h)$	stat only	12.6	16.0	16.5
	stat + syst	13.2	16.7	17.7
$\delta_\mu(b\bar{b}\tau_h\tau_l)$	stat only	7.4	8.2	9.2
	stat + syst	7.6	8.8	10.4
$\delta_{\kappa_\lambda}(b\bar{b}\tau_h\tau_l)$	stat only	14.3	16.3	18.6
	stat + syst	14.7	17.5	21.0
$\delta_\mu(\text{comb.})$	stat only	5.6	6.5	7.0
	stat + syst	5.8	7.0	7.9
$\delta_{\kappa_\lambda}(\text{comb.})$	stat only	9.4	11.4	12.3
	stat + syst	9.8	12.2	13.8

**Event selection and results** In order to ensure fully efficient online triggers, the event selection starts by requiring the presence of at least four b-jets with  $p_T(b) > 30 \text{ GeV}$  and  $|\eta(b)| < 4$ . The b-jets are identified with the ‘Medium’ working point defined in Table 10.4. The Higgs candidates are reconstructed as the pairing of b-jet pairs that minimises the difference between the invariant masses of the two b-jet pairs. A BDT discriminant is built out of the set of kinematic properties of the final-state objects.

The precision expected for the signal strength and the Higgs self-coupling are derived from a 1D maximum likelihood fit on the BDT discriminant (see Ref. [6] for the details). The combined expected precision on the  $b\bar{b}b\bar{b}$  channel is shown in Fig. 10.9. The coloured lines correspond to the different



Table 10.8: Expected precision at 68% CL on the di-Higgs production cross-section and Higgs self coupling using the  $b\bar{b}b\bar{b}$  channel at the FCC-hh with  $30 \text{ ab}^{-1}$ . The symmetrised value  $\delta = (\delta^+ + \delta^-)/2$  is given in %.

		@68% CL	Scenario I	Scenario II	Scenario III
$\delta_\mu$	stat only		8.4	9.1	10.8
	stat + syst		10.4	12.2	17.9
midrule $\delta_{\kappa_\lambda}$	stat only		18.0	20.0	24.2
	stat + syst		22.3	27.1	32.0

systematic uncertainty assumptions summarised in Table 10.5. The 68% and 95% confidence intervals on  $\delta_\mu$  and  $\delta_{\kappa_\lambda}$  for the various systematics assumptions can be extracted from Fig. 10.9, and the results are summarised in Table 10.8. Depending on the scenario assumed,  $\mu$  and  $\kappa_\lambda$  can be measured with a precision of  $\delta_\mu = 8\text{--}18\%$  and  $\delta_{\kappa_\lambda} = 18\text{--}32\%$  respectively at 68% C.L., limited by statistics. Notice however that, despite the large statistical uncertainty, the systematic uncertainties are important. This is the result of the significant contamination in the signal region from single-Higgs background events. Since this background is assumed to be estimated from Monte Carlo, its uncertainty, even though at the percent level, is reflected in a larger signal systematics.

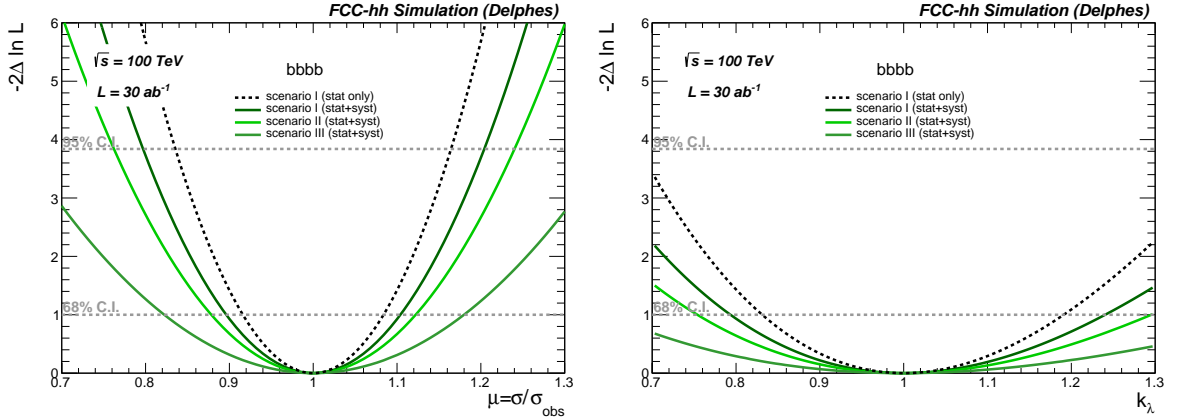


Fig. 10.9: Expected negative log-likelihood scan as a function of the signal strength  $\mu$  (left) and trilinear self-coupling modifier  $\kappa_\lambda$  (right) in the  $b\bar{b}b\bar{b}$  channel. The various lines correspond to the different systematic uncertainty assumptions summarised in Table 10.5. The black dashed line shows the likelihood profile when only the statistical uncertainty is included under scenario I.

### 10.2.3.4 $HH \rightarrow b\bar{b}ZZ(4\ell)$

The large Higgs pair production cross section at 100 TeV means that rare but cleaner final states become accessible. One example is the  $HH \rightarrow b\bar{b}ZZ(4\ell)$  decay channel (where  $l = e^\pm, \mu^\pm$ ). Despite a small cross section ( $\sigma_{b\bar{b}4\ell} = 178 \text{ ab}$ ), the presence of four leptons in association with two b-jets leads to a very clean final state topology allowing a rather good signal selection efficiency to be maintained while controlling the background. The main background processes are  $t\bar{t}(b\bar{b})H(4\ell)$ ,  $gg(H) + b\bar{b}$ ,  $Z(b\bar{b})H(4\ell)$  and  $t\bar{t}Z(2l)$ , followed by minor negligible contributions such as  $4\ell + b\bar{b}$  continuum,  $t\bar{t}(bl\nu_l bl\nu_l)H(4\ell)$  and  $t\bar{t}ZZ(4\ell)$ .



**Monte Carlo events** Signal events were generated at LO accounting for the full  $m_t$  dependence, for several values of the self-coupling modifier  $k_\lambda = \lambda/\lambda_{SM}$  ranging from  $k_\lambda = -1$  to  $k_\lambda = 3$ . The  $t\bar{t}H$ ,  $gg(H) + b\bar{b}$ ,  $Z(b\bar{b})H$  and  $t\bar{t}Z(2l)$  background samples were generated at LO and higher order radiative corrections were accounted for by applying K-factors of  $K(ttH) = 1.22$ ,  $K(ggH) = 3.2$  and  $K(ZH) = 1.1$  (from [5]). The contribution of the  $4\ell + \text{jets}$  ( $ZZ^*$ ,  $Z^*Z^*$ ,  $ZZ$ ) continuum is evaluated using an  $\ell\ell\ell\ell jj$  ( $\ell = e^\pm, \mu^\pm$ ) sample, generated with the four leptons invariant mass in the range [100, 150] GeV and only heavy flavour partons (b/c). This background contribution was found to be negligible. The cross sections are summarised in Table 10.9.

Table 10.9: Cross section times branching ratio for the signal and the background processes [5].

Cross sections [fb]				
$HH \rightarrow b\bar{b}ZZ(4\ell)$	$t\bar{t}H \rightarrow b\bar{b}4\ell$	$gg(H) + b\bar{b} \rightarrow b\bar{b}4\ell$	$ZH \rightarrow b\bar{b}4\ell$	$t\bar{t}Z \rightarrow b\bar{b}4\ell$
0.178	4.013	0.369	0.071	2594

**Event Selection** Events are required to have exactly four identified and isolated muons (electrons) with  $p_T > 5(7)$  GeV and  $|\eta| < 4.0$ .  $Z$  boson candidates are formed from pairs of opposite-charge leptons ( $\ell^+\ell^-$ ). At least two di-lepton pairs are required. The  $Z$  candidate with the invariant mass closest to the nominal  $Z$  mass is denoted as  $Z_1$ ; then, among the other opposite-sign lepton pairs, the one with the highest  $p_T$  is labelled as  $Z_2$ .  $Z$  candidates must pass a set of kinematic requirements that improve the sensitivity to the Higgs boson decay: the  $Z_1$  and  $Z_2$  invariant masses have to be in the [40, 120] GeV and [12, 120] GeV ranges, respectively. At least one lepton is required to have  $p_T > 20$  GeV and a second is required to have  $p_T > 10$  GeV. A minimum angular separation between two leptons is required to be  $\Delta R(\ell_i, \ell_j) > 0.02$ . The four leptons invariant mass,  $m_{4\ell}$ , is requested to be in the range  $120 < m_{4\ell} < 130$  GeV.

At least two identified b-jets, reconstructed with the anti- $k_T$  algorithm inside a cone of radius  $R = 0.4$ , are required. Their invariant mass is required to be in the range  $80 < m_{b\bar{b}} < 130$  GeV and the angular distance between the 2 b-jets has to be  $0.5 < \Delta R_{b\bar{b}} < 2$ . These cuts are particularly effective to reject the  $t\bar{t}H$  background.

**Results** The invariant mass spectrum of the four leptons after the full event selection is shown in Fig. 10.10 (left). The event yield, normalised to an integrated luminosity of  $30 \text{ ab}^{-1}$ , is  $N_S = 489$  for the signal sample,  $N_{t\bar{t}H} = 1162$  for the  $t\bar{t}H$  background,  $N_{b\bar{b}H} = 317$  for the  $gg(H) + b\bar{b}$  sample,  $N_{ZH} = 52$  and  $N_{t\bar{t}Z} = 179$  for the  $ZH$  and the  $t\bar{t}Z$  process respectively.

The negative log-likelihood on the self-coupling modifier  $k_\lambda$  is shown in Figure 10.10, (centre), for three different systematics assumptions:

1. Statistical uncertainties only
2. 1% systematic uncertainty on signal and background:  $\frac{\Delta S}{S} = \frac{\Delta B}{B} = 1\%$
3. 3% systematic uncertainty on signal and background:  $\frac{\Delta S}{S} = \frac{\Delta B}{B} = 3\%$

The expected precision on the Higgs self-coupling modifier  $k_\lambda$  without systematics is 14% at 68% CL, while when assuming a 1% systematic uncertainty on the signal and the backgrounds the precision on  $k_\lambda$  becomes 15% while with a 3% systematic uncertainty it decreases to 24%. Figure 10.10 (right) shows how the precision on the self-coupling is affected by the variation of the detector configuration (for example, assuming a larger tracker and/or higher magnetic field and consequently a minimum  $p_T$  for muons and electrons of 10 GeV). The precision on  $k_\lambda$  degrades from 14% to 15% at 68% CL, considering statistical uncertainties only.

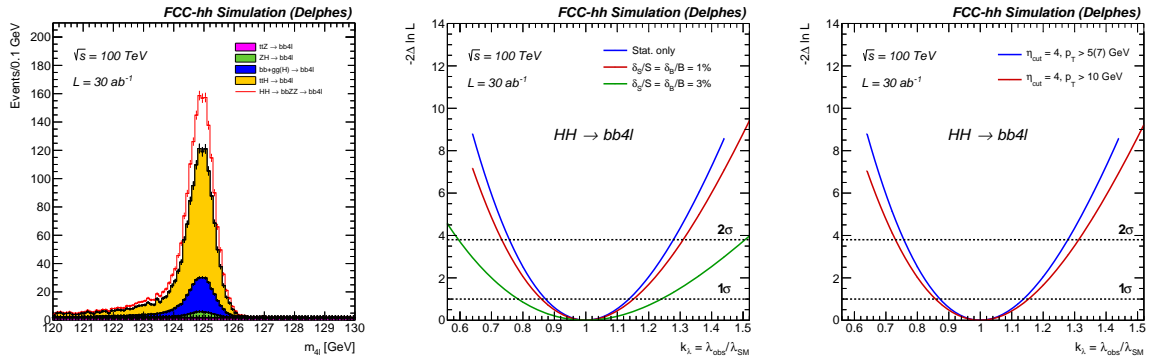


Fig. 10.10: Left: Stacked plot of the four leptons invariant mass for the  $HH \rightarrow \bar{b}b\bar{Z}Z(4\ell)$  signal and all the analysed background processes after the full selection for  $30 \text{ ab}^{-1}$ . Centre: Expected precision on the Higgs-self coupling. Right: Comparison of two scenarios (without systematics) with a cut on muon (electron)  $p_T$  larger than 5 (7) GeV and 10 (10) GeV.

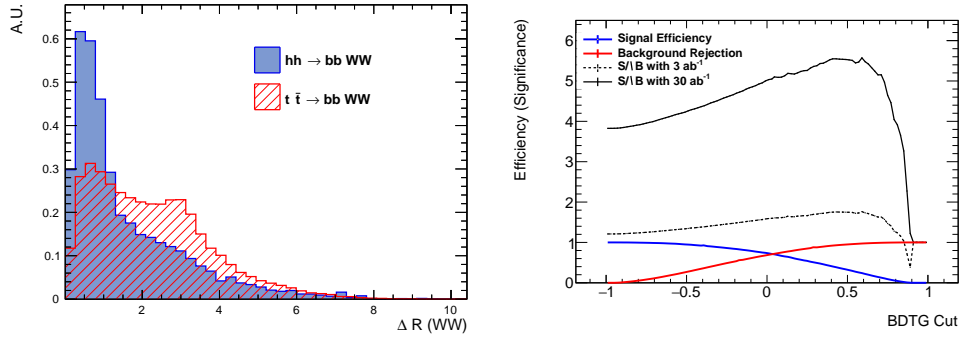


Fig. 10.11: Left: The distribution of one of the most discriminant variables used in the BDT training for signal and background samples: the  $\Delta R$  between the two  $W$ 's. Right: The BDT efficiency and significance as a function of the applied cut on the BDT response for two reference integrated luminosity values:  $3000 \text{ fb}^{-1}$  and  $30000 \text{ fb}^{-1}$ . The significance curves is estimated by using  $S/\sqrt{B}$ .

### 10.2.3.5 $HH \rightarrow bbWW$

The  $bbWW$  channel is a compromise between signal efficiency and background reduction. We require one  $W$  boson to decay hadronically and the other leptonically. The dominant backgrounds are  $t\bar{t}$  and multi-jet background, with smaller contributions from Drell-Yan and single top-quark production. Events are required to meet the following requirements:  $p_T(WW) > 150 \text{ GeV}$ , an invariant mass of the two b-jets system of  $80 \text{ GeV} < m_{bb} < 180 \text{ GeV}$  and  $\Delta R$  and invariant mass of the two b-jets system of  $\Delta R_{bb} < 2.0$ .

The signal is identified using a boosted decision tree (BDT). The input variables used by the BDT are the leptons, the jets, the neutrino and angular correlations between objects. The BDT is trained to discriminate the signal from the dominant background  $t\bar{t}$ . The BDT cut is optimised to ensure a high  $S/\sqrt{B}$  ratio (where  $S$  is the number of signal events and  $B$  the number of background events).

An example of an input distribution used in the BDT is shown in Fig. 10.11 (a), which is the angular separation between the two  $W$  bosons. The output BDT distribution for the signal and background is shown in Fig. 10.11 (b). With a luminosity of  $30 \text{ ab}^{-1}$ , a significance of  $5 \sigma$  can be achieved corresponding to a 40% precision on  $\kappa_\lambda$ .

### 10.2.3.6 Combined precision

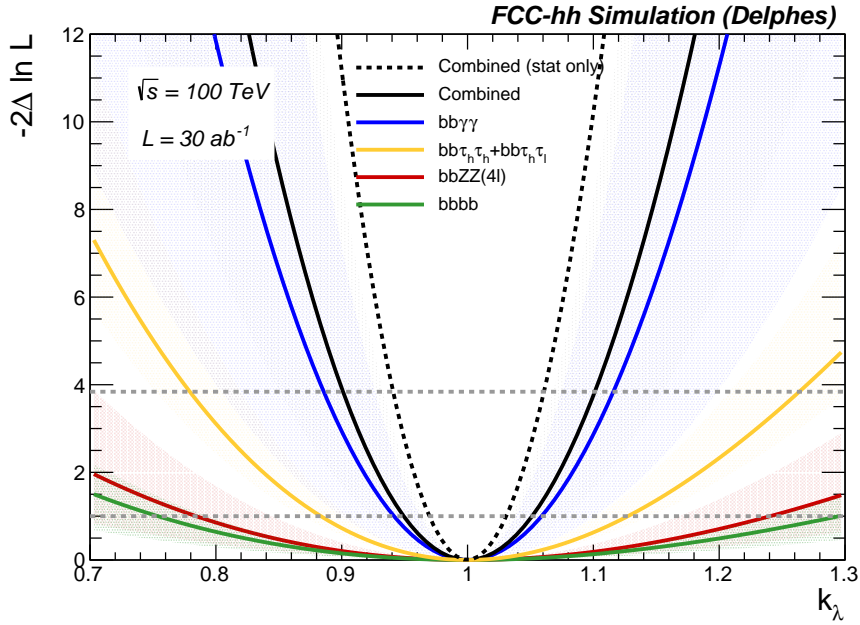


Fig. 10.12: Expected negative log-likelihood scan as a function of the trilinear self-coupling modifier  $\kappa_\lambda$  in all channels, and their combination. The solid line corresponds to the scenario II for systematic uncertainties. The band boundaries represent respectively scenario I and III. The dashed line represents the sensitivity obtained including statistical uncertainties only, under the assumptions of scenario I.

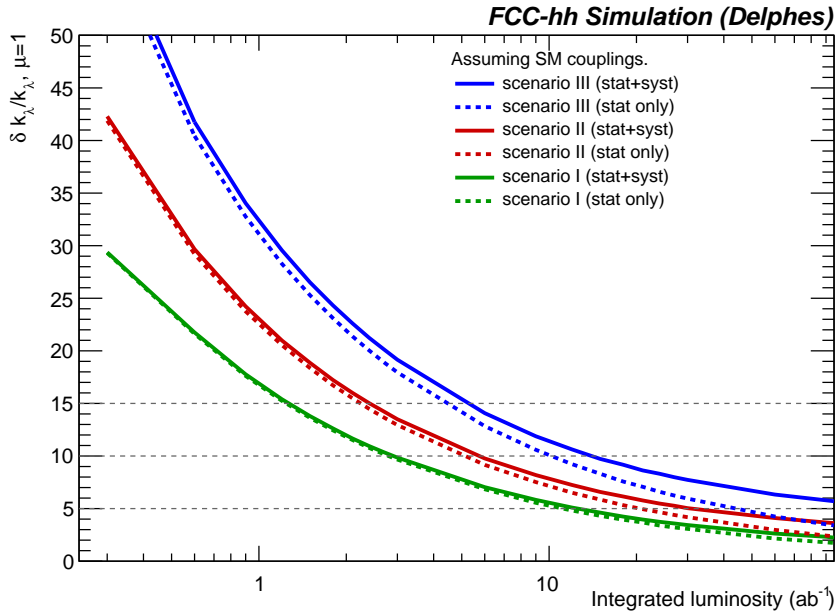


Fig. 10.13: Expected precision on the Higgs self-coupling as a function of the integrated luminosity.

In view of the higher precision emerging from the  $b\bar{b}\gamma\gamma$ ,  $b\bar{b}\tau\tau$  and  $b\bar{b}b\bar{b}$  channels, we focus at this time on the evaluation of the combined precision to these three final states. A contribution from the  $b\bar{b}l^+l^-l^+l^-$  channel discussed above, not optimised to reflect the more extensive study of the other three

Table 10.10: Combined expected precision at 68% CL on the di-Higgs production cross- and Higgs self coupling using all channels at the FCC-hh with  $\mathcal{L} = 30 \text{ ab}^{-1}$ . The symmetrised value  $\delta = (\delta^+ + \delta^-)/2$  is given in %.

@68% CL		Scenario I	Scenario II	Scenario III
$\delta_\mu$	stat only	2.2	2.8	3.7
	stat + syst	2.4	3.5	5.1
$\delta_{\kappa_\lambda}$	stat only	3.0	4.1	5.6
	stat + syst	3.4	5.1	7.8

channels, is nevertheless included.

When combining results from the various channels, the systematic uncertainties from the various sources affecting those processes that we assume to be estimated from Monte Carlo simulations (HH, single Higgs, and ZZ) are accounted for as follows. Lepton ( $e/\mu$ ,  $\tau$ ) uncertainties are correlated across all process and across the  $b\bar{b}\tau_h\tau_h$  and  $b\bar{b}\tau_h\tau_l$  channels. In the  $b\bar{b}\gamma\gamma$  channel, the photon uncertainty for the single and double Higgs processes are correlated. The luminosity uncertainty is correlated across all these processes and all channels. The same applies, for each process independently, to the overall normalisation uncertainty. The uncertainties on lepton ID, luminosity and normalisation are assumed to only affect the overall normalisation of signal and background shapes and not to introduce a significant deformation of their shapes. For the b-jets ID, we take into account both the shape and normalisation uncertainty due to the b-jets systematic uncertainties. This is achieved by shifting the efficiency for each jet by the ( $p_T$ -dependent) values reported in Table 10.4, and re-computing the resulting BDT distributions.

Overall normalisation uncertainties are cancelled out when a background is estimated from a control region. Moreover, we expect all control regions to be well populated at the FCC-hh and their systematic uncertainties to be negligible, excluding them in the fit procedure.

The combined expected negative log-likelihood scan is shown in Fig. 10.12. The expected precision for the single channels is also shown. The expected combined precision on the Higgs self-coupling obtained after combining the channels  $b\bar{b}\gamma\gamma$ ,  $b\bar{b}\tau\tau$ ,  $b\bar{b}b\bar{b}$  and  $b\bar{b}l^+l^-l^+l^-$  can be inferred from the intersection of black curves with the horizontal 68% and 95% CL lines. The expected statistical precision for Scenario I, neglecting systematic uncertainties, can be read from the dashed black line in Fig. 10.12, and gives  $\delta_{\kappa_\lambda} = 3.0\%$  at 68% CL. The solid line corresponds to scenario II, while the boundaries of the shaded area represent the alternative scenarios I and III respectively. From the shaded black curve one can infer the final precision when including systematic uncertainties. Depending on the assumptions, the expected precision for the Higgs self-coupling is  $\delta_{\kappa_\lambda} = 3.4\text{--}7.8\%$  at 68% CL. The signal strength and self-coupling precision for the combination are summarised in Table 10.10.

The expected precision on the Higgs self-coupling as a function of the integrated luminosity is shown in Fig. 10.13, for the three scenarios, with and without systematic uncertainties. With the most aggressive scenario I, a precision of  $\delta_{\kappa_\lambda} = 10\%$  can be reached with only  $3 \text{ ab}^{-1}$  of integrated luminosity, whereas approximately  $20 \text{ ab}^{-1}$  are required for the most conservative scenario III. Therefore, assuming scenario I, the 10% target should therefore be achievable during the first five years of FCC-hh operation, combining the datasets of two experiments. Even including the duration of the FCC-ee phase of the project, and the transition period from FCC-ee to FCC-hh, this timescale is competitive with the time required by the proposed future linear colliders, which need to complete their full programme at the highest beam energies to achieve this precision.

The self-coupling precision in scenarios where the measured value of  $\kappa_\lambda$  differs from the SM value of 1 is shown in Fig. 10.14. A more complete discussion of the assumptions used to compile this result is given in Ref. [6].

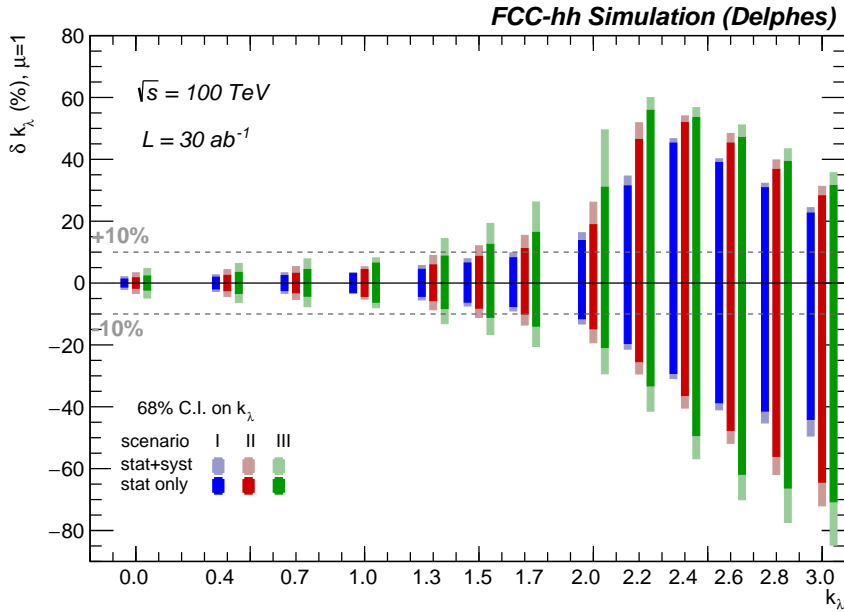


Fig. 10.14: Expected precision on the Higgs self-coupling as a function of the  $\kappa_\lambda$  value for each scenario. To improve readability, the positions of scenario I (III) bands are slightly offset in the negative (positive) direction along the  $\kappa_\lambda$  axis.

#### 10.2.4 Measurement of vector boson scattering

**Introduction** In the absence of the Higgs boson in the Standard Model (SM) the scattering of longitudinally polarised vector bosons ( $V_L V_L$  scattering where  $V=W,Z$ ) grows at high energy beyond the unitarity limit. In particular, if the couplings of the Higgs boson to vector bosons deviate from the SM value, the delicate balance that preserves unitarity can be spoiled and lead to large enhancements in  $VV$  scattering at high energy, potentially providing hints of new physics. Vector boson scattering (VBS) at high energies can therefore help to elucidate the nature and the mechanism of electro-weak symmetry breaking (EWSB) in a model independent way. At hadron colliders VBS occurs via the reaction  $qq \rightarrow VVjj$ . Due to the absence of colour exchange, the final state typically features the presence of two very forward jets, with very little central activity. The average pseudo-rapidity of the most forward jet is  $|\eta| \approx 4.5$  at  $\sqrt{s} = 100$  TeV compared to  $|\eta| \approx 3.5$  at  $\sqrt{s} = 14$  TeV.

VBS processes can be studied in several channels but we focus here only on the  $W^\pm W^\pm$  same sign production, which is the most sensitive. Projections for the High-Luminosity LHC indicate an expected significance of  $3\sigma$  for the discovery of  $W_L W_L$  scattering, after  $3 \text{ ab}^{-1}$  [203]. The FCC-hh provides a unique opportunity to measure  $V_L V_L$  processes at the percent level.

The VBS process interferes with other electro-weak (EWK) production channels, as well as with QCD  $W^\pm W^\pm$  production (see Fig. 10.15). However the interference between EWK and QCD is very small and can be neglected. In the fully leptonic mode this channel features two same-sign leptons in addition to the characteristic forward jets. The main prompt backgrounds for same-sign leptons are  $W^\pm W^\pm$  (QCD) and  $WZ$ +jets production. Other potential backgrounds such as non-prompt backgrounds coming from  $t\bar{t}$ ,  $WW$  and double parton scattering are neglected in this study.

Here, we explore the prospects of measuring the longitudinal  $W_L W_L$  VBS cross section at the FCC-hh. The robustness of the sensitivity as a function of various scenarios of detector acceptance is also discussed.

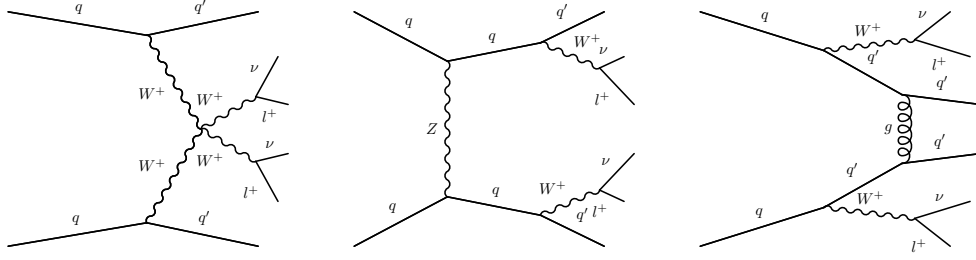


Fig. 10.15: Representative Feynman diagrams for Vector Boson Scattering (left), EWK t-channel production (centre) and QCD (right)  $W^\pm W^\pm jj$  production.

**Monte Carlo events** The EWK  $pp \rightarrow W^\pm W^\pm qq \rightarrow \ell^\pm \nu \ell^\pm \nu qq$  sample was generated at LO for the three polarisations (TT, TL and LL) components separately. Fiducial requirements were applied in the generation to increase the generation efficiency. Both partons were required to have  $p_T > 20$  GeV and  $|\eta| < 6$ . We also require a rapidity gap  $\Delta\eta_{qq} > 2.5$  and a large di-jet invariant mass  $m_{qq} > 200$  GeV to enhance the VBS contribution. The total fiducial cross section for this process at  $\sqrt{s} = 100$  TeV is  $\sigma(W^\pm W^\pm jj)^{\text{EWK}} = 0.39$  pb. The contribution of the LL component is around 10%. Since the interference with the EWK contribution is small, the QCD contribution was generated in a separate sample with the same selection at generator level. The LO cross section for this process is  $\sigma(W^\pm W^\pm jj)^{\text{QCD}} = 0.17$  pb. Finally the WZ contribution was generated at LO with up to 2 jets merged. The inclusive cross section  $\sigma(WZ) = 611$  pb was used, including a  $K=1.7$  to account for higher order corrections [15].

**Event selection and signal extraction** We require at least two same-sign leptons (electrons and muons) with  $p_T^\ell > 20$  GeV and  $|\eta_\ell| < 4$ . The relative isolation is computed using the momentum sum of particle-flow candidates [52] inside a cone of size  $R = 0.3$  around the reconstructed particle (excluding the particle itself) divided by the particle  $p_T$ . We then require at least two jets with  $p_T^j > 30$  GeV and  $|\eta_j| < 6$  reconstructed with the anti- $k_T$  [54] algorithm with a parameter  $R = 0.4$ .

Specific cuts designed to enhance the VBS topology contribution relative the other EWK and QCD  $W^\pm W^\pm jj$  contributions are then applied. Events with a large di-jet invariant mass  $m_{jj} > 600$  GeV and rapidity gap between the two leading jets  $\Delta\eta_{jj} > 3.5$  GeV are selected. We substantially reduce the WZ background by vetoing events with the presence of an additional lepton and require  $E_T^{\text{miss}} > 50$  GeV as well as  $m_{\ell\ell} > 50$  GeV.

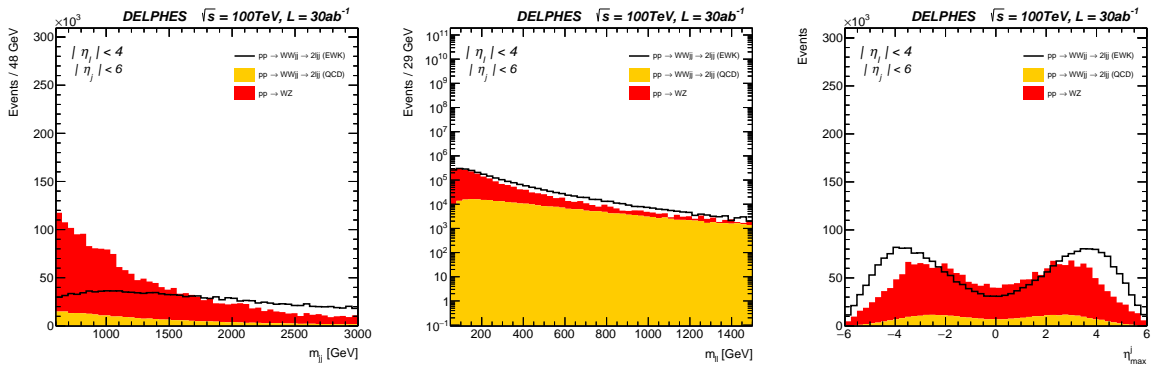


Fig. 10.16: Distributions of the di-jet (left), di-lepton (centre) invariant mass and pseudo-rapidity of the most forward reconstructed jet (right). The background contributions WZ and  $W^\pm W^\pm$  (QCD) are stacked, while the  $W^\pm W^\pm$  (EWK) process is not.

Figure 10.16 shows the WZ and the  $W^\pm W^\pm$  QCD background contributions to three key observables together with the total EWK contribution normalised to  $\mathcal{L} = 30 \text{ ab}^{-1}$ . Figure 10.16 (left) shows the di-jet invariant mass. The centre plot shows the dilepton invariant mass distribution, as a proxy for the WW invariant mass. Several thousand events will be available at large diboson mass to probe the unitarisation of the vector boson scattering. In Fig. 10.16 (right) we show the pseudo-rapidity distribution of the most forward jet.

Two observables are used for the signal extraction. The azimuthal angle between the two leptons  $\Delta\phi_{\ell\ell}$  discriminates between the LL and TT/TL polarisations as can be seen in Fig. 10.17 (left). The leading jet rapidity distribution discriminates against the large WZ+jets and the  $W^\pm W^\pm$  QCD backgrounds. The extraction of the longitudinal component of the  $W^\pm W^\pm$  (EWK) process is performed via a 2-dimensional fit of these two observables. The fit uncertainties are driven by an uncertainty of 10% on shapes, 1% on luminosity, 1% on the PDF and 0.5% on lepton efficiency.

**Results and discussion** The relative uncertainty of the same-sign  $W_L W_L$  scattering is shown in Fig. 10.17 (right) as a function of the integrated luminosity. Under the nominal detector assumption (red curve), i.e. with the ability of reconstructing leptons up to  $|\eta_\ell| < 4$  and jets up to  $|\eta_j| = 6$ , this process can be measured with precision of  $\delta\sigma(W_L W_L) \approx 2\%$  with the full  $\mathcal{L} = 30 \text{ ab}^{-1}$  of the FCC-hh programme.

We also studied the effect on the sensitivity of a reduced acceptance (similar to that of the LHC experiments) for leptons and jets ( $|\eta_\ell| < 2.5$  and  $|\eta_j| = 4.5$ ). With these assumptions the precision expected is degraded  $\delta\sigma(W_L W_L) \approx 6\%$ .

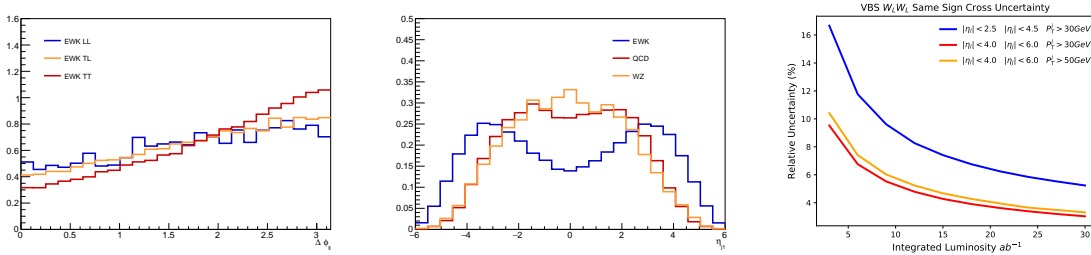


Fig. 10.17: Left: The distribution azimuthal angle between the two leptons  $\Delta\phi_{\ell\ell}$  for the 3 polarisations components (TT,TL and LL) of the  $W^\pm W^\pm \rightarrow \ell^\pm \nu \ell^\pm \nu$  process. Right: The distribution of the leading jet pseudo-rapidity for the inclusive  $W^\pm W^\pm \rightarrow \ell^\pm \nu \ell^\pm \nu$  (EWK) signal sample and the  $W^\pm W^\pm \rightarrow \ell^\pm \nu \ell^\pm \nu$  (QCD) and WZ+jets backgrounds. Bottom: Relative uncertainty of the same-sign  $W^\pm W^\pm$  scattering as a function of the integrated luminosity.

With 1000 simultaneous interactions per bunch cross (pile-up events) it may be impossible to accurately reconstruct jets down to  $p_T^j > 30 \text{ GeV}$ , in particular in the forward region. We studied the impact of raising this threshold to  $p_T^j > 50 \text{ GeV}$  (yellow) and we observe a relatively negligible degradation in the sensitivity. Nevertheless, pile-up rejection in the forward region, for example with the help of timing detectors, is essential for the success of this measurement.

## 10.3 Searches for new physics

### 10.3.1 Resonances: $ee, \mu\mu, \tau\tau$

#### 10.3.1.1 Introduction

Models with extended gauge groups often feature additional U(1) symmetries with corresponding heavy spin-1 bosons. These bosons, generally referred to as  $Z'$ , could manifest themselves as a narrow resonance in the dilepton mass spectrum. These models include those inspired by Grand Unified Theories,



motivated by gauge unification or a restoration of the left-right symmetry violated by the weak interaction. Examples include the  $Z'$  bosons of the E6 motivated theories [204–206] and Minimal models [207]. The Sequential Standard Model (SSM) [206] has a  $Z'_{\text{SSM}}$  boson with fermionic couplings identical to those of the Standard Model Z boson. For more details on the models considered here, and on the analysis, see Ref. [19].

The decay products of heavy resonances are in the multi-TeV regime and the capability to reconstruct their momentum imposes stringent requirements on the detector design. In particular, reconstructing the curvature of multi-TeV muon tracks requires excellent position resolution and a large lever arm. In this section, the expected sensitivity is presented for a  $Z' \rightarrow \ell\ell$  (where  $\ell = e, \mu$ ) and  $Z' \rightarrow \tau\tau$  separately.

### 10.3.1.2 Monte Carlo samples

Monte Carlo (MC) simulated event samples were used to simulate the response of the FCC detector to signal and backgrounds. The muon momentum resolution is assumed to be  $\sigma(p)/p \approx 20\%$  at  $p_T = 20$  TeV. Signals are generated with PYTHIA 8.230 [102] using the leading order cross section from the generator. All lepton flavour decays of the  $Z'_{\text{SSM}}$  are generated assuming universality of the couplings. The Drell-Yan background has been generated using MG5\_aMC@NLO 2.5.2 [25] at leading order only. A K-factor of 2 is applied to all the background processes.

### 10.3.1.3 Event selection

Events are required to contain two leptons with  $p_T > 1$  TeV,  $|\eta| < 4$  and an invariant mass  $m_{\ell\ell} > 2.5$  TeV. For di- $\tau$  final state we focus on the most sensitive fully hadronic channel only. The di- $\tau$  event selection requires two jets with  $p_T > 0.5$  TeV and  $|\eta| < 2.5$  identified as  $\tau$ 's. To ensure no overlap between the  $\ell$  and  $\tau$  final states, jets containing leptons with  $p_T > 100$  GeV are vetoed. Finally, requirements of  $\Delta\phi(\tau_1, \tau_2) > 2$  and  $2.5 < \Delta R(\tau_1, \tau_2) < 4$  are applied. Mass dependent cuts applied to maximise the signal to background ratio are summarised in Table 10.11.

Figure 10.18 (left and centre) shows the invariant mass for a 30 TeV signal for the  $ee$  and  $\mu\mu$  channels. The mass resolution is better for the  $ee$  channel, as expected. Figure 10.18 (right) shows the transverse mass<sup>1</sup> of a 10 TeV signal for the  $\tau\tau$  channel. Several proxies for the true resonance mass have been tested, such as the invariant mass of the two taus, with and without correction for the missing energy. The transverse mass provided the best sensitivity and was therefore used to set limits and determine the discovery reach.

Table 10.11: List of mass dependent cuts optimised to maximise the sensitivity for the  $Z' \rightarrow \tau\tau$  search.

$Z'$ mass [TeV]	$\Delta\phi(\tau_1, \tau_2)$	$\Delta R(\tau_1, \tau_2)$	$E_T^{\text{miss}}$
4 – 8	$> 2.4$	$> 2.5$ and $< 3.5$	$> 400$ GeV
10	$> 2.4$	$> 2.7$ and $< 4$	$> 300$ GeV
12 – 14	$> 2.6$	$> 2.7$ and $< 4$	$> 300$ GeV
16 – 18	$> 2.7$	$> 2.7$ and $< 4$	$> 300$ GeV
$> 18$	$> 2.8$	$> 3$ and $< 4$	$> 300$ GeV

### 10.3.1.4 Results and discussion

Hypothesis testing is performed using a modified frequentist method based on a profile likelihood that takes into account the systematic uncertainties as nuisance parameters that are fitted to the expected Monte-Carlo. For the  $ee$  and  $\mu\mu$  analyses, the di-lepton invariant mass is used as the discriminant, while

<sup>1</sup>The transverse mass is defined as  $m_T = \sqrt{2p_T^{Z'} * E_T^{\text{miss}} * (1 - \cos\Delta\phi(Z', E_T^{\text{miss}}))}$ .

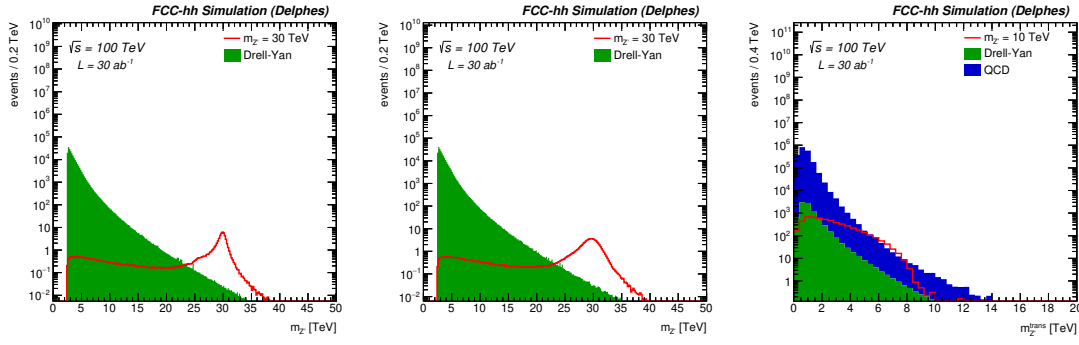


Fig. 10.18: Left, centre: Invariant mass for a 30 TeV signal after full event selection for  $ee$  channel (left) and  $\mu\mu$  channel (centre). Right: Transverse mass for a 10 TeV signal after full event selection for the  $\tau\tau$  channel.

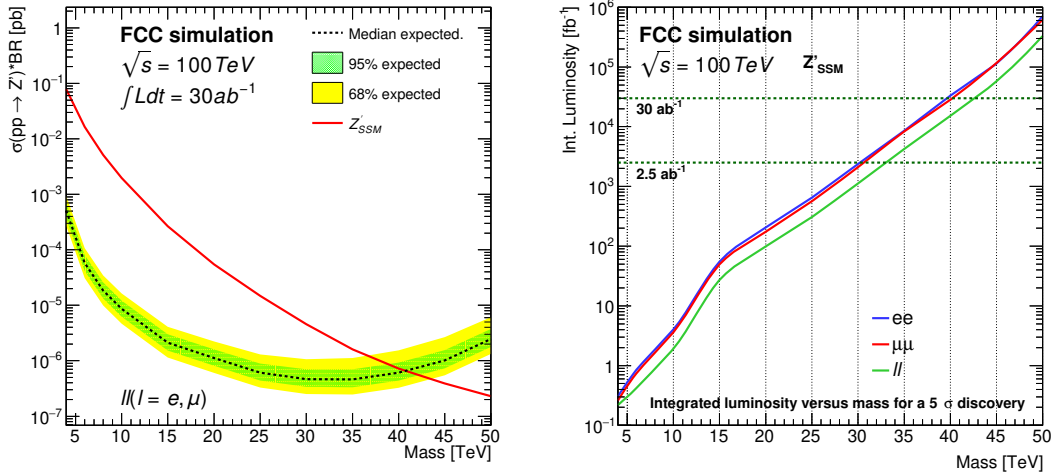


Fig. 10.19: Limit versus mass for the di-lepton ( $ee, \mu\mu$ ) channel (left) and luminosity for a  $5\sigma$  discovery (right) comparing  $ee, \mu\mu$  and combined channels.

for the  $\tau\tau$  channel the transverse mass is used. A 50% uncertainty on the background normalisation is assumed.

The exclusion limit obtained with  $\mathcal{L} = 30 \text{ ab}^{-1}$  of data for the combination of the  $ee$  and  $\mu\mu$  channels is shown in Fig. 10.19 (left). Figure 10.19 (right) shows the integrated luminosity required to reach a  $5\sigma$  discovery for the leptonic resonances as a function of the mass of the heavy resonance. The  $Z' \rightarrow ee$  and  $Z' \rightarrow \mu\mu$  channel display very similar performance, due to the low background rates. We conclude therefore that the reference detector design features near to optimal performance for searches involving high  $p_T$  muon final states. Figure 10.20 shows the exclusion limits for  $30 \text{ ab}^{-1}$  of data (left) and the required integrated luminosity versus mass to reach a  $5\sigma$  discovery (right) for the di-tau resonances.

The discovery potential for high mass resonances decaying to  $ee, \mu\mu$  and  $\tau\tau$  has been studied using as a benchmark the  $Z'_{\text{SSM}}$  model. The very large centre of mass energy provides a correspondingly large mass reach. For the  $ee$  and  $\mu\mu$  cases masses up to 42 TeV can be excluded or discovered. Heavy resonance decaying to  $\tau$  leptons reconstructed in the hadronic decay mode are more challenging, but we would be able to probe masses up to 18 TeV.

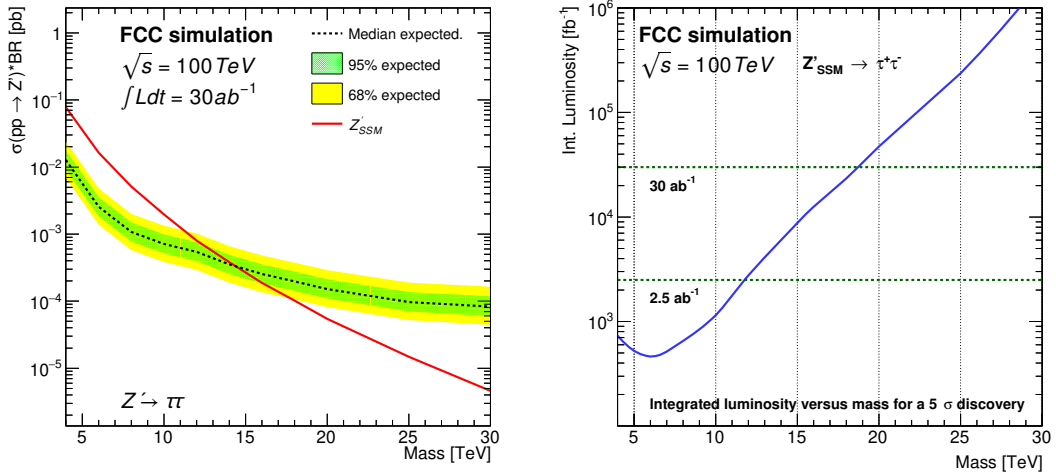


Fig. 10.20: Limit versus mass for the di-tau channel (left) and luminosity for a  $5\sigma$  discovery (right).

### 10.3.2 Resonances: $WW$ , $t\bar{t}$ , $jj$

#### 10.3.2.1 Introduction

Many models of beyond the SM (BSM) physics predict additional particles with masses at the TeV scale. The presence of new resonant states [208–216] decaying to two highly boosted particles decaying hadronically could be observed as an excess in the QCD dijet distribution. We focus here on three specific benchmark models: a  $Z'_{SSM}$  [206], a Randall-Sundrum graviton [215], and an excited quark resonance [217, 218]. We study the sensitivity using hadronic decay modes:  $Z' \rightarrow t\bar{t}$ ,  $G_{RS} \rightarrow WW$  and  $Q^* \rightarrow jj$ .

The decay products are typically in the multi-TeV regime and their reconstruction imposes stringent requirement on the detector design. Precise jet energy resolution requires full longitudinal shower containment. Highly boosted top quarks and W bosons decay into highly collimated jets that need to be disentangled from standard QCD jets by studying their substructure. High discrimination power and sensitivity for these searches at such extreme energies, requires excellent granularity both in the tracking detectors and calorimeters.

#### 10.3.2.2 Monte Carlo samples

Signal models were generated with PYTHIA 8.230 [102] and the LO cross-section is used. The SM backgrounds are di-jet (QCD), top pairs ( $t\bar{t}$ ),  $VV$  and  $V + \text{jets}$  where  $V = W/Z$ , which were generated using MG5\_aMC@NLO 2.5.2 [25] at LO. A K-factor of 2 is applied to all the background processes.

#### 10.3.2.3 Multivariate tagger

An important ingredient of the  $Z' \rightarrow t\bar{t}$  and  $G_{RS} \rightarrow WW$  searches is the identification of heavy boosted top quarks and W bosons. Two jet taggers using Boosted Decision Trees (BDTs) were developed to discriminate W and top jets against the di-jet background.

Top and W taggers were optimised using jets with a transverse boost of  $p_T = 10$  TeV. At these extreme energies, W and top jets have a characteristic angular size  $R = 0.01\text{--}0.02$ , i.e smaller than the typical electromagnetic and hadronic calorimeter cells. Following the approach described in [219], we exploit the superior track angular resolution and reconstruct jets from tracks only (track jets) using the anti- $k_T$  algorithm with a parameter  $R = 0.2$ . The missing neutral energy is corrected for by rescaling the track 4-momenta by the factor  $p_T^{trk} / p_T^{PF}$ , where  $p_T^{trk}$  is the track-jet  $p_T$  and  $p_T^{PF}$  is the particle-

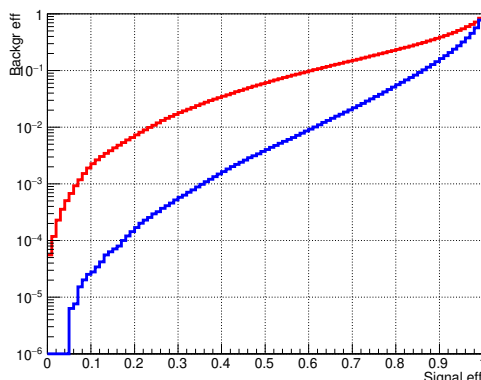


Fig. 10.21: Left: Energy-flow ( $E_F(1, 0.05)$ ) observable for W and QCD jets. Right: Di-jet rejection versus signal efficiency for the two taggers, W in blue and top in red.

flow-jet  $p_T$ . In what follows, we will simply refer to ‘track jets’ as the jet collection that includes the aforementioned rescaling.

The boosted top tagger is built from jet substructure observables: the soft-dropped jet mass [56] and N-subjettiness [55] variables  $\tau_{1,2,3}$  and their ratios  $\tau_2/\tau_1$  and  $\tau_3/\tau_2$ . The W-jet versus QCD-jet tagger also uses an ‘isolation-like’ variable that exploits the absence of high  $p_T$  final state-radiation (FSR) in the vicinity of the W decay products. We call these variables  $E_F(n, \alpha)$  and define them as:

$$E_F(n, \alpha) = \frac{\sum_{\frac{n-1}{5}\alpha < \Delta R(k, jet) < \frac{n}{5}\alpha} p_T^{(k)}}{\sum_{\Delta R(k, jet) < \alpha} p_T^{(k)}} \quad (10.1)$$

We use  $\alpha = 0.05$ . We construct 5 variables  $E_F(n, \alpha)$  with  $n = 1 - 5$  and provide them as input to the BDT. The  $E_F(1, 0.05)$  observable is shown in Fig. 10.21 (left). The final performance of the W and top tagger is shown in Fig. 10.21 (right). The W tagging performance has significantly better performance due to the use of the energy-flow variables. We choose our working points with a top and W tagging efficiencies of  $\epsilon_S^{\text{top}} = 60\%$  and  $\epsilon_S^{\text{W}} = 90\%$  corresponding respectively to a background efficiency of  $\epsilon_B^{\text{top}} = \epsilon_B^{\text{W}} = 10\%$ .

#### 10.3.2.4 Event selection

**Dijet analysis** Jets are clustered using particle-flow candidates with the anti- $k_T$  [54] algorithm with parameter  $R=0.4$ . We require at least two jets with  $p_T > 3$  TeV and  $|\eta| < 3$  and the rapidity difference between the two leading jets to be small,  $\Delta(\eta) < 1.5$  as di-jet events will tend to be more central. The dijet invariant mass of the  $Q^* \rightarrow jj$  signal for  $m_Q^*$  and QCD contributions after the full event selection is shown in Fig. 10.22 (left).

**Boosted Top and W analyses** As track jets are better able to resolve the jet sub-structure compared to particle-flow jets, the jet selection for the  $G_{RS} \rightarrow WW$  and  $Z' \rightarrow t\bar{t}$  searches uses track jets. As no lepton veto is applied, there is also some acceptance for leptonic decays. The sensitivity to semi-leptonic WW or  $t\bar{t}$  decays is enhanced by adding the  $p_T^{\text{miss}}$  vector to the closest jet 4-momentum (among the two leading jets).

We require two jets with  $p_T > 3$  TeV,  $|\eta| < 3$  and  $\Delta(\eta) < 2.4$ . Both jets must either be W or top tagged. Both high- $p_T$  jets must be  $b$ -tagged for the  $Z' \rightarrow t\bar{t}$  analysis. Finally, to further reject QCD, we

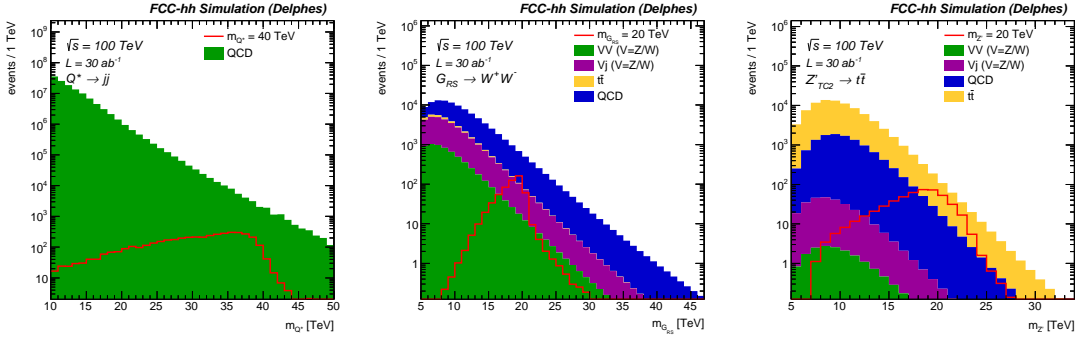


Fig. 10.22: Invariant mass distribution of the two leading jets for the for the  $Q^* \rightarrow jj$  (left,  $m_{Q^*} = 40$  TeV),  $Z' \rightarrow t\bar{t}$  (centre,  $m_{Z'} = 20$  TeV) and  $G_{RS} \rightarrow WW$  (right,  $m_{G_{RS}} = 20$  TeV) analyses.

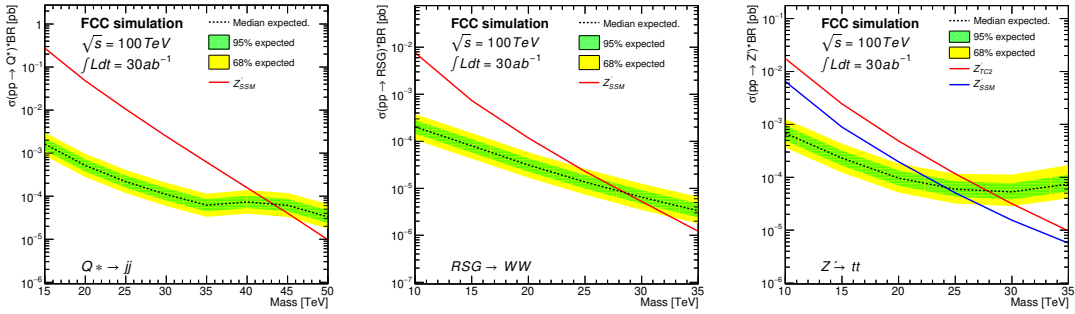


Fig. 10.23: Exclusion limit at 95% CL versus heavy resonance mass decaying into di-jet (left), WW (centre),  $t\bar{t}$  (right).

require  $m_{SD} > 40$  GeV for both jets. In Fig. 10.22 we show the di-jet invariant mass distribution after the final cuts for the  $G_{RS} \rightarrow WW$  (centre) and  $Z' \rightarrow t\bar{t}$  (right) analyses respectively.

### 10.3.2.5 Signal extraction and results

Hypothesis testing is performed using a modified frequentist method based on a profile likelihood fit that takes into account the systematic uncertainties as nuisance parameters. The di-jet invariant mass is used as a discriminant. In order to reduce large statistical fluctuations from high Monte Carlo weight events, we parameterise the background invariant mass distribution with the following function (conservatively assuming 50% uncertainty on the background normalisation)  $f(z) = p_1(1-z)^{p_2}z^{p_3}z^{p_4 \log z}$ , where  $z = m_{jj}/\sqrt{s}$ .

The expected exclusion limits at 95% CL, and the  $5\sigma$  discovery reach, are shown in Figs. 10.23 and 10.24, respectively. For the  $Q^* \rightarrow jj$  masses, up to 40 TeV could be discovered with  $\mathcal{L} = 30 \text{ ab}^{-1}$ . Reconstructing heavy resonances decaying to WW and  $t\bar{t}$  is more challenging and requires the use of novel approaches to boosted object tagging to reduce the backgrounds. The reach for  $Z' \rightarrow t\bar{t}$  (in TC2 models) and  $G_{RS} \rightarrow WW$  is 24 TeV and 22 TeV respectively and it is possible to discover a  $Z'_{SSM} \rightarrow t\bar{t}$  up to  $m_{Z'} = 18$  TeV.

### 10.3.3 Supersymmetry: top squarks

SUSY provides a theoretical framework that can address some of the most fundamental shortcomings of the standard model (SM), such as the hierarchy problem [220, 221] and the origin of dark matter [222–224]. The quantum corrections to the value of the Higgs boson mass [187, 188, 225–228] from SUSY

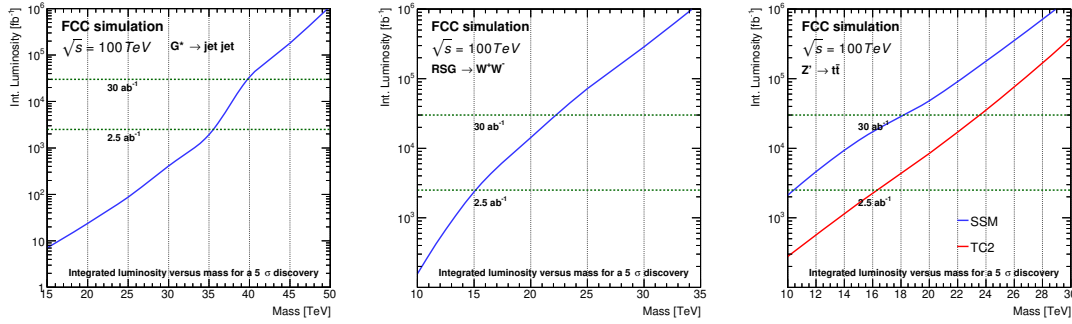


Fig. 10.24: Integrated luminosity for a  $5\sigma$  discovery as a function of the heavy resonance mass decaying into di-jet (left), WW (centre),  $t\bar{t}$  (right).

particles (sparticles) could cancel the otherwise problematic SM contributions [229–232]. In this way, SUSY can protect the value of Higgs mass. This is especially important for the superpartners of the top quark, because they have the largest couplings to the Higgs boson, and hence produce the largest corrections. Moreover, SUSY models with R-parity [233, 234] conservation require sparticles to be produced in pairs, with the LSP stable on cosmological time scales. If the lightest neutralino, denoted  $\tilde{\chi}_0^1$ , is the LSP, then it is also a very promising dark matter candidate [235] that would remain at the end of all R-parity conserving sparticle cascade decays. Taking into consideration the observed Higgs mass, a plethora of SUSY models predict scalar masses below the  $\mathcal{O}(10 \text{ TeV})$  regime. Therefore, the hunt of top squarks at a future 100 TeV hadron collider is of critical importance not only for understanding the naturalness of the electroweak scale, but also for the viability of SUSY in general.

Based on these motivating principles, we explore the reach of a search for top squarks at  $\sqrt{s}=100 \text{ TeV}$  in the framework of the FCC-hh. We consider the simplified model [236–238] with the  $\tilde{t}_1 \rightarrow t + \tilde{\chi}_0^1$  decay mode with R-parity conservation, where  $\tilde{t}_1$  is the lightest mass eigenstate of the top squark and  $\tilde{\chi}_0^1$  is the lightest neutralino. All other sparticles are assumed to be much heavier and hence neglected. We consider a variety of  $m_{\tilde{t}_1}$  and  $m_{\tilde{\chi}_0^1}$  combinations and focus on all-hadronic final states, defined as those for which the visible content is made up solely of hadronic jets. This would be expected for signal processes in which all W bosons decay to quarks, and thus have the largest accessible branching fraction.

The  $\tilde{t}_1 \rightarrow t + \tilde{\chi}_0^1$  decay mode has a very unique signature, with the presence of two on-shell top (t) quarks, decaying to multiple jets and b jets, and containing a large value of missing transverse momentum due to the presence of the two  $\tilde{\chi}_0^1$ . Nevertheless, the search for t squarks at this energy frontier is challenging, since many of the methods that have been used at the LHC are no longer effective. Highly boosted t quarks will be produced from the decay of the massive top squarks and top quark reconstruction techniques used at the LHC including methods based upon jet substructure will be highly inefficient, requiring breakthroughs in object reconstruction and search design. Moreover, the production of SM processes that are considered rare at the LHC will be significantly enhanced to create new sources of background.

### 10.3.3.1 Simulated events

MC simulated events are used to study the signal and background processes. The details of the generation of the signal and background processes are discussed in Section 10.1. Simulated events originating from  $t\bar{t}V$ , where  $V$  collectively refers to the Z and W bosons, and  $t\bar{t}H$ , are generated with up to one additional parton, whereas events stemming from  $t\bar{t}$ ,  $tV$ , single-t,  $VV$ , and the signal events, are generated with up to two additional partons. The  $V$ +jets background is generated with up to three additional partons. No additional partons are generated for rare background processes, as  $t\bar{t}t\bar{t}$ , and  $t\bar{t}VV$ . In all cases, the parton showering and fragmentation is simulated using PYTHIA v8.201 [102]. The most precise cross



section calculations are used to normalize the signal and background samples, corresponding to NLO accuracy [15, 239].

### 10.3.3.2 Event reconstruction and search design

Events are reconstructed using the particle flow (PF) algorithm, in a similar way to Ref. [52]. The PF algorithm aims to reconstruct each particle in the event by combining information from all subdetectors and provides a list of mutually exclusive candidates. Jets are produced by clustering the PF candidates using the anti- $k_T$  algorithm [54] with a distance parameter,  $R$  of value 0.4. Jets are required to have  $p_T > 50$  GeV. We consider electrons and muons with  $p_T > 30$  GeV. In addition, we require the scalar sum of the  $p_T$  of the PF candidates within a cone of  $\Delta R = 0.5$  around the lepton to be less than 30% of the lepton  $p_T$ .

An important ingredient of the searches for  $\tilde{t}_1$  quarks is the identification of jets associated with the decays of  $t$  quarks and  $W$  bosons to quarks, which can be used to suppress most of the backgrounds. As discussed in the introduction, the identification of ultra-boosted (e.g.  $p_T > 5$  TeV) hadronically decaying  $t$  quarks requires new techniques. On the other hand, a plethora of models with moderately boosted  $t$  quarks will still be viable at the end of the HL-LHC physics programme. To this end, we have developed an algorithm to reconstruct hadronically decaying  $t$  quarks over a wide range of  $p_T$  values.

**Identification of hadronically decaying  $t$  quarks** The decay products of  $t$  quarks are typically contained within a cone of radius  $\sim 2m_t/p_T$ . It is therefore evident that in the context of this search, there is no single cone radius that would be useful over a wide range of top  $p_T$ . There are two main considerations for the choice of the  $R$ : (a)  $R$  should be large enough to contain the  $t$  quark decay products, and (b) not so large that it leads to excessive contributions to the jet mass from the underlying event, initial and final state radiation, and pile-up. Taking these considerations into account, we developed the ‘multi- $R$ ’  $t$  quark tagging algorithm. The algorithm begins with the following steps:

1. Consider all PF-jets with  $R = 0.8$  to be potential  $t$  quark candidates. Apply the ‘modified mass drop tagger’ algorithm [240], also known as the ‘soft drop’ (SD) algorithm [56], with angular exponent  $\beta = 0$ , soft cutoff threshold  $z \leq 0.1$ , and characteristic radius  $R_0 = 0.8$ , to remove soft, typically wide-angle, radiation from the jet.
2. Recluster the jet constituents using smaller  $R$  (i.e. 0.2, 0.4 and 0.6)
3. Calculate  $m_{SD}$  and N-subjettiness ratios [241] ( $\tau_3/\tau_2$ ,  $\tau_3/\tau_1$  and  $\tau_2/\tau_1$ ) for all jet variants (i.e. the jets clustered using different  $R$ )

A multivariate boosted decision tree (BDT) is then trained to identify candidates for the quark decays of boosted  $t$  quarks. The input variables to the BDT are the 4-vectors of each jet variant along with  $m_{SD}$  and the N-subjettiness ratios.

However, another challenge we have to face when tagging ultra-boosted  $t$  quarks is the spatial separation of the  $t$  quark decay products, which is extremely small compared to the granularity of the calorimeters. For example, the spatial separation between the decay products of a 5 TeV  $t$  quark is  $\Delta R = \Delta\eta \times \Delta\phi \sim 0.07$ , smaller than the cell size of the proposed hadronic calorimeter with  $\Delta\eta \times \Delta\phi \sim 0.1$ . Inspired by the approach taken in Ref. [219], we make a first attempt at overcoming the limited granularity of the calorimeter by constructing purely track-based observables in order to take advantage of the much finer spatial resolution of the tracking system. We cluster tracks to form jets with  $R$  values of 0.2, 0.4, 0.6 and 0.8, and use them to calculate  $m_{SD}$  and N-subjettiness ratios. A separate BDT is trained using the 4-vectors of the track-based jets and the corresponding substructure variables in addition to the ‘multi- $R$ ’ tagger inputs. We refer to this as the ‘multi- $R$ +Tracks’ tagging algorithm.

The performance of the ‘multi- $R$ ’ algorithm and that of the ‘multi- $R$ +Tracks’ algorithm are compared by means of the receiver operating characteristic (ROC) curves shown in Fig. 10.25 along with



that of an approach based on techniques widely used at the LHC based upon PF-jets with  $R = 0.8$ , and cutting on  $m_{SD}$  and  $\tau_3/\tau_2$ . The new techniques show significantly enhanced performance, particularly in the high  $p_T$  regime. We would like to highlight the fact that the method presented here is not limited to the identification of t quarks, but can be exploited for the reconstruction of other hadronically decaying heavy SM particles, such as Higgs, Z and W bosons. For the 100 TeV analysis reported in this section, we use the multi-R+Tracks algorithm and operate with a working point that corresponds to  $\sim 10\%$  mistag rate.

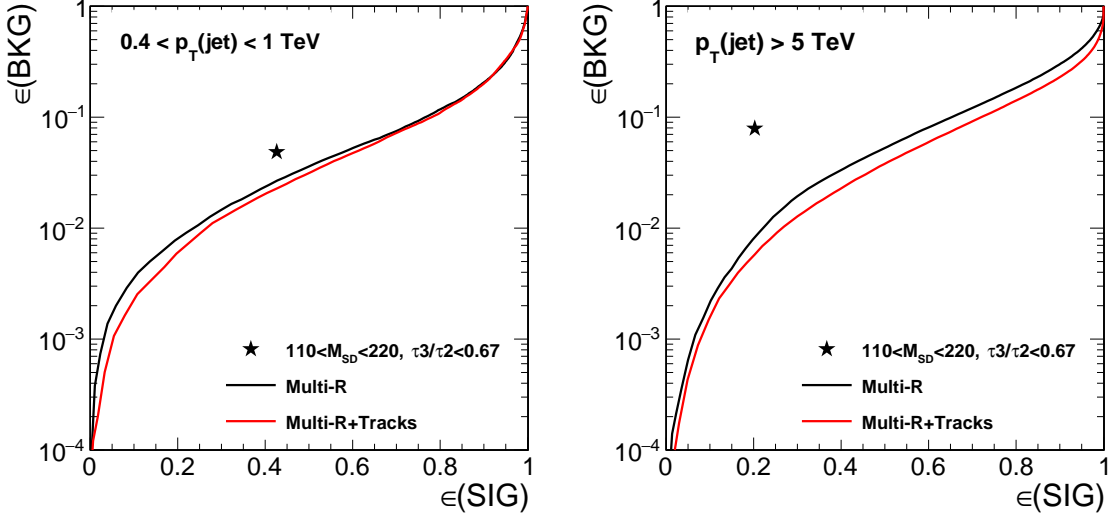


Fig. 10.25: Performance of the multi-R (black) and multi-R+Tracks (red) algorithms in terms of Receiver Operating Characteristic (ROC) curves. The curve labelled LHC corresponds to the performance of a t quark tagging algorithm using current LHC techniques based on PF-jets with  $R = 0.8$  that satisfy  $110 < m_{SD} < 220$  GeV and  $\tau_3/\tau_2 < 0.67$ .

**Event categorisation** For the all-hadronic final state we define a baseline selection that requires the absence of electrons or muons,  $p_T^{\text{miss}} > 2$  TeV, at least two jets with  $p_T > 1$  TeV, of which at least one is b-tagged ( $N_b \geq 1$ ), and at least one top-tagged jet ( $N_t \geq 1$ ).

In the search sample defined by the above requirements, the dominant sources of SM background with intrinsic  $p_T^{\text{miss}}$  arise from  $t\bar{t}$  and  $t\bar{t}V$  production. The contribution from  $t\bar{t}$  processes arises from events in which one or more W bosons decay leptonically to produce  $p_T^{\text{miss}}$  associated with an energetic neutrino, but the charged lepton either falls outside of the kinematic acceptance, or more likely, is misidentified as a jet after failing to be identified as a lepton. Contributions arising from  $t\bar{t}W$ ,  $t\bar{t}H$  and single-t quark processes also enter this category at lower levels. This background is collectively referred to as the ‘lost lepton’ (LL) background. The contributions from  $t\bar{t}Z$  events arise primarily when the Z boson decays to neutrinos, thereby producing significant  $p_T^{\text{miss}}$ . The azimuthal angles between the direction of  $p_T^{\text{miss}}$  and those of each reconstructed t quarks in the event provide powerful means to reduce the LL and  $t\bar{t}Z$  backgrounds. The  $p_T^{\text{miss}}$  in LL and  $t\bar{t}Z$  events is typically aligned with one of the two t quarks. However, in signal events, due to the presence of the two  $\tilde{\chi}_0^1$ ,  $p_T^{\text{miss}}$  is distributed more democratically and therefore frequently points to a region between the two t quarks. Based on these arguments we define the observable  $|\Delta\phi(t, p_T^{\text{miss}})| = \min|\Delta\phi(t_{1,2}, p_T^{\text{miss}})|$  as the minimum azimuthal angle of  $p_T^{\text{miss}}$  with the two reconstructed t quarks. In the case of a single reconstructed t quark, the observable is simply defined relative to it. We select events with  $|\Delta\phi(t, p_T^{\text{miss}})| > 0.5$ .

Contributions arising from electroweak (e.g. V+jets), single-t quark,  $t\bar{t}VV$  and  $t\bar{t}t$  processes represent much smaller backgrounds and will be collectively referred to as ‘rare’ backgrounds in the

following. Contributions from the QCD multijet process enter the search sample in cases where severe mis-measurements of jet momenta produce significant artificial  $p_T^{\text{miss}}$ , or when neutrinos arise from leptonic decays of heavy-flavor hadrons produced during jet fragmentation. However, in these cases  $p_T^{\text{miss}}$  is aligned with one of the highest- $p_T$  jets in the event. We therefore require  $|\Delta\phi(j_{1,2}, p_T^{\text{miss}})| > 0.5$  and  $|\Delta\phi(j_3, p_T^{\text{miss}})| > 0.3$ , where  $j_1, j_2, j_3$  are the three leading- $p_T$  jets. This selection greatly reduces the contribution from this background.

Events passing the baseline selection are divided into two categories based on the number of  $t$  quark candidates;  $N_t = 1$  and  $N_t \geq 2$ . Each category is further subdivided by the number of  $b$  tagged jets;  $N_b = 1$  and  $N_b \geq 2$ . To increase the sensitivity of the search in different signal models we consider the shape of the  $p_T^{\text{miss}}$  distribution in each of the four categories of events. In the current incarnation of the search we define eight exclusive regions in  $E_T^{\text{miss}}$ . Figure 10.26 displays the expected signal and background contributions in two of the search categories.

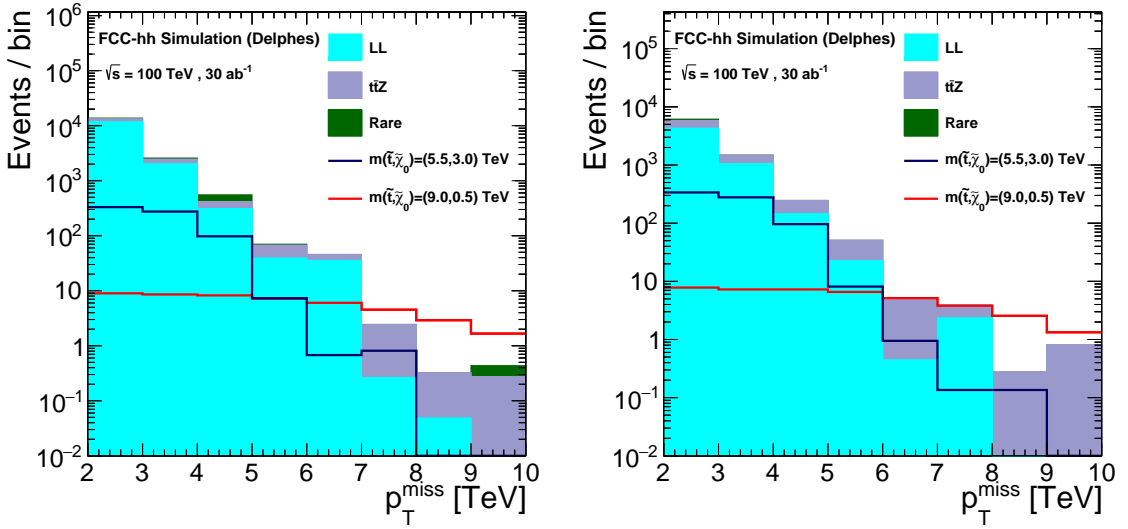


Fig. 10.26: The  $p_T^{\text{miss}}$  distribution in background and signal events with  $N_t \geq 2$  and  $N_b = 1$  (left) or with  $N_t \geq 2$  and  $N_b \geq 2$  (right). The background processes are displayed with solid histograms and the distribution of one signal model is shown with solid red line. The expected yields are scaled to  $30 \text{ ab}^{-1}$ .

### 10.3.3.3 Background estimation

The contribution of the dominant SM backgrounds (i.e. LL and  $t\bar{t}Z$ ) to the search sample is estimated via measurements carried out in dedicated control regions (CR) that are then translated to predictions for event counts in corresponding search regions (SR) with the aid of simulation samples. The rare backgrounds are estimated directly from simulation with generous uncertainties to account for possible differences between data and simulation.

The LL background is estimated from a single-lepton control sample that is obtained by inverting the electron or muon veto requirements described in Section 10.3.3.2. Potential signal contamination is suppressed by requiring the transverse mass of the lepton and  $p_T^{\text{miss}}$  to be less than 100 GeV, which is in the ballpark of expectation for real  $W$  decays. The LL estimation in each SR is based upon the event count in the corresponding single-lepton CR. The count is translated to a prediction in the SR by means of a transfer factor obtained from simulation, defined as:

$$N_{\text{LL}}^{\text{pred}}(\text{SR}) = N_{\text{LL}}^{\text{MC}}(\text{SR}) \frac{N_{\text{LL}}^{\text{data}}(\text{CR})}{N_{\text{LL}}^{\text{MC}}(\text{CR})}, \quad (10.2)$$

where  $N_{LL}^{\text{pred}}(\text{SR})$  is the predicted number of LL events in the SR,  $N_{LL}^{\text{MC}}(\text{SR})$  the expected number of events in the SR, and  $N_{LL}^{\text{MC}}(\text{CR})$  and  $N_{LL}^{\text{'data'}(\text{CR})}$ , the expected and observed events in the CR.

The  $t\bar{t}Z$  background is estimated using a three-lepton control sample. We require the presence of exactly three leptons (electrons or muons) that satisfy  $p_T > 30$  GeV and no additional lepton with  $p_T > 10$  GeV. We further require at least two jets, of which at least two are b-tagged. The same-flavor, opposite-sign lepton pair with the highest dilepton  $p_T$  is assumed to originate from Z boson decay. We require the presence of such a pair with the invariant mass near the Z boson mass (80–100 GeV) and  $p_T$  greater than 1 TeV to probe boson kinematic properties similar to those in the search sample. A small, yet not negligible  $t\bar{t}$  contribution is expected in the three-lepton control sample. The region outside the Z boson mass window is used to constrain the  $t\bar{t}$  background. Correction factors are extracted by comparing the expected and ‘observed’ yields in bins of  $p_T(Z)$  in the three-lepton sample; These correction factors are then used to correct the  $t\bar{t}Z$  expectation.

The dominant systematic uncertainty in the background estimation, especially in the SRs with tight selection in  $p_T^{\text{miss}}$  and  $N_t$ , arises from the limited statistics of the CRs. Other possible sources are expected to be more relevant in regions with moderate  $p_T^{\text{miss}}$ . Based on the current searches at the LHC (e.g. that in Ref. [242]) we consider two scenarios for the remaining systematic uncertainties, which we label as ‘nominal’ and ‘conservative’. In the nominal (conservative) scenario we assume a 10% (20%) uncertainty, uncorrelated across all SRs and between the background processes. For signal we assign a 10% systematic uncertainty uncorrelated across the SRs.

### 10.3.3.4 Results

The statistical interpretation of the results in terms of exclusion and  $5\sigma$  discovery potential for the signal models being considered in this analysis are based on a binned likelihood fit to the expected background and signal yields in the SRs. The extraction of the exclusion potential is based on a modified frequentist approach using the CLs criterion [243,244] under the asymptotic approximation for the test statistic [245, 246]. All of the SRs, and their corresponding CRs, are fitted simultaneously to determine the signal cross section excluded at a 95% confidence level (CL) for each signal point. Models for signal in which the 95% CL upper limit on the production cross section falls below the theoretical value are considered to be excludable. The discovery potential is based on the CLs criterion for the background only hypothesis and is presented in terms of standard deviations ( $\sigma$ ) in the following.

To define the FCC-hh physics programme, an important parameter to define is the integrated luminosity required to exploit the full potential of a 100 TeV machine. To this end we consider two luminosity scenarios,  $3 \text{ ab}^{-1}$  and  $30 \text{ ab}^{-1}$ . Figure 10.27 show the exclusion and discovery potential for the different luminosity and systematics scenarios. With  $3 \text{ ab}^{-1}$  of integrated luminosity,  $\tilde{t}_1$  with mass up to 9 TeV can be excluded for models that predict light  $\tilde{\chi}_0^1$ . A factor of ten increase in luminosity would allow the discovery of  $\tilde{t}_1$  with mass  $\sim 10$  TeV for light  $\tilde{\chi}_0^1$ , independent of the systematic scenario.

## 10.3.4 Dark matter: monojet + DM, $t\bar{t}$ + DM, VBF + DM

### 10.3.4.1 Introduction

An important component of the dark matter search is the search for the Higgs decaying to invisible particles. For a large class of models, the Higgs boson can act as a portal between matter and dark matter. In these models, the Higgs is capable of interacting with both matter and dark matter. In some cases, the Higgs mixes with a dark sector scalar particle and decays to dark sector particles as a result of the mixing. In other cases, the Higgs couples directly to a dark matter particle without any additional particles.

The search for Higgs decaying invisibly uses the  $E_T^{\text{miss}}$  distribution since the  $E_T^{\text{miss}}$  reflects the  $p_T$  spectrum of the Higgs boson. The  $p_T$  of the Higgs boson is, on average, larger than the  $p_T$  of background

processes, which typically originate from quark induced processes. The Higgs  $p_T$  spectrum is particularly advantageous in the tails where Higgs production is significantly enhanced relative to background processes as a result of the larger average Higgs  $p_T$ .

Multiple Higgs production modes can be used. The total Higgs production cross section is dominated by gluon fusion and vector boson fusion. However, at high  $p_T$ , the relative proportion of gluon fusion with respect to the rest of the other production modes is reduced, including Higgs produced in association with top quarks and vector boson fusion. The vector boson fusion production mode (VBF) and the Higgs production produced in association with top quarks both have advantageous properties that allow for further signal vs background separation.

The VBF production mode has the characteristic signature of two jets with relatively large  $\eta$  corresponding to additional quarks as a result of the W pair boson radiation necessary to produce the Higgs boson. With the current 13 TeV searches, the VBF production mode is the dominant channel for the

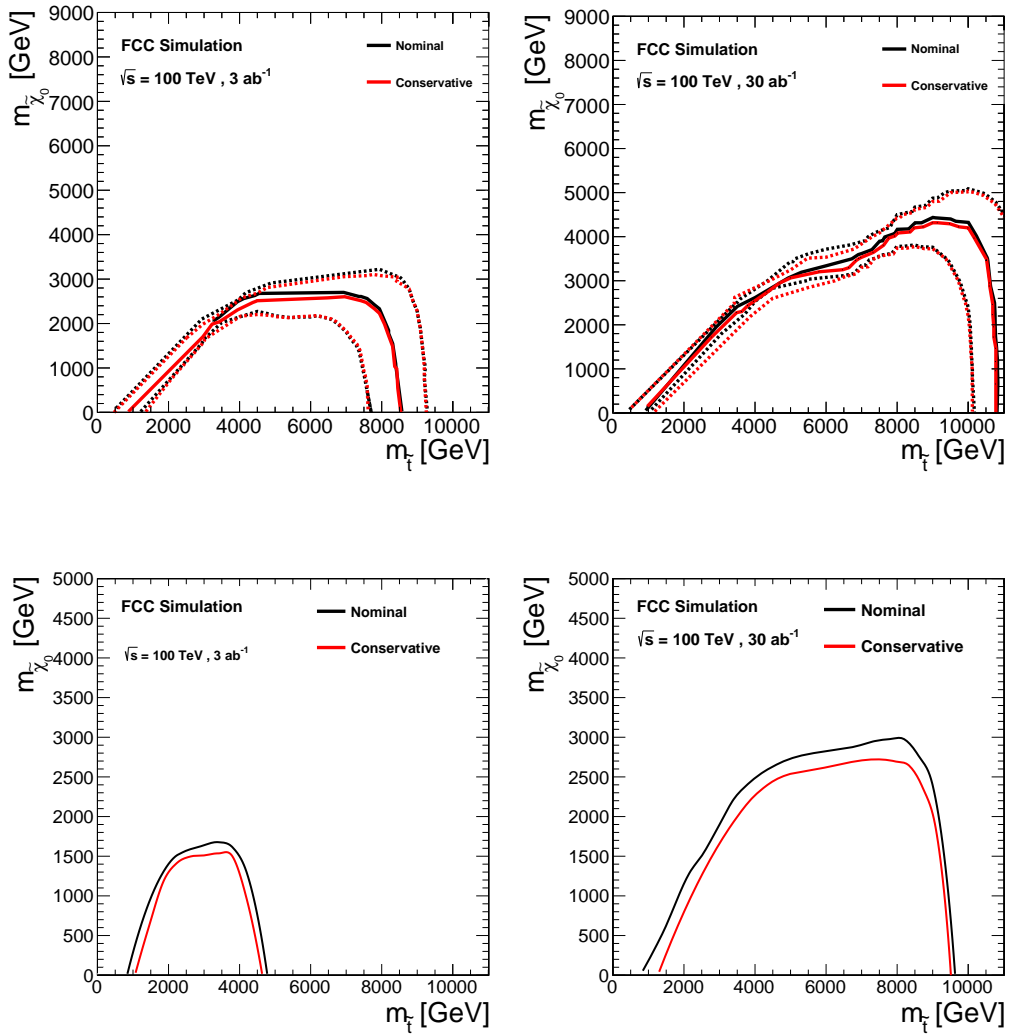


Fig. 10.27: Upper row: Exclusion potential for  $3 \text{ ab}^{-1}$  (left) and  $30 \text{ ab}^{-1}$  (right) of integrated luminosity. The area to the left of and below the solid red (black) curve represents the expected exclusion and the  $\pm 1$  standard deviation contours for the nominal (conservative) scenario of associated systematic uncertainties. Lower row: Discovery potential for  $3 \text{ ab}^{-1}$  (left) and  $30 \text{ ab}^{-1}$  (right) of integrated luminosity. The area to the left and below the solid red (black) curve represents the expected  $5\sigma$  discovery reach for the nominal (conservative) scenario of associated systematic uncertainties.

Higgs invisible search. The vector boson production mode does not have a significantly different  $p_T$  spectrum when compared with background processes largely as a result of the quark initial state. Consequently, the most powerful approach to searching for the Higgs invisible decay in this mode is to look for events with large missing transverse energy and large di-jet pair mass  $m_{jj}$ . The current 13 TeV search is performed by fitting the dijet mass pair with a  $E_T^{\text{miss}}$  requirement above 200 GeV.

The search for Higgs decaying invisibly and produced with pairs of top quarks is perhaps the most promising channel, since the relative cross section is hugely enhanced with respect to background processes, when compared to 13 TeV. Higgs production and the top pair decays allow for a very distinct signature that can significantly reduce the background. In this study, a dedicated analysis isolating Higgs production produced in association with tops is not performed; its addition would likely lead to a further enhancement in sensitivity.

#### 10.3.4.2 Event selection

Events are required to have large missing energy and no additional leptons, including taus. Events are triggered with a missing energy trigger. For this study a trigger that yields 100% efficiency at a  $E_T^{\text{miss}}$  value of 200 GeV is required. This choice of trigger is consistent with the current plateau in both the LHC ATLAS and CMS experiments. Projections with the high luminosity upgrade for the LHC also indicate that with the addition of tracking in the level one trigger system, this plateau can be maintained during high intensity running of the LHC.

#### 10.3.4.3 Backgrounds

The main backgrounds consist of Z boson production, where the Z boson decays to neutrinos ( $Z \rightarrow \nu\nu$ ) and W boson production, where the W boson decays leptonically and the lepton is not identified. The lepton is missed either because the lepton transverse momentum is too low or the lepton falls out of the acceptance of detectors capable of identifying the lepton (e.g. tracking detector and muon chambers in the case of muons). The next largest background consists of top pair production where one of the top quarks decays leptonically and the lepton fails to be identified. This background is very similar to single W boson production with additional jets.

Current monojet analysis in ATLAS and CMS [247,248] use a series of control regions to precisely predict the backgrounds. The Z boson background where the Z boson decays to neutrinos, is predicted by constructing a control region by selecting electron or muon pairs, consistent with the Z boson decay. The leptons are then treated as ‘invisible’ and removed from the event to effectively mimic the Z to neutrino topology. The overall shape of these Z events matches the Z to neutrino events very well, excluding the regions where the leptons would not be selected in the detector. The normalisation of the Z boson events can then be determined from the data and is limited by the uncertainty in the lepton pair selection efficiency.

W events are selected by requiring a lepton, electron or muon, and missing transverse energy. The lepton is removed from the computation of the  $E_T^{\text{miss}}$  so as to match the final  $E_T^{\text{miss}}$  selection. These events are then used to predict the shape of the W boson events where the lepton is not selected, by adding extrapolation uncertainties reflecting the accuracy of the lepton rapidity distribution and the lepton efficiency. In addition, W boson events can be used to predict Z boson events, and single isolated photon events can be used to predict the background shape of both Z boson and W boson events. To use these events in the prediction, we exploit the fact that the prediction of the production ratios is known to a significantly higher precision than the production of the individual processes [249]. This is because W, Z and photon production have the same QCD production diagrams at leading order in the electroweak production. The differences at higher orders have been characterised [249], leading to a predicted uncertainty in the production modes that varies from 1-5% as a function of the single boson  $p_T$ .

#### 10.3.4.4 Monte Carlo samples

Background processes are generated using AMC@NLO [25]. The generation of Z events includes all instances where a Z boson decays to neutrinos, including both diboson production and single Z production. W boson events, including both single boson and diboson production, are relevant as long as there is one leptonically decaying W boson. W and Z boson events are generated at NLO with up to 2 jets and merged following the FxFx merging prescription [250]. Top pair events are generated separately at NLO with up to one additional jet and at least one top is required to have a W boson decaying leptonically. Electroweak production of W and Z boson through vector boson fusion is generated separately at LO. These processes consist of W and Z boson fusion into a single boson. Such backgrounds are necessary when trying to characterise the sensitivity to vector boson fusion, since they constitute the largest irreducible backgrounds. For all backgrounds, DELPHES with the FCC run card is used for the simulation; no additional pileup events are added to the simulation. Events are generated using a weighted generation scheme so that the tails of the distribution correspond to an equivalent luminosity of  $30 \text{ ab}^{-1}$ .

#### 10.3.4.5 Signal extraction and results

The signal is extracted using a simultaneous fit of all background control regions. The fit is performed using the same Monte Carlo where the total number of Monte Carlo events is fixed to a specific luminosity choice. The luminosity is then scanned ranging from  $1 \text{ fb}^{-1}$  to the full  $30 \text{ ab}^{-1}$ . At each luminosity point the asymptotic limit is extracted using the fit with all control regions. The performance is examined considering multiple systematic uncertainty approaches:

- **Experimental systematics:** The driving experimental systematic uncertainties originate from the extrapolation from the control regions to the signal region. For W boson and top events falling in the signal region, a lepton must not be found within the signal region acceptance. The leading uncertainty is the uncertainty on the lepton efficiency. We assume a lepton efficiency uncertainty of 0.5%, 0.25%, and 5% for the electron, muon, and hadronic taus respectively. We assume a luminosity uncertainty of 1%.
- **‘Conservative’ theoretical systematics:** When performing the signal extraction, the uncertainties on the fit are driven by the uncertainty on the ratio of the production of single bosons. To simplify the implementation we take three sets of uncertainties: an increasing slope going from 5% at a  $p_T$  of 0 GeV to 15% at a  $p_T$  of 3 TeV, which mimics the NLO electroweak correction shape; a flat uncertainty of 8%, which matches the orthogonal eigen-component of the factorisation and renormalisation scales and a 5% uncertainty at a  $p_T = 0 \text{ GeV}$  that then goes to a negative 5% uncertainty at a  $p_T$  of 3 TeV. Each suite of three uncertainties are combined for each respective process production ratio W/Z and  $\gamma/Z$ .
- **‘Aggressive’ theoretical systematics:** The same uncertainty scheme as the previous one is used, except now the uncertainty is reduced by an order of magnitude.

Figure 10.28 shows the sensitivity of the Higgs boson invisible branching ratio, as a function of luminosity. Either approach to the theoretical uncertainties appears to be sub-dominant to the impact of the experimental uncertainties. In all cases, however, the uncertainties continue to scale with  $\sqrt{\mathcal{L}}$ . With  $30 \text{ ab}^{-1}$  we reach a branching ratio of the Higgs boson to invisible of  $10^{-4}$ . This is well below the Standard Model branching ratio ( $\sim 2 \times 10^{-3}$ ) of the Higgs boson to neutrinos ( $H \rightarrow ZZ \rightarrow \nu\nu\nu\nu$ ), and consequently we would be able to observe a signal which would look very much like an actual dark matter signature. No actual loss in sensitivity is incurred by the observation of the Standard Model production because we assume that the Standard Model production rate is known. The signal was extracted either from the  $E_T^{\text{miss}}$  distribution or from a two-category extraction, where in the one-jet exclusive category the  $E_T^{\text{miss}}$  is fitted while for events with at least two jets the two highest  $p_T$  jets are combined and their dijet mass  $m_{jj}$  is fitted. The two-category extraction enhances the sensitivity to vector boson fusion



production. In both scenarios, the sensitivity is within 20% of each other and the scaling with respect to luminosity is roughly the same.

The results are translated to compare to direct detection results following [251]. Figure 10.28 shows that a result comparable to that of the expected ultimate limit of direct detection, as defined by the bound induced from neutral current neutrino interactions known as the neutrino floor.

In summary, by performing a simultaneous fit of the hadronic recoil (e.g.  $E_T^{\text{miss}}$ ) spectra of five control regions defined by  $Z$  and  $W$  to lepton decays and  $\gamma$ +jets, it is possible to constrain both theory and experimental systematics to obtain an extremely precise prediction of the  $Z \rightarrow \nu\nu$  spectrum. This simultaneous fit is used to probe the decay of the Higgs to invisible particles. The resulting sensitivity shows a sensitivity to a branching ratio of the Higgs to invisible particles of roughly  $10^{-4}$ ; a bound that is sensitive to Standard Model  $H \rightarrow \nu\nu\nu\nu$  and which extends to the maximal bound of the direct detection searches.

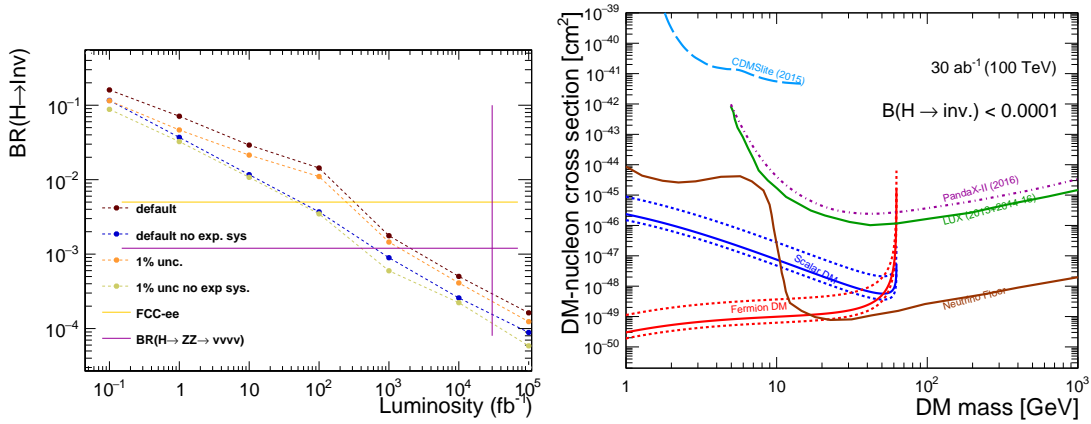


Fig. 10.28: (Left) Expected limit as a function luminosity for the Higgs to invisible, for multiple uncertainty schemes. (Right) Translation of the limit at  $30 \text{ ab}^{-1}$  to the direct detection plane and comparison with LUX [252], PandaX-II [253], CDMSlite [254], and the neutrino floor [255].

### 10.3.5 Dark matter: disappearing tracks

Astrophysical observations of galaxies and the large-scale structure in the universe strongly indicate that dark matter predominate the matter contents in the universe. The nature of dark matter is, however, still unknown and the Standard Model (SM) of particle physics has no states acting as dark matter. Within the theory of supersymmetry (SUSY), a dark matter candidate is a neutralino, which is a mixed state of neutral supersymmetric partners of the SM  $U(1) \times SU(2)$  gauge bosons and the two  $SU(2)$  Higgs doublets. The lightest neutralino ( $\tilde{\chi}_1^0$ ) is often assumed to be the lightest supersymmetric particle (LSP). If we assume that dark matter is the neutral wino (higgsino), which is a supersymmetric partner of the SM  $SU(2)$  gauge boson (Higgs boson) and that it was produced in thermal processes, the upper limit of the LSP mass is determined by the observed relic density of dark matter to be 3 (1) TeV for the wino (higgsino) LSP scenario. In this section, the discovery potential of the FCC-hh with the reference detector is assessed, for wino and higgsino dark matter up to the limits set by thermal production.

When the pure wino or higgsino state is the LSP and has a large mass, the  $\tilde{\chi}_1^0$  is highly degenerate with the lightest chargino ( $\tilde{\chi}_1^\pm$ ), because the wino/higgsino belong to the same  $SU(2)$  multiplets. The mass difference between the  $\tilde{\chi}_1^\pm$  and the  $\tilde{\chi}_1^0$  is typically 160 (355) MeV for the wino (higgsino) LSP scenario, as evaluated from the calculation of radiative correction in Refs. [256, 257]. Due to the small mass difference, the  $\tilde{\chi}_1^\pm$  has a long lifetime of approximately 0.2 (0.023) ns for the 3 TeV wino (1 TeV higgsino) LSP scenario.



gsgino) at the thermal limit [258]. With this mass difference, the  $\tilde{\chi}_1^\pm$  decays into a  $\tilde{\chi}_1^0$  and a charged pion predominantly. The  $\tilde{\chi}_1^0$  passes through the detector without any electromagnetic or strong interactions while the pion is not reconstructed as a track in the inner-tracking detector due to very low transverse momentum ( $p_T$ ). Therefore, such long-lived charginos are observed in the detector as a short ‘disappearing’ track with a typical length of  $\mathcal{O}(1-10)$  cm in collider experiments [259–261]. In this section, a search strategy with the reference FCC-hh detector for the long-lived charginos with a disappearing-track signature is discussed and the expected sensitivity is presented under possible running scenarios of the FCC-hh.

**Monte Carlo events** Simulated samples of Monte Carlo (MC) events are used to obtain the kinematic distributions of the signal and background processes. The wino mass spectrum is calculated using SOFTSUSY 3.7.3 [262] assuming the minimum Anomaly Mediated SUSY Breaking (AMSB) model with  $\tan\beta = 5$ , positive sign of the higgsino-mass term and the universal scalar mass ( $m_0$ ) of 20 TeV. This setting naturally accommodates the Higgs boson mass observed of 125 GeV without maximal mixing. The higgsino mass spectrum is calculated by SUSYHIT [263] assuming the general minimal supersymmetric extension of the SM (MSSM) with  $\tan\beta = 5$ . Other SUSY particle masses are set to 100 TeV to prevent the higgsino from being affected from loop effects. Only the pure wino and higgsino LSP scenarios are considered here. The production cross sections for the winos and higgsinos in 100 TeV pp collisions are calculated using PROSPINO2 [264]. The kinematic distributions are simulated using MADGRAPH5\_AMC@NLO 2.3.3 [25] assuming the wino spectra. The same kinematic distributions are assumed for the wino and higgsino if they have the same masses. In this study, pair productions of the charginos and neutralinos are considered:  $\tilde{\chi}_1^\pm \tilde{\chi}_1^\mp$  and  $\tilde{\chi}_1^\pm \tilde{\chi}_1^0$  for the wino scenario, and  $\tilde{\chi}_1^\pm \tilde{\chi}_1^\mp$ ,  $\tilde{\chi}_1^\pm \tilde{\chi}_1^0$  and  $\tilde{\chi}_1^\pm \tilde{\chi}_2^0$  for the higgsino scenario. As the  $\tilde{\chi}_1^0$  and  $\tilde{\chi}_2^0$  are degenerate in the higgsino case, the difference in the cross section or decay processes between  $\tilde{\chi}_1^\pm \tilde{\chi}_1^0$  and  $\tilde{\chi}_1^\pm \tilde{\chi}_2^0$  is negligible. Therefore, only the  $\tilde{\chi}_1^\pm \tilde{\chi}_1^0$  process is generated and the cross section is doubled to account for  $\tilde{\chi}_1^\pm \tilde{\chi}_2^0$ . Minimum-bias collisions are produced using PYTHIA 8.230 [102], and are overlaid to evaluate contribution from non-genuine tracks caused by the random combination of hits in the inner-tracking detector, which are referred to as fake tracks hereafter.

SM background processes such as W/Z-boson production in association with jets, top-quark pair and single top-quark production are simulated using MADGRAPH5\_AMC@NLO and the generated samples are used to evaluate the selection efficiency. The kinematic distributions of jets, leptons and the magnitude of missing transverse momentum ( $E_T^{\text{miss}}$ ) are processed using the DELPHES simulation [34] to account for the detector reconstruction efficiency and energy/momentum measurement.

**Event selection** The events produced are required to contain at least one high- $p_T$  jet, large  $E_T^{\text{miss}}$  and no lepton (electron or muon) with  $p_T$  above 10 GeV as a pre-selection. The jet  $p_T$  and  $E_T^{\text{miss}}$  thresholds are determined by maximising the sensitivity at each  $\tilde{\chi}_1^\pm$  mass point based on the signal acceptance and background rate. Figure 10.29 shows the leading jet  $p_T$  and  $E_T^{\text{miss}}$  distributions of signal and background events selected with the lepton veto and no requirement on the jet  $p_T$  or  $E_T^{\text{miss}}$ . While the background yield can be reduced significantly by applying high thresholds to the leading jet  $p_T$  and to the  $E_T^{\text{miss}}$ , FCC has no discovery power for the wino or higgsino at the thermal limit if the disappearing-track information is not used in the search.

**Track requirement** As the chargino lifetime becomes short, the acceptance for the chargino-track reconstruction increases with decreasing radial position of the outermost layer necessary for the track reconstruction. On the other hand, the use of short tracks with few layer hits will usually increase fake tracks (discussed later). In order to assess the impact on the sensitivity from different requirements of the number of hits used in the track reconstruction ( $N_{\text{layer}}^{\text{hit}}$ ), the track reconstruction is performed with the requirements of  $N_{\text{layer}}^{\text{hit}} = 4$  and  $N_{\text{layer}}^{\text{hit}} = 5$  separately. Since the contribution from fake tracks

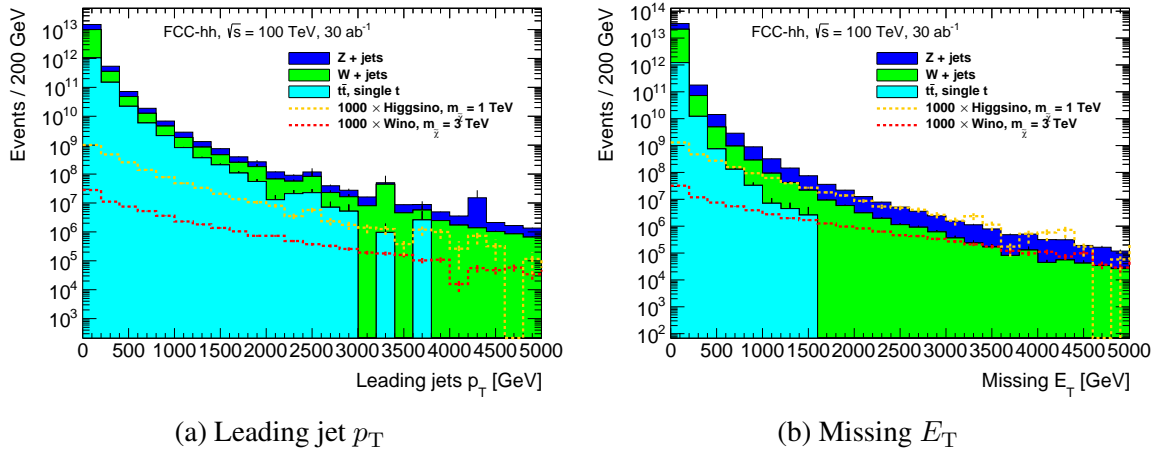


Fig. 10.29: (a) Leading-jet  $p_T$  and (b)  $E_T^{\text{miss}}$  distributions after removing events containing leptons with  $30 \text{ ab}^{-1}$ . The SM backgrounds from W/Z+jets and top production are shown as filled histograms. Also shown as dashed lines are the 3 (1) TeV wino (higgsino) signals, scaled up by a factor 1000.

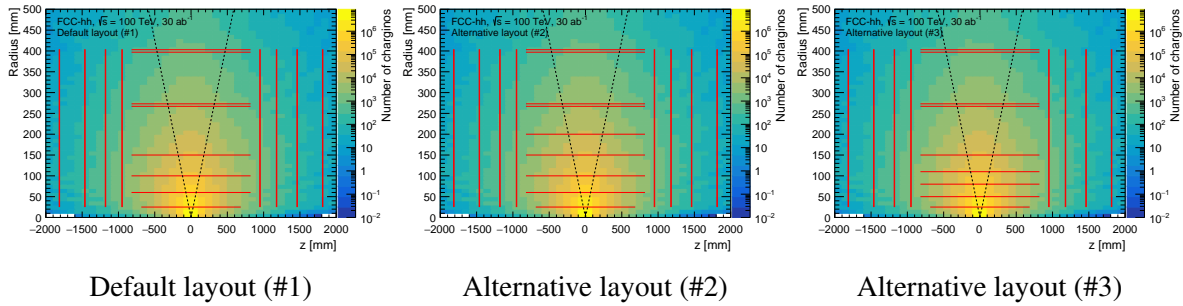


Fig. 10.30: Three barrel inner-tracker layouts considered in this study. The difference between different layouts is restricted within  $R \leq 200 \text{ mm}$  and  $|z| \leq 82 \text{ cm}$ , and the detector configuration is identical outside the region. The contour drawn behind the layouts shows the number of charginos in 3 TeV wino signal events with  $30 \text{ ab}^{-1}$  at a given  $\tilde{\chi}_1^\pm$  decay position. The analysis considers the region  $|\eta| < 1$ , denoted by the dotted lines.

increases significantly at high  $|\eta|$  due to higher hit occupancy, the analysis requires a candidate track to be within  $|\eta| < 1$

**Inner tracker layout** Three types of the tracker layout are considered in this study. The first one is the default layout (#1) containing four pixel layers within 150 mm in radial distance from the beam axis, as shown in Fig 10.30. The second and third ones are alternative layouts where a new layer is added. In the second layout (#2) the new layer is added at 200 mm to the default layout and the other layers are unchanged. In the third layout (#3) the new layer is added at 150 mm and the inner four pixel layers are moved closer to the beam line (as shown in Fig. 10.30). The radial positions of the inner pixel layers considered in the three tracker layouts are summarised in Table 10.12.

**Signal acceptance** The estimation of the signal acceptance is based on the tracker geometry and the chargino lifetime by assuming that the chargino tracks can be reconstructed with 100% efficiency if the charginos traverse at least four or five inner-most layers before decay. Table 10.13 summarises the signal acceptances for the wino and higgsino under the three scenarios of the inner-tracker layouts.

Table 10.12: Radial distances (in mm) of the first five layers from the beam line for the three inner-tracker layouts considered in this study.

Layer #	1	2	3	4	5
Default layout (#1)	25	60	100	150	270
Alternative layout (#2)	25	60	100	150	200
Alternative layout (#3)	25	50	80	110	150

Table 10.13: Signal acceptance for the 3 TeV wino and 1 TeV higgsino with  $|\eta| < 1$  for the three inner-tracker layouts. The acceptances are provided separately for the requirements of  $N_{\text{layer}}^{\text{hit}} = 4$  and 5. The alternative layout #3 has significantly higher acceptance than the others because the relevant layers are located closer to the beam line, particularly for the higgsino case with  $N_{\text{layer}}^{\text{hit}} = 5$ .

Layout	Default (#1)	Alternative (#2)	Alternative (#3)
wino ( $m_{\tilde{\chi}_1^\pm} = 3 \text{ TeV}$ )			
$N_{\text{layer}}^{\text{hit}} = 4$	2.5 %	2.5 %	4.4 %
$N_{\text{layer}}^{\text{hit}} = 5$	0.57 %	1.3 %	2.5 %
higgsino ( $m_{\tilde{\chi}_1^\pm} = 1 \text{ TeV}$ )			
$N_{\text{layer}}^{\text{hit}} = 4$	0.0043 %	0.0043 %	0.016 %
$N_{\text{layer}}^{\text{hit}} = 5$	0.00022 %	0.0011 %	0.0043 %

**Background estimation** Backgrounds are mainly categorised in two components [265]. The first one is physical background, which arises from a charged particle (electron or charged pion) scattered by the material in the inner tracker. The second one is an unphysical background, called fake-tracks, which arises from an incorrect combination of sensor hits. The two background components are evaluated separately in this study.

The rate of the physical background is estimated by scaling the background rate estimated at ATLAS [265] by the ratio of the amount of the material in the FCC tracker to that in the ATLAS inner tracker [266]. A support structure in the FCC tracker has not been defined yet, but the expected impact of particle scattering with support material is taken into account by assuming the same relative amount of tracker layer and support material measured in ATLAS. The dominant process in the physical background is  $W(\rightarrow \ell\nu)+\text{jets}$ , which has large  $E_T^{\text{miss}}$  and a high  $p_T$  track from a decay product of a W boson. Therefore, only the W+jets process is considered for the scaling of the cross section and kinematic-selection efficiency.

The fake-track rate is evaluated by counting the reconstructed tracks with good quality using simulated minimum bias events. Minimum bias events with 200 or 500 pileup collisions are simulated by GEANT4 [37]. Pileup collisions are produced with two different models of soft QCD processes. In the first model, only non-diffractive processes are considered, while in the second model the mixture of diffractive and non-diffractive processes are considered according to PYTHIA cross sections. The former model leads to more fake-track background than the latter due to the absence of diffractive events, and is used as the nominal pileup model, to be more conservative. In the track reconstruction, hits are first identified in narrow regions around nearly straight lines across the tracker layers. Second, a track is reconstructed by fitting the hits with a large curvature line. Third, a track having a large average residual is discarded. The following track quality selection is applied: high  $p_T$  ( $> 100 \text{ GeV}$ ), small  $\eta$  ( $|\eta| < 1$ ), good fit quality ( $\chi^2$ -probability  $> 0.1$ ), at least one hit on each layer and a small impact parameter ( $|d_0| < 0.05 \text{ mm}$  and  $|z_0| < 0.5 \text{ mm}$ ). To estimate the final number of fake tracks after track selection, the fake

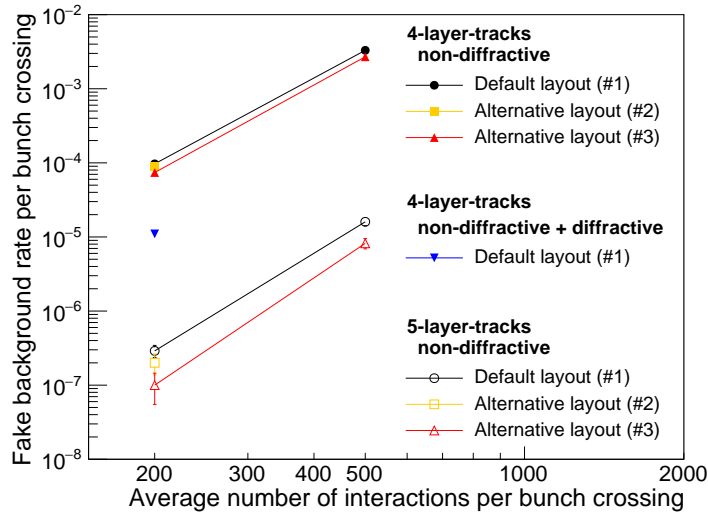


Fig. 10.31: Probability of finding a fake track in an event as a function of the  $\langle\mu\rangle$  occurring in the same event. The probabilities for the tracks reconstructed with  $N_{\text{layer}}^{\text{hit}} = 4$  (5) are shown by the filled (open) markers, and they are presented separately for the three tracker layouts: the default layout (#1) in black circles, the alternative layouts of #2 in orange squares and #3 in red upward triangles. The probabilities for the layout #2 are shown only at  $\langle\mu\rangle = 200$ . The estimate from the mixed sample of non-diffractive and diffractive events for the default layout is shown by the blue downward triangle for comparison purpose.

tracks in the MC samples with a loose impact parameter requirement ( $|d_0| < 1$  mm,  $|z_0| < 250$  mm) are counted and the estimated rate is scaled to the nominal selection ( $|d_0| < 0.05$  mm,  $|z_0| < 0.5$  mm), assuming a uniform distribution of  $d_0$  and  $z_0$ . Figure 10.31 shows the estimated probability of finding a fake track per event as a function of the number of interactions per bunch crossing ( $\langle\mu\rangle$ ). The number of fake tracks increases significantly with increasing  $\langle\mu\rangle$ . The number of fake-track background events is estimated by scaling the number of the SM background events passing the kinematic selection by this probability.

The time resolution of pixel detectors can be better than 50 ps by using, for example, low-gain avalanche detectors [267, 268]. Therefore, the time information could be used in the track fitting as an additional track parameter. The reduction of fake-track background by requiring a good fit quality (i.e. small  $\chi^2$  in the estimation of track timing using pixel hits associated to it) was estimated using minimum-bias MC samples with pile-up of 500. In the simulation, the  $x$ ,  $y$ ,  $z$  positions and the time of pp collisions are distributed randomly according to Gaussian probability-density functions with the standard deviations of 0.5 mm, 0.5 mm, 50 mm and 160 ps, respectively (without assuming any correlations among them). The  $\chi^2$  is computed assuming the constant time resolution of 50 psec for a single layer hit. The fake-track background was found to be reduced by 96% by requiring the  $\chi^2$ -probability to be larger than 0.05 for tracks reconstructed with  $N_{\text{layer}}^{\text{hit}} = 4$  when pp collisions occur in bunch crossings separated by 25 ns. The signal efficiency for this selection was estimated to be 95 % using a sample of single-muon events.

**Results** The discovery sensitivity with the requirements of  $N_{\text{layer}}^{\text{hit}} = 5$  is better than that with  $N_{\text{layer}}^{\text{hit}} = 4$ , due to the lower fake-track background yield. Figure 10.32 shows the expected discovery significance at  $30 \text{ ab}^{-1}$  with the requirement of  $N_{\text{layer}}^{\text{hit}} = 5$  in the wino (higgsino) LSP model with a lifetime of 0.2 (0.023) ns without using time information, assigning 30% systematic uncertainty on the background yields. The significance well exceeds  $5\sigma$  for the 3 TeV wino, while it is at the level of  $2\text{--}3\sigma$

for the 1 TeV higgsino when using the alternative layout (#3). On the other hand, the significance using the default layout (#1) is worse and it is lower than the discovery level. Figure 10.33 shows expected discovery sensitivities when the time information is used in the analysis. With the time information, the  $5\sigma$  discovery can be reached with sufficient margin for the 1 TeV higgsino with less than  $30 \text{ ab}^{-1}$ . The discovery sensitivities for the three tracker layouts at the pile-up scenarios of  $\langle\mu\rangle = 200$  and 500 (without time information) are summarised in Table 10.14 and 10.15, respectively.

The discovery potential for 3 TeV wino and 1 TeV higgsino at FCC-hh with a disappearing-track search has been evaluated. The FCC-hh detector will have a high discovery sensitivity both for the 3 TeV wino and 1 TeV higgsino by using optimised inner tracker design even in the high pileup environment ( $\langle\mu\rangle = 500$ ). If timing resolution of at least  $\sim 50$  psec is available in the pixel detector, such dark matter would be discovered earlier and eventually with a higher significance with the full data.

Finally, we discuss several ideas that could potentially improve the sensitivity further. The  $|\eta|$  range could be expanded from  $|\eta| < 1$  (used in the present analysis) to e.g.  $|\eta| < 4$ , to improve the overall signal acceptance, then split into smaller  $|\eta|$  regions to optimise the sensitivity. The contribution from fake tracks, that grows very rapidly with increasing  $|\eta|$ , will have to be evaluated for the determination of the  $|\eta|$  regions. By tilting the sensor modules and making overlaps between them, the charginos produced at the interaction region may pass through multiple modules in a single layer. This will potentially help improving the acceptance for a short-lifetime signal without decreasing the required number of hits in the track reconstruction, therefore without increasing the fake-track background level. Also it would be beneficial if the barrel pixel layers can be moved even closer to the beam line than the alternative layout #3. This has a large impact on the higgsino signal acceptance. Another interesting avenue to pursue is to use the speed of particles relative to the speed of light ( $\beta$ ), which can be measured using the time information of pixel hits, to reject background and characterise the observed disappearing-track signature. With the single-muon sample, the  $\beta$  resolution is found to be about 14% (with the pixel-hit time resolution of 50 ps) for the tracks with  $N_{\text{layer}}^{\text{hit}} = 5$  under the alternative tracker layouts. The estimated  $\beta$  resolution is roughly proportional to the pixel-hit time resolution. The fake-track background will be reduced by requiring the measured  $\beta$  to be compatible with a particle (produced from the primary pp collision vertex) with a certain range of momentum and mass. Because new heavy particles move more slowly in the detector than SM particles, the  $\beta$  could be used as an additional discriminant to separate the signal from scattered SM particles.

### 10.3.6 Top quark FCNC couplings

In the SM, flavor-changing neutral current (FCNC) couplings of the top quark are highly suppressed by the GIM mechanism [269] and are not detectable at current experimental sensitivity. However, they can be significantly enhanced in various SM extensions. Possible new contributions can be encoded in an effective field theory through higher-dimensional gauge-invariant operators [270, 271]. Direct limits on top quark FCNC parameters have been established by the CDF [272], D0 [273], ATLAS [274], and CMS [275] Collaborations.

#### 10.3.6.1 $tq\gamma$ coupling

**Introduction** Searches for FCNC in top quark decays have been performed in the previous experiments and no indication of FCNC  $t \rightarrow u\gamma$  and  $t \rightarrow c\gamma$  transitions were found. The most stringent upper limits at 95% CL on the  $\text{Br}(t \rightarrow u\gamma) < 0.016\%$  and  $\text{Br}(t \rightarrow c\gamma) < 0.182\%$  are set by the CMS experiment through single-top quark production in association with a photon [276]. In comparison the branching fractions for the  $t \rightarrow u\gamma$  and  $t \rightarrow c\gamma$  decays expected in the SM are approximately  $10^{-16}$  and  $10^{-14}$  respectively. Extensions of the SM predict branching fractions several orders of magnitude larger [277] and detection of these decays would therefore be a clear indication of BSM phenomena.

FCNC searches in the top quark sector are typically based on the selection of events with isolated,

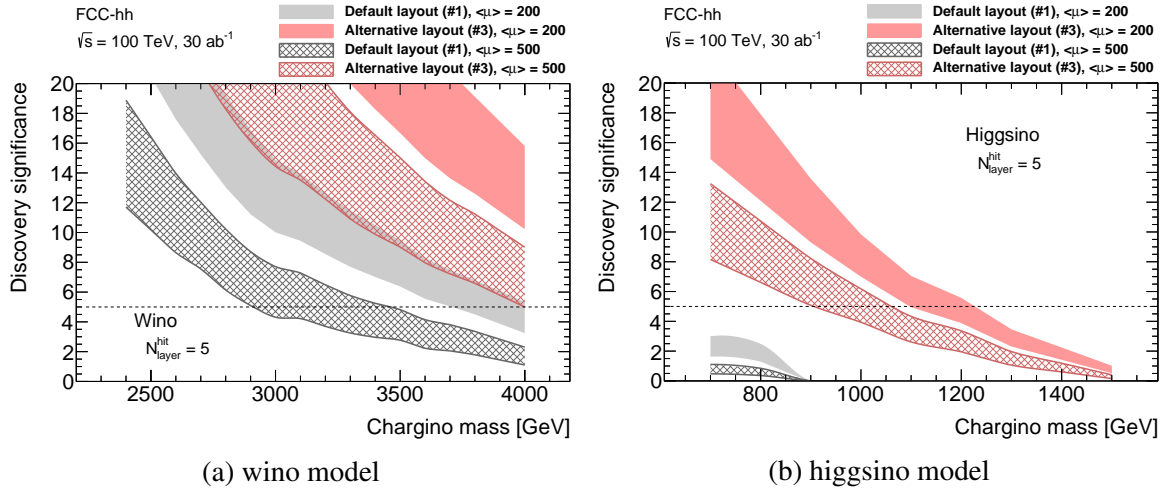


Fig. 10.32: Expected discovery significance for the (a) wino and (b) higgsino models with  $30 \text{ ab}^{-1}$  with the requirement of  $N_{\text{layer}}^{\text{hit}} = 5$ . The grey (red) bands show the significance using the default (alternative) layout #1 (#3). The difference between the solid and hatched bands corresponds to the different pile-up conditions of  $\langle\mu\rangle = 200$  and  $500$ . The band width corresponds to the significance variation due to the two models assumed for soft QCD processes.

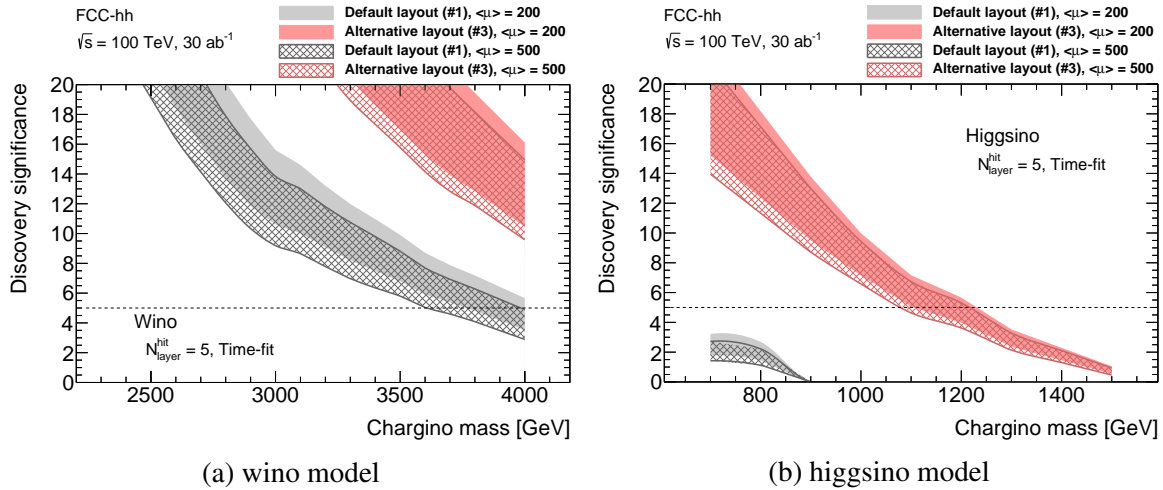


Fig. 10.33: Expected discovery significance for the (a) wino and (b) higgsino models with  $30 \text{ ab}^{-1}$  with the requirements of  $N_{\text{layer}}^{\text{hit}} = 5$  and a good time-fit quality. The background reduction rate with the time information is assumed to be the same for both pile-up conditions. The grey (red) bands show the significance using the default (alternative) layout #1 (#3). The difference between the solid and hatched bands corresponds to the different pile-up conditions of  $\langle\mu\rangle = 200$  and  $500$ . The band width corresponds to the significance variation due to the two models assumed for soft QCD processes.



Table 10.14: Signal and background yields as well as the discovery significance for the 3 TeV wino and 1 TeV higgsino with  $30 \text{ ab}^{-1}$  with the requirements of  $N_{\text{layer}}^{\text{hit}} = 5$  under the pile-up condition of  $\langle \mu \rangle = 200$ . The fake-track background rate is assumed to be same for both layouts. The kinematic selection requirements on the leading jet  $p_T$  and  $E_T^{\text{miss}}$  are also given.

Layout	Default (#1)	Alternative (#2)	Alternative (#3)
wino ( $m_{\tilde{\chi}_1^\pm} = 3 \text{ TeV}$ )			
Leading jet $p_T$ threshold [TeV]	1	1	1
$E_T^{\text{miss}}$ threshold [TeV]	4	3	2
Signal yield	28.5	86.5	287
Background yield	1.9	7.2	42.6
Significance	10.4	17.8	26.8
higgsino ( $m_{\tilde{\chi}_1^\pm} = 1 \text{ TeV}$ )			
Leading jet $p_T$ threshold [TeV]	1	1	1
$E_T^{\text{miss}}$ threshold [TeV]	1	4	4
Signal yield	2.7	6.6	19.0
Background yield	673	1.8	1.6
Significance	0.0	3.4	8.0

well separated objects. On the other hand, due to the expected increase of the energy of future collider experiments, a significant number of events will contain highly energetic, boosted objects that require an exploration of a different analysis strategy. We study the sensitivity of the FCC-hh to  $t \rightarrow q\gamma$  FCNC transition using the  $pp \rightarrow t\bar{t} \rightarrow tq\gamma$  process where  $q$  is a  $u$  or  $c$  quark. This analysis focuses on the boosted regime where the top-quark  $p_T$  is much larger than its mass and the signature of the signal processes includes high transverse momentum  $b$ -tagged fat jet and a fat jet clustered around a collinear photon and light-flavour jet.

**Monte Carlo samples** We consider the following processes as backgrounds: QCD  $\gamma$ +jets,  $t\bar{t}$ ,  $t\bar{t} + \gamma$ ,  $W + \text{jets}$ ,  $Z + \text{jets}$ , single  $t$  production and single  $t$  in association with a photon. All signals and backgrounds are generated at leading order with the MG5\_AMC@NLO 2.5.2 [185] package, showered and hadronised with PYTHIA 8.230 [102]. The detector simulation has been performed with the fast simulation tool DELPHES 3.4.2 [34] using the reference FCC-hh detector parameterisation. No pile-up is assumed in the simulation. In order to take into account higher order QCD corrections, K-factors are applied to the signal and background samples [278, 279].

**Event selection and signal extraction** Events are selected by requiring exactly one photon with  $p_T > 200 \text{ GeV}$ , at least two jets with cone  $R = 0.4$  and  $p_T > 30 \text{ GeV}$  (one of which must be  $b$ -tagged), at least two fat jets with cone  $R = 0.8$  and  $p_T > 30 \text{ GeV}$  and one or zero leptons ( $e$  or  $\mu$ ) with  $p_T > 25 \text{ GeV}$ . All objects must have  $|\eta| < 3$ . The  $\Delta R$  between selected photon and  $b$ -tagged jet should be greater than 0.8. The fat jets matching photon and  $b$ -tagged jet are required to have  $p_T > 400 \text{ GeV}$ .

A Boosted Decision Tree (BDT) constructed within the TMVA framework [280, 281] is used to separate the signal signature from the background contributions. The following input variables are used:  $\tau_{21}$  [241] of the fat jet matched to the photon ( $\gamma$ -jet),  $\tau_{21}$  and  $\tau_{32}$  of  $b$ -tagged fat jet ( $b$ -jet), masses of soft-dropped [56]  $\gamma$ -jet and  $b$ -jet,  $p_T$  of the photon,  $\gamma$ -jet and  $b$ -jet, scalar product of the photon and  $\gamma$ -jet four-vectors, scalar product of  $b$ -jet and  $\gamma$ -jet four-vectors; the masses of two soft-dropped fat jets



Table 10.15: Signal and background yields as well as the discovery significance for the 3 TeV wino and 1 TeV higgsino with  $30 \text{ ab}^{-1}$  with the requirements of  $N_{\text{layer}}^{\text{hit}} = 5$  under the pile-up condition of  $\langle \mu \rangle = 500$ . The fake-track background rate is assumed to be same for both alternative layouts. The kinematic selection requirements on the leading jet  $p_T$  and  $E_T^{\text{miss}}$  are also given.

Layout	Default (#1)	Alternative (#2)	Alternative (#3)
wino ( $m_{\tilde{\chi}_1^\pm} = 3 \text{ TeV}$ )			
Leading jet $p_T$ threshold [TeV]	1	1	1
$E_T^{\text{miss}}$ threshold [TeV]	4	4	4
Signal yield	28.5	55.7	92.6
Background yield	27.0	14.5	14.5
Significance	4.6	15.2	15.1
higgsino ( $m_{\tilde{\chi}_1^\pm} = 1 \text{ TeV}$ )			
Leading jet $p_T$ threshold [TeV]	1	2	8
$E_T^{\text{miss}}$ threshold [TeV]	1	6	8
Signal yield	2.7	3.1	4.7
Background yield	8214	1.6	0.17
Significance	0	1.8	4.5

Table 10.16: The 95% C.L. expected exclusion limits on the branching fractions and coupling strengths  $\lambda$  [282] for integrated luminosities of  $30 \text{ ab}^{-1}$  and  $3 \text{ ab}^{-1}$ .

Process	Branching fraction for $30 \text{ ab}^{-1}$ ( $3 \text{ ab}^{-1}$ )	Coupling strengths $\lambda$ for $30 \text{ ab}^{-1}$ ( $3 \text{ ab}^{-1}$ )
$t \rightarrow u\gamma$	$1.8 \cdot 10^{-7}$ ( $9.8 \cdot 10^{-7}$ )	$6.5 \cdot 10^{-4}$ ( $15.1 \cdot 10^{-4}$ )
$t \rightarrow c\gamma$	$2.4 \cdot 10^{-7}$ ( $12.9 \cdot 10^{-7}$ )	$7.5 \cdot 10^{-4}$ ( $17.3 \cdot 10^{-4}$ )

corresponds mostly to the mass of the top quark. The samples are divided into two parts: 10% of events selected for training and the remainder are used in the statistical analysis of the BDT discriminants with the CombinedLimit package. For each background a 30% normalisation uncertainty is assumed and incorporated in the statistical model as a nuisance parameter. The asymptotic frequentist formula [245] is used to obtain an expected upper limit on the signal cross section based on an Asimov data set of background-only models.

**Results and conclusions** The 95% C.L. expected exclusion limits on the branching fractions and coupling strengths [282] are given in Table 10.16. Figure 10.34 (right) shows the expected exclusion limits on the FCNC branching fractions as a function of integrated luminosity. This would improve the existing experimental limits [276] on the branching fractions by about three-four orders of magnitude.

### 10.3.6.2 $tq$ couplings

**Introduction** Processes with FCNC vertices in the decay of the top quark are negligible because the current limits to the branching fractions are about  $10^{-5}$ . In addition, the final states of such decays are difficult to distinguish from the backgrounds. This search assumes negligible contributions of the FCNC decay modes to the total width of top quark and searches for FCNC interactions in top quark production. The FCNC  $tq$  and  $tq$  interactions can be written in a model-independent form using the

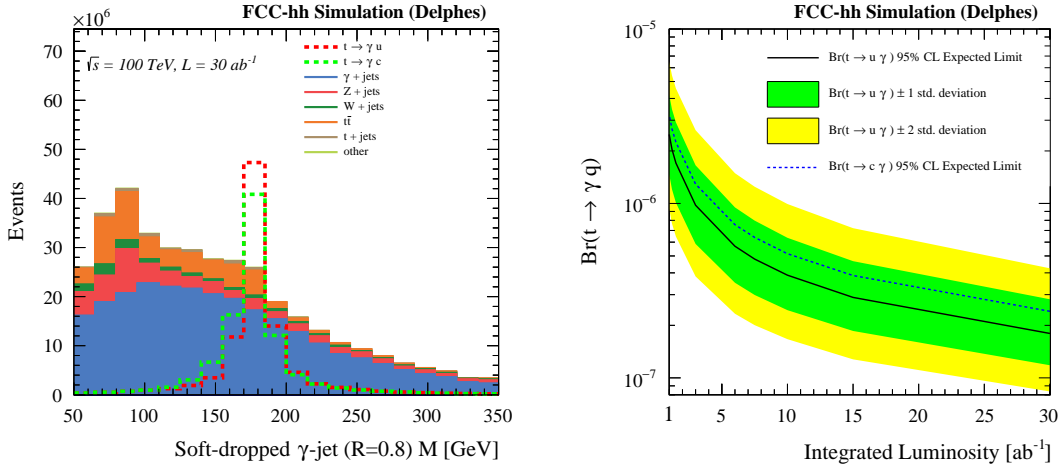


Fig. 10.34: Distribution of mass of the soft-dropped light fat jet matched to the photon with arbitrary normalisation of the signal processes for the illustration purpose (left) and expected exclusion limits at 95% C.L. on the FCNC branching fractions as a function of integrated luminosity (right).

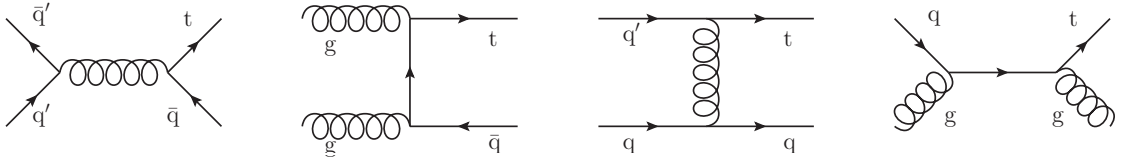


Fig. 10.35: Representative Feynman diagrams for the FCNC processes with  $tqg$  interactions ( $q=u,c$ ).

following effective Lagrangian [283]:

$$\mathcal{L} = \frac{\kappa_{tqg}}{\Lambda} g_s \bar{q} \sigma^{\mu\nu} \frac{\lambda^a}{2} t G_{\mu\nu}^a, \quad (10.3)$$

where  $\Lambda$  is the scale of new physics ( $\gtrsim 1\text{TeV}$ ),  $q$  refers to either the  $u$  or  $c$  quarks,  $\kappa_{tqg}$  defines the strength of the FCNC interactions in the  $tqg$  or  $tcg$  vertices,  $\lambda^a/2$  are the generators of the  $SU(3)$  colour gauge group,  $g_s$  is the coupling constant of the strong interaction, and  $G_{\mu\nu}^a$  is the gluon field strength tensor. The Lagrangian is assumed to be symmetric with respect to the left and right projectors. The cross section of single top quark production through FCNC interactions is proportional to  $(\kappa_{tqg}/\Lambda)^2$ .

**Monte Carlo samples** There are two complementary strategies to search for FCNC in single top quark production. A search can be performed in the  $s$ -channel for resonance production through the fusion of a gluon ( $g$ ) with an up ( $u$ ) or charm ( $c$ ) quark, as was the case in analyses by the CDF and ATLAS Collaborations. In alternative, the  $t$ -channel cross section and its corresponding kinematic properties have been measured accurately at the LHC [284–286], with an important feature being that the  $t$ -channel signature contains a light-quark jet produced in association with the single top quark. This light-quark jet can be used to search for deviations from the SM prediction caused by FCNC in the top quark sector. This strategy was applied by the D0 [273] and CMS [275] collaborations and is used in the present analysis as well. Representative Feynman diagrams for the FCNC processes are shown in Fig. 10.35.

**Monte Carlo events** The SingleTop Monte Carlo generator [287] based on the COMPHEP 4.5.2 package [288] was used to generate the signal events. The values of the LO cross sections for different

Table 10.17: The LO cross sections of the FCNC processes for different pp collision energies and values of the anomalous FCNC couplings ( $\kappa_{tqq}/\Lambda = 0.03 \text{ TeV}^{-1}$ ) with all lepton decays of the W-boson from the top quark are included.

$\sqrt{s}$ , [TeV]	FCNC tgu CS, [pb]	FCNC tgc CS, [pb]
7	33.2	4.9
8	41.7	6.7
13	91.6	18.5
14	102.8	21.4
27	268.6	71.1
100	1720.0	575.0

pp collision energies are listed in the Table 10.17. The NLO K-factors [289] of 1.52 and 1.4 for tug and tgc processes were applied to normalise to the NLO cross sections of 2614 and 805 pb for tug and tgc production, respectively. The reference tug and tgc couplings are taken as  $|\kappa_{tug}|/\Lambda = 0.03$  and  $|\kappa_{tgc}|/\Lambda = 0.03 \text{ TeV}^{-1}$  and can be quadratically rescaled to any necessary value. The backgrounds from  $t\bar{t}$  ( $4.3 \times 10^4$  pb), single top ( $7.5 \times 10^3$  pb), W+jets ( $1.6 \times 10^6$  pb) and Drell-Yan ( $5.1 \times 10^5$  pb) processes are estimated with the MG5\_AMC@NLO 2.5.2 [185] package, showered and hadronised with PYTHIA 8.230 [102]. The detector simulation has been performed with the fast simulation tool DELPHES 3.4.2 [34] using the reference FCC-hh detector parametrisation. No pile-up is included in the simulation.

**Event selection and signal extraction** We select events by requiring only one muon or electron with  $p_T > 26 \text{ GeV}$  and  $|\eta| < 2.8$  and relative isolation  $I_{\text{rel}} < 0.15$ . Events are rejected if they contain additional muons or electrons with  $p_T > 10 \text{ GeV}$ ,  $|\eta| < 2.8$ , and  $I_{\text{rel}} < 0.25$ . Events are required to have two or three jets reconstructed using the anti- $k_T$  algorithm with a distance parameter of  $R = 0.4$ , with  $p_T > 30 \text{ GeV}$  and  $|\eta| < 4.7$ . We require exactly one  $b$ -tagged jet. Simulation of the multijet background is a serious problem, and often dedicated data-driven templates are used to model it. Neither such templates nor an MC-based sample are available and the multijet background is not considered in the current analysis. However, we simulate the suppression of the QCD background by requiring  $m_T(W) = \sqrt{2p_T(\mu)E_T^{\text{miss}}(1 - \cos[\Delta\phi(\mu, \vec{p}_T^{\text{miss}})])} > 40 \text{ GeV}$ . We perform full kinematic reconstruction of the top quark and W boson candidates. For the kinematic reconstruction of the top quark, the W boson mass constraint is applied to extract the component of the neutrino momentum along the beam direction ( $p_z$ ) leading to a quadratic equation in  $p_z$ . When there are two real solutions of the equation, the smaller value of  $p_z$  is used as the solution. For events with complex solutions, the imaginary components are eliminated by modifying  $E_T^{\text{miss}}$  such that  $m_T(W) = M_W$ . The expected numbers of signal and background events are shown in Table 10.18.

The Bayesian Neural Network technique (BNN) and the slightly adapted FBM package [290, 291] are used to distinguish signal events from the SM background. The input variables for each BNN are summarised in Table 10.19. Their choice is based on the difference in the structure of the Feynman diagrams contributing to the signal and background processes [292]. The BNN discriminant distributions of all SM and FCNC processes are shown in Fig. 10.36. The shape of the neural networks discriminants are used in the statistical analysis to estimate the expected sensitivity to the contribution from FCNC. The statistical analysis is done in the conservative assumption to have 15% prior cross-section rate uncertainty for the single and pair top quark production, 30% for the  $Z/\gamma^*$ +jets and 50% for the W+jets backgrounds. These independent normalisation uncertainties are paired with additional general Gaussian blur of 15%, modelling experimental uncertainty. The uncertainties owing to finite MC statistics are taken into account with the Barlow-Beeston method [295].

Table 10.18: The predicted event yields before and after the  $m_T(W)$  requirement for integrated luminosity of  $30 \text{ ab}^{-1}$ . The given event numbers for tug and tcg processes assume a coupling values of  $|\kappa_{\text{tug}}|/\Lambda = 0.03$  and  $|\kappa_{\text{tcg}}|/\Lambda = 0.03 \text{ TeV}^{-1}$ .

Process	Basic selections	$m_T(W) > 40 \text{ GeV}$
FCNC tcg	3,036,000,000	2,320,000,000
FCNC tug	7,710,000,000	5,560,000,000
Single Top	10,223,000,000	7,934,000,000
$t\bar{t}$	39,517,000,000	30,617,000,000
W+jets	28,709,000,000	23,588,000,000
Z/ $\gamma^*$ +jets	2,591,000,000	1,031,000,000

Table 10.19: Input variables for the BNNs used in the analysis. The symbol X represents the variables used for each particular BNN. The notations ‘leading’ and ‘next-to-leading’ refer to the highest- $p_T$  and second-highest- $p_T$  jet, respectively. The notation ‘best’ jet is used for the jet that gives a reconstructed mass of the top quark closest to the value of 172.5 GeV, which is used in the MC simulation.

Variable	Description	tug FCNC BNN	tcg FCNC BNN
$p_T(j_1)$	$p_T$ of the leading jet	X	X
$p_T(j_2)$	$p_T$ of the leading jet	X	X
$p_T(j_1, j_2)$	Vector sum of the $p_T$ of the leading and the next-to-leading jet	X	X
$p_T(j_L)$	$p_T$ of the light-flavour jet (untagged jet with the highest value of $ \eta $ )	X	X
$p_T(j_{\text{not best}})$	$p_T$ of the all jets without one, best to reconstruct the top quark	X	X
$p_T(\text{lep})$	$p_T$ of the lepton	X	X
$p_T(\text{top})_{b_1}$	$p_T$ of the top quark reconstructed with leading c jet (the b-tagged jet with the highest $p_T$ )	X	X
$H_T(j)$	Scalar sum of the $p_T$ of the all jets	X	X
$\eta(\text{lep})$	$\eta$ of the lepton	X	X
$\eta(j_L)$	$\eta$ of the light-flavour jet	X	X
$m(j)$	The invariant mass of the all jets	X	X
$m(j, W)$	The invariant mass of the W boson and all jets	X	X
$m(\text{top})_{b_1}$	The invariant mass of the top quark reconstructed with leading c jet	X	X
$N(j)$	The number of the selected jets	X	X
$\cos(\theta_{\text{lep}, j_L}) _{\text{top}}$	The cosine of the angle between the lepton and the light-flavour jet in the top quark rest frame, for top quark reconstructed with the leading c jet [293]	X	X
$\cos(\theta_{\text{lep}, W}) _W$	The cosine of the angle between the lepton momentum in the W boson rest frame and the direction of the W boson boost vector [294]	X	X
$Q(\text{lep})$	Charge of the lepton	X	

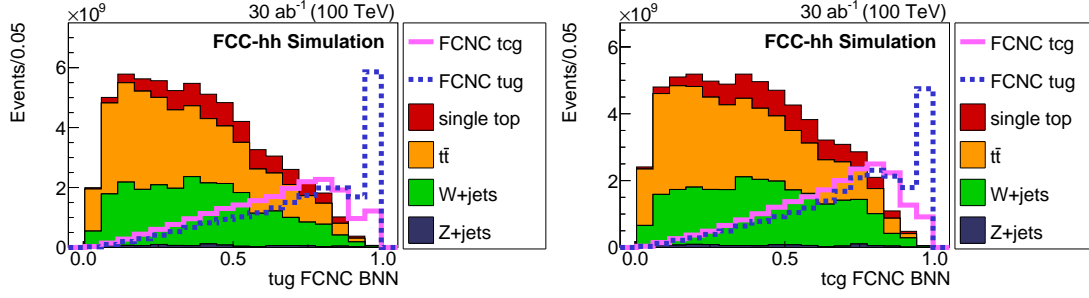


Fig. 10.36: The FCNC BNN discriminant distributions to distinguish FCNC tug (left) or tcg (right) processes from the SM contribution. The solid and dashed lines of FCNC production corresponds a coupling values of  $|\kappa_{\text{tug}}|/\Lambda = 0.06$  and  $|\kappa_{\text{tcg}}|/\Lambda = 0.09 \text{ TeV}^{-1}$ .

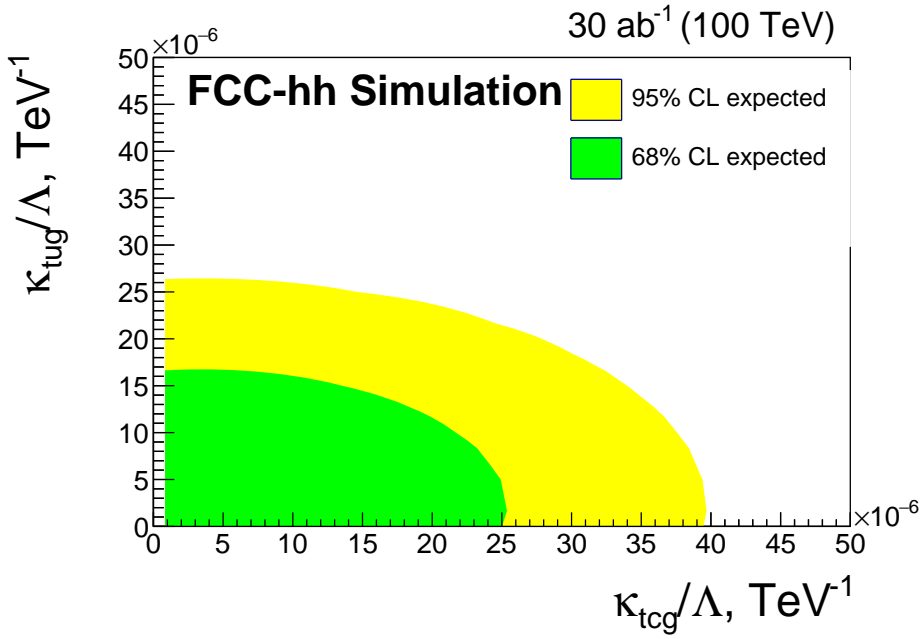


Fig. 10.37: Two-dimensional expected limits on the FCNC couplings at 68% and 95% C.L. for an integrated luminosity of  $30 \text{ ab}^{-1}$ .

**Results and conclusions** A direct search for model-independent FCNC  $|\kappa_{\text{tug}}|/\Lambda$  and  $|\kappa_{\text{tcg}}|/\Lambda$  couplings of the tug and tcg interactions has been projected for FCC pp collisions at  $\sqrt{s} = 100 \text{ TeV}$ . To obtain the individual exclusion limits on  $|\kappa_{\text{tug}}|/\Lambda$  and  $|\kappa_{\text{tcg}}|/\Lambda$  we assume the presence of only one corresponding FCNC parameter in the FCNC signal Monte-Carlo model. The 95% C.L. expected exclusion limits on the coupling strengths are  $|\kappa_{\text{tug}}|/\Lambda < 2.2 \times 10^{-5} \text{ TeV}^{-1}$  and  $|\kappa_{\text{tcg}}|/\Lambda < 3.3 \times 10^{-5} \text{ TeV}^{-1}$  for the integrated luminosity of  $30 \text{ ab}^{-1}$ . The corresponding limits on branching fractions [289] are  $\mathcal{B}(t \rightarrow ug) < 5.8 \cdot 10^{-10}$  and  $\mathcal{B}(t \rightarrow cg) < 1.3 \cdot 10^{-9}$  which demonstrate about five orders of magnitude improvement in comparison with existing limits [275] on the branching fractions of rare FCNC top quark decays. The two-dimensional contours that reflect the possible simultaneous presence of both FCNC parameters are shown in Fig. 10.37. In this case both FCNC couplings are implemented in the FCNC signal Monte-Carlo model.

# Cost goals, strategic R&D

---

## 11.1 Cost goals

The FCC-hh reference detector is to a large extent based on technologies that are employed in the LHC detectors and their upgrades. For the magnet system, calorimetry, muon system and for tracker radii larger than 40 cm from the beam axis these represent viable solutions. Research and development is needed for the improvement of granularity and the verification of the adequate rate capability and radiation hardness. For tracker radii smaller than 40 cm there is at this moment no technology that is capable of handling the large amount of radiation and a significant R&D is needed on this topic.

For the existing technologies we can, therefore, relate the cost to the LHC experiments, while the absence of a viable technology for the vertex tracker makes the estimate of this component difficult. The cost estimates are given according to the ‘core cost’ definition for the LHC experiment technical design reports.

The estimated cost of the magnet system, consisting of the main solenoid, two forward solenoids, cryostats and support structures together with the cryogenics system, and power supply, is 350 MCHF. The complete liquid argon calorimeter system is estimated at 220 MCHF. The barrel and endcap HCAL is estimated at 30 MCHF, while 200 MCHF is the assumed cost for the silicon tracker and beampipe vacuum system. Further, it is assumed that the muon system and the trigger and DAQ system will cost 100 MCHF each. This leads to an overall cost of about 1000 MCHF, a value that is about twice that for ATLAS and CMS as defined around the year 2000. The FCC-hh reference detector is similar to the LHC detectors in the overall scale, but in terms of channel numbers and readout data rates, it is significantly more challenging. This estimate, therefore, already assumes significant economies for the readout electronics as a result of performance improvements in the silicon world.

## 11.2 Detector research and development

The key challenge for an FCC-hh detector is of course the vertex tracker at radii smaller than 40 cm where no sufficiently radiation hard technology exists for the sensor, front-end electronics and optical readout. The question of how to read out the enormous data volume in this high radiation environment, while still keeping the detector material at an absolute minimum level, is, therefore, crucial.

Timing at the 5 ps level is also an R&D challenge. For the HL-LHC the goal is to achieve 25 ps time resolution with LGAD and SiPM technology. Pushing the performance to 5 ps is a serious challenge, not only in terms of sensor resolution, but also in terms of the readout and calibration system.

For the liquid argon calorimetry, the question of how to read out the required granularity, through dedicated PCBs and feedthroughs, is an important R&D challenge. The proposed geometry of inclined plates differs from the ATLAS accordion geometry and, therefore, needs prototyping and testing. For the

scintillator calorimeter, SiPMs are very interesting devices that allow economic high granularity readout.

The size and stored energy of the magnet system goes significantly beyond the LHC experiments. The technology is however conventional and the system, therefore, mainly represents a sizeable engineering challenge.

The rates in the muon system allow the use of present day gas detectors over most of its surface. Only the rates in the inner part of the forward muon system at radii of less than 1 m, which exceed those in the present day LHC muon systems and Micropattern detectors or silicon detectors, have to be considered.

The activation of the detector material poses stringent limits on the access to the detector for maintenance. The design of the detector, therefore, has to include automated opening scenarios, automated insertion of radiation shielding infrastructure as well as deployment of robotic systems for remote operations.

All the above-mentioned technologies represent natural developments of those employed at the LHC. With the significant timescale of the FCC-hh detector there is time to develop alternative ideas and technologies. An ultra-thin cryostat and magnet coil in front of the calorimeter system could represent a very economic detector system. Large-scale monolithic silicon sensors, produced using commercial CMOS technology, can also be a game changer for the performance and the cost of the tracker system.

It is important to conduct these developments in line with the further exploitation of the LHC and related upgrades of the LHC detectors, which will naturally lead towards the required performance for the FCC-hh.



---

# Bibliography

---

- [1] A. Abada *et al.*, FCC physics opportunities: Future Circular Collider conceptual design report Volume 1, *Eur. Phys. J. C*, **79**(6):474, 2019, doi: [10.1140/epjc/s10052-019-6904-3](https://doi.org/10.1140/epjc/s10052-019-6904-3).
- [2] A. Abada *et al.*, FCC-ee: The Lepton Collider: Future Circular Collider conceptual design report Volume 2, *Eur. Phys. J. ST*, **228**(2):261–623, 2019, doi: [10.1140/epjst/e2019-900045-4](https://doi.org/10.1140/epjst/e2019-900045-4).
- [3] M. Benedikt *et al.*, FCC-hh: The Hadron Collider: Future Circular Collider conceptual design report Volume 3, *Eur. Phys. J. ST*, **228**(4):755–1107, 2019, doi: [10.1140/epjst/e2019-900087-0](https://doi.org/10.1140/epjst/e2019-900087-0).
- [4] T. Golling *et al.*, Physics at a 100 TeV pp collider: beyond the Standard Model phenomena, *CERN Yellow Rep. Monogr.*, **3/2017**:441–634, 2017, doi: [10.23731/CYRM-2017-003.441](https://doi.org/10.23731/CYRM-2017-003.441).
- [5] R. Contino *et al.*, Physics at a 100 TeV pp collider: Higgs and EW symmetry breaking studies, *CERN Yellow Rep. Monogr.*, **3/2017**:255–440, 2017, doi: [10.23731/CYRM-2017-003.255](https://doi.org/10.23731/CYRM-2017-003.255).
- [6] M. L. Mangano, G. Ortona, and M. Selvaggi, Measuring the Higgs self-coupling via Higgs-pair production at a 100 TeV p-p collider, *Eur. Phys. J. C*, **80**:1030, 2020, doi: [10.1140/epjc/s10052-020-08595-3](https://doi.org/10.1140/epjc/s10052-020-08595-3).
- [7] G. F. Giudice, T. Han, K. Wang, and L.-T. Wang, Nearly degenerate gauginos and dark matter at the LHC, *Phys. Rev. D*, **81**:115011, 2010, doi: [10.1103/PhysRevD.81.115011](https://doi.org/10.1103/PhysRevD.81.115011).
- [8] P. Schwaller and J. Zurita, Compressed electroweakino spectra at the LHC, *JHEP*, **03**:060, 2014, doi: [10.1007/JHEP03\(2014\)060](https://doi.org/10.1007/JHEP03(2014)060).
- [9] Z. Han, G. D. Kribs, A. Martin, and A. Menon, Hunting quasidegenerate Higgsinos, *Phys. Rev. D*, **89**(7):075007, 2014, doi: [10.1103/PhysRevD.89.075007](https://doi.org/10.1103/PhysRevD.89.075007).
- [10] N. Arkani-Hamed, A. Gupta, D. E. Kaplan, *et al.*, Simply unnatural supersymmetry, *arXiv:1212.6971 [hep-ph]*, 12 2012, doi: [10.48550/arXiv.1212.6971](https://doi.org/10.48550/arXiv.1212.6971).
- [11] J. L. Feng, T. Moroi, L. Randall, *et al.*, Discovering supersymmetry at the Tevatron in wino LSP scenarios, *Phys. Rev. Lett.*, **83**:1731–1734, 1999, doi: [10.1103/PhysRevLett.83.1731](https://doi.org/10.1103/PhysRevLett.83.1731).
- [12] A. Falkowski, J. T. Ruderman, T. Volansky, and J. Zupan, Hidden Higgs decaying to lepton jets, *JHEP*, **05**:077, 2010, doi: [10.1007/JHEP05\(2010\)077](https://doi.org/10.1007/JHEP05(2010)077).
- [13] J. A. Evans and J. Shelton, Long-lived staus and displaced leptons at the LHC, *JHEP*, **04**:056, 2016, doi: [10.1007/JHEP04\(2016\)056](https://doi.org/10.1007/JHEP04(2016)056).
- [14] M. J. Strassler and K. M. Zurek, Echoes of a hidden valley at hadron colliders, *Phys. Lett. B*, **651**:374–379, 2007, doi: [10.1016/j.physletb.2007.06.055](https://doi.org/10.1016/j.physletb.2007.06.055).
- [15] M. Mangano *et al.*, Physics at a 100 TeV pp collider: Standard Model processes, *CERN Yellow Rep. Monogr.*, **3/2017**:1–254, 2017, doi: [10.23731/CYRM-2017-003.1](https://doi.org/10.23731/CYRM-2017-003.1).
- [16] CMS Collaboration, The Phase-2 Upgrade of the CMS tracker, CERN-LHCC-2017-009, CMS-TDR-014, CERN, Geneva, Jun 2017, doi: [10.17181/CERN.QZ28.FLHW](https://doi.org/10.17181/CERN.QZ28.FLHW).

- [17] L. Borgonovi, S. Braibant, B. D. Micco, *et al.*, Higgs measurements at FCC-hh, CERN-ACC-2018-0045, CERN, Geneva, Oct 2018, <https://cds.cern.ch/record/2642471>.
- [18] C. Helsens and M. Selvaggi, Search for high-mass resonances at FCC-hh, CERN-ACC-2019-0028, CERN, Geneva, Oct 2018, <https://cds.cern.ch/record/2642473>.
- [19] C. Helsens, D. Jamin, M. L. Mangano, *et al.*, Heavy resonances at energy-frontier hadron colliders, *Eur. Phys. J. C*, **79**(2):569, 2019, doi: 10.1140/epjc/s10052-019-7062-3.
- [20] T. Carli, C. Helsens, A. Henriques Correia, and C. Solans Sánchez, Containment and resolution of hadronic showers at the FCC, *JINST*, **11**(09):P09012, 2016, doi: 10.1088/1748-0221/11/09/P09012.
- [21] M. Selvaggi, A Delphes parameterisation of the FCC-hh detector, CERN-FCC-PHYS-2020-0003, CERN, Geneva, May 2020, <https://cds.cern.ch/record/2717698>.
- [22] C. H. Yeh, S. V. Chekanov, A. V. Kotwal, *et al.*, Studies of granularity of a hadronic calorimeter for tens-of-TeV jets at a 100 TeV  $pp$  collider, *JINST*, **14**(05):P05008, 2019, doi: 10.1088/1748-0221/14/05/P05008.
- [23] E. Perez Codina and P. G. Roloff, Hit multiplicity approach to b-tagging in FCC-hh, CERN-ACC-2018-0023, CERN, Geneva, Jul 2018, <https://cds.cern.ch/record/2631478>.
- [24] H. Brooks and P. Skands, Average event properties from LHC to FCC-hh, *Eur. Phys. J. C*, **78**:963, 2018, doi: 10.1140/epjc/s10052-018-6460-2.
- [25] J. Alwall, R. Frederix, S. Frixione, *et al.*, The automated computation of tree-level and next-to-leading order differential cross sections, and their matching to parton shower simulations, *JHEP*, **07**:079, 2014, doi: 10.1007/JHEP07(2014)079.
- [26] A. Ferrari, P. R. Sala, A. Fasso, and J. Ranft, FLUKA: A multi-particle transport code (Program version 2005), CERN-2005-010, SLAC-R-773, INFN-TC-05-11, CERN, Geneva, 2005, doi: 10.5170/CERN-2005-010.
- [27] G. Battistoni *et al.*, Overview of the FLUKA code, *Annals Nucl. Energy*, **82**:10–18, 2015, doi: 10.1016/j.anucene.2014.11.007.
- [28] V. Boccone *et al.*, Beam-machine Interaction at the CERN LHC, *Nucl. Data Sheets*, **120**:215–218, 2014, doi: 10.1016/j.nds.2014.07.050.
- [29] M. Besana, F. Cerutti, A. Ferrari, *et al.*, Evaluation of the radiation field in the future circular collider detector, *Phys. Rev. Accel. Beams*, **19**(11):111004, 2016, doi: 10.1103/PhysRevAccelBeams.19.111004.
- [30] S. Roesler, R. Engel, and J. Ranft, The Monte Carlo event generator DPMJET-III, in *Advanced Monte Carlo for radiation physics, particle transport simulation and applications. Proc. Monte Carlo 2000 Conf., Lisbon, Portugal, 23–26 Oct. 2000*, pp. 1033–1038, 2000, doi: 10.1007/978-3-642-18211-2\_166.
- [31] A. Fedynitch and R. Engel, Revision of the high energy hadronic interaction models PHOJET/DPMJET-III, in *Proc. 14th Int. Conf. on Nuclear Reaction Mechanisms, Villa Monastero, Varenna, Italy, 15–19 Jun. 2015*, pp. 291–299, 2015, <https://cds.cern.ch/record/2115393>.
- [32] M. Cattaneo *et al.*, Status of the GAUDI event-processing framework, in *CHEP 2001: Proc. Int. Conf. on Computing in High Energy and Nuclear Physics*, 2001, <https://inspirehep.net/literature/2088868>.
- [33] F. Gaede, B. Hegner, and P. Mato, PODIO: An event-data-model toolkit for high energy physics experiments, *J. Phys. Conf. Ser.*, **898**:072039. 6 p, 2017, doi: 10.1088/1742-6596/898/7/072039.

- [34] J. de Favereau, C. Delaere, P. Demin, *et al.*, DELPHES 3, A modular framework for fast simulation of a generic collider experiment, *JHEP*, **02**:057, 2014, doi: [10.1007/JHEP02\(2014\)057](https://doi.org/10.1007/JHEP02(2014)057).
- [35] J. Allison *et al.*, Recent developments in GEANT4, *Nucl. Instrum. Meth. A*, **835**:186–225, 2016, doi: [10.1016/j.nima.2016.06.125](https://doi.org/10.1016/j.nima.2016.06.125).
- [36] J. Allison *et al.*, GEANT4 developments and applications, *IEEE Trans. Nucl. Sci.*, **53**:270, 2006, doi: [10.1109/TNS.2006.869826](https://doi.org/10.1109/TNS.2006.869826).
- [37] S. Agostinelli *et al.*, GEANT4: A simulation toolkit, *Nucl. Instrum. Meth. A*, **506**:250, 2003, doi: [10.1016/S0168-9002\(03\)01368-8](https://doi.org/10.1016/S0168-9002(03)01368-8).
- [38] A. A. Alves, Jr. *et al.*, The LHCb Detector at the LHC, *JINST*, **3**:S08005, 2008, doi: [10.1088/1748-0221/3/08/S08005](https://doi.org/10.1088/1748-0221/3/08/S08005).
- [39] M. Frank, F. Gaede, C. Grefe, and P. Mato, DD4hep: A Detector Description Toolkit for High Energy Physics Experiments, *J. Phys. Conf. Ser.*, **513**:022010, 2014, doi: [10.1088/1742-6596/513/2/022010](https://doi.org/10.1088/1742-6596/513/2/022010).
- [40] H. J. Drescher, M. Hladik, S. Ostapchenko, *et al.*, Parton based Gribov-Regge theory, *Phys. Rept.*, **350**:93–289, 2001, doi: [10.1016/S0370-1573\(00\)00122-8](https://doi.org/10.1016/S0370-1573(00)00122-8).
- [41] W. Lukas, Fast simulation for ATLAS: Atfast-II and ISF, *J. Phys. Conf. Ser.*, **396**(2):022031, 2012, doi: [10.1088/1742-6596/396/2/022031](https://doi.org/10.1088/1742-6596/396/2/022031).
- [42] M. Selvaggi, Delphes 3: Latest developments, *J. Phys. Conf. Ser.*, **762**:012051, Oct 2016, doi: [10.1088/1742-6596/762/1/012051](https://doi.org/10.1088/1742-6596/762/1/012051).
- [43] S. Mersi, D. Abbaneo, N. De Maio, and G. Hall, Software package for the characterization of Tracker layouts, in *Proc. 13th ICATPP Conf. on Astroparticle, Particle, Space Physics and Detectors for Physics Applications (ICATPP 2011)*, pp. 1015–24, 2012, doi: [10.1142/9789814405072\\_0153](https://doi.org/10.1142/9789814405072_0153).
- [44] G. Grindhammer and S. Peters, The Parameterized simulation of electromagnetic showers in homogeneous and sampling calorimeters, in *Int. Conf. on Monte Carlo Simulation in High-Energy and Nuclear Physics - MC 93 Tallahassee, Florida, February 22-26, 1993*, 1993, doi: [10.48550/arXiv.hep-ex/0001020](https://doi.org/10.48550/arXiv.hep-ex/0001020).
- [45] A. Zaborowska, Geant4 fast and full simulation for Future Circular Collider studies, *J. Phys. Conf. Ser.*, **898**:042053, 2017, doi: [10.1088/1742-6596/898/4/042053](https://doi.org/10.1088/1742-6596/898/4/042053).
- [46] A. Salzburger, Optimisation of the ATLAS Track Reconstruction Software for Run-2, *J. Phys. Conf. Ser.*, **664**(7):072042, May 2015, doi: [10.1088/1742-6596/664/7/072042](https://doi.org/10.1088/1742-6596/664/7/072042).
- [47] C. Gumpert *et al.*, ACTS: from ATLAS software towards a common track reconstruction software, *J. Phys. Conf. Ser.*, **898**(4):042011, 2017, doi: [10.1088/1742-6596/898/4/042011](https://doi.org/10.1088/1742-6596/898/4/042011).
- [48] R. Brun and F. Rademakers, ROOT—An object oriented data analysis framework, *Nucl. Instrum. Meth. A*, **389**:81–86, 1997, doi: [10.1016/S0168-9002\(97\)00048-X](https://doi.org/10.1016/S0168-9002(97)00048-X).
- [49] Delphes releases, <https://github.com/delphes/delphes/releases>.
- [50] FCCSW—Software for the Future Circular Collider: FCC-hh detector DELPHES card, <http://hep-fcc.github.io/FCCSW/>, last accessed 24 May 2022.
- [51] M. Selvaggi, Physics requirements for the FCC-hh calorimeter system, *J. Phys. Conf. Ser.*, **1162**(1):012010, 2019, doi: [10.1088/1742-6596/1162/1/012010](https://doi.org/10.1088/1742-6596/1162/1/012010).
- [52] A. M. Sirunyan *et al.*, Particle-flow reconstruction and global event description with the CMS detector, *JINST*, **12**(10):P10003, 2017, doi: [10.1088/1748-0221/12/10/P10003](https://doi.org/10.1088/1748-0221/12/10/P10003).
- [53] M. Cacciari, G. P. Salam, and G. Soyez, FastJet User Manual, *Eur. Phys. J. C*, **72**:1896, 2012, doi: [10.1140/epjc/s10052-012-1896-2](https://doi.org/10.1140/epjc/s10052-012-1896-2).
- [54] M. Cacciari, G. P. Salam, and G. Soyez, The anti- $k_t$  jet clustering algorithm, *JHEP*, **04**:063, 2008, doi: [10.1088/1126-6708/2008/04/063](https://doi.org/10.1088/1126-6708/2008/04/063).

- [55] J. Thaler and K. Van Tilburg, Identifying boosted objects with N-subjettiness, *JHEP*, **03**:015, 2011, doi: [10.1007/JHEP03\(2011\)015](https://doi.org/10.1007/JHEP03(2011)015).
- [56] A. J. Larkoski, S. Marzani, G. Soyez, and J. Thaler, Soft drop, *JHEP*, **05**:146, 2014, doi: [10.1007/JHEP05\(2014\)146](https://doi.org/10.1007/JHEP05(2014)146).
- [57] M. Mentink *et al.*, Evolution of the conceptual fcc-hh baseline detector magnet design, *IEEE Trans. Appl. Supercond.*, **28**:1–10, 2017, doi: [10.1109/TASC.2017.2782708](https://doi.org/10.1109/TASC.2017.2782708).
- [58] M. Mentink *et al.*, FCC-hh detector magnet, Presentation at the FCC Week 2017, Berlin, Germany (2017), <https://indico.cern.ch/event/556692/contributions/2465157>.
- [59] A. Yamamoto *et al.*, ATLAS superconducting solenoid: Conceptual design report, ATLAS Internal Note, TECH-NO-020, KEK, Tsukuba, 1996, doi: [10.17181/CERN.5WIZ.HMJA](https://doi.org/10.17181/CERN.5WIZ.HMJA).
- [60] ATLAS Collaboration, ATLAS magnet system: Technical design report, 1, CERN-LHCC-97-018, CERN, Geneva, 1997, doi: [10.17181/CERN.905C.VDTM](https://doi.org/10.17181/CERN.905C.VDTM).
- [61] J. P. Badiou, J. Beltramelli, J. M. Baze, and J. Belorgey, ATLAS barrel toroid: Technical Design Report, CERN-LHCC-97-019, CERN, Geneva, 1997, doi: [10.17181/CERN.RF2A.CP5T](https://doi.org/10.17181/CERN.RF2A.CP5T).
- [62] ATLAS Collaboration, ATLAS end-cap toroids: Technical Design Report, CERN-LHCC-97-020, CERN, Geneva, 1997, doi: [10.17181/CERN.P03D.WQLV](https://doi.org/10.17181/CERN.P03D.WQLV).
- [63] ATLAS Collaboration, ATLAS central solenoid: Technical Design Report, CERN-LHCC-97-021, CERN, Geneva, 1997, doi: [10.17181/CERN.ZZVJ.2JYE](https://doi.org/10.17181/CERN.ZZVJ.2JYE).
- [64] G. Acquistapace *et al.*, CMS, the magnet project: Technical design report, CERN-LHCC-97-10, CMS-TDR-1, CERN, Geneva, 1997, doi: [10.17181/CERN.6ZU0.V4T9](https://doi.org/10.17181/CERN.6ZU0.V4T9).
- [65] L. Rossi, G. Volpini, C. Berriaud, *et al.*, Progress on the conductor for the superconducting toroids of the ATLAS experiment, *IEEE Trans. Appl. Supercond.*, **10**(1):369–372, 2000, doi: [10.1109/77.828250](https://doi.org/10.1109/77.828250).
- [66] B. Blau *et al.*, The CMS conductor, *IEEE Trans. Appl. Supercond.*, **12**(1):345–348, 2002, doi: [10.1109/TASC.2002.1018416](https://doi.org/10.1109/TASC.2002.1018416).
- [67] C. Berriaud, A. Dudarev, A. Gaddi, *et al.*, Preliminary conductor layouts for the detector magnets of the Future Circular Collider, *IEEE Trans. Appl. Supercond.*, **26**(4):4802305, 2016, doi: [10.1109/TASC.2016.2537651](https://doi.org/10.1109/TASC.2016.2537651).
- [68] T. Kulenkampff *et al.*, Development of conductors for thin solenoids for ultra radiation-transparent detector magnets, Presentation at MT25, Amsterdam, the Netherlands (2017), <https://indico.cern.ch/event/445667/contributions/2678596/>.
- [69] V. Ilardi *et al.*, Development of thin, highly radiation transparent cryostats for the detector magnets of the Future Circular Collider, Presentation at ICEC/ICMC2018, Oxford, UK (2018), <https://indico.stfc.ac.uk/event/2/contributions/161/>.
- [70] H. ten Kate, Detector magnets study for a 100 TeV proton-proton collider, Presentation at ICEC25-ICMC2014, Enschede, the Netherlands (2014), <https://indico.cern.ch/event/244641/contributions/1563325/>.
- [71] H. ten Kate *et al.*, Concepts for detectors magnets for a 100 TeV proton-proton collider, Presentation at FCC Kickoff Meeting, Geneva, Switzerland (2014), <https://indico.cern.ch/event/282344/contributions/1630776/>.
- [72] H. ten Kate, Principle design demonstration of the twin solenoid detector magnet, option 2, for a 100 TeV proton-proton collider, Presentation at FCC Kickoff Meeting, Geneva, Switzerland (2014), <https://indico.cern.ch/event/282344/contributions/1630776/>.
- [73] H. ten Kate, Superconducting detector magnets for the 100 TeV Future Circular Collider, Presentation at MT24, Seoul, South Korea (2015), <https://indico.cern.ch/event/727555/contributions/3431121/>.

- [74] H. ten Kate, Detector Magnets for the 100 TeV Future Circular Collider, a first look, Presentation at EUCAS2015, Lyon, France (2015).
- [75] M. Mentink *et al.*, Design of a 56-GJ Twin Solenoid and Dipoles Detector Magnet System for the Future Circular Collider, *IEEE Trans. Appl. Supercond.*, **26**(3):4003506, 2016, doi: [10.1109/TASC.2016.2528988](https://doi.org/10.1109/TASC.2016.2528988).
- [76] H. ten Kate *et al.*, Detector magnets for the 100 TeV future circular p-p collider (FCC-hh), Presentation at CEC-ICMC2015, Tucson, USA (2015), <https://indico.cern.ch/event/344330/contributions/806384/>.
- [77] H. ten Kate *et al.*, Superconducting detector magnets for the 100 TeV Future Circular Collider (FCC-hh), Presentation at ICEC26-ICMC2016, New Delhi, India (2016).
- [78] H. ten Kate *et al.*, Detector magnets for the Future Circular Collider - evolution and new baseline design, Presentation at CEC-ICMC2017, Madison, USA (2017), <https://indico.cern.ch/event/578092/contributions/2538209/>.
- [79] H. ten Kate *et al.*, Detector magnets for the Future Circular Collider - evolution and new baseline design, Presentation at MT25, Amsterdam, the Netherlands (2017), <https://indico.cern.ch/event/445667/contributions/2561791/>.
- [80] H. ten Kate *et al.*, FCC-hh detector magnets - requirements and options, Presentation at the FCC Week 2015, Washington, USA (2015), <https://indico.cern.ch/event/340703/contributions/802200>.
- [81] H. ten Kate *et al.*, FCC-hh detector magnets design study, Presentation at the FCC Week 2016, Rome, Italy (2016), <https://indico.cern.ch/event/438866/contributions/1084958/>.
- [82] M. Mentink *et al.*, Magnet options - forward dipoles vs. forward solenoids, Presentation at the FCC Week 2016, Rome, Italy (2016), <https://indico.cern.ch/event/438866/contributions/1085181/>.
- [83] H. Pais da Silva *et al.*, FCC-hh detector - integration and opening-closing scenarios, Presentation at the FCC Week 2017, Berlin, Germany (2017), <https://indico.cern.ch/event/556692/contributions/2592515/>.
- [84] E. Bielert *et al.*, FCC-hh detector magnet - baseline and options, Presentation at the FCC Week 2018, Amsterdam, the Netherlands (2018), <https://indico.cern.ch/event/656491/contributions/2939178/>.
- [85] M. Mentink, A. Dudarev, T. Mulder, *et al.*, Quench Protection of Very Large, 50-GJ-Class, and High-Temperature-Superconductor-Based Detector Magnets, *IEEE Trans. Appl. Supercond.*, **26**(4):4500608, 2016, doi: [10.1109/TASC.2015.2510078](https://doi.org/10.1109/TASC.2015.2510078).
- [86] M. Mentink *et al.*, Iron-free detector magnet options for the future circular collider, *Phys. Rev. Accel. Beams*, **19**:111001, 2016, doi: [10.1103/PhysRevAccelBeams.19.111001](https://doi.org/10.1103/PhysRevAccelBeams.19.111001).
- [87] M. Mentink, H. Pais Da Silva, A. Dudarev, *et al.*, Design of 4 Tm forward dipoles for the FCC-hh detector Magnet System, *IEEE Trans. Appl. Supercond.*, **27**(4):4500306, 2017, doi: [10.1109/TASC.2017.2658951](https://doi.org/10.1109/TASC.2017.2658951).
- [88] V. I. Klyukhin *et al.*, Superconducting magnet with the reduced barrel yoke for the Hadron Future Circular Collider, in *Proc. 2015 IEEE Nuclear Science Symp. and Medical Imaging Conf. (NSS/MIC 2015): San Diego, California, United States, 31 Oct.–7 Nov. 2015*, p. 7581877, 2015, doi: [10.1109/NSSMIC.2015.7581877](https://doi.org/10.1109/NSSMIC.2015.7581877).
- [89] V. I. Klyukhin *et al.*, Superconducting magnet with a minimal steel yoke for the Future Circular Collider detector, *J. Supercond. Nov. Mag.*, **30**:2309–2313, 2017, doi: [10.1007/s10948-016-3660-6](https://doi.org/10.1007/s10948-016-3660-6).
- [90] E. R. Bielert *et al.*, Design of the optional forward superconducting dipole magnet for the FCC-hh detector, *IEEE Trans. Appl. Supercond.*, **28**(4):4500204, 2018, doi: [10.1109/TASC.2018.2813535](https://doi.org/10.1109/TASC.2018.2813535).



- [91] U. Wagner, Conceptual design of cryogenics for the FCC-hh detector magnet system, Internal note FCC-INF-RPT-0067 v.1, CERN, Geneva, Switzerland, <https://edms.cern.ch/document/2747847/1>.
- [92] M. Morpurgo, A large superconducting dipole cooled by forced circulation of two phase helium, *Cryogenics*, **19**:411–414, 1979, doi: 10.1016/0011-2275(79)90126-7.
- [93] W. Riegler *et al.*, FCC-hh detector and experiments CDR outline and status, Presentation at the FCC Week 2017, Berlin, Germany (2017), <https://indico.cern.ch/event/556692/contributions/2483417/>.
- [94] V. Klyukhin, A. Ball, C. Berriaud, *et al.*, Comparison of the baseline and the minimal steel yoke superconducting magnets for the Future Circular Hadron-Hadron Collider, , CERN, Geneva, Jan. 2022, doi: 10.48550/arXiv.2201.07101, Pres. 6th Int. Conf. on Superconductivity and Magnetism (ICSM2018), 29 Apr.–4 May 2018, Antalya Turkey.
- [95] H. ten Kate *et al.*, Ultra-light 2T/4m bore detector solenoid for FCC-ee, Presentation at the FCC Week 2018, Amsterdam, the Netherlands (2018), <https://indico.cern.ch/event/656491/contributions/2939122/>.
- [96] G. Aad *et al.*, The ATLAS Experiment at the CERN Large Hadron Collider, *JINST*, **3**:S08003, 2008, doi: 10.1088/1748-0221/3/08/S08003.
- [97] S. Chatrchyan *et al.*, The CMS Experiment at the CERN LHC, *JINST*, **3**:S08004, 2008, doi: 10.1088/1748-0221/3/08/S08004.
- [98] L. Linssen, A. Miyamoto, M. Stanitzki, and H. Weerts, Physics and Detectors at CLIC: CLIC Conceptual Design Report, *CERN Yellow Rep.*, **3**, 2012, doi: 10.5170/CERN-2012-003.
- [99] G. Bianchi, tkLayout: a design tool for innovative silicon tracking detectors, *JINST*, **9**:C03054, 2014, doi: 10.1088/1748-0221/9/03/C03054.
- [100] G. Bianchi *et al.*, tkLayout-lite SW: Github repository of a tkLayout version adapted for FCC-hh needs, 2017, <https://github.com/tkLayout/tkLayout/tree/masterLite>.
- [101] Wolfram Research, Inc., Champaign, IL, Mathematica, Version 11.2, 2018, <https://reference.wolfram.com/legacy/language/v11.2/>, last accessed 31 May 2022.
- [102] T. Sjöstrand, S. Ask, J. R. Christiansen, *et al.*, An Introduction to PYTHIA 8.2, *Comput. Phys. Commun.*, **191**:159–177, 2015, doi: 10.1016/j.cpc.2015.01.024.
- [103] W. J. Fawcett, A. Sfyrla, and G. Iacobucci, A self-seeded track trigger for the FCC-hh, CERN-ACC-2018-0046, CERN, Geneva, Oct 2018, <https://cds.cern.ch/record/2645273>.
- [104] M. Petric, M. Frank, F. Gaede, *et al.*, Detector simulations with DD4hep, *J. Phys. Conf. Ser.*, **898**(4):042015, 2017, doi: 10.1088/1742-6596/898/4/042015.
- [105] N. Graf and J. McCormick, Simulator for the linear collider (SLIC): A tool for ILC detector simulations, *AIP Conf. Proc.*, **867**:503–512, 2006, doi: 10.1063/1.2396991.
- [106] N. A. Graf, org.lcsim: Event reconstruction in Java, *J. Phys. Conf. Ser.*, **331**:032012, 2011, doi: 10.1088/1742-6596/331/3/032012.
- [107] E. Perez Codina and P. G. Roloff, Tracking and flavour tagging at FCC-hh, CERN-ACC-2018-0027, CERN, Geneva, Aug 2018, <https://cds.cern.ch/record/2635893>.
- [108] M. A. Thomson, Particle flow calorimetry and the PandoraPFA algorithm, *Nucl. Instrum. Meth. A*, **611**:25–40, 2009, doi: 10.1016/j.nima.2009.09.009.
- [109] J. S. Marshall and M. A. Thomson, The Pandora software development kit for pattern recognition, *Eur. Phys. J. C*, **75**(9):439, 2015, doi: 10.1140/epjc/s10052-015-3659-3.
- [110] T. Suehara and T. Tanabe, LCFIPlus: A framework for jet analysis in linear collider studies, *Nucl. Instrum. Meth. A*, **808**:109–116, 2016, doi: 10.1016/j.nima.2015.11.054.

- [111] A. Zaborowska, GEANT4 fast and full simulation for Future Circular Collider studies, *J. Phys. : Conf. Ser.*, **898**(4):042053, 2017, doi: [10.1088/1742-6596/898/4/042053](https://doi.org/10.1088/1742-6596/898/4/042053).
- [112] J. Hrdinka, *Tracker performance studies at the 100 TeV future circular hadron collider at extreme pile-up conditions*, PhD thesis, TU Wien, 2019, doi: [10.34726/hss.2019.36084](https://doi.org/10.34726/hss.2019.36084).
- [113] C. Gumpert, A. Salzburger, M. Kiehn, *et al.*, ACTS: from ATLAS software towards a common track reconstruction software, ATL-SOFT-PROC-2017-030. 4, CERN, Geneva, 01 2017, <https://cds.cern.ch/record/2243297>.
- [114] V. Völkl, Tricktrack: An experiment-independent, cellular-automaton based track seeding library, 2018, doi: [10.5281/zenodo.6618944](https://doi.org/10.5281/zenodo.6618944).
- [115] Z. Drasal *et al.*, Official FCC-hh tracker layout repository: Tracker in flat configuration - v3.03, 2017, [http://fcc-tklayout.web.cern.ch/fcc-tklayout/FCChh\\_v3.03/index.html](http://fcc-tklayout.web.cern.ch/fcc-tklayout/FCChh_v3.03/index.html).
- [116] Z. Drasal *et al.*, Official FCC-hh tracker layout repository: Tracker in tilted configuration - v4.01, 2017, [http://fcc-tklayout.web.cern.ch/fcc-tklayout/FCChh\\_v4.01/index.html](http://fcc-tklayout.web.cern.ch/fcc-tklayout/FCChh_v4.01/index.html).
- [117] Z. Drasal and W. Riegler, An extension of the Gluckstern formulae for multiple scattering: Analytic expressions for track parameter resolution using optimum weights, *Nucl. Instrum. Meth. A*, **910**:127–132, 2018, doi: [10.1016/j.nima.2018.08.078](https://doi.org/10.1016/j.nima.2018.08.078).
- [118] Z. Drasal, The Basics of Tracking Formalism by GLS Method: An Application to Optimal Design of Tracking Detectors, in preparation, 2018.
- [119] ATLAS Collaboration, Technical Design Report for the ATLAS Inner Tracker Pixel Detector, CERN-LHCC-2017-021. ATLAS-TDR-030, CERN, Geneva, Sep 2017, doi: [10.17181/CERN.FOZZ.ZP3Q](https://doi.org/10.17181/CERN.FOZZ.ZP3Q).
- [120] G. Bianchi *et al.*, CMS phase 2 tracker layout repository, 2017, <http://cms-tklayout.web.cern.ch/cms-tklayout/layouts/repository-git-master>.
- [121] E. Perez Codina and P. G. Roloff, Initial study of the reconstruction of boosted B-hadrons and  $\tau$ -leptons at FCC-hh, CERN-ACC-2018-0035, CERN, Geneva, Oct 2018, <https://cds.cern.ch/record/2643897>.
- [122] S. Fartoukh, Pile up management at the high-luminosity LHC and introduction to the crab-kissing concept, *Phys. Rev. ST Accel. Beams*, **17**(11):111001, 2014, doi: [10.1103/PhysRevSTAB.17.111001](https://doi.org/10.1103/PhysRevSTAB.17.111001).
- [123] B. T. Huffman, C. Jackson, and J. Tseng, Tagging  $b$  quarks at extreme energies without tracks, *J. Phys. G*, **43**(8):085001, 2016, doi: [10.1088/0954-3899/43/8/085001](https://doi.org/10.1088/0954-3899/43/8/085001).
- [124] B. T. Huffman, T. Russell, and J. Tseng, Tagging  $b$  quarks without tracks using an Artificial Neural Network algorithm, *arXiv:1701.06832 [hep-ex]*, 2017, doi: [10.48550/arXiv.1701.06832](https://doi.org/10.48550/arXiv.1701.06832).
- [125] N. Alipour Tehrani and P. Roloff, Optimisation Studies for the CLIC Vertex-Detector Geometry, CLICdp-Note-2014-002, CERN, Geneva, 7 2014, <https://cds.cern.ch/record/1742993>.
- [126] ATLAS Collaboration, Optimisation and performance studies of the ATLAS  $b$ -tagging algorithms for the 2017-18 LHC run, ATL-PHYS-PUB-2017-013, CERN, Geneva, 2017, <http://cds.cern.ch/record/2273281>.
- [127] M. Aaboud *et al.*, Performance of the ATLAS track reconstruction algorithms in dense environments in LHC Run 2, *Eur. Phys. J. C*, **77**(10):673, 2017, doi: [10.1140/epjc/s10052-017-5225-7](https://doi.org/10.1140/epjc/s10052-017-5225-7).
- [128] J. Troska, Talk: Optical Link Technology @ FCC Week in Berlin, 29 May 2017 to 2 June 2017, 2017, <https://indico.cern.ch/event/556692/contributions/2611072>.
- [129] M. Aaboud *et al.*, Performance of the ATLAS Trigger System in 2015, *Eur. Phys. J. C*, **77**(5):317, 2017, doi: [10.1140/epjc/s10052-017-4852-3](https://doi.org/10.1140/epjc/s10052-017-4852-3).



- [130] A. Clark *et al.*, Final Report: ATLAS Phase-2 Tracker Upgrade Layout Task Force, ATL-UPGRADE-PUB-2012-004, CERN, Geneva, Oct 2012, <https://cds.cern.ch/record/1482960>.
- [131] CMS Collaboration, The Phase-2 Upgrade of the CMS Endcap Calorimeter, CERN-LHCC-2017-023. CMS-TDR-019, CERN, Geneva, Nov 2017, doi: 10.17181/CERN.IV8M.1JY2.
- [132] J. Repond *et al.*, Hadronic Energy Resolution of a Combined High Granularity Scintillator Calorimeter System, *JINST*, **13**(12):P12022, 2018, doi: 10.1088/1748-0221/13/12/P12022.
- [133] ATLAS and CMS Collaborations, Addendum to the report on the physics at the HL-LHC, and perspectives for the HE-LHC: Collection of notes from ATLAS and CMS, *CERN Yellow Rep. Monogr.*, **7**:Addendum, 2019, doi: 10.23731/CYRM-2019-007.Addendum.
- [134] ATLAS Collaboration, ATLAS liquid-argon calorimeter: Technical Design Report, CERN-LHCC-96-041, CERN, Geneva, 1996, doi: 10.17181/CERN.FWRW.FOOQ.
- [135] H. Zumbahlen, *Linear circuit design handbook*, Elsevier, Burlington, MA, 2008, <https://cds.cern.ch/record/1520867>.
- [136] ATLAS Collaboration, Technical Design Report for the Phase-II Upgrade of the ATLAS LAr Calorimeter, CERN-LHCC-2017-018. ATLAS-TDR-027, CERN, Geneva, Sep 2017, doi: 10.17181/CERN.6QIO.YGHO.
- [137] M. Aharrouche *et al.*, Study of the response of ATLAS electromagnetic liquid argon calorimeters to muons, *Nucl. Instrum. Meth. A*, **606**:419–431, 2009, doi: 10.1016/j.nima.2009.05.021.
- [138] ATLAS Collaboration, *ATLAS tile calorimeter: Technical Design Report*, Technical Design Report ATLAS, CERN, Geneva, 1996, doi: 10.17181/CERN.JRBJ.7028.
- [139] H. Jivan, B. Mellado, E. Sideras-Haddad, *et al.*, Radiation hardness of plastic scintillators for the Tile Calorimeter of the ATLAS detector, *J. Phys. Conf. Ser.*, **623**(1):012016, 2015, doi: 10.1088/1742-6596/623/1/012016.
- [140] A. Heering, Y. Musienko, R. Ruchti, *et al.*, Effects of very high radiation on SiPMs, *Nucl. Instrum. Meth. A*, **824**:111–114, 2016, doi: 10.1016/j.nima.2015.11.037.
- [141] J. Abdallah *et al.*, The optical instrumentation of the ATLAS tile calorimeter, *JINST*, **8**(01):P01005–P01005, 2013, doi: 10.1088/1748-0221/8/01/p01005.
- [142] D. Pont™, Tyvek®, <http://www.dupont.com/products-and-services/fabrics-fibers-nonwovens/protective-fabrics/brands/tyvek.html>.
- [143] G. Aad *et al.*, Readiness of the ATLAS Tile Calorimeter for LHC collisions, *Eur. Phys. J. C*, **70**:1193–1236, 2010, doi: 10.1140/epjc/s10052-010-1508-y.
- [144] J. S. Schliwinski, Light response study of FCC-hh plastic-scintillator tiles with SiPM readout, *CERN-STUDENTS-Note-2019-136*, 2019, <https://cds.cern.ch/record/2687718>.
- [145] P. Adragna *et al.*, Testbeam studies of production modules of the ATLAS tile calorimeter, *Nucl. Instrum. Meth. A*, **606**:362–394, 2009, doi: 10.1016/j.nima.2009.04.009.
- [146] FCCSW: FCC software, common to FCC-hh, -ee, and -eh, <https://github.com/HEP-FCC/FCCSW>, last accessed 1 June 2022.
- [147] DD4hep, a detector description toolkit for high energy physics, <https://dd4hep.web.cern.ch/dd4hep/>, last accessed 1 June 2022.
- [148] R. Craun and D. Smith, Analysis of response data for several organic scintillators, *Nucl. Instrum. Meth.*, **80**(2):239 – 244, 1970, doi: 10.1016/0029-554X(70)90768-8.
- [149] W. Lampl *et al.*, Calorimeter clustering algorithms: Description and performance, ATL-LARG-PUB-2008-002. ATL-COM-LARG-2008-003, CERN, Geneva, Apr 2008, <https://cds.cern.ch/record/1099735>.

- [150] G. Aad *et al.*, Topological cell clustering in the ATLAS calorimeters and its performance in LHC Run 1, *Eur. Phys. J. C*, **77**:490, 2017, doi: [10.1140/epjc/s10052-017-5004-5](https://doi.org/10.1140/epjc/s10052-017-5004-5).
- [151] S. Baffioni, C. de La Taille, D. Fournier, *et al.*, Electrical measurements on the ATLAS electromagnetic barrel calorimeter, ATL-LARG-PUB-2007-005, ATL-COM-LARG-2006-009, CERN, Geneva, 2006, <http://cds.cern.ch/record/986702>.
- [152] K. Fukushima, A neural network for visual pattern recognition, *IEEE Computer*, **21**(3):65–75, 1988, doi: [10.1109/2.32](https://doi.org/10.1109/2.32).
- [153] K. Fukushima, Increasing robustness against background noise: Visual pattern recognition by a neocognitron, *Neural Networks*, **24**(7):767–778, 2011, doi: [10.1016/j.neunet.2011.03.017](https://doi.org/10.1016/j.neunet.2011.03.017).
- [154] K. Fukushima, S. Miyake, and T. Ito, Neocognitron: A neural network model for a mechanism of visual pattern recognition, *IEEE Trans. Systems, Man, and Cybernetics*, **13**(5):826–834, 1983, doi: [10.1109/TSMC.1983.6313076](https://doi.org/10.1109/TSMC.1983.6313076).
- [155] Y. LeCun, B. E. Boser, J. S. Denker, *et al.*, Backpropagation applied to handwritten zip code recognition, *Neural Computation*, **1**(4):541–551, 1989, doi: [10.1162/neco.1989.1.4.541](https://doi.org/10.1162/neco.1989.1.4.541).
- [156] Y. LeCun, B. E. Boser, J. S. Denker, *et al.*, Handwritten digit recognition with a back-propagation network, in *Advances in Neural Information Processing Systems 2, [NIPS Conference, Denver, Colorado, USA, November 27-30, 1989]*, pp. 396–404, 1989, <https://dl.acm.org/doi/10.5555/109230.109279>.
- [157] Y. LeCun, P. Haffner, L. Bottou, and Y. Bengio, Object recognition with gradient-based learning, in *Shape, Contour and Grouping in Computer Vision*, p. 319, 1999, doi: [10.1007/3-540-46805-6\\_19](https://doi.org/10.1007/3-540-46805-6_19).
- [158] K. He, X. Zhang, S. Ren, and J. Sun, Deep residual learning for image recognition, *arXiv:1512.03385 [cs.CV]*, 2015, doi: [10.48550/arXiv.1512.03385](https://doi.org/10.48550/arXiv.1512.03385).
- [159] F. Chollet *et al.*, Keras, <https://keras.io>, 2015, last accessed 2 June 2022.
- [160] M. Abadi *et al.*, TensorFlow: Large-scale machine learning on heterogeneous systems, *arXiv:1603.04467 [cs.DC]*, 2016, <https://arxiv.org/abs/1603.04467>.
- [161] D. P. Kingma and J. Ba, Adam: A method for stochastic optimization, *arXiv:1412.6980 [cs.LG]*, 2014, doi: [10.48550/arXiv.1412.6980](https://doi.org/10.48550/arXiv.1412.6980).
- [162] P. J. Huber, Robust estimation of a location parameter, *Ann. Math. Statist.*, **35**(1):73–101, 1964, doi: [10.1214/aoms/1177703732](https://doi.org/10.1214/aoms/1177703732).
- [163] G. Aad *et al.*, Expected performance of the ATLAS experiment—Detector, trigger and physics, SLAC-R-980, CERN-OPEN-2008-020, CERN, Geneva, 2009, doi: [10.48550/arXiv.0901.0512](https://doi.org/10.48550/arXiv.0901.0512).
- [164] ATLAS Collaboration, Technical proposal: A high-granularity timing detector for the ATLAS Phase-II upgrade, CERN-LHCC-2018-023. LHCC-P-012, CERN, Geneva, Jun 2018, doi: [10.17181/CERN.CIUJ.KS4H](https://doi.org/10.17181/CERN.CIUJ.KS4H).
- [165] CMS Collaboration, Technical proposal for a MIP timing detector in the CMS experiment Phase 2 upgrade, CERN-LHCC-2017-027. LHCC-P-009, CERN, Geneva, Dec 2017, doi: [10.17181/CERN.2RSJ.UE8W](https://doi.org/10.17181/CERN.2RSJ.UE8W).
- [166] P. Barria, The CMS ECAL upgrade for precision crystal calorimetry at the HL-LHC, CMS-CR-2017-162, CERN, Geneva, Jun 2017, <http://cds.cern.ch/record/2273277>.
- [167] Z. Ajaltouni *et al.*, Results from a combined test of an electromagnetic liquid argon calorimeter with a hadronic scintillating tile calorimeter, *Nucl. Instrum. Meth. A*, **387**:333–351, 1997, doi: [10.1016/S0168-9002\(97\)00075-2](https://doi.org/10.1016/S0168-9002(97)00075-2).
- [168] ATLAS Collaboration, Pile-up subtraction and suppression for jets in ATLAS, ATLAS-CONF-2013-083, CERN, Geneva, 2013, <https://cds.cern.ch/record/1570994>.

- [169] D. Bertolini, P. Harris, M. Low, and N. Tran, Pileup Per Particle Identification, *JHEP*, **10**:059, 2014, doi: [10.1007/JHEP10\(2014\)059](https://doi.org/10.1007/JHEP10(2014)059).
- [170] C. Neubüser, C. Helsens, Jet sub-structure studies of highly boosted topologies at the FCC-hh experiment, *soon available*, 2019.
- [171] M. Aaboud *et al.*, Jet energy scale measurements and their systematic uncertainties in proton-proton collisions at  $\sqrt{s} = 13$  TeV with the ATLAS detector, *Phys. Rev.*, **D96**(7):072002, 2017, doi: [10.1103/PhysRevD.96.072002](https://doi.org/10.1103/PhysRevD.96.072002).
- [172] J. Repond *et al.*, Design and Electronics Commissioning of the Physics Prototype of a Si-W Electromagnetic Calorimeter for the International Linear Collider, *JINST*, **3**:P08001, 2008, doi: [10.1088/1748-0221/3/08/P08001](https://doi.org/10.1088/1748-0221/3/08/P08001).
- [173] S. Collaboration, N. Watson, *et al.*, DESY PRC Report, , DESY, Hamburg, Oct 2009, <http://www.hep.ph.imperial.ac.uk/calice/official/091105prc/spider.pdf>.
- [174] M. Inaba, T. Chujo, and M. Hirano, Development of the FoCal-E PAD detector and its electronics for the ALICE experiment at the LHC, *Nucl. Instrum. Meth. A*, **824**:299–301, 2016, doi: [10.1016/j.nima.2015.10.055](https://doi.org/10.1016/j.nima.2015.10.055).
- [175] M. Munker, M. Benoit, D. Dannheim, *et al.*, Simulations of CMOS pixel sensors with a small collection electrode, improved for a faster charge collection and increased radiation tolerance, *JINST*, **14**:C05013, 2019, doi: [10.1088/1748-0221/14/05/C05013](https://doi.org/10.1088/1748-0221/14/05/C05013).
- [176] T. Price, *Digital calorimetry for future  $e^+e^-$  colliders and their impact on the precision measurement of the top Higgs Yukawa coupling*, PhD thesis, Birmingham U., 2013, <http://etheses.bham.ac.uk/id/eprint/4515>.
- [177] T. Price, Maps technology for vertexing, tracking, and calorimetry, *Physics Procedia*, **37**:932–939, 2012, doi: [10.1016/j.phpro.2012.02.437](https://doi.org/10.1016/j.phpro.2012.02.437).
- [178] I. Kopsalis, First tests of a reconfigurable depleted MAPS sensor for digital electromagnetic calorimetry, *Nucl. Instrum. Meth. A*, **958**:162654, 2020, doi: [10.1016/j.nima.2019.162654](https://doi.org/10.1016/j.nima.2019.162654).
- [179] T. Price, Silicon ECal for FCC-hh, Presentation at the FCC Week 2018, Amsterdam, Netherlands, 2018, <https://indico.cern.ch/event/656491/contributions/2939182/>.
- [180] M. L. Mangano, M. Moretti, F. Piccinini, *et al.*, ALPGEN, a generator for hard multiparton processes in hadronic collisions, *JHEP*, **07**:001, 2003, doi: [10.1088/1126-6708/2003/07/001](https://doi.org/10.1088/1126-6708/2003/07/001).
- [181] J. M. Campbell and R. K. Ellis, An update on vector boson pair production at hadron colliders, *Phys. Rev.*, **D60**:113006, 1999, doi: [10.1103/PhysRevD.60.113006](https://doi.org/10.1103/PhysRevD.60.113006).
- [182] ATLAS Collaboration, Technical Design Report for the Phase-II Upgrade of the ATLAS TDAQ System, CERN-LHCC-2017-020, ATLAS-TDR-029, CERN, Geneva, Sep 2017, doi: [10.17181/CERN.2LBB.4IAL](https://doi.org/10.17181/CERN.2LBB.4IAL).
- [183] CMS Collaboration, The Phase-2 Upgrade of the CMS L1 Trigger Interim Technical Design Report, CERN-LHCC-2017-013, CMS-TDR-017, CERN, Geneva, Sep 2017, doi: [10.17181/CERN.CZTV.E00A](https://doi.org/10.17181/CERN.CZTV.E00A).
- [184] J. Duarte *et al.*, Fast inference of deep neural networks in FPGAs for particle physics, *JINST*, **13**(07):P07027, 2018, doi: [10.1088/1748-0221/13/07/P07027](https://doi.org/10.1088/1748-0221/13/07/P07027).
- [185] J. Alwall, M. Herquet, F. Maltoni, *et al.*, MadGraph 5 : Going beyond, *JHEP*, **06**:128, 2011, doi: [10.1007/JHEP06\(2011\)128](https://doi.org/10.1007/JHEP06(2011)128).
- [186] M. Mangano (ed), Physics at the FCC-hh, a 100 TeV pp collider, *CERN Yellow Rep.*, **3/2017**, 2017, doi: [10.23731/CYRM-2017-003](https://doi.org/10.23731/CYRM-2017-003).
- [187] G. Aad *et al.*, Observation of a new particle in the search for the Standard Model Higgs boson with the ATLAS detector at the LHC, *Phys. Lett. B*, **716**:1–29, 2012, doi: [10.1016/j.physletb.2012.08.020](https://doi.org/10.1016/j.physletb.2012.08.020).

- [188] S. Chatrchyan *et al.*, Observation of a new boson at a mass of 125 GeV with the CMS experiment at the LHC, *Phys. Lett.*, **B716**:30–61, 2012, doi: [10.1016/j.physletb.2012.08.021](https://doi.org/10.1016/j.physletb.2012.08.021).
- [189] CMS Collaboration, Projected performance of Higgs analyses at the HL-LHC for ECFA 2016, CMS-PAS-FTR-16-002, CERN, Geneva, 2017, <https://cds.cern.ch/record/2266165>.
- [190] ATLAS Collaboration, Projections for measurements of Higgs boson signal strengths and coupling parameters with the ATLAS detector at a HL-LHC, ATL-PHYS-PUB-2014-016, CERN, Geneva, Oct 2014, doi: [10.17181/CERN.B5WP.VPT7](https://doi.org/10.17181/CERN.B5WP.VPT7).
- [191] J. Alwall, R. Frederix, S. Frixione, *et al.*, Comparative study of various algorithms for the merging of parton showers and matrix elements in hadronic collisions, *Eur. Phys. J. C*, **53**:473, 2008, doi: [10.1140/epjc/s10052-007-0490-5](https://doi.org/10.1140/epjc/s10052-007-0490-5).
- [192] B. Mellado Garcia, P. Musella, M. Grazzini, and R. Harlander, CERN Report 4: Part I Standard Model Predictions, LHCHSWG-DRAFT-INT-2016-008, CERN, Geneva, May 2016, <https://cds.cern.ch/record/2150771>.
- [193] C. Anastasiou, C. Duhr, F. Dulat, *et al.*, Higgs boson gluon-fusion production in QCD at three loops, *Phys. Rev. Lett.*, **114**:212001, 2015, doi: [10.1103/PhysRevLett.114.212001](https://doi.org/10.1103/PhysRevLett.114.212001).
- [194] A. M. Sirunyan *et al.*, Measurements of Higgs boson properties in the diphoton decay channel in proton-proton collisions at  $\sqrt{s} = 13$  TeV, *JHEP*, **11**:185, 2018, doi: [10.1007/JHEP11\(2018\)185](https://doi.org/10.1007/JHEP11(2018)185).
- [195] A. M. Sirunyan *et al.*, Observation of  $t\bar{t}H$  production, *Phys. Rev. Lett.*, **120**:231801, 2018, doi: [10.1103/PhysRevLett.120.231801](https://doi.org/10.1103/PhysRevLett.120.231801).
- [196] M. Aaboud *et al.*, Observation of Higgs boson production in association with a top quark pair at the LHC with the ATLAS detector, *Phys. Lett. B*, **784**:173–191, 2018, doi: [10.1016/j.physletb.2018.07.035](https://doi.org/10.1016/j.physletb.2018.07.035).
- [197] M. L. Mangano, T. Plehn, P. Reimitz, *et al.*, Measuring the Top Yukawa Coupling at 100 TeV, *J. Phys. G*, **43**(3):035001, 2016, doi: [10.1088/0954-3889/43/3/035001](https://doi.org/10.1088/0954-3889/43/3/035001).
- [198] A. M. Sirunyan *et al.*, Search for Higgs boson pair production in events with two bottom quarks and two tau leptons in proton–proton collisions at  $\sqrt{s} = 13$  TeV, *Phys. Lett. B*, **778**:101–127, 2018, doi: [10.1016/j.physletb.2018.01.001](https://doi.org/10.1016/j.physletb.2018.01.001).
- [199] CMS Collaboration, Prospects for HH measurements at the HL-LHC, CMS-PAS-FTR-18-019, CERN, Geneva, 2018, <https://cds.cern.ch/record/2652549>.
- [200] S. Banerjee, C. Englert, M. L. Mangano, *et al.*,  $hh + \text{jet}$  production at 100 TeV, *Eur. Phys. J. C*, **78**(4):322, 2018, doi: [10.1140/epjc/s10052-018-5788-y](https://doi.org/10.1140/epjc/s10052-018-5788-y).
- [201] J. K. Behr, D. Bortoletto, J. A. Frost, *et al.*, Boosting Higgs pair production in the  $b\bar{b}b\bar{b}$  final state with multivariate techniques, *Eur. Phys. J. C*, **76**:386, 2016, doi: [10.1140/epjc/s10052-016-4215-5](https://doi.org/10.1140/epjc/s10052-016-4215-5).
- [202] D. E. Ferreira de Lima, A. Papaefstathiou, and M. Spannowsky, Standard model Higgs boson pair production in the  $(b\bar{b})(b\bar{b})$  final state, *JHEP*, **08**:030, 2014, doi: [10.1007/JHEP08\(2014\)030](https://doi.org/10.1007/JHEP08(2014)030).
- [203] R. A. Gerosa, Vector boson scattering prospects for High-Luminosity LHC at CMS in the same sign WW final state, CMS-CR-2015-219, CERN, Geneva, Oct 2015, <http://cds.cern.ch/record/2058229>.
- [204] D. London and J. L. Rosner, Extra gauge bosons in  $E_6$ , *Phys. Rev. D*, **34**:1530, 1986, doi: [10.1103/PhysRevD.34.1530](https://doi.org/10.1103/PhysRevD.34.1530).
- [205] A. Joglekar and J. L. Rosner, Searching for signatures of  $E_6$ , *Phys. Rev.*, **D96**(1):015026, 2017, doi: [10.1103/PhysRevD.96.015026](https://doi.org/10.1103/PhysRevD.96.015026).
- [206] P. Langacker, The physics of heavy  $Z'$  gauge bosons, *Rev. Mod. Phys.*, **81**:1199–1228, 2009, doi: [10.1103/RevModPhys.81.1199](https://doi.org/10.1103/RevModPhys.81.1199).

- [207] E. Salvioni, G. Villadoro, and F. Zwirner, Minimal Z-prime models: Present bounds and early LHC reach, *JHEP*, **11**:068, 2009, doi: [10.1088/1126-6708/2009/11/068](https://doi.org/10.1088/1126-6708/2009/11/068).
- [208] R. M. Harris and K. Kousouris, Searches for Dijet Resonances at Hadron Colliders, *Int. J. Mod. Phys.*, **A26**:5005–5055, 2011, doi: [10.1142/S0217751X11054905](https://doi.org/10.1142/S0217751X11054905).
- [209] N. Boelaert and T. Åkesson, Dijet angular distributions at  $\sqrt{s} = 14$  TeV, *Eur. Phys. J. C*, **66**:343–357, 2010, doi: [10.1140/epjc/s10052-010-1268-8](https://doi.org/10.1140/epjc/s10052-010-1268-8).
- [210] T. D. Lee, A theory of spontaneous T violation, *Phys. Rev.*, **D8**:1226–1239, 1973, doi: [10.1103/PhysRevD.8.1226](https://doi.org/10.1103/PhysRevD.8.1226).
- [211] G. C. Branco, P. M. Ferreira, L. Lavoura, *et al.*, Theory and phenomenology of two-Higgs-doublet models, *Phys. Rept.*, **516**:1–102, 2012, doi: [10.1016/j.physrep.2012.02.002](https://doi.org/10.1016/j.physrep.2012.02.002).
- [212] C. T. Hill, Topcolor assisted technicolor, *Phys. Lett.*, **B345**:483–489, 1995, doi: [10.1016/0370-2693\(94\)01660-5](https://doi.org/10.1016/0370-2693(94)01660-5).
- [213] D. B. Kaplan, H. Georgi, and S. Dimopoulos, Composite Higgs scalars, *Phys. Lett.*, **136B**:187–190, 1984, doi: [10.1016/0370-2693\(84\)91178-X](https://doi.org/10.1016/0370-2693(84)91178-X).
- [214] B. Bellazzini, C. Csáki, and J. Serra, Composite Higgses, *Eur. Phys. J. C*, **74**(5):2766, 2014, doi: [10.1140/epjc/s10052-014-2766-x](https://doi.org/10.1140/epjc/s10052-014-2766-x).
- [215] L. Randall and R. Sundrum, A Large mass hierarchy from a small extra dimension, *Phys. Rev. Lett.*, **83**:3370–3373, 1999, doi: [10.1103/PhysRevLett.83.3370](https://doi.org/10.1103/PhysRevLett.83.3370).
- [216] A. Pomarol, Gauge bosons in a five-dimensional theory with localized gravity, *Phys. Lett.*, **B486**:153–157, 2000, doi: [10.1016/S0370-2693\(00\)00737-1](https://doi.org/10.1016/S0370-2693(00)00737-1).
- [217] U. Baur, I. Hinchliffe, and D. Zeppenfeld, Excited quark production at hadron colliders, *Int. J. Mod. Phys.*, **A2**:1285, 1987, doi: [10.1142/S0217751X87000661](https://doi.org/10.1142/S0217751X87000661).
- [218] U. Baur, M. Spira, and P. M. Zerwas, Excited quark and lepton production at hadron colliders, *Phys. Rev.*, **D42**:815–824, 1990, doi: [10.1103/PhysRevD.42.815](https://doi.org/10.1103/PhysRevD.42.815).
- [219] A. J. Larkoski, F. Maltoni, and M. Selvaggi, Tracking down hyper-boosted top quarks, *JHEP*, **06**:032, 2015, doi: [10.1007/JHEP06\(2015\)032](https://doi.org/10.1007/JHEP06(2015)032).
- [220] K. G. Wilson, The renormalization group and strong interactions, *Phys. Rev. D*, **3**:1818, 1971, doi: [10.1103/PhysRevD.3.1818](https://doi.org/10.1103/PhysRevD.3.1818).
- [221] G. F. Giudice, Naturalness after LHC8, *PoS*, **EPS-HEP2013**:163, 2013.
- [222] F. Zwicky, Die Rotverschiebung von extragalaktischen Nebeln, *Helv. Phys. Acta*, **6**:110, 1933, doi: [10.5169/seals-110267](https://doi.org/10.5169/seals-110267).
- [223] V. C. Rubin and J. Ford, W. Kent, Rotation of the Andromeda Nebula from a spectroscopic survey of emission regions, *Astrophys. J.*, **159**:379, 1970, doi: [10.1086/150317](https://doi.org/10.1086/150317).
- [224] Particle Data Group, Review of particle physics, *Chin. Phys. C*, **40**:100001, 2016, doi: [10.1088/1674-1137/40/10/100001](https://doi.org/10.1088/1674-1137/40/10/100001).
- [225] S. Chatrchyan *et al.*, Observation of a new boson with mass near 125 GeV in p p collisions at  $\sqrt{s} = 7$  and 8 TeV, *JHEP*, **06**:081, 2013, doi: [10.1007/JHEP06\(2013\)081](https://doi.org/10.1007/JHEP06(2013)081).
- [226] G. Aad *et al.*, Measurement of the Higgs boson mass from the  $H \rightarrow \gamma\gamma$  and  $H \rightarrow ZZ^* \rightarrow 4\ell$  channels with the ATLAS detector using  $25 \text{ fb}^{-1}$  of p p collision data, *Phys. Rev. D*, **90**:052004, 2014, doi: [10.1103/PhysRevD.90.052004](https://doi.org/10.1103/PhysRevD.90.052004).
- [227] V. Khachatryan *et al.*, Precise determination of the mass of the Higgs boson and tests of compatibility of its couplings with the standard model predictions using proton collisions at 7 and 8 TeV, *Eur. Phys. J. C*, **75**:212, 2015, doi: [10.1140/epjc/s10052-015-3351-7](https://doi.org/10.1140/epjc/s10052-015-3351-7).
- [228] ATLAS and CMS Collaborations, Combined measurement of the Higgs boson mass in pp collisions at  $\sqrt{s} = 7$  and 8 TeV with the ATLAS and CMS experiments, *Phys. Rev. Lett.*, **114**:191803, 2015, doi: [10.1103/PhysRevLett.114.191803](https://doi.org/10.1103/PhysRevLett.114.191803).



- [229] R. Barbieri and G. F. Giudice, Upper bounds on supersymmetric particle masses, *Nucl. Phys.*, **B306**:63–76, 1988, doi: [10.1016/0550-3213\(88\)90171-X](https://doi.org/10.1016/0550-3213(88)90171-X).
- [230] B. de Carlos and J. A. Casas, One loop analysis of the electroweak breaking in supersymmetric models and the fine tuning problem, *Phys. Lett.*, **B309**:320–328, 1993, doi: [10.1016/0370-2693\(93\)90940-J](https://doi.org/10.1016/0370-2693(93)90940-J).
- [231] S. Dimopoulos and G. F. Giudice, Naturalness constraints in supersymmetric theories with nonuniversal soft terms, *Phys. Lett.*, **B357**:573–578, 1995, doi: [10.1016/0370-2693\(95\)00961-J](https://doi.org/10.1016/0370-2693(95)00961-J).
- [232] R. Barbieri, G. R. Dvali, and L. J. Hall, Predictions from a U(2) flavor symmetry in supersymmetric theories, *Phys. Lett.*, **B377**:76–82, 1996, doi: [10.1016/0370-2693\(96\)00318-8](https://doi.org/10.1016/0370-2693(96)00318-8).
- [233] J. Wess and B. Zumino, Supergauge transformations in four-dimensions, *Nucl. Phys. B*, **70**:39, 1974, doi: [10.1016/0550-3213\(74\)90355-1](https://doi.org/10.1016/0550-3213(74)90355-1).
- [234] G. R. Farrar and P. Fayet, Phenomenology of the production, decay, and detection of new hadronic states associated with supersymmetry, *Phys. Lett. B*, **76**:575, 1978, doi: [10.1016/0370-2693\(78\)90858-4](https://doi.org/10.1016/0370-2693(78)90858-4).
- [235] J. L. Feng, Dark matter candidates from particle physics and methods of detection, *Ann. Rev. Astron. Astrophys.*, **48**:495, 2010, doi: [10.1146/annurev-astro-082708-101659](https://doi.org/10.1146/annurev-astro-082708-101659).
- [236] J. Alwall, P. Schuster, and N. Toro, Simplified models for a first characterization of new physics at the LHC, *Phys. Rev. D*, **79**:075020, 2009, doi: [10.1103/PhysRevD.79.075020](https://doi.org/10.1103/PhysRevD.79.075020).
- [237] J. Alwall, M.-P. Le, M. Lisanti, and J. G. Wacker, Model-independent jets plus missing energy searches, *Phys. Rev. D*, **79**:015005, 2009, doi: [10.1103/PhysRevD.79.015005](https://doi.org/10.1103/PhysRevD.79.015005).
- [238] LHC New Physics Working Group, D. Alves, *et al.*, Simplified models for LHC new physics searches, *J. Phys. G*, **39**:105005, 2012, doi: [10.1088/0954-3899/39/10/105005](https://doi.org/10.1088/0954-3899/39/10/105005).
- [239] C. Borschensky, M. Kraemer, A. Kulesza, *et al.*, Squark and gluino production cross sections in pp collisions at  $\sqrt{s} = 13, 14, 33$  and 100 TeV, *Eur. Phys. J. C*, **74**(12):3174, 2014, doi: [10.1140/epjc/s10052-014-3174-y](https://doi.org/10.1140/epjc/s10052-014-3174-y).
- [240] M. Dasgupta, A. Fregoso, S. Marzani, and G. P. Salam, Towards an understanding of jet substructure, *JHEP*, **09**:029, 2013, doi: [10.1007/JHEP09\(2013\)029](https://doi.org/10.1007/JHEP09(2013)029).
- [241] J. Thaler and K. Van Tilburg, Maximizing boosted top identification by minimizing N-subjettiness, *JHEP*, **02**:093, 2012, doi: [10.1007/JHEP02\(2012\)093](https://doi.org/10.1007/JHEP02(2012)093).
- [242] A. M. Sirunyan *et al.*, Search for direct production of supersymmetric partners of the top quark in the all-jets final state in proton-proton collisions at  $\sqrt{s} = 13$  TeV, *JHEP*, **10**:005, 2017, doi: [10.1007/JHEP10\(2017\)005](https://doi.org/10.1007/JHEP10(2017)005).
- [243] T. Junk, Confidence level computation for combining searches with small statistics, *Nucl. Instrum. Meth. A*, **434**:435, 1999, doi: [10.1016/S0168-9002\(99\)00498-2](https://doi.org/10.1016/S0168-9002(99)00498-2).
- [244] A. L. Read, Presentation of search results: The  $CL_s$  technique, *J. Phys. G*, **28**:2693, 2002, doi: [10.1088/0954-3899/28/10/313](https://doi.org/10.1088/0954-3899/28/10/313).
- [245] G. Cowan, K. Cranmer, E. Gross, and O. Vitells, Asymptotic formulae for likelihood-based tests of new physics, *Eur. Phys. J. C*, **71**:1554, 2011, doi: [10.1140/epjc/s10052-011-1554-0](https://doi.org/10.1140/epjc/s10052-011-1554-0), [Erratum: *Eur. Phys. J. C* **73** (2013) 2501, doi: [10.1140/epjc/s10052-013-2501-z](https://doi.org/10.1140/epjc/s10052-013-2501-z)].
- [246] ATLAS, CMS, LHC Higgs Combination Group, Procedure for the LHC Higgs boson search combination in summer 2011, ATL-PHYS-PUB-2011-011, CMS-NOTE-2011-005, CERN, Geneva, 2011, <http://cds.cern.ch/record/1379837>.
- [247] A. M. Sirunyan *et al.*, Search for new physics in final states with an energetic jet or a hadronically decaying  $W$  or  $Z$  boson and transverse momentum imbalance at  $\sqrt{s} = 13$  TeV, *Phys. Rev.*, **D97**(9):092005, 2018, doi: [10.1103/PhysRevD.97.092005](https://doi.org/10.1103/PhysRevD.97.092005).

- [248] M. Aaboud *et al.*, Search for dark matter and other new phenomena in events with an energetic jet and large missing transverse momentum using the ATLAS detector, *JHEP*, **01**:126, 2018, doi: [10.1007/JHEP01\(2018\)126](https://doi.org/10.1007/JHEP01(2018)126).
- [249] J. M. Lindert *et al.*, Precise predictions for  $V+$  jets dark matter backgrounds, *Eur. Phys. J. C*, **77**(12):829, 2017, doi: [10.1140/epjc/s10052-017-5389-1](https://doi.org/10.1140/epjc/s10052-017-5389-1).
- [250] R. Frederix and S. Frixione, Merging meets matching in MC@NLO, *JHEP*, **12**:061, 2012, doi: [10.1007/JHEP12\(2012\)061](https://doi.org/10.1007/JHEP12(2012)061).
- [251] A. Djouadi, A. Falkowski, Y. Mambrini, and J. Quevillon, Direct detection of Higgs-portal dark matter at the LHC, *Eur. Phys. J. C*, **73**(6):2455, 2013, doi: [10.1140/epjc/s10052-013-2455-1](https://doi.org/10.1140/epjc/s10052-013-2455-1).
- [252] D. S. Akerib *et al.*, Results from a search for dark matter in the complete LUX exposure, *Phys. Rev. Lett.*, **118**(2):021303, 2017, doi: [10.1103/PhysRevLett.118.021303](https://doi.org/10.1103/PhysRevLett.118.021303).
- [253] A. Tan *et al.*, Dark matter results from first 98.7 days of data from the PandaX-II experiment, *Phys. Rev. Lett.*, **117**(12):121303, 2016, doi: [10.1103/PhysRevLett.117.121303](https://doi.org/10.1103/PhysRevLett.117.121303).
- [254] R. Agnese *et al.*, New results from the search for low-mass weakly interacting massive particles with the CDMS Low Ionization Threshold experiment, *Phys. Rev. Lett.*, **116**(7):071301, 2016, doi: [10.1103/PhysRevLett.116.071301](https://doi.org/10.1103/PhysRevLett.116.071301).
- [255] J. Billard, L. Strigari, and E. Figueroa-Feliciano, Implication of neutrino backgrounds on the reach of next generation dark matter direct detection experiments, *Phys. Rev.*, **D89**(2):023524, 2014, doi: [10.1103/PhysRevD.89.023524](https://doi.org/10.1103/PhysRevD.89.023524).
- [256] M. Ibe, S. Matsumoto, and R. Sato, Mass splitting between charged and neutral winos at two-loop level, *Phys. Lett. B*, **721**:252–260, 2013, doi: [10.1016/j.physletb.2013.03.015](https://doi.org/10.1016/j.physletb.2013.03.015).
- [257] S. D. Thomas and J. D. Wells, Phenomenology of Massive Vectorlike Doublet Leptons, *Phys. Rev. Lett.*, **81**:34–37, 1998, doi: [10.1103/PhysRevLett.81.34](https://doi.org/10.1103/PhysRevLett.81.34).
- [258] A. J. Barr, C. G. Lester, M. A. Parker, *et al.*, Discovering anomaly-mediated supersymmetry at the LHC, *JHEP*, **03**(03):045, 2003, doi: [10.1088/1126-6708/2003/03/045](https://doi.org/10.1088/1126-6708/2003/03/045).
- [259] C.-H. Chen, M. Drees, and J. F. Gunion, A nonstandard string / SUSY scenario and its phenomenological implications, *Phys. Rev. D*, **55**:330–347, 1997, doi: [10.1103/PhysRevD.60.039901](https://doi.org/10.1103/PhysRevD.60.039901), [Erratum: *Phys.Rev.D* 60, 039901 (1999)].
- [260] C.-H. Chen, M. Drees, and J. F. Gunion, Addendum/erratum for ‘searching for invisible and almost invisible particles at  $e^+e^-$  colliders’ [hep-ph/9512230] and ‘a nonstandard string/SUSY scenario and its phenomenological implications’ [hep-ph/9607421], *arXiv:hep-ph/9902309*, 1999, <https://arxiv.org/abs/hep-ph/9902309>.
- [261] S. Asai, T. Moroi, and T. T. Yanagida, Test of anomaly mediation at the LHC, *Phys. Lett. B*, **664**(3):185–189, 2008, doi: [10.1016/j.physletb.2008.05.019](https://doi.org/10.1016/j.physletb.2008.05.019).
- [262] B. C. Allanach, SOFTSUSY: a program for calculating supersymmetric spectra, *Comput. Phys. Commun.*, **143**:305–331, 2002, doi: [10.1016/S0010-4655\(01\)00460-X](https://doi.org/10.1016/S0010-4655(01)00460-X).
- [263] A. Djouadi, M. M. Muhlleitner, and M. Spira, Decays of supersymmetric particles: The Program SUSY-HIT (SUSpect-SdecaY-Hdecay-INterface), *Acta Phys. Polon.*, **B38**:635–644, 2007.
- [264] W. Beenakker, R. Höpker, M. Spira, and P. Zerwas, Squark and gluino production at hadron colliders, *Nucl. Phys. B*, **492**:51–103, 1997, doi: [10.1016/S0550-3213\(97\)00084-9](https://doi.org/10.1016/S0550-3213(97)00084-9).
- [265] M. Aaboud *et al.*, Search for long-lived charginos based on a disappearing-track signature in  $pp$  collisions at  $\sqrt{s} = 13$  TeV with the ATLAS detector, *JHEP*, **22**, 2018, doi: [10.1007/JHEP06\(2018\)022](https://doi.org/10.1007/JHEP06(2018)022).
- [266] M. Aaboud *et al.*, Study of the material of the ATLAS inner detector for Run 2 of the LHC, *JINST*, **12**(12):P12009, 2017, doi: [10.1088/1748-0221/12/12/P12009](https://doi.org/10.1088/1748-0221/12/12/P12009).



- [267] G. Pellegrini, P. Fernández-Martínez, M. Baselga, *et al.*, Technology developments and first measurements of Low Gain Avalanche Detectors (LGAD) for high energy physics applications, *Nucl. Instrum. Meth. A*, **765**:12–16, 2014, doi: [10.1016/j.nima.2014.06.008](https://doi.org/10.1016/j.nima.2014.06.008).
- [268] J. Lange, M. Carulla, E. Cavallaro, *et al.*, Gain and time resolution of 45  $\mu\text{m}$  thin Low Gain Avalanche Detectors before and after irradiation up to a fluence of  $10^{15} \text{ n}_{\text{eq}}/\text{cm}^2$ , *JINST*, **12**:P05003, 2017, doi: [10.1088/1748-0221/12/05/P05003](https://doi.org/10.1088/1748-0221/12/05/P05003).
- [269] S. L. Glashow, J. Iliopoulos, and L. Maiani, Weak interactions with lepton-hadron symmetry, *Phys. Rev. D*, **2**:1285–1292, 1970, doi: [10.1103/PhysRevD.2.1285](https://doi.org/10.1103/PhysRevD.2.1285).
- [270] J. A. Aguilar-Saavedra, A minimal set of top anomalous couplings, *Nucl. Phys. B*, **812**:181, 2009, doi: [10.1016/j.nuclphysb.2008.12.012](https://doi.org/10.1016/j.nuclphysb.2008.12.012).
- [271] S. Willenbrock and C. Zhang, Effective field theory beyond the Standard Model, *Ann. Rev. Nucl. Part. Sci.*, **64**:83, 2014, doi: [10.1146/annurev-nucl-102313-025623](https://doi.org/10.1146/annurev-nucl-102313-025623).
- [272] T. Aaltonen *et al.*, Search for top-quark production via flavor-changing neutral currents in W+1 jet events at CDF, *Phys. Rev. Lett.*, **102**:151801, 2009, doi: [10.1103/PhysRevLett.102.151801](https://doi.org/10.1103/PhysRevLett.102.151801).
- [273] V. M. Abazov *et al.*, Search for flavor changing neutral currents via quark-gluon couplings in single top quark production using  $2.3 \text{ fb}^{-1}$  of  $p\bar{p}$  collisions, *Phys. Lett. B*, **693**:81, 2010, doi: [10.1016/j.physletb.2010.08.011](https://doi.org/10.1016/j.physletb.2010.08.011).
- [274] G. Aad *et al.*, Search for single top-quark production via flavour-changing neutral currents at 8 TeV with the ATLAS detector, *Eur. Phys. J. C*, **76**:55, 2016, doi: [10.1140/epjc/s10052-016-3876-4](https://doi.org/10.1140/epjc/s10052-016-3876-4).
- [275] V. Khachatryan *et al.*, Search for anomalous Wtb couplings and flavour-changing neutral currents in t-channel single top quark production in pp collisions at  $\sqrt{s} = 7$  and 8 TeV, *JHEP*, **02**:028, 2017, doi: [10.1007/JHEP02\(2017\)028](https://doi.org/10.1007/JHEP02(2017)028).
- [276] V. Khachatryan *et al.*, Search for anomalous single top quark production in association with a photon in pp collisions at  $\sqrt{s} = 8 \text{ tev}$ , *Journal of High Energy Physics*, **2016**(4):35, 2016, doi: [10.1007/JHEP04\(2016\)035](https://doi.org/10.1007/JHEP04(2016)035).
- [277] K. Agashe *et al.*, Working Group Report: Top Quark, in *Proceedings, 2013 Community Summer Study on the Future of U.S. Particle Physics: Snowmass on the Mississippi (CSS2013): Minneapolis, MN, USA, July 29-August 6, 2013*, 2013, <https://arxiv.org/abs/1311.2028>.
- [278] K. Melnikov, M. Schulze, and A. Scharf, Qcd corrections to top quark pair production in association with a photon at hadron colliders, *Phys. Rev. D*, **83**:074013, 2011, doi: [10.1103/PhysRevD.83.074013](https://doi.org/10.1103/PhysRevD.83.074013).
- [279] R. Boughezal, X. Liu, and F. Petriello, Phenomenology of the  $z$  boson plus jet process at nnlo, *Phys. Rev. D*, **94**:074015, 2016, doi: [10.1103/PhysRevD.94.074015](https://doi.org/10.1103/PhysRevD.94.074015).
- [280] A. Hoecker *et al.*, TMVA - Toolkit for multivariate data analysis, *arXiv:physics/0703039*, 2007, doi: [10.48550/arXiv.physics/0703039](https://doi.org/10.48550/arXiv.physics/0703039).
- [281] H. Voss *et al.*, TMVA, the Toolkit for Multivariate Data Analysis with ROOT, *PoS, ACAT*:040, 2007, doi: [10.22323/1.050.0040](https://doi.org/10.22323/1.050.0040).
- [282] J. A. Aguilar-Saavedra, Top flavor-changing neutral interactions: Theoretical expectations and experimental detection, *Acta Phys. Polon.*, **B35**:2695–2710, 2004, doi: [10.48550/arXiv.hep-ph/0409342](https://doi.org/10.48550/arXiv.hep-ph/0409342).
- [283] M. Beneke *et al.*, Top quark physics, in *1999 CERN Workshop on standard model physics (and more) at the LHC, CERN, Geneva, Switzerland, 25–26 May: Proceedings*, pp. 419–529, 2000, doi: [10.5170/CERN-2000-004.419](https://doi.org/10.5170/CERN-2000-004.419).

- [284] V. Khachatryan *et al.*, Measurement of the  $t$ -channel single-top-quark production cross section and of the  $|V_{tb}|$  CKM matrix element in pp collisions at  $\sqrt{s} = 8$  TeV, *JHEP*, **06**:090, 2014, doi: [10.1007/JHEP06\(2014\)090](https://doi.org/10.1007/JHEP06(2014)090).
- [285] V. Khachatryan *et al.*, Measurement of top quark polarisation in  $t$ -channel single top quark production, *JHEP*, **04**:073, 2016, doi: [10.1007/JHEP04\(2016\)073](https://doi.org/10.1007/JHEP04(2016)073).
- [286] G. Aad *et al.*, Comprehensive measurements of  $t$ -channel single top-quark production cross sections at  $\sqrt{s} = 7$  TeV with the ATLAS detector, *Phys. Rev. D*, **90**:112006, 2014, doi: [10.1103/PhysRevD.90.112006](https://doi.org/10.1103/PhysRevD.90.112006).
- [287] E. E. Boos, V. E. Bunichev, L. V. Dudko, *et al.*, Method for simulating electroweak top-quark production events in the NLO approximation: SingleTop event generator, *Phys. Atom. Nucl.*, **69**:1317, 2006, doi: [10.1134/S1063778806080084](https://doi.org/10.1134/S1063778806080084).
- [288] E. Boos *et al.*, CompHEP 4.4: automatic computations from Lagrangians to events, *Nucl. Instrum. Meth. A*, **534**:250, 2004, doi: [10.1016/j.nima.2004.07.096](https://doi.org/10.1016/j.nima.2004.07.096).
- [289] J. J. Zhang, C. S. Li, J. Gao, *et al.*, Next-to-leading order QCD corrections to the top quark decay via model-independent FCNC couplings, *Phys. Rev. Lett.*, **102**:072001, 2009, doi: [10.1103/PhysRevLett.102.072001](https://doi.org/10.1103/PhysRevLett.102.072001).
- [290] M. N. Radford, *Bayesian learning for neural networks*, Springer, 1996, doi: [10.1007/978-1-4612-0745-0](https://doi.org/10.1007/978-1-4612-0745-0).
- [291] M. N. Radford, Software for flexible Bayesian modeling and Markov chain sampling, 2004-11-10, Dept. of Statistics and Dept. of Computer Science, University of Toronto, 2004, <http://www.cs.toronto.edu/~radford/fbm.software.html>.
- [292] E. Boos *et al.*, Method of optimum observables and implementation of neural networks in physics investigations, *Phys. Atom. Nucl.*, **71**:383–393, 2008, doi: [10.1134/S1063778808020191](https://doi.org/10.1134/S1063778808020191).
- [293] G. Mahlon and S. J. Parke, Improved spin basis for angular correlation studies in single top quark production at the Tevatron, *Phys. Rev. D*, **55**:7249, 1997, doi: [10.1103/PhysRevD.55.7249](https://doi.org/10.1103/PhysRevD.55.7249).
- [294] J. A. Aguilar-Saavedra and R. V. Herrero-Hahn, Model-independent measurement of the top quark polarisation, *Phys. Lett. B*, **718**:983, 2012, doi: [10.1016/j.physletb.2012.11.031](https://doi.org/10.1016/j.physletb.2012.11.031).
- [295] R. J. Barlow and C. Beeston, Fitting using finite Monte Carlo samples, *Comput. Phys. Commun.*, **77**:219, 1993, doi: [10.1016/0010-4655\(93\)90005-W](https://doi.org/10.1016/0010-4655(93)90005-W).